Environmental Science and Engineering

Long Ni
Peng Wang
Jiqin Li
Yongxin Liu *Editors*

Proceedings of the 12th International Conference on Cold Climate HVAC & Energy (Volume 2)

CCHVAC 2025

Springer

Environmental Science and Engineering

Series Editors

Ulrich Förstner, *Buchholz, Germany*
Wim H. Rulkens, *Department of Environmental Technology, Wageningen University and Research Centre, Wageningen, Gelderland, The Netherlands*

The ultimate goal of this series is to contribute to the protection of our environment, which calls for both profound research and the ongoing development of solutions and measurements by experts in the field. Accordingly, the series promotes not only a deeper understanding of environmental processes and the evaluation of management strategies, but also design and technology aimed at improving environmental quality. Books focusing on the former are published in the subseries Environmental Science, those focusing on the latter in the subseries Environmental Engineering.

Long Ni · Peng Wang · Jiqin Li · Yongxin Liu
Editors

Proceedings of the 12th International Conference on Cold Climate HVAC & Energy (Volume 2)

CCHVAC 2025

Springer

Editors
Long Ni
Research Center of Building Science
and Engineering for Cold Region
Harbin Institute of Technology
Harbin, Heilongjiang, China

Peng Wang
Research Center of Building Science
and Engineering for Cold Region
Harbin Institute of Technology
Harbin, Heilongjiang, China

Jiqin Li
Research Center of Building Science
and Engineering for Cold Region
Harbin Institute of Technology
Harbin, Heilongjiang, China

Yongxin Liu
Research Center of Building Science
and Engineering for Cold Region
Harbin Institute of Technology
Harbin, Heilongjiang, China

ISSN 1863-5520 ISSN 1863-5539 (electronic)
Environmental Science and Engineering
ISBN 978-981-95-3252-0 ISBN 978-981-95-3253-7 (eBook)
https://doi.org/10.1007/978-981-95-3253-7

© The Editor(s) (if applicable) and The Author(s), under exclusive license
to Springer Nature Singapore Pte Ltd. 2025

This work is subject to copyright. All rights are solely and exclusively licensed by the Publisher, whether the whole or part of the material is concerned, specifically the rights of translation, reprinting, reuse of illustrations, recitation, broadcasting, reproduction on microfilms or in any other physical way, and transmission or information storage and retrieval, electronic adaptation, computer software, or by similar or dissimilar methodology now known or hereafter developed.
The use of general descriptive names, registered names, trademarks, service marks, etc. in this publication does not imply, even in the absence of a specific statement, that such names are exempt from the relevant protective laws and regulations and therefore free for general use.
The publisher, the authors and the editors are safe to assume that the advice and information in this book are believed to be true and accurate at the date of publication. Neither the publisher nor the authors or the editors give a warranty, expressed or implied, with respect to the material contained herein or for any errors or omissions that may have been made. The publisher remains neutral with regard to jurisdictional claims in published maps and institutional affiliations.

This Springer imprint is published by the registered company Springer Nature Singapore Pte Ltd.
The registered company address is: 152 Beach Road, #21-01/04 Gateway East, Singapore 189721, Singapore

If disposing of this product, please recycle the paper.

Preface

The series of Cold Climate HVAC Conferences was initiated by the Scandinavian Federation of HVAC and Sanitary Engineering Societies (SCANVAC). It has since evolved into a premier international forum, with the previous eleven conferences successfully held in Rovaniemi, Finland, in 1994; Reykjavik, Iceland, in 1997; Sapporo, Japan, in 2000; Trondheim, Norway, in 2003; Moscow, Russia, in 2006; Sisimiut, Greenland, in 2009; Calgary, Canada, in 2012; Dalian, China, in 2015; Kiruna, Sweden, in 2018; Tallinn, Estonia, in 2021; and Anchorage, USA, in 2023.

The 12th Cold Climate HVAC & Energy Conference 2025 is proudly hosted by Harbin Institute of Technology (HIT). Harbin is one of the coldest cities in China, making it a fitting venue for these international gatherings. The conference attracted approximately 230 participants from 15 countries. Topics covered included renewable and waste energy utilization, sustainable district heating and cooling, heat pumps, smart energy systems, and zero-energy buildings. Eight outstanding scientists and experts, including Prof. Yi Jiang, Prof. Risto Kosonen, Prof. Peter V. Nielsen, Prof. Matti Lehtonen, Prof. Müslüm Arıcı, Prof. Katsunori Nagano, Prof. Man-Hoe Kim, and Mr. Allan Bertelsen, delivered keynote speeches. The conference featured 18 workshops with 140 presentations, including both selected papers and invited talks. The conference proceedings include 95 papers selected from 134 submitted full papers.

We would like to express our sincere gratitude to all members of the organizing and scientific committees for their dedicated efforts. We also extend our appreciation to all authors and participants for their valuable contributions and active engagement in the conference. We are deeply grateful to our sponsors for their generous support. Special thanks go to the other three editors of the proceedings: Dr. Peng Wang, Dr. Jiqin Li, and Dr. Yongxin Liu, for their meticulous work and unwavering commitment.

We hope this collection of papers will inspire continued research and innovation in HVAC technologies for cold climates and foster lasting collaborations among researchers, practitioners, and policymakers around the globe.



Long Ni
President of Cold Climate HVAC &
Energy Conference 2025, Professor,
School of Architecture and Design

Organization

Organization Committee

President

Long Ni (Professor)	Harbin Institute of Technology

Secretary

Peng Wang (Assoc. Professor)	Harbin Institute of Technology
Jiqin Li (Assoc. Professor)	Harbin Institute of Technology

Members

Yang Yao (Professor)	Harbin Institute of Technology
Jing Liu (Professor)	Harbin Institute of Technology
Zhigang Zhou (Professor)	Harbin Institute of Technology
Chenghu Zhang (Professor)	Harbin Institute of Technology
Jiankai Dong (Professor)	Harbin Institute of Technology
Chao Shen (Professor)	Harbin Institute of Technology
Haibo Guo (Professor)	Harbin Institute of Technology
Huizhe Cao (Assoc. Professor)	Harbin Institute of Technology
Fang Wang (Assoc. Professor)	Harbin Institute of Technology
Tiantian Zhang (Assoc. Professor)	Harbin Institute of Technology
Wenke Zheng (Assoc. Professor)	Harbin Institute of Technology
Yongxin Liu (Assoc. Professor)	Harbin Institute of Technology
Qi Dong (Assoc. Professor)	Harbin Institute of Technology
Yanshu Miao (Lecturer)	Harbin Institute of Technology
Subo Fan (Lecturer)	Harbin Institute of Technology

Contents

Heat Pump

Experimental Investigation on the Effect of Volume Flow Rates and EEV Openings on the Regeneration Process of a Solution Regenerator Unit Using Freezing Concentration 3
Chong Han, YiNuo Yao, and Long Ni

Frosting and Heating Performance of Electric Vehicle Heat Pump Air Conditioning System in Cold Area 13
Ying Sun, Ying Wang, Haoran Ning, Shicheng Yao, and Haochen Yu

Experimental and Numerical Investigation on Effects of PCM Phase Change on Thermo-Mechanical Behaviours of Energy Pipe Pile with PCM Backfill 26
Weibo Yang, Jiayan Zhao, Tianzheng Qiao, and Feng Wang

Application of Superhydrophobic Coatings in Air-Source Heat Pump Evaporators Under Frosting and Defrosting Conditions 38
Yifan Yang, Zhen Shen, Yixuan Jin, Leshan Shen, Hao Peng, Huadong Huang, Chenxi Li, Zhifu Qi, Zhouyang Luo, Shien Sun, and Weiming Teng

Dynamic Characteristics in the Startup Stage of a Transcritical CO_2 Heat Pump 48
Hongzhi Liu, Minglu Qu, and Jing Lv

Applicability Analysis of Freezing Concentration Method Applied in Frost-Free Air Source Heat Pumps' Solution Regeneration for Cold Regions 58
Liutao Zhu, Xiaosong Zhang, and Shifang Huang

Frost Suppression Mechanism of Superhydrophobic Coating in Air Source Heat Pump 66
Rui Tang, Wenzhe Wei, Yunfeng Wang, Wei Wang, and Yuying Sun

Study on Operation Characteristics of Solar-Assisted Enhanced Jet Enthalpy Air Source Heat Pump 75
Shirui Su and Guodong Qiu

Experimental Investigation on the Indoor Thermal Environment During the Dynamic Frosting-Defrosting Process of Air Source Heat Pump 86
Wenzhe Wei, Jianfei Zhang, Xinyue Jin, Wei Wang, and Yuying Sun

Performance Evaluation of a CO_2 Air Source Heat Pump Integrated with Binary Hydrate Salt Composite for Frost Mitigation under Cold and Humid Conditions 97
Minglu Qu, Zhenfang Ma, Jing Lv, Hongzhi Liu, and Jiajie Chen

Performance Enhancement of CO_2 Air Source Heat Pumps via Photovoltaic-Thermal (PV/T) Air Preheating: A Simulation and Experimental Study 105
Minglu Qu, Haoqiang Zhao, Guoqing Yu, Zhenfang Ma, and Changling Lu

Field Performance Study of Distributed Small-Capacity Air Source Heat Pumps for Centralized Heating in Residential Buildings 114
Wenju Hu, Jian Cao, Lingyan Yang, and Dan Wang

Freezing and Accompanying Frosting Characteristics of Alcohol Binary Droplet on Cold Surface 123
Feng Wang, Mengting Xiang, Weibo Yang, and Caihua Liang

Analysis for Parameters Affecting Cycle Performance of CO_2 Two-Stage Compression Cycles 132
Aruna, Xu Jin, Zheng Qiu, Zhongyan Liu, Jiapeng Zhang, Hao Zhang, Xin Meng, Xianglai Xu, and Wei Su

A Universal Prediction Model for Initial Frosting Rate of Air Source Heat Pumps Based on the Enthalpy Diagram 143
Wenzhe Wei, Yutao Guo, Zhike Jiang, Xinyu Zhang, Wei Wang, Yuying Sun, Shiquan Wang, and Chunxiao Zhang

Performance of Annual CO_2 Space Heating and Cooling System integrated with Soil Cold Storage 154
Baomin Dai, Ronghua Miao, Tongyu Duan, and Shengchun Liu

Optimization of Low-Grade Waste Heat Recovery in District Heating Systems Using Zeotropic Mixture Heat Pump 163
Yumiao Wang, Sijing Zhang, Fang Zhou, Xiaosong Zhang, and Jian Liu

Performance Evaluation of a Hybrid Solar-Heat Pump Dual-Source Heating System for Interactive Cascade Ventilation 174
Gaoqi Lai, Tong Sang, Han Li, Xiangfei Kong, and Man Fan

Construction of CO_2 Heat Pump Cycles for Space Heating in Cold Regions Using the Intelligent GraPHsep Method 182
Mengdi Cui and Baolong Wang

Preliminary Simulation Study of a Novel Open-Loop Air Cycle CO_2 Heat Pump Dryer 191
Jay Wang and Ding Mao

Study on Field Performance Testing Methods for Air-Source Heat Pump Refrigerant-Direct Radiant Systems 200
Fan Xu, Gang Wang, Yu Du, and Encan Jia

Turbulence Control Simulation Inside the Defoulant Hydrocyclone for Sewage Source Heat Pump 209
Tao Song, Jing Li, Xin Yang, Qisheng Yang, Changhua Hu, and Bo Wang

Absorption Chiller Design for Liquid Cooling in Data Centers 217
Zixuan Peng, Haojun Duan, and Xiaoyun Xie

Smart Energy System

Decoupling Simulation of Thermal Processes with Two-Time Scale for Heated Buildings in Cold Regions 231
Wei Jiang and Peng Wang

Research on the Collaborative Benefits of Energy Conservation and Emission Reduction in the Blast Furnace Process Technology Based on the CSC Method 239
Yan Long, Qiuyan Lu, and Tianyi Hua

Automatic Hourly Calibration of a Multi-Purpose Building Simulation Model in an Adaptive Framework Using IDA-Python API 250
Hamed Amini, Hang Yin, Kari Alanne, Mohamed Hamdy, and Risto Kosonen

Mitigating Data Imbalance in Neural Network-Based Building Energy Prediction Using Multi-Task Learning 260
Chaobo Zhang, Feng Wang, and Jian Zhang

A City-Level Carbon Emissions Prediction Method Based on Open-Source Data and LLMs: A Case Study of 65 Winter Cities Worldwide 268
Biaoqing Tao, Cheng Sun, Xiran Cui, Jingrong Ma, and Yunsong Han

A Two-Stage Optimal Design Framework for Improving the Energy Flexibility of District Energy System 277
Chenxin Feng, Jiayu Xu, Yang Zhao, and Xiao Peng

Centralized Demand Response Control for a Finnish Apartment Building Considering Indoor Air Conditions 287
Yuchen Ju, Perttu Karjalainen, Juha Jokisalo, and Risto Kosonen

Performance Investigation and Design Principles of PEMFC Integrated Energy Supply Systems Based on Flexible Load Regulation 296
Ruyi Zhang, Xu Li, Jintao Wu, and Shanshan Cai

Study on Thermal Environment and Energy-Saving Control of Radiant Terminals in Winter Based on Operative Temperature 307
Haiying Wang, Hang Meng, Junli Sun, and Renjie Yan

Automatic Wiring Method of Fire Alarm System in Metro Station Based on BIM and Ant Colony Algorithm 315
Ruiying Jin, Peng Xu, Junjie Li, Hongxin Wang, and Jiefan Gu

EfficientWiPose: A Lightweight and High-Accuracy WiFi-Based Human Pose Estimation System for Energy-Efficient Smart Buildings 326
Weili Wang, Weixiong Zhang, Linjun Zhao, Benying Tan, Huijun Wu, and Huakun Huang

A Mean Room Temperature Prediction LSTM Model for Heating Buildings ... 334
Yongjie Wang, Yangming Liu, Guanjing Lin, and Changhong Zhan

Zero Energy Buildings

Feasibility Study on Low-temperature Transformation of Air Conditioning Heating in Existing Buildings: A Case Study of Industrial Parks 345
Siqi Wu and Peng Wang

A Study on the Optical and Thermal Performance and Energy Efficiency Analysis of a Novel Adjustable Wall-Like Window 354
Huiyan Tang and Zhengrong Li

Design and Application of a Novel Intelligent Building Envelope with Adjustable Window-to-Wall Ratio 364
Shijun Ni and Cui Li

Effects of Surface Painting on Indoor Hygrothermal Performance and Energy Consumption in Pile-Dwellings 374
Yin Ying-de, Li Yuan-yu, Shi Heng-lin, Li Hou-ying, Qin Xin-ping, Tan Shu-hao, and Lu Da-ji

Impact of Hygrothermal Transfer in Pile-Dwellings' Walls on Indoor Hot-Humid Environments and Energy Consumption 385
Yin Ying-de, Shi Heng-lin, Li Yuan-yu, Li Hou-ying, Lin Fei, Chen Guan-yu, and Pan Li-rong

Optimization of Architectural Design to Improve Thermal Performance in Standard Housing in Daqing, China 396
Samanta López Salazar, Dong Li, Ruitong Yang, E. Simá, and Zhe Yuan

Carbon Emission Index System and Effectiveness Evaluation of Carbon Reduction Measures in Substation Operational Phase 406
Yanfeng Wang, Can Fang, Huijun Wu, Jia Liu, Yanchen Liu, and Zhuwei Xie

Study on a Simplified Heat Transfer Model for the Roof Ventilated Desiccant Bed 414
Sheng Liu and Xinhua Xu

Performance Simulation Study of Air Compression System Applied to Residential Air Conditioning 424
Rong Weilai, Ma Guoyuan, Sun Shangyu, Xu Shuxue, and Nie Junrui

Research on the Influence of Curtain Settings on the Indoor Thermal Environment of Heated Dormitories 432
Kaiyue Liu, Chenyu Ma, Donghai Zhang, Shuang Ma, and Zhe Liu

Are Heating Electrification and Mechanical Ventilation Viable Approaches for Cold Climate Rural Buildings? 441
Xinyi Hu, Juha Jokisalo, Risto Kosonen, and Matti Lehtonen

A Boundary Heat Transfer Model for CFD Simulation of Floor Radiant Heating Systems 449
Guiqiang Wang and Guixin Huang

Energy Performance Comparison of Diffuse Ceiling Ventilation and Mixing Ventilation Strategies in Heating Conditions 458
Rui Guo and Shady Attia

Research on Ice Restaurant Form Design Based on Indoor Thermal Environment Simulation 467
Xianglu Ding, Peng Luo, Yongxin Liu, and Tianshuo Ren

Percentage of Dissatisfied Model of Thermal Environment Based on Beta Distribution 476
Yongxin Liu and Peng Wang

Energy Efficient Thermal Comfort in Temporarily Occupied Space for Winter Heating Mode: A Case Study of Ceiling Fan Aided Diffuse Ceiling Ventilation System 486
Bin Yang, Xinrou Han, Bin Zhou, and Zhe Li

A Nodal Model for Predicting Vertical Air Temperature Difference in a Radiant Floor Cooling Room with Mechanical Ventilation 494
Xiaozhou Wu, Zhaoyi Liu, Diqi Yu, and Hao Gao

Comparison of Air Quality Between Mechanical Ventilation Systems and Portable Air Cleaners with Research on Synergistic Integration Mechanisms 506
Mingqi Liu, Yiqun Li, and Wei Ye

Author Index 517

Heat Pump

Experimental Investigation on the Effect of Volume Flow Rates and EEV Openings on the Regeneration Process of a Solution Regenerator Unit Using Freezing Concentration

Chong Han[1,2], YiNuo Yao[1], and Long Ni[3(✉)]

[1] Qibang Construction Engineering (Shandong) Co., Ltd, Yantai, China
[2] Shandong Provincial Key Laboratory of Civil Engineering Disaster Prevention and Mitigation, Shandong University of Science and Technology, QingDao, China
[3] Harbin Institute of Technology, Harbin 150090, China
nlonggn@163.com

Abstract. This experimental study investigates the impacts of volume flow rates (4–7 m^3/h) and electronic expansion valve (EEV) openings (50–100%) on the regeneration process of a 6% dilute sodium formate solution in a solution regenerator unit using freezing concentration. Key findings reveal that latent heat exchange dominates the heat transfer process, with a stable latent heat ratio of approximately 80%, while sensible heat exchange increases slightly (by 6%) only at 50% EEV opening due to reduced refrigerant flow. Volume flow rates affect ice growth in stages: high flow rates (6–7 m^3/h) accelerate initial ice formation, but low flow rates (4–5 m^3/h) promote faster late-stage growth, with a 0.001 mm/s higher thickness growth rate by the experiment's end. EEV openings significantly influence ice layer uniformity; lower openings (50%) increase ice layer slope (up to 6.57%), enhancing separation efficiency via gravity-driven melting, with the maximum separation ratio reaching 0.75. These results provide critical insights for optimizing system performance in dilute solution regeneration.

Keywords: Freezing concentration · Solution regeneration · Volume flow rate

1 Introduction

Air-source heat pump (ASHP)-based clean heating is critical for carbon peak/neutrality in buildings. However, its actual efficiency lags behind design expectations [1], with frost prevention being key to performance optimization. Existing strategies fall into defrosting [2] and frost suppression [3]: defrosting removes frost via high-temperature melting [4], ultrasonic vibration [5], etc., to reduce energy loss, while frost suppression prevents frost by disrupting its formation conditions [6, 7], which is preferred for avoiding defrost-related energy fluctuations and comfort issues. Heat source tower heat pumps (HSTHPs) enhance frost suppression by spraying high-concentration anti-frost solution on evaporators to form a protective film, enabling winter frost-free operation with proven

© The Author(s), under exclusive license to Springer Nature Singapore Pte Ltd. 2025
L. Ni et al. (Eds.): CCHVAC 2025, ESE, pp. 3–12, 2025.
https://doi.org/10.1007/978-981-95-3253-7_1

low-temperature efficiency [8]. The solution's mass concentration is pivotal, as it affects freezing point and hygroscopicity, thus system stability. Prolonged operation dilutes the solution via moisture absorption, raising its freezing point and reducing hygroscopicity. Below the minimum allowable concentration, the film loses anti-frost ability and may freeze, worsening heat exchange. Hence, developing low-carbon, cost-effective solution concentration methods is a research priority.

In practical heat pump applications, water removal methods offer simple structure and easy operation. Among them, thermally driven separation [9] is widely used in HSTHP systems for good regeneration efficiency. However, during winter operation, their evaporation requires extra heat [10], and the reverse cooling tower principle is constrained by outdoor conditions [11]. Without available heat sources, freeze concentration becomes a suitable choice. Previous studies on freeze concentration focused mostly on water treatment and food industry [12], showing freeze regeneration has promising prospects and high efficiency. Its process involves three stages: cooling to freezing point, ice crystal formation/growth on heat exchanger surfaces, and ice separation via physical/thermal melting. The freezing stage, key to concentration [13], dictates HSTHP regeneration feasibility/efficiency, necessitating research on its variations.

Enhancing the separation ratio mitigates meltwater's impact on regeneration concentration and reduces extra regeneration energy consumption. Since the solution regenerator unit using freezing concentration (SRFCHP) system uses reverse-cycle deicing, with operational patterns/logics similar to air-source heat pump defrosting, defrosting research informs its ice-melting process. Frost layer structure/distribution directly affects defrosting performance, shaped by formation conditions: environmental factors (air velocity, temperature, humidity) and heat pump parameters (exchanger surface temperature, edge structures). These characteristics influence melting efficiency. Notably, SRFCHP deicing targets incomplete melting: high-temperature refrigerant melts surface ice, enabling gravity-driven separation of intact ice layers to avoid solution dilution. Thus, rapid ice-plate separation is key for regeneration efficiency. Moreno et al. [14], Miyawaki et al. [15] explored how ice-melting methods and ice morphologies affect separation. Raventós et al. [16] identified optimal ice melting thickness on falling-film exchangers via sugar solution tests. For SRFCHP, improving separation ratio and rapid deicing are critical. This research will analyze ice layer non-uniformity under varying concentrations, flow rates, and EEV openings, and their impacts on separation. In the SRFCHP system,. the EEV opening (O_{EEV}) and volume flow rate has a great impact on the icing process. Hence, to research the effects of O_{EEV} and volume flow rate on the freezing process, the SRFCHP unit worked in the same 6% inlet solution concentration. Ice covering process and ice thickness growth are analyzed to compare the difference in freezing process under different operating parameters. The main propose of SRFCHP system is solution regeneration, therefore, influences of different freezing processes on the regeneration efficiency are compared.

2 Experimentations

2.1 Experimental Setup

To examine the deicing energy efficiency of the SRFCHP system, a test rig was built in an enthalpy difference laboratory following GB/T 17758–2010. As shown in Fig. 1, the system consists of a solution regeneration unit, a heat pump unit, and a waste heat utilization unit. Dilute sodium formate solution is concentrated in the regeneration unit via progressive freezing. The heat pump unit provides refrigeration, with refrigerant-absorbed phase change heat and compressor heat released into hot water through the waste heat utilization unit.

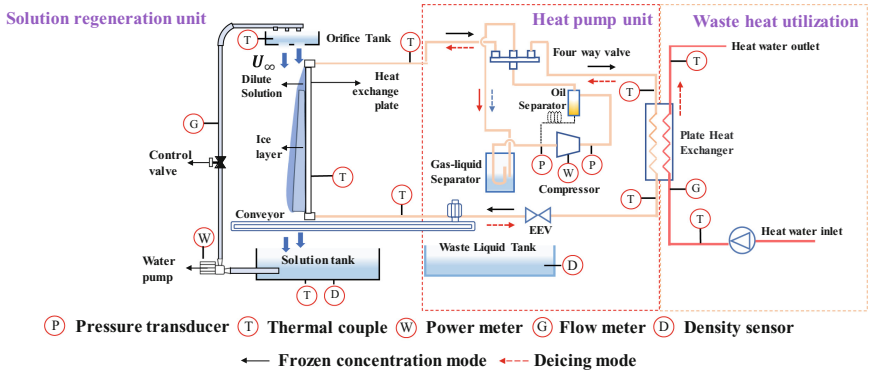


Fig. 1. Schematic diagram of the SRFCHP system.

The core function of the SRFCHP system is to remove excess water from diluted anti-frost solution via freeze concentration: water in the solution freezes into ice, reducing water content and gradually increasing solution concentration until reaching the target level. Its regeneration process (Fig. 2) involves three stages.

First, the system provides cooling to lower the solution to its freezing point; in tests, initial temperatures of dilute solutions with different concentrations were maintained at 0 °C. Next, progressive freezing forms an ice layer on the heat exchanger plate, fixing excess water as ice while retaining solute in the solution to elevate concentration—though minor solute entrainment in ice causes losses.

Upon reaching the shutdown condition, the heat pump switches to reverse cycle to melt the ice layer. As shown in Fig. 2, part of the melted ice returns to the solution tank, and the rest is separated into a wastewater tank. For energy efficiency, solute residue reduces the proportion of input power used for ice production; thus, actual effective water removal equals ice separation minus solute residual.

In this experiment, the inlet solution concentration was 6%. The corresponding freeze temperature was −3.52 °C. Volumetric flow rate of pre-concentration solution was 7 ~ 4 m^3/h. The change of deicing energy consumption of the unit was recorded through multiple tests. The photograph of measuring instruments is displayed in the Fig. 3.

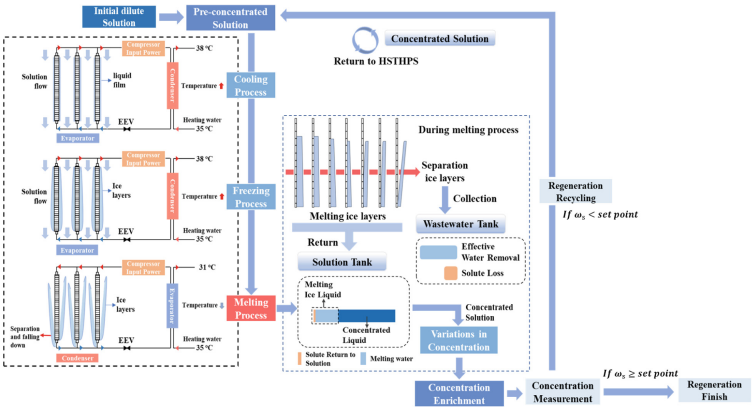


Fig. 2. The process of solution regeneration in the SRFCHP system.

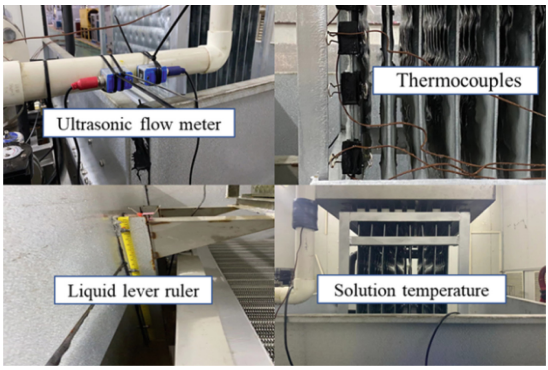


Fig. 3. Photo of measuring instruments.

2.2 Data Collection and Analysis

The separation ratio of the ice is defined as:

$$SR = \frac{M_{icec}}{M_{ice}} \times 100\% \tag{1}$$

where SR is the separation ratio of the ice, %; M_{icec} is the effective separation mass of ice and can be collected by waste liquid tank, kg; M_{ice} is the total mass of ice production, kg.

The total heat transfer coefficient is calculated as:

$$K_m{}^i = \frac{Q_s{}^i}{A_p\left(\overline{T_s}^i - T_E{}^i\right)} \tag{2}$$

where $K_m{}^i$ is the total heat transfer coefficient at moment i, W/m^2•°C; $Q_s{}^i$is the refrigeration capacity of the system at moment i, kWh; A_p is the total heat exchange area, m^2;

$\overline{T_s}^i$ is the average solution temperature at moment i, °C; $\overline{T_E}^i$ is the system evaporation temperature at moment i, °C

3 Results and Discussion

To analyze the impact of volume flow rate variations on the heat transfer performance of the SRFCHP system, Fig. 4 illustrates the changes in evaporation temperature, average heat transfer coefficient, and ice thickness across different volume flow rate groups, where the average heat transfer coefficient is calculated using Eq. 3. As observed from the figure, the variation trend of evaporation temperature under each volume flow rate group reflects the icing rate. Altering the solution volume flow rate exerts little influence on the evaporation temperature of the refrigeration regeneration system, with the variation patterns and temperature values remaining essentially consistent among all groups. When the throttle valve opening is set within the range of 100% to 65%, the evaporation temperatures under different volume flow rates begin to converge after 10 min of operation. At a throttle valve opening of 50%, the evaporation temperature stabilizes between −24 °C and − 26 °C, indicating stable operation of the refrigeration regeneration system under all working conditions.

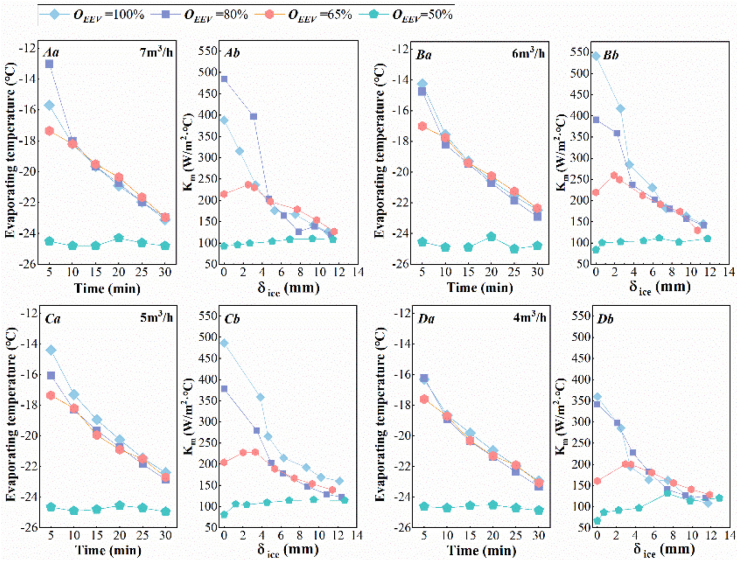
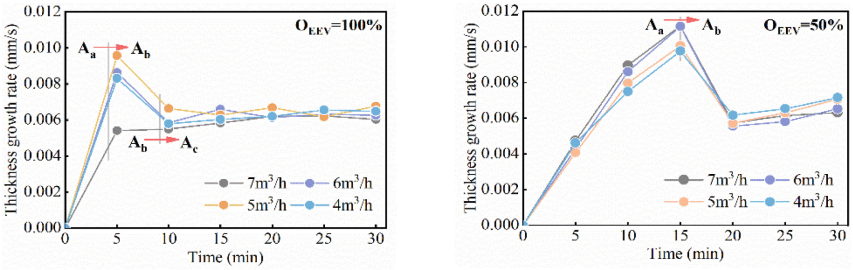


Fig. 4. Effect of mass flow of weak solution and opening of EEV on coefficient of heat transfer, evaporating temperature and thickness of ice.

As shown in Fig. 4, the average heat transfer coefficient is jointly affected by three factors: solution volume flow rate, throttle valve opening, and ice layer thickness. The impact of solution volume flow rate on heat transfer capacity is mainly manifested in the initial stage of icing operation. A comparison of the average heat transfer coefficients

at 100% valve opening under different flow rates indicates that, at the state where the ice layer thickness ranges from 0 mm to 4 mm, the maximum average heat transfer coefficient appears in the 6 m^3/h circulation group, reaching 550 W/(m^2·K), while the minimum value is observed in the 4 m^3/h circulation group, being 350 W/(m^2·K). In the initial stage of icing, the solution cools down from the initial temperature of 0 °C to the corresponding freezing point, and sensible heat exchange dominates this stage. A higher volume flow rate is conducive to the rapid cooling of the solution to the regeneration stage, while simultaneously improving the average heat transfer coefficient of the system. During operation with a low valve opening, the average heat transfer coefficients of all circulation test groups show a consistent variation trend at 65% EEV opening. When operating at 50% EEV opening, the heat transfer coefficient remains around 100 W/(m^2·K). This is because the lower refrigerant flow rate, to a certain extent, restricts the heat exchange process between the solution and the evaporator, weakening the impact of flow rate changes on the convective heat exchange between the solution and the plates during the regeneration process.

Notable differences exist in the variation of ice layer thickness between 100% and 50% EEV opening degrees. Therefore, to analyze the influence of volume flow rate on the uneven distribution of ice layers, the average growth rates of ice layer thickness under variable volume flow rates at 100% and 50% EEV opening degrees were selected to examine their variation processes, as shown in Fig. 5. The arrows in the figure indicate the direction of change in ice layer area, which corresponds to the ice layer variation processes at 100% and 50% EEV opening degrees reported in previous studies.



EEV opening=100% EEV opening=50%

Fig. 5. The calculation results of latent heat ratios.

As shown in the figure, except for the fifth minute at 100% EEV opening, the 7 m^3/h and 6 m^3/h groups (high-flow) have similar ice growth rate variations, while the 5 m^3/h and 4 m^3/h groups (low-flow) show consistent patterns. Thus, they are categorized into high-flow and low-flow groups.

At 50% EEV opening: In the first 15 min, high-flow groups ice faster, with 7 m^3/h peaking. But in the next 15 min, low-flow groups accelerate, and by experiment end, their growth rate exceeds high-flow groups by 0.001 mm/s. Early icing: High flow speeds up cooling from 0 °C to freezing point, shortening initial response time and boosting early growth. Post-cooling, low flow benefits ice expansion—lower flow reduces scouring of thin ice, raising icing probability and final average growth rate.

At 100% EEV opening: The cooling phase is much shorter than at 50%, weakening high flow's cooling advantage. Within 5 min, all flows cover surface Aa and shift to Ab, with low-flow groups dominating ice formation (peaks at $^{5th,\ 10th,\ 20th,\ 30th}$ min). However, growth rate differences between groups are only 0.0003–0.0005 mm/s, smaller than at 50%. This is because ice fully covers plates by 15th min, entering a stable growth phase (vs. 50% opening, where ice still grows between 15–20 min). In stable phase, flow has negligible impact, leading to similar growth rates across groups. Still, low flow overall benefits solution regeneration.

The variations in ice layer thickness under different volume flow rates and their corresponding ice layer slopes are presented in Figs. 6 and 7. When the EEV opening ranges from 100% to 65%, the ice layer slopes exhibit two distinct trend distributions based on the volume flow rates. Compared to the high-volume flow rate groups (7 m^3/h and 6 m^3/h), the low-volume flow rate groups (5 m^3/h and 4 m^3/h) tend to enhance the unevenness of the ice layer during the icing process. At an EEV opening of 50%, the slopes under all volume flow rates increase significantly: the ice layer slope reaches 6.57% at 7m^3/h, while the minimum slope of 6.13% is observed at 4 m^3/h. As the difficulty of icing increases, low volume flow rates are more conducive to ice layer growth.

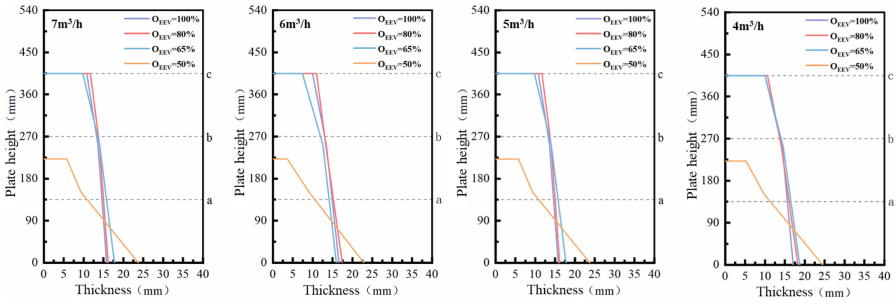


Fig. 6. Variations of ice thickness under different volume flow rates.

By comparing the ice layer variations under different volume flow rates as shown in Fig. 7, it can be noted that at 100% EEV opening, the ice layer distribution in the 7 m^3/h group is relatively uniform, whereas the ice layer thickness at the lower end slightly increases in the 4 m^3/h group. However, at 50% EEV opening, there is no significant difference in thickness between the ice layers in the 4 m^3/h and 7 m^3/h groups.

In the same reverse-cycle ice-melting process, ice layer unevenness critically affects separation. Table 1 shows icing conditions at 100–50% EEV openings: melted liquid mass decreases with increasing ice layer slope. At 100% and 80% openings, both with a 1.23% slope, melted liquid masses are 30.7 kg and 30.1 kg, indicating nearly identical separation under high openings.

Table 1 also shows the icing mass difference between 80% and 65% openings is ~0.4 kg, but melted liquid at 65% drops by ~4 kg (to 26.1 kg) due to slope effects. At 50% opening, unevenness impacts separation more significantly: reduced upper ice thickness and effective coverage height let refrigerant stay hotter when contacting thicker

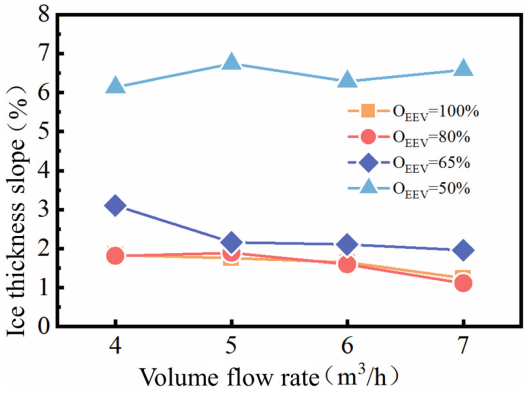


Fig. 7. The average slope of ice thickness under different volume flow rates.

ice, enabling faster melting of lower thick regions with the same heat input. A steeper slope also aids gravity-driven separation. Overall, greater ice layer unevenness benefits separation and markedly improves ice removal efficiency.

Table 1. Change in ice mass under different EEV.

EEV openings	Icing conditions
100%	60.94 kg
80%	62.43 kg
65%	62.88 kg
50%	44.94 kg

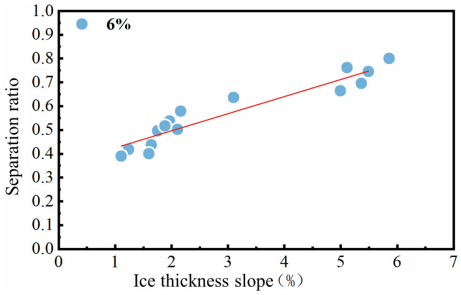


Fig. 8. Effect of ice percentage slope on ice segregation ratio under 6% concentration.

Figure 8 illustrates how ice thickness slope affects separation ratio under variable flow rates. With fixed concentration (6%), the 16 experimental groups reveal that reverse-cycle separation ratio rises with increasing slope. At slopes of 1%–2% (corresponding

to 100% and 80% EEV openings), separation ratios range 0.4–0.5, with low slopes leading to poor efficiency. At 2%–3% slopes (mainly 65% EEV opening), ratios reach 0.5–0.6. Despite a large slope span due to flow rate effects, the overall area shrinks with steeper slopes, reducing melting mass loss and improving efficiency. At 3.0%–6.0% slopes, solution loss is minimal, with a maximum separation ratio of 0.75, showing significantly enhanced efficiency.

By fitting the relationship between ice layer slope and separation ratio at a 6% concentration, the fitting equation represented by the red dashed line in the figure is obtained, as shown in Equation:

$$\theta = 35.29\gamma + 0.0718 \tag{3}$$

Where θ is separation ratio, γ is ice layer slope.

The degree of fitting R^2 is 0.88. In this equation, both the ice layer slope and ice separation ratio are expressed in decimal form. This formula can effectively analyze the influence of ice layer slope on the separation efficiency during the regeneration process.

4 Conclusions

This study explores the effects of volume flow rates (4–7 m^3/h) and EEV openings (50%–100%) on the regeneration of 6% dilute solution in SRFCHP. Results show latent heat ratio dominates heat transfer. Low flow rates benefit late-stage ice growth; EEV openings affect latent heat, with higher ice slope improving separation efficiency. The details are as:

1. Volume flow rate has little effect on latent heat ratio, while EEV opening directly affects the latent and sensible heat processes.
2. Volume flow rate affects ice layer growth in stages: high flow rates (6–7 m^3/h) facilitate rapid initial icing, while low flow rates (4–5 m^3/h) promote faster ice growth in the later stage, being more favorable for ice layer development, especially at low EEV openings.
3. EEV opening and ice layer slope significantly influence separation efficiency. Ice layer slope increases with decreasing EEV opening; higher slope (e.g., at 50% EEV opening) improves ice separation efficiency, and low flow rates are conducive to ice layer growth under difficult icing conditions.

Acknowledgement. This work is supported financially by the supported by China Postdoctoral Science Foundation (2025 M773227).

References

1. Wei, W.Z., et al.: Frosting performance variations of variable-frequency air source heat pump in different climatic regions[J]. Appl. Therm. Eng. **219**, 119356 (2022)
2. Song, M.J., et al.: A modeling study on the revere cycle defrosting of an air source heat pump with the melted frost downwards flowing away and local drainage[J]. Energ. Buildings. **226**, 110257 (2020)

3. Liang, S.M., et al.: A novel characteristic index for frosting suppression based on the configuration and operation of air source heat pumps[J]. Int. J. Refrig. **109**, 161–171 (2020)
4. Song, M.J., Mao, N.: Experimental study on the melted frost influence on the metal energy storage during an air source heat pump defrosting[J]. Energ. Buildings. **214**, 109809 (2020)
5. Tan, H.H., et al.: Investigation on the ultrasonic propagation mechanism and its application on air-source heat pump defrosting[J]. Appl. Therm. Eng. **107**, 479–492 (2016)
6. Wei, W.Z., et al.: Experimental and theoretical investigation on defrosting characteristics of a multi-split air source heat pump with vapor injection[J]. Energ. Buildings. **217**, 109938 (2020)
7. Mahvi, A.J., et al.: Superhydrophobic heat exchangers delay frost formation and enhance efficiency of electric vehicle heat pumps[J]. Int. J. Heat Mass Transf. **172**, 121162 (2021)
8. Huang, S.F., et al.: Performance evaluation of heating tower heat pump systems over the world[J]. Energy Convers. Manag. **186**, 500–515 (2019)
9. Song, P., et al.: Experimental investigation of the regeneration performance of an internally heated regenerator used for heating tower solution regeneration. Energy Convers. Manag. **189**, 184–194 (2019)
10. Ahmetović, E., et al.: Simultaneous optimisation and heat integration of evaporation systems including mechanical vapour recompression and background process. Energy. **158**, 1160–1191 (2018)
11. Zhang, Q., et al.: Calculations on performance characteristics of counterflow reversibly used cooling towers. Int. J. Refrig. **35**(2), 424–433 (2012)
12. Najim, A., Krishnan, S.: Experimental and theoretical investigation of a novel system for progressive freeze-concentration based desalination process. Chem. Eng. Process. Process Intensif. **173**, 108821 (2022)
13. Kalista, B., et al.: Current development and future prospect review of freeze desalination. Desalination. **447**, 167–181 (2018)
14. Moreno, F.L., et al.: Effect of separation and thawing mode on block freeze-concentration of coffee brews [J]. Food Bioprod. Process. **91**(4), 396–402 (2013)
15. Miyawaki, O., et al.: Integrated system of progressive freeze-concentration combined with partial ice-melting for yield improvement [J]. J. Food Eng. **184**, 38–43 (2016)
16. Raventós, M., et al.: Concentration of aqueous sugar solutions in a multi-plate cryoconcentrator [J]. J. Food Eng. **79**(2), 577–585 (2007)

Frosting and Heating Performance of Electric Vehicle Heat Pump Air Conditioning System in Cold Area

Ying Sun(✉), Ying Wang, Haoran Ning, Shicheng Yao, and Haochen Yu

Harbin University of Commerce, Harbin, Heilongjiang 150028, China
tlsunying@126.com

Abstract. Electric vehicles (EVs) cannot utilize waste heat for cabin heating. Most EVs rely on PTC (Positive Temperature Coefficient) systems, which consume high energy and reduce driving range. This study proposes an air-source heat pump system for summer cooling and winter heating. Experiments evaluated its frosting and heating performance in low-temperature environments. Results show that lower ambient temperatures worsen frosting on the outdoor heat exchanger, reducing heating capacity; at −10 °C, the system fails to meet heating demands. Airflow velocity extremes (high or low) exacerbate frosting and degrade efficiency, while lower humidity mitigates frosting and improves performance. After 600 s of operation, the system's COP drops below 1, indicating reduced energy efficiency. Integrating auxiliary heating is recommended to enhance overall performance in extreme cold conditions.

Keywords: Electric Vehicle · Air-source Heat Pump · Heating Performance

1 Introduction

With the development of society and the environment, electric vehicles (EVs) have gradually become the primary mode of transportation. Unlike conventional vehicles, EVs lack an internal combustion engine and therefore cannot utilize engine waste heat for cabin heating [1]. Currently, EVs air conditioning systems commonly employ PTC heaters for heating purposes. However, PTC systems consume significant amounts of electricity, which greatly reduces the driving range of EVs. Thus, it is necessary to develop new heat pump air conditioning systems for EVs [2]. Nevertheless, heat pump systems suffer from frost formation on the outdoor heat exchanger in winter. To address this issue, this study conducts theoretical calculations to determine the winter heating load of the EVs air-source heat pump system and designs a retrofit air-source heat pump air conditioning system based on the original vehicle air conditioning system, enabling both cooling in summer and heating in winter [3]. An experimental platform was built to investigate the frosting characteristics and heating performance of the EV heat pump air conditioning system under low-temperature conditions, with analysis of the effects of various influencing factors [4].

© The Author(s), under exclusive license to Springer Nature Singapore Pte Ltd. 2025
L. Ni et al. (Eds.): CCHVAC 2025, ESE, pp. 13–25, 2025.
https://doi.org/10.1007/978-981-95-3253-7_2

2 EVs Air-Source Heat Pump System Design

2.1 System Principle

The experimental setup used in this study is modified from an existing refrigeration air conditioning system of an electric vehicle (see Fig. 1) [5]. In heating mode, the circulating refrigerant is compressed by the electric compressor into a high-temperature, high-pressure gas. It then flows through tubing to the indoor heat exchanger in the passenger compartment, where it condenses and releases heat. The refrigerant subsequently enters the liquid storage tank, passes through a thermal expansion valve, and flows into the outdoor heat exchanger, where it absorbs heat and evaporates. The refrigerant is then drawn back into the compressor to complete the heat pump cycle [6].

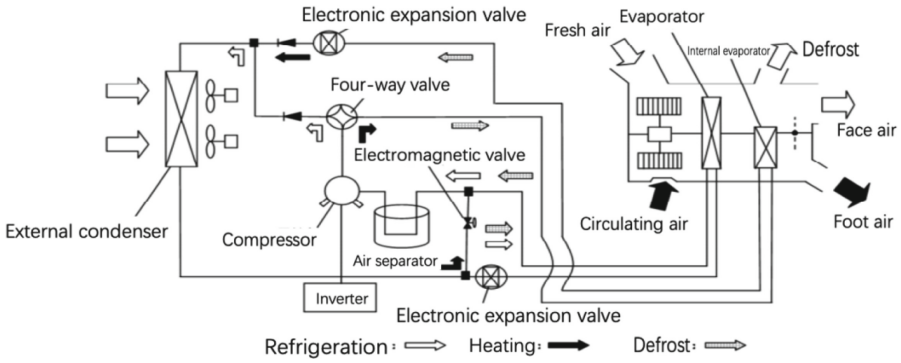


Fig. 1. Principle diagram of electric vehicle heat pump air conditioning system.

2.2 Air Calculation Parameters

The outside air temperature is one of the primary parameters for calculating the thermal load of an air conditioning system [7]. As a mode of transportation, changes in geographical location and climate during a vehicle's operation directly affect the outcome of the air conditioning system's thermal load calculation. This study focuses on the Harbin, located in Heilongjiang Province, China and Table 1 providing the air parameters used in this calculation [8].

Table 1. Winter air calculation parameters.

Parameter	Value
Average temperature outside the car	−15 °C
Average humidity outside the car	50%
Average temperature inside the car	20 °C

(*continued*)

Table 1. (*continued*)

Parameter	Value
Average humidity inside the car	50%
Average wind speed inside the car	0.4 m/s

2.3 Heat Load Calculation

In this study, the 2022 BYD Tang EV is used as the experimental model, with interior cabin dimensions of 2820 mm × 1940 mm × 1650 mm. The formula for calculating the body heat transfer coefficient is shown in Eq. (1) [9]. Table 2 provides the surface areas and corresponding heat transfer coefficients for the various structures of this vehicle model [10].

$$K = \left[\sum_{i=1}^{n} R_i + R_w + R_n\right]^{-1} \tag{1}$$

Table 2. 2022 BYD Tang EV heat transfer area and heat transfer coefficient.

Part	Area	heat transfer coefficient
Car roof	2.24m^2	1.94 W/m^2·K
Car body	7.49m^2	2.07 W/m^2·K
Car floor	3.92m^2	2.34 W/m^2·K
Car glass	4.81m^2	6.20 W/m^2·K

Calculate the heat load based on the methods and data mentioned earlier. Table 3 shows the heat load of the 2022 BYD Tang EV.

Table 3. Heat load of the 2022 BYD Tang EV.

Project	Heat load
Car enclosure structure	1016.08 W
Car window glass	1044.05 W
Fresh Air	1764.61 W
People in car	−794.44 W
Total	3030.31 W

3 Experimental Design

3.1 Experimental Instruments

The structure of the passenger compartment is too complex to model directly, so it has been simplified into a rectangular prism that matches the original vehicle's passenger compartment volume [11]. This simplified model is constructed using insulated panels (see Fig. 2). The performance parameters of the main instruments of the experimental system are shown in Table 4.

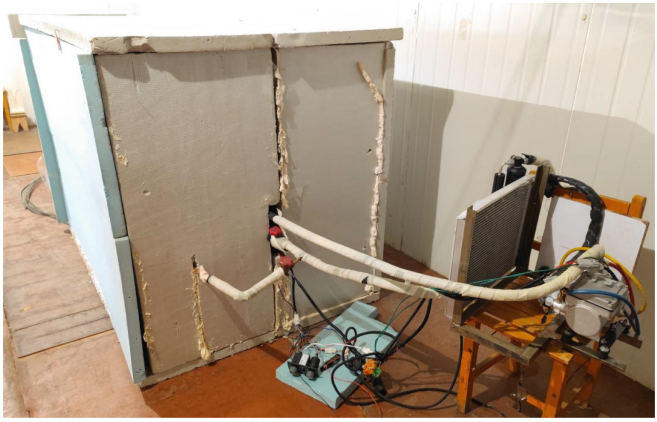


Fig. 2. Principle diagram of electric vehicle heat pump air conditioning system.

Table 4. The performance parameters of the main instruments of the experimental system.

Instruments	Parameter	Value
Electric compressor	Compression method	Scroll
	Rated power	760 W
Internal heat exchanger	Maximum cooling capacity	5200 W
	Heat exchanger type	Stacked
	Heat Exchange Area	3.2m^2
Auxiliary heat exchanger	Heat exchanger type	Parallel flow
	Heat Exchange Area	1.3m^2
External heat exchanger	Heat exchanger type	Parallel flow
	Heat Exchange Area	4m^2
Internal fan	Rated power	36 W
	Rated air volume	500m^3/h
External fan	Rated power	36 W

(*continued*)

Table 4. (*continued*)

Instruments	Parameter	Value
	Rated air volume	4000m^3/h

3.2 Experimental Plan

This experiment includes four variable groups: ambient temperature, ambient humidity, outdoor wind speed(External wind speed), and wind speed inside passenger compartment(Internal wind speed) [12]. These variables are used to investigate how the frosting behavior and heating performance of the heat pump system change under different conditions. Tables 5, 6, 7 and 8 present the experimental operating conditions for the various test scenarios.

Table 5. Experimental conditions at different ambient temperature.

Ambient temperature	Internal wind speed	External wind speed	Ambient humidity
−3 °C	4 m/s	9 m/s	40–50%
−5 °C	4 m/s	9 m/s	40–50%
−7 °C	4 m/s	9 m/s	40–50%
−10 °C	4 m/s	9 m/s	40–50%

Table 6. Experimental conditions at different internal wind speed.

Ambient temperature	Internal wind speed	External wind speed	Ambient humidity
−5 °C	3 m/s	9 m/s	40–50%
−5 °C	4 m/s	9 m/s	40–50%
−5 °C	5 m/s	9 m/s	40–50%

Table 7. Experimental conditions at different external wind speed.

Ambient temperature	Internal wind speed	External wind speed	Ambient humidity
−5 °C	3 m/s	4 m/s	40–50%
−5 °C	4 m/s	9 m/s	40–50%
−5 °C	5 m/s	12 m/s	40–50%

Table 8. Experimental conditions at different ambient humidity.

Ambient temperature	Internal wind speed	External wind speed	Ambient humidity
−5 °C	4 m/s	9 m/s	30–40%
−5 °C	4 m/s	9 m/s	40–50%

4 Experimental Results

4.1 Ambient Temperature

The frost layer on the outdoor evaporator surface, once it reaches a stable state, affects the system's heating capacity (see Fig. 3) [13]. As the ambient temperature decreases, the time at which the evaporator surface begins to frost is extended. With continued operation of the compressor, the frosted area gradually increases until it reaches a stable state. Although the onset of frosting is delayed at lower ambient temperatures, the time to reach a stable frost layer also increases. Moreover, the thickness of the stable frost layer becomes significantly greater at lower temperatures, leading to higher thermal resistance on the evaporator surface and more severely impacting its heat exchange efficiency.

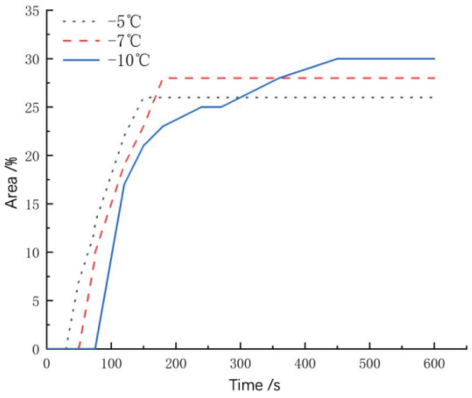


Fig. 3. Frost area variation curve of evaporator at different ambient temperature.

As shown in Fig. 4, at −5 °C, the heating capacity of the system after 600 s of operation is 453.15w; at −7 °C, the heating capacity of the system after 600 s of operation is 374.80w, meeting the basic requirements. At −10 °C, due to the low condensation temperature of the system, the heating effect in the passenger compartment is poor. Currently, the heating capacity of the system is only 232.13w. The frosting on the surface of the evaporator outside the vehicle is also more serious, and the heat exchange effect of the evaporator is poor, resulting in the reduction of evaporation pressure, compressor suction pressure and system heating capacity. At the same time, the ambient temperature is too low, and the heat consumption of the passenger compartment envelope increases. Therefore, the heat consumption of the system increases, the heating capacity decreases, and the heating effect of the system is not ideal.

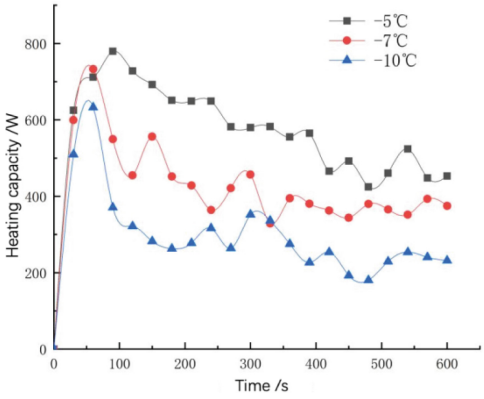


Fig. 4. Variation curve of system heating capacity at different ambient temperature.

4.2 Internal Wind Speed

At the different wind speeds of the heat exchanger inside the vehicle, the frosting start time and maximum frosting area of the heat exchanger outside the vehicle are different (see Fig. 5). When the wind speed is 2 m/s, the system starts to frost after 45 s, and reaches the maximum frost area after 285 s; When the wind speed is 4 m/s, the frosting starts at 30 s at the earliest, reaches the maximum frosting area after 150 s, and the overall frosting area is the minimum; When the wind speed is 5 m/s, the frost starts to form after 60 s, and reaches the maximum frost area after 240 s. Among them, when the wind speed is 4 m/s, the frosting rate is the fastest but the area is the smallest, indicating that the frosting rate is the fastest at this wind speed. Due to the same ambient temperature, different wind speeds mainly affect the frosting speed and maximum frosting area, but have little effect on the overall frosting trend.

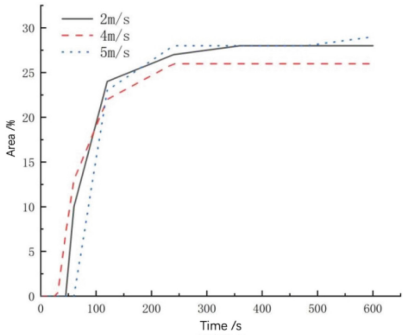


Fig. 5. Frost area variation curve of evaporator at different internal wind speed.

As shown in Fig. 6, increasing the indoor heat exchanger wind speed leads to a decrease in system condensing pressure, which in turn reduces the compressor power. Under environmental conditions of −5 °C ambient temperature, 40%–50% relative humidity (RH), and an outdoor wind speed of 9 m/s, the heating capacity at 600 s after startup decreases from 427.83 W at 2 m/s to 339.26 W at 5 m/s, representing a reduction of approximately 20.7%. At a wind speed of 4 m/s, the heating capacity is 453.15 W. As the wind speed of the heat exchanger in the vehicle increases, the compressor power gradually decreases, and the heating capacity of the system also decreases.

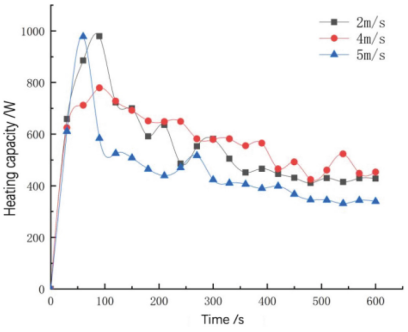


Fig. 6. Variation curve of system heating capacity at different internal wind speed.

4.3 External Wind Speed

When the surface wind speed of the external heat exchanger is 4 m/s and 12 m/s, the time for the maximum frost formation on the surface of the external heat exchanger is later than that when the surface wind speed of the external heat exchanger is 9 m/s (see Fig. 7). The reason is that the surface heat exchange effect of the external heat exchanger is poor when the external wind speed is too low or too high. When the wind speed outside the vehicle is too low, the frost layer grows faster in the early stage, but when the frost layer area increases to a certain size, it further reduces the heat exchange capacity of the heat

exchanger outside the vehicle, resulting in a slow frost formation rate in the late stage and an increase in the time to reach the maximum frost formation area; When the wind speed outside the vehicle is too high, the heat exchange between the heat exchanger outside the vehicle and the air is insufficient. At the same time, the faster wind speed makes the driving force of the water vapor in the wet air to frost on the surface of the evaporator outside the vehicle worse, so the frosting speed is slow, and the frosting layer is not dense when the wind speed outside the vehicle is 4 m/s.

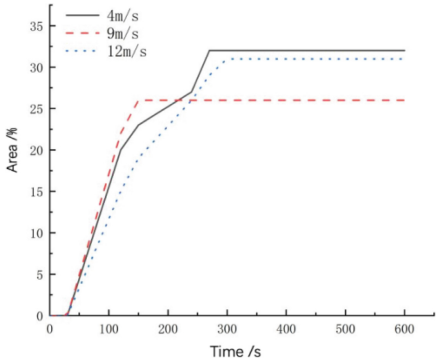


Fig. 7. Frost area variation curve of evaporator at different external wind speed.

As shown in Fig. 8, when the system operates for 600 s, the heating capacity of the system is only 338.58w at the outside wind speed of 4 m/s, 403.37w at the outside wind speed of 12 m/s, and 453.15w at the outside wind speed of 9 m/s. Compared with the heating capacity at the outside wind speed of 9 m/s, the heating capacity at the outside wind speed of 4 m/s and 12 m/s is reduced by 25.3% and 11.0% respectively. On the other hand, due to the insufficient air flow rate, the water vapor in the wet air fully exchanges heat with the external heat exchanger, which further promotes the growth rate of frost layer on the surface of the external heat exchanger and further worsens the heat transfer conditions of the external heat exchanger. With the acceleration of air flow rate, the driving force of water vapor in wet air condensing into frost on the surface of heat exchanger outside the vehicle is reduced, and the amount of frost is reduced. Therefore, at the same time, the increase of heating capacity under the external wind speed of 12 m/s is slightly better than that under the external wind speed of 4 m/s, but both are less than 9 m/s.

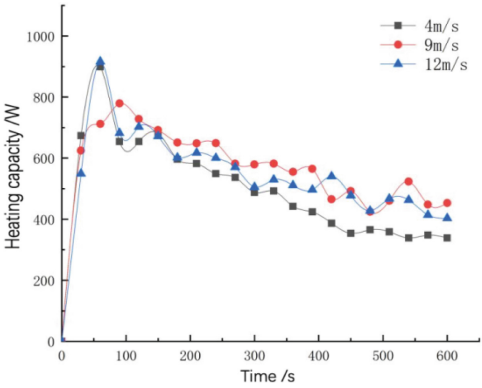


Fig. 8. Variation curve of system heating capacity at different external wind speed.

4.4 Ambient Humidity

When the ambient humidity is 30–40%, the frosting time on the surface of the heat exchanger outside the vehicle is delayed compared with 40–50%, and the growth rate of the frost layer is slower (see Fig. 9). This is due to the low content of water vapor in the air in the low humidity environment, which is difficult to adhere to the surface of the heat exchanger. At the same time, although the frost layer grows slowly in low humidity environment, its compactness is poor, and the final maximum frost area is far less than that in high humidity environment. Under the condition of 30–40%, the frost layer is very thin, which has little effect on the heat exchange effect. Even when the frost is slight, the heat exchange area can be slightly increased, so that the heat exchange performance can be improved.

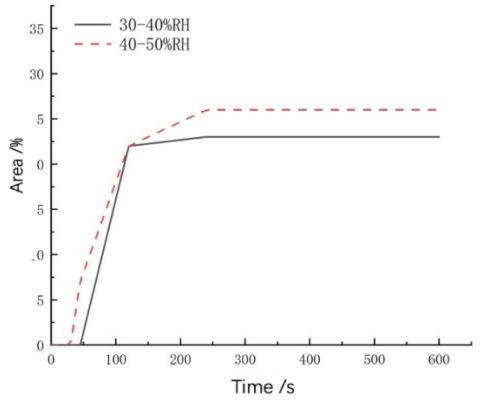


Fig. 9. Frost area variation curve of evaporator at different ambient humidity.

Figure 10 shows that different ambient humidity has significant effects on frosting and system performance of heat pump system external heat exchanger. When the relative humidity is 30–40%, due to the low content of water vapor in the air and the weak driving force for frosting, the frosting is slow and the frost layer is thin, and the heating capacity of the system can reach 541.49 W after 600 s of operation. However, when the relative humidity is 40–50%, the water vapor in the air is easier to condense into frost on the surface of the heat exchanger, and the frost layer is more compact, which seriously affects the heat exchange effect, reducing the heating capacity of the system to 453.15 W, which is only 80.4% of the heating capacity under low humidity environment. When the humidity increases by about 10%, the heating capacity of the system decreases by about 20%, indicating that the higher the humidity, the more serious the frosting, and the more obvious the attenuation of the heating performance of the heat pump system.

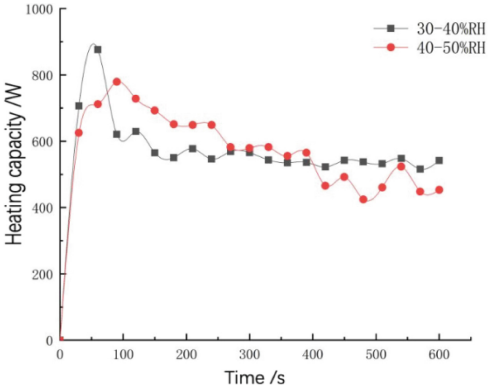
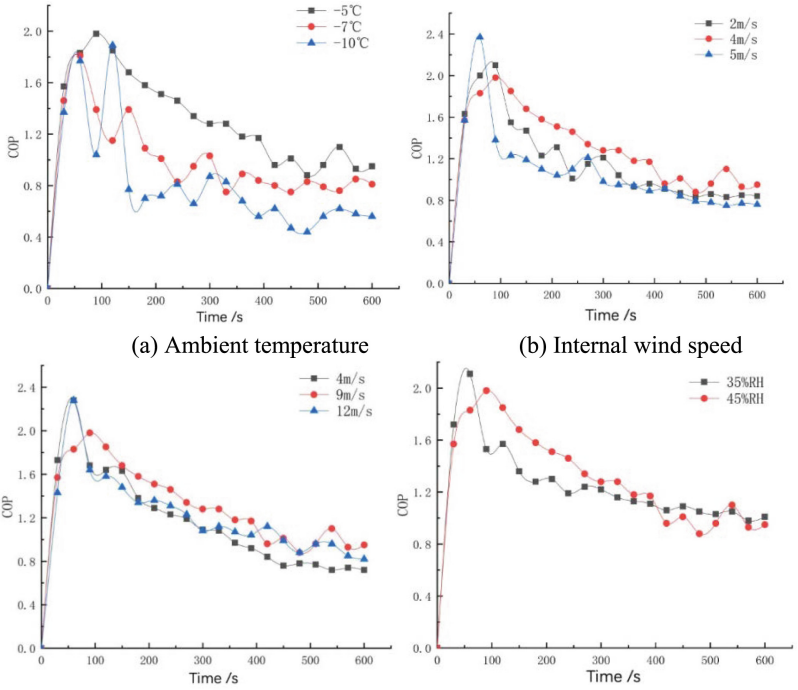


Fig. 10. Variation curve of system heating capacity at different ambient humidity.

4.5 System COP

After the initial start of the system, the COP of the system decreases to varying degrees after the system starts frosting. When the heat pump system is started for 600 s, the cop of the system is 1.01 when the ambient humidity is 30–40%, and the COP of the system is lower than 1 under other conditions. At this time, the energy-saving advantage of using the heat pump system to heat the passenger compartment is not obvious, and other heating systems can be set up for auxiliary heating (Fig. 11).



(a) Ambient temperature (b) Internal wind speed

(c) External wind speed (d) Ambient humidity

Fig. 11. Variation curve of system COP.

5 Conclusion

Lower ambient temperatures delay the onset of frosting on the heat pump air conditioning system of electric vehicles but result in larger frost areas and a stepwise decrease in heating capacity. At −10 °C, auxiliary heating becomes necessary. The COP decreases with decreasing temperature, with similar reductions observed at −5 °C and − 7 °C, while the greatest decline occurs at −10 °C.

At an indoor air outlet wind speed of 4 m/s, the heat pump air conditioning system exhibits the smallest frost area, highest heating capacity, and optimal COP. In contrast, at 5 m/s, the heating performance is poorest, requiring auxiliary heating, and the COP experiences the largest drop.

At an outdoor wind speed of 9 m/s, the system shows the smallest frost area, highest heating capacity, and best COP. Conversely, at 4 m/s, the frost area is largest, heating performance is worst, and the COP reduction is most significant.

Lower ambient humidity (30–40%) delays frosting, reduces frost layer area, and enhances heating capacity. Although the initial COP is slightly lower, it stabilizes to levels comparable to those under 40–50% conditions.

References

1. Wang, A., et al.: Principle and performance optimization analysis of a frost-free control for electric vehicle heat pumps. Appl. Therm. Eng. **2**(26), 120–126 (2023)
2. Huang, Y., Wu, X., Jing, J.: Research on the electric vehicle heat pump air conditioning system based on R290 refrigerant. Energy Rep. **8**(S7), 10–15 (2022)
3. Wang, A., Cao, F., Fang, J., Jia, F., Yin, X., Wang, X.: Research on efficient defrosting control logic for transcritical CO2 electric vehicle heat pump air-conditioning system. Int. J. Refrig. **2**(138), 13–22 (2022)
4. Meyer, J., Yang, G., Papoulis, E.: R134a heat pump for improved passenger comfort. Electr. Electr. Avionics. **6**(9), 136–144 (2004)
5. Ju-Suk, B., Jinho, L., Chang-Duk, J.: Frost retardation of an air-source heat pump by the hot gas bypass method. Int. J. Refrig. **31**(2), 328–334 (2008)
6. Huang, D., Li, Q., Yuan, X.: Comparison between hot-gas bypass defrosting and reverse-cycle defrosting methods on an air-to-water heat pump. Appl. Energy. **86**(9), 1697–1703 (2009)
7. Qi, Z., Zhao, Y., Chen, J.: Performance enhancement study of mobile air conditioning system using microchannel heat exchangers. Int. J. Refrig. **33**(2), 301–312 (2010)
8. Dingyuan, W., Tangfei, T., Guanghua, X.: Experimental study on frosting suppression for a finned-tube evaporator using ultrasonic vibration. Exp. Thermal Fluid Sci. **36**(1), 1–11 (2012)
9. Dong-Yeon, L., Chung-Won, C., Jong-Phil, W.: Performance characteristics of mobile heat pump for a large passenger electric vehicle. Appl. Therm. Eng. **50**(1), 660–669 (2013)
10. Dong, L., Zhenqian, C.: Experimental study on instantaneously shedding frozen water droplets from cold vertical surface by ultrasonic vibration. Exp. Thermal Fluid Sci. **53**(2), 17–25 (2014)
11. Steiner, A., Rieberer, R.: Parametric analysis of the defrosting process of a reversible heat pump system for electric vehicles. Appl. Therm. Eng. **61**(2), 393–400 (2013)
12. Song, M., Wang, X., Liao, L., Deng, S.: Termination control temperature study for an air source heat pump unit during its reverse cycle defrosting. Energy Procedia. **10**(5), 335–342 (2017)
13. Mahvi Allison, J., Boyina, K., Musser, A., Elbel, S., Miljkovic, N.: Superhydrophobic heat exchangers delay frost formation and enhance efficiency of electric vehicle heat pumps. Int. J. Heat Mass Transf. **17**(2), 121–126 (2021)

Experimental and Numerical Investigation on Effects of PCM Phase Change on Thermo-Mechanical Behaviours of Energy Pipe Pile with PCM Backfill

Weibo Yang(✉), Jiayan Zhao, Tianzheng Qiao, and Feng Wang

College of Electrical, Energy and Power Engineering, Yangzhou University, Yangzhou, Jiangsu 225127, People's Republic of China
yangwb2004@163.com, wbyang@yzu.edu.cn

Abstract. A model experimental bench is built to compare the differences in thermo-mechanical (TM) behaviours of traditional energy pipe pile (TEPP) and phase-change energy pipe pile(PCEPP), and obtain the TM performance of enhanced PCEPP. The results show that the PCEPP can significantly enhance the heat transfer performance (HTP), slow down the temperature and mechanical properties variation of pile and soil. The composite enhancement has the most significant enhancement in HTP, but it has also the greatest influence on the temperature of the pile and soil and the greatest change in the mechanical characteristics of pile. A 3-D CFD model was built to explore the impact of the PCM backfill form. The findings indicate that the cylindrical backfill has the best HTP and mechanical properties of the pile body. When using radial layered backfill with PCM, the backfill with increasing phase-change temperatures(PCT) from the inside to outside can increase the long-term HTP of pile while slowing down pile temperature change and minimizing thermal impact on soil.

Keywords: GSHP · Phase-change energy pipe pile · Thermo-mechanical behaviours

1 Introduction

Ground source heat pump (GSHP) is an efficient method of shallow geothermal energy utilization. Nevertheless, it requires a large occupied area and expensive initial investment due to drilling borehole [1, 2]. For this reason, some researchers introduced the idea of energy pipe pile (EPP), which can effectively solves the above problem of traditional GSHP, but its long-term operation inevitably produces irreversible changes in mechanical properties due to temperature change of pile body. Thus, some scholars proposed the use of PCM for backfilling at the center of EPP and form phase change energy pipe pile(PCEPP), utilizing their latent heat to enhance heat transfer performance(HTP) and slow down the deformation of pile body. However, the impact mechanism of PCM on TM properties of EPPs needs to be further revealed.

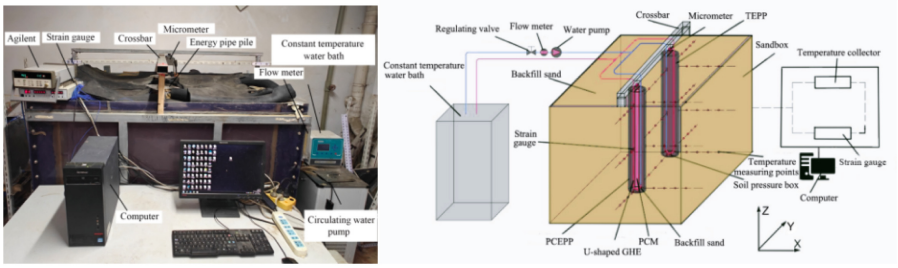
© The Author(s), under exclusive license to Springer Nature Singapore Pte Ltd. 2025
L. Ni et al. (Eds.): CCHVAC 2025, ESE, pp. 26–37, 2025.
https://doi.org/10.1007/978-981-95-3253-7_3

Existing studies have shown that energy pile (EP) with PCM backfill exhibit significant advantages compared to traditional EP in terms of thermodynamic properties. Bao et al. [3] tested the effectiveness of PCM in EPs by creating lab-scale phase-change EPs in unsaturated clay, revealing lower temperature change and higher heat transfer efficiency. Elkezza et al. [4, 5] investigated the effect of PCM on EPs and concluded that the addition of PCM to piles could effectively reduce the thermal radius of the soil and structural damage caused by thermal strain. Han et al. [6] concluded that the use of PCM in concrete significantly improves the heat transfer efficiency by comparing the HTP of conventional EPs with that of phase-change EPs. Du et al. [7] compared the TM properties of traditional and phase-change EPs and concluded that phase-change EPs have a much smaller effect on the mechanical characteristics of pile body. Xia et al. [8] integrated metal fins and spiral heat exchange tubes in pipe piles and concluded that the integration resulted in better HTP and reduced thermal stresses in the pile body, which can significantly improve the utilization of PCM.

The existing studies have shown that the PCEPP has significant advantages in TM properties compared with TEPP. In this work, a set of model test bench is constructed to find the difference between TEPP and PCEPP and performance change under various enhancement forms. Also, a 3-D model is built to obtain the TM behaviours of PCEPP under various PCM layout forms and layered backfills forms.

2 Experimental Bench

A model experimental bench of PCEPP was built [9]. As shown in Fig. 1, the experimental bench includes a sandbox, constant temperature water bath, flow meter, water pump and data collection system. Two model EPPs, one EPP backfilled with PCM while the other does not have PCM, are made to compare the effects of PCM. Two types of PCMs are used for summer and winter conditions, respectively. Among them, the butyl stearate with PCT of 20.15 °C is used as summer PCM (PCM-S) and encapsulated on the inner wall of pipe pile. The oleic acid with PCT of 8.11 °C is used as winter PCM (PCM-W), which is encapsulated inside a circular tube and placed at center of pipe pile. The data collection system is used to monitor parameter changes by using thermocouple, dial indicator, strain gauge and soil pressure box.



(a) Picture of experimental system (b) Schematic diagram of experimental system

Fig. 1. Experimental system of PCEPP.

3 Experimental Results and Discussion

3.1 Comparative Experiments of TEPP and PCEPP

The comparative experiments of PCEPP and TEPP are conducted to find the difference in their TM characteristics. First, run for one day in summer mode, and then run for one day in winter mode.

Figure 2 indicates the total heat exchange rate, Q of PCEPP are higher than those of TEEP in both summer and winter conditions. During the initial 2 h of operation, the decrease in Q of PCEPP in summer condition is significantly lower than that of TEPP.

Based on the temperature change curves of PCM-S in Fig. 3a, it is evident that the temperature of PCM-S is around its PCT in the first 2 h. Therefore, the Q of PCEPP decreases slowly in the first 2 h resulting from phase change of PCM-S, while the Q of TEPP decreases sharply. This phenomenon indicates that the PCM-S is able to maintain a stable heat release during the initial operation. Under winter condition, the Q of both PCEPP and TEPP shows a steep decrease. This is because the PCM-W in EPP is filled in the center of the pipe pile and has not yet reached its PCT, As shown in Fig. 3b. However, since the temperature of PCM-W is always maintained in the range of PCT, its phase change latent heat can be released continuously so that the Q of PCEPP in winter condition is always higher than that of TEPP.

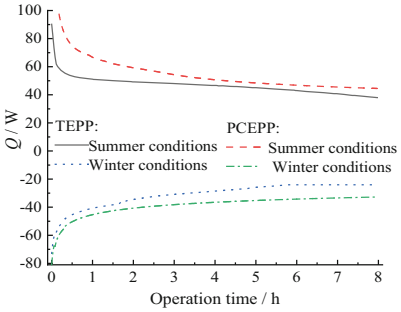
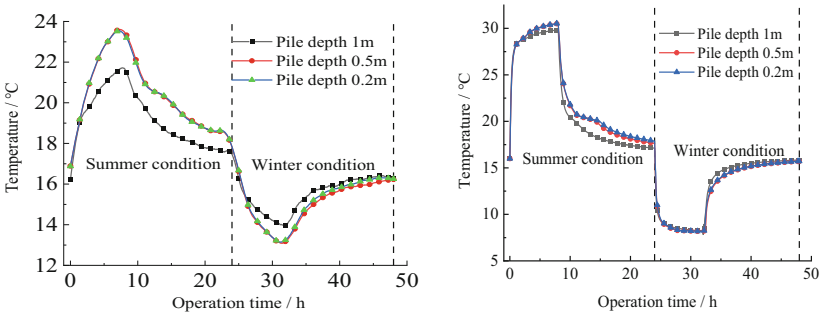


Fig. 2. Variations of total heat exchange rate with time for PCEPP and TEPP.

Figure 3a shows that under summer condition, the temperatures of PCM-S at pile depths of 0.2 and 0.5 m reach 20 °C after 2 h of operation, while the temperature of PCM-S at pile depth of 1 m is 19.4 °C. This indicates that the PCM-S at pile depths of 0.2 and 0.5 m began to melt at this moment, but the PCM-S at pile depths of 1 m does not reach its PCT. After running for 8 h, the highest temperature of PCM-S at pile depths of 0.2 and 0.5 m reach around 23.6 °C, which is higher than its PCT. This indicates that PCM-S has completely undergone phase change at this time. Under the winter condition, the temperature variation law of PCM-S with time is similar to summer condition. Additional examination of Fig. 3b indicates that the temperature of PCM-W under summer condition gradually rises with time, and reaches a maximum of about 30.5 °C at pile depths of 0.2 and 0.5 m and 29.8 °C at pile depths of 1 m at the end of 8 h operation. Under winter condition, the temperature of PCM-W drops sharply with time

and drops to 8.1 °C after running for 6 h. This is exactly the PCT of PCM-W, indicating that PCM-W is starting to melt at this moment. After 8 h of operation, the temperature of PCM-W remains at around 8.1 °C, but reaches a minimum temperature of 7.8 °C at the time of 10 h. This indicates that the temperature of PCM-W under winter condition is always around its PCT of 8.11 °C.



(a) PCM-S (b) PCM-W

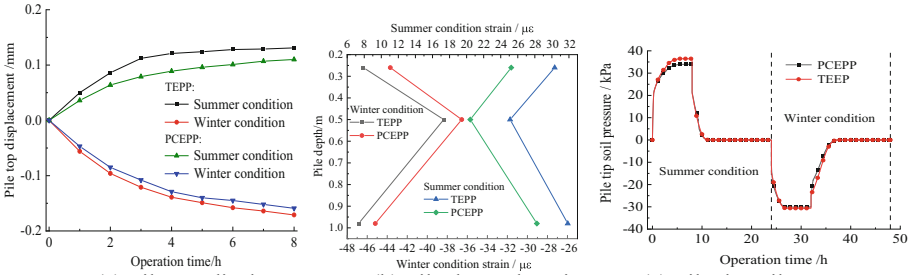
Fig. 3. Variations of temperature of PCM-S and PCM-W at different pile depths with time.

As illustrated in Fig. 4a, the pile top displacements of PCEPP are always smaller than that of TEPP, which indicates that both PCM-S and PCM-W can effectively mitigate the changes in pile displacement due to the buffering effect of PCM on temperature changes of piles. Additional examination of Fig. 4b shows that under summer condition, the minimum strains of PCEPP is obviously smaller than that of TEPP. Under the winter condition, the thermal strains of both TEEP and PCEPP show an opposite trend to that under summer condition, that is, first increase and then decrease along the depth of pile, and the strain of PCEPP is less than that of TEPP. It can be further found from Fig. 4c that both summer and winter condition, the pile tip soil pressure of PCEPP is lower than that of TEPP after stabilization. It can be concluded that under both winter and summer conditions, backfilling PCM in EPP can significantly enhance HTP, slow down the temperature variations and the influence of heat transfer on the mechanical properties of the pile body.

3.2 Enhanced PCEPP

Three types of enhancement form experiments are conducted to find the differences in TM characteristics of EPP under various enhancement forms. Among which, enhanced PCM-S refers to that insert a cylindrical wire mesh into the PCM-S encapsulated in the cylinder to enhance its thermal conductivity. Enhanced backfill sand is by uniformly mixing iron filings with sand in the mass ratio of 3:7 to improve its thermal conductivity. Composite enhancement is by enhancing both PCM-S and backfill sand based above methods.

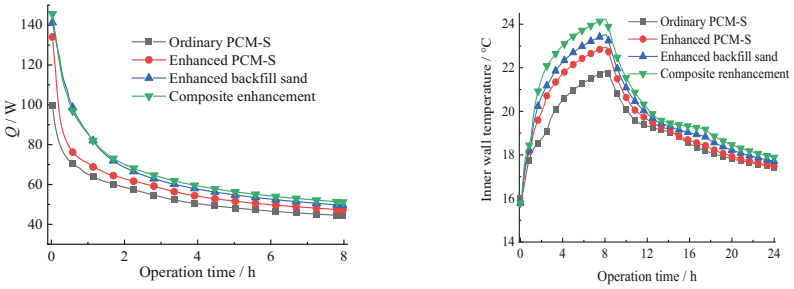
Figure 5a illustrates that the total heat exchange rate, Q, of PCEPP under the composite enhancement is always the largest throughout the operation cycle, followed by



(a) Pile top displacement (b) Pile thermal strain (c) Pile tip soil pressure

Fig. 4. Changes of mechanical properties of pile body for TEEP and PCEPP.

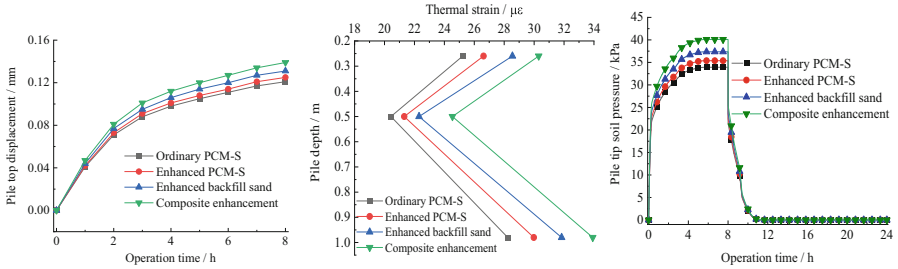
enhanced backfill sand and enhanced PCM-S respectively, and the ordinary PCM-S is the smallest. Further analysis on Fig. 5b indicates under composite enhancement, the inner wall temperature is the highest, followed by enhanced backfill sand and enhanced PCM-S, and the ordinary PCM-S has the least inner wall temperature. This is mainly due to the different heat transfer enhancement effects caused by various enhancement forms. It can be inferred that the enhancement of the backfill material and PCM-S will weaken the buffering effect of PCM-S on the pile temperature change to a certain extent.



(a) Total heat exchange rate (b) Inner wall temperature

Fig. 5. Variations of total heat exchange rate and inner wall temperature of PCEPP with time for different enhancement forms.

As demonstrated in Fig. 6, the patterns of pile top displacement, thermal strain, and tip soil pressure exhibit similarities across various enhancement methods. Notably, the largest values are observed in the composite enhancement, followed by enhanced backfill sand and enhanced PCM-S, and the ordinary PCM-S backfill are the smallest. This phenomenon can be attributed to that the PCEPP under different enhancement forms have different heat transfer capacity and temperature changes of the pile. As shown in Fig. 5, the composite enhancement has the best HTP and the largest temperature variation of pile body, followed by enhanced backfill sand and enhanced PCM-S, and the ordinary PCM-S backfill has the worst HTP and the smallest temperature variation of pile body. This indicates that the enhanced PCEPP improve its heat transfer performance, but it also



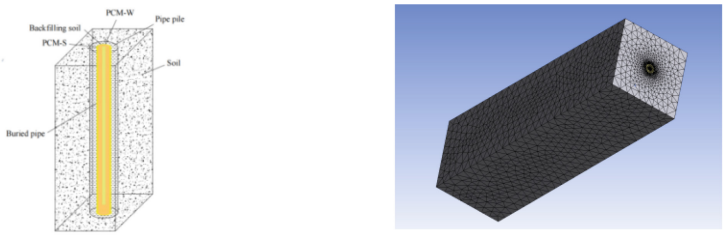
(a) Pile top displacement (b) Thermal strain (c) Pile tip soil pressure

Fig. 6. Changing law of mechanical properties of pile body with different enhancement forms.

increases its temperature change amplitude, resulting in an increase in its mechanical characteristic parameters.

4 Numerical Model

The physical model of PCEPP shown in Fig. 7a is built, and its specific parameters are presented in Table 1. According to above physical model, the numerical model of PCEPP shown in Fig. 7b is constructed based on SpaceClaim module of Workbench platform, and the mesh module is utilized for meshing. The upper half of the model is meshed with larger spacing by sweeping to reduce the number of meshes due to the regular structure and larger depth. The lower half of the model is meshed with six-sided mesh to ensure quality. Face mesh division is used for pipe pile structures to reduce the number of meshes. Mesh encryption is implemented in soil region around pile, and the grid density decreases from inside to outside.



(a) Schematic diagram of physical model (b) Schematic diagram of model meshing.

Fig. 7. Physical and numerical model of PCEPP.

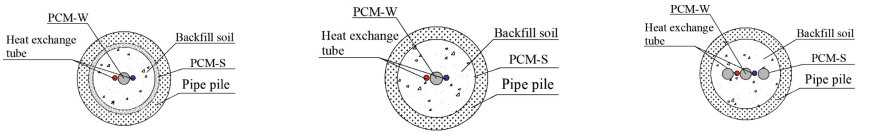
Table 1. Geometric parameters of the PCEPP model.

Parameters	Values	Parameters	Values
U-tube outer diameter/m	0.032	Pile depth/m	14
U-tube inner diameter/m	0.025	Outer diameter of pipe pile/m	0.5
U-tube center distance/m	0.2	Inner diameter of pipe pile/m	0.25
U-tube depth/m	13.5	Soil calculation area/m^3	$2 \times 2 \times 15$
PCM-W backfill radius/m	0.035	PCM-S backfill radius/m	0.104
PCM-W backfill depth/m	13	PCM-S backfill depth/m	14

5 Simulation Results and Discussion

5.1 Influence of PCM Backfill Forms

Three kinds of PCM-S backfill forms shown in Fig. 8 are designed to compare the HTP, thermal influence range and mechanical properties of PCEPP under various PCM-S backfill forms. Among them, the cylindrical backfill refers to the cylindrical backfilling of PCM-S along the inner wall of pipe pile. Layered backfill is that backfilling PCM-S at depths of 1, 7, and 13 m respectively. Columnar backfill encapsulates PCM-S equally in two cylindrical bodies and locates them on both sides of heat exchange tubes.



(a) Cylindrical backfill (b) Layered backfill (c) Columnar backfill

Fig. 8. PCM-S backfill forms.

Figure 9 illustrates that on the 1st day of operation, the heat exchange rate per unit pile depth, q_l, for columnar backfill is the largest, succeeded by cylindrical backfill and the smallest for layered backfill. But on the 2nd day of operation, the q_l of the cylindrical backfill exceeds that of the columnar backfill. This is mainly due to the differences in the liquid phase ratio and contribution ratio of PCM-S under different backfill forms, which can be found in Fig. 10. On the 10th day of operation, The cylindrical backfill has the largest q_l, which is due to the fact that under cylindrical backfill, the radial position of PCM-S is the farthest and its thickness is the thinnest, and therefore has the least effect on heat transfer and the best heat exchange effect. The PCM-S under the cylindrical and columnar backfill forms have completely changed phase by the 10th day of operation, while the layered backfill is still in the stage of slow phase change, and its contribution ratio is low, so the q_l is mainly affected by the heat exchange between the pile and soil.

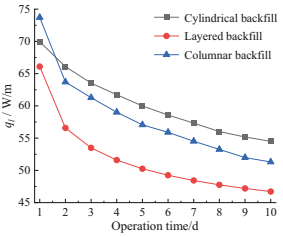


Fig. 9. Variation of heat exchange rate per unit pile depth with time under different backfill forms.

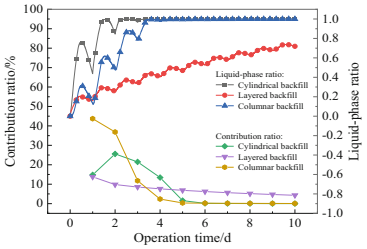
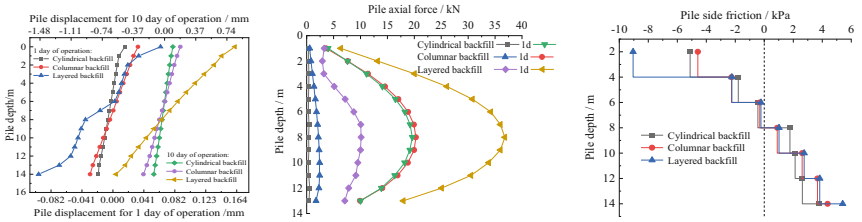


Fig. 10. Changes of liquid phase ratio and contribution ratio of PCM-S with time for different backfill forms.

As can be seen in Fig. 10, the liquid phase ratio of PCM-S under columnar backfill changes the most dramatically, followed by the cylindrical backfill, and the layered backfill is the slowest. Among them, PCM-S with cylindrical and columnar backfill has completely melted on the third day of operation, while the liquid phase ratio of PCM-S with layered backfill shows a periodic slow upward trend over the 10-day operating cycle, and has not completely melted. Further analysis of Fig. 10 can see that in the first 2 days of operation, the contribution ratio of PCM-S is the largest for the columnar backfill, and the utilization effect is good. The cylindrical backfill has a good contribution ratio in the first 5 days, but the contribution ratio of layered backfill is always low throughout the entire operation cycle. This indicates that, from a short-term operational perspective, the PCM-S under the cylindrical and columnar backfill have higher contribution ratio. However, from a long-term operational perspective, although the layered backfill has a lower contribution ratio, it remains in a contributing state during the operation.



(a) Pile displacemnt (b) Pile axial force (c) Pile side friction

Fig. 11. Distribution of pile mechanical properties with pile depth for different backfill forms of PCM.

Figure 11a shows that the pile displacement increases with time under different backfill forms. After one day of operation, the changes are small. But after 10 days of operation, there is a significant cumulative increase in pile displacements, with the largest pile displacements occurring for the layered backfill, followed by the columnar backfill, and the smallest for the cylindrical backfill. Figure 11b reveals that after one day of operation, the pile axial force under cylindrical and columnar backfill changes slightly, while under the layered backfill, the pile axial forces are larger and show an S-shaped fluctuation with pile depth. As the running time increases, the pile axial force increases for three backfill forms, and exhibits an initial upward trend and then decreasing along the depth, with the maximum axial force at the center of the pile. Further analysis of Fig. 11c can see that after 10 days of operation, the maximum pile side friction is achieved under layered backfill, and there is not much difference between cylindrical and columnar backfill.

5.2 Effects of Layered Backfill with Various PCMs

To examine the impacts of various types of PCM-S layered backfills on the TM properties of PCEPP, the radial layered backfill with n-butyl stearate, mixed acid and paraffin wax is used. The PCTs of n-butyl stearate, mixed acid and paraffin wax are 20.1, 8.11 and 24 °C, respectively. The specific layering modes are shown in Table 2.

Table 2. Different types of PCM-S layered backfill modes.

Mode	First layer	Second layer	Third layer
1	Mixed acids	N-butyl stearate	Paraffin
2	Paraffin	N-butyl stearate	Mixed acids
3	Mixed acids		

Figure 12 displays that on the 1st day of operation, the q_l of mode 1 is smaller than that of modes 2 and 3. This is principally due to that the third layer of mode 2 and 3

is backfilled with mixed acid with low PCT. As illustrated in Fig. 13, on the first day of operation, the liquid phase and contribution ratio of the third layer PCM-S under modes 2 and 3 are significantly higher than those under mode 1, resulting in a larger heat transfer capacity. In contrast, the third layer of paraffin in mode 1 has a higher PCT and a lower liquid phase and contribution ratio, resulting in a smaller heat exchange capacity. Further examination of Fig. 12 indicates that the q_l of mode 1 will exceed that of modes 2 and 3 with time. This is due to the fact that the third layer PCM-S of modes 2 and 3 has undergone a complete phase change over a long period of operation, while the third layer PCM-S of mode 1 is still in phase-change state and has a higher PCM-S contribution ratio, resulting in a larger heat transfer capacity.

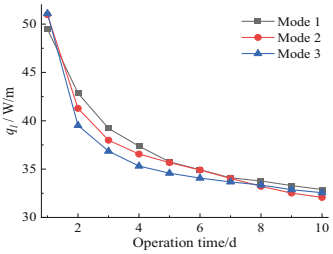
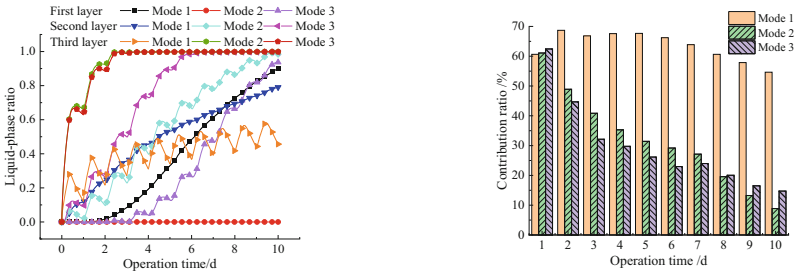


Fig. 12. Heat exchange rate per unit pile depth with time for different types of PCM-S layered backfill modes.

Figure 13a shows that for the third layer, the modes 2 and 3 use PCM-S with low PCT, which completely phase changes in a very short time, while the mode 1 uses PCM-S with high PCT, which does not completely phase change, and the phase change latent heat cannot be fully utilized. For the second layer, mode 3 uses PCM-S with a low PCT, which can be fully phase transitioned during the operation time, while modes 1 and 2 use PCM-S with a moderate PCT, which can continue to function during the operation. For the first layer, modes 1 and 3 use PCM-S with a low PCT, which can always effectively function, while mode 2 hardly undergoes any phase transition due to the high PCT. This implies that the PCT of PCM-S should be decreased sequentially from the center to the outside to improve the use efficiency of PCM-S. Meanwhile, it can be seen through Fig. 13b that except for the first day of operation, the PCM contribution ratio of mode 1 is always higher than that of the other two backfill modes, indicating that increasing the PCT of PCM sequentially from the inside to the outside can improve the use of PCM-S.



(a) Liquid phase ratio of PCM-S (b) Contribution ratio of PCM-S

Fig. 13. Variations of liquid phase ratio and contribution ratio of PCM-S with time for different types of PCM-S layered forms.

6 Conclusions

(1) The PCEPP can significantly improve HTP, slow down the impact on temperature variation of pile and soil, and decrease the impact of mechanical characteristics of pile body. When PCM is backfilled on the inner wall of pipe pile, it can effectively slow down the temperature variations of the pile body, while the effect is not significant when backfilled to the center of the pipe pile.

(2) The enhanced PCEPP improve its HTP, but it also increases its temperature change, resulting in an increase in its mechanical parameters. The composite enhancement has the most obvious effect on the heat transfer enhancement of PCEPP, but it has the greatest influence on temperature and mechanical property change of pile and soil, followed by backfill sand enhancement and PCM-S enhancement.

(3) After studying the different layout forms of PCM-S, it is found that the heat exchange effect is best by using cylindrical backfill, followed by columnar backfill and layered backfill, and the cylindrical backfill has the least effect on the mechanical properties of the pile body.

(4) When using PCM-S with lower PCT for inner backfill, the temperature change of pile-soil can be slowed down in a short period of operation. When the PCT of PCM-S is gradually reduced from the inside to out during backfilling, it can significantly alleviate the impact of pile-soil temperature during long-term operation.

References

1. Sani, A.K., et al.: A review on the performance of geothermal energy pile foundation, its design process and applications. Renew. Sust. Energ. Rev. **106**, 54–78 (2019)
2. Sharmin, T., et al.: A state-of-the-art review on geothermal energy extraction, utilization, and improvement strategies: conventional, hybridized, and enhanced geothermal systems. Int. J. Thermofluids. **18**, 100323 (2023)
3. Bao, X., et al.: Experimental study on thermal response of a PCM energy pile in unsaturated clay. Renew. Energy. **185**, 790–803 (2022)

4. Elkezza, O., et al.: Experimental investigation on the use of PCM heat exchangers in Geo-energy piles and walls. Geothermics. **119**, 102950 (2024)
5. Elkezza, O., Mohamed, M.: Experimental assessment of using Phase Change Lightweight Aggregates to enhance the thermal storage of geo-energy structures. J. Energy Storage. **79**, 109981 (2024)
6. Han, C., Yu, X.B.: An innovative energy pile technology to expand the viability of geothermal bridge deck snow melting for different United States regions: computational assisted feasibility analyses. Renew. Energy. **123**, 417–427 (2018)
7. Du, T., et al.: Thermo-mechanical performance of a phase change energy pile in saturated sand. Symmetry. **12**(11), 1781 (2020)
8. Xia, C., et al.: Thermal performance of heat storage-enhanced PCM energy pipe pile with heat conduction fin. Appl. Therm. Eng., 126407 (2025)
9. Qiao, T.Z.: Theoretical analysis and experimental research on the thermal-mechanical characteristics of phase change energy pipe piles under the influence of different factors, Master thesis. Yangzhou. Yangzhou University; 2025(in Chinese).

Application of Superhydrophobic Coatings in Air-Source Heat Pump Evaporators Under Frosting and Defrosting Conditions

Yifan Yang, Zhen Shen, Yixuan Jin, Leshan Shen, Hao Peng, Huadong Huang, Chenxi Li, Zhifu Qi, Zhouyang Luo(✉), Shien Sun(✉), and Weiming Teng(✉)

Zhejiang Baima Lake Laboratory Co., Ltd, Hangzhou 310051, China
{luozhouyang,sunse,tengweiming}@zjenergy.com.cn

Abstract. Air-source heat pumps (ASHPs) suffer from significant efficiency degradation under low-temperature, high-humidity conditions due to evaporator frosting. To address this, superhydrophobic coatings were applied to the aluminum fins of an ASHP evaporator to delay frost formation and accelerate defrosting. This study evaluates the frosting/defrosting performance of superhydrophobic coatings under real-world operating conditions using commercially residential ASHP units. Three configurations were tested: original hydrophilic fins with default defrost strategy, superhydrophobic-coated fins with default strategy, and superhydrophobic-coated fins with a modified COP-based defrost strategy. Results demonstrate that the superhydrophobic coating alone extended the first defrost interval to 323% of the hydrophilic baseline, reduced average defrost time by 61.1% and defrost energy consumption 60.7% over 8-h operation. After defrosting, residual moisture was significantly minimized on coated surfaces, and frost layer detachment during defrosting contributed to accelerating melting. Implementing the COP-based strategy on coated fins further enhanced system efficiency, increasing the 8-h average COP by 2.3% compared to the default strategy. This integrated approach—combining superhydrophobic coatings with optimized defrost strategy—enables sustained high-efficiency ASHP operation in cold, humid climates while ensuring user comfort.

Keywords: Superhydrophobic · Coatings · Defrosting

1 Introduction

Air-source heat pumps (ASHPs) are widely employed for hot water production and space heating during winter in southern China, thanks to their high coefficient of performance (COP) of approximately 3 ~ 4, which far exceeds the 90% thermal efficiency of modern gas boilers. However, under low-temperature, high-humidity winter conditions, frost readily forms on the evaporator surface of ASHPs during heating production. The frost accumulation leads to a sharp increase in airflow resistance through the evaporator and a significant decrease in heat transfer rate. Severe frosting on the surface of evaporator may cause the ASHP to be unable to heat properly.

© The Author(s), under exclusive license to Springer Nature Singapore Pte Ltd. 2025
L. Ni et al. (Eds.): CCHVAC 2025, ESE, pp. 38–47, 2025.
https://doi.org/10.1007/978-981-95-3253-7_4

To solve the problem of evaporator frosting, various defrost strategies have been developed, including the traditional reverse-cycle defrost (RCD), hot-gas bypass defrost, electric heating defrost and so on. Reverse-cycle defrost switches the system from heating to cooling mode, yielding lower power consumption and shorter defrost duration. However, frequent reverse-cycle defrosting may compromise indoor thermal comfort due to intermittent heating interruption [1]. Hot-gas bypass defrost employs compressor discharge gas to directly purge the coil. Although this method requires significantly longer defrosting time than reverse-cycle defrosting, it produces smaller temperature fluctuations indoor and better user comfort [2–4]. Electric heating defrost uses embedded heating elements to melt frost but requires additional defrosting energy consumption. Li [5] et al. proposed a novel frost-free ASHP which use solution to extract heat from the environment and release heat to evaporator. The present work mainly integrates superhydrophobic coating with reverse-cycle defrost to prolong the defrost interval, shorten defrost time, and reduce defrosting energy consumption.

Numerous studies demonstrated that applying superhydrophobic or superhydrophilic coatings to heat exchanger fins to suppress frost formation and enhance defrost performance. Wang [6] et al. reported a sprayable superhydrophobic coating reduced frost-layer thickness by 33% after 60 min of frosting. Gu [7] et al. demonstrated that a superhydrophobic aluminum surface exhibited only 69.8% of the frost mass compared to bare aluminum, and the defrost time was reduced to 64% of the uncoated case. Li [8] et al. demonstrated that a wet-chemically etched super-hydrophobic finned-tube evaporator enhanced heat transfer rates by 17 ~ 44%, improved COP by 11.2 ~ 31.9%, reduced frost accumulation by 59.2 ~ 76.3%, and extended defrosting intervals compared to conventional units under multiple frosting conditions.

Although studies above demonstrate notable improvements under laboratory conditions, they predominantly rely on small-scale test rigs and controlled environments. To bridge the gap between laboratory and real-world performance, this study is the first to verify the superhydrophobic coating and modified defrosting strategy through long-period testing on a commercial air source heat pump system, thereby providing more engineering-representative performance data.

2 Experimental Approach

2.1 Facility and Instrumentation

The test facility comprised a 1-HP “VARKI” ASHP hot-air unit (VKFR-3) coated with superhydrophobic layer. Major components included a compressor (Panasonic 5PS102EAA22), a four-way reversing valve (SANHUA SHF-4H-23 U-P), a fin-tube condenser (VARKI VHF-G3), R410A refrigerant, and an electronic expansion valve (SANHUA PQM10058). The ASHP evaporator was the main focus of the study; the test evaporator was an L-shaped copper-tube, aluminum-fin heat exchanger with S-shaped tube circuitry and no manifolds, featuring vertically oriented fins with the spacing of 1.8 mm. The long leg of L-shaped heat exchanger is 60 cm long, the short leg is 19 cm long, and the curved corner radius is 8.5 cm.

The enthalpy-difference laboratory used in this study is located in the College of Architectural Engineering at Jiaxing University which comprises a 5-HP enthalpy measurement rig. The laboratory is divided into two separate chambers: one chamber simulates the outdoor environment in which installed the outdoor test unit. The outdoor-side temperature and humidity are controlled by a heat pump system, a heater, and a humidifier. The other chamber simulates the indoor environment, in which installed the indoor test unit. The indoor-side temperature and humidity were similarly controlled by a heat pump system, a heater and a humidifier. By deploying high-precision temperature and humidity sensors at the airflow inlet and outlet of the condenser heat exchanger and testing the velocity of airflow, the system calculates the enthalpy rise or drop through the coil according to the enthalpy-difference method to evaluate thermal performance (Fig. 1).

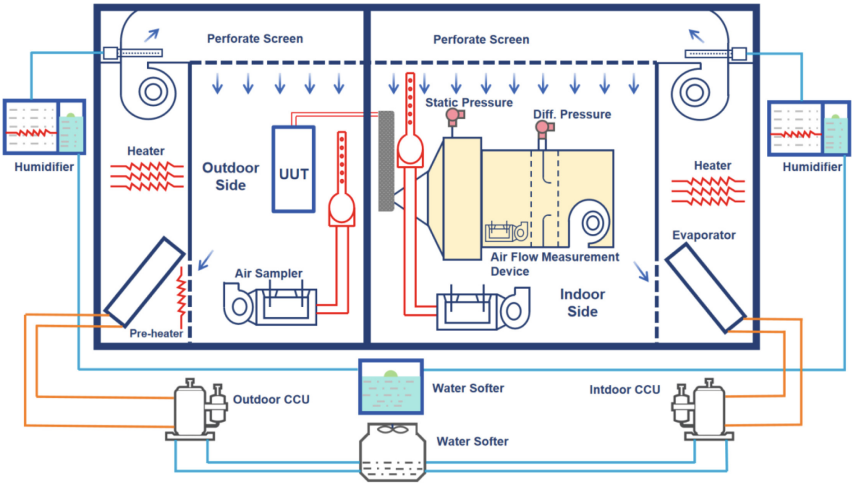


Fig. 1. Layout & Equipment Schematic of enthalpy-difference laboratory.

To comprehensively characterize the unit's heating and defrosting cycle, the following instrumentation was deployed: a thermocouple at the compressor discharge pipe to record discharge temperature; a thermocouple upstream of the electronic expansion valve for pre-valve temperature; temperature and humidity probes at the outdoor unit fan inlet to monitor outdoor ambient conditions; two thermocouples located on different locations of evaporator; a power meter in the main power line to measure total electrical consumption; an anemometer inside the indoor unit air duct to measure airflow velocity; two temperature and humidity probes at the indoor-unit airflow inlet and outlet; a temperature and humidity probe in the indoor environment to monitor indoor ambient conditions. The airflow velocities at the evaporator air inlet were measured using a handheld hot-wire anemometer (TES-1341).

2.2 Data Collection and Processing

The total heating capacity of the test unit was determined using the air enthalpy difference method on the condenser side. Specifically, the dry-bulb temperature $T_{d,\,in}$ and wet-bulb temperature $T_{w,\,in}$ at the condenser inlet were measured, and the corresponding air enthalpy h_{in} was obtained using thermo-physical database software. Similarly, the dry-bulb temperature $T_{d,\,out}$ and wet-bulb temperature $T_{w,\,out}$ at the condenser outlet were measured to determine the outlet air enthalpy h_{out}. The air mass flow rate M was calculated based on the measured airflow velocity $v_{airflow}$, the cross-sectional area of the air duct A, and the air density ρ_{air} using the following equation:

$$\mathrm{M} = v_{airflow} A \rho_{air} \tag{1}$$

The total heating capacity Q of the unit was calculated using the following equation:

$$\mathrm{Q} = \mathrm{M}(h_{out} - h_{in}) \tag{2}$$

The coefficient of performance COP of the test unit was calculated as the ratio of the heating capacity Q to the input power P using the following equation:

$$\mathrm{COP} = \frac{\mathrm{Q}}{\mathrm{P}} \times 100\% \tag{3}$$

The aforementioned airflow velocity, heating capacity and COP data were measured and calculated by the enthalpy-difference laboratory's system. Since the ASHP unit itself cannot directly obtain indoor-side airflow data, heating capacity and COP values are challenging to calculate onboard. To address this, we developed an empirical correlation to estimate heating capacity based on fan motor current and indoor-side air inlet/outlet temperatures, achieving a root-mean-square deviation (RMSD) of 9.47%. Subsequently, COP was calculated using the unit electrical current and voltage data.

2.3 COP-Based Defrost Control Strategy

The traditional defrost control strategy of the ASHP unit uses operating time, ambient temperature, and fin temperature as criteria for the start of defrosting. When the operating time exceeds a preset value (45 min under the test conditions) and the difference between ambient and fin temperatures exceeds 8 °C, a defrost cycle is triggered. The COP-based control strategy abandons the traditional temperature-based criterion and instead uses the coefficient of performance (COP) calculated by the unit itself to serve as the basis for determining the start of defrosting. In the modified defrost strategy, the overall COP for one complete heating–defrosting cycle is calculated using the following equation:

$$COP_c = \frac{H}{E + E_{defrost}} \tag{4}$$

Here, H denotes the cumulative heating capacity from the compressor startup in the current heating–defrosting cycle up to present. E denotes the cumulative electrical energy consumption of the unit from compressor startup in the current cycle up to present.

$E_{defrost}$ denotes the electrical energy consumption during the last defrost time(for the first heating–defrosting cycle, a default value is used).

In actual defrost control, it is often difficult to obtain COP. The units in the tests were equipped additionally with a power meter for the total unit and a power meter for the indoor fan. The power meter for the total unit was used to obtain the total electric consumption data of the unit, while the power meter for the indoor fan was used to obtain the electric consumption data of the fan, from which the airflow rate data is estimated. The modified defrost strategy adjusts the original defrost-entry and defrost-exit setpoints based on the unit's overall COP.

3 Results and Discussion

3.1 Wettability Test (Contact Angle Measurement)

The surface wettability of superhydrophobic-coated aluminum plates was evaluated using a contact angle measurement platform. Deionized water droplets (volume: 5 μL) were gently deposited onto the horizontal sample surface, and the static water contact angle (WCA) was measured at ambient conditions (23 ± 1 °C, RH 50 ± 5%) following ASTM D7334. Advancing and receding contact angles were also recorded to assess hysteresis, yielding values of 165° and 155°, respectively. The resulting static WCA of 164° and a sliding angle below 7.5° confirmed the coating's superhydrophobic character by Wenzel and Cassie–Baxter criteria. This methodology demonstrates reliability and reproducibility of following frosting and defrosting experiments.

3.2 Frosting and Defrosting Test

All tests were carried out under standard defrost conditions (outdoor dry-bulb temperature of 2 °C and wet-bulb temperature of 1 °C; indoor dry-bulb temperature of 20 °C and wet-bulb temperature of 15 °C). During the testing procedure, the test unit was permitted to commence operation only after the temperature and humidity on both the indoor and outdoor chambers of the enthalpy-difference laboratory had reached their preset values and stabilized.

During the testing procedure, the ASHP unit undergoes a heating–frosting–defrosting cycle, i.e., startup → heating (frosting) → defrosting → heating (frosting) → defrosting, and so on. The period between initial startup and the first defrost (marked by compressor first shutdown for defrost) is defined as the first defrost interval. The period between the end of defrost (marked by compressor start for heating) and the start of the next defrost (marked by compressor shutdown for defrost) is defined as a defrost interval. The period between the start of defrost (marked by compressor shutdown for defrost) and the end of defrost (marked by compressor start for heating) is called the defrost time. A consecutive heating (frosting) → defrosting sequence constitutes a single heating–defrosting cycle.

The tests were divided into three groups. Group 1: the evaporator heat exchanger employed with original hydrophilic aluminum fins, Group 2: the evaporator heat exchanger employed with superhydrophobic-coated aluminum fins, while retaining the same factory-default defrost control strategy as Group 1, Group 3: the evaporator heat

exchanger employed with superhydrophobic-coated aluminum fins, with the defrost control strategy switched to a modified COP-based strategy.

The real-time heat capacity curves for heating–defrosting cycles are shown in Fig. 2. During defrosting, the indoor-unit fan is shut off, resulting in heat capacity of zero. The defrost intervals for the three test groups over 3 heating–defrosting cycles are shown in Fig. 3. Defrost energy consumption for three test groups during three cycles are shown in Fig. 4. After 8 h of consecutive operation, the overall defrost energy consumption and average COP (total heating capacity divided by total electrical consumption) for three test group are shown in Fig. 5. Surface images of the evaporator before the second defrosting are shown in Fig. 6. The phenomenon of solid-state bulk delamination of frost layers during defrosting is shown in Fig. 7.

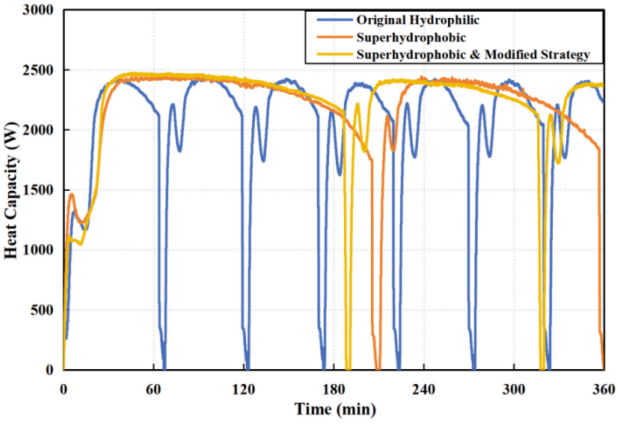


Fig. 2. Heat capacity as a function of time for original hydrophilic unit, superhydrophobic-coated unit and superhydrophobic unit with modified defrost strategy.

As shown in Fig. 2, the original hydrophilic evaporator started its first defrosting after 63.6 min. In contrast, the superhydrophobic-coated evaporator started its first defrost after 205.5 min, which is 323% of that of the original hydrophilic evaporator unit. Meanwhile, as shown in Fig. 6, after 60 min of continuous operation, the frost layer on the original hydrophilic evaporator surface was significantly thicker than that on the superhydrophobic-coated evaporator surface, which can be revealed by visual inspection. These results demonstrate the superhydrophobic coating's strong frost-delay effect. The third group, employing modified COP-based control strategy, reached its first defrosting at 186.6 min—slightly earlier than the second group with unmodified defrost control strategy—because the modified control strategy triggered defrosting early to avoid prolonged low-efficiency operation under condition of severe surface frosting.

As shown in Fig. 3, the average defrost interval for the first three heating-defrosting cycles of the original hydrophilic evaporator was 55.3 min, whereas the superhydrophobic-coated evaporator averaged 155.3 min—281% of the original's average interval. After long time operation, the original hydrophilic evaporator's defrost interval stabilized at 46 $\pm$ 0.1 min, while the superhydrophobic-coated evaporator's

defrost interval stabilized at 79.6 ± 5.1 min—roughly 173% of the former—demonstrating that the superhydrophobic coating continues to provide effective frost-delay performance after long time operation.

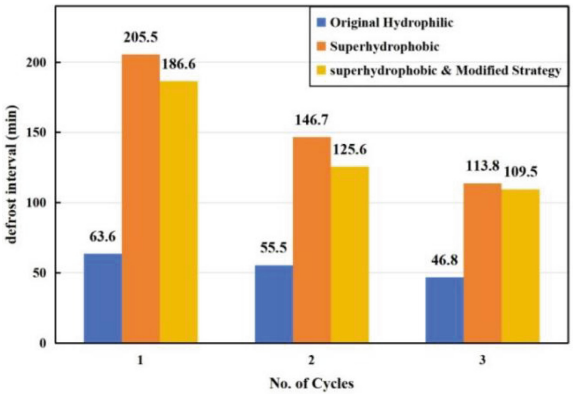


Fig. 3. Defrost interval over 3 heating-defrosting cycles for three test groups.

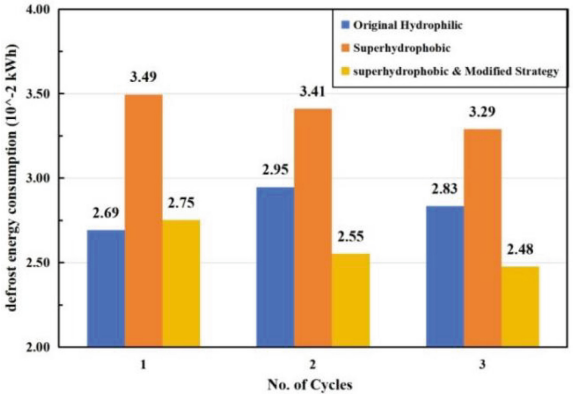


Fig. 4. Defrost energy consumption over 3 heating-defrosting cycles for three test groups.

As shown in Fig. 4, the average energy consumption over three defrost cycles was 0.0282 kWh for the original hydrophilic evaporator and 0.0340 kWh for the superhydrophobic-coated evaporator, with the single-cycle defrost energy consumption of the latter being 120% of the former. For the superhydrophobic evaporator using the modified defrost control strategy, the average energy consumption over three defrost cycles was 0.0259 kWh, with its single-cycle consumption being 92% of the original hydrophilic evaporator and 76% of the superhydrophobic evaporator with the original defrost control strategy. Although the superhydrophobic coating showed no significant reduction in single-cycle defrost energy consumption—even exceeding that of the

original hydrophilic evaporator—its advantage in defrost energy consumption per unit time becomes evident when considering the extended defrost intervals enabled by the coating's frost-delaying effect.

As shown in Fig. 5a, after 8 h of operation, the total defrost energy consumption was 0.2595 kWh for the original hydrophilic evaporator, 0.1020 kWh for the superhydrophobic evaporator, and 0.0788 kWh for the superhydrophobic evaporator with the modified strategy. The superhydrophobic evaporator reduced defrost energy consumption by 61% compared to the hydrophilic evaporator over 8 h, while superhydrophobic evaporator with modified defrost strategy achieved a 70% reduction versus the hydrophilic evaporator and a 24% reduction versus the superhydrophobic evaporator with the original strategy. Thus, the superhydrophobic coating substantially reduces defrost energy consumption during prolonged operation of ASHPs, and the modified defrost control strategy enables further reduction.

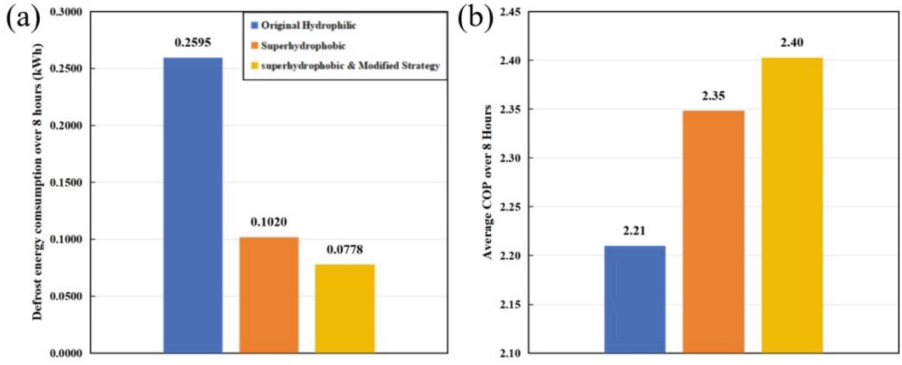


Fig. 5. Overall defrost energy consumption (a) and average COP (b) over 8 h for three test groups.

Beyond providing frost-delaying effect, the superhydrophobic coating, as observed in Fig. 6, multiplies the defrost interval. Moreover, the superhydrophobic-coated evaporator exhibits distinct defrost phenomena during the defrosting process. During reverse-cycle defrosting, solid-state bulk delamination of frost layers occurred on the superhydrophobic surface (Fig. 7). This phenomenon, where intact frost slabs separated from the exchanger, accelerated defrosting by reducing latent heat absorption. It is precisely this reduction in latent heat absorption that enables the superhydrophobic-coated evaporator with modified defrost strategy to complete defrosting with less energy consumption when its surface frosting conditions are comparable.

As shown in Fig. 5b, over 8 h of operation, the unit equipped with original hydrophilic evaporator attained an average COP of 2.21, while the superhydrophobic-coated evaporator unit attained an average COP of 2.35, and the superhydrophobic-coated evaporator unit using modified COP-based defrost strategy attained an average COP of 2.40. The superhydrophobic-coated evaporator unit's average COP attained an 6.3% increase over the original hydrophilic evaporator unit, and implementing modified COP-based defrost strategy attained a 2.3% increase compared to the default defrost strategy. Although unit with modified COP-based defrost strategy slightly shortens the defrost interval, it

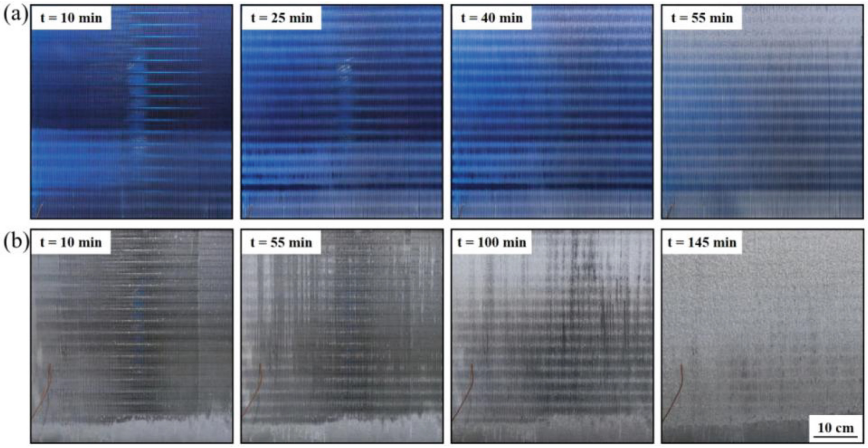


Fig. 6. Front-view photographs of original hydrophilic evaporator (a) and superhydrophobic-coated evaporator (b) during the frosting process.

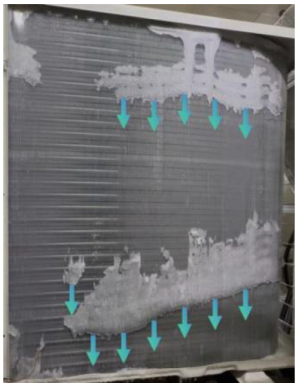


Fig. 7. Phenomenon of solid-state bulk delamination of frost layers during defrosting.

raises the eight-hour average COP. Compared with the original hydrophilic evaporator unit with default defrost strategy, the COP-based strategy together with application of superhydrophobic coating reduces the defrost time to 31% and the eight-hour average COP by 8.6%, demonstrating that the modified COP-based defrost control strategy is a suitable defrost strategy when retrofitting with superhydrophobic-coated evaporators.

Although the superhydrophobic coating demonstrates excellent performance in extending defrost intervals and reducing defrost energy consumption, its direct application to commercial ASHP evaporators presents challenges. During reverse-cycle defrosting, bulk delamination of frost layers occurs on the superhydrophobic-coated evaporator surface. The baseplate of existing commercial units captures these unmelted frost blocks. Due to the non-fluidic nature of frost blocks, ice progressively accumulates and freezes within the baseplate over time, causing severe ice buildup inside the outdoor unit. During defrost cycles, this accumulated ice may be ejected through the outlet vent by the fan or

impact the fan blades, posing operational risks. Subsequent testing will involve refitting current units to accommodate the superhydrophobic-coated evaporator.

4 Conclusion

To address the critical challenge of evaporator frosting in ASHPs, this study implemented a superhydrophobic coating on evaporator fins with COP-based defrost strategy. Key findings demonstrate that: the superhydrophobic coating extended the first defrost interval to 323% of the hydrophilic baseline, with stabilized defrost intervals maintained at 173% of the original after prolonged operation. Despite a 20.6% increase in per-cycle defrost energy under default logic, cumulative energy consumption over 8 h decreased by 61% due to extended defrost interval. The modified COP-based strategy further reduced total defrost energy by 24% versus the coated baseline, achieving a 70% reduction compared to the uncoated system. Unique frost detachment behavior minimized latent heat absorption, enabling faster defrost completion at comparable frosting levels. Eight-hour average COP increased by 6.3% with the coating alone and by 8.6% with the integrated coating-strategy approach.

Our future work will focus on mitigating operational risks from frost accumulation by testing fan reverse rotating during defrost cycles, redesigning baseplate geometries in commercial units to prevent frost buildup, validating long-term coating durability under real-world cyclic frosting/ defrosting stresses.

This synergistic approach—combining surface engineering with adaptive control—establishes a pathway for high-efficiency ASHP operation in cold, humid climates while ensuring reliability and user comfort.

References

1. Cao, S., Wang, Y.: A review of defrosting technologies for air source heat pumps. Front. Sci. Eng. **5**(1), 48–55 (2025)
2. Huang, D., Li, Q., Yuan, X.: Comparison between hot-gas bypass defrosting and reverse-cycle defrosting methods on an air-to-water heat pump. Appl. Energy. **86**(9), 1697–1703 (2009)
3. Ye, Z., Wang, Y., Yin, X., Song, Y., Cao, F.: Comparison between reverse cycle and hot gas bypass defrosting methods in a transcritical CO_2 heat pump water heater. Appl. Therm. Eng. **196**, 117356 (2021)
4. Martin, C., Oppenheim, P., Bush, J., Stillman, H.: Alternative defrost strategies for residential heat pumps. In: Proceedings of the International Refrigeration and Air Conditioning Conference, p. 1898. Purdue University, West Lafayette (2018)
5. Li, Y., Chen, G., Tang, L., Liu, L.: Analysis on performance of a novel frost-free air-source heat pump system. Build. Environ. **46**(10), 2052–2059 (2011)
6. Wang, F., Zhou, Y., Yang, W., Ni, M., Zhang, X., Liang, C.: Anti-frosting performance of sprayable superhydrophobic coating suitable for outdoor coil of air source heat pump. Appl. Therm. Eng. **169**, 114967 (2020)
7. Gu, Y., He, G., Li, S., Ding, W., Li, H., Duan, J.: Study on frost-suppression characteristics of superhydrophobic aluminum surface heat exchanger applied in air source heat pump. Sustainability. **14**(4), 1954 (2022)
8. Li, R., et al.: Performance improvement of vapor compression heat pump with superhydrophobic finned-tube evaporator. J. Build. Eng. **87**, 109013 (2024)

Dynamic Characteristics in the Startup Stage of a Transcritical CO_2 Heat Pump

Hongzhi Liu[1](✉), Minglu Qu[2], and Jing Lv[3]

[1] Environmental System Research Laboratory, Faculty of Engineering, Hokkaido University, Kita-ku, Sapporo, Hokkaido 060-8628, Japan
liuhz@eng.hokudai.ac.jp

[2] School of Environment & Architecture, University of Shanghai for Science & Technology, No.516, Jungong Road, Shanghai 200093, China

[3] Architecture Engineering College, Qingdao Bin Hai University, Qingdao 2066555, China

Abstract. The transcritical CO_2 heat pump is highly efficient and environmentally friendly, making it a promising technology for water heating. This study investigates the startup characteristics of a transcritical CO_2 heat pump water heater, focusing on the effects of inlet water temperature, flow rate, expansion valve opening, and startup strategy on the heating performance. An optimized startup strategy was proposed to improve startup efficiency and reduce energy consumption. Results show that lower inlet water temperatures and smaller expansion valve openings shorten the startup time. A comparison of cold and hot startup modes reveals that the hot startup method can reduce the stabilization times by over 30%, with significant reductions in power consumption.

Keywords: CO_2 heat pump · COP · Startup

1 Introduction

The need for energy-efficient, environmentally friendly technologies in the residential heating sector has led to a growing interest in heat pump water heaters. Among these, transcritical carbon dioxide (CO_2) systems stand out due to their high efficiency and favorable environmental properties—namely, zero ozone depletion potential (ODP = 0) and an exceptionally low global warming potential (GWP = 1) [1]. CO_2-based systems face practical limitations. One key issue is the extended startup time compared to conventional systems. During this transient period, it takes time for the heat pump to raise water to the desired outlet temperature. This delay impacts user satisfaction, especially on residential applications where hot water demand is immediate and often irregular. In transcritical CO_2 systems, the startup dynamics are complex due to the thermodynamic behavior of CO_2 near and above its critical point. This sensitivity necessitates precise control during startup. Numerous studies have focused on the steady-state performance of transcritical CO_2 systems [2]. Fewer studies have addressed the transient startup behavior, which is critical for real-world application. Therefore, the startup performance of a CO_2 heat pump water heater will be studied experimentally in order to decrease the startup time and increase energy efficiency.

© The Author(s), under exclusive license to Springer Nature Singapore Pte Ltd. 2025
L. Ni et al. (Eds.): CCHVAC 2025, ESE, pp. 48–57, 2025.
https://doi.org/10.1007/978-981-95-3253-7_6

2 Experimental Setup and Method

2.1 System Configuration and Component

The experimental CO_2 heat pump system includes four primary components: a semi-hermetic piston-type CO_2 compressor (Dorin CD 180H), a gas cooler (tube-in-tube counterflow type), an electronic expansion valve (JKV-24D27), and a fin-tube type evaporator. Figure 1 provides the schematic diagram of the system, showing all components and sensor locations, whose picture is shown in Fig. 2. The CO_2 flows through the gas cooler and transfers heat to the domestic water loop. The refrigerant circuit is designed to handle pressures exceeding 10 MPa, with all piping and fittings tested for safety compliance. The water-side circuit consists of a circulation pump, temperature-controlled inlet system, and flow meters. The specifications of the main four components are listed in Table 1. Measurements were recorded at 2-s intervals, and the main sensors are listed in Table 2.

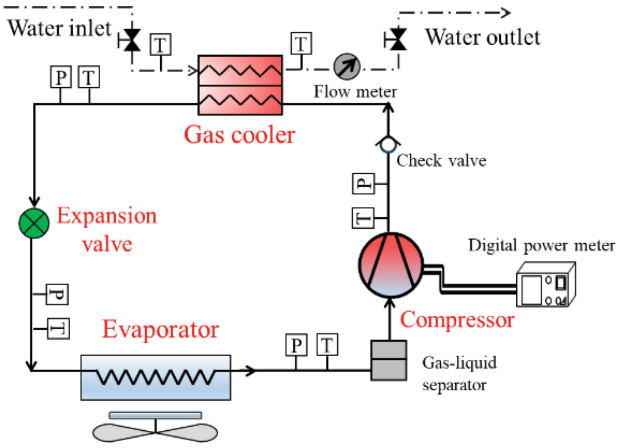


Fig. 1. Schematic diagram of experimental CO_2 heat pump system.

Table 1. Main components of the heat pump prototype.

Component	Type	Manufacturer	Model	Specification
Compressor	Semi-hermetic piston-type	Dorin	CD 180H	Power: 1.4 kW Displacement: 1.12 m^3/h Rated Speed: 1450 rpm

(*continued*)

Table 1. (*continued*)

Component	Type	Manufacturer	Model	Specification
Gas cooler	Multi-tubular tube-in-tube	–	–	Inner Tube: (DE) = 9.52 mm, Thickness = 1.5 mm Outer Tube: (OD) = 16 mm, Thickness = 1.5 mm
Expansion valve	Electronic	Saginomiya, Tokyo, Japan	JKV-24D27	Maximum Working Pressure: 15 MPa Operating Temperature Range: −30 to 70 °C
Evaporator	fin-tube type	–	–	Tube Length: 0.86 m Outer Tube: OD = 7 mm, Thickness = 0.41 mm Fins: Flat fins, Fin spacing = 1.9 mm

Table 2. Measurement sensors set in the heat pump prototype.

Sensors	Type	Manufacturer	Model	Properties
Temperature sensor	Pt100	Heraeus, Germany	–	$-200 < T < 550$ °C, ±0. 5%
Pressure sensor	Digital	Shanghai Tianmu Automation Instrument Co., Ltd. China	NS-F NS-I7	$0 < P < 20$ MPa, ±0.3% F.S.
Mass flow meter	Turbin	Hangzhou Meacon, China	LWGY-MIK-DN6	0.06 to 0.6 m^3/h, ±1.0% F.S.
Power meter	–	Fujian Hongrun Precision Instrument Co., Ltd., China	OHR-C300	AC Voltage: 100–500 V AC Current: 0.5–5 A
Thermo-Hygrometer	–	Testo, Germany	Testo 625	−10 ~ 60 °C, ±0.5 °C 0 ~ 100% RH, ±2.5%RH

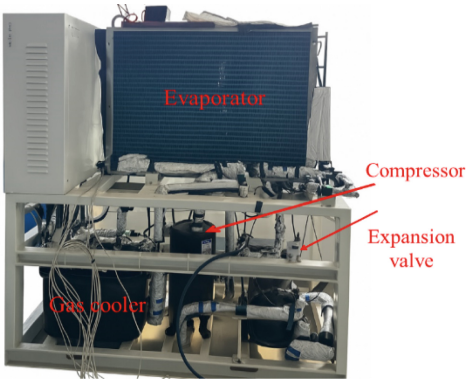


Fig. 2. Picture of experimental heat pump system.

2.2 Test Procedures and Conditions

Before each test, the system was stabilized to the desired initial condition. For cold startups, the unit was powered off for at least 30 min, ensuring thermal equilibrium. For hot startups, the unit was reinitiated after 9 or 15 min to simulate rapid cycling. Each test was performed three times for repeatability, and averaged values were used for analysis. The startup phase was defined as the period from compressor start until the outlet water temperature stabilized within ±0.5 °C of the target temperature. The experimental conditions are listed in Table 3.

Table 3. Experimental conditions.

Parameters	Values					
Inlet Water Temperature (°C)	8	12	16	20	24	28
Water Flow Rate (L/h)	80	100		120	140	
Ambient Temperature (°C)	10	15		20	25	
Expansion Valve Opening (%)	20	25		30	35	

2.3 Data Reduction and Uncertainty Analysis

Thermodynamic properties of CO_2 were computed using REFPROP 10.0. The transient water heating capacity Q_w can be calculated from the sensible heat of water as shown in Eq. 1.

$$Q_w = \dot{m}_w \cdot c_{p,w} \cdot \left(T_{w,out} - T_{w,in}\right) \tag{1}$$

The water heating COP was calculated as the ratio of the heating capacity Q_w to the electric power consumption of the compressor W.

$$\mathrm{COP} = \frac{Q_w}{W} \tag{2}$$

An uncertainty analysis was conducted according to the theory of measurement uncertainty [3]. The equation to calculate uncertainty of calculation variables can be seen in Eq. 3 [3], where R and δR presents calculated variable based on several measured variables and its uncertainty, X_i represents the ith measured variable, and δX_i is uncertainty of the ith variable.

$$\delta R = \left[\sum_{i=1}^{N} \left(\frac{\partial R}{\partial X_i} \delta X_i \right)^2 \right]^{1/2} \tag{3}$$

The uncertainties of the heating capacity Q_{tw} and heating COP were calculated as ±2.4%, ±2.4%, respectively.

3 Results and Discussion

3.1 Effect of Inlet Water Temperature

Under outdoor conditions of a dry-bulb temperature of 15 °C, a wet-bulb temperature of 12 °C, a water inlet flow rate of 100 L/h, and an expansion valve opening of 30%, experiments were conducted by varying the inlet water temperature at 8 °C, 12 °C, 16 °C, 20 °C, 24 °C, and 28 °C. As shown in Fig. 3, within the first 20 s after the compressor starts, under conditions of higher inlet water temperature, the outlet water temperature remains unchanged. In contrast, when the inlet water temperature is lower, the outlet temperature shows a slight increase due to the influence of a higher discharge temperature. Subsequently, between 20 and 90 s, the outlet water temperature rises rapidly. From 90 to 300 s, the outlet water temperature continues to rise, with a similar increase of about 17.1 °C under all conditions. During startup, the time required to reach stable outlet temperature for inlet water temperatures of 8 °C, 12 °C, 16 °C, 20 °C, 24 °C, and 28 °C is 820 s, 840 s, 870 s, 925 s, 970 s, and 1030 s respectively.

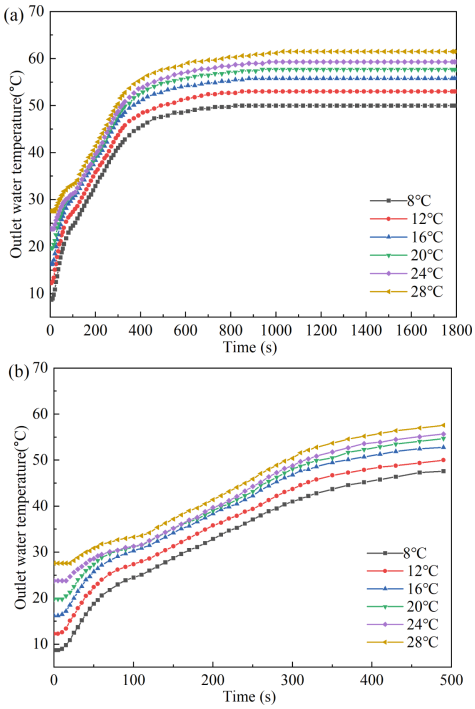


Fig. 3. Outlet water temperature variation for different inlet water temperatures (a) 1800s and (b) first 500 s.

Discharge pressure increased more rapidly due to the larger thermal load, and this is reflected in the steeper pressure gradient shown in Fig. 4 increases. Due to the initial opening of the expansion valve being 80%, the discharge pressure does not continue to rise indefinitely. As a result, the higher the inlet water temperature, the faster the discharge pressure reaches a steady state. Between 90 and 150 s, the expansion valve opening decreases to 60%, and the discharge pressure begins to rise more rapidly. From 150 to 210 s, the valve opening further reduces to 45%, and the discharge pressure continues to increase. It is observed that the lower the inlet water temperature, the sooner the pressure curve tends to stabilize.

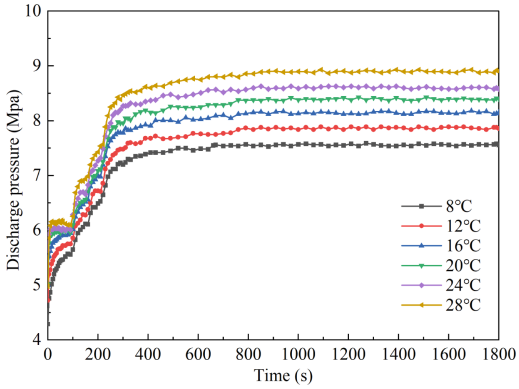


Fig. 4. Discharge pressure variations at different inlet temperatures.

Figure 5 illustrates that the variation trends of instantaneous COPs under different inlet water temperatures are generally similar. Specifically, within the first 90 s following compressor startup, the COPs increase rapidly. Subsequently, during the period from 90 to 250 s, the COPs exhibit an overall upward trend with noticeable fluctuations, particularly more pronounced under lower inlet water temperatures. Finally, from 250 to 1030 s, the COPs increase gradually and smoothly, eventually reaching a steady-state after a transitional phase.

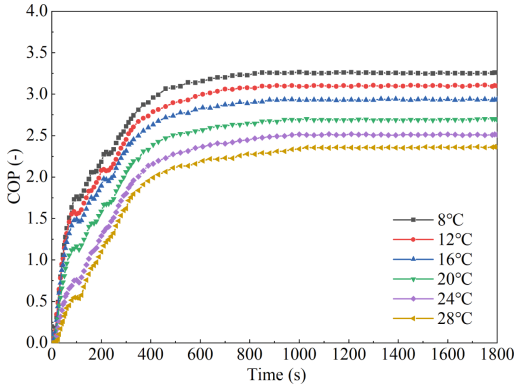


Fig. 5. Variations of COP at different inlet temperatures.

3.2 Effect of Water Flow Rate

Under ambient conditions of a dry-bulb temperature of 25 °C, a wet-bulb temperature of 21 °C, an inlet water temperature of 24 °C, and an expansion valve opening of 30%, an experimental analysis was conducted by varying the inlet water flow rates. Higher flow rates facilitated greater heat transfer rates but also increased the thermal inertia of the water side, delaying temperature stabilization.

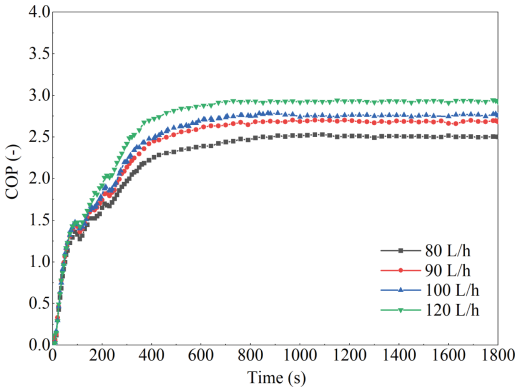


Fig. 6. COP variations for flow rates of 80, 90, 100, and 120 L/h.

Figure 6 presents the variation curves of the system's instantaneous COPs under different inlet water flow rates. Within the first 90 s after the compressor starts, the system COPs rise rapidly, with the smallest increase observed at the flow rate of 80 L/h. Then, during the period from 90 to 300 s, the system COPs exhibit oscillating growth. This is caused by the adjustment of the expansion valve opening, which leads to a sudden increase in compressor power consumption, while the heat transfer rate cannot increase immediately, resulting in a slight drop in COPs. The startup times for COPs under inlet water flow rates of 80 L/h, 90 L/h, 100 L/h, and 120 L/h are 1030 s, 970 s, 760 s, and 670 s, respectively, which correspond to the startup times of the outlet water temperature under the same conditions.

3.3 Effect of Expansion Valve Opening

Under ambient conditions with a dry-bulb temperature of 25 °C, a wet-bulb temperature of 21 °C, an inlet water temperature of 24 °C, and an inlet water flow rate of 100 L/h, experimental analysis was conducted. Figure 7 presents the variation of the system's instantaneous COPs during startup under different expansion valve openings. Larger openings result in increased mass flow as shown in Fig. 8, but lower discharge pressure. Increasing the valve opening from 20% to 35% decreased startup time from 1030 s to 730 s (a 29.1% improvement). However, openings beyond 35%) could reduce outlet temperature due to lower discharge temperature.

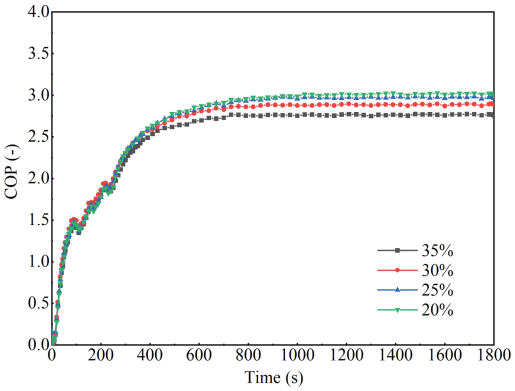


Fig. 7. Variations of COP for expansion valve openings (20% to 35%).

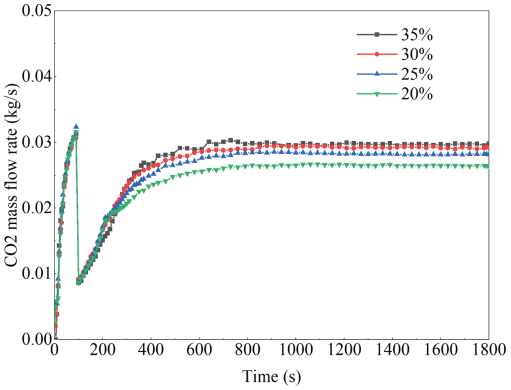


Fig. 8. Variations of CO_2 mass flow rate for expansion valve openings (20% to 35%).

3.4 Cold vs. Hot Startup Behavior

In the nominal condition, the dry-bulb temperature is 6 °C with a wet-bulb temperature of 12 °C. The inlet water flow rate is maintained at 100 L/h, and the inlet water temperature is set to 17 °C. The opening of expansion valve is 30%. Figure 9 compares COP stabilization between hot and cold modes. The COPs for the 9-min hot start rapidly increase to 1.76 within the first 90 s after the compressor starts, whereas the COPs for the cold start reach only 1.08 during the same period. This difference is attributed to the lower heat transfer and higher power consumption observed during the early stage of the cold start. Subsequently, between 90 and 300 s, the COPs under the hot start condition exhibit a significant decline, primarily due to the sharp increase in power consumption while the outlet water temperature rises at a slower rate. During this period, the gap between the COPs of the hot and cold start modes gradually narrows. Finally, from 300 to 880 s, the system COPs under both startup modes gradually stabilize and enter a steady-state condition.

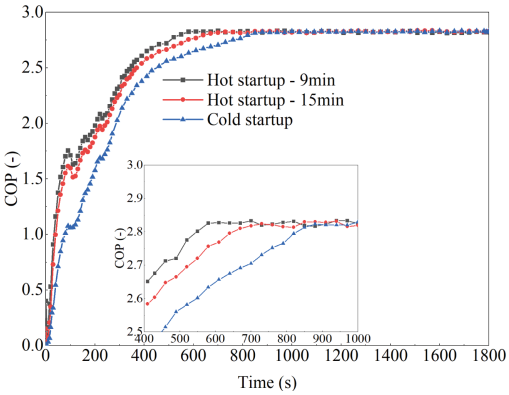


Fig. 9. COP comparison – hot vs. cold startup under nominal condition.

4 Conclusion

This study presented an investigation into the startup performance of a transcritical CO_2 heat pump water heater. (1) Lowering the inlet water temperature significantly shortened the time required to reach stable outlet conditions. A drop from 28 °C to 8 °C reduced startup time by 25.6% due to an enhanced thermal gradient driving more effective heat exchange in the gas cooler. (2) Increased flow rates reduced the time to reach target outlet temperature and the peak outlet temperature. (3) Modulating the valve opening can obtain a high COP because of the optimized discharge pressure of compressor. (4) Hot startup scenarios offered substantial benefits. Stabilization times were reduced by over 30%, with significant reductions in power consumption.

References

1. Otón-Martínez, R.A., Illán-Gómez, F., García-Cascales, J.R., Velasco, F.J.S., Reda Haddouche, M.: Optimal-pressure performance of CO_2 heat pump with IHX. Appl. Therm. Eng. **215**, 118991 (2022)
2. Wang, J., Belusko, M., Evans, M., Liu, M., Zhao, C., Bruno, F.: A comprehensive review and analysis on CO_2 heat pump water heaters. Energ. Conv. Manag. **15**, 100277 (2022)
3. Moffat, R.J.: Describing the uncertainties in experimental results. Exp. Thermal Fluid Sci. **1**(1), 3–17 (1988)

Applicability Analysis of Freezing Concentration Method Applied in Frost-Free Air Source Heat Pumps' Solution Regeneration for Cold Regions

Liutao Zhu[1], Xiaosong Zhang[1,2], and Shifang Huang[1,2(✉)]

[1] School of Energy and Environment, Southeast University, Nanjing, China
shifang_huang@seu.edu.cn

[2] MOE Engineering Research Center of Building Energy Equipment and Environment, Nanjing 210096, China

Abstract. The application of air source heat pumps in cold regions is severely limited by frost accumulation during winter. The frost-free air source heat pump (FFASHP) employs antifreeze solution as an intermediate heat transfer medium between the refrigerant and air, effectively resolving the frosting issue in finned-tube heat exchangers. However, this approach introduces additional energy consumption for solution regeneration and concentration regulation. Conventional thermal regeneration methods require overcoming the latent heat of vaporization of water, whereas freezing concentration circumvents this by utilizing the latent heat of fusion. To investigate the applicability of this method, this study proposes a progressive freeze concentration model to simulate the regeneration dynamics of calcium chloride solution using a vapor-compression refrigeration cycle. Simulation results reveal that the regeneration process can be divided into two stages: an initial period dominated by sensible cooling, and a subsequent phase characterized by ice formation and latent heat removal. The coefficient of performance (COP) declines steadily throughout the process—from approximately 3.8 initially to below 1—mainly due to the increasing thermal resistance induced by ice accumulation. The average COP was found to be around 1.4. Additionally, the evaporation temperature has a significant influence on regeneration performance. Lower evaporation temperatures accelerate ice formation but also reduce energy efficiency. These findings demonstrate the trade-off between regeneration speed and system efficiency, highlighting the importance of staged or optimized operation strategies. The proposed model provides a theoretical foundation for the design and optimization of low-energy regeneration schemes in FFASHP systems.

Keywords: Frost-free air-source heat pump · Solution regeneration · Freezing concentration

1 Introduction

In the global effort to decarbonize the building sector, heat pumps have become an increasingly important solution due to their high energy efficiency and ability to utilize low-grade environmental heat. By transferring heat from ambient sources—such as air,

© The Author(s), under exclusive license to Springer Nature Singapore Pte Ltd. 2025
L. Ni et al. (Eds.): CCHVAC 2025, ESE, pp. 58–65, 2025.
https://doi.org/10.1007/978-981-95-3253-7_7

water, or ground—rather than generating it through combustion, heat pumps significantly reduce both primary energy consumption and greenhouse gas emissions. According to the International Energy Agency, heat pumps could supply more than 20% of the global heating demand in buildings by 2050 under net-zero scenarios [1].

Among various types, air-source heat pumps (ASHPs) are particularly popular due to their simple installation, low capital cost, and relatively mature market deployment. They are also flexible enough to be integrated with renewable energy sources, thermal storage, and smart grid control systems, enabling their participation in future resilient and low-carbon energy infrastructures [2]. However, in cold and humid conditions, frost formation on the outdoor evaporator remains one of the main operational challenges for ASHPs. As ambient air passes over the cold evaporator surface, moisture condenses and freezes, forming frost layers that reduce heat transfer efficiency, increase air-side pressure drops, and degrade system performance. To remove frost, conventional ASHPs rely on periodic reverse-cycle defrosting, which interrupts heating, consumes additional energy, and shortens compressor lifespan [3].

To overcome this limitation, frost-free air-source heat pump systems (FFASHPs) have been proposed. These systems typically separate the evaporator from direct contact with ambient air by using an indirect antifreeze loop, in which a secondary fluid (e.g., a calcium chloride solution or ethylene glycol mixture) circulates between the outdoor heat exchanger and a hydronic loop exposed to ambient air [4]. The evaporator remains frost-free by operating below the freezing point of water but above the freezing point of the antifreeze solution. Such systems allow for continuous operation in sub-zero temperatures without the need for defrost cycles, making them highly suitable for cold-region applications.

Nonetheless, the long-term stability of the antifreeze loop is challenged by dilution of the solution. Moisture ingress can gradually reduce the concentration of the antifreeze, thereby increasing its freezing point and reducing its ability to function safely under low-temperature conditions. Periodic regeneration of the antifreeze solution becomes necessary to restore its concentration and ensure frost protection. Traditional regeneration methods, such as thermal evaporation or vacuum distillation, rely on substantial thermal energy input, which is often scarce and difficult to access during the heating season, especially in decentralized building-scale systems. In contrast, cold energy—readily available from the heat pump's refrigeration cycle—is more accessible under winter conditions. Freeze concentration offers a promising alternative by utilizing cold energy to remove water through ice formation, rather than vaporization. Moreover, this method requires overcoming only the latent heat of fusion, which is approximately one-seventh of the latent heat of vaporization required in thermal regeneration processes, thus significantly reducing energy consumption in theory.

However, existing freeze concentration studies have primarily focused on food processing (e.g., fruit juice, dairy) or seawater desalination [5, 6]. Although the feasibility of freeze concentration for antifreeze regeneration has been experimentally demonstrated in prior studies [7, 8], its advantages and performance characteristics in the context of solution regeneration for frost-free air-source heat pump systems in cold climates remain insufficiently investigated.

To address this gap, we propose and apply a progressive freeze concentration numerical model tailored to the regeneration of calcium chloride ($CaCl_2$) solutions used in frost-free ASHP systems. The model simulates the coupled heat and mass transfer during ice formation, using a flat-plate heat exchanger where the solution is progressively frozen by the R22 refrigerant flowing inside the evaporator tubes. It integrates thermodynamic and transport property data of both refrigerant and solution, considers wall and ice-layer thermal resistances, and accounts for dynamic changes in concentration and freezing point.

This study aims to evaluate the feasibility and energy performance of the proposed method for antifreeze regeneration. Specifically, the simulation investigates how several critical operating parameters affect regeneration performance. The results provide insight into the practical application potential of freeze concentration in ASHP antifreeze loops, and offer guidance for system design and operational optimization.

2 Model and Methods

To investigate the application of freeze concentration in antifreeze regeneration for FFASHP systems, a transient numerical model of progressive freeze concentration was developed. The model simulates the gradual freezing of a calcium chloride ($CaCl_2$) solution on a flat-plate heat exchanger surface, where a vapor-compression refrigeration cycle provides the required cold energy. The governing framework couples heat transfer, mass transfer, phase change dynamics, and solution property variations to evaluate the regeneration performance under various operating conditions.

2.1 System Configuration and Assumptions

The modeled system comprises:

1. A vapor-compression cycle using R22 as the working fluid, including a scroll compressor, condenser, expansion valve, and evaporator.
2. A horizontal flat-plate evaporator, where R22 flows inside the tubes and the antifreeze solution flows outside.
3. A calcium chloride solution with an initial concentration between 13–15 wt.%, targeted to be concentrated via ice removal.

It is assumed that ice is presumed to form uniformly on the outer surface of the heat exchanger plate, which is made of copper with a known thermal conductivity. Additionally, the freezing point of the solution is treated as a function of concentration and is calculated using established empirical correlations.

2.2 Heat Transfer and Ice Growth Modeling

The cold energy is supplied by a vapor-compression refrigeration cycle modeled based on the empirical performance curves of a Copeland scroll compressor. The heat flux

transferred from the antifreeze solution through the ice layer and metal wall to the evaporating refrigerant is given by:

$$Q_e = \frac{T_{sol} - T_{eva}}{R_{sol} + R_{ice} + R_{wall} + R_{refe}} = m_{ref}\,\Delta h_e \tag{1}$$

Where T_{sol} is the bulk temperature of solution, T_{eva} is the evaporating temperature of R22. R_{sol}, R_{ice}, R_{wall}, and R_{refe} are the thermal resistances of solution-surface heat convection, the ice layer and copper wall and refrigeration-wall heat convection, respectively. m_{ref} is the mass flow of refrigerant and Δh_e is the specific enthalpy change in evaporator. The ice increases over time as:

$$\frac{dm_{ice}}{dt} = \frac{Q_e}{r_{ice}} \tag{2}$$

Where r_{ice} is the latent heat of fusion of ice. The heat flux transferred from refrigerant to the outdoor air is given by:

$$Q_e = \frac{T_{con} - T_{air}}{R_{air} + R_{wall} + R_{refc}} = m_{ref}\,\Delta h_c \tag{3}$$

Where T_{air} is the temperature of outdoor air, T_{eva} is the condensing temperature of R22. R_{air}, R_{wall}, and R_{refc} are the thermal resistances of air-surface heat convection, the ice layer and copper wall and refrigeration-wall heat convection, respectively. Δh_c is the specific enthalpy change in condenser.

2.3 Simulation Parameters

The following Table 1 gives a summary of base parameters set.

Table 1. Base parameters set.

Initial solution mass	Initial solution temperature	Evaporation temperature	Superheat	Outdoor air temperature
1000 kg	0 °C	−30 °C	5 °C	5 °C

3 Results and Discussion

3.1 Regeneration Dynamics and Freezing Characteristics

At the beginning of the regeneration process, the solution remains above its freezing point, and the available cooling capacity is primarily used to lower the solution temperature (see Fig. 1a). During this stage, the temperature drops rapidly due to the absence of latent heat absorption and minimal thermal resistance at the evaporator wall. Once the solution temperature reaches its equilibrium freezing point, ice formation begins on

the heat exchanger surface. As the process progresses, the cooling capacity is divided between further lowering the solution temperature and overcoming the latent heat of fusion required for ice formation. This transition leads to a noticeable decrease in the rate of temperature drop, while the ice mass begins to accumulate. Importantly, the ice layer growing on the evaporator surface introduces an additional thermal resistance, which slows down the heat transfer and reduces the freezing rate over time. As shown in Fig. 1a, the ice growth rate decreases progressively, reflecting the increased difficulty in extracting latent heat through the thickening ice layer. Furthermore, the accumulation of ice not only impedes heat transfer but also affects the refrigeration system performance. As shown in Fig. 1b, during the regeneration process, the condensing temperature gradually increases, resulting in a corresponding rise in compressor power consumption.

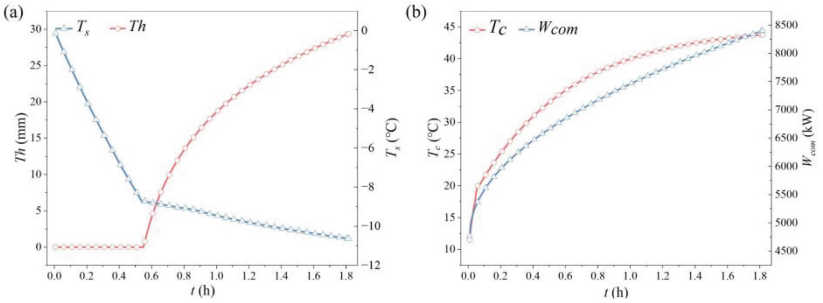


Fig. 1. Variation of (a) solution temperature, ice thickness, (b) condensing temperature, and compressor power with time.

The coefficient of performance (COP) of the refrigeration system drops significantly with time, indicating reduced energy efficiency. The system exhibited a high COP during the initial phase of regeneration, with values around 3.8. However, as the regeneration progressed and the ice layer gradually thickened, the COP dropped steadily throughout the process, eventually falling below 1 in the later stages. The average COP over the entire regeneration period was only approximately 1.4, reflecting a considerable decline in energy efficiency due to the progressive accumulation of ice. These findings highlight the necessity of adopting a staged regeneration strategy rather than attempting continuous, single-pass operation (Fig. 2).

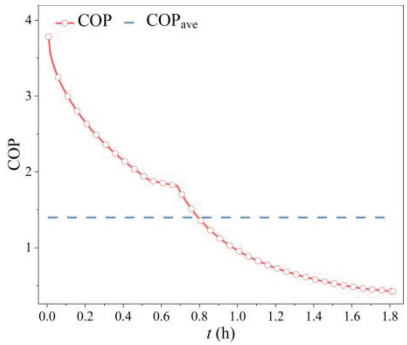


Fig. 2. Variation of COP with time and average COP.

3.2 Effect of Evaporation Temperature

The evaporation temperature plays a critical role in determining both the regeneration rate and the energy efficiency of the freeze concentration system. Simulation results show that a lower evaporation temperature significantly accelerates the regeneration process. This is primarily due to the increased temperature difference between the refrigerant and the antifreeze solution, which enhances the heat transfer rate at the evaporator wall. As a result, more latent heat is extracted from the solution in a shorter period, leading to a faster formation of ice and a more rapid concentration increase.

However, the benefit of faster regeneration at lower evaporation temperatures comes at the cost of reduced system efficiency. Specifically, the average COP decreases with decreasing evaporation temperature. This is a fundamental thermodynamic characteristic of vapor-compression refrigeration cycles: lower evaporation temperatures correspond to larger enthalpy lifts and thus higher compressor work for the same cooling effect. Consequently, although low-temperature operation enhances the rate of antifreeze recovery, it compromises the energy efficiency of the system. Therefore, a balance must be struck between regeneration speed and energy consumption, and the selection of evaporation temperature should be carefully optimized based on specific application priorities (Fig. 3).

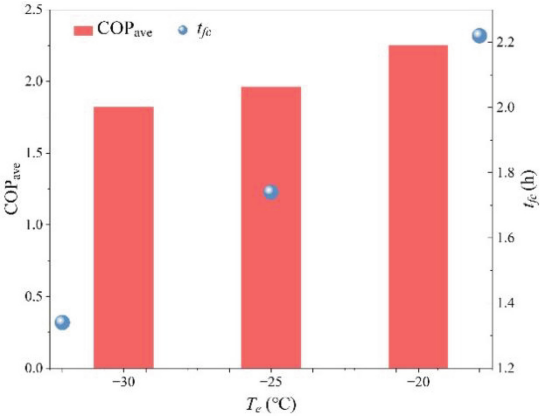


Fig. 3. Average COP and regeneration time under different evaporation temperatures.

4 Conclusion

This study numerically investigated the application of freeze concentration as a regeneration method for antifreeze solutions in FFASHP systems. A progressive freezing model was developed to simulate the dynamic behavior of the regeneration process, considering ice growth, thermal resistance evolution, and system performance coupling. The analysis revealed that the regeneration process is characterized by distinct thermal stages: during the initial phase, cooling capacity is primarily used to reduce solution temperature, while in the later stage, it is increasingly consumed to overcome the latent heat of ice formation. The accumulation of ice significantly increases thermal resistance, which in turn reduces the system COP from about 3.8 initially to below 1 in the final stages. The average COP over the full process was only approximately 1.4, highlighting the limitations of continuous single-stage regeneration.

Furthermore, the effect of evaporation temperature was explored. Lower evaporation temperatures enhanced the heat transfer rate and reduced regeneration time due to the larger temperature gradient at the evaporator interface. However, this came at the cost of reduced energy efficiency, as lower evaporation temperatures inherently lead to higher compressor work in vapor-compression systems. These findings suggest that optimizing the regeneration strategy—such as adopting multi-stage regeneration or adaptive temperature control—may be essential to achieve both high regeneration speed and acceptable energy performance. Future work should consider experimental validation and system-level integration with actual ASHP operations under real-world conditions.

References

1. Installation of About 600 Million Heat Pumps Covering 20% of Buildings Heating Needs Required by 2030. IEA, Paris (2022).

2. Cao, J., et al.: Advances in coupled use of renewable energy sources for performance enhancement of vapour compression heat pump: a systematic review of applications to buildings. Appl. Energy. **328**, 120571 (2023)
3. Kim, J., et al.: Development and validation of a dynamic modeling framework for air-source heat pumps under cycling of frosting and reverse-cycle defrosting. Energy. **278**, 127030 (2023)
4. Huang, S., et al.: Advances, challenges and outlooks in frost-free air-source heat pumps: a comprehensive review from materials, components to systems. Appl. Therm. Eng. **234**, 121163 (2023)
5. Hernández, E., et al.: Two strategies for freeze desalination of seawater by progressive and block techniques. Desalin. Water Treat. **215**, 1–9 (2021)
6. Najim, A., Krishnan, S.: Experimental and theoretical investigation of a novel system for progressive freeze-concentration based desalination process. Chem. Eng. Process. **185**, 108821 (2022)
7. Han, C., et al.: Deicing performance analysis of the solution regenerator unit using freeze concentration. Appl. Therm. Eng. **230**, 124194 (2024)
8. Han, C., et al.: Experimental investigation on heating performance of a solution regenerator unit using freezing concentration for heat source tower heat pump system. Energ. Buildings. **300**, 114166 (2024)

Frost Suppression Mechanism of Superhydrophobic Coating in Air Source Heat Pump

Rui Tang[1], Wenzhe Wei[1(✉)], Yunfeng Wang[2], Wei Wang[1,3(✉)], and Yuying Sun[1]

[1] Beijing Key Laboratory of Green Built Environment and Energy Efficient Technology, Beijing University of Technology, Beijing 100124, China
weiwzhe@126.com, mrwangwei@bjut.edu.cn
[2] Qingdao Haier Smart Technology R&D Co., Ltd., Qingdao, China
[3] School of Mechatronic Engineering, Beijing Polytechnic University, Beijing 100176, China

Abstract. Superhydrophobic coatings exhibit excellent frost suppression performance. However, it remains unclear whether superhydrophobic ASHPs can maintain such performance during operation, given the complex influences of structural configuration and environmental parameters. In this study, based on a visualization test platform and an enthalpy difference laboratory, the microscopic frosting characteristics and frost suppression performance of superhydrophobic ASHPs were revealed. Furthermore, the frost suppression mechanism and failure modes were clarified through theoretical analysis. The experimental results showed that, compared to those of hydrophilic ASHP, its heating duration increased by 16.00%, while the surface temperature decline rate of the hydrophilic ASHP was approximately 54.84% higher than that of the superhydrophobic one. The condensation droplets remained condensation for extended periods, and detached from the fins on both the inner and outer heat exchangers was identified as the primary reason for its frost suppression performance. The droplets on the outer-row heat exchanger detached solely under the influence of their own gravity. On the inner-row superhydrophobic heat exchanger, droplet detachment was promoted by both gravity and fan-induced drag forces.

Keywords: Frost suppression mechanism · Droplet detachment · Superhydrophobic ASHPs

1 Introduction

The air source heat pump(ASHP), as an efficient and clean heating technology, not only demonstrates excellent energy utilization efficiency, but also holds significant importance in achieving energy savings, emission reductions, and promoting the development of zero-carbon buildings. With the expansion of application scale and geographical coverage, some technical issues in the application of ASHPs are becoming increasingly prominent. Especially in practical engineering applications, where frosting issues arise

© The Author(s), under exclusive license to Springer Nature Singapore Pte Ltd. 2025
L. Ni et al. (Eds.): CCHVAC 2025, ESE, pp. 66–74, 2025.
https://doi.org/10.1007/978-981-95-3253-7_8

due to low temperature and high humidity environment [1–4]. When the ASHPs operate in low-temperature and high-humidity environment, the outdoor heat exchanger fin surface is prone to frosting. Although the initially formed frost layer increases the heat transfer area and improves the heat transfer coefficient to some extent, as the frost layer thickens, a series of problems occur. For example, frost will increase resistance to air passing through the fin tubes, reduce air flow, and diminish heating capacity. In severe cases, these issues can lead to catastrophic accidents such as compressor burnout [5, 6]. Some previous researchers had suggested in their studies that frosting problems can increase the energy consumption of ASHP by about 20%, and lead to a decrease in heating performance by 30% to 60% [7, 8]. Therefore, the ASHP units must be equipped with appropriate defrosting operations in the winter for space heating.

Wang et al. [9] compared the droplet condensation characteristics of hydrophilic, bare and superhydrophobic surfaces. The results found that the superhydrophobic surface was sparsely distributed with condensation droplets, and the surface coverage was only 15%; while the hydrophilic and bare surfaces coverage reached 91% and 63%. He et al. [10] studied the effect of superhydrophobicity on condensation droplets by preparing different superhydrophobic surfaces of ZnO nanorod arrays. It was found that the prepared surface had superhydrophobicity to the condensation droplets at a temperature below the freezing point, and delayed the droplets freezing. Kim et al. [11] investigated the frosting characteristics of hydrophobic and superhydrophobic surfaces, and the results showed that the ice crystals formation and propagation were delayed as the static contact angle increased. Kim et al. [12] quantitatively analyzed the anti-freezing properties of superhydrophobic and bare surfaces. The freezing propagation velocity on the bare and superhydrophobic surfaces was 0.032 cm^2/s and 0.026 cm^2/s, respectively, and the freezing propagation velocity on superhydrophobic surface was reduced by 17%. Liu et al. [13] observed the frosting phenomenon on superhydrophobic surface with a contact angle of 162°. Compared with the frost layer formed on bare copper surface, the frost layer thickness on superhydrophobic surface was only 52% of bare copper surface at the end of the test, and the frost deposition time was delayed by 55 min. Wang et al. [14] found that the superhydrophobic finned tube heat exchanger exhibited the lowest air-side pressure drop and the best heat transfer performance during the frosting process.

Although superhydrophobic surfaces have shown strong frost suppression in previous studies, most were limited to simple surface. Moreover, chilled water was often used instead of actual refrigerants, leading to differences in thermal behavior. As a result, existing results cannot fully represent frost suppression performance in real ASHPs, leaving their frost suppression performance unclear.

Therefore, in this paper, three types of fin-tube heat exchangers (hydrophilic and superhydrophobic) with different surface characteristics were prepared, and based on a Psychrometer testing room, the operating performance and frost suppression mechanism with different surface wettability under different frosting conditions were measured and analyze.

2 Experimentations

2.1 Superhydrophobic Heat Exchanger Fabrication Process

To investigate the frosting and suppression behavior of a superhydrophobic ASHP, a heat exchanger was coated using vapor-deposited perfluorooctyltrichlorosilane (FOTS, $CF_3(CF_2)_5CH_2CH_2SiCl_3$). The fabrication involved three steps: (1) Surface pretreatment – the aluminum heat exchanger was ultrasonically cleaned, chemically etched in NaOH and neutralized in HNO_3 to generate an Al_2O_3 layer. (2) Hydrothermal treatment – the sample was boiled in deionized water to form a nano-sheet boehmite (AlO(OH)) structure, increasing surface –OH group density. (3) Vapor deposition – FOTS vapor was deposited under vacuum and elevated temperature, followed by annealing and rinsing to enhance crosslinking and coating stability. The resulting surface achieved ultra-low surface energy (~10–12 mN/m), enabling superhydrophobicity.

The fabrication of the superhydrophobic surface and its scanning electron microscopy (SEM) image were shown in Fig. 1.

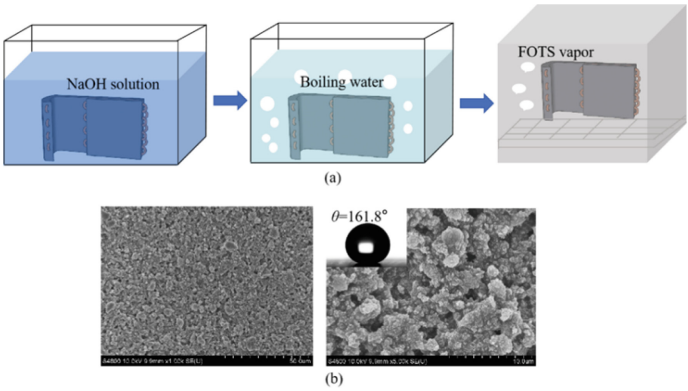


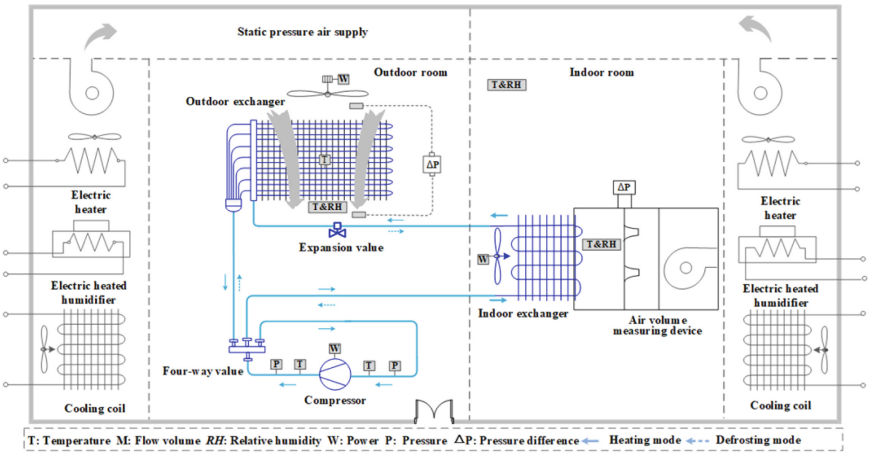
Fig. 1 The fabrication process and its scanning electron microscopy (SEM) image of the superhydrophobic surface.

2.2 Experimental Apparatus

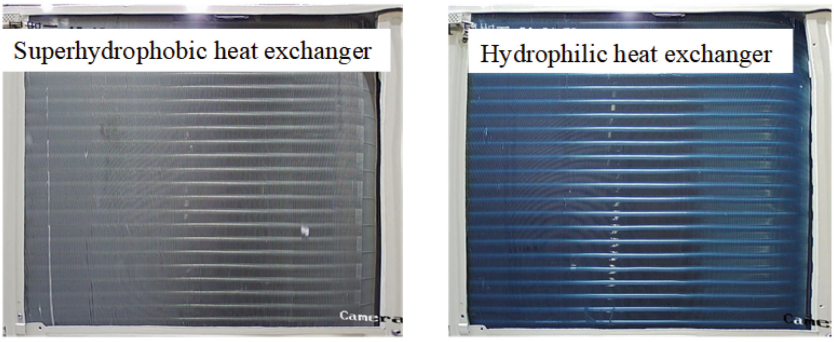
Frosting-defrosting experiments for superhydrophobic and hydrophilic ASHPs were carried out in a psychrometric testing room built in accordance with GB/T 32146–2015 standards. The system included air handling, temperature/humidity monitoring, airflow detection, control, and data acquisition components (Fig. 2a), enabling precise control of environmental conditions for testing.

The data acquisition system recorded ambient temperature, humidity, refrigerant temperatures (via ten platinum RTDs), and power input. Sensors were calibrated and insulated to improve accuracy. Dry-bulb and relative humidity were also measured, then converted into wet-bulb temperatures. All readings were cross-validated with lab data.

An image acquisition system, comprising a microscope (CK-500GT), a high-definition camera (Hikvision DS-2CD2626F), a cold light source, and a computer, was used to capture both localized and overall frost formation on fin surfaces with different coatings.



(a) The psychrometer testing room



(b) The evaporators with different wettability coatings

Fig. 2 Schematic diagram of the experimental setup.

To evaluate the frost suppression capability of the superhydrophobic ASHP, two identical outdoor heat exchangers were prepared—one coated with a superhydrophobic layer and the other with a hydrophilic layer, as illustrated in Fig. 2b. These exchangers were alternately installed as the evaporator in the same ASHP system.

2.3 Experimental Conditions

To investigate the frosting behavior and heating performance of the superhydrophobic ASHP, this study selected the standard frosting condition of 2/1 °C as the experimental condition. The condition of 2 °C (outdoor dry-bulb temperature) / 1 °C (wet-bulb temperature) lies near the typical frosting boundary for air-source heat pumps, where high humidity and low temperature are most conducive to frost formation, effectively triggering the frosting process on the heat exchanger. Under this condition, the unit can still maintain a certain heating capacity, while the impact of frost on heat transfer performance becomes pronounced, making it suitable for investigating the effects of anti-frost strategies on heating continuity and efficiency improvement.

3 Frost Suppression Performance Analysis of Superhydrophobic ASHP

Figure 3 illustrates the surface temperature variations of the outdoor heat exchanger in different surface wettability air source heat pumps (ASHPs) under different heating conditions. At the 2/1 °C condition, the average surface temperature of the superhydrophobic ASHP was found to be 1.07 °C higher than that of the hydrophilic counterpart during the initial 12 min. From 12 to 36 min, both systems exhibited nearly identical surface temperatures. However, beyond 36 min, the temperature profiles diverged notably, the surface temperature of the superhydrophobic ASHP declined at a rate of 0.31 °C/min, whereas the hydrophilic ASHP experienced a faster drop at 0.48 °C/min. This indicates that the surface temperature decline rate in the hydrophilic system exceeded that of the superhydrophobic one by approximately 54.84%. Consequently, the hydrophilic ASHP reached the defrosting threshold at 50 min, while the superhydrophobic ASHP took 58 min, representing a 16.00% extension in frosting duration.

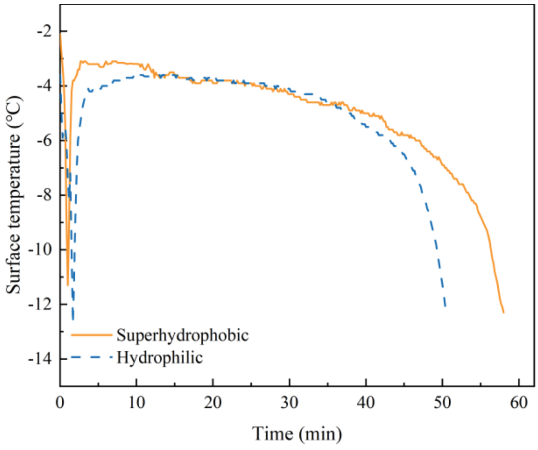


Fig. 3 Variation of surface temperature over time for heat pump units with different wettability.

4 Frost Suppression Mechanism Analysis of Superhydrophobic ASHP

By analyzing the dynamic frosting behavior of superhydrophobic fins, it was found that the superhydrophobic heat exchanger demonstrated good frost suppression performance at 2/1 °C. To further investigate this, the frost suppression mechanism of the superhydrophobic heat exchanger was examined. This mechanism mainly involved three aspects. Firstly, the superhydrophobic surface showed outstanding anti-freezing properties. As illustrated in Fig. 4a, the condensation droplet freezing was significantly delayed, occurring only after 50 min and 20 s. No liquid film was observed on the hydrophilic heat exchanger during the frosting process. Frost formed rapidly and grew uniformly, with the frost layer reaching a height of 0.65 mm in 50 min, completely blocking the fins, as shown in Fig. 4b

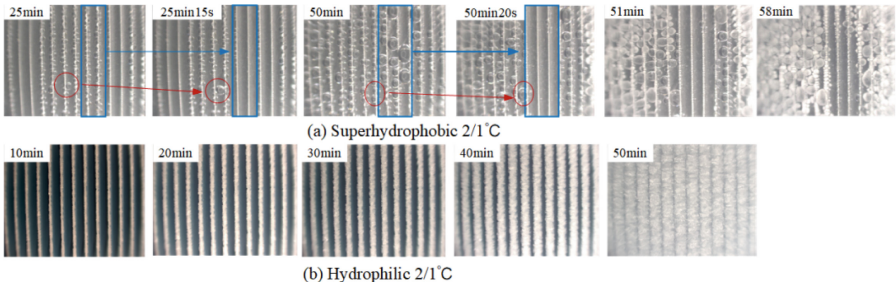


Fig. 4 The microscopic and overall frost formation process of superhydrophobic heat exchangers at the 2/1 °C.

Secondly, condensation droplets on both inner-row and outer-row superhydrophobic heat exchangers detached easily from the fin surfaces, reducing frost coverage. As shown in Fig. 4a, different detachment modes outer-row in superhydrophobic heat exchangers were observed at various condensation stages. In the early stage (25–25 min 15 s), small droplets were removed by larger ones falling from above. In the later stage (50–50 min 20 s), larger coalesced droplets detached due to gravity, dragging smaller ones along. This sweeping effect reduced droplet retention and helped suppress frost formation.

On the inner-row superhydrophobic heat exchanger, droplet detachment was promoted by both gravity and fan-induced drag forces. During heating, the outdoor fan operated at a constant speed, generating shear and pressure difference forces on the droplets in addition to gravity. These forces jointly drove droplet detachment, while surface tension resisted motion. A detailed force analysis is shown in Fig. 5, with corresponding equations in Eqs. (1)–(4).

As a driving force, gravity force in x component is [15]:

$$F_{g,x} = \frac{\pi}{3} r^3 \left(2 - \cos\theta_e + \cos^3\theta_e\right)\left(\rho_l - \rho_g\right) g \sin\beta \tag{1}$$

The fan-induced drag force in x component is another driving force, which is:

$$F_d = F_{\Delta P} + F_\tau = \frac{1}{2}\rho_g \upsilon^2 C_d \frac{2\theta_e - \sin(2\theta_e)}{2} r^2 \tag{2}$$

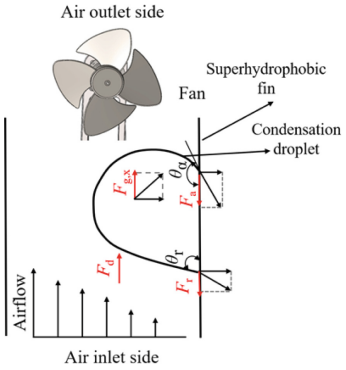


Fig. 5 Analysis of forces acting on a condensation droplet.

Combining Eqs. (1) and (2), the detachment force can be derived, which is:

$$F_{g,x} + F_d = F_{detach} \tag{3}$$

The net surface tension force in x component is:

$$F_{\sigma,x} = -\frac{4}{\pi} r\sigma \sin\theta_e(\cos\theta_r - \cos\theta_a) \tag{4}$$

Up to now, the force balance principle writes

$$F_{g,x} + F_d + F_{\sigma,x} = 0 \tag{5}$$

Among them: r is the droplet radius, mm; θe is the contact angle, 161.8°; ρ_l is the density of water, 1000 kg/m^3; ρ_g is the density of air, 1.225 kg/m^3; g is the gravity, 9.18 m/s^2; β is the angle of inclination for the fin, 90°; C_d is the drag coefficient (for a spherical droplet), 0.47; υ is the wind speed, 5.02 m/s; σ is the air liquid surface tension, 0.072 N/m; θ_r is the receding angle, 158.4°; θ_a is the advancing angle, 163.2°.

Substituting Eqs. (1), (2) and (3) into Eq. (5) yields the critical radius for droplet detachment from the surface. the value of R_c can be obtained, and it was 78.19 μm. To investigate the dynamic characteristics of condensation droplets under the 2/1 °C frosting condition, this study conducted a statistical analysis of droplet sizes during the condensation process. The measured droplet radii ranged from 0.021 to 0.650 mm. As shown in Fig. 6, both the detachment force and surface tension increase with growing droplet radius. However, the detachment force exhibits a significantly steeper growth rate compared to surface tension. When the droplet radius was below the critical value of 78.19 μm, surface tension was equal to or greater than the detachment force, preventing droplet separation from the superhydrophobic fin surface. Once this threshold radius was exceeded, the detachment force surpassed the surface tension, enabling droplet departure. Specifically, as the radius grew from 78.19 μm to 0.65 mm, the detachment force rose from 1.23×10^{-7} N to 210.13×10^{-7} N, an increase of 170.84 times, while the surface tension only increased by a factor of 4.15, from 1.23×10^{-7} N to 5.11×10^{-7} N. This disparity in growth trends indicates that larger droplets are significantly more likely to detach from the superhydrophobic surface as condensation proceeds.

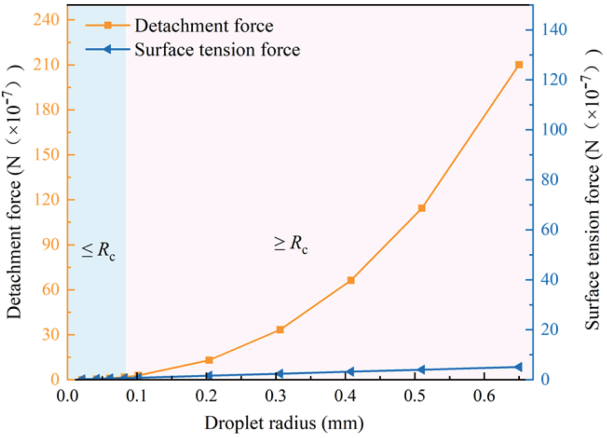


Fig. 6 The relationship between the radius of condensation droplets and both the detachment force and the surface tension force.

From the above analysis, it can be concluded that the prolonged anti-condensation performance of the superhydrophobic coating and the detachment of condensate droplets from the fin surfaces of both the inner and outer heat exchangers are the most critical factors contributing to frost suppression in superhydrophobic air-source heat pumps. On the inner heat exchanger, droplets detach under the combined effect of fan-induced drag force and gravity. Since the fan-induced drag is related to the wind speed, increasing the fan speed in the future could be considered as a means to further enhance the frost suppression performance of superhydrophobic ASHP.

5 Conclusion

To reveal the frost suppression performance of the superhydrophobic heat pump under the 2/1 °C frosting conditions, this study installed outdoor heat exchangers with different surface wettability on ASHPs. Through microscopic observations, the frost formation characteristics on superhydrophobic and hydrophilic fins were revealed. Based on the experimental data and theoretical analysis, the frost suppression differences and the underlying mechanisms were analyzed under different frosting conditions. The following conclusions are summarized below:

(1) The superhydrophobic ASHP showed excellent frost suppression performance. Compared to those of hydrophilic ASHP, its heating duration, average heating capacity and average COP increased by 16.00%, 10.91%, and 6.35%, respectively.
(2) The condensation droplets remained condensation for extended periods, and detached from the fins on both the inner and outer heat exchangers was identified as the primary reason for its frost suppression performance.

References

1. Sun, Y., Chen, X., Wu, S., Wei, W., Wang, W., Deng, S.: Performance analysis of air source heat pump space heating system with an adaptive control for supply water temperature. Appl. Therm. Eng. **211**, 118401 (2022)
2. Wang, F., Tang, R., Wang, Z., Yang, W.: Experimental study on anti-frosting performance of superhydrophobic surface under high humidity conditions. Appl. Therm. Eng. **217**, 119193 (2022)
3. Li, Z., et al.: A method for sizing air source heat pump considering the joint effect of outdoor air temperature and relative humidity. J. Build. Eng. **65**, 105815 (2023)
4. Pu, J., Shen, C., Zhang, C., Liu, X.: A semi-experimental method for evaluating frosting performance of air source heat pumps. Renew. Energy. **173**, 913–925 (2021)
5. Song, M., Deng, S., Dang, C., Mao, N., Wang, Z.: Review on improvement for air source heat pump units during frosting and defrosting. Appl. Energy. **211**, 1150–1170 (2018)
6. Wang, W., Feng, Y., Zhu, J., Li, L., Guo, Q., Lu, W.: Performances of air source heat pump system for a kind of mal-defrosting phenomenon appearing in moderate climate conditions. Appl. Energy. **112**, 1138–1145 (2013)
7. Tudor, V.: Control of Frost Growth in Refrigeration Systems Using the EHD Technique. Ph.D. Thesis of the University of Maryland, Maryland. 32–36 (2003).
8. Hewitt, N., Huang, M.J.: Defrosting cycle performance for a circular shape evaporator air source heat pump. Int. J. Refrig. **31**, 444–452 (2008)
9. Wang, F., Liang, C.H., Zhang, X.S.: Research of anti-frosting technology in refrigeration and air conditioning fields: a review. Renew. Sust. Energ. Rev. **81**, 707–722 (2018)
10. He, M., Wang, J.J., Li, H.L., Song, Y.L.: Super-hydrophobic surfaces to condensed micro-droplets at temperatures below the freezing point retard ice/frost formation. Soft Matter. **7**(8), 3993–4000 (2011)
11. Kim, M.H., Kim, H., Lee, K.S., Kim, D.R.: Frosting characteristics on hydrophobic and superhydrophobic surfaces: a review. Energy Conv. Manag. **138**, 1–11 (2017)
12. Kim, J., Jeon, J., Kim, D.R., Lee, K.S.: Quantitative analysis of anti-freezing characteristics of superhydrophobic surfaces according to initial ice nuclei formation time and freezing propagation velocity. Int. J. Heat Mass Transf. **126**, 109–117 (2018)
13. Liu, Z.L., Gou, Y.J., Wang, J.T., Cheng, S.Y.: Frost formation on a super-hydrophobic surface under natural convection conditions. Int. J. Heat Mass Transf. **15**, 5975–5982 (2008)
14. Wang, F., Liang, C.H., Yang, M.T., Fan, C., Zhang, X.S.: Effects of surface characteristic on frosting and defrosting behaviors of fin tube heat exchangers. Appl. Therm. Eng. **75**, 1126–1132 (2015)
15. Schillberg, C.H., Kandlikar, S.G.: A review of models for water droplet detachment from the gas diffusion layer-gas flow channel interface in PEMFCs. In: International Conference on Nanochannels, Microchannels, and Minichannels, 4272, 299–310 (2007).

Study on Operation Characteristics of Solar-Assisted Enhanced Jet Enthalpy Air Source Heat Pump

Shirui Su and Guodong Qiu(✉)

Laboratory of Thermo-fluid Science and Nuclear Engineering, School of Energy and Power Engineering, Northeast Electric Power University, Jilin 132012, China
qiugd@neepu.edu.cn

Abstract. Jet enthalpy technology can improve the low-temperature performance degradation of air source heat pumps, but it is still necessary to integrate auxiliary heat sources to supplement the heating gap in extremely cold regions. Solar energy is widely used as one of the most commonly used auxiliary heat sources. However, the traditional integrated system of solar energy and air source heat pumps is difficult to achieve efficient operation under wide-range working conditions. Therefore, this paper proposes a new solar-assisted enhanced jet enthalpy air source heat pump. Solar energy is used to heat the refrigerant in the jet branch to increase the flow rate of the jet branch, which enhances the effect of jet enthalpy. The operational performance of the new system is studied and analyzed by combining experimental and simulation methods. The results show that the new system is highly efficient in the utilization of medium-grade solar energy and has a significant effect on improving quality and increasing quantity. Its heating capacity and coefficient of performance are both superior to the existing integrated systems. The research in this paper provides a new idea for promoting the popularization of air source heat pump heating technology in extremely cold regions.

Keywords: solar energy · jet enthalpy air source heat pump · heating

1 Introduction

Air source heat pumps are highly efficient, energy-saving, clean, and environmentally friendly, and have occupied an important position in the clean transformation of building heating. However, their heating performance will decline sharply as the decrease of outdoor temperature. Jet enthalpy technology improves the low-temperature adaptability of air source heat pumps through intermediate gas replenishment, but the improvement in heating performance at low temperatures is limited. For extremely cold regions, the conventional jet enthalpy system is still difficult to independently meet the heating demand, and auxiliary heat sources need to be integrated to supplement the heating gap [1]. Solar energy is widely used as one of the most commonly used auxiliary heat sources.

The existing solar-assisted air source heat pump heating systems can essentially be divided into two categories. The first type is the system in which solar collectors and

© The Author(s), under exclusive license to Springer Nature Singapore Pte Ltd. 2025
L. Ni et al. (Eds.): CCHVAC 2025, ESE, pp. 75–85, 2025.
https://doi.org/10.1007/978-981-95-3253-7_9

heat pump condensers are connected in parallel [2, 3]. Solar energy directly supplies heat to users. It performs well under high radiation conditions, but its heat-collecting efficiency is relatively low under low radiation. Another type is the system in which solar energy is used as a low-temperature heat source and connected in parallel with the heat pump evaporator [4, 5]. It has a relatively high heat-collecting efficiency under low-radiation conditions, but only collects heat to the evaporation temperature under high radiation, resulting in a serious loss of solar energy grade. To adapt to different weather conditions, some researchers aim to integrate the above integrated models and propose a hybrid system that can switch operation modes according to outdoor meteorological conditions [6]. However, the system is overly complex and has a relatively high cost.

Therefore, traditional solar-assisted air source heat pump systems are difficult to achieve efficient operation under wide operating conditions, resulting in limited energy efficiency improvement. Therefore, this paper proposes a new solar-assisted enhanced jet enthalpy air source heat pump, placing solar heating in the jet branch. The solar energy and air sources in the system operate at different evaporation temperatures and can operate efficiently under wide-range solar radiation. The operational performance of the new system is studied and analyzed by combining experimental and simulation methods.

2 System Principle

The principle of the new system proposed in this paper is shown in Fig. 1. This system is based on the traditional jet enthalpy air source heat pump and places the solar collector in the middle branch. This integration method effectively increases the refrigerant pressure of the middle branch of the system and enhances the effect of jet enthalpy, thereby increasing the circulating refrigerant flow rate of the system and improving the heating capacity.

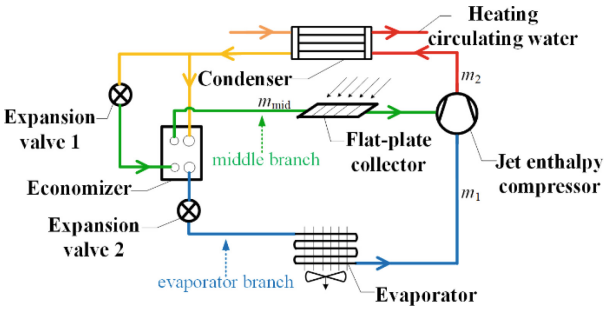


Fig. 1. Solar-assisted enhanced jet enthalpy air source heat pump system.

3 Experimental Research

3.1 Experimental Testing Platform

An experimental platform is built to verify the feasibility of the new system proposed in this paper, as shown in Fig. 2. This experimental platform consists of a jet enthalpy air source heat pump system, a condensation temperature regulation system, an evaporation temperature regulation system, and a simulated solar heating system. The compressor adopts the Invotech YW160C1-V100 jet enthalpy compressor. The middle branch uses an electric heater to simulate solar heating. The evaporator side uses a 50% ethylene glycol aqueous solution to simulate the outdoor environmental conditions. The heating capacity of the system is transferred through the cooling water in the condenser. This experimental platform can independently control the evaporation temperature and condensation temperature through its own cold and heat sources.

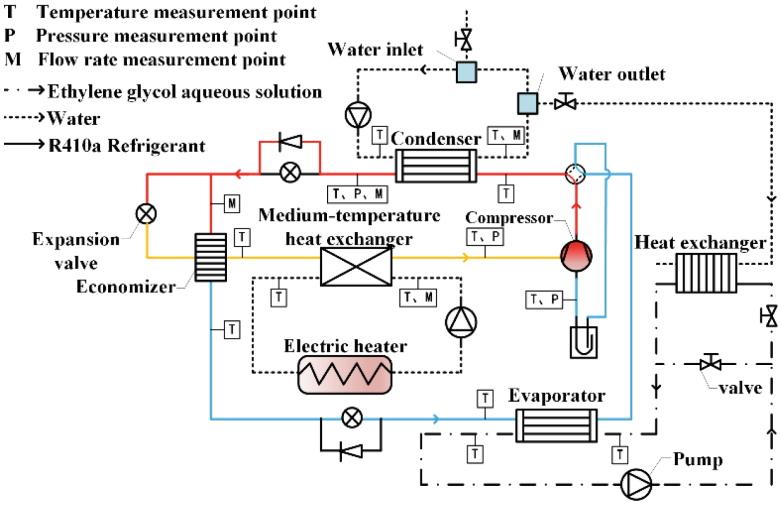


Fig. 2. Diagram of experimental platform.

3.2 Performance Evaluation Indicators

The key performance indicators of the heat pump system include the heating capacity and the COP (coefficient of performance). The parameters and measuring instruments required for their calculation are shown in Table 1.

The heating capacity of the system is transferred through the cooling water in the condenser, so the heat gained from the cooling water is the heating capacity Q_g of the heat pump system.

$$Q_g = m \cdot C_p \cdot (t_o - t_i) \tag{1}$$

Table 1. Measurement parameters and instruments.

Parameter	Instrument	Measurement range
Temperature	Four-wire armored platinum resistance measuring instrument	−40 °C ~ 160 °C
Pressure	Pressure transmitter	3.5 MPa, 2.5 MPa, 1 MPa
Flow rate	Turbine flowmeter	1.6 L/min ~ 10 L/min
Power	Three-phase electrical parameter measuring instrument	

where m is the mass flow rate of circulating cooling water, kg/s; C_p is the specific heat capacity of water, kJ/(kg•°C); t_o is the outlet temperature of condenser water side, °C; t_i is the inlet temperature of condenser water side, °C.

COP is the ratio of heating capacity to power consumption.

$$\mathrm{COP} = \frac{Q_g}{W} \tag{2}$$

where W is the power consumption of the compressor, kW.

3.3 Analysis of Experimental Results

The traditional jet enthalpy air source heat pump system was selected as the control, and the performance improvement effect of the enhanced system was experimentally explored. The comprehensive influence of solar heating capacity Q_{mid} on the operational performance of the enhanced system is further analyzed. The experimental test conditions are shown in Table 2. Due to the limitation of the rated power of the compressor motor, some working conditions are not tested.

Table 2. Experimental test conditions.

Parameter	Condition
Outdoor temperature	−30 °C ~ 10 °C
Water supply temperature	45 °C
Solar heating capacity	0 kW ~ 6 kW

The test results of the heating capacity Q_g and COP are shown in Figs. 3 and 4. The heating performance of the enhanced system is significantly improved at low temperatures. Under the condition of −30 °C outdoor temperature and 2 kW solar heating capacity, the heating capacity and COP of the enhanced system increased by 30.77% and 20.96% compared with the traditional jet enthalpy system, and the increase in heating capacity (3.82 kW) is higher than that of the solar heating capacity (2 kW). This is because the solar heating in the middle branch enhances the jet enthalpy effect of the

system. As shown in Fig. 5, the refrigerant pressure P_{mid} and flow rate m_{mid} in the middle branch are increased by 24.28% and 63.62%. As shown in the Y-Z plane projections in Figs. 3 and 4, the heating capacity and COP of the enhanced system are positively correlated with the solar heating capacity, but the increase gradually slows down. Meanwhile, the continuous increase in the temperature of solar heating will reduce the cooling effect on the compressor exhaust, as shown in Fig. 6. Therefore, under the condition of meeting the heating demand, the solar heating capacity should not be too large.

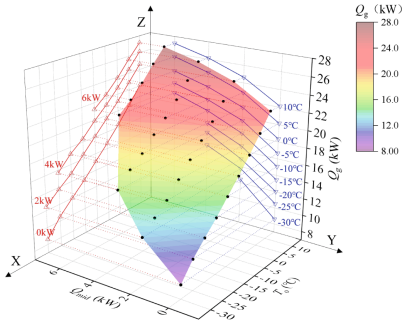


Fig. 3. Heating capacity.

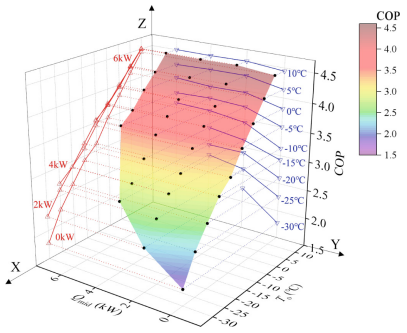


Fig. 4. COP.

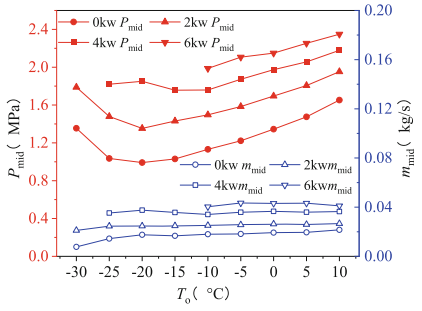


Fig. 5. Refrigerant pressure and flow rate in the middle branch.

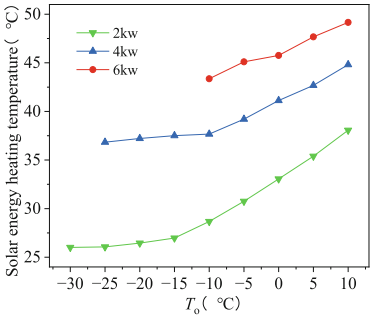


Fig. 6. Solar energy heating temperature.

4 Simulation Research

The experimental results show that the enhanced system has obvious effects of improving quality and increasing quantity. To further explore the performance advantages and development prospects of the enhanced system, this paper selects the traditional solar integrated system with the same component composition but different integration methods as the control for simulation analysis.

4.1 Types and Principles of Integrated Systems

The traditional integrated systems of solar energy and air source heat pumps can be classified into two types based on the heat-collecting temperature. As shown in Fig. 7, the solar collector is connected in parallel with the heat pump evaporator, and its heat-collecting temperature is close to the evaporation temperature. This system is called SLAS (solar low-temperature assisted system). This system has two operation modes. When the outdoor temperature is low and the solar radiation is strong, it operates in the single-heat source mode where the collector works alone. In other working conditions, it operates in the dual-heat source mode where both the evaporator and the collector work simultaneously. As shown in Fig. 8, the solar collector is connected in parallel with the heat pump condenser, and its heat-collecting temperature is close to the condensation temperature. This system is called SHAS (solar high-temperature assisted system). The heating capacity of this system consists of two parts, which come from the heat pump and the solar collector. Different from SLAS and SHAS, the heat-collecting temperature of the enhanced system proposed in this paper is the middle branch temperature between the evaporation temperature and the condensation temperature. Therefore, this system can be called SMAS (solar medium-temperature assisted system).

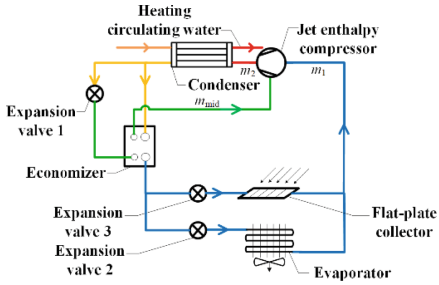


Fig. 7. SLAS schematic diagram.

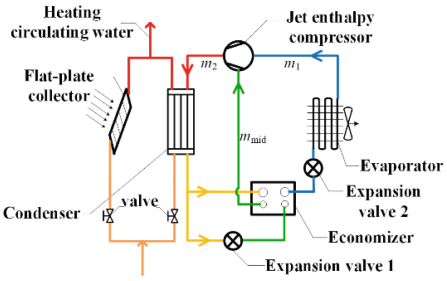


Fig. 8. SHAS schematic diagram.

4.2 System Model

In this paper, the mathematical model of the system is built using MATLAB software and solved by iterative programming. The steady-state models of three systems are established.

(1) Compressor model

In this paper, a five-horsepower swirl jet enthalpy compressor is adopted. Ignoring the complex internal compression process, the jet enthalpy compressor is simplified to a two-stage compression for modeling. The flow rate m and power consumption w of each stage compressor are as follows:

$$m = \varepsilon \cdot V^* \cdot \rho \tag{3}$$

where ε is the compressor volumetric efficiency; V^* is the compressor theoretical displacement, m^3/s; ρ is the compressor import refrigerant density, kg/m^3.

$$w = \varepsilon \cdot V^* \cdot P_{\text{in}} \cdot \frac{k}{k-1} \cdot \left((P_{\text{out}}/P_{\text{in}})^{\frac{k-1}{k}} - 1 \right) / \eta \tag{4}$$

where P_{in} is the suction pressure, kPa; k is the polytropic index of the compression; P_{out} is the exhaust pressure, kPa; η is the compressor efficiency.

(2) Heat exchanger model

The heat transfer of the condenser Q_{c} is:

$$Q_{\text{c}} = m_2 \cdot (h_{2\text{o}} - h_{\text{c}}) \tag{5}$$

where h_c is the enthalpy of refrigerant at the condenser outlet, kJ/kg; $h_{2\text{o}}$ is the enthalpy of refrigerant at the second-stage compressor outlet, kJ/kg; m_2 is the mass flow rate of the compressor (second stage), kg/s.

The heat transfer of the economizer Q_{eco} is given by:

$$Q_{\text{eco}} = m_1 \cdot (h_{\text{c}} - h_{\text{eco}}) \tag{6}$$

where h_{eco} is the enthalpy of refrigerant at the outlet of the economizer connected to the evaporator, kJ/kg; m_1 is the mass flow rate of the compressor (first stage), kg/s.

The heat transfer of the evaporator Q_{e} is:

$$Q_{\text{e}} = m_{\text{e}} \cdot (h_{\text{e}} - h_{\text{eco}}) \tag{7}$$

where m_{e} is the mass flow rate of refrigerant in the evaporator, kg/s; h_{e} is the enthalpy of refrigerant at the evaporator outlet, kJ/kg.

The evaporation temperature T_{e} and outdoor temperature T_{o} satisfy:

$$Q_{\text{e}} = k \cdot A_{\text{e}} \cdot (T_{\text{o}} - T_{\text{e}}) \tag{8}$$

where A_{e} is the evaporator's heat exchange surface area, m^2; k is the evaporator's heat exchange coefficient, $k = 0.036$ kW/(m^2·°C).

(3) Expansion valve model

The electronic expansion valve is used to control the superheat of the refrigerant. Among them, the superheat of the evaporator outlet is 10 °C, and the superheat of the economizer outlet is 5 °C.

(4) Flat-plate solar collector model

The solar flat plate collector is selected, and its heat-collecting capacity Q_{sol} is:

$$Q_{\text{sol}} = I \cdot \eta_c \cdot A_{\text{sol}}/1000 \tag{9}$$

where I is the solar radiation value, W/m^2; η_c is the heat-collecting efficiency of flat-plate collector; A_{sol} is the flat-plate collector's heat exchange area, m^2.

From the efficiency curve provided by the manufacturer, the heat-collecting efficiency η_{c} is:

$$\eta_c = 0.77 - 4.47 \cdot (T_{\text{sol}} - T_{\text{o}})/I \tag{10}$$

where T_{sol} is the heat-collecting temperature of flat-plate collector, °C.

4.3 Model Verification

The simulation results of heating capacity and COP are compared with the experimental data, and the results are shown in Figs. 9 and 10. Due to the influence of the experimental testing environment, there is a certain error between the experimental values and the simulated values. Among them, the maximum relative error of the heating capacity is 5.96%, and the average relative error is 2.74%. The maximum relative error of COP is 5.93%, and the average relative error is 4.47%. The model accuracy meets the requirements.

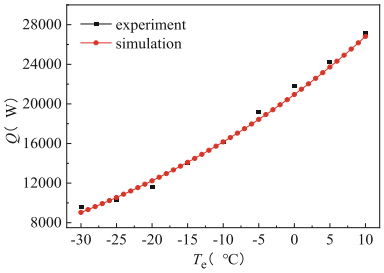


Fig. 9. Heating capacity verification.

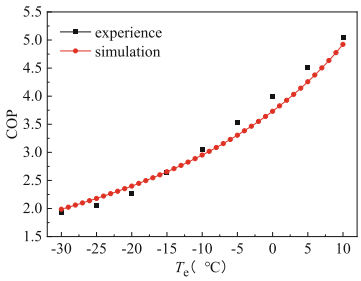


Fig. 10. COP verification.

4.4 Analysis of Simulation Results

The operating conditions and equipment parameters of the simulation calculation are shown in Table 3.

Table 3. Simulation parameters.

Equipment	Condition	Parameter	Condition
Compressor	Rated power 5827 W	Outdoor temperature	−30 °C ~ 10 °C
Expansion valve	Superheat 5 °C ~ 10 °C	Condensation temperature	50 °C
Evaporator	Heat exchange area 110 m^2	Radiation intensity	500 W/m^2
Solar collector	Area 20 m^2		

The simulation results of the system heating capacity Q_g and COP are shown in Figs. 11 and 12. Among them, SMAS exhibits the highest Q_g and COP, followed by SLAS, and the SHAS exhibits the lowest This is because the heat-collecting temperature difference of SHAS is the largest, while the heat-collecting capacity and efficiency are

the lowest, as shown in Fig. 13. There is an inflection point in the characteristic curve of SLAS. This is because the system switches to dual heat source mode at $T_o = -22$ °C. Compared with the single heat source mode, the total heat absorption of the system increases, but due to mutual interference between dual heat sources, the total heat absorption of the system are the lowest among the three integrated systems, as shown in Fig. 14. Therefore, the improvement effect is the least among the three integrated systems. For SMAS, solar heating enhances the effect of jet enthalpy, and there is no problems with low heat-collecting efficiency and mutual interference between dual heat sources. The total heat absorption of the system is the largest. Therefore, the heating capacity and COP of the system have the most significant improvement effect, especially under the condition of $T_o = -30$ °C, where the Q_g is higher approximately 45.8% and COP is higher approximately 22.5% than the other two systems.

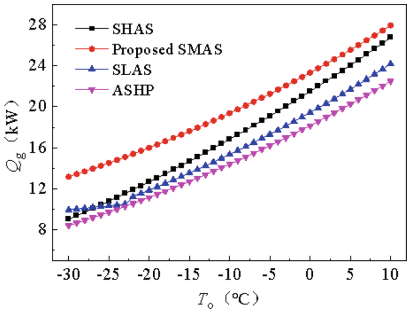


Fig. 11. Heating capacity comparison

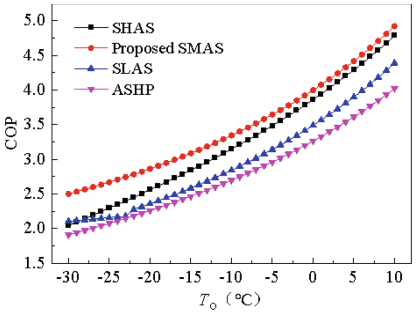


Fig. 12. COP comparison

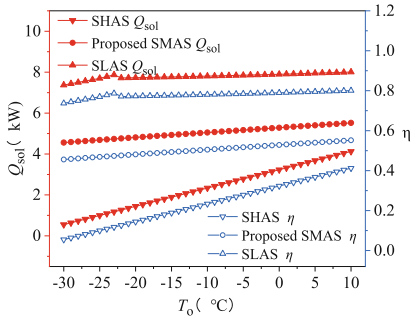


Fig. 13. Heat-collecting capacity and efficiency

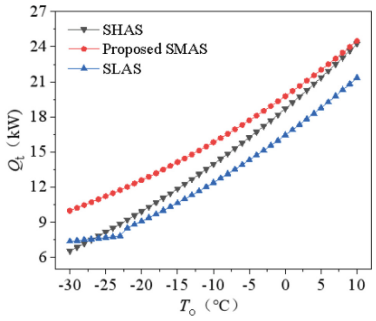


Fig. 14. Total heat absorption of the system

5 Conclusions

This paper proposes a new solar-assisted enhanced jet enthalpy air source heat pump. The operational performance of the new system is studied and analyzed by combining experimental and simulation methods. Several conclusions can be drawn as follows:

(1) The solar heating of the new system is placed in the middle branch, which can enhance the jet enthalpy effect of the system. Especially in low-temperature environments, the improvement effect is more significant. Under the condition of −30 °C outdoor temperature and 2 kW solar heating capacity, the heating capacity and COP of the new system increased by 30.77% and 20.96% compared with the traditional jet enthalpy system, and the increase in heating capacity (3.82 kW) is higher than that of the solar heating capacity (2 kW).
(2) The new system has obvious improvements compared with the existing integrated system. It does not add additional equipment but enhances the heating performance of the system by changing the integration method. Compared with the existing two integrated systems, its heating capacity increases by about 45.8%, and COP increases by about 22.5% when the outdoor temperature is −30 °C and the radiation value is 500 W/m^2.
(3) The improvement effect of traditional integration methods on system performance is limited. The heat-collecting temperature of the traditional solar high-temperature assisted system is relatively high, the heat-collecting temperature difference is large, and there exist problems of low heat-collecting capacity and efficiency. Solar heating in the traditional solar low-temperature assisted system will increase the evaporation temperature, resulting in a decrease in the total heat absorption of the system, and there is a problem of mutual interference between the two heat sources.
(4) The new system proposed in this paper has a medium heat-collecting capacity and efficiency, and the two heat sources will not interfere with each other. Solar energy can be replaced by other medium and low-grade heat sources. The system can be flexibly configured according to the characteristics of the auxiliary heat source to achieve the complementary advantages of " low-temperature heat source accessibility" and " medium-temperature heat source efficiency".

References

1. Navarro, E., et al.: Characterization of a vapor injection scroll compressor as a function of low, intermediate and high pressures and temperature conditions [J]. Int. J. Refrig. **36**(7), 1821–1829 (2013)
2. Yerdesh, Y., Abdulina, Z., Aliuly, A., Belyayev, Y., Mohanraj, M., Kaltayev, A.: Numerical simulation on solar collector and cascade heat pump combi water heating systems in Kazakhstan climates. Renew. Energy. **145**, 1222–1234 (2020)
3. Long, T., et al.: Performance analysis and optimization of a solar-air source heat pump heating system in Tibet. China Energy Build. **220**, 110084 (2020)
4. Yuan, P., Huang, F., Zhu, C., Gao, S., Fu, P., Gao, K.: Review on research progress of solar coupled air source heat pump system for domestic space heating. Therm. Sci. Eng. Progress. **53**, 102709 (2024)

5. Wang, Y., Quan, Z., Zhao, Y., Wang, L., Bai, Z., Shi, J.: Energy and exergy analysis of a novel dual-source heat pump system with integrated phase change energy storage. Renew. Energy. **222**, 119905 (2024)
6. Li, J., Qu, C., Li, C., Liu, X., Novakovic, V.: Technical and economic performance analysis of large flat plate solar collector coupled air source heat pump heating system. Energ. Buildings. **277**, 112564 (2022)

Experimental Investigation on the Indoor Thermal Environment During the Dynamic Frosting-Defrosting Process of Air Source Heat Pump

Wenzhe Wei[1], Jianfei Zhang[1], Xinyue Jin[1], Wei Wang[1,2(✉)], and Yuying Sun[1]

[1] Beijing Key Laboratory of Green Built Environment and Energy Efficient Technology, Beijing University of Technology, Beijing, China
mrwangwei@bjut.edu.cn

[2] School of Mechatronic Engineering, Beijing Polytechnic University, Beijing, China

Abstract. During the defrosting operation of air source heat pump (ASHP), it stops supplying heating, or even absorbs heat from indoors. This results in the significant fluctuation of indoor thermal environment. However, the variation rule of indoor thermal environment during frosting-defrosting is still unclear, which severely restricts the heating quality improvement of ASHPs. To solve this problem, two test rigs, an air-water heat pump (AWHP) heating system and an air-air heat pump (AAHP) heating system, were built in an artificial environmental chamber. Through creating the frosting environmental condition, the practical space heating experiments of ASHPs during frosting-defrosting process were conducted. Then, the indoor thermal environment variation rules of the two ASHPs and their differences were analyzed. Results show that the indoor temperature during the defrosting process of both the AWHP and AAHP decreases obviously, and the decline amplitude in rooms using AWHP is greater. The temperature decline in rooms using AWHP is 2.99–4.66 °C, while 1.58–1.79 °C in the room using AAHP. For AAHP, during the later stage of its defrosting operation, the supply water temperature drops below the indoor air temperature, causing the indoor fan coil units to absorb heat from the indoor air instead of providing heating.

Keywords: air source heat pump · frosting · indoor temperature fluctuation

1 Introduction

To reduce building heating energy consumption, China has actively promoted renewable energy technologies like heat pumps in building heating [1]. Among heat pumps, air source heat pumps (ASHPs) extract heat from ambient air [2]; due to advantages such as extensive heat sources, easy installation, and low initial cost, they have become the most widely used [3]. Under low-temperature and high-humidity conditions, if the outdoor coil surface temperature drops below ambient dew point and 0 °C, moisture

© The Author(s), under exclusive license to Springer Nature Singapore Pte Ltd. 2025
L. Ni et al. (Eds.): CCHVAC 2025, ESE, pp. 86–96, 2025.
https://doi.org/10.1007/978-981-95-3253-7_10

condenses and freezes into frost. Frost accumulation reduces coil air flow and increases thermal resistance, degrading heat transfer capacity, cutting heating capacity and COP by over 30%, and even causing shutdowns or damage. Periodic defrosting, most commonly reverse cycle, is needed to maintain high COP. Reverse cycle defrosting switches the four-way valve, directing high-temperature refrigerant to the outdoor coil to melt frost, outdoor coil as condenser, indoor unit as evaporator. This stops indoor heating or absorbs indoor heat, causing significant temperature drops and disrupting indoor thermal environment, a key challenge for ASHP heating quality, especially in low-thermal-inertia rural buildings. To enhance comfort during frosting-defrosting, researchers focused on two solutions: 1) improving defrosting accuracy [4], e.g., Wang et al.'s optimal initiation time theory [5]; Li et al. and Wang et al.'s image recognition-based methods [6], which reduces heating loss and temperature fluctuations; 2) shortening defrost duration [7], e.g., Dong et al. and Zhang et al.'s phase-change material heat storage [8], cutting duration by 59.41% and 65.00%; Wei et al.'s vapor injection in quasi-two-stage compression [9], reducing duration by 20.61%, which shortens heating interruption and temperature drops.

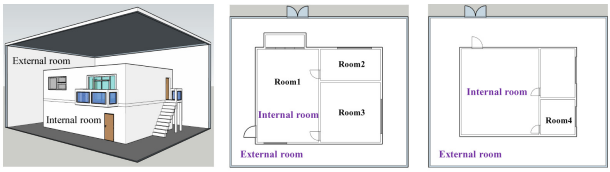
However, existing studies were in psychrometric chambers, focusing on ASHP defrosting performance but ignoring impacts on indoor environment. Qu et al. [10] used the PMV model to assess comfort in practical projects, but PMV is unsuitable for dynamic frosting-defrosting conditions. Additionally, outdoor temperature variations in practical heating affect ASHP capacity and indoor environment, leaving indoor thermal environment variation rules during frosting-defrosting unclear—restricting defrost control strategy improvements.

To fill the research gap above, the indoor thermal environment of AHSP during dynamic frosting-defrosting process was investigated in an artificial environmental chamber. To realize the actual space heating effect, a typical rural residential building widely distributed in the Yangtze River Basin was constructed in the artificial environmental chamber. Then, two test rigs, an air-water heat pump (AWHP) heating system and an air-air heat pump (AAHP) heating system, were built and used for supplying heating. At last, under the standard frosting condition of 2/1 °C (dry-bulb/wet-bulb temperature), the dynamic frosting-defrosting experiments were conducted with different indoor temperature setpoints, and the variations of indoor thermal environment were analyzed for both the two types of ASHPs. The originalities of present work are: 1) the variation rules of indoor thermal environment during the dynamic frosting-defrosting process of ASHP is firstly explored; and 2) the frosting environment and indoor thermal environment are controlled precisely through constructing actual buildings and creating frosting environment in the artificial environmental chamber. This work can provide guidance for the defrosting control strategies design of ASHP, and further improve the indoor thermal environment.

2 Experimentations

2.1 The Artificial Environment Chamber

To reveal the variation rules of indoor thermal environment during dynamic frosting-defrosting process, the actual space heating experiments of ASHPs were conducted in an artificial environmental chamber, as shown in Fig. 1. The external room was used to create the outdoor frosting environment condition. The internal room was a two-story building. The building envelope of the internal room follows the construction standards for actual buildings in Hot Summer and Cold Winter climatic region of China. The floor plans of the first and second stories are presented in Fig. 1 (a) and 1 (b), respectively. The first story was used to conduct the space heating experiments using AAHP, while the second story was used to conduct the space heating experiments using AWHP. The areas of the three rooms on the second story were 62.08 m^2, 20.99 m^2, and 38.92 m^2 respectively. All the three rooms were supplied heating by the AWHP, and used for investigating the indoor thermal environment. For the first floor, only Room 4 with the area of 15.57 m^2 was supplied heating by AAHP, and used for investigating the indoor thermal environment.



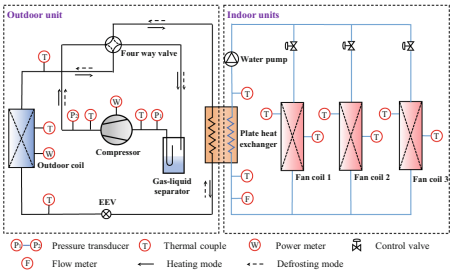
(a) artificial environmental chamber (b) second floor (c) first floor

Fig. 1. Three-dimensional diagram of artificial environmental chamber and floor plan of the artificial environment room.

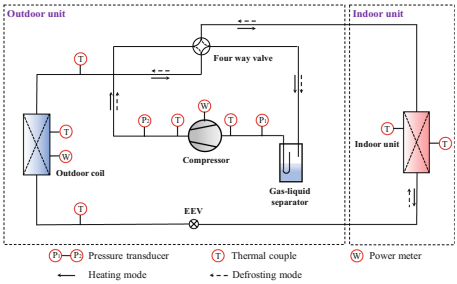
2.2 The Experimental Air Source Heat Pumps

At present, ASHPs are mainly classified into two types: AWHP and AAHP. To comprehensively reveal the variation rules of indoor thermal environment during dynamic frosting-defrosting process, an AWHP and an AAHP are chosen for experiments. Their schematic diagrams are presented in Fig. 2 (a) and 2 (b), respectively. The AWHP heating system comprises one outdoor unit and three indoor fan-coils. The three indoor fan-coils are respectively installed in the three rooms on the second floor of the artificial environmental chamber to provide heating. The rated heating capacity and COP of AWHP are 18 kW and 3.1, respectively. The refrigerant used in it is R410A. The AAHP heating system comprises one outdoor unit and one indoor unit. The indoor unit is installed in Room 4 on the first floor of the artificial environmental chamber to provide heating. The rated heating capacity and COP of AAHP are 3.5 kW and 3.3, respectively, and the R32 refrigerant is employed.

For both the AWHP and AAHP, the reverse-cycle defrosting is adopted. The most widely used temperature difference-time (ΔT–T) defrosting control method is adopted



(a) air-water heat pump



(b) air-air heat pump

Fig. 2. Schematic diagrams of the experimental air source heat pumps.

by both the two ASHPs. For the two experimental ASHPs, when ΔT exceeds 7 °C and the operation time exceeds 40 min, the compressor speed decreases rapidly to 0 and prepare to defrosting through switching the four-way valve. During defrosting process, when the tube surface temperature of the lowest refrigerant circuit of outdoor heat exchanger (Tc) reaches 20 °C, the defrosting operation of both the two ASHPs terminates. Then, the four-way valve switches again, and the ASHP restarts to supply heating. To reduce the pressure difference between the two sides of four-way valve during its switching, the AWHP is turned off for 2 min before each switching. Meanwhile, the AAHP is turned off for only 1 min before each switching because of its lower pressure difference. During defrosting process, the indoor fan-coils of AWHP are turned on and continue to supply heating for indoors, while the indoor unit of AAHP is shut down.

2.3 Data Acquisition System

To obtain the experimental data, plenty of measuring instruments were installed to monitor the operating parameters of the two ASHPs, and the indoor and outdoor environmental parameters. Among them, the arrangement method of relative humidity sensors and thermocouples in heated rooms is carried out in accordance with the Standard of Test Methods for Thermal Environment of Buildings (JGJ/T 347–2014). The specific instruments and quantities are shown in Table 1.

Table 1. Detailed specifications of measuring instruments.

Name	Measuring range	Error	Number
Thermocouple	−20–100 °C	± 0.1 °C	738
Temperature & humidity sensor	Temp: 0–50 °C RH: 0–100%	±0.15 °C ±3%	33
Electromagnetic flow meter	0.1–3.0 m^3/h	0.5% FS	1
Power meter	0–6.6 kW	0.25% FS	4
Black bulb temperature	0–80 °C	±0.1 °C	13
Hot-wire anemometer	0–30 m/s	±0.5%	31
Pressure transducer	0–3.0 MPa	0.3% FS	4

2.4 Experimental Conditions and Procedures

In the US, EN, China, etc., ASHP frosting tests are all conducted at 2/1 °C, where frosting is fast and typical. Thus, the external chamber of the artificial environmental chamber here was set to this condition to ensure universal results. In Hot-Summer and Cold-Winter regions, ASHP heating systems usually set indoor temperatures at 22–24 °C. To accurately quantify frosting-defrosting impacts on indoor thermal environment, Rooms 1–3 (heated by AWHP) were set at 22 °C, 23 °C, and 24 °C, respectively, and Room 4 (heated by AAHP) at 23 °C. All four rooms had a 2 °C temperature return difference (allowed fluctuation) during heating, so actual temperatures were 22 ± 2 °C, 23 ± 2 °C, 24 ± 2 °C for the AWHP rooms and 23 ± 2 °C for the AAHP room.

The experimental process is displayed in Fig. 3. Firstly, the outdoor environmental condition was regulated to 2/1 °C. Then, the preliminary experiments were conducted. After the ASHP was turned on, its heating capacity was regulated by adjusting the compressor speed and outdoor fan frequency. When the indoor temperature stabilized around the setting valve, it is regarded that the heating capacity of ASHP is equal to the building heating load. To avoid the effect of frosting on the follow-up experiments, both the two ASHPs executed one defrosting operation before the termination of preliminary experiments.

At last, the indoor thermal environment experiments during the dynamic frosting-defrosting process were conducted. Since the regulation of the compressor speed and outdoor fan frequency can affect the heating capacity of the ASHPs, and further influence the indoor thermal environment. To eliminate their influence, the compressor speed and outdoor fan frequency were both fixed at constant values throughout the experiment process. Once the operation parameters of ASHPs met the defrosting initiation criteria introduced in Sect. 2.2, the defrosting was initiated automatically. To mitigate random errors, four groups of repeated experiments were conducted for both the AWHP and AAHP.

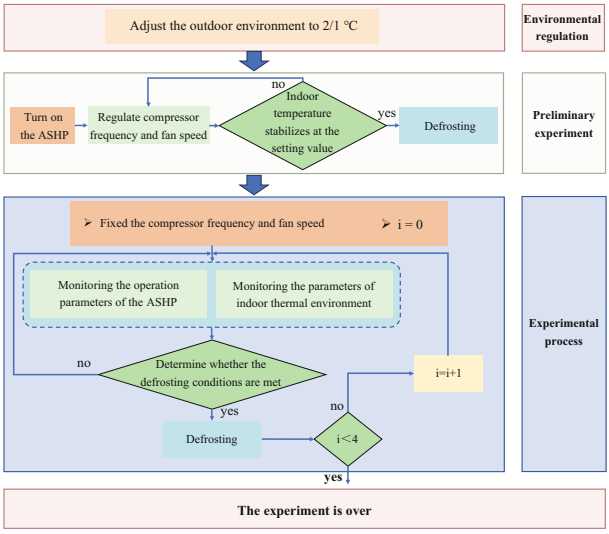


Fig. 3. Experimental process.

3 Experimental Results

3.1 Heating Performance Analysis of ASHP

Fig. 4 illustrates the variations of supply and return water temperature during the four groups of repeated frosting-defrosting experiments of the AWHP. As expressed in Sect. 2.4, before the experiments, a defrosting operation was executed at the end of preliminary experiment to eliminate the effect from frost accumulated on outdoor coil. In all the four groups of experiments, the supply and return water temperature ultimately stabilized at approximately 40 °C and 34 °C. At the time of 47.75, 98.75, 151.67, and 202.83 min, the operation parameters of AWHP met the initiation criteria of defrosting expressed in Sect. 2.2. The four-way valve switched, and the AWHP was shut down for 2 min. During the four groups of experiments, when the defrosting went on 1.33 min, 1.17 min, 1.41 min, and 1.59 min respectively, the heat absorption of refrigerant from the circulating water reached the maximum. The corresponding temperature difference between supply and return water temperature was −12.2 °C, −12.8 °C, −12.7 °C, and − 12.7 °C in turn. When the surface temperature of outdoor coil reached 20 °C, the defrosting terminated, and the AWHP was shut down automatically for 2 min again. Then, the four-way valve switched again, and the AWHP restarted to supply heating.

In the four groups of experiments, the defrosting durations, i. e. the time duration between two four-way valve switching, were 2.25 min, 2.08 min, 2.25 min, and 2.34 min respectively. Considering the two 2-min shutdown before each four-way valve switching, the total interruption intervals of space heating caused by defrosting were 6.25 min, 6.08 min, 6.25 min and 6.34 min, respectively. Although the total interruption intervals are not long, the fan-coils and refrigerant absorbed heat from the circulating water

simultaneously. This made return water temperature drop to approximately 16.0 °C in all the four groups of experiments. After the second four-way valve switching, the AWHP restarted to supply heating, and experienced a heating-resume period to make the supply water temperature rise to 38.0 °C, at which point the heating performance of AWHP was considered to have returned to normal. In the four groups of experiments, the heating-resume period was 8.75–10.00 min. Therefore, the total abnormal space heating durations caused by defrosting, including defrosting, two shutdowns, and heating-resume period, were 14.83–16.34 min.

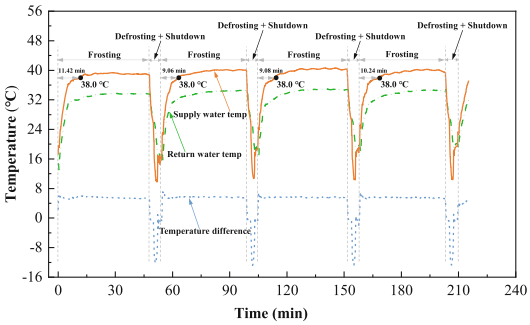


Fig. 4. Water temperature variations of the AWHP during experimental process.

Figure 5 illustrates the supply and return air temperature variations during the four groups of frosting-defrosting experiments of the AAHP. The total experimental duration was 228 min. The experiment was also started when the AAHP restarted to supply heating after the defrosting operation in the preliminary experiment, and stopped when the supply air temperature reached 36.0 °C after the defrosting in the fourth group of experiment. During the four groups of experiments, when the space heating of AAHP reached stability, the supply and return air temperature maintained at around 36.0 °C and 25.0 °C, respectively. The defrosting operation initiated at the time of 44.00 min, 93.58 min, 151.33 min, and 214.17 min, and the defrosting durations were 2.25 min, 2.42 min, 2.75 min, and 2.91 min in turn. As expressed in Sect. 2.2, the AAHP experienced a 1-min shutdown before the two four-way valve switching. Consequently, for AAHP, the total interruption intervals of space heating caused by defrosting were 4.25, 4.42, 4.75, and 4.91 min. During the defrosting process, the indoor fan-coil was turned off. This made the air temperature near its inlet just decrease slightly. However, owing to the natural-convection heat transfer, the air temperature at the outlet of indoor fan-coils decreased significantly to around 20.0 °C. When AWHP had restarted to supply heating, the supply air temperature increased rapidly. In the four groups of experiments, the heating-resume durations, during which time the supply air temperature returned to 34.0 °C, were 6.33 min, 5.67 min, 5.67 min, and 5.09 min in turn. Therefore, the total abnormal space heating durations caused by defrosting, including defrosting, two shutdowns, and heating-resume period, were 10.00–10.58 min.

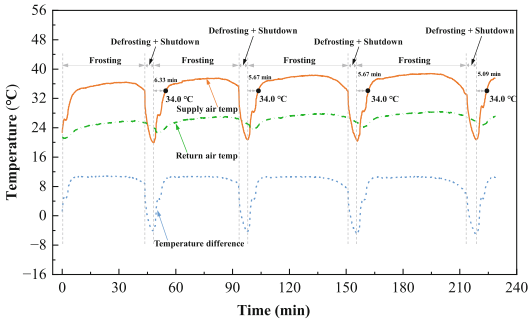


Fig. 5. Air temperature variations of the AAHP during experimental process.

The comparison of Figs. 4 and 5 reveals that the variation trends of supply and return water temperature in AWHP heating system agreed well with the variation trends of supply and return air temperature in AAHP heating system. Specifically, the temperature increased gradually during the frosting process, while dropped rapidly during the defrosting process. However, the recovery speed of temperatures varies a lot between the AWHP heating system and AAHP heating system.

3.2 Variations of Indoor Thermal Environment

Figures 6 and 7 present the variations in indoor air temperature and relative humidity in the four rooms during the experiments. As described in Sect. 2.3, 270, 150, 90, and 210 thermocouples were respectively installed in the four rooms to monitor the indoor temperature. Since the temperature varied across different locations, the average values of all thermocouple readings in each room are displayed in Figs. 6 and 7. Throughout the experiment, although the temperature in all four rooms overall exhibited a slight upward trend, they remained stable near the setpoint values. For both the AWHP and AAHP, a significant drop in indoor temperature was observed during the defrosting process. The maximum indoor temperature drop reached 4.66 °C in rooms heated by the AWHP (Rooms 1–3), while it was only 1.79 °C for the room heated by the AAHP (Room 4). Furthermore, the average temperature decline in each room during four groups of frosting-defrosting was calculated. The average temperature drop in the three rooms heated by the AWHP was 3.61 °C, 3.28 °C and 4.27 °C respectively, while only 1.71 °C in the room heated by the AAHP. This indicates that the temperature drop in the rooms heated by the AWHP is significantly larger than that in the room heated by the AAHP. Additionally, the temperature recovery rate in the room heated by AWHP was notably slower than that heated by AAHP. Taking Room 1 as an example, in the first three groups of experiments, the time for the indoor temperature to recover to the value before defrosting operation was 31.17 min, 31.50 min, and 29.58 min, respectively. Meanwhile, for Room 4, the time was 19.33 min, 24.92 min, and 25.54 min, respectively (Table 2).

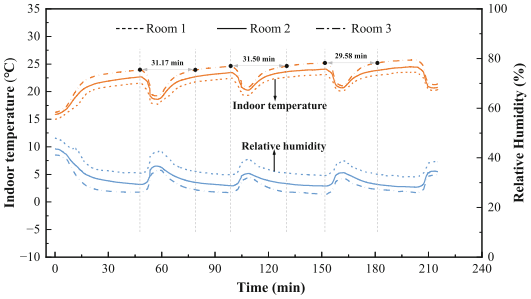


Fig. 6. Variations of indoor temperature during experimental process.

Table 2. Temperature drop magnitude after each frosting-defrosting process.

Item	1st defrosting (°C)	2nd defrosting (°C)	3rd defrosting (°C)	4th defrosting (°C)	Average value (°C)
Room 1	4.06	3.18	3.41	3.79	3.61
Room 2	3.73	3.12	2.99	3.28	3.28
Room 3	4.66	3.78	4.16	4.49	4.27
Room 4	1.58	1.70	1.77	1.79	1.71

In Figs. 6 and 7, it can be observed that the variation trend of relative humidity in all the four rooms was opposite to that of indoor temperature. Throughout the experimental process, for all the four rooms, noticeable fluctuations in indoor relative humidity could be observed. Specifically, the relative humidity in the rooms heated by AWHP increased by 13.73%–25.01%, while 9.05%–10.66% in the room heated by AAHP. This indicates that the frosting-defrosting of AWHP has a greater impact on indoor relative humidity. As the heating resumed after the defrosting operation, the relative humidity gradually decreased again, and reached its minimum value just before the next defrosting operation.

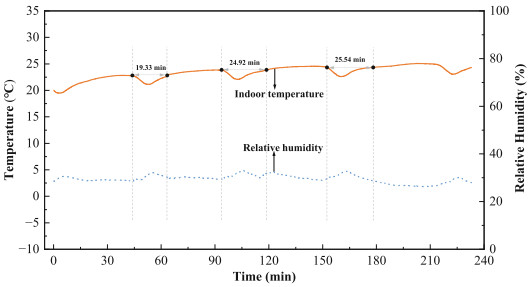


Fig. 7. Variations of indoor relative humidity during experimental process.

4 Conclusions

To reveal the of indoor thermal environment variation rules during the dynamic frosting-defrosting process of air source heat pump (ASHP), two test rigs, an air-water heat pump (AWHP) heating system and an air-air heat pump (AAHP) heating system, were built in an artificial environmental chamber. Through creating the frosting environmental condition, the practical space heating experiments of ASHP during frosting-defrosting process were conducted. Then, based on the experimental results, the indoor thermal environment variation rules of the two ASHPs and their differences were analyzed. The main findings are as follows.

(1) During the defrosting process, the indoor temperature using both AWHP and AAHP decreases obviously, and the decline amplitude in rooms using AWHP is greater. During the four groups of frosting-defrosting experiments, the temperature decline in rooms using AWHP is 2.63–5.48 °C, with an average of 3.72 °C. Meanwhile, the temperature decline in the room using AAHP is 1.58–1.79 °C, with an average of 1.71 °C.
(2) For AWHP, during the late stage of its defrosting operation, the indoor fan-coils will absorb heat from indoor air, rather than supply heating. At the 0.58th min of defrosting operation, the supply water temperature decreased to 18.10 °C, and became lower than indoor air temperature. The circulating water started to absorb heat from indoor air. Owing to the coupled effect of heat absorption of fan-coil and heat dissipation to outdoor environment, the indoor temperature decline speed was greater.

References

1. Xu, Y., Huang, Y., Jiang, N., Song, M., Xie, X., Xu, X.: Experimental and theoretical study on an air-source heat pump water heater for northern China in cold winter: effects of environment temperature and switch of operating modes. Energ. Buildings. **191**, 164–173 (2019)
2. Ma, G., Lu, T., Liu, F., Niu, J., Xu, S.: Experimental study on hot liquid subcooling defrosting of an air source heat pump with multi-connected outdoor units. Energ. Buildings. **291**, 113104 (2023)
3. Rogeau, A., Vieubled, J., Ruche, L., Girard, R.: A generic methodology for mapping the performance of various heat pumps configurations considering part-load behavior. Energ. Buildings. **318**, 114490 (2024)
4. Xu, Y.J., Zhang, H.R., Wu, K., Jin, H.Q., Song, M.J., Shen, X.: Comparative study on adaptable intelligent frost recognition method for air-source heat pump and cold chain based on image texture features under complex lighting conditions. Int. J. Refrig. **175**, 273–287 (2025)
5. Wang, W., Zhang, S., Li, Z., Sun, Y., Deng, S., Wu, X.: Determination of the optimal defrosting initiating time point for an ASHP unit based on the minimum loss coefficient in the nominal output heating energy, Pergamon. Energy. **191**, 116505 (2020)
6. Li, Z.Y., Wang, W., Sun, Y.Y., Wang, S.Q., Deng, S.M., Lin, Y.: Applying image recognition to frost built-up detection in air source heat pumps. Energy. **233**, 121004 (2021)
7. Wei, P., Wang, Z.W., Feng, H.L., Wang, S., Fan, J.F.: Frost suppression performance of an air source heat pump using sensible heat from indoor air to preheat outdoor air. Build Serv Eng Res Technol. **44**, 537–555 (2023)

8. Dong, J.K., Jiang, Y.Q., Yao, Y., Zhang, X.D.: Operating performance of novel reverse-cycle defrosting method based on thermal energy storage for air source heat pump. J. Cent. S. Univ. Technol. **18**, 2163–2169 (2011)
9. Wei, W.Z., Ni, L., Dong, Q., Wang, W., Ye, J.Y., Xu, L.F., Yang, Y.H., Yao, Y.: Experimental investigation on improving defrosting performance of air source heat pump through vapor injection. Energ. Buildings. **25**, 111696 (2022)
10. Qu, M.L., Xia, L.A., Deng, S.M., Jiang, Y.Q.: Improved indoor thermal comfort during defrost with a novel reverse-cycle defrosting method for air source heat pumps. Build. Environ. **45**, 2354–2361 (2010)

Performance Evaluation of a CO_2 Air Source Heat Pump Integrated with Binary Hydrate Salt Composite for Frost Mitigation under Cold and Humid Conditions

Minglu Qu[1(✉)], Zhenfang Ma[1], Jing Lv[2], Hongzhi Liu[3], and Jiajie Chen[1]

[1] School of Environment and Architecture, University of Shanghai for Science and Technology, Shanghai 200093, China
quminglu@126.com

[2] Architecture Engineering College, Qingdao Bin Hai University, Qingdao 266555, China

[3] Environmental System Research LaboratoryFaculty of Engineering, Hokkaido University, Sapporo, Japan

Abstract. CO_2 air source heat pumps (ASHPs) present significant advantages for residential and commercial heating applications due to their high thermodynamic efficiency and environmental benefits. However, evaporator frosting during winter operation leads to substantial performance degradation cold-humid climates. To address this challenge, this research introduces a novel frost mitigation strategy through integration of a binary hydrated salt composite (BHSC) dehumidification device within a CO_2 ASHP. The composite material was synthesized via vacuum impregnation of LiCl/$CaCl_2$ into mesoporous diatomaceous earth (WSS) and experimentally optimized. The 4LiCl/$CaCl_2$ formulation (4,1 M ratio) demonstrated superior moisture sorption performance, achieving a maximum equilibrium moisture uptake of 0.482 $g{\cdot}g^{-1}$. A comprehensive model of the CO_2 ASHP system integrated with BHSC dehumidification device was developed and experimentally validated. Simulations under varied outdoor temperature (−4 °C ~ 0 °C) and humidity (70% ~ 100%) conditions revealed significant performance improvements: evaporation temperature increased by up to 1.0 °C, evaporator heat exchange capacity enhanced by up to 17.8%, system heating capacity boosted by up to 5.3%, and COP elevated by up to 5.3%. These results demonstrate that the effectiveness of BHSC in enhancing operational stability and thermal performance in low-temperature, high-humidity conditions. The study provides a validated material-based solution to mitigate winter performance degradation in CO_2 ASHPs.

Keywords: Frost mitigation · CO_2 air source heat pumps · Binary hydrate salt composite

1 Introduction

China's 'Carbon Peak Carbon Neutrality' targets necessitate urgent advancements in decarbonized heating technologies. CO2 air source heat pumps (ASHPs), recognized for their high volumetric heating capacity and efficient hot water production [1], represent

© The Author(s), under exclusive license to Springer Nature Singapore Pte Ltd. 2025
L. Ni et al. (Eds.): CCHVAC 2025, ESE, pp. 97–104, 2025.
https://doi.org/10.1007/978-981-95-3253-7_11

promising solutions. However, these systems frequently experience evaporator frosting in cold and humid climates, causing significant performance degradation and potential operational instability or shutdown [2]. To mitigate these issues, research into advanced defrosting and anti-frosting technologies has become imperative.

Conventional defrosting strategies primarily include reverse cycle defrosting and hot gas bypass defrosting [3]. However, these approaches often cause temporary interruptions in indoor heating and consume additional energy [4]. In contrast, anti-frosting technologies prevent frost formation by preconditioning inlet air conditions, offering a more fundamental solution. Recent studies have explored dehumidification-based anti-frosting approaches: LiCl solution [5] silica gel desiccant [6], and solid $CaCl_2 \cdot 6H_2O$ [7] have demonstrated effectiveness in reducing evaporator surface humidity and improving Coefficient of Performance (COP). Furthermore, Zheng et al. [8] developed carbon-based composite desiccants by impregnating LiCl into the pores of activated carbon and activated carbon fibers for desiccant-coated heat exchanger systems. Studies have found that compared to liquid desiccants, solid desiccants, despite having limited air handling capacity, offer advantages such as high dehumidification efficiency, fewer system components, smaller footprint, simpler control, lower regeneration power consumption, and reduced operation and maintenance costs [9].

Despite these advances, Existing literature predominantly focuses on single-salt composites, while binary salt applications remain underexplored despite their superior stability and hygroscopicity. Therefore, this study develops a composite desiccant by impregnating binary hydrated salts ($LiCl/CaCl_2$) onto mesoporous diatomaceous earth (WSS) substrate, subsequently integrating into a CO_2 ASHP system. The performance impact is quantitatively evaluated via validated simulation models.

2 Methodology

2.1 System Description

The system schematic of the CO_2 ASHP integrated with binary hydrate salt composite (BHSC) dehumidification device is shown in Fig. 1, illustrating airflow preconditioning for evaporator frosting mitigation. The proposed system integrates a BHSC dehumidification unit upstream of the finned-tube evaporator. Unlike conventional CO_2 ASHP configurations, this arrangement enables preconditioning of outdoor airflow prior to entering the evaporator. During operation, ambient outdoor air passes sequentially through the dehumidification device and the evaporator. This process reduces the dew point attainment probability of the processed air, thereby effectively suppressing frost formation on the evaporator surface.

2.2 Material Synthesis and Characterization

The composite desiccant material was synthesized by impregnating a binary hydrated salt mixture ($LiCl/CaCl_2$) into a WSS through vacuum impregnation. with. WSS was chosen as the porous matrix due to its favorable pore characteristics and structural stability post-impregnation [10]. The $LiCl–CaCl_2$ binary system leverages the complementary

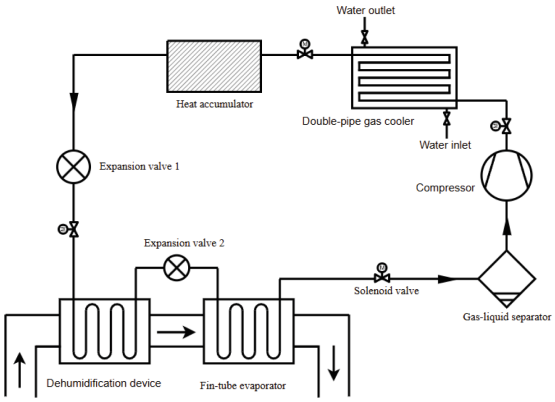


Fig. 1. System schematic of the CO_2 ASHP integrated with BHSC dehumidification device.

properties of both salts: LiCl provides superior hygroscopicity while $CaCl_2$ enhances composite stability, collectively reducing deliquescence risk and solution leakage under high-humidity conditions

Seven composite formulations with varying LiCl: $CaCl_2$ molar ratios were synthesized and characterized under controlled environmental conditions. The 4:1 M ratio variant (designated 4LiCl/$CaCl_2$-WSS) exhibited optimal dehumidification performance, achieving a maximum equilibrium moisture uptake of 0.482 $g{\cdot}g^{-1}$ at 0 °C/80% RH. This formulation was consequently selected for system integration.

2.3 Dehumidification Device Design

The BHSC dehumidification device was engineered as a fixed honeycomb-structured wheel incorporating the 4LiCl/$CaCl_2$-WSS composite. The monolithic structure features uniformly distributed hexagonal flow channels, each fully impregnated with the composite material. The geometric configuration maximizes the air-composite contact area while maintaining mechanical stability under operational stresses.

2.4 Simulation

CO2 ASHP Modeling. A dynamic simulation model of the CO_2 ASHP integrated with BHSC dehumidification device was developed using MATLAB/Simulink. Mathematical representations of core thermodynamic components, including the compressor, gas cooler, expansion valve, and evaporator, were established based on mass and energy conservation principles. Components models were implemented using the Thermolib library to ensure physically accurate representations of transcritical CO_2 behavior. The dehumidification device was simulated using the enthalpy difference method [11], accounting for moisture adsorption kinetics and latent heat effects. The modular components were integrated into a system-level simulation platform to evaluate operational performance at ambient temperatures of 0 °C, −2 °C, and − 4 °C (at 85% relative humidity), and at relative humidity levels of 70%, 85%, and 100% (at −2 °C), both with and without the BHSC dehumidification device.

Validation. Experimental validation was performed using a 3.2 kW CO_2 ASHP test unit, with specifications summarized in Table. 1. Under controlled laboratory conditions: water inlet temperature of 9 °C, water flow rate of 80 L/h, ambient temperature of 2 °C and RH of 80%, the EEV opening was systematically varied from 15% to 21%. As shown in Fig. 2, simulated COP values demonstrated strong agreement with experimental data across all operating points, with all points falling within ±10% error bounds. This statistical confirmation establishes model reliability for subsequent performance analysis.

Table 1. Specification of the experimental CO_2 ASHP unit.

Items	Parameters	Values
Compressor	Refrigerant	CO_2
	Displacement (m^3/h)	1.12
	Rated input power (kW)	1.4
	Nominal heating capacity (kW)	4.1
Evaporator	Type	Finned tube
	Fin pitch (mm)	1.9
	External diameter (mm)	7
	Pipe distance (mm)	18.2
	Number of pipe rows	3
	Air volume (m^3/h)	1500
Gas cooler	Type	Double pipe
	External diameter (mm)	16
	Pipe length (mm)	12
	Unit length heat exchange area (m^2)	3.73×10^{-2}
Electronic expansion valve	Maximum working pressure (MPa)	15
	Operating temperature range (°C)	−3-70

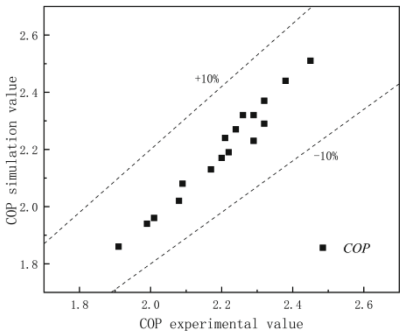


Fig. 2. Verification of CO_2 ASHP with BHSC dehumidification device.

3 Results and Discussion

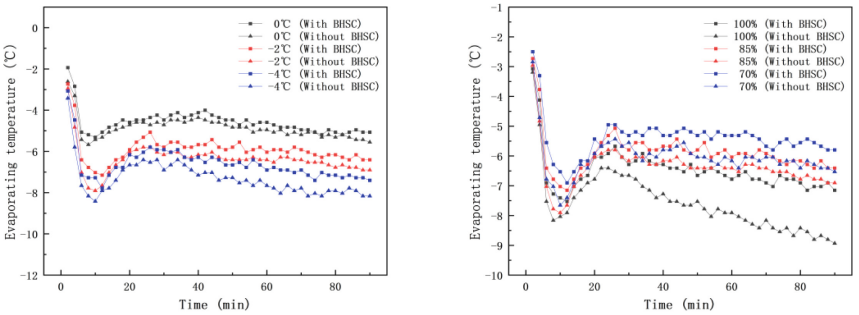
The heating performance of CO_2 ASHP system integrated with BHSC dehumidification device was evaluated through validated simulations across varied outdoor conditions. Comparative analysis against a conventional CO_2 ASHP (without dehumidification) was conducted at controlled operating parameters: constant water inlet temperature (9 °C), flow rate (80 L/h), and EEV opening (15%). Test conditions comprised:

- Ambient temperatures: 0 °C, −2 °C, −4 °C (at 85% RH)
- Relative humidity: 70%, 85%, 100% (at −2 °C)

Figure 3 illustrates the effect of BHSC dehumidification device on evaporating temperature. When the ambient temperature decreased from 0 °C to −4 °C at 85% RH, the system with the BHSC dehumidification device maintained evaporating temperatures up to 1.0 °C higher than the conventional system. Additionally, at ambient temperature of −2 °C, increasing RH from 70% to 100% resulted in a maximum evaporating temperature elevation of 0.85 °C. These improvements are attributed to the strong hygroscopic properties of the BHSC dehumidification device, which effectively preconditions the inlet air, though moisture content reduction, latent-to-sensible heat conversion during adsorption and thus decreased frost nucleation potential on evaporator surfaces.

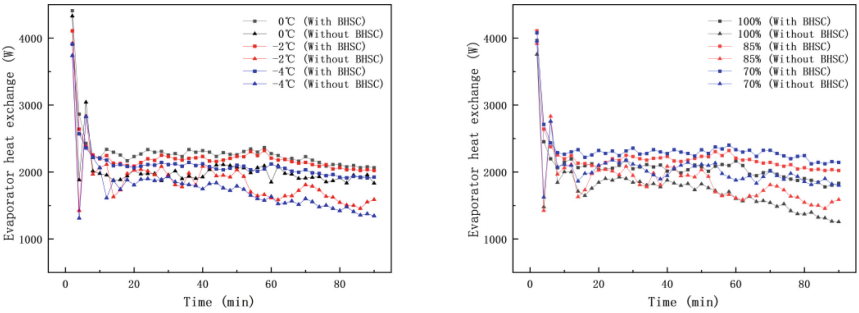
Figure 4 presents the enhancement in the heat exchange of the evaporator when adopting the BHSC dehumidification device. When the ambient temperature fell from 0 °C to −4 °C, the heat exchange was boosted by 14.9% to 15.9%. At −2 °C, as the RH increased from 70% to 100%, the heat exchange increased from 14.2% to 17.8%. This enhancement stems from reduced frost formation on the evaporator surface due to lowered air humidity. Thus, the air-side heat transfer coefficient through sustained dry-surface operation was maintained.

Figure 5. depicts the influence of the dehumidification device on the system heating capacity. As the ambient temperature decreased from 0 °C to −4 °C, the heating capacity was elevated from 3.4% to 4.7%. Likewise, at an ambient temperature of −2 °C, the heating capacity gain ranged from 5.1% to 5.3% as the RH increased from 70% to 100%. The direct correlation between evaporator performance (Fig. 4) and system heating capacity confirms that frost mitigation preserves refrigerant-side heat transfer efficiency, enabling greater heating output.



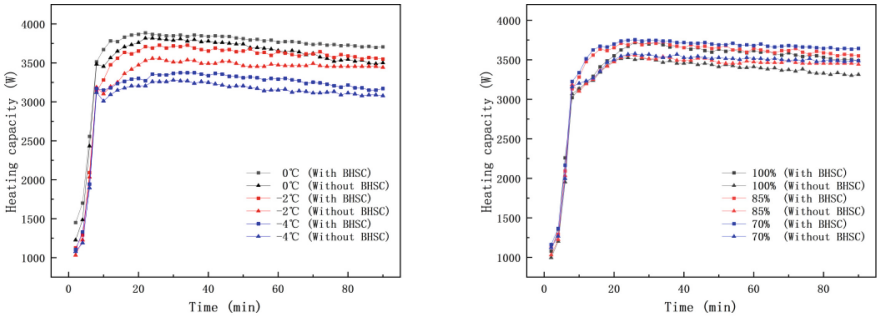
(a) Different Temperature (b) Different RH

Fig. 3. The effect of dehumidification device on evaporation temperature.



(a) Different Temperature (b) Different RH

Fig. 4. The effect of BHSC dehumidification device on heat exchange of evaporator.

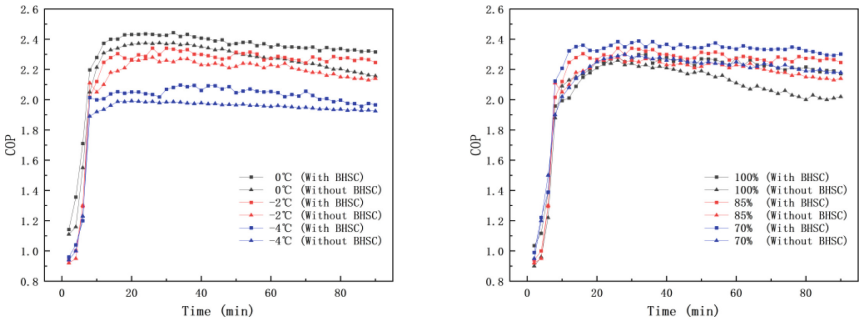


(a) Different temperature (b) Different RH

Fig. 5. The effect of dehumidification device on system heating capacity.

Figure 6 demonstrates the COP enhancement of the BHSC dehumidification device versus conventional system. Within the ambient temperature range of 0 °C to −4 °C, average COP increased from 3.4% to 5.3% when adopting the BHSC dehumidification device comparing with that of conventional system. At ambient temperature of

−2 °C, the average COP improved by 3.8–5.1% as RH climbed from 70% to 100%This improvement results from the BHSC device's dual effect: substantial heating capacity augmentation (Fig. 5) with minimal additional compressor power input. The COP gain is particularly pronounced at higher humidity levels where frost accumulation would otherwise cause disproportionate performance degradation.



(a) Different temperature (b) Different RH

Fig. 6. The effect of dehumidification device on system COP.

4 Conclusions

To mitigate frosting in CO_2 ASHPs, this study proposed a BHSC dehumidification device integrated within a CO_2 ASHP system. Based on validated simulations and material characterization, the following conclusions are drawn:

1. A high-performance desiccant composite was synthesized by vacuum impregnation of $LiCl/CaCl_2$ binary salts (4:1 M ratio) into WSS substrate. This formulation achieved a maximum equilibrium moisture uptake of 0.482 $g{\cdot}g^{-1}$ at 0 °C/80% RH.
2. The BHSC-integrated system significantly outperformed conventional CO_2 ASHPs under frost-prone conditions (−4 °C to 0 °C; 70–100% RH). The BHSC significantly improved heating performance, evaporator heat exchange capacity increased by 14.2–17.8%, system heating capacity improved by 3.4–5.3%, and COP elevated by 3.4–5.3%. Peak enhancements occurred at −4 °C/100% RH - conditions where conventional systems experience severe frosting.
3. Performance improvements are attributed to 1) dew-point depression via air preconditioning, and 2) reduced thermal resistance from suppressed frost formation.

This research establishes BHSC integration as a viable solution for frost-induced performance degradation in CO_2 ASHPs operating in cold-humid climates. Future work should explore long-term material stability and scalability.

Acknowledgments. This research was sponsored by Shanghai Pujiang Program (No. 23PJ1409400).

References

1. Song, Y., Cui, C., Yin, X., Cao, F.: Advanced development and application of transcritical CO_2 refrigeration and heat pump technology—a review. Energy Rep. **8**, 7840–7869 (2022)
2. Eom, Y.H., Chung, Y., Park, M., Hong, S.B., Kim, M.S.: Deep learning-based prediction method on performance change of air source heat pump system under frosting conditions. Energy. **228**, 120542 (2021)
3. Huang, S., et al.: Advances, challenges and outlooks in frost-free air-source heat pumps: a comprehensive review from materials, components to systems. Appl. Therm. Eng. **234**, 121163 (2023)
4. Zhang, Y., Zhang, G., Leng, X., Qu, X., Tian, M.: Research progress on frost-free air source heat pump technology. CIESC J. **71**(12), 5400–5415 (2020)
5. Zhang, Y., et al.: Experimental study and performance evaluation of an air source heat pump (ASHP) system with a frost-free evaporator. J. Clean. Prod. **448**, 141469 (2024)
6. Wang, Z., Li, G., Wang, F., Li, K., Lou, Y.: Techno-economic evaluation of a frost-free air source heat pump water heater. Sustain. Cities Soc. **57**, 102102 (2020)
7. Wang, F., et al.: Performance investigation of a novel frost-free air-source heat pump water heater combined with energy storage and dehumidification. Appl. Energy. **139**, 212–219 (2015)
8. Zheng, X., Wang, R.Z., Ge, T.S.: Experimental study and performance predication of carbon-based composite desiccants for desiccant coated heat exchangers. Int. J. Refrig. **72**, 124–131 (2016)
9. Zhang, Y., He, F., Wang, Y., Li, C., Zhang, G., Zhou, D.: Recent advances, challenges and future prospects on frost-free air source heat pump technology with integrated solid desiccant dehumidification. Renew. Sust. Energ. Rev. **219**, 115877 (2025)
10. Thoruwa, T.F.N., Johnstone, C.M., Grant, A.D., Smith, J.E.: Novel, low cost CaCl2 based desiccants for solar crop drying applications. Ren. Energy. **19**, 513–520 (2000)
11. Kuehn, T.H., Ramsey, J.W., Threlkeld, J.L.: Thermal Environmental Engineering. Prentice Hall, Upper Saddle River. (12)

Performance Enhancement of CO_2 Air Source Heat Pumps via Photovoltaic-Thermal (PV/T) Air Preheating: A Simulation and Experimental Study

Minglu Qu(✉), Haoqiang Zhao, Guoqing Yu, Zhenfang Ma, and Changling Lu

School of Environment and Architecture, University of Shanghai for Science andTechnology, Shanghai 200093, China
quminglu@126.com

Abstract. Solar energy plays a crucial role in global energy transformation due to its cleanliness, renewability and environmental benefits. Concurrently, transcritical carbon dioxide (CO_2) heat pump systems offer high efficiency with low carbon footprint. The study proposes a novel integration of these technologies: a CO_2 air source heat pump (ASHP) synergistically coupled with upstream photovoltaic-thermal (PV/T) air heaters. The configuration preheats evaporator, inlet air through solar-thermal conversion, thereby increasing the evaporation temperature and enhancing system performance. Mathematical models developed in MATLAB and Excel experimentally validated and employed for comparative winter operating analysis against a conventional CO_2 ASHP. The research results show that the novel system exhibited a 14.2% increase in heat output and a 1.6% reduction in power consumption compared to the conventional system throughout the winter, with peak monthly heating output improvements reaching 16.9%. Crucially, the PV/T-integrated seasonal coefficient of performance ($SCOP_{PVT}$) exhibits 48.5% average enhancement over the conventional system. This work provides a validated strategy for significantly improving the energy efficiency and decarbonization in cold climates space heating.

Keywords: CO_2 air-source heat pump · Photovoltaic-thermal air heater · Renewable energy integration

1 Introduction

Buildings account for nearly 40% of global energy consumption, and their energy demand is projected to increase further in the future [1]. Therefore, the research and application of low-carbon clean energy systems have gained critical importance. Solar photovoltaic/thermal (PV/T) technology has seen significant advancements due to solar energy's inherent advantages as a clean and renewable resource. Recent studies have increasingly focused on integrating solar PV/T systems with air source heat pump

© The Author(s), under exclusive license to Springer Nature Singapore Pte Ltd. 2025
L. Ni et al. (Eds.): CCHVAC 2025, ESE, pp. 105–113, 2025.
https://doi.org/10.1007/978-981-95-3253-7_12

(ASHP). For example, Han et al. [2] established a mathematical model for the PV/T heat pump system, analyzed the impact of environmental conditions on the system performance, and established operational boundaries through condenser temperature analysis. Their case study in Lhasa demonstrated, the life cycle carbon emission reduction advantage of the system compared to standalone PV system.

Refrigerants such as CO_2, possessing zero-ozone depletion potential (ODP = 0) and low greenhouse gas potential (GWP = 1), demonstrates significant application potential in heating and cooling via CO_2 heat pump systems. There is a lot of current research on CO_2 heat pump systems [3, 4]. For example, Ma et al. [5] developed models to compare the performance of indirect-expansion solar-assisted heat pumps using one-stage transcritical CO_2, two-stage transcritical CO_2, and one-stage R410a cycles for space heating in cold climates. They found that the two-stage CO_2 cycle was more competitive, achieving a significantly higher free energy ratio at a much smaller optimal compressor output compared to the other cycle. Rocha et al. [6] presented an experimental study of a direct expansion solar-assisted heat pump (DX-SAHP) using a transcritical CO_2 cycle, where CO_2 directly absorb heat within the solar collector. The results showed that increased solar irradiance could elevate heat output by 58% and improve the performance coefficient of performance (COP) from 2.19 to 3.12.

The existing literature reveals that most studies focus on relatively simple configurations of PV/T and CO_2 ASHP, with limited analysis on the long-term performance. To address this gap, this study introduces a configuration incorporating a PV/T air heater to preheat the incoming air, and seasonal COP (SCOP) metric is employed to evaluate the long-term operation efficiency of the system comprehensively.

2 System Description

Figure 1 presented the schematic diagram of the novel CO2 ASHP system coupled with PV/T air heater, highlighting airflow and energy pathways. The PV/T simultaneously air heater harnesses solar radiation via concurrent photovoltaic-electrical conversion and thermal energy collection for air preheating. The preconditioned supply air exiting the PV/T air heater is delivered to the evaporator, elevating its inlet air temperature. This preheating effect significantly enhances the thermodynamic efficiency and heating output of the heat pump cycle. Detailed specifications of the system components are provided in Table. 1. Based on the airflow requirements of the evaporator, the system configuration necessitates 11 parallel PV/T air heaters.

3 Methodology

Mathematical models for the novel CO_2 ASHP system coupled with PV/T air heater were developed to simulate system performance. The PV/T air heater model was implemented in Microsoft Excel, while the CO_2 ASHP model was developed in MATLAB. All model were consistent with the experimental setup specifications. The PV/T air heater model calculates key performance parameters for solar energy collection and electrical power generation. The simulated outlet air temperature from the PV/T air heater served as the critical inlet air temperature boundary condition for the evaporator in the CO_2 ASHP. In

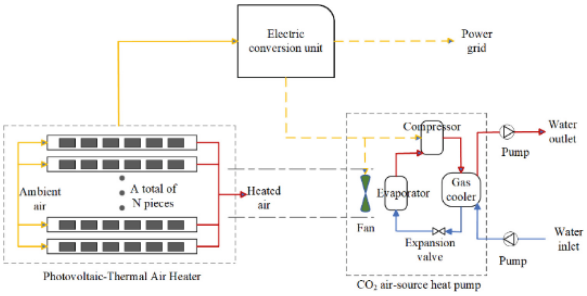


Fig. 1. Schematic diagram of novel CO_2 ASHP system coupled with PV/T air heater.

the mathematical model of the CO_2 ASHP, Component-level models (compressor, gas cooler, evaporator, expansion device) were developed sequentially based on fundamental thermodynamic equations and heat transfer correlations. Theses component models were integrated into a complete system-level simulation. The encapsulated system model output key performance indicators, including system heating output, compressor power consumption and SCOP for the PV/T-integrated system ($SCOP_{PVT}$).

3.1 Mathematical Model

PV/T air heater: a simplified heat transfer model was employed, establishing energy balance equations for each structural layer node. The model incorporating key assumptions and structural characteristics, with balance equations and heat transfer parameters derived from established calculation methodologies [7].

Gas cooler: A distributed parameter approach was implemented. The gas cooler was discretized into multiple segments along the pipe length. Calculations were performed iteratively, with outlet parameters of each segment serving as inlet conditions of the subsequent segment. The energy balance of each infinitesimal segment is given by:

$$Q_j = K_j A_j \Delta t_{m,j} \tag{1}$$

where K_j is the total heat transfer coefficient for the segment j, and $\Delta t_{m,j}$ is the logarithmic average temperature difference for segment j.

The total refrigerant-side heat release is:

$$Q_{r,j} = m_{r,j}\left[h(T,P)_{i,j} - h\left(T,P\right)_{o,j}\right] \tag{2}$$

Evaporator: steady-state lumped parameter modeling is adopted, accounting for CO_2 phase change during evaporation. Refrigerant and air flows were treated as one-dimensional steady-state flows with uniform air distribution. The governing equations for any segment are:

Refrigerant heat absorption:

$$Q_j = m_{r,j}\left(h_{ro,j} - h_{ri,j}\right) \tag{3}$$

Air-side heat transfer:

$$Q_j = m_{a,j}\left(h_{ai,j} - h_{ao,j}\right) \tag{4}$$

where $h_{ri,\,j}$ and $h_{ro,\,j}$ represent the refrigerant enthalpies at the inlet and outlet, while $h_{ai,\,j}$ and $h_{ao,\,j}$ represent the air enthalpies at the inlet and outlet.

Compressor: Isentropic compression was assumed with steady refrigerant flow and negligible heat losses. Isentropic efficiency ef_{isen} were determined using empirical correlations from Reference [8].

Shaft power is given by:

$$W_c = \frac{M_r\left(h_{dis,isen} - h_{suc}\right)}{ef_{isen}ef_{\,mc}} \tag{5}$$

where $h_{dis,\,isen}$ represents discharge enthalpy, h_{suc} represents suction enthalpy and $ef_{\,mc}$ represents mechanical efficiency.

Electronic expansion Valve (EEV): An isenthalpic process was assumed. Pressure-drop Δp_{mv} of the electronic expansion valve is obtained according to the fitting formula in reference [8]. The pressure at the valve outlet is:

$$p_{vo} = p_{vi} - \Delta p_{mv} \tag{6}$$

where p_{vo} and p_{vi} represent outlet and inlet pressure.

Table 1. Specification of novel CO_2 ASHP system coupled with PV/T air heater.

Items	Type	Parameter
Compressor	Reciprocating	Nominal heating output: 4.61 kW Rated power input: 1.4 kW Displacement: 1.12m^3/h (50 Hz) Speed: 1450 rpm (50 Hz)
Evaporator	Finned-tube	3 rows × 30 tubes Single tube length: 0.86 mm Outer diameter: 7 mm Wall thickness: 0.41 mm Fin type: straight fins Fin spacing: 1.9 mm
Gas cooler	Double-pipe	Inner pipe diameter: 9.52 mm (wall: 1.5 mm) Outer pipe diameter: 16 mm (wall: 1.5 mm)
EEV	JKV-24D27	Maximum working pressure: 15 MPa Operating temperature: −30 ~ 70 ° C
PV/T air heater	Flexible monocrystalline	Size: 1200 mm * 600 mm Area: 0.72 m^2 PV layer: 2 mm mono-Si Rated power: 100 W

3.2 Performance Indices

To comprehensively evaluate winter operational efficiency SCOP [9] and $SCOP_{PVT}$ are adopted:

$$SCOP = \frac{\sum Q_h}{\sum W_c} \tag{7}$$

where Q_h is heating output and W_c is compressor power consumption.

$$SCOP_{PVT} = \frac{\sum Q_h + \frac{\sum E_e}{0.38}}{\sum W_c} \tag{8}$$

This metric incorporates the electrical energy generated by the PV/T air heaters (E_e). The factor 0.38 is the conventional electrical efficiency.

4 Results and Discussion

4.1 Validation

Experimental validation of the PV/T air heater was conducted on November 26, 2022. Under the following conditions:

The average outdoor ambient temperature was 20.8 °C, with the highest ambient temperature of 24.9 °C. The average irradiance was 356 W/m^2, with the maximum solar irradiance of 433 W/m^2.

Figure 2 compares the simulated and experimental results for heat collection and power generation of the PV/T air heater. Simulated and experimental results exhibited congruent trends, peaking synchronously with solar irradiance. The average errors of the heat collection and the power generation were 4.3% and 6.5%, respectively.

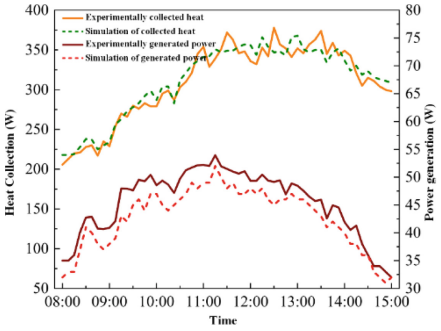


Fig. 2. Simulated and experimental comparison of the heat collection and the power generation of the PV/T air heater.

The CO_2 ASHP was validated under variable ambient temperature conditions with:

Water flow rate: 320 L/h

EEV opening: 45%
Inlet/outlet water temperature: 17 °C/ 60 °C

Figure 3 compared simulated and experimental of COP for the CO_2 ASHP under variable ambient temperatures. Both COP curves show positive correlation with ambient temperature. The peak values of the simulated COP and the experimental COP were 4.63 and 4.45, respectively. The average error of the COP in the simulation and experiment was 4.3%, with the maximum error of 5.9%. These validation errors fall within acceptable range, confirming model reliability for subsequent analysis.

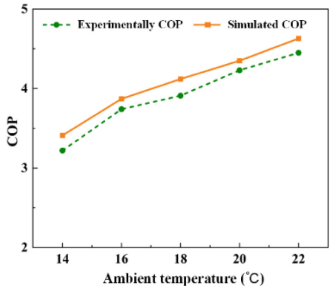


Fig. 3. Comparison of simulated and experimental COP for the CO_2 ASHP under variable ambient temperatures.

4.2 System Comparison

The novel CO_2 ASHP system coupled with PV/T air heater was evaluated against a conventional CO_2 heat pump (without PV/T preheating) under typical Beijing winter conditions. Operational parameters were simulated using meteorological data from existing literature [10], with key system setting as follows: PV/T air heater channel wind speed was 3 m/s, PV/T air heater volumetric flow rate was 0.06m^3/s. The heat pump inlet and outlet water temperatures were 15 °C/60 °C, with the water flow rate of 100 L/h, and the heating output was 3.51 kW. The power consumption was 1.74 kW.

Figure 4 compares the monthly heating output and power consumption of both systems during winter operation. The novel CO2 ASHP system coupled with PV/T air heater demonstrated consistent power consumption trends with the conventional system while achieving a 1.6% average reduction in total energy consumption. More significantly, the novel system increased seasonal heating output by 14.2%—primarily driven by evaporator inlet air preheating from PV/T thermal conversion. Performance differentials peaked in December with a 16.9% heating capacity enhancement, correlating with optimal solar-thermal contribution during peak heating demand periods.

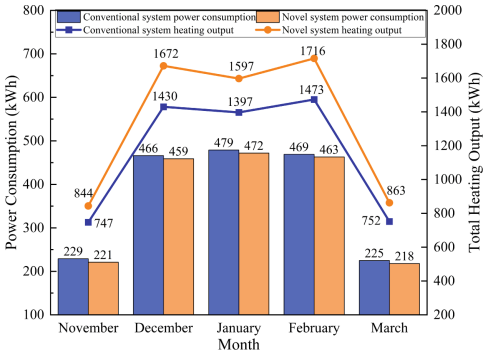


Fig. 4. Comparison of monthly heating output and power consumption for both systems during winter operation.

Figure 5 presents the comparison of monthly SCOP and $SCOP_{PVT}$ of both systems during winter operation. It could be seen the $SCOP_{PVT}$ of the novel system consistently exceeded the SCOP of the conventional system throughout the winter period. March delivered peak performance gains of 52.3% with $SCOP_{PVT}$, driven by substantially elevated solar irradiance while compressor power consumption remained relatively stable. Conversely, the minimum enhancement of 45.7% occurred in November, attributable to diminished solar irradiance coupled with milder ambient temperatures that constrained PV yield. Across the entire winter season, the novel system achieved a 48.5% average improvement in $SCOP_{PVT}$ over conventional operation. These results confirm that the synergistic integration of PV generation and thermal preheating delivers the greatest efficiency advantage when abundant solar resources coincide with persistent heating demands.

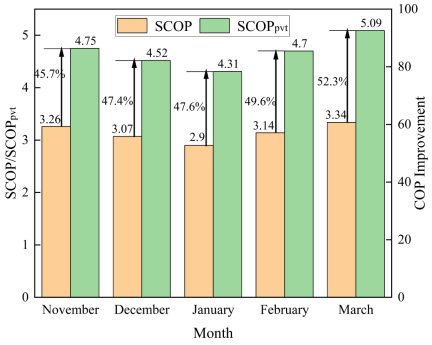


Fig. 5. Comparison of monthly SCOP and $SCOP_{PVT}$ of both systems during winter operation.

5 Conclusions

This study presents a novel integration of PV/T air heater and CO_2 ASHP, introducing comprehensive $SCOP_{PVT}$ analysis to evaluate long-term operational efficiency. Through validated MATLAB and EXCEL modeling, the novel CO_2 ASHP system coupled with PV/T air heater demonstrates significant performance advantages:

1. Compared to the conventional system, the novel system exhibited a 14.2% increase in average heat production and a 1.6% reduction in average total power consumption throughout the winter operation.
2. The $SCOP_{PVT}$ of the novel CO_2 ASHP system coupled with PV/T air heater reveals 48.5% average efficiency improvement across winter months, confirming superior thermodynamic performance under variable climatic conditions.

This integrated approach fundamentally addresses traditional ASHP efficiency limitations by synergizing renewable energy harvesting with environmentally benign refrigerant technology. The dual mechanism of solar-electrical conversion and thermal preheating enables operational resilience through reduced compressor lift during low-ambient conditions, carbon mitigation via displacement of grid electricity and enhanced energy sovereignty through on-site generation-consumption coupling. Future work should investigate lifecycle cost analysis and scalability in diverse climatic regions to accelerate practical implementation of this carbon-neutral heating paradigm.

Acknowledgments. This research was sponsored by Shanghai Pujiang Program (No. 23PJ1409400).

References

1. Cao, X., Dai, X., Liu, J.: Building energy-consumption status worldwide and the state-of-the-art technologies for zero-energy buildings during the past decade. Energ. Buildings. **128**, 198–213 (2016)
2. Han, Y., Feng, L., Fu, Z., Sui, J.: Performance and application boundary analysis of a solar PV/T heat pump system. Sustainab Energy Fuels. **8**, 2451–2460 (2024)
3. Peng, X., Xie, J., Liu, X., Wang, G., Wang, D., Yang, Y.: Experimental investigation and comparison on heating performance characteristics of two transcritical CO_2 heat pump systems. Energ. Buildings. **250**, 111296 (2021)
4. Liu, X., Hu, Y., Wang, Q., Yao, L., Li, M.: Energetic, environmental and economic comparative analyses of modified transcritical CO_2 heat pump system to replace R134a system for home heating. Energy. **229**, 120544 (2021)
5. Ma, J., Fung, A.S., Brands, M., Juan, N., Mohammad Abul Moyeed, O.: Performance analysis of indirect-expansion solar assisted heat pump using CO2 as refrigerant for space heating in cold climate. Sol. Energy. **208**, 195–205 (2020)
6. Rocha, T.T.M., De Paula, C.H., Maia, A.A.T., Paulino, T.D.F., De Oliveira, R.N.: Experimental assessment of a CO_2 direct-expansion solar-assisted heat pump operating with capillary tubes and air-solar heat source. Sol. Energy. **218**, 413–424 (2021)
7. Wang, Y., Tian, W., Ren, J., Zhu, L., Wang, Q.: Influence of a building's integrated-photovoltaics on heating and cooling loads. Appl. Energy. **83**, 989–1003 (2006)

8. Sun, Z., Wang, Y.: Comprehensive performance analysis of cascade refrigeration system with two-stage compression for industrial refrigeration. Case Stud. Therm. Eng. **39**, 102400 (2022)
9. Lan, T., Hu, R., Tang, Q., Han, M., Wu, S., Liu, G.: A multivariate nonlinear regression prediction model for the performance of cooling tower assisted ground source heat pump system. Energy Convers. Manag. **325**, 119333 (2025)
10. Chang, K., Zhang, Q.: Development of a solar radiation model considering the hourly sunshine duration for all-sky conditions – a case study for Beijing, China. Atmos. Environ. **234**, 117617 (2020)

Field Performance Study of Distributed Small-Capacity Air Source Heat Pumps for Centralized Heating in Residential Buildings

Wenju Hu[1], Jian Cao[1], Lingyan Yang[2,3(✉)], and Dan Wang[1(✉)]

[1] Beijing University of Civil Engineering and Architecture, Beijing, China
wangdan1@bucea.edu.cn
[2] China Academy of Building Research, Beijing, China
yly8111@163.com
[3] Jianke EET Co., Ltd., Beijing, China

Abstract. Air source heat pumps (ASHPs) have enormous potential for promotion and application in China due to their excellent efficiency and economic viability. However, the application of large-capacity units or clusters are plagued by severe issues such as noise and vibration, poor heating stability during defrosting, and efficiency degradation under part-load operation. To address these challenges, this paper proposes a novel form of distributed small-capacity ASHP system for centralized heating in residential buildings and conducts field tests on two systems in a community in Zhengzhou. The heating performance of the system form and the influence of heat source configurations were analyzed during a typical week, including system efficiency and defrosting behavior. Then the long-term energy consumption performance of different control modes was compared during an 81-day testing period. As the results show, the system form could achieve the higher efficiency and show the better heating reliability when defrosting is frequency during high-humidity conditions. For the case systems, when the rated capacity increased by 19%, the System COP (SCOP) increased 6.2% in the typical week and increased 7.66% in the mid-to-late testing period, showing the significant impact of configuration. Regarding to defrosting performance, the cycle could be extended and the degree of frosting would be decreased by operating at the efficiency status. The sudden supply water temperature drops could be limited at lower than 2 °C when the simultaneous defrosting ratio is less than 15%. Of course, cluster defrosting should not exhibit high concentration and decentralized defrosting is necessary for stable heating.

Keywords: Distributed small-capacity ASHP · Defrost behavior · Performance analysis

1 Introduction

In recent years, with the advancement of China's "dual carbon" strategy, air source heat pump (ASHP) technology has been widely applied in the field of clean heating [1, 2]. However, when large-capacity ASHPs are applied individually or in groups in actual

© The Author(s), under exclusive license to Springer Nature Singapore Pte Ltd. 2025
L. Ni et al. (Eds.): CCHVAC 2025, ESE, pp. 114–122, 2025.
https://doi.org/10.1007/978-981-95-3253-7_13

engineering projects, a series of critical issues that need to be addressed arise. These include prolonged defrosting times under high humidity conditions leading to a decrease in supply water temperature, long-term partial load operation under low-load conditions resulting in reduced system efficiency, and severe noise from fans and compressors. These issues have become key constraints to the promotion and application of ASHPs in urban areas.

Many scholars have conducted extensive research on these critical issues and identified the main problems as follows. Firstly, the key to improving the energy efficiency of heat pump units is to ensure that the units operate at their efficient load rate, which is often overlooked during operation and regulation [3, 4]. Deng et al. [5] observed that the peak efficiency of heat pumps occurs at load rates above 80%, but in their survey of 32 different systems in China's cold regions, low load rates were prevalent. Xu et al. [6] believe that the part-load factor is a major factor affecting efficiency. Secondly, under high humidity conditions, severe frosting and frequent defrosting have a significant impact on the heating stability and energy efficiency of heat pump units. Li et al. [7] identified frosting as an accelerated accumulation process. Xiong et al. [8] conducted typical operating condition tests on an ASHP heating system in Handan. The COP (Coefficient of Performance) of unit is only 1.56 under continuous high-humidity conditions at −0.9 °C, with significant fluctuations in heating output and supply water temperature. Finally, the severe noise and vibration issues of large-capacity units are the main reasons for public resistance to the application in urban areas. Zou et al. [9] conducted noise tests with a rated thermal capacity of 80 kW under full-load conditions. The results showed that the average sound pressure levels of the fan at low speeds would still have a significant impact on the surrounding environment. In summary, when dealing with partial load rate conditions, large-capacity ASHP clusters often operate at inefficient loads due to improper adjustment [10]. Heating stability under low-temperature and high-humidity conditions is hard to guarantee and severe noise also limits their widely application in urban areas too. All of these factors overshadow the outstanding economic and energy-saving advantages of ASHPs. The existing researches are only effective in improving the efficiency [11], but the improvement in the inherent short board of large capacity units is very limited [12]. However, when the research thinking is boarded, these limitations may be significantly overcome through optimization of system form and configuration.

To address the aforementioned issues, this study proposes a distributed small-capacity ASHP modular heating system. Through filed testing, the thermal stability and energy-saving potential of the system's operation strategies under complex and variable conditions were evaluated. A comparative analysis was conducted to assess the effects of two different heat-supply combinations on system efficiency. It was also proved that the units are allowed to operating at the more efficient status when the heat source configuration is increased, which could boost the system COP to a large extent.

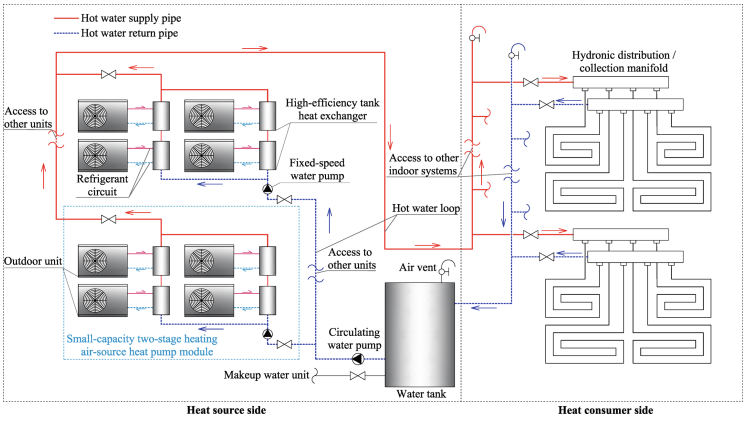


Fig. 1. Schematic diagram of the small-capacity ASHP module heating system.

2 System Description and Control Strategy Analysis

2.1 System Description

The schematic of the distributed small-capacity ASHP heating system is shown in Fig. 1. After dividing the building into heating zones, each zone is equipped with modules composed of multiple small-capacity ASHP units connected in parallel. The heat generated by each small-capacity unit is first delivered to the main heating supply line and then distributed to individual households. Each module consists of four units, with each unit comprising an outdoor unit and a high-efficiency tank heat exchanger forming a loop. The four high-efficiency tanks are connected in pairs in series and then in parallel. Within the energy station, all modules are connected in a homologous manner and linked via the main supply and return water lines to the radiant floor heating systems of each floor in the building units.

There are many advantages of the small-capacity ASHP modular system:

1. Improves system response to complex variable conditions and increases unit load rates under partial loads, elevating heating efficiency.
2. The four outdoor units per module enable independent defrost control, reducing impact on stability and demonstrating less efficiency degradation under high humidity.
3. This helps to reduce noise and vibration of ASHP.
4. Smaller system scale is stable during variable operation and reduces distribution energy losses.
5. Enables installation on rooftops and building facades while ensuring low noise impact, ideal for centralized heating in residential units or small standalone buildings.

2.2 Tested System Configuration and Control Strategy

Two residential heating systems (System A and B) in Zhengzhou, China, were monitored from December 23, 2023 to March 15, 2024, both employing distributed parallel ASHP modules with 28 kW rated capacity per module. Individual units featured 7 kW capacity

(nominal condition), compressors operating at 30–120 Hz (rated 60 Hz, COP 3.45, noise <60 dB). System A utilized a tightly constrained configuration designed at 90 Hz operation (10 modules/40 units serving 3,324 m^2), whereas System B adopted redundant capacity based on 60 Hz conditions (6 modules/24 units serving 1,675 m^2).

Both systems employed indoor temperature-based control (2-h feedback interval, 18 ± 1 °C setpoint) prioritizing operation within the 50–80 Hz range. During low-load periods, activation priority was given to units within the efficient 50–80 Hz band. This hierarchical strategy balanced thermal stability with efficiency. Defrosting utilized time-temperature feedback control (evaporator coil/supply water temperatures, dynamic intervals), executing at fixed 70 Hz compressor frequency to ensure high accuracy and minimal cycle duration.

3 Operation Performance Analysis

The performance of ASHPs under complex and variable weather conditions could better reflect their energy-saving and heating-stability characteristics, especially in low-temperature and high-humidity conditions. So, the period of January 31 to February 6, 2024 was selected as a typical week (avg. −2.4 °C, RH 79.5%), when the snowfall was existed. For facilitate assessment, operations were divided into 9 periods Fig. 2.

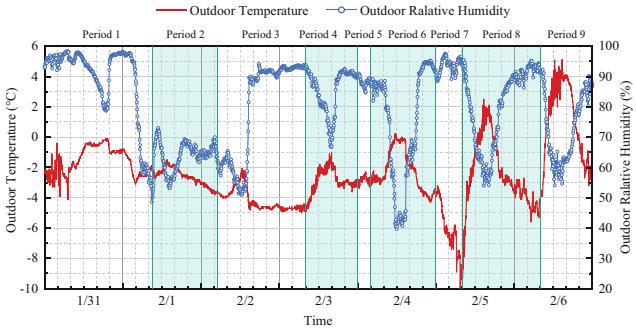


Fig. 2. Change of outdoor temperature and relative humidity in the typical week.

3.1 Operation Analysis during the Typical Week

Figure 3 shows both systems' hourly indoor temperatures, heat supply, and power consumption during the typical week. System B achieved higher thermal comfort (avg. 17.7 °C vs. 16.7 °C) and greater heat output (64.4 W/m^2 vs. 60.1 W/m^2) with comparable power consumption (26.6 Wh/m^2 vs. 26.4 Wh/m^2). Despite System A's high-frequency operation (shown as Fig. 4), it failed to maintain adequate indoor temperatures, indicating its tight capacity configuration cannot meet extreme condition demands. Conversely, System B ensured stable comfort while maintaining economic operation.

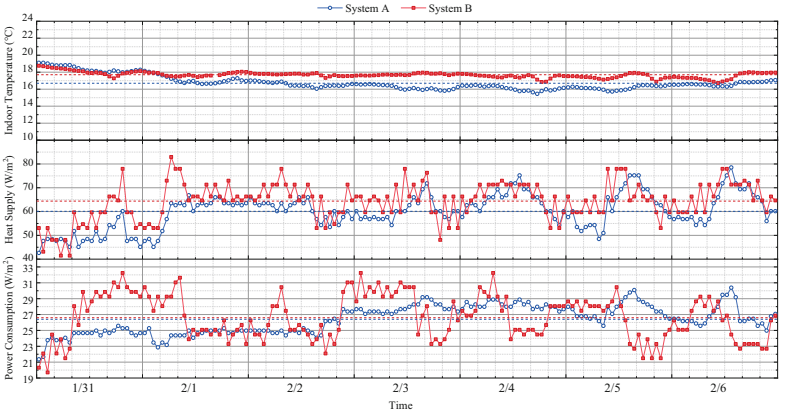


Fig. 3. Indoor temperature, heating and power consumption in the typical week.

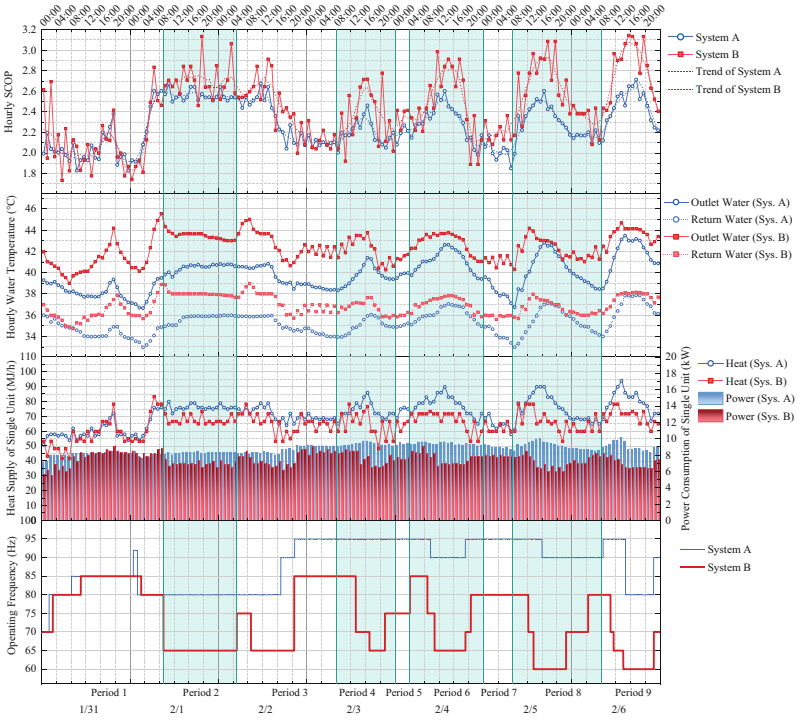


Fig. 4. Hourly variation diagram of unit operation status of both systems in the typical week.

Figure 4 shows both systems' operating frequencies, hourly SCOP (incorporating circulation pump, makeup pump, and heat pump unit consumption, source-side metered), electricity/heat profiles, and water temperatures during the typical week. Period #1 showed matched frequencies yielding near-identical SCOPs (85 Hz: 2.024 vs. 2.012),

confirming the feasibility of comparison. In Period #2 (−2.6 °C/RH 63.8%), System B (65 Hz, circulating water 43.4 °C/38.0 °C) achieved 8% higher SCOP (2.70 vs. 2.50) than System A (80 Hz, circulating water 40.7 °C/36.0 °C), aligning with the 2% COP gain per 1 °C supply temperature reduction principle and demonstrating frequency-efficiency inverse proportionality above rated frequency.

System A's constrained capacity limited its adjustment range. During Period #6's temperature/humidity fluctuations, its 5 Hz frequency reduction resulted in wider supply water temperature variations (39.7–42.6 °C) and lower SCOP (2.31 vs. System B's 2.47 at 41–43.7 °C), with efficiency gaps widening to 11.3% (Period 8) and 13.9% (Period #9). Crucially, delayed responses to RH spikes (Period #3: 1.2 h/5.7 h lag caused 1.3 °C/2.7 °C supply drops and 1 °C room temperature decline) and untimely frequency recovery (Period #4: 3.5 °C drop) underscore the necessity for prompt dynamic regulation via frequent room feedback and thermal mass/outdoor analysis. Overall, System A's high-frequency constrained operation averaged SCOP 2.277, while System B's dynamic modulation achieved 2.418 (6.2% higher).

3.2 Influence Analysis of Simultaneous Defrosting

The typical week's diverse outdoor conditions effectively demonstrate defrosting impacts and system performance differences during frequent frost/defrost cycles. Distributed small-capacity systems reduce simultaneous defrosting impacts by allowing autonomous unit-level defrost initiation, thereby attenuating supply water temperature fluctuations and heat output decline rates. The System Simultaneous Defrosting Ratio (SSDR)—defined as minute-level defrosting units versus active units— quantifies this effect. Figure 5 shows SSDR and supply/return temperatures, with insets detailing high-SSDR periods, while Fig. 6 statistically analyzes SSDR time distribution across five intervals.

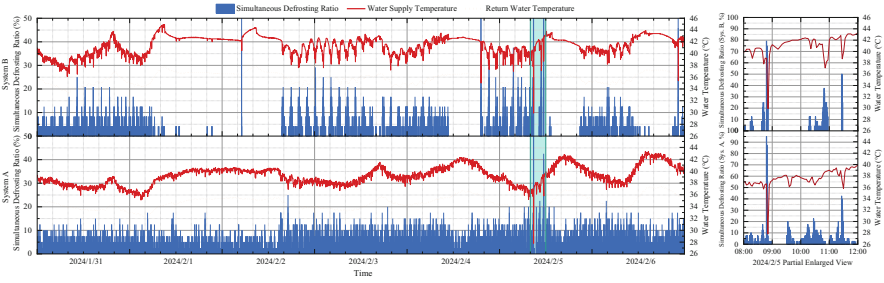


Fig. 5. Variation of SSDR and water temperature of both systems in the typical week.

Figure 5 shows the difference of both systems' defrosting performance. Under medium humidity (Period I: RH 63%), System B's low-frequency operation minimized defrosting, achieving stable temperatures and high SCOP of 2.70 at −2.6 °C, while System A's high-frequency operation caused frequent defrosting (75% time at 2.5–10% SSDR) and $\leq$ 1.5 °C supply water temperature fluctuations. Under high humidity (Periods II/III: RH $>$ 90%), System B's centralized periodic defrosting (2-h cycles, peak

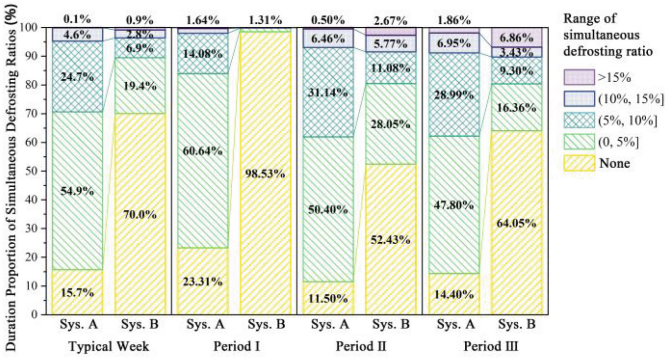


Fig. 6. Scale chart of total duration corresponding to different SSDR.

SSDR 20%) induced significant temperature drops (avg. 3.2 °C at outdoor −5 °C; 4.0 °C during outdoor −2 °C → -10 °C transition), whereas System A's non-periodic defrosting (SSDR 2.5–10% for 82% time, peak 15%) maintained stability with <2 °C instantaneous drops despite higher efficiency losses. SSDR critically governs stability: minute-level peaks of 95%/79% caused 8.8 °C/8.9 °C drops within 3 min; sustained 24% SSDR for 12 min caused 4.2 °C drop. Threshold analysis confirms: SSDR <10% (<3 min) limits drops to <1.0 °C; <15% (<3 min) to <1.5 °C; while 10%/15% SSDR sustained 5 min cause 1.5 °C/ 2.0 °C drops. Thus, System B optimizes efficiency-stability balance at low-medium humidity, System A excels in high-humidity/sudden-load scenarios, and SSDR must be capped at <15% with durations ≤10 min.

3.3 Operation Analysis During the Test Period

Based on the typical week analysis, System B demonstrates higher efficiency under complex and variable conditions, especially pronounced efficiency gains at warmer conditions. Its performance during the testing period is shown in Fig. 7. During routine load fluctuations, System B balances supply and demand by adjusting only one modular unit's frequency (dashed lines) while maintaining other units' operating status. From January 13–21, 2024 (avg. 0.4 °C/RH 75%), when System B operated at sustained higher frequencies (similar to System A), its average SCOP was 2.35. During comparable conditions from February 5–9, 2024 (avg. 0.6 °C/RH 74%), System B's optimized operation achieved a SCOP of 2.70, a 14.9% improvement. The optimization effect is more significant at higher outdoor temperatures where SCOP exceeds 3.0, with maximum daily SCOP gains reaching 0.57; even under low-temperature/high-humidity conditions, efficiency gains still reached 0.3. After January 22, 2024, System B consistently operated with its optimized strategy, while System A operated with its original strategy constrained by initial capacity configuration. During this period, System B achieved the SCOP of 2.95 (*vs.* System A's of 2.74), representing a 7.66% improvement. Thus, implementing System B's strategy delivers substantial energy-saving benefits across all heating season conditions.

Economically, System B demonstrates superior performance. After January 22, 2024, Systems A and B delivered average daily heat supplies of 4.60 MJ/(m^2·d) and 4.71 MJ/(m^2·d), with corresponding energy consumptions of 0.465 kWh/(m^2·d) and 0.443 kWh/(m^2·d). This confirms that System B—featuring redundant capacity design and "dynamic regulation within high-efficiency load ranges"—achieves better economic performance, making it particularly suitable for the long-term cost-effective operation of residential buildings.

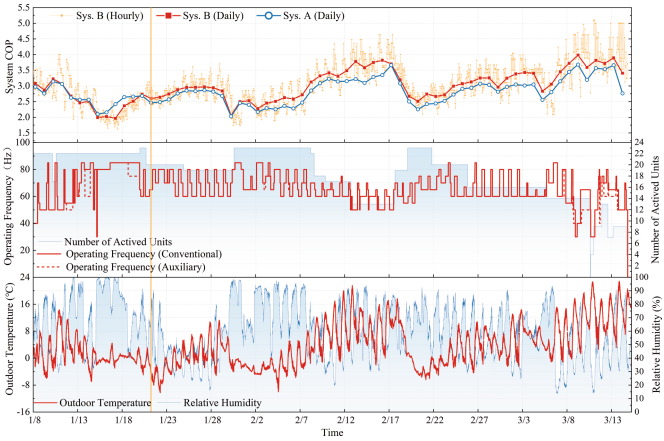


Fig. 7. Comparison diagram of system B operation and SCOP during the test period.

4 Conclusion

This research investigates the capacity configuration and regulation strategies of distributed small-capacity ASHP heating systems. By comparing the operational performance of two systems with different capacity configurations, the following conclusions are drawn:

1. Efficiency & Economics: During the typical week, System B achieved a SCOP of 2.418, representing a 6.2% improvement over System A. Under specific operating conditions, the efficiency gain ranged from 6.9% to 13.9%. In the mid-to-late testing phase, System B's SCOP reached 2.95, outperforming System A by 7.66%.
2. Defrosting Characteristics: Although System B exhibits higher efficiency under high-humidity conditions, its group defrosting demonstrates high centralization and periodicity (2 h per cycle), causing short-term supply water temperature fluctuations of up to 4.0 °C, which compromises heating stability. Critically, limiting the simultaneous defrosting ratio (SSDR) is key to stabilizing supply temperature: When the short-term (<3 min) SSDR is under 15%, supply temperature fluctuations can be controlled within 2 °C. When SSDR exceeds 25%, temperature drops reach upon 4 °C. Therefore, the group SSDR should be capped at lower than 15%.

3. Impact of Capacity Configuration: System B's greater regulation redundancy enables it to maintain efficient operating frequencies (50–80 Hz) under complex conditions. In contrast, System A's tight capacity constraints force high-frequency operation, resulting in increased defrosting frequency, higher defrosting efficiency losses, and lower room temperatures.

References

1. Building energy efficiency research center of Tsinghua University, 2025 annual report on China building energy efficiency (2025)
2. Yang, C., et al.: Assessing climate adaptability and low-carbon efficiency of air source heat pumps in China's diverse climates. J. Buil. Eng. **99**, 111584 (2025)
3. Wu, C., et al.: Optimizing the selection and combined operation of multiple air-source heat pumps for sustainable heating systems. Energ. Buildings. **310**, 114052 (2024)
4. Ling, J., et al.: Simulation and optimization of the operation strategy of ASHP heating system: a case study in Tianjin. Energ. Buildings. **226**, 110349 (2020)
5. Deng, J., Wei, Q., Liang, M., He, S., Zhang, H.: Does heat pumps perform energy efficiently as we expected: field tests and evaluations on various kinds of heat pump systems for space heating. Energ. Buildings. **182**, 172–186 (2019)
6. Xu, Z., et al.: Investigation on the efficiency degradation characterization of low ambient temperature air source heat pump under partial load operation. Int. J. Refrig. **133**, 99–110 (2022)
7. Li, Z., et al.: Experimental study on the effects of melted frost icing on the operating performances of air source heat pump. Appl. Therm. Eng. **238**, 122136 (2024)
8. Xiong, C., et al.: Performance analysis of an air-source heat pump heating system in Handan area. J. Refrig. **42**(01), 111–116+139 (2021)
9. Zou, C., et al.: Noise characteristics of enhanced vapor injection heat pump under heating condition. CIESC J. **69**(S2), 109–115 (2018)
10. Sun, Y., et al.: Study on operation optimization of air source heat pump heating system based on particle swarm optimization algorithm. Renew Energy Resources. **40**(11), 1465–1472 (2022)
11. Li, L., et al.: Simulation of economic, energy-saving, and environmental benefits of the centralized-decentralized two-stage heating mode. Energ. Buildings. **341**, 115869 (2025)
12. Huchtemann, K.D.: Müller: simulation study on supply temperature optimization in domestic heat pump systems. Build. Environ. **59**, 327–335 (2013)

Freezing and Accompanying Frosting Characteristics of Alcohol Binary Droplet on Cold Surface

Feng Wang[1], Mengting Xiang[1], Weibo Yang[1], and Caihua Liang[2(✉)]

[1] Yangzhou University, Yangzhou 225127, PR China
[2] Southeast University, Nanjing 210096, PR China
caihualiang@163.com

Abstract. Although spraying antifreeze solution onto cold surface has been proven effective for frost inhibition, the freezing characteristics of alcohol binary droplet and the accompanying frosting behavior on freezing droplet surface remain unclear. Visualization experiments were carried out to achieve the freezing-frosting processes of ethylene glycol and glycerol solution droplets on cold surface under varying conditions. Experimental results demonstrate that alcohol droplet exhibits prolonged freezing duration and reduced deformation. The formation of an annular dry zone surrounding the droplet inhibits frost crystal propagation, increasing propagation time by 3–6.2 times. Different from water droplet, the freezing mechanism of alcohol droplet is attributed to frost crystal on the cold surface initiating nucleation upon contacts with the droplet. The solution membrane formed on the freezing droplet surface rises along the frost crystal inducing localized melting, which results in the frost crystals sparse and freezing droplet forming circular table-shaped morphology.

Keywords: Alcohol binary droplet · Freezing · Dry zone

1 Introduction

Frost formation is inevitable in various industries, including aviation, aerospace, wind turbine, refrigeration, heat pump, and cryogenic engineering. The accumulated frost layer detrimentally impacts equipment operational efficiency, thereby inducing substantial energy waste [1, 2]. For instance, during winter heating with an air source heat pump, frost layer can obstruct fin gaps in outdoor heat exchanger, reducing airflow and consequently diminishing both the heating capacity and the operational efficiency [3]. Spraying antifreeze solution onto frosted cold surface, primarily composed of salt or alcohol, has been proven to be an effective method for frost inhibition and even frost melting [4, 5]. Moreover, freezing concentration or desalination has become a promising technique for regeneration of antifreeze solution [6]. In the development and application of these technologies, it is a critical scientific problem to reveal the freezing characteristics of antifreeze droplet on cold surface and the accompanying frosting behavior on freezing droplet surface.

© The Author(s), under exclusive license to Springer Nature Singapore Pte Ltd. 2025
L. Ni et al. (Eds.): CCHVAC 2025, ESE, pp. 123–131, 2025.
https://doi.org/10.1007/978-981-95-3253-7_14

In recent years, numerous scholars have conducted investigations on freezing characteristics of deionized water (DW) droplet. The droplet freezing process on cold surface is classified into 5 stages: liquid cooling, nucleation, recoalescence, freezing, and solid cooling. When the droplet temperature reaches the critical nucleation temperature, it undergoes nucleation and recoalescence. In this stage, the temperature rapidly increases to approximately 0 °C, resulting in a loss of light transmission and initiating the freezing stage. The freezing process is characterized by the initiation of an internal freezing front at the base of the droplet, which progresses upward and ultimately forms a freezing tip at the top of the droplet [7]. Wildeman et al. [8] found that rupture occurred during the freezing process of droplet larger than 50 μm. The solidification led to an accumulation of internal pressure, ultimately resulting in rupture. Chu et al. [9] conducted droplet freezing experiments on hydrophobic and superhydrophobic surfaces. They observed the bubble-dissolving phenomenon and demonstrated that the freezing droplet was a kind of porous medium. Starostin et al. [10] conducted experimental and theoretical studies on the formation of freezing tip. Their results showed that the direction of the freezing tip was determined by the direction of heat flux. Zhang et al. [11] experimentally investigated the formation mechanism of freezing tip under forced convection condition. Their finding revealed that elevated airflow velocity induced a transition from peak-mode to peakless-mode freezing pattern. Miao et al. [12] discovered that the competitive relationship between heat conduction and convection influenced the convex-concave morphology of freezing front. This morphological evolution controlled the generation and disappearance of freezing tip. Their study further demonstrated that enhanced convection intensity, reduced supercooling degree, or increased contact angle effectively inhibited tip formation.

In practical engineering applications, alcohol-based antifreeze is widely adopted due to its good aqueous solubility, high thermal conductivity, low corrosiveness, low dynamic viscosity, and cost-effectiveness. Sun et al. [13] found that frost formation was completely prevented between propylene glycol solution and salt-saturated water droplet with spacing of less than twice the radius. Jiang et al. [14] reported that the combination of ethanol solution spray and passive superhydrophobic coating effectively prevented the formation of condensation icing/frosting. The defrosting of air source heat pump with ethylene glycol solution spray not only had obvious defrosting effect, but also the average COP of the unit was improved compared with traditional reverse cycle defrosting. However, the freezing characteristics of alcohol binary droplet on cold surface and the accompanying frosting behavior on freezing droplet surface have not been reported. In summary, the freezing and accompanying frosting characteristics of alcohol binary droplet are not yet clear, and the anti-frosting mechanism in the dry zone remains elusive. Therefore, this study carried out visual experiments to achieve freezing-frosting processes of ethylene glycol solution (ES) and glycerol solution (GS) droplets on cold surface under various experimental conditions. These findings contribute to understand the freezing and frosting mechanisms of alcohol binary droplet, and provide foundation for optimizing anti-frosting strategies by using alcohol solution.

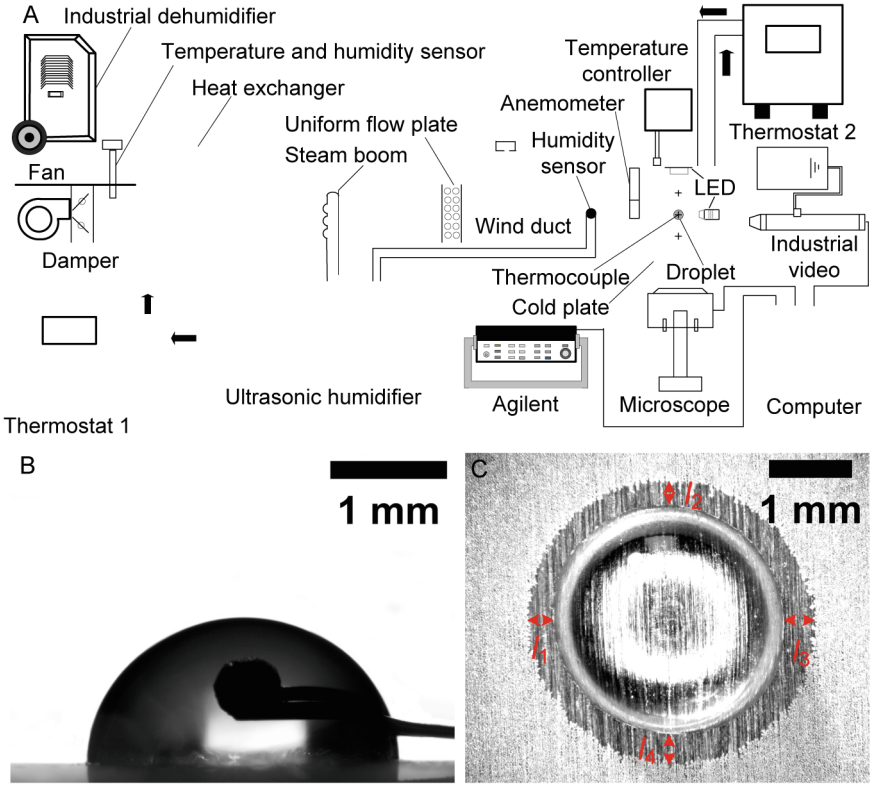


Fig. 1. Experimental system and parameter measurement: (A) schematic diagram of experimental system; (B) measuring of droplet internal temperature; and (C) measuring of dry zone length.

2 Experimental Methods

The experimental system is illustrated in Fig. 1. The air conditioning and supply module included an industrial dehumidifier, an adjustable-speed fan, and an air valve. Additional components such as heat exchanger, thermostat 1 (cooling capacity 3900 W, accuracy ± 0.05 °C), ultrasonic humidifier, steam boom, and wind tunnel were integrated into this module. The cold platform module (SLTD1-600S high-precision semiconductor constant-temperature test system) featured a cold plate, thermostat 2, and LED cold lights. This module enabled precise temperature control of the sample with an adjustable range spanning from −30 to 60 °C. The parameter measurement module included analytical balance, hand anemometer, temperature and humidity sensor, and T-type thermocouple. Thermocouples were affixed to the back surface of the sample (Fig. 1A). To ensure the accuracy of droplet temperature, a T-type thermocouple was positioned at the inner center of droplet (Fig. 1B). The image acquisition system consisted of an industrial-grade video microscope and an optical microscope, enabling simultaneous acquisition of front and lateral droplet views. The droplet height (H) and dry zone length (l) were quantified using ImageJ software. Since the distribution of dry zone presents anisotropy,

4 radial measurements (l_1, l_2, l_3, l_4) were recorded along the annular region (Fig. 1C). The l was the average of l_1, l_2, l_3 and l_4. To ensure the repeatability of experimental results, each experiment was conducted to 3 replicate tests. The H and l were calculated as the average values from 3 repeated tests.

3 Experimental Results and Analysis

The droplet volume was 5 μL. The w ranged from 20% to 30% for ES droplet and 30% to 40% for GS droplet, with an interval of 5%. Ambient temperature was controlled at 10.0 ± 0.3 °C. The T_d and T_p was set at −1.48 °C and −10 °C, respectively. Figure 2 illustrates the side and top views of the freezing-frosting processes of ES and GS droplets at different w. Unlike deionized water (DW) droplet, the alcohol binary droplets lack a distinct freezing tip during solidification, and membrane of alcohol solution forms on the surface of the freezing droplet. As w increases, the freezing duration is significantly prolonged, with complete freezing inhibition observed in 30% ES and 40% GS droplets. The antifreeze behavior promotes the formation of an annular dry zone surrounding the droplet (Fig. 2C–D). In the initial 90 s, the condensation droplets outside the dry zone on the cold surface remain unfrozen. The dry zone progressively expanded outward until 330 s, at which all the condensation droplets freeze. At this point, the length of dry zone reaches its maximum value. At 1230 s, the dry zone shrinks obviously due to solution dilution on the droplet surface, resulting in the appearance of uneven frost crystals inward. The droplet freezes upon the contact between the frost crystal and the droplet. As the frost crystal pierces the solution membrane and grows inward, lateral leakage appears in the droplet, as indicated by the yellow circle in the images. As w increases, the dry zone exhibits substantial expansion, thereby delaying the freezing time.

It is noteworthy that the surface of 30% GS droplet still has no frost crystal even after 2830 s, just with some sparse frost particles adhering to the freezing droplet surface. Partial freezing is observed on the surface of 25% ES and 35% GS droplets, indicating incomplete freezing due to the lower freezing point. When the freezing point is significantly higher than T_p, in the case of DW droplet, rapid freezing occurs once the droplet reaches supercooling. When the freezing point is slightly higher than T_p, in the case of 20% ES and 30% GS droplets, the cold surface cannot induce sufficient supercooling for freezing. As a result, the freezing time is determined by the rate of frost crystal propagating in the dry zone. When frost crystal contacts the droplet surface and provide nucleation site for freezing, the droplet will freeze rapidly. In contrast, when the droplet freezing point is lower than T_p, as 25% ES and 35% GS droplets, the frost crystals make contact with the droplet surface, leading to localized freezing while the interior remains unfrozen.

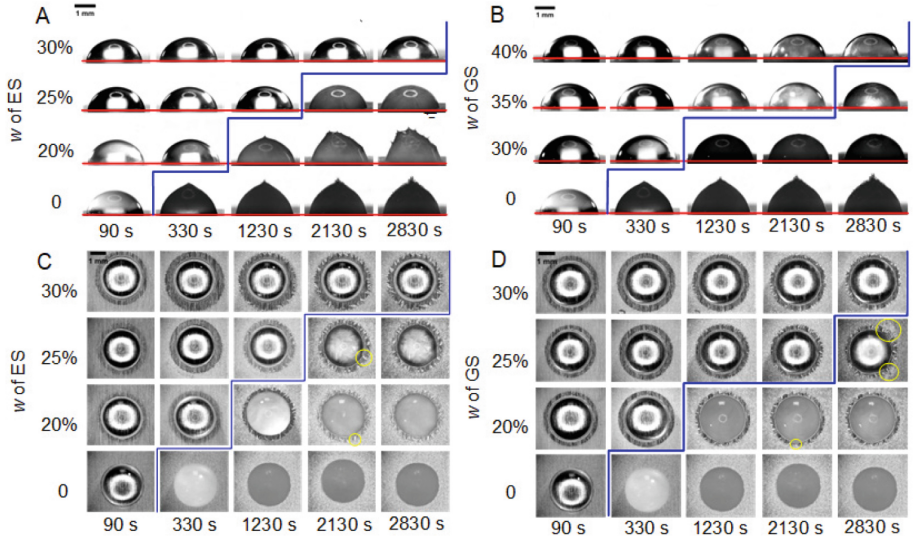


Fig. 2. Freezing-frosting processes of ES and GS droplets at different *w*: (A) side view of ES droplets; (B) side view of GS droplets; (C) top view of ES droplets; and (D) top view of GS droplets. The red line denotes the cold surface, the blue line represents before and after droplet freezing, and the yellow circle highlights the contact between droplet and frost crystal.

Figure 3 shows the droplet characteristic parameters during freezing-frosting processes. The height differences between the initial and final states of DW, 20%–30% ES, and 30%–40% GS droplets are as follows: 656.25, 399.00, 71.00, 61.25, 85.00, −286.20 and 83.00 μm (Fig. 3A). The reduction in height of 35% GS droplet at 2900 s is primarily due to the lateral leakage, as indicated by the images in Fig. 3A. The variations in droplet height of DW and 20% ES are more pronounced compared to those of other droplets. However, unlike the DW droplet, the droplet height of 20% ES droplet does not undergo sharp rise because no significant deformation occurs. Interestingly, the droplet height of 20% ES droplet has several significant drops. This is because the high concentration of ES on the surface of the freezing droplet rises along the frost crystal under the action of capillary force, leading to localized melting of the frost crystal (Fig. 3B). The localized ES after melting frost crystal falls back under the action of gravity and then freezes. Whereafter, the frost crystal will grow again on the new freezing surface. As a result, the droplet height of 20% ES is lower than that of the DW droplet, and the frost crystal on the droplet surface is sparser and thicker.

Figure 3C illustrates the duration of each stage during freezing-frosting process. The time proportion of the first stage (droplet cooling) for DW, 20%–30% ES and 30%–40% GS droplets is 6.35%, 27.51%, 56.98%, 100%, 37.21%, 72.43% and 100%, respectively. In the third stage (frost growth), the time proportion of DW, 20% ES and 30% GS droplets is 89.57%, 58.80% and 43.52%, respectively. Figure 3D demonstrates the change of dry zone length with time. As *w* increases, the *l* gradually increases and shows a trend of first increasing and then decreasing with time. The maximum *l* of 20%–30% ES droplets is 290.25, 350.75 and 566.75 μm, while for 30%–40% GS droplets is 320.25, 351.50

and 389.75 μm, respectively. The time required for frost crystal propagation around the droplet is shown in Fig. 3E. The time for frost crystal propagation around DW, 20%–30% ES and 30–40% GS droplets is 17, 77, 96, 105, 51, 79 and 99 s, respectively. The alcohol solution extends the time of frost crystal propagation by approximately 3 to 6.2 times.

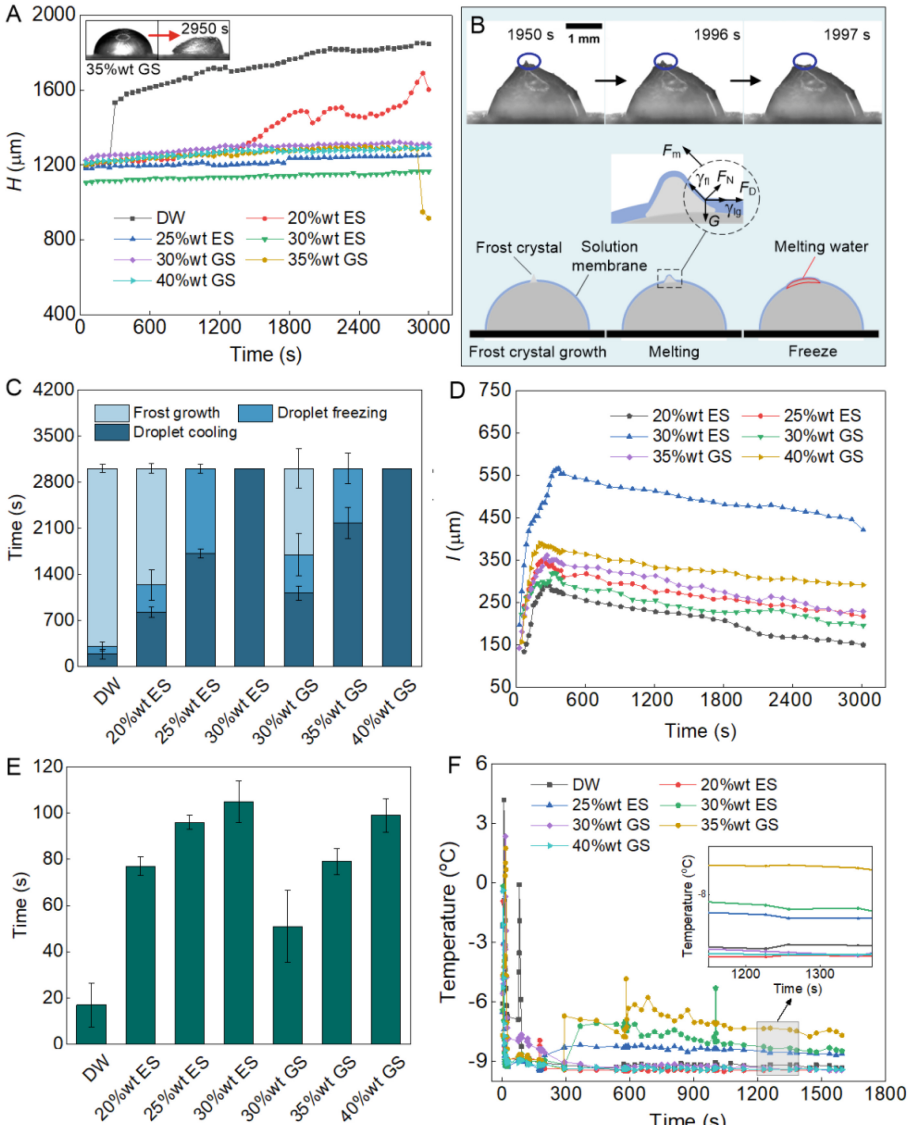


Fig. 3. Droplet characteristic parameters during freezing-frosting processes: (A) droplet height; (B) schematic diagram of frost crystal melting; (C) duration of each stage in freezing-frosting process; (D) dry zone length; (E) propagation duration of frost crystal; and (F) internal temperature of droplet.

Figure 3F presents the internal temperature of droplet during freezing-frosting process. The internal temperatures of DW, 20% ES and 30% GS droplets decrease and ultimately achieve stability. The temperature reaches peak at 77, 172 and 221 s, respectively, indicating that the droplet begins to freeze. Following a period of temperature stability, the 25% ES droplet experiences a sharp temperature increase at 199 s due to incomplete freezing, resulting in a solid-liquid mixture. The temperature of 30% ES and 35% GS droplets rises twice. After the second rise, the temperature continues to cool down slowly. The first temperature increase for 30% ES and 35% GS droplets occurs at 366 and 289 s, respectively. The former is because of the droplet rupture, which prevents the thermocouple from making contact with the droplet surface, while the latter is due to the freezing of droplet surface. Subsequent temperature rises are observed at 580 and 1001 s. This is caused by the dilution of the residual solution on the thermocouple surface absorbing water vapor in the environment after the droplet rupture, resulting in a reoccurrence of freezing or direct rupture. The temperature of 40% GS droplet remains stable once it reaches T_p. The local magnification shows that the internal temperature after stability, from high to low, is as follows: 35% GS, 30% ES, 25% ES, DW, 30% GS, 40% GS and 20% ES. The above analysis further verified that under this experimental condition, the 20% ES droplet and 30% GS droplet are completely freezing, the 25% ES droplet is in solid-liquid mixed state, the surface of 35% GS droplet is locally freezing, and the 30% ES droplet and 40% GS droplet do not freeze.

Figure 4 shows the morphological evolution of droplet in initial freezing stage. Figure 4A-4B provides side and top views of DW, 20% ES and 30% GS droplets. The surface of DW droplet initiates freezing under certain level of supercooling and rapidly transitions to opaque state. Subsequently, a concave freezing front emerges at the base of droplet and rises vertically until a tip forms at the top of the droplet. The freezing characteristics of alcohol binary droplet are different from that of DW droplet in the following aspects. Firstly, the trigger mechanisms of freezing are different. The freezing of alcohol binary droplet is caused by the contact of frost crystal with the droplet surface, which promotes nucleation and freezing. Secondly, the freezing front exhibits different characteristics. The irregular freezing front of alcohol binary droplet initially advances diagonally upward and then deflects vertically upward. Finally, the morphology of droplet is different after freezing. The alcohol binary droplet does not form a tip. A comparison of the top views of DW and alcohol binary droplet after freezing reveals that the top view of freezing alcohol binary droplet has stronger light transmission than that of DW droplet, indicating the presence of solution membrane on the droplet surface. Figure 4C illustrates the evolution of droplet profile of DW, 20% ES and 30% GS droplets. The deformation of DW droplet is larger than that of alcohol binary droplet due to the anomalous expansion of water. Moreover, the deformation of 20% ES droplet is more prominent than that of 30% GS droplet, because the water content in 20% ES droplet is higher than 30% GS droplet and the 30% GS droplet exhibits a lower freezing point than 20% ES droplet.

Furthermore, we also investigated the effects of key factors such as ambient air dew point temperature, droplet volume, cold surface temperature, and cold surface wettability on freezing and accompanying frosting characteristics of alcohol binary droplet. Due to

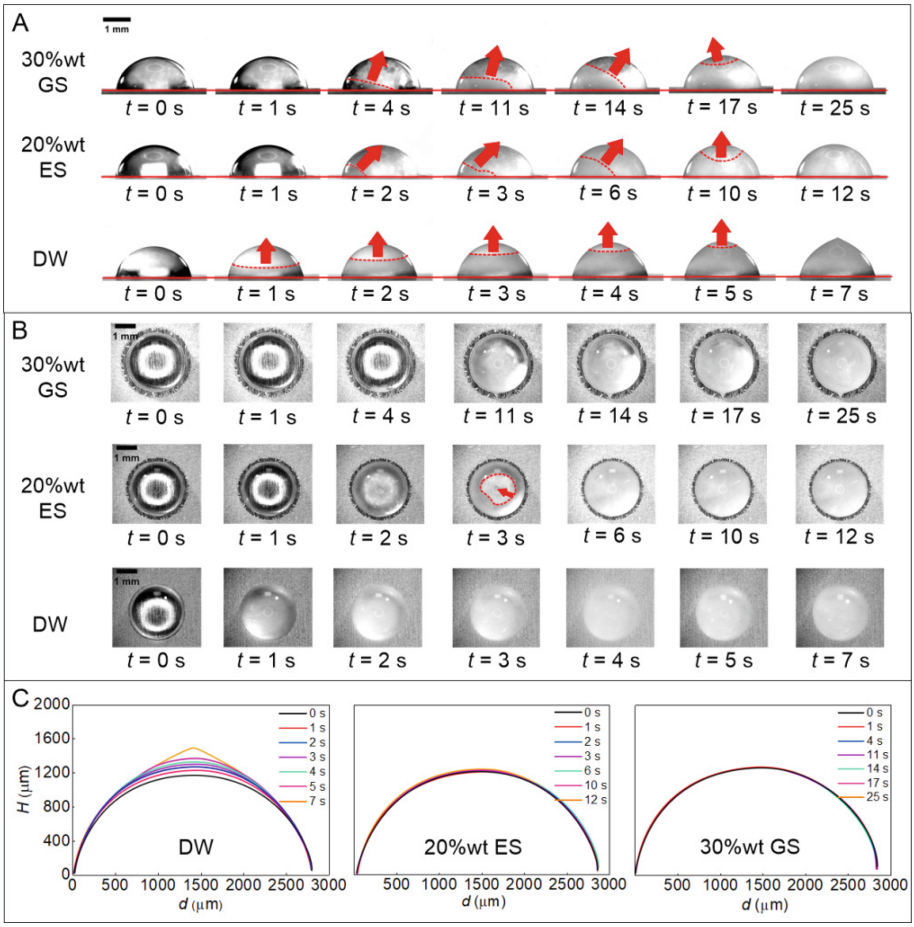


Fig. 4. Morphological evolution of droplet in initial freezing stage: (A) side view; (B) top view; and (C) droplet profile. The solid red line represents the cold surface, the dotted red line indicates the freezing front of droplet, and the red arrow represents the propagation direction of freezing front.

the limited length of the paper, no further elaboration is provided here. These results are only summarized briefly in the conclusion section.

4 Conclusion

Compared to DW droplet, alcohol binary droplet exhibits prolonged freezing duration and reduced deformation. The formation of an annular dry zone surrounding the droplet inhibits frost crystal propagation, increasing propagation time by 3–6.2 times. The length of dry zone decreases with the increase of T_d and increases with the increase of V or T_p. Furthermore, based on the experimental data, an empirical correlation for predicting dry zone length is proposed. Different from DW droplet, the freezing mechanism of alcohol

binary droplet is attributed to frost crystal on the cold surface initiating nucleation upon contacts with the droplet. The thickness of solution membrane formed on the freezing droplet surface demonstrates direct proportionality to V and inverse correlation with T_p. The solution rises along the frost crystal inducing localized melting, which results in the frost height on the droplet surface lower than that of DW droplet.

References

1. Boinovich, B., Emelyanenko, M.: Recent progress in understanding the anti-icing behavior of materials. Adv. Colloid Interface Sci. **323**, 103057 (2024)
2. Zhang, L., Zhao, Y., Guo, Y., et al.: Research on wind turbine icing prediction data processing and accuracy of machine learning algorithm. Renew Energy. **237**, 121566 (2024)
3. Lyu, N., Feng, G., He, H., et al.: Impact of ambient temperature and humidity on the performance of a novel anti-frosting air source heat pump system. Energy. **314**, 134190 (2025)
4. Li, N., Jiang, J., Yang, M., et al.: Anti-icing mechanism of combined active ethanol spraying and passive surface wettability. Appl. Therm. Eng. **220**, 119805 (2023)
5. Li, D., Xu, Z., Liu, Y., et al.: Developing a durable anti-frost surface: Integrating the passive anti-icing properties of salt, saline, and bulk ice for enhanced frost prevention. Surf Interfaces. **51**, 104722 (2024)
6. Rasmussen, A., Jannat, M., Wang, H.: Fundamentals of freeze desalination: critical review of ion inclusion and rejection studies from molecular dynamics perspective. Desalination. **573**, 117216 (2024)
7. Strub, M., Jabbour, O., Strub, F., et al.: Experimental study and modelling of the crystallization of a water droplet. Int. J. Refrig. **26**(1), 59–68 (2003)
8. Wildeman, S., Sterl, S., Sun, C., et al.: Fast dynamics of water droplets freezing from the outside in. Phys. Rev. Lett. **118**(8), 084101 (2017)
9. Chu, F., Zhang, X., Li, S., et al.: Bubble formation in freezing droplets. Phys. Rev. Fluids. **4**(7), 071601 (2019)
10. Starostin, A., Strelnikov, V., Dombrovsky, A., et al.: Effect of asymmetric cooling of sessile droplets on orientation of the freezing tip. J. Colloid Interface Sci. **620**, 179–186 (2022)
11. Zhang, C., Zhang, H., Fang, W., et al.: Axisymmetric lattice Boltzmann model for simulating the freezing process of a sessile water droplet with volume change. Phys. Rev. E. **101**(2), 023314 (2020)
12. Miao, S., Zhang, C., Liu, X.: Tunable tip singularity of a water droplet freezing on surfaces under forced convection. Appl. Therm. Eng. **241**, 122362 (2024)
13. Sun, X., Damle, G., Uppal, A., et al.: Inhibition of condensation frosting by arrays of hygroscopic antifreeze drops. Langmuir. **31**(51), 13743–13752 (2015)
14. Jiang, Y., Fu, H., Yao, Y., et al.: Experimental study on concentration change of spray solution used for a novel non-frosting air source heat pump system. Energy Build. **68**, 707–712 (2014)

Analysis for Parameters Affecting Cycle Performance of CO_2 Two-Stage Compression Cycles

Aruna[1,2,3], Xu Jin[1,2,3](✉), Zheng Qiu[1,2,3], Zhongyan Liu[1,2,3], Jiapeng Zhang[1,2,3], Hao Zhang[1,2,3], Xin Meng[1,2,3], Xianglai Xu[1,2,3], and Wei Su[1,2,3]

[1] School of Energy and Power Engineering, Northeast Electric Power University, Jilin 132012, China
jinxu7708@sina.com
[2] School of New Energy Industry, Xing An Vocational and Technical College, Hinggan League 137400, China
[3] Huaneng Jilin Power Generation Co., Ltd., Changchun 130012, Jilin, China

Abstract. The application of CO_2 in air source heat pumps has the advantages of environmentally friendly, non-toxic and harmless, and superior thermal performance, however, it still suffers from the problems of high system pressure and high compressor pressure ratio under large temperature span conditions in cold regions. To address these issues, a CO_2 two-stage throttling intermediate complete cooling dual-compression cycle (TCDC) is adopted to improve cycle performance. Based on this, dynamic simulation modeling of the TCDC has been carried out using the Dymola software. The impact of different parameters, such as the low/high-stage compressor volume ratio (R_v), high pressure (P_H), outlet temperature of gas cooler ($T_{gs,out}$) and evaporating temperature (T_L), on the heating performance of the TCDC is analyzed, and the calculation formulas for the optimal low/high-stage compressor volume ratio ($R_{v,opt}$) is derived. The results show that the optimal low/high-stage compressor volume ratio ($R_{v,opt}$) of the TCDC depends solely on TL and has a significant impact on both the heating coefficient of performance (COP_{hot}) and heating capacity (Q_{hot}). Since the impact of R_v on system Q_{hot} is greater than its impact on COP_{hot}, the Q_{hot} demand can be prioritized by adjusting R_v, laying the foundation for a heat priority control strategy.

Keywords: CO_2 · Dymola · optimal low/high-stage compressor volume ratio ($R_{v,opt}$)

1 Introduction

Transcritical CO_2 heat pump heating systems have drawn interest in the heating industry recently because of their superior low-temperature adaptation, high energy efficiency, and environmental friendliness. A dynamic compressor model for a variable-capacity two-stage compression system was established by Jin et al. [1] and supported by experimental validation, revealing that two-stage compression is not performed as a continuous

© The Author(s), under exclusive license to Springer Nature Singapore Pte Ltd. 2025
L. Ni et al. (Eds.): CCHVAC 2025, ESE, pp. 132–142, 2025.
https://doi.org/10.1007/978-981-95-3253-7_15

compression process, with the theoretical displacement ratio of the low-stage to high-stage compressors identified as having the largest effect on intermediate pressure, which was found to be highly sensitive to changes in heating capacity but minimally impacted heating COP. A two-stage compression cycle with an external intercooler was proposed by Niu et al. [2], demonstrating that system performance can potentially be enhanced by adjusting intermediate pressure, and relationships for optimal high and intermediate pressures were provided. Variance analysis was applied by Qin et al. [3] to evaluate the effects of evaporating temperature, outlet temperature of gas cooler, evaporator outlet superheat, internal heat exchanger efficiency, and isentropic efficiency on optimal high pressure and COP, with the conclusion drawn that outlet temperature of gas cooler accounts for 98.03% and 47.11% of optimal high pressure and optimal COP, respectively. The existence of an optimal discharge pressure (PH,opt) in transcritical cycles and an optimal intermediate pressure (PM,opt) in two-stage cycles, both significantly impacting the performance of CO_2 transcritical two-stage cycles, was identified by Kauf [4].

To address these issues. Firstly, a simulation model for a CO_2 variable-capacity two-stage compression heat pump system was established. Moreover the effects of four parameters, including low/high-stage compressor volume ratio (R_v), outlet temperature of gas cooler ($T_{gs,out}$), evaporating temperature (T_L) and high pressure (P_H), on the heating performance of the two-stage throttling intermediate complete cooling dual-compression cycle (TCDC) was comprehensively analyzed. Finally, based on the roles of these four parameters in determining the optimal low/high-stage compressor volume ratio ($R_{v,opt}$) and optimal intermediate pressure ($P_{M,opt}$), relationships for the optimal low/high-stage compressor volume ratio and intermediate pressure for the TCDC were derived, providing theoretical guidance for the optimization and control of the system.

2 Model

To evaluate the system's performance, a dynamic simulation model was developed using Dymola [5] and the TLK Thermal System Library [6], as illustrated in the TCDC schematic diagram shown in Fig. 1. The reliability of this approach has been validated in several studies [7–14], where Dymola and the TLK Thermal System Library were employed to investigate optimal control strategies for two-stage compression systems. Figure 2 shows the P-h diagram of the TCDC used in this study.

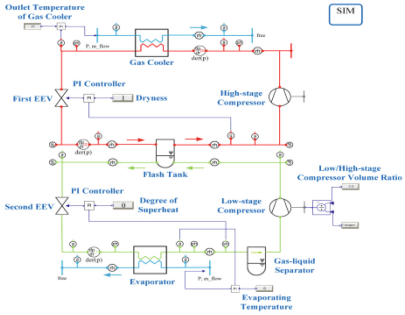


Fig. 1. Schematic diagram of TCDC.

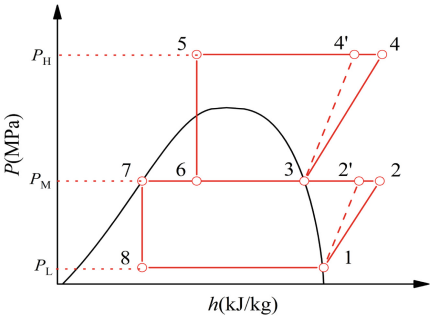


Fig. 2. *P-h* diagram of TCDC

2.1 Model Description

2.1.1 Compressor Model

The compressor is the core component of the vapor compression refrigeration system. Its volumetric efficiency and isentropic efficiency are primarily influenced by the pressure ratio. Therefore, the compressor model is established using the isentropic efficiency correlation based on experimental fitting from literature [15] (Eq. 1) and the volumetric efficiency correlation provided in literature [16] (Eq. 2). The CO_2 compressor efficiency correlation is as follows:

$$\eta_{is} = 0.8014 - 0.04842(P_{out}/P_{in}) \tag{1}$$

$$\eta_v = -0.0096(P_{out}/P_{in})^2 + 0.0065(P_{out}/P_{in}) + 0.85 \tag{2}$$

2.1.2 Evaporator Model

The evaporator is divided into two-phase and superheating regions. The two-phase region uses the correlation developed by Longo [17], while the superheating region applies the General Reynolds Prandtl correlation. Detailed information on the heat transfer correlations can be found in the references.

2.1.3 Gas Cooler Model

The gas cooler was configured with a double-pipe heat exchanger, using a modeling methodology analogous to that implemented for the evaporator. Within the gas cooler, the refrigerant flowing through the gas cooler operates under supercritical conditions. A modified Gnielinski correlation proposed by Chaobin et al. [18] was adopted for the supercritical refrigerant heat transfer calculation. On the cooling water side, the Dittus-Boelter correlation was employed to characterize the convective heat transfer process. Detailed formulations of these heat transfer correlations are comprehensively documented in the cited references.

3 Effect of Rv

3.1 Effect of R_v on Cycle Performance

As observed in Fig. 3, for P_H in the range of 8.6–11.0 MPa, COP_{hot} increases initially and then decreases with the increase in R_v, reaching its maximum value at R_v=1.4. This the low/high-stage compressor volume ratio is defined as the optimal low/high-stage compressor volume ratio, $R_{v,opt}$=1.4. At P_H=8.6 MPa, as R_v increases from 0.6 to 1.4, COP_{hot} increases from 2.10 to the maximum value of 2.34, representing an increment of 11.43%. $COP_{hot,max}$ at $R_{v,opt}$=1.4 is explained by the relationship between the system's heating coefficient of performance, COP_{hot}, and the heating capacity, Q_{hot}, as well as the total compressors power consumption, W_{total}. Both Q_{hot} and W_{total} increase with the continuous rise in R_v, but their respective rates of change differ. According to Fig. 4, at P_H=8.6MPa, the slope of W_{total} remains nearly constant as R_v increases, whereas the rate of change of Q_{hot} decreases initially and then stabilizes around R_v=1.4. This stabilization of the Q_{hot} rate of change results in the maximum value of COP_{hot} being achieved at R_v=1.4.

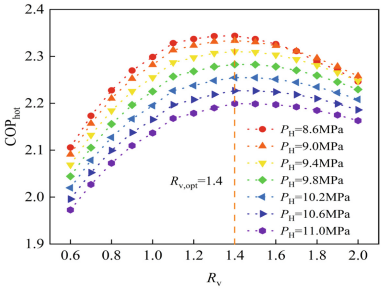


Fig. 3. Variation of COP_{hot} with P_H under different R_v conditions for the TCDC.

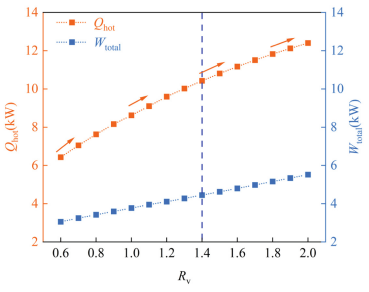


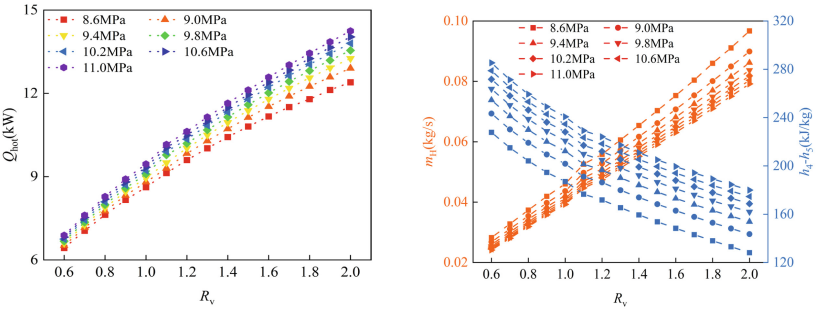
Fig. 4. Variation of W_{total} and Q_{hot} with R_v under P_H=8.6MPa for the TCDC.

From Fig. 5(a), it can be observed that when P_H is constant, Q_{hot} increases with an increase in R_v. For example, at P_H=8.6MPa, as R_v increases from 0.6 to 2.0, Q_{hot} rises from 6.43 kW to 12.40 kW, an increment of 92.85%, with an average growth of 0.43 kW for every 0.1 increase in R_v. When R_v is constant, Q_{hot} increases with an increase in P_H. Taking $R_{v,opt}$=1.4 as an example, as P_H increases from 8.6 MPa to 11.0 MPa, Q_{hot} rises from 10.42 kW to 11.64 kW, an increment of 11.71%, with an average growth of 0.05 kW for every 0.1 MPa increase in P_H. According to Eq. (3), Q_{hot} is primarily determined by m_H and h_4-h_5. When P_H is constant, as R_v increases, m_H increases correspondingly, leading to an increase in P_M. Meanwhile, since $T_{gs,out}$ remains constant, h_4-h_5 decreases. As shown in Fig. 5(b), the growth rate of m_H exceeds the reduction rate of h_4-h_5. For instance, at P_H=8.6MPa, as R_v increases from 0.6 to 2.0, m_H increases from 0.028 kg s^{-1} to 0.097 kg s^{-1}, an increment of 246.43%, while h_4-h_5 decreases from 227.78 kJ kg^{-1} to 128.17 kJ kg^{-1}, a reduction of 43.73%. Consequently, when P_H is constant, the trend of Q_{hot} aligns closely with the trend of m_H, increasing as R_v increases. When R_v is constant, as P_H increases, both m_H and P_M increase, while h_4-h_5 also increases due

to the constant $T_{gs,out}$. For example, at $R_{v,opt}$=1.4, as P_H increases from 8.6 MPa to 11.0 MPa, m_H decreases from 0.065 kg s^{-1} to 0.055 kg s^{-1}, a reduction of 15.38%, while h_4-h_5 rises from 159.40 kJ kg^{-1} to 210.93 kJ kg^{-1}, an increment of 32.33%. Since the magnitude of h_4-h_5 is significantly greater than that of m_H, the trend of Q_{hot} is primarily influenced by h_4-h_5, resulting in an increase in Q_{hot} as P_H increases. When the outlet temperature of cooling water T_{wout}=50°C, Q_{hot} increases from 6.43 kW at R_v=0.6 to 13.62 kW at R_v=2.0, an increment of 111.82%, further demonstrating the significant impact of the volumetric ratio on the heat transfer rate.

It can thus be concluded that R_v plays a significant role in the TCDC. This finding provides a theoretical basis for the rational selection of R_v under different operating conditions, enabling the optimization of system performance.

$$Q_{hot} = m_H(h_4 - h_5) \tag{3}$$



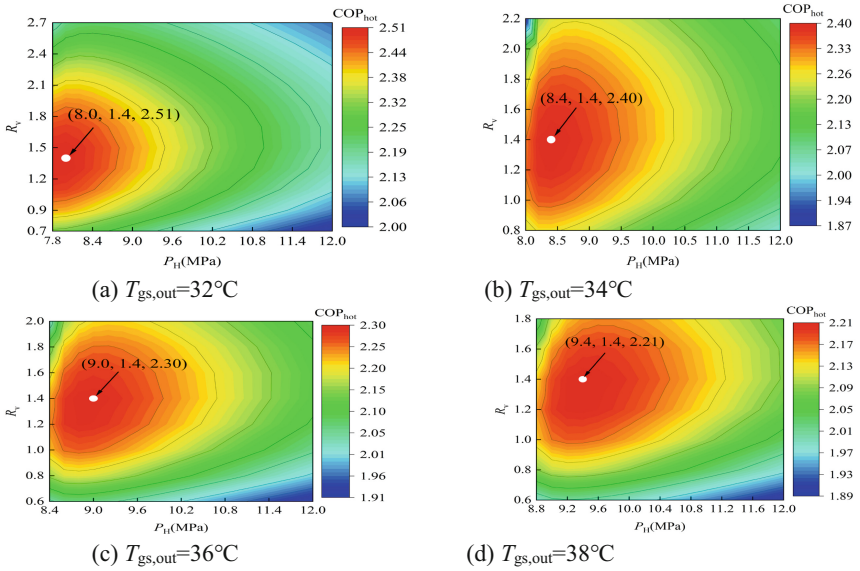
(a) Q_{hot} (b) m_H and h_4-h_5

Fig. 5 Variation of (a) Q_{hot}, (b) m_H and h_4-h_5 with R_v under different P_H conditions for the TCDC.

3.2 Effect of $T_{gs,out}$

3.2.1 Effect of $T_{gs,out}$ on Cycle Performance

As $T_{gs,out}$=increases from 32 °C to 38 °C, the optimal high pressure $P_{H,opt}$ increases from 8.0 MPa to 9.4 MPa. For every 1 °C increase in $T_{gs,out}$, $P_{H,opt}$ rises by 0.2 MPa. This indicates that $T_{gs,out}$ has a significant effect on $P_{H,opt}$, which is consistent with the findings in reference [19]. Furthermore, as $T_{gs,out}$ increases, $R_{v,opt}$ remains constant at 1.4, indicating that $T_{gs,out}$ has almost no effect on the optimal low/high-stage compressor volume ratio. Finally, as $T_{gs,out}$ increases from 32 °C to 38 °C, the maximum COP_{hot} decreases from 2.51 to 2.21, with a decrease of 0.05 for every 1 °C increase in $T_{gs,out}$, indicating that the $T_{gs,out}$ significantly affects $COP_{hot,max}$ (Fig. 6).

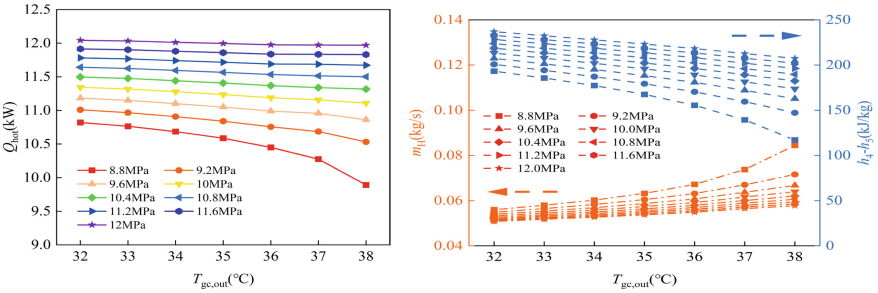


(a) $T_{gs,out}$=32°C (b) $T_{gs,out}$=34°C

(c) $T_{gs,out}$=36°C (d) $T_{gs,out}$=38°C

Fig. 6. Variation of COP_{hot} with P_H under different $T_{gs,out}$ and R_v conditions for the TCDC.

From Fig. 7(a), it can be seen that, at $R_{v,opt}$=1.4, as $T_{gs,out}$ increases, the Q_{hot} decreases. However, as P_H increases, the effect of $T_{gs,out}$ on Q_{hot} gradually weakens. For instance, when P_H=8.8 MPa, as $T_{gs,out}$ increases from 32 °C to 38 °C, Q_{hot} decreases from 10.82 kW to 9.89 kW, a decrease of 8.60%. When P_H=12.0 MPa, as $T_{gs,out}$ increases from 32°C to 38°C, Q_{hot} decreases from 12.04 kW to 11.97 kW, a decrease of 0.58%. From Eq. (3), Q_{hot} is mainly determined by m_H and h_4-h_5. When P_H is fixed, as $T_{gs,out}$ increases, h_4-h_5 decreases P_M and m_H increases, and. As shown in Fig. 7(b), for P_H=8.8MPa, as $T_{gs,out}$ increases from 32°C to 38°C, m_H increases from 0.056 kg s^{-1} to 0.084 kg s^{-1}, an increase of 50.00%, while h_4-h_5 decreases from 193.23 kJ kg^{-1} to 117.13 kJ kg^{-1}, a decrease of 39.36%. Since the magnitude of h_4-h_5 is greater than that of m_H, the trend of Q_{hot} follows the trend of h_4-h_5, meaning that as $T_{gs,out}$ increases, both h_4-h_5 and Q_{hot} decrease. Since the isothermal line of CO_2 in the transcritical region is "S"-shaped, when $T_{gs,out}$ is fixed, as P_H increases further, the rate of decrease of h_5 slows down, and the rate of decrease of h_4-h_5 slows, constraining the downward trend of Q_{hot}. Therefore, as P_H increases, the effect of $T_{gs,out}$ on Q_{hot} gradually weakens. When the outlet temperature of cooling water T_{wout}=50°C, for $T_{gs,out}$=32°C, Q_{hot}=11.26 kW, and for $T_{gs,out}$=38 °C, Q_{hot}=10.53 kW.



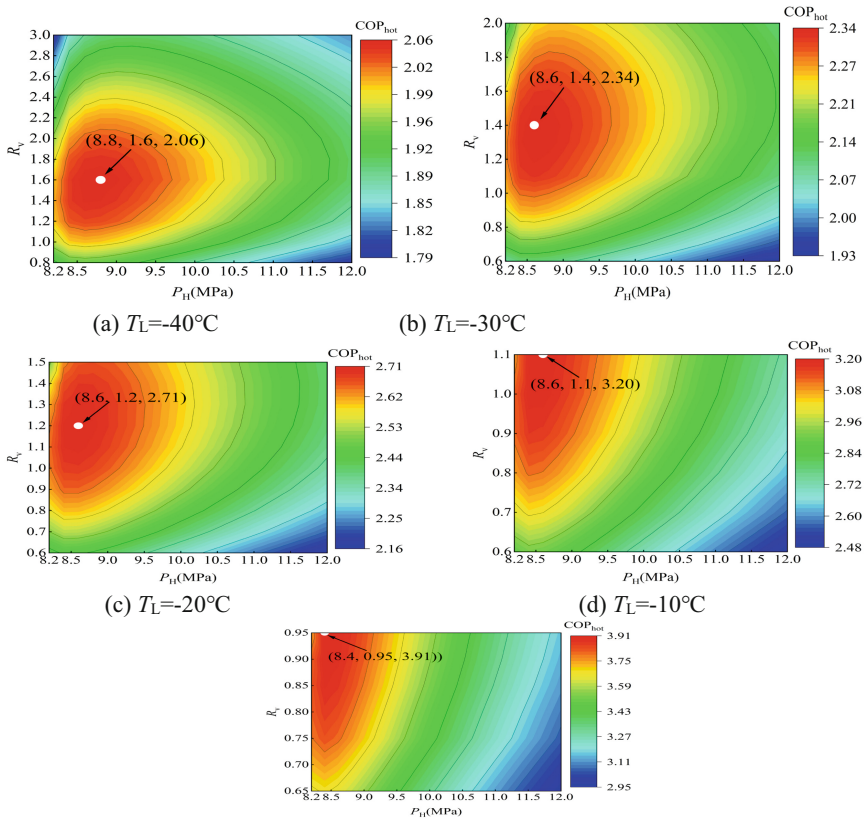
(a) Q_{hot} (b) m_H and h_4-h_5

Fig. 7 Variation of (**a**) Q_{hot}, (**b**) m_H and h_4-h_5 with $T_{gs,out}$ under different P_H conditions for the TCDC.

3.3 Effect of T_L

3.3.1 Effect of T_L on Cycle Performance

As depicted in Fig. 8, with an increase in T_L, the $COP_{hot,max}$ also increases. Specifically, when T_L=–40 °C, $COP_{hot,max} = 2.06$, and when $T_L = 0$ °C, $COP_{hot,max} = 3.91$, representing an average increase of 0.46 for every 10°C rise in T_L. Additionally, as T_L increases, the corresponding $P_{H,opt}$ slightly decreases; however, the variation is not significant. This indicates that T_L does not have a substantial impact on $P_{H,opt}$, which is consistent with the findings presented in reference [15]. As shown in Fig. 17, for T_L=–40 °C, –30 °C and –20 °C, with P_H held constant, $COP_{hot,max}$ initially increases and then decreases with the increase in R_v. In contrast, for T_L=–10 °C and 0°C, with P_H held constant, COP_{hot} continuously increases as R_v increases. As previously discussed, with the increase in T_L, $P_{M,opt}$ gradually approaches P_{crit}, thereby constraining $R_{v,opt}$ and limiting $COP_{hot,max}$. In summary, it can be concluded that T_L and R_v exert significant influences on $P_{H,opt}$ and the cycle performance of the TCDC cycle. This conclusion underscores the critical roles of T_L and R_v in determining the optimal operating conditions and overall efficiency of the system.



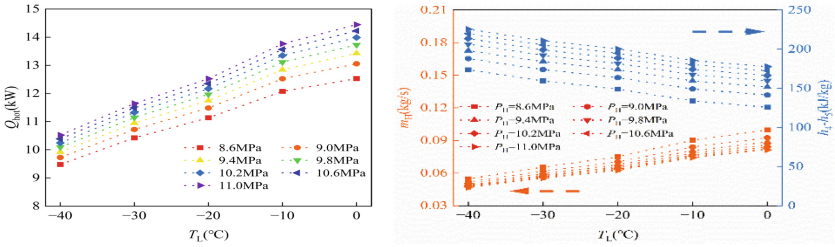
(a) T_L=-40°C (b) T_L=-30°C

(c) T_L=-20°C (d) T_L=-10°C

(e) T_L=-0°C

Fig. 8. Variation of COP_{hot} with P_H under different T_L and R_v conditions for the TCDC.

From Fig. 9(a), it is evident that Q_{hot} increases progressively as T_L rises. When P_H=8.8MPa, Q_{hot} increases from 9.48 kW to 12.53 kW as T_L rises from –40 °C to 0°C, representing an increase of 32.17%. Similarly, at P_H=11.0MPa, Q_{hot} increases from 10.52 kW to 14.44 kW, corresponding to a rise of 37.26%. According to Eq. (1), Q_{hot} is primarily determined by m_H and h_4-h_5. Fig. 9(b) indicates that the growth rate of m_H is greater than the reduction rate of h_4-h_5. For example, at P_H = 8.6 MPa, m_H increases from 0.055 kg s^{-1} to 0.100 kg s^{-1} as T_L rises from –40 °C to 0 °C, an increase of 81.82%, while h_4-h_5 decreases from 173.57 kJ kg^{-1} to 125.68 kJ kg^{-1}, a reduction of 27.59%. Consequently, when P_H is constant, the trend of Q_{hot} aligns closely with the trend of m_H, such that Q_{hot} increases with increasing T_L. When the outlet temperature of cooling water T_{wout} = 50 °C, Q_{hot} is 9.83 kW at T_L = –40 °C and increases to 13.79 kW at T_L = 0 °C, corresponding to an increase of 40.28%. This demonstrates the significant impact of T_L on Q_{hot}.



(a) Q_{hot} (b) m_H and h_4-h_5

Fig. 9. Variation of (a)Q_{hot}, (b)m_H and h_4-h_5 with $T_{gs,out}$ under different P_H conditions for the TCDC.

3.4 The Optimal Low/High-Stage Compressor Volume Ratio

Based on the analysis above, the following conclusions can be drawn. First, when other parameters remain constant, R_v initially causes COP_{hot} to increase and then decrease as R_v increases, indicating the existence of $R_{v,opt}$. Furthermore, $R_{v,opt}$ does not vary with changes in P_H, demonstrating that P_H is not a key factor influencing $R_{v,opt}$. Second, $R_{v,opt}$ shows minimal variation with changes in $T_{gs,out}$, suggesting that $T_{gs,out}$ is also not a critical factor affecting $R_{v,opt}$. Finally, $R_{v,opt}$ decreases with increasing T_L, indicating that T_L is a key factor influencing $R_{v,opt}$. Thus, $R_{v,opt}$ is solely dependent on T_L. Through fitting analysis, the functional relationship of $R_{v,opt}$ with the corresponding T_L (P_L) is derived as follows:

$$R_{v,opt} = 0.921 - 0.015P_L \tag{4}$$

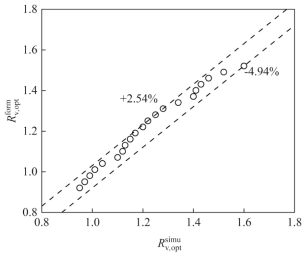


Fig. 10. Comparison between simulated and formulated values of $R_{v,opt}$

The fitting dataset spanning T_L = –40–0°C was constructed with 2°C increments, as illustrated in Fig. 10. The parametric optimization of $R_{v,opt}$ demonstrated a maximum negative fitting discrepancy of –4.94%, with Eq. (4) retaining predictive validity across the entire studied range of –40 °C≤T_L≤0°C.

4 Conclusion

(1) $R_{v,opt}$ depends only on the T_L. Based on this, a functional relationship between $R_{v,opt}$ and T_L (P_L) was proposed.

(2) The influence of R_v on the system's Q_{hot} is greater, while its effect on COP_{hot}. Therefore, the Q_{hot} demand can be prioritized by adjusting R_v to meet the required Q_{hot}.
(3) Impact of outlet temperature of gas cooler $T_{gs,out}$:$T_{gs,out}$ has almost no effect on $R_{v,opt}$, but its influence on $COP_{hot,max}$ is more significant. As P_H increases, the impact of $T_{gs,out}$ on Q_{hot} gradually weakens.
(4) $T_{gs,out}$ has almost no effect on $R_{v,opt}$, but has a significant effect on COP_{hot}, and its effect on Q_{hot} gradually weakens as P_H increases.

References

1. Zhang, Z., Wang, H., Tian, L., Huang, C.: Thermodynamic analysis of double-compression flash intercooling transcritical CO_2 refrigeration cycle. J. Supercrit. Fluids. **109**, 100–108 (2016). https://doi.org/10.1016/j.supflu.2015.09.002.2
2. Jin, X., Wang, S., Zhang, T.T., et al.: Intermediate pressure of two-stage compression system under different conditions based on compressor coupling model. Int. J. Refrig. **35**(4), 827–840.1 (2012)
3. Qin, X., Zhang, F., Zhang, D., Gao, Z., Tang, S., 2022b. Experimental and theoretical analysis of the optimal high pressure and peak performance coefficient in transcritical CO_2 heat pump. Appl. Therm. Eng. 210, 118372 10.1016/j.applthermaleng.2022.118372.3
4. Kauf, F.: Determination of the optimum high pressure for transcritical CO2-refrigeration cycles. Int. J. Therm. Sci. **38**, 325–330 (1999). https://doi.org/10.1016/S1290-0729(99)80098-2.4
5. Dymola – Dassault Syst'emes® [WWW Document], URL, https://www.3ds.com/products-services/catia/products/dymola/, 2023. Accessed 15 May 22.
6. TLK-Thermo GmbH" TLK-Thermo GmbH [WWW Document]. URL. https://www.tlk-thermo.com (2023). Accessed 16May 22
7. Hu, B., Li, Y., Cao, F., Xing, Z.: Extremum seeking control of COP optimization for air-source transcritical CO_2 heat pump water heater system. Appl. Energy. **147**, 361–372 (2015). https://doi.org/10.1016/j.apenergy.2015.03.010
8. Wang, W., Li, Y.: Intermediate pressure optimization for two-stage air-source heat pump with flash tank cycle vapor injection via extremum seeking. Appl. Energy. **238**, 612–626 (2019). https://doi.org/10.1016/j.apenergy.2019.01.083
9. Wang, W., Li, Y., Cao, F.: Extremum seeking control for efficient operation of an air-source heat pump water heater with internal heat exchanger cycle vapor injection. Int. J. Refrig. **99**, 153–165 (2019). https://doi.org/10.1016/j.ijrefrig.2019.01.002.[1]
10. Wang, W.: Real-time efficiency optimization of a cascade heat pump system via multivariable extremum seeking. Appl. Therm. Eng. **18** (2020)
11. Cui, C., Ren, J., Song, Y., Yin, X., Wang, W., Yang, X., Cao, F.: Multi-variable extreme seeking control for efficient operation of sub-cooler vapor injection trans-critical CO2 heat pump water heater. Appl. Therm. Eng. **184**(116), 261 (2021). https://doi.org/10.1016/j.applthermaleng.2020.116261
12. Michael, M.: Tiller, Modelica by Example [WWW Document], Modelica by Example, 2022. URL, https://mbe.modelica.university/. Accessed 22Aug 22
13. Wang, W., Hu, B., Wang, R.Z., Luo, M., Zhang, G., Xiang, B.: Model predictive control for the performance improvement of air source heat pump heating system via variable water temperature difference. Int. J. Refrig. **138**, 169–179 (2022). https://doi.org/10.1016/j.ijrefrig.2022.03.001

14. Jiang, S., Yu, Y., Li, S., et al.: Simulation and optimum control of a two-stage compression air source heat pump system: a comparison of two kinds of variable volume approaches. Appl. Therm. Eng. **226**, 120149 (2023)
15. Wang, S., Tuo, H., Cao, F., Xing, Z.: Experimental investigation on air-source transcritical CO_2 heat pump water heater system at a fixed water inlet temperature. Int. J. Refrig. **36**, 701–716 (2013)
16. Ma, Y.T.: Research and Development on Refrigeration and Heat Pump Cycle with Natural Working Fluid Carbon Dioxide. Science Press, Beijing (2017)
17. Longo, G.A., Mancin, S., Righetti, G., Zilio, C.: A new model for refrigerant boiling inside Brazed Plate Heat Exchangers (BPHEs). Int. J. Heat Mass Transf. **91**, 144–149 (2015)
18. C, H.E.D.: In-Tube Cooling Heat Transfer of Supercritical Carbon Dioxide. Elsevier Ltd (2004)
19. Niu, H., Xiao, H., Li, W., Wang, P., Zhang, X.: W. shi, Performance of CO2 transcritical two-stage compression refrigeration cycle with complete inter-cooling and double-stage throttling. J. Refriger. **43**, 1–9 (2022)

A Universal Prediction Model for Initial Frosting Rate of Air Source Heat Pumps Based on the Enthalpy Diagram

Wenzhe Wei[1], Yutao Guo[1], Zhike Jiang[1], Xinyu Zhang[2(✉)], Wei Wang[1,3(✉)], Yuying Sun[1], Shiquan Wang[1], and Chunxiao Zhang[4]

[1] Beijing Key Laboratory of Green Built Environment and Energy Efficient Technology, Beijing University of Technology, Beijing, China
mrwangwei@bjut.edu.cn
[2] State Key Laboratory of Building Safety and Built Environment, Beijing, China
[3] School of Mechatronic Engineering, Beijing Polytechnic University, Beijing, China
[4] Institute of Building Energy and Thermal Science, Henan University of Science and Technology, Luoyang, China

Abstract. To maintain the high efficiency of air source heat pump (ASHP) under frosting conditions, the periodic defrosting is required. The earlier and later defrosting can both cause a decrease in its average coefficient of performance (COP) throughout the frosting-defrosting process. Accurately predicting the frosting rate and using it for defrosting control is a fundamental method to solve this problem. However, there is still lack of a universal model for predicting the frosting rate. To solve this problem, a mathematical model for variable-frequency ASHP was developed firstly, which can simulate its operating parameters under different conditions. Combining with the enthalpy diagram, a calculation method for the initial frosting rate of ASHPs was proposed. Then, an initial frosting rate prediction model suit for all operating conditions was developed utilizing the calculation results. Results indicate that the developed frosting rate prediction model for ASHPs demonstrates well predictive performance. The deviations between the predicted values and actual values are mainly within ±15%. Besides, the initial frosting rate can characterize the overall frosting degree and be used to predict the total frost mass throughout the frosting process. The maximum relative error between the predicted total frosting mass and the experimental results is 9.25%.

Keywords: Air source heat pump · Initial frosting rate · Prediction model

1 Introduction

Air source heat pumps (ASHPs) have emerged as an energy-efficient alternative to conventional HVAC systems due to their high performance and environmental benefits [1]. However, frosting remains a critical operational challenge, occurring when the outdoor heat exchanger surface temperature (STOHE) falls below both dew point and freezing point. Frost accumulation can reduce heating capacity and COP by up to 60%, increase discharge temperature, and potentially cause system shutdowns [2].

© The Author(s), under exclusive license to Springer Nature Singapore Pte Ltd. 2025
L. Ni et al. (Eds.): CCHVAC 2025, ESE, pp. 143–153, 2025.
https://doi.org/10.1007/978-981-95-3253-7_16

To maintain the high energy efficiency of ASHPs under frosting condition, the periodic defrosting is necessary. But the earlier and later defrosting can both cause a decrease in the average COP of ASHPs throughout the frosting and defrosting process [3]. Thus, it is imperative to initiate the defrosting operation at the optimal defrosting time [4]. However, in actual heating projects, the frosting rate of ASHPs varies significantly, and the optimal defrosting initiating time also changes accordingly. To realize the goal of accurate defrosting, accurately predicting the frosting rate and using it for defrosting control is a fundamental method.

To obtain the frosting rate of ASHPs under various environmental conditions, researchers have systematically developed frosting rate prediction models for ASHPs through progressive studies. While these studies have established valuable empirical models through experimental and numerical approaches, their applicability remains constrained to specific operational parameters, as displayed in Table 1. There is still lack of a universal frosting rate prediction model for ASHPs, which is applicable to all operating conditions.

Table 1. The applicable conditions of the frosting rate prediction models in previous investigations.

Item	Authors	Applicable conditions			
		Outdoor air temperature (°C)	STOHE (°C)	Relative humidity	Air velocity
1	Tokura et al. [5]	20	−16–−11	45–65%	2–4 m/s
2	Yang et al. [6]	5–15	−35–−15	3.22–8.47 g/kg	1–2 m/s
3	Lee et al. [7]	25	–15	50%–80%	0–2 m/s
4	Guo et al. [8]	–15–5	—	55%–90%	6500 m^3/h
5	Cheng et al. [9]	28.15–30.85	28.15–19.85	3.9–17 g/kg	1.08–2.92 m/s
6	W. Wang et al. [10]	–8–25	–16—4	30%–80%	0.7–5 m/s
7	D. Wang et al. [11]	–10–10	–20—8	50%–90%	0.5–2.5 m/s
9	Seker et al. [12]	–35–0	—	30–100%	0.1–0.5 kg/s
10	Ye et al. [13]	3–11	–15–7	3.27–5.69 g/kg	1.5–2.5 m/s

To address the above research gap, a mathematical model of variable-frequency ASHP was established to supply the operating parameters under diverse conditions. Using the enthalpy diagram, a method for calculating the initial frosting rate of ASHPs was proposed and extended into a universal predictor of outdoor temperature, relative humidity, inlet air velocity, and STOHE. The originalities of this research are: 1) proposing a calculation method of initial frosting rate for ASHPs based on enthalpy diagram;

and 2) developing an initial frosting rate prediction model of ASHPs, which is suit for all kinds of operating conditions.

2 Mathematical Model Development and Validation

2.1 Residential Building Thermal Dynamic Prediction Model

To further investigate the initial frosting rate of ASHPs, the mathematical model of variable-frequency ASHP as shown in Fig. 1 was developed based on the Ref. [14], and its detailed parameters refer to Ref. [18]. The variable-frequency ASHP model is primarily composed of six component sub-models, including quasi-two-stage compressor, evaporator, economizer, condenser and two electric expansion valves.

The compressor model divides the process into three stages: (1) low-pressure compression with efficiencies calculated though AHRI method [15] and adjusted for variable speeds [16]; (2) medium-pressure mixing [17] treated as constant-pressure; and (3) high-pressure compression. The economizer employs partitioned lumped parameter methods for heat exchange between refrigerant branches. Similar approaches model the condenser and evaporator, while expansion valves are treated as isenthalpic processes. Minor pipe losses are neglected due to minimal impact (Fig. 2).

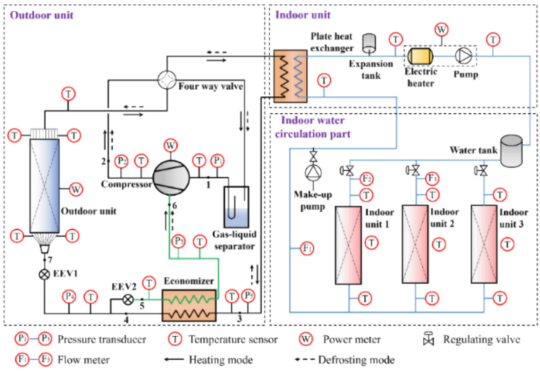


Fig. 1. Schematic of the used variable-frequency ASHP.

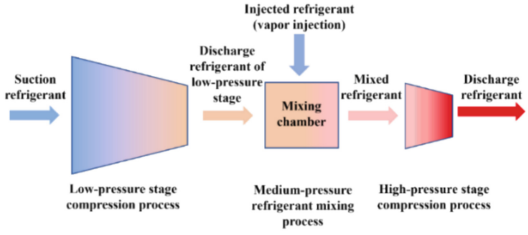


Fig. 2. Schematic of the refrigerant compression process within the quasi-two stage compressor.

2.2 Model Verification

To validate the variable-frequency ASHP model's accuracy, a two-step verification was conducted. First, simulations at the rated compressor speed (80 r/s) and fixed water temperature (41°C) showed strong agreement with experimental data [17] for refrigerant pressures and heating capacity (Fig. 3), with maximum 7.56% relative error in heating capacity. Second, variable-speed operation validation through STOHE comparisons across different outdoor temperatures [19] demonstrated model accuracy at non-rated speeds (Fig. 4). These results confirm the model's reliability for initial frosting rate investigations under all operational conditions

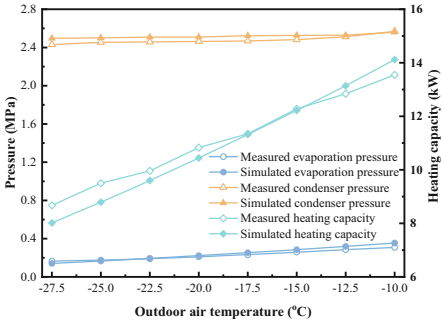


Fig. 3. Comparison of the main heating performance parameters obtained through simulations and tests at the rated speed of the compressor.

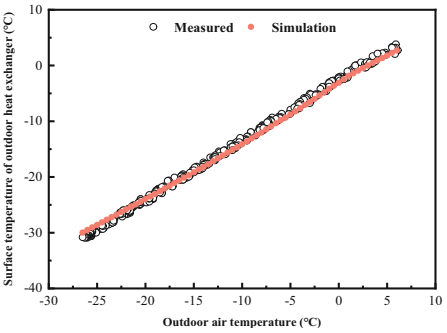


Fig. 4. Comparison of the surface temperatures of outdoor heat exchanger derived from simulations and tests at various compressor speeds.

3 Calculation Method for the Initial Frosting Rate of ASHP Based on enthalpy Diagram

3.1 Variations of Wet Air State During the Frosting Process of ASHP

During ASHP frosting operation, refrigerant absorbs heat from outdoor air, causing temperature reduction and part of the water vapor to condense and subsequently freeze into frost on the heat exchanger. This process parallels the treatment process of wet air in fresh air system. Therefore, the state changes of wet air during the frosting process of ASHP can also be exhibited by enthalpy diagram. Fig. 6 demonstrates wet air state transitions, at low relative humidity (points C-E), no frosting occurs and state points descend vertically (constant humidity ratio). At high relative humidity (point A), both simultaneous temperature and humidity reduction occur with state points moving toward the lower left.

The boundary layer reaches 100% relative humidity (point B in Fig. 5), determinable through the variable-frequency ASHP model's STOHE calculations. While air state theoretically progresses along line AB toward point B, finite heat exchanger size limits the final state to an intermediate point A_n.

3.2 Calculation Method for the Initial Frosting Rate of ASHP

During the space heating of ASHP under frosting condition, the initial frosting rate on the outdoor heat exchanger is given by Eq. (1). In the initial frosting stage, when frost deposition is minimal, the dry air mass flow rate (m_a) can be approximated as the rated flow, while the inlet air humidity ratio (d_A) is determined from ambient temperature and relative humidity. Thus, the frosting rate depends solely on the outlet air humidity ratio (d_{A_n}).

$$v_0 = m_a\left(d_A - d_{A_n}\right)/A \tag{1}$$

Figure 6 displays the relationship between the air state at point A_n and the air states at points A and B, with Eq. (2) derived using similar triangles. Since the air states at A and B are known (Sect. 3.1), Eq. (2) contains two unknown parameters, t_{A_n} and d_{A_n}. Rearranging Eq. (2) expresses d_{A_n} as a function of t_{A_n} (Eq. (3)).

$$\frac{d_A - d_B}{t_A - t_B} = \frac{d_A - d_{A_n}}{t_A - t_{A_n}} \tag{2}$$

$$d_{A_n} = d_A - \frac{d_A - d_B}{t_A - t_B}\left(t_A - t_{A_n}\right) = f\left(t_{A_n}\right) \tag{3}$$

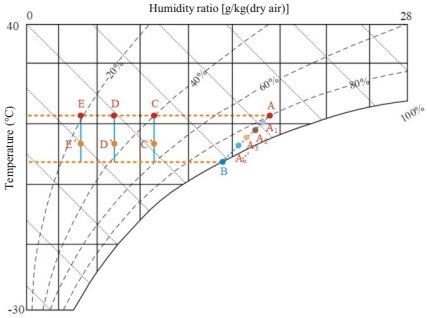


Fig. 5. Variations of wet air state during the space heating process of ASHP in enthalpy diagram.

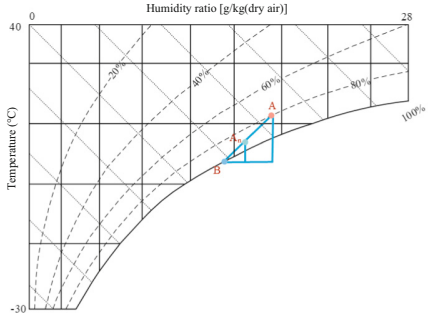


Fig. 6. The mathematical relationship of wet air during the frosting process

The total heat transfer (Q_0) between outdoor air and the heat exchanger consists of sensible and latent heat exchange from air state changes (Eqs. (4)–(6)), calculated via wet air enthalpy (Eq. (7)), and latent heat from condensate freezing. Substituting Eqs. (3), (5)–(7) into Eq. (4) yields Q_0 as a function of t_{A_n} (Eq. (8)). Using the ASHP's variable-frequency model, Q_0 is computed numerically, with t_{A_n} iteratively adjusted by the bisection method until the calculated Q_0 converges with the actual value. Once t_{A_n} is determined, d_{A_n} is obtained from Eq. (3), allowing the initial frosting rate to be calculated by Eq. (1) . The detailed calculation process of the initial frosting rate is shown in Fig. 7.

$$Q_0 = Q_a + Q_l \tag{4}$$

$$Qa = m_a\left(h_A - h_{A_n}\right) \tag{5}$$

$$Ql = 0.001 m_a l\left(d_{A_n} - d_A\right) \tag{6}$$

$$h = 1.005ta + 0.001d(2500 + 1.84t_a) \tag{7}$$

$$Q_o = m_a\left[1.005\left(t_A - t_{A_n}\right) + (2.5 + 0.001l)\left(d_A - f\left(t_{A_n}\right)\right) + 0.00184\left(t_A d_A - t_{A_n} f\left(t_{A_n}\right)\right)\right] \tag{8}$$

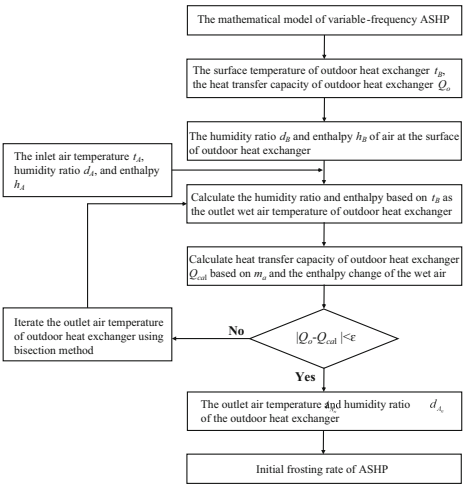
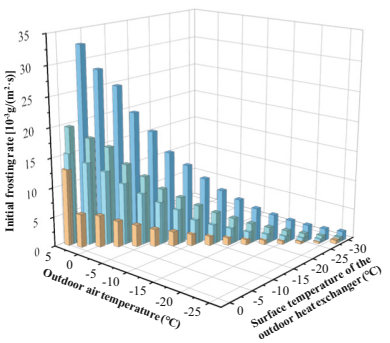


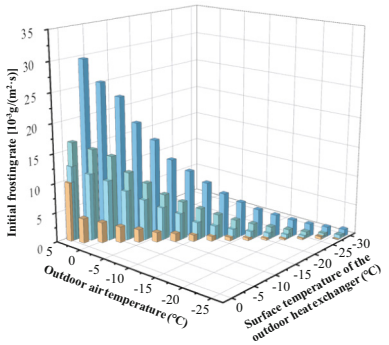
Fig. 7. Flowchart for detailed calculation of initial frosting rate.

4 Initial Frosting Rate Prediction Model

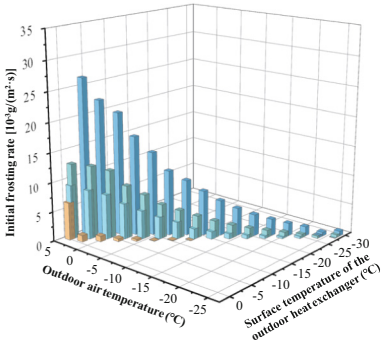
The initial frosting rate of ASHPs is mainly affected by the outdoor air temperature, relative humidity, the STOHE, and inlet air velocity through outdoor heat exchanger. To develop a prediction model applicable to all operating conditions, 1360 sets of initial frosting rates under different combinations of the four factors were obtained by combining: temperature ranges (–26 °C to 4 °C [18] with 2 °C intervals), relative humidity levels (70–90% [18] with 5% intervals), four compressor speeds (25–100% of rated), and three air velocities (2.0–3.0 m/s). As shown in Fig. 8, the strong dependence of initial frosting rates on these parameters at 2.5 m/s air velocity is demonstrated, with a 43.5% decrease (32.7–18.5 $\times 10^{-3}$ g/(m^2·s)) being observed when relative humidity drops from 90% to 70% at 4 °C. When the relative humidity is ≤80%, the frosting will not occur or the initial frosting rate is close to 0 under some conditions, the initial frosting rates were not displayed. Under the same relative humidity, the initial frosting rate is positively correlated with the outdoor air temperature, while negatively correlated with the STOHE.



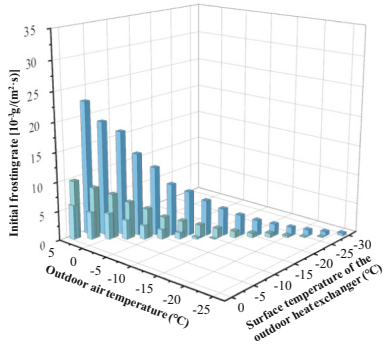
(a) Relative humidity of 90%.



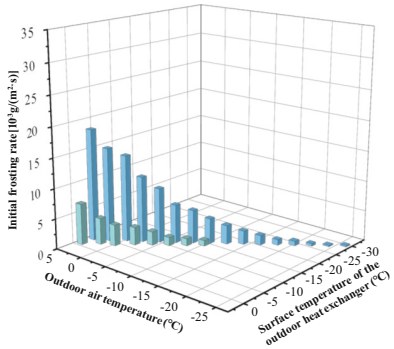
(b) Relative humidity of 85%.



(c) Relative humidity of 80%.



(d) Relative humidity of 75%.



(e) Relative humidity of 70%.

Fig. 8. Initial frosting rates under different relative humidity conditions when the inlet air velocity is 2.5 m/s.

Based on the results in Fig. 8, the prediction model of the initial frosting rate of ASHP at the inlet air velocity of 2.5 m/s was obtained, as displayed in Eq. (9). The M in it is a 5 × 5 matrix, and its values are given in Eq. (10). Considering all the frosting rates

under the inlet air velocity of 2.5 m/s, the R^2 value of the initial frosting rate prediction model is 0.997.

$$v_0 = \begin{bmatrix} RH^4 & RH^3 & RH^2 & RH & 1 \end{bmatrix} M \begin{bmatrix} 1 \\ t_A \\ t_A^2 \\ t_B \\ t_B^2 \end{bmatrix} \tag{9}$$

$$M = \begin{bmatrix} 0.000331962 & -4.452E-05 & -7.637E-07 & 5.84E-05 & 8.479E-07 \\ -0.10726572 & 0.01443838 & 0.00024238 & -0.01885680 & -0.00026874 \\ 12.93309893 & -1.74920640 & -0.02863707 & 2.27242377 & 0.03169022 \\ -688.79579748 & 93.83482799 & 1.49106772 & -121.09181109 & -1.64525061 \\ 13639.79341924 & -1875.85957637 & -28.72775890 & 2400.77040297 & 31.56649607 \end{bmatrix} \tag{10}$$

To validate the accuracy of the model above, the predicted initial frosting rates under various operating conditions were calculated though Eq. (9) and compared with theoretical values (Fig. 9).

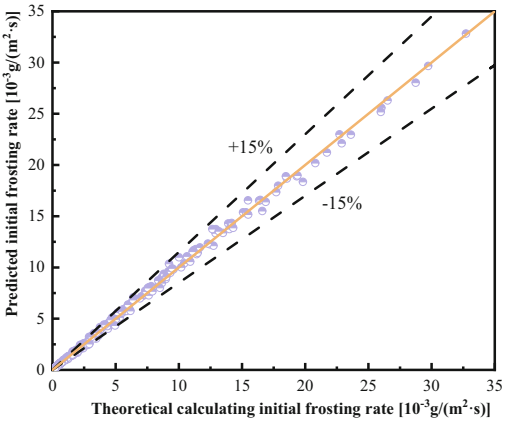


Fig. 9. Relative error analysis of the ASHP initial frosting rate prediction model.

In Fig. 9, relative errors remained within ±15% for initial frosting rates ≥3 × 10^{-3} g/(m^2·s). However, when the initial frosting rate is <3 × 10^{-3} g/(m^2·s), seven data points exceeded ±15% error (maximum: 55%). In practical application of ASHP, once the obvious frost can be observed, the initial frosting rate is always ≥3 × 10^{-3} g/(m^2·s). On the other hand, the model demonstrated high accuracy with an average relative error of 4.68%, confirming its practical for ASHP.

Similarly, at the inlet air velocities of 2.0 m/s and 3.0 m/s, the frosting rate prediction models were also obtained, as displayed in Appendix A (Eqs. 1A–4A).

5 Conclusions

To calculate the optimal defrosting initiation time and further realize the accurate defrosting of ASHP, a mathematical model for variable-frequency ASHP was established firstly in present work to obtain the operating parameters under various conditions. Then, combining the enthalpy diagram, a method for calculating the initial frosting rate of ASHPs was proposed. Utilizing the initial frosting rates under different operating conditions, an initial frosting rate prediction model suit for all operating conditions was developed and its accuracy was verified. The findings are summarized below. The initial frosting rate of ASHPs under different operating conditions can be calculated theoretically based on the enthalpy diagram. Through the mathematical model of variable-frequency ASHP, the STOHE can be calculated, and the state point of wet air on the surface of outdoor heat exchanger can be determined in enthalpy diagram. By analyzing the heat and mass transfer process, the initial frosting rate under different operating conditions can be calculated accurately. The developed initial frosting rate prediction model for ASHPs demonstrated well predictive performance in various operating conditions. When the inlet air velocity is 2.5 m/s, all the relative errors fall into the range of ±15% when the initial frosting rate is $\geq 3 \times 10^{-3}$ g/(m^2·s), and the average error of all points is 4.68%. Under different inlet air velocities, the R^2 of all prediction models exceed 0.996.

Appendix A

The frosting rate prediction model at the inlet air velocity of 2.0 m/s:

$$v = \begin{bmatrix} RH^4 & RH^3 & RH^2 & RH & 1 \end{bmatrix} N \begin{bmatrix} 1 \\ t_A \\ t_A^2 \\ t_B \\ t_B^2 \end{bmatrix} \tag{1A}$$

$$N = \begin{bmatrix} 0.00029 & -0.00004442 & -5.08661\text{E}-07 & 0.00005528 & 6.097585\text{E}-07 \\ -0.09346 & 0.014324489 & 0.000164039 & -0.0178029 & -0.00019606 \\ 11.23962 & -1.7257582 & -0.01975658 & 2.14108 & 0.0235043 \\ -597.28541 & 92.081798 & 1.05138325 & -113.93542 & -1.244012 \\ 11807.36311 & -1832.0777656 & -20.763904 & 2258.21829 & 24.419352 \end{bmatrix} \tag{2A}$$

The frosting rate prediction model at the inlet air velocity of 3.0 m/s:

$$v_0 = \begin{bmatrix} RH^4 & RH^3 & RH^2 & RH & 1 \end{bmatrix} P \begin{bmatrix} 1 \\ t_A \\ t_A^2 \\ t_B \\ t_B^2 \end{bmatrix} \tag{3A}$$

$$P = \begin{bmatrix} 0.0005016 & -0.00004509 & -3.983132\text{E}-06 & 0.0001142 & 5.15752003\text{E}-06 \\ -0.1629452 & 0.014726671 & 0.0012905596 & -0.0370867 & -0.0016698 \\ 19.765763 & -1.79640626 & -0.156315966 & 4.5002769 & 0.2020816 \\ -1060.3593 & 97.027934 & 8.38730355 & -241.79134 & -10.8335354 \\ 21191.9256 & -1952.63927 & -168.06851 & 4846.05744 & 216.9101788 \end{bmatrix} \tag{4A}$$

References

1. Jiang, S., Zhao, H., Ni, L.: Review and prospect of air source heat pump research: a bibliometric insight. Int. J. Refrig. **170**, 172–191 (2025)
2. Liu, J., Sun, Y., Wang, W., Zhu, J.: Performance evaluation of air source heat pump under unnecessary defrosting phenomena for nine typical cities in China. Int. J. Refrig. **74**, 385–398 (2017)
3. Jin, X., Zhang, K., Liu, Z., Li, X., Jiang, S.: Numerical research on coupling performance of inter-stage parameters for two-stage compression system with injection. Appl. Therm. Eng. **128**, 1430–1445 (2018)
4. Wang, S., Wei, W., Luo, J., Wang, W., Sun, Y., Li, Z., Huang, C., Tang, R., Deng, S.: A prediction model of the optimal defrosting initiating time for the air source heat pumps with different configurations and operations. Energy Build. **326**, 115079 (2025)
5. Tokura, I., Saito, H., Kishinami, K.: Prediction of growth rate and density of frost layer developing under forced convection. Heat Mass Transf. **22**, 285–290 (1988)
6. Yang, D.-K., Lee, K.-S.: Dimensionless correlations of frost properties on a cold plate. Int. J. Refrig. **27**(1), 89–96 (2004)
7. Lee, K.S., Lee, T.H., Kim, W.S.: A one-dimensional model for frost formation on a cold flat surface. Int. J. Heat. Mass. Tran. **40**, 4359–4365 (1997)
8. Guo, X.-M., Chen, Y.-G., Wang, W.-H., Chen, C.-Z.: Experimental study on frost growth and dynamic performance of air source heat pump system. Appl. Therm. Eng. **28**(17-18), 2267–2278 (2008)
9. Cheng, C.H., Cheng, Y.C.: Predictions of frost growth on a cold plate in atmospheric air. Int. Commum. Heat Mass Transf. **28**, 953–962 (2001)
10. Wang, W., Guo, Q.C., Lu, W.P., Feng, Y.C., Na, W.: A generalized simple model for predicting frost growth on cold flat plate. Int. J. Refrig. **35**(2), 475–486 (2012)
11. Wang, D., Sun, Y., Wang, W., Guo, Q., Liu, J.: Semi-empirical dimensionless correlations of dynamic frosting process under practical conditions for air source heat pump. Heat Transf. Res. **49**, 915–927 (2018)
12. Seker, D., Karatas, H., Egrican, N.: Frost formation on fin-and-tube heat exchangers. Part I—Modeling of frost formation on fin-and-tube heat exchangers. Int. J. Refrig. **27**(4), 367–374 (2004)
13. Ye, H.-Y., Lee, K.-S.: Performance prediction of a fin-and-tube heat exchanger considering air-flow reduction due to the frost accumulation. Int. J. Heat. Mass. Transfer. **67**, 225–233 (2013)
14. Wei, W., Ni, L., Xu, L., Yang, Y., Yao, Y.: Application characteristics of variable refrigerant flow heat pump system with vapor injection in severe cold region. Energy Build. **211**, 109798 (2020)
15. Lumpkin, D., Bahman, A., Groll, E.: Two-phase injected and vapor-injected compression: experimental results and mapping correlation for a R-407C scroll compressor. Int. J. Refrig. **86**, 449–462 (2018)

16. Li, W.: Simplified steady-state modeling for variable speed compressor. Appl. Therm. Eng. **50**, 318–326 (2013)
17. Wei, W., Ni, L., Zhou, C., Yao, Y., Xu, L., Yang, Y.: Performance analysis of a quasi-two stage compression air source heat pump in severe cold region with a new control strategy. Appl. Therm. Eng. **174**, 115317 (2020)
18. Wei, W., Ni, L., Li, S., Wang, W., Yao, Y., Xu, L., Yang, Y.: A new frosting map of variable-frequency air source heat pump in severe cold region considering the variation of heating load. Renew. Energy. **161**, 184–199 (2020)

Performance of Annual CO_2 Space Heating and Cooling System integrated with Soil Cold Storage

Baomin Dai[1,2,3], Ronghua Miao[1,2,3], Tongyu Duan[1,2,3], and Shengchun Liu[1,2,3](✉)

[1] Tianjin Key Laboratory of Refrigeration Technology, Tianjin University of Commerce, Tianjin 300134, China
liushch@tjcu.edu.cn

[2] International Centre in Fundamental and Engineering Thermophysics, Tianjin University of Commerce, Tianjin 300134, China

[3] Key Lab of Agricultural Products Low Carbon Cold Chain of Ministry of Agriculture and Rural Affairs, Tianjin University of Commerce, Tianjin 300134, China

Abstract. Aiming at the demand for energy saving and carbon reduction in heating and cooling systems of civil buildings and to achieve the "carbon neutrality" goal in the building sector, an annual CO_2 heating and cooling system with soil cold storage is proposed in this study. The results show that the annual CO_2 heating and cooling system with soil cold storage and subcooling is superior to the basic CO_2 system in terms of thermodynamic performance. The annual average COP of Beijing is increased by 14.04%. The maximum improvement ratio of the annual performance coefficient is 12.91% in Harbin. The maximum subcooling degree in Beijing is 13.47°C. This study can provide a theoretical reference for the application of carbon dioxide refrigeration and heat pump technologies.

Keywords: Soil cold storage · CO_2 system · Subcooling

1 Introduction

1.1 Background

The implementation of the "double carbon" goal is an important task for China's medium and long-term energy development and utilization. In the field of refrigeration and air conditioning, the entry into force of the Kigali Amendment to the Montreal Protocol [1] has accelerated the replacement process of refrigerants with high global warming potential (GWP). Therefore, using clean and environmentally friendly working fluids, improving the energy efficiency of refrigeration systems, and reducing carbon emissions are urgent for the development of the refrigeration industry. Besides, soil as a typical low-temperature sensible heat storage material, can be used as an energy storage tank to store cold energy from the external environment and extract it when needed.

© The Author(s), under exclusive license to Springer Nature Singapore Pte Ltd. 2025
L. Ni et al. (Eds.): CCHVAC 2025, ESE, pp. 154–162, 2025.
https://doi.org/10.1007/978-981-95-3253-7_17

1.2 Literature Review

CO_2 as a natural refrigerant is clean, non-toxic, non-flammable, has zero ODP, and negligible GWP [3]. Its use in trans-critical direct cooling ice-making at the Beijing Winter Olympics highlighted its potential. While CO_2 systems with soil cold storage/subcooling are gaining traction in Europe [2], high ambient temperatures in China limit their efficiency. Specifically, heat cannot be fully rejected from the CO_2 fluid leaving the gas cooler in trans-critical systems, causing excessive throttling losses and low efficiency. To address this, subcooling technology [4] is applied. This involves storing winter "cold" energy in the soil and releasing it in summer to subcool the CO_2 after the gas cooler, boosting system performance in hot climates.

1.3 Scope and Contributions

Against the background of providing better heating and cooling for civil buildings, a mathematical model of the annual CO_2 space heating and cooling system integrated with soil cold storage is established to analyze the soil temperature field and the dynamic performance of the CO_2 refrigeration system, providing a theoretical reference for improving the performance of CO_2 refrigeration systems. The contributions and innovations of this study are that load prediction models, CO_2 system models, and soil energy storage system models are established respectively. After predicting the building load requirements in eight cities such as Beijing and Shanghai, the two systems are modeled, and the above three models are integrated to establish a model of the CO_2 cooling and heating system with cross-seasonal soil cold storage and subcooling.

2 System Description

Figure 1 shows the schematic diagram of the CO_2 heating and cooling system using soil cold energy storage (SCES). This system adds a soil cold storage device to the basic CO_2 cycle, including a subcooler, multiple valves, and a set of buried pipes. Heating and cooling are switched via a three-way valve. In the heating mode, the soil stores cold energy; conversely, in the cooling mode, the soil releases cold energy. The switching of operating modes is shown in Table 1.

Table 1 Different Operating Modes of the System

Model	Operating conditions	Operating model
1	$T_{amb} < 18$ °C	Heating mode
2	$T_{amb} > 26$ °C	Cooling mode
3	18 °C $\leq T_{amb} \leq$ 26 °C	stop mode

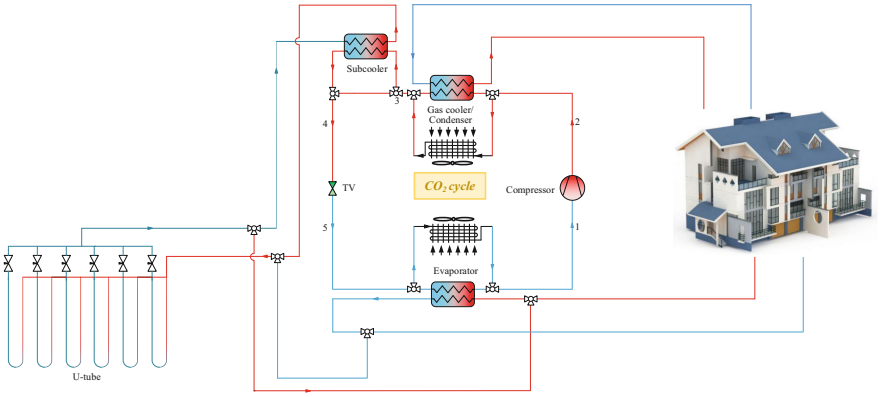


Fig. 1. Soil cold energy storage subcooling CO_2 system.

3 Model Development

3.1 Soil Energy Storage Model

3.1.1 Related Assumptions and Parameter Settings

As shown in Fig. 2, the U-shaped pipe is vertically placed in the borehole, which is filled with backfill material.

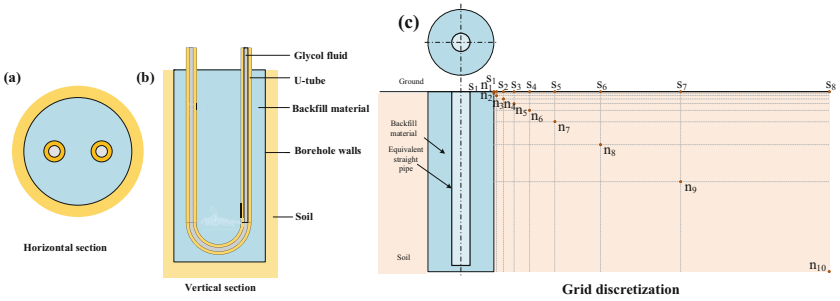


Fig. 2. Vertical U-shaped pipe section diagram. (a) Horizontal section. (b) Vertical section (c) Soil Energy Storage System Diagram.

3.1.2 Thermal Resistance-Capacitance Method Heat Transfer Model

The thermal resistance-capacitance method (TRCM) has fast calculation speed, high accuracy, and can handle complex heat transfer conditions, making it more suitable for establishing the buried pipe model [5, 6]. Figure 3 shows the thermal resistance-capacitance network diagram established in this study.

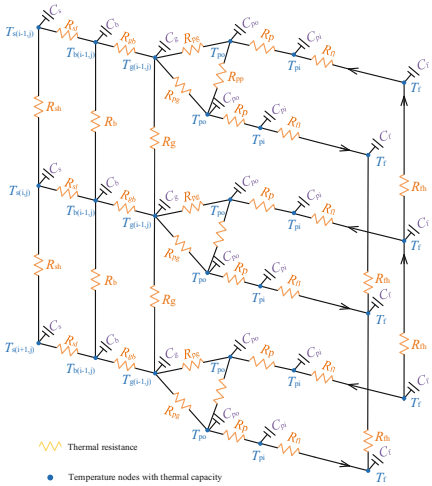


Fig. 3. Thermal resistance heat capacity network diagram.

3.2 Annual CO_2 Space Heating and Cooling System Integrated with Soil Cold Storage

The system's mathematical model is shown in Table 2.

Table 2 Key equations of the soil-integrated CO_2 heating/cooling system

Eq.	Equation	Description
(1)	$C_{\mathrm{j}} \frac{\mathrm{d}T_{\mathrm{j}}}{\mathrm{d}\tau} = \sum_{\mathrm{k}=1}^{n} \frac{T_{\mathrm{k}} - T_{\mathrm{j}}}{R_{\mathrm{k}}} + Q_{\mathrm{j}}$	Thermal Resistance-Capacitance Method
(2)	$\dot{Q}_{\mathrm{H,GC}} = \dot{m}_{\mathrm{ref}}(h_2 - h_3)$	Heating capacity of the SCES system:
(3)	$\dot{\mathrm{Q}}_{\mathrm{f}} = \mathrm{c_f}\dot{\mathrm{m}}_{\mathrm{f}}\left(\mathrm{T}_{\mathrm{sin\,k,out}} - \mathrm{T}_{\mathrm{sin\,k,in}}\right)$	Soil energy storage system
(4)	$\dot{Q}_{C,\mathrm{Evap}} = \dot{m}_{\mathrm{r}}(\mathrm{h}_1 - \mathrm{h}_4)$	CO_2 refrigeration system and CO_2 refrigeration cycle: Evaporator
(5)	$\dot{W}_{Comp} = \dot{m}_r(h_2 - h_1)$	Compressor power consumption
(6)	$\eta_{\mathrm{isen}} = 0.7325 - 0.0155p_r - 0.0021{p_r}^2$	Compressor isentropic efficiency (empirical correlation) [7]
(7)	$\mathrm{COP_H} = \frac{\dot{Q}_{\mathrm{H,Cond}}}{\dot{W}_{\mathrm{Comp}}}$	Heating Coefficient of Performance
(8)	$COP_{\mathrm{C}} = \frac{\dot{Q}_{C,Evap}}{\dot{\mathrm{W}}_{Comp}}$	Cooling Coefficient of Performance
(9)	$\dot{m}_{\mathrm{f,Evap}} = \frac{\dot{m}_r(h_1 - h_4)}{\mathrm{c}_f\left(T_{\mathrm{source,in}} - T_{\mathrm{source,out}}\right)}$	Ethylene glycol mass flow rate (from evaporator energy balance)

(*continued*)

Table 2 (*continued*)

Eq.	Equation	Description
(10)	$T_{\mathrm{U}} = \frac{\dot{m}_{\mathrm{f,Evap}} \cdot T_{\mathrm{source,out}}}{\dot{m}_{\mathrm{f,Evap}}}$	Inlet temperature of cold storage fluid entering soil system
(11)	$\dot{m}_{\mathrm{SC}} = \frac{\dot{m}_r (\mathrm{h}_3 - \mathrm{h}_4)}{\mathrm{c}_f (\mathrm{T}_{f,out} - \mathrm{T}_{f,in})}$	Ethylene glycol mass flow rate (dynamically adjusted for subcooler)
(12)	$\mathrm{T_U} = \mathrm{T_{f,\,out}}$	Inlet temperature of cold release fluid entering soil system
(13)	$\mathrm{APF} = \frac{\mathrm{Q_{tot}}}{W_{\mathrm{tot}}}$	Annual Performance Factor [8]
(14)	$\mathrm{Q_{tot}} = \sum \mathrm{Q_{H,\,tot}} + \sum \mathrm{Q_{C,\,tot}}$	Annual total heating + cooling load
(15)	$\mathrm{W_{tot}} = \sum \mathrm{W_{Comp}} + \sum \mathrm{W_{Pump}} + \sum \mathrm{W_{Fan}}$	Annual total compressor power consumption

4 Results and Discussion

4.1 Model Validation

To validate the accuracy of the used model, The experimental setup conditions were as follows: the initial soil temperature was 18.2 °C, the water supply temperature was 35.13 °C, and the operation lasted for 3 h. The outlet water temperature was recorded. Other simulation parameters were set consistently with the experiment [9]. As shown in Fig. 4, the numerical calculations are in good agreement with the experimental results. This comparison confirms the reliability and predictive capability of the present model.

4.2 Performance Analysis of the CO_2 System

To observe the performance of the SCES system, Fig. 5 shows the comparison of COP and COP improvement rate with time and ambient temperature in Beijing under two modes (four seasons). The COP of SCES is higher than that of the Base system in all seasons, with an average COP improvement rate of 14.04% in Beijing. It can be seen from the figure that the winter COP is directly proportional to the ambient temperature, while the summer COP is inversely proportional. The COP in spring and autumn has no correlation with the ambient temperature. The maximum COP in summer in Beijing can reach 3.01. In summary, the SCES can greatly improve the COP throughout the year.

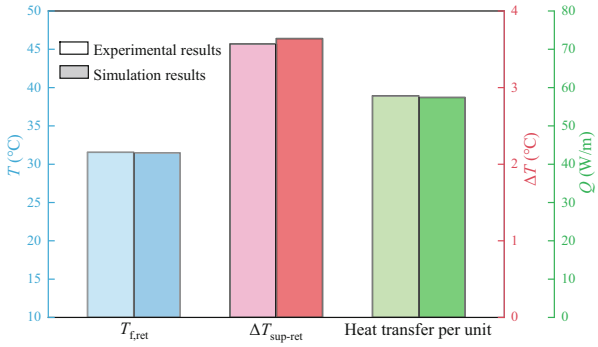


Fig. 4. Validation of soil subsystem.

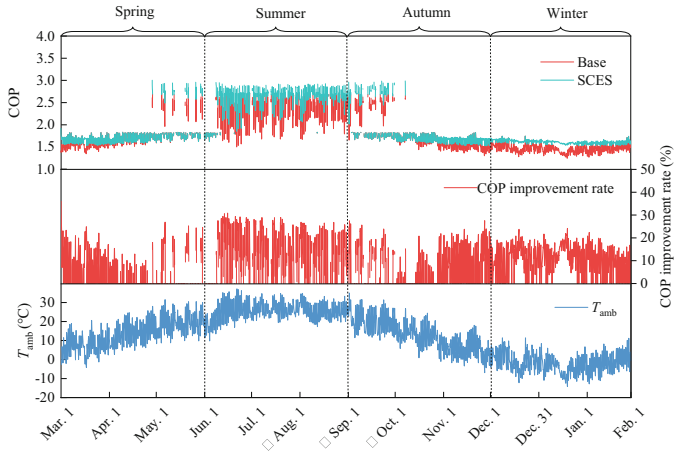


Fig. 5. Year-round COP comparison in Beijing.

Figure 6 shows the annual compressor discharge pressure of the base system and the SCES system in Beijing. The change trends of the two are consistent, with the annual compressor discharge pressure not exceeding 11.4 kPa, and the discharge pressure of the SCES system is much lower than that of the Base system. In addition, the discharge pressure is relatively stable in winter, spring, and autumn, with more obvious fluctuations in summer.

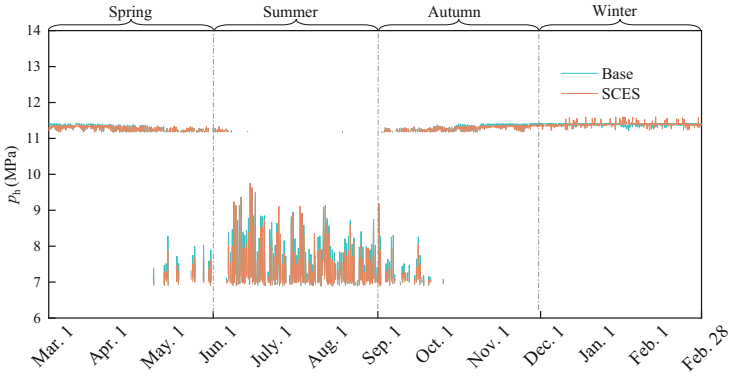


Fig. 6. Comparison of discharge pressure throughout the year in Beijing.

Figure 7 shows the variations in summer subcooling degree and ambient temperature over time during summer operation in Beijing. As shown in the figure, the subcooling degree of the system decreases with time because as the building's cooling demand increases, the soil energy storage system gradually releases cold energy, reducing the soil cold storage amount. In addition, the maximum subcooling degree in Beijing is 13.47 °C.

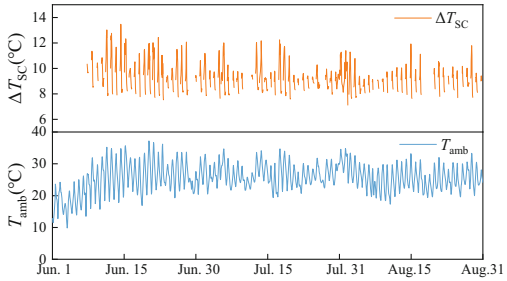


Fig. 7. Changes in summer subcooling over time in Beijing.

4.3 Fifteen-Year Continuous Operation of Soil Temperature Changes

Figure 8 shows radial soil temperatures in Beijing after 15 years of operation, revealing continuous cooling (cold accumulation) under both modes. The average soil temperature dropped from 13.05 °C (Year 1) to 10.21 °C (Year 15)—a 2.84 °C decline—due to subcooling < cold storage. This imbalance necessitates solutions to prevent ecological impacts.

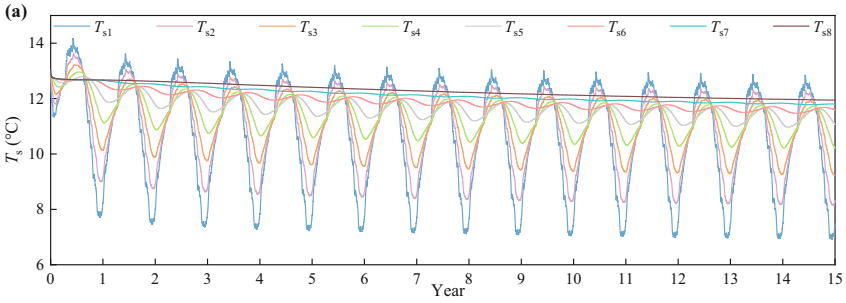


Fig. 8. 15 years of changes in soil temperature. Beijing.

4.4 Annual Performance Factor

Figure 9 shows the Annual Performance Factor (APF) of the SCES and base systems in eight cities after 10 years of operation. The SCES system outperformed the base system in all cities, with APF increases ranging from 3.34% (Kunming) to 12.91% (Harbin) and an average increase of 8.57%. This improvement stems from the SCES system's "winter cold storage for summer use" capability. APF was significantly higher in low-latitude regions, confirming the system's greater suitability for these areas.

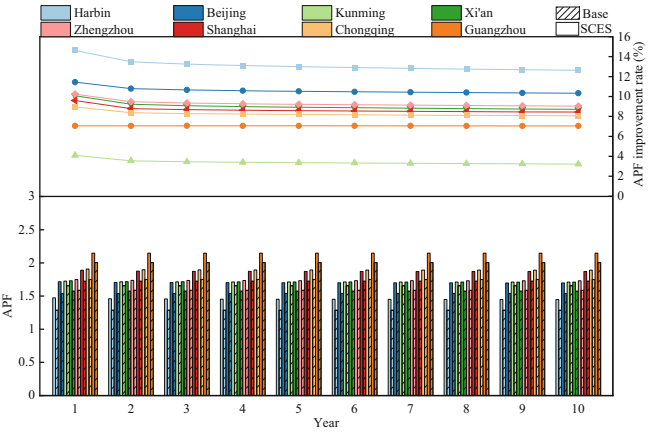


Fig. 9. The APF varies over time throughout the year.

5 Conclusions

This work presents and assesses an annual CO_2 heating/cooling system with soil cold storage and subcooling (SCES). Results validate cross-seasonal soil energy storage feasibility, aiding CO_2 thermal system theory and low-carbon buildings. Yet long-term use

may cause soil cold accumulation, disturbing thermal balance, which can be eased by solar energy as a secondary heat source. Future research should optimize the system (e.g., buried pipe layout, dynamic control) to improve soil heat-cold exchange balance and long-term stability.

References

1. Ministry of ecology and environment of the people's republic of China. (2021, June 21). China formally accepts the Kigali Amendment to the Montreal Protocol on Substances That Deplete the Ozone Layer. http://www.mee.gov.cn/xxgk/hjyw/202106/t20210621_841062.shtml
2. Skačanová, K.Z., Battesti, M.: Global market and policy trends for CO_2 in refrigeration. Int. J. Refrig. **107**, 98–104 (2019)
3. Tsamos, K.M., Ge, Y.T., Santosa, I.D., et al.: Energy analysis of alternative co_2 refrigeration system configurations for retail food applications in moderate and warm climates. Energy Convers. Manag. **150**, 822–829 (2017)
4. Llopis, R., Nebot-Andrés, L., Sánchez, D., et al.: Subcooling methods for CO_2 refrigeration cycles: a review. Int. J. Refrig. **93**, 85–107 (2018)
5. Pasquier, P., Marcotte, D.: Short-term simulation of ground heat exchanger with an improved TRCM. Renew. Energy. **46**, 92–99 (2012)
6. Bakar, H.A., Zarrouk, S.J.: Transient pressure analysis of geothermal wells fractured during well testing. Geothermics. **76**, 26–37 (2018)
7. Gullo, P., Elmegaard, B., Cortella, G.: Energy and environmental performance assessment of R744 booster supermarket refrigeration systems operating in warm climates. Int. J. Refrig. **64**, 61–79 (2016)
8. Low ambient temperature air source heat pump (water chilling) packages: GB/T 25127.1-2020. Standards Press of China, Beijing (2020)
9. Gao, J., Zhang, X., Liu, J., et al.: Thermal performance and ground temperature of vertical pile-foundation heat exchangers: a case study. Appl. Thermal Eng. **28**(17–18), 2295–2304 (2008)

Optimization of Low-Grade Waste Heat Recovery in District Heating Systems Using Zeotropic Mixture Heat Pump

Yumiao Wang, Sijing Zhang, Fang Zhou, Xiaosong Zhang, and Jian Liu(✉)

Southeast University, Nanjing 210096, China
liujian8@seu.edu.cn

Abstract. With increasing global energy constraints and stricter carbon emission targets, building operations account for 44.8% of total energy consumption. Enhancing the efficiency of heating and cooling load responses is essential for achieving carbon neutrality in the building sector.

This study focuses on the dual temperature demand of space heating and domestic hot water in office buildings. A stratified thermal storage heat pump system is proposed, employing a zeotropic mixture (CO_2/R1234yf) and industrial wastewater as a representative low-temperature heat source, as shown in Fig. 1. A typical office unit in Nanjing is selected for simulation, with annual thermal loads modeled using DeST-C software. A load-shifting operation strategy, nighttime heat storage, and daytime stratified supply are implemented. Furthermore, a Particle Swarm Optimization (PSO) algorithm is applied to optimize the control logic for heat pump operation dynamically.

The results show that the temperature glide of the zeotropic mixture significantly enhances the temperature matching degree during evaporation and condensation processes. Under high-temperature output conditions ($\geq$60 °C), the system achieves a seasonal average *COP* above 6.7 and reduces compressor energy consumption by 15%. This work offers both theoretical insights and practical guidance for the cascaded utilization of low-grade waste heat in urban buildings, supporting scalable and sustainable district energy applications.

Keywords: District heating · Low-grade waste heat recovery · Zeotropic mixture

1 Introduction

Municipal sewage exhibits favorable characteristics as a heat source, including stable temperatures and large, continuous flow throughout the year. It is suitable for winter space heating and annual DHW supply in urban buildings. The DHW system typically involves a significant temperature lift, with outlet temperatures ranging from 55 to 65 °C, depending on national standards. Experimental and simulation studies show that SSHPs can achieve coefficients of performance (*COP*) between 4.0 and 5.7 [1–4].

© The Author(s), under exclusive license to Springer Nature Singapore Pte Ltd. 2025
L. Ni et al. (Eds.): CCHVAC 2025, ESE, pp. 163–173, 2025.
https://doi.org/10.1007/978-981-95-3253-7_18

For conventional single-component working fluids, a significant mismatch between the refrigerant and heat source temperatures during the evaporation and condensation processes leads to inefficient heat transfer. In addition, low-boiling-point refrigerants often require high operating pressures, which increase system cost and introduce safety concerns [5]. To address this issue, high-boiling-point components can be added to form zeotropic mixtures. These mixtures exhibit temperature glide behavior, improving the thermal match during heat exchange and enhancing system efficiency [6].

CO_2 (R744), with a critical temperature of 31.1 °C, is lower than the condensation temperatures typically observed in subcritical vapor compression systems. This results in better temperature matching with the heating medium and reduced irreversible losses. As a result, CO_2 is widely investigated among natural refrigerants [7]. Saikawa and Koyama [8] compared the *COP* limits of R744, R134a, and R22 under a 16 °C heat source, 17 °C inlet water, and 65 °C outlet water, with CO_2 achieving the highest *COP* of 6.0. Liu et al. [5] evaluated 15 zeotropic mixtures consisting of low-boiling-point components (R744, R41, R170) and high-boiling-point components (RE170, R600a, R1234yf, R1234ze(E), R290), and proposed the Temperature Matching Degree (TMD) index to assess the thermal matching of the heat exchanger. Results showed that zeotropic mixtures outperformed pure refrigerants in energy efficiency, with the maximum energy efficiency ratio (*EER*) of R1234yf-based blends increased by 20.8% to 28.5%, and a maximum TMD of 76%.

The main contributions of this study are as follows:

System Design: A zeotropic-refrigerant sewage-source heat pump system coupled with a thermal storage tank is proposed to meet the dual heating demands (space heating and DHW) of office buildings. Its feasibility under real climate and load conditions is verified.

Operational Strategy: A “nighttime charging-daytime discharging” strategy is developed to reduce frequent compressor cycling and improve system stability.

Control Optimization: A dynamic control framework based on the PSO algorithm is established, reducing compressor power consumption by approximately 15% and increasing system *COP* to over 6.7.

Most importantly, this study verifies the advantages of zeotropic mixtures in heat pumps for waste heat recovery and further elucidates the energy efficiency enhancement mechanism of zeotropic mixtures. These findings provide a valuable reference for selecting zeotropic mixtures and optimizing their concentration fractions in various waste heat recovery applications.

2 Methods

2.1 System Configuration

An SSHP utilising a low-GWP zeotropic mixture fluid is illustrated in Fig. 1. The system primarily comprises a sewage-source heat pump, a sewage storage tank, a medium-temperature hot water storage tank (M-WTES), and a heating terminal system, which includes domestic hot water and indoor space heating subsystems. Industrial wastewater serves as the primary heat source.

The selected working fluid in this study is a zeotropic mixture of CO_2/R1234yf with a mass fraction ratio of 0.17/0.83. The thermophysical properties of the *mix* are presented in Table 1. Considering the time-staggered characteristics of space heating and domestic hot water demands, the system adopts a "nighttime heat storage and daytime heat supply" strategy. During peak demand periods, the M-WTES acts as the primary heat source.

Table 1. Basic data for selected refrigerants.

Refrigerant	Atmospheric lifetime, years	NBP at atm, °C	Tcrit, °C	Pcrit, kPa	GWP	ODP
R744	NA	–78.0	31.0	7377.3	1	0
R1234yf	0.029	–29.4	94.7	3382	<1	0

The operation of the heat pump unit is dynamically regulated based on real-time monitoring of the upper and lower temperature layers of the M-WTES. During the heating season, the heat pump starts operating at midnight daily and stops when the upper-layer temperature of the M-WTES reaches 60 °C. During the daytime, the M-WTES supplies heat to the end users. When the upper-layer temperature drops to or below 40 °C, the heat pump resumes operation to recharge the M-WTES.

2.2 Building Model

The target building is a single office room located in an office building in Nanjing, China. The model was generated using the DeST-C simulation software. This region belongs to the hot-summer and cold-winter climate zone. The heating room faces 45° northwest, and its window orientation is also 45° northwest. The room area is 40 m^2 with a floor height of 3 m. According to the Code for Thermal Design of Civil Buildings and the General Code for Energy Efficiency and Renewable Energy Application in Buildings, the parameters of the building envelope and construction materials are summarized in Tables 2 and 3.

Table 2. Envelope construction of buildings.

Component Name	Building Materials (from inside to outside, top to bottom)	Thermal Conductivity, W/m^2•K
External Wall	20 mm mixed mortar + 240 mm solid clay brick + 20 mm mixed mortar	0.384
Internal Wall	15 mm mixed mortar + 240 mm solid clay brick + 15 mm mixed mortar	0.375
Floor	20 mm cement mortar + 40 crushed stone or pebble concrete	20.83
Roof	20 mm mixed mortar + 100 mm reinforced concrete slab + 20 mm mixed mortar	3.827
External Window	Aluminum alloy frame + Low-e coated insulating glass (high-transmittance) 6 (Low-e) + 9A + 6	2.4
External Door	Single-layer solid wooden external door	0.35
Internal Door	Single-layer wooden internal door	0.35

Table 3. Parameters of construction materials.

Material	Thermal Conductivity, W/m^2•K	Density, kg/m^3	Specific Heat Capacity, kJ/kg•K	Correction Coefficient	Corrected Thermal Conductivity, W/m^2•K
Reinforced Concrete	1.74	2500	0.92	1	1.74
Crushed Stone or Pebble Concrete	1.51	2300	0.92	1	1.51
Cement Mortar	0.93	1800	1.05	1	0.93
Mixed Mortar (lime-cement mortar)	0.87	1700	1.05	1	0.87
Solid Clay Brick	0.81	1800	1.05	1	0.81
Extruded Polystyrene Board (XPS)	0.03	35	1.38	1.1	0.033
FTC Insulation Mortar	0.07	300	1.05	1.25	0.0875

The heating period spans from November 15 to March 15 of the following year. Based on the nearly zero energy building technical standard, the daily heating operation period is defined as 8:00–18:00. The cooling period is set from June 15 to October 15. Equipment start/stop times and air conditioning settings are shown in Table 4.

Table 4. Equipment runtime and air conditioning settings.

System	Period	Time	Temperature, °C	Humidity,%
Lighting	All year	08:00–20:00	-	-
Equipment	All year	08:00–20:00	-	-

(*continued*)

Table 4. (*continued*)

System	Period	Time	Temperature, °C	Humidity,%
Heating (HVAC)	Nov. 15-Mar. 15	08:00–18:00	Upper limit: 23 Lower limit: 21	Upper limit: 40 Lower limit: 35
Cooling (HVAC)	June 15-Oct. 15	08:00–18:00	Upper limit: 27 Lower limit: 23	Upper limit: 60 Lower limit: 50

2.3 Meteorological Conditions

The meteorological data used in this study were obtained from the standard weather dataset of Nanjing provided by the DeST-C software. The annual outdoor dry-bulb temperature and humidity profiles are shown in Fig. 2 and Fig. 3, respectively. During the heating season, the indoor design temperature is set to 18 °C for heated spaces and 12 °C for non-heated spaces. In the summer, the design temperature for air-conditioned rooms is set to 26 °C with 60% relative humidity.

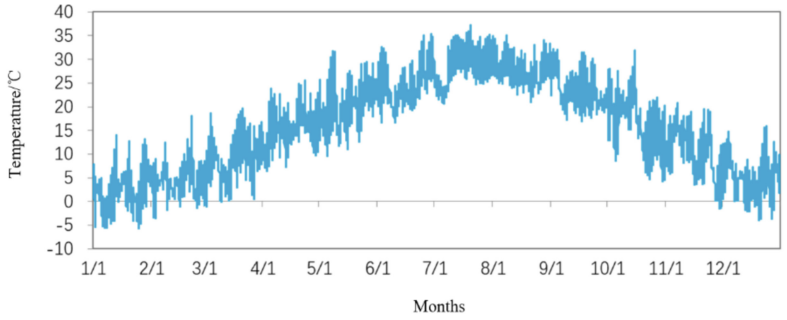


Fig. 2. Diagram of outdoor dry bulb hour-by-hour temperatures throughout the year.

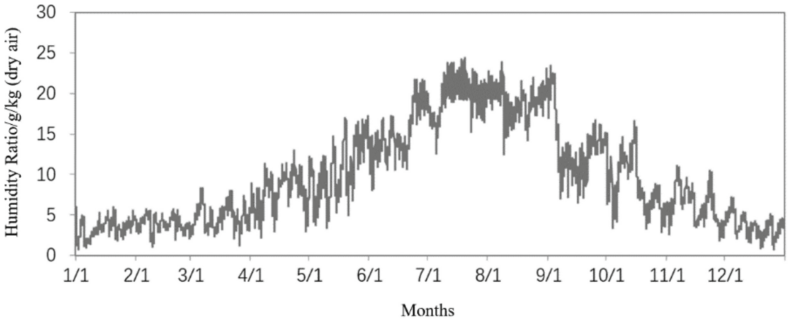


Fig. 3. Diagram of outdoor humidity throughout the year.

2.4 Optimization Algorithm

The PSO algorithm is a population-based optimization technique inspired by the collective behavior observed in flocks of birds and schools of fish. The algorithm was first proposed by Russell Eberhart and James Kennedy in 1995. The core idea of PSO is to find the optimal solution through cooperation and information sharing among particles in the population. Each "particle" represents a potential solution, and it adjusts its position in the solution space based on its individual best position (personal best) and the best position found by the entire swarm (global best).

2.5 Constraint Conditions

Sewage-source Heat Pump: To prevent frequent start-stop cycles of the heat pump, the following constraint is applied:

$$-1 \leq (s_{HP}(k+1) - s_{HP}(k)) - (s_{HP}(k) - s_{HP}(k-1)) \leq 1 \tag{1}$$

Where $s_{HP}(k)$ represents the operational state of the heat pump at time step k, with on being one and off being 0.

M-WTES: When the M-WTES is large and the water remains static or flows slowly, significant temperature stratification can occur inside the tank. The lower layer of the tank tends to be cooler, which helps improve the system's heat collection efficiency and energy utilization. In this study, a multi-node model, consisting of three nodes, is adopted for the storage tank. For simplification, it is assumed that the tank is always at the whole water level, and the temperature in each layer is evenly distributed and treated as a single node. Fluid exchange between nodes is assumed to be homogeneous.

The energy balance equation for node i is:

$$\begin{aligned} \dot{m}_i \tfrac{dT_{s,i}}{dt} = \left(\tfrac{UA}{C_p}\right)_i \left(T_a - T_{s,i}\right) + F_i^c \dot{m}_c \left(T_{c,o} - T_{s,i}\right) + F_i^L \dot{m}_L \left(T_{L,r} - T_{s,i}\right) \\ + \begin{cases} \dot{m}_{m,i}\left(T_{s,i-1} - T_{s,i}\right), \dot{m}_{m,i} > 0 \\ \dot{m}_{m,i+1}\left(T_{s,i} - T_{s,i+1}\right), \dot{m}_{m,i} < 0 \end{cases} \end{aligned} \tag{2}$$

Where:

$\dot{m}_i$: mass flow rate at node i, kg/s;
F_i^c, F_i^L: control functions for heat source and load;
$\dot{m}_c$, $\dot{m}_L$: circulation mass flow rates on the heat source and load sides, kg/s;
T_a: ambient temperature, °C;
$T_{s,i}$: temperature at node i, °C;
UA: product of heat loss coefficient and surface area;
$T_{L,r}$: return water temperature on the load side, °C;
$T_{c,o}$: outlet temperature on the heat source side, °C;
$\dot{m}_{m,i}$: net flow entering node i from node i−1, kg/s.

During water injection and withdrawal, heat losses occur. The energy efficiencies during these processes are defined as:

$$\eta_{\text{ht,in}} = \eta_{\text{ht,out}} = 0.9 \tag{3}$$

Due to temperature differences, continuous heat exchange occurs between the s M-WTES and the surrounding environment. The storage efficiency is defined as:

$$\eta_{\mathrm{ht}} = 0.98 \tag{4}$$

3 Results and Discussion

3.1 Building Energy Demand

Figure 5 illustrates the hourly heating load profile of the target office room located in Nanjing. The peak heating load reaches 3.12 kW, corresponding to a specific heat load of 87.19 W/m^2. The cumulative annual heating demand is 1386.11 kWh (Fig. 6). The heating demand is characterized by clear diurnal fluctuations, with higher loads during early morning and late afternoon, aligning with typical office occupancy patterns and outdoor temperature variations. These findings highlight the need for a dynamic heating system capable of effectively responding to intermittent peak demands while minimizing energy waste during off-peak hours.

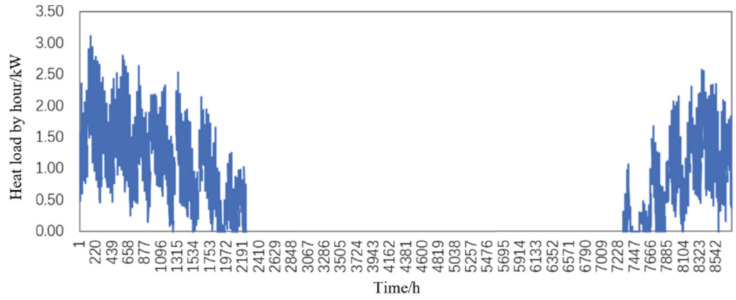


Fig. 5. Diagram of load dynamics of a building hour by hour throughout the year.

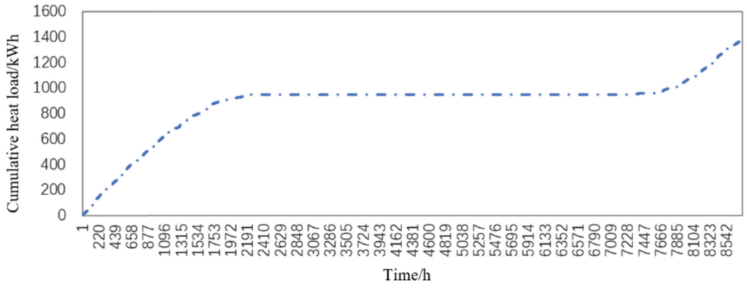


Fig. 6. Diagram of the cumulative annual heat load of the building.

3.2 M-WTES Temperature Performance

Figure 7 presents the temperature profile of the M-WTES throughout the heating season. It can be observed that the upper-layer temperature of the tank fluctuates around 60 °C, while the lower-layer temperature remains below 40 °C, indicating good thermal stratification characteristics. This distinct stratification confirms the effectiveness of the multi-node tank model and reflects the low flow velocity design, which minimizes thermal mixing and supports efficient heat utilization. Nighttime charging and daytime discharging were adopted as the system operation strategy, leveraging off-peak electricity periods and load shifting. This strategy not only ensures a stable daytime heating supply but also avoids frequent heat pump startup/shutdown cycles, thereby extending equipment life and improving system stability. Moreover, by maintaining higher tank outlet temperatures during peak periods, the heat pump can operate under more favorable conditions, improving the seasonal average *COP*.

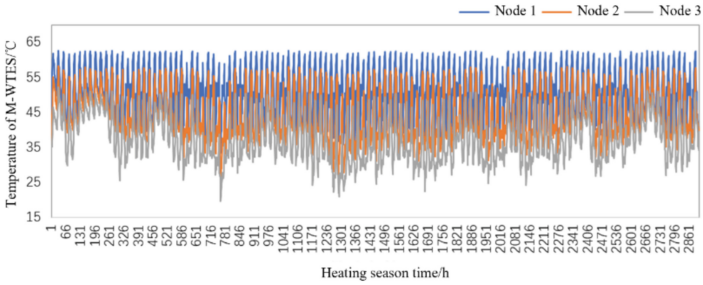


Fig. 7. Diagram of temperature changes in M-WTES during the heating season.

3.3 System Optimization and Energy Efficiency Improvement

To evaluate the effectiveness of the optimization control strategy, Fig. 8 compares the compressor power consumption before and after optimization. Before optimization, the compressor power fluctuates cyclically between 0.34–0.37 kW, reflecting unstable system operation and frequent load-following behavior. Post-optimization, the compressor operates within a lower and narrower range of 0.25–0.29 kW, indicating smoother operation and more efficient energy conversion. As a result, the total electricity cost during the heating season is reduced from the baseline scenario to 136.26 CNY, representing a notable economic benefit.

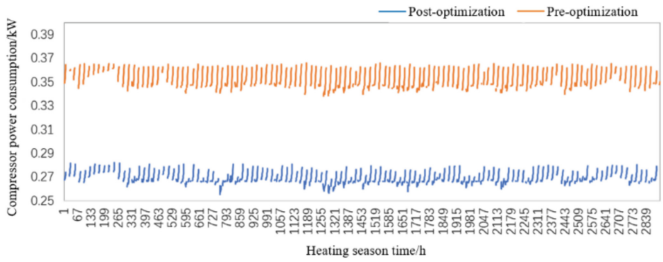


Fig. 8. Diagram of power consumption temperature variation of the heat pump compressor during the heating season.

This optimization also aligns the compressor's operating mechanism with the efficient operating zone of the CO_2/R1234yf mixture. Since this mixture has a high volumetric cooling capacity and good heat transfer characteristics at medium temperatures, the optimized system can take better advantage of these characteristics. More importantly, the temperature glide characteristics of CO_2/R1234yf with a mass fraction ratio of 0.17/0. 83 allows for a more minor heat transfer temperature difference between the refrigerant and the heat transfer fluid, which can be more accurately matched to evaporation/condensation conditions.

Figure 9 presents the system's *COP* variation trend. The optimized system exhibits consistently higher *COP* values across most periods, with average improvement of 0.4–0.5, and peak improvements reaching 0.7. The pre-optimization *COP* was mainly in the 6.0–6.5 range with significant fluctuations, indicating sensitivity to instantaneous loads. After optimization, the *COP* becomes more stable and centered between 6.5–7.0, with the highest value reaching 7.07. This improvement results from better coordination between heat pump operation and tank charging/discharging schedules, enabled by the PSO algorithm.

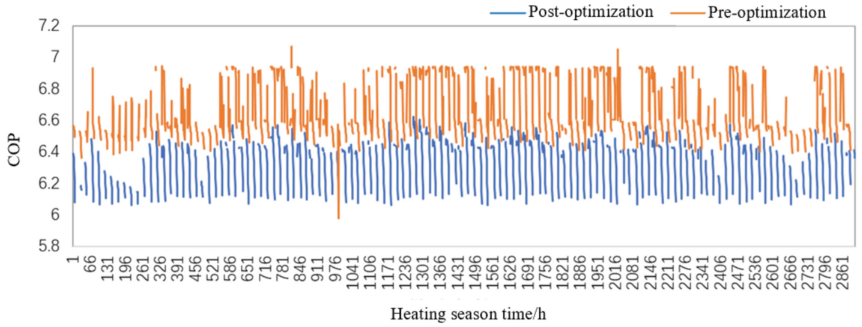


Fig. 9. Diagram of *COP* changes during the heating season.

4 Conclusion

This study proposes a low-GWP, large-temperature-glide zeotropic refrigerant-based heat pump heating system that utilizes urban sewage as the primary heat source to supply heating and domestic hot water at 45–65 °C. A typical office building in Nanjing was selected as the case study, and full-season energy consumption simulations along with an optimized control strategy were conducted for the heating season. The main conclusions are summarized as follows:

The integration of an M-WTES and zeotropic refrigerant enables a more energy-efficient, cost-effective, and operationally stable heating system. The system not only shifts load from peak to off-peak periods through intelligent storage utilization but also exploits the glide properties of CO_2/R1234yf to improve heat exchange performance.

The control strategy developed using a PSO algorithm significantly enhances the system's economic performance and operational stability. After optimization, compressor power consumption is reduced by approximately 15% with significantly lower fluctuation amplitudes, indicating smoother operation. Simultaneously, the system *COP* increases to above 6.7 on average, an improvement of 0.4–0.5 compared to pre-optimization conditions. In some periods, *COP* exceeds 7.0, reflecting a notable enhancement in heat pump efficiency.

In practical applications, such a system can significantly reduce operational costs and carbon emissions, especially in urban buildings with intermittent heating demand. The favorable environmental profile of R1234yf and the natural origin of CO_2 also make this mixture a low-GWP and policy-compliant choice, promoting both decarbonization and regulatory alignment.

Future research can further explore the impact of different refrigerant mixture ratios on system performance, validate the model accuracy through experimental data, and incorporate more environmental variables (e.g., climatic variations and heat source fluctuations) to improve the model's adaptability and generalizability. These efforts will provide more comprehensive support for the design of high-efficiency intelligent building heating systems.

Acknowledgement. The authors gratefully acknowledge the financial support from the Fundamental Research Funds for the Jiangsu Province fundamental research project (Grant No. BK20230846) and Jiangsu Province innovation capacity project (Grant No.BM2023013).

References

1. Wang, Q., Zhang, X., Geng, X., Chen, X., Xing, M.: Experiments on the characteristics of a sewage water source heat pump system for heat recovery from bath waste. Appl. Therm. Eng. **204**, 117956 (2022)
2. He, Z., Zeng, L., Meng, S., Hao, J., He, T., Mao, N.: An experimental study on the effects of oily content on flow pattern transition over horizontal tubes in a sewage source heat pump system. Int. J. Therm. Sci. **181**, 107779 (2022)
3. Gao, C., Hao, Y., Liu, Q.: Design and analysis of a small sewage source heat pump triple supply system. Energy Eng. **118**, 667–678 (2021)

4. Qin, N., Hao, P.Z.: The operation characteristics of the sewage source heat pump system and the analysis of its thermal economic benefits. Appl. Therm. Eng. **124**, 1083–1089 (2017)
5. Liu, J., Zhou, L., Lin, Z., Zhang, X.: Performance evaluation of low GWP large glide temperature zeotropic mixtures applied in air source heat pump for DHW production. Energy Convers. Manag. **274**, 116457 (2022)
6. Garimella, S., Milkie, J., Macdonald, M.: Condensation of zeotropic mixtures of low-pressure hydrocarbons and synthetic refrigerants. Int. J. Heat Mass Transf. **162**, 120301 (2020)
7. Hao, Z., He, G., Wu, A., Lin, Y., Cai, D.: Dynamic characteristics and performance enhancement of a novel hybrid system integrating transcritical CO_2 heat pump and absorption thermal energy storage. Energy. **330**, 136874 (2025)
8. Saikawa, M., Koyama, S.: Thermodynamic analysis of vapor compression heat pump cycle for tap water heating and development of CO_2 heat pump water heater for residential use. Appl. Therm. Eng. **106**, 1236–1243 (2016)

Performance Evaluation of a Hybrid Solar-Heat Pump Dual-Source Heating System for Interactive Cascade Ventilation

Gaoqi Lai, Tong Sang, Han Li(✉), Xiangfei Kong, and Man Fan

School of Energy and Environmental Engineering, Hebei University of Technology, Tianjin 300401, China
lihan18113@hebut.edu.cn

Abstract. Based on the optimization of a hybrid heat source heating system integrated with interactive cascade ventilation (ICV) systems terminals under the global energy transition and the "dual carbon" strategy, this study investigates five operation strategies: PHEH, PHAP, SHAP, ISHS, and DSHS, incorporating Multistage Solar Energy Resource Utilization. The results demonstrate that PHAP emerges as the optimal strategy in cold climate zones, while maintaining the lowest annual electricity consumption 589.7 kWh. The direct solar supply mode attains a COP exceeding 8. Meanwhile, Under the climatic conditions of the Tianjin region, the PHAP mode demonstrates the optimal energy efficiency performance, reducing power consumption by 21.3–35.3% compared to other modes. PHEH mode shows weaker performance across various indicators, while the ISHS and DSHS modes utilize tank heat more efficiently, exhibiting minimal heat loss throughout the entire heating season. When the system operates in solar direct supply mode, its energy-saving performance is excellent. These findings provide a foundation for optimizing energy allocation in interactive cascade ventilation systems.

Keywords: Interactive cascade ventilation · System strategy · Solar coupled heat pump

1 Introduction

In the future, global energy consumption is set to grow significantly, projected to increase by 50% from current levels by 2050 [1], and driven by China's commitment to peak CO_2 emissions by 2030 and achieve carbon neutrality by 2060 [2, 3], decarbonizing building energy systems has become critical. Buildings account for over 30% of societal energy use [4], with heating/cooling dominating this share. Transitioning to renewable-based technologies like heat pumps and solar energy is essential to alleviate energy constraints [5]. Air-source heat pumps (ASHPs) offer significant operational and environmental advantages [6, 7], while water-source variants excel in stability and efficiency [8]. Solar energy, though abundant in China, requires hybridization due to intermittency [9].

Recent research focuses on integrating solar with IX-SAASHPs to enhance performance. Studies demonstrate improved efficiency and cost-effectiveness in dual-source

© The Author(s), under exclusive license to Springer Nature Singapore Pte Ltd. 2025
L. Ni et al. (Eds.): CCHVAC 2025, ESE, pp. 174–181, 2025.
https://doi.org/10.1007/978-981-95-3253-7_19

systems [10], with applications in space heating (SH) and hot water production. Parallel advances in load-side management, such as Interactive Cascade Ventilation (ICV), optimize thermal distribution by stratifying airflow to reduce energy waste [11, 12]. However, a significant gap persists: existing work rarely couples multi-energy source systems with advanced end-use technologies like ICV. Most studies prioritize either source-side hybridization [13, 14] or terminal load optimization independently, neglecting their synergistic potential.

This study bridges this gap by proposing and evaluating five novel heating strategies integrating SAASHP configurations with ICV. The goal is to harmonize source-side multi-energy complementarity (solar + heat pump) with demand-side cascade energy utilization to maximize overall efficiency, leveraging the strengths of both approaches while mitigating their individual limitations.

2 Methodology

2.1 System Description and the Operating Strategy

Figure 1 shows a schematic of these five systems. First, the green line is the solar input heat energy part, the blue line is the water source heat pump input heat energy part, and the yellow line is the air source heat pump input heat energy part. Next is the heat exchange part: the red line is the direct heat exchange between the solar water tank and the air, and the purple part is the heat exchange between the dual source heat pump and the air. By controlling the switching valves, five operation strategies are achieved:

Auxiliary Heating Parallel Heat Exchange Mode (PHEH): In this mode, valves 1, 4, 6, 7, 8, and 11 are opened, while the rest are closed. The mode uses the outlet water from the thermal storage tank to heat the upper-side supply air alone, maximizing the use of solar energy to meet the upper-side thermal demand. An electric heater ensures the stability of the tank temperature in extreme weather, and an air-source heat pump heats the lower-side supply air. This mode focuses on the system's energy-saving characteristics when solar resources are insufficient.

Air-Source Heat Pump Parallel Heat Exchange Mode (PHAP): This mode has two operation strategies. When solar energy is sufficient, the direct solar supply mode is adopted (the tank outlet water directly heats the supply air). When the system's heating capacity can be fully provided by solar energy, valves 1, 7, 8, and 9 are opened, and the rest are closed. At this time, only fans and water pumps consume energy, achieving the optimal energy efficiency. When solar energy is insufficient, the air-source heat pump is activated for secondary heating of the supply air, with valves 4, 6, 10, and 11 opened. Compared with PHEH, PHAP removes the tank electric heating, uses the direct solar supply mode to conduct primary heating for both air ducts simultaneously to maximize solar energy utilization, and adds an air-source heat pump for secondary heating to ensure the stability of the supply air temperature.

Air-Source Heat Pump Series Heat Exchange Mode (SHAP): In this mode, valves 1, 4, 5, 7, 8, and 9 are opened, and the rest are closed. The mode ensures the tank temperature through dual heating by solar collectors and an air-source heat pump. The air-source heat pump is connected in series to the lower-side loop of the collectors, meaning that when solar energy is sufficient, the solar collectors prioritize heat collection for the tank. If the

system demand is met, the air-source heat pump remains off, while an electric heater ensures the supply air temperature in extreme weather. Compared with PHAP, SHAP focuses on the primary heating process.

Indirect Solar Thermal Storage Mode (ISHS). To explore efficient utilization of thermal storage tank heat, a water-source heat pump is added, using the tank as a stable low-temperature heat source to enhance heating efficiency and enabling more thorough solar energy utilization. Compared with the previous three modes (PHEH, PHAP, SHAP), ISHS adds a water-source heat pump, removes the electric heater and direct solar supply mode, and uses the water-source heat pump for heating (valves 1, 2, 3, 6, 10, 11 opened). When the tank temperature is insufficient, the air-source heat pump is activated (valve 4 opened).

Direct Solar Thermal Storage Mode (DSHS): It is divided into three operation strategies. When solar energy is sufficient, the direct solar supply mode is adopted (valves 1, 7, 8, and 9 are opened, and the rest are closed). At this time, only fans and water pumps consume energy, achieving the optimal energy efficiency. When solar energy is insufficient, the water-source heat pump is activated (valves 2, 3, 6, 10, and 11 are opened), simultaneously operating the direct solar supply heating mode and the water-source heat pump heating mode. When the tank temperature is too low, the air-source heat pump is activated for heating (valve 4 is opened). Compared with ISHS, DSHS reintroduces the direct solar supply mode.

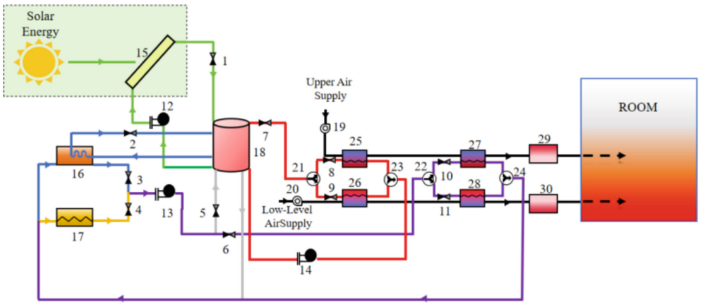


Fig. 1. Schematic diagram of the composite energy system (1–11: Valves; 12–14: Circulating water pump; 15: Collector; 16: Water source heat pump; 17: Air source heat pump; 18: Hot water storage tank; 19–20: Fan; 21–22: Diverter valve; 23–24: Manifold valve; 25–28: Heat exchanger 29–30: Electric heater).

2.2 Simulation method

The configuration of composite system, including five operation strategies, is established in TRNSTS. The running time of this simulation is from November 15 of the heating season to March 15 of the following year, and the running time step is 1h. The system runs from the 7632nd hour 0 minutes to the 10536th hour 0 minutes. The initial water temperature of the solar water tank is 20 °C.In the simulation, the room area is set at 4.8 m × 4.9 m. Considering the occupied area of the roof equipment, the solar collector area is set to 10 square meters.

2.3 Performance Indicator

The performance of the heating system is evaluated by a number of indicators, including the heating capacity of the system, the indoor air temperature, the performance index of the heat pump, the energy consumption of the system, and the performance index COP of the system.where *Qsys* are the thermal energies supplied by the system for SH, respectively, and *Wsys* is the total electricity consumed by the system by *Eq.* (1):

$$W_{sys} = W_{pumps} + W_{fans} + W_{electricty} + W_{HP} \tag{1}$$

where W_{HP} is the electricity consumed by the HP calculated by *Eq.* (2):

$$W_{HP} = j_{ASHP} \times W_{ASHP} + j_{SWHP} \times W_{SWHP} \tag{2}$$

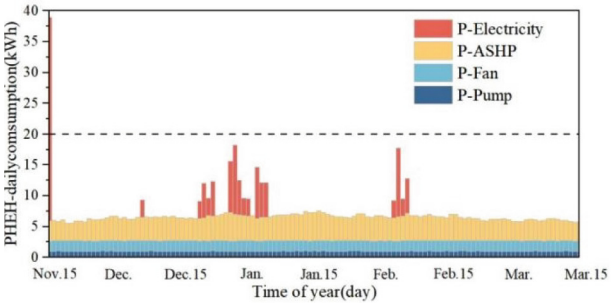
Where W_{ASHP} and W_{SWHP} are the power consumed by ASHP and SWHP respectively, the value of j_{ASHP} and j_{SWHP} is 1 or 0. For systems 1, 2, $j_{SWHP} = 0$. For system 4 and 5, j_{ASHP} and j_{SWHP} may be 1 or 0, depending on the condition, depending on their switching state. The COP of the system is defined by *Eq.* (3):

$$COP = \frac{Q_{sys}}{W_{sys}} \tag{3}$$

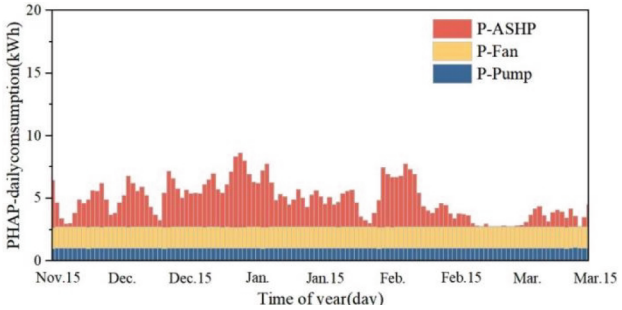
3 Result and Discussion

3.1 Energy Consumption

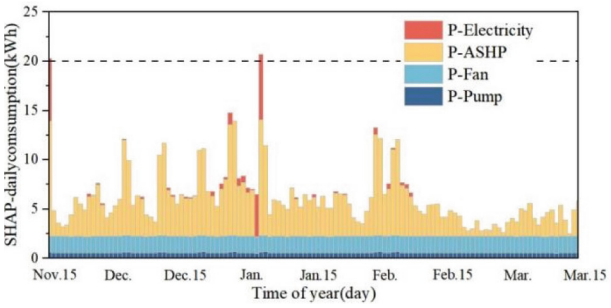
Figure 2 displays daily electricity consumption variations across five heating systems during the winter season. Stacked column components include dark blue representing pump power consumption, light blue representing fan power consumption, light yellow representing air source heat pump consumption, and red representing either electric heating or water source heat pump consumption. Systems PHAP, ISHS, and DSHS exhibit stable consumption patterns by eliminating electric heating. Annual energy consumption values confirm PHAP as the most efficient at 589.61 kilowatt-hours, while other systems consumed significantly more: PHEH used 54.7% more, ISHS used 42.7% more, SHAP used 27.6% more, and DSHS used 27.0% more. ISHS demonstrates minimal consumption fluctuations since all solar thermal energy stored in the tank serves exclusively as the low-grade heat source for the water source heat pump, without direct solar heating modes. Both PHAP and DSHS employ solar-direct heating after thermal storage, reducing operational energy to fundamental pump and fan loads during this mode. Despite this shared efficiency mechanism, PHAP consumes 21.3% less electricity than DSHS. Comparatively, DSHS uses 11.0 % less power than ISHS. While ISHS experiences fewer heat pump start-stop events. The DSHS mode has incorporated a solar direct supply mode, improving the system COP. The PHAP system integrates the solar direct supply mode with supplementary heat pump heating, making it the most energy-efficient configuration, whereas PHEH's dependence on electric heating and unharnessed solar potential results in the poorest efficiency.



(a) The daily power consumption distribution map of PHEH.

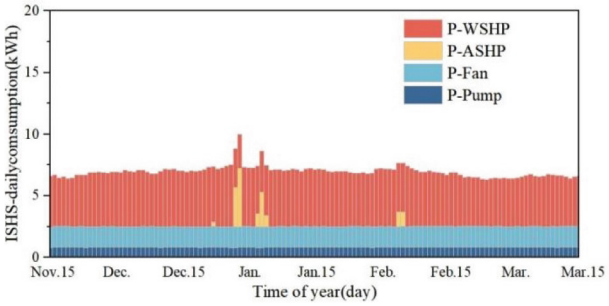


(b) The daily power consumption distribution map of PHAP.

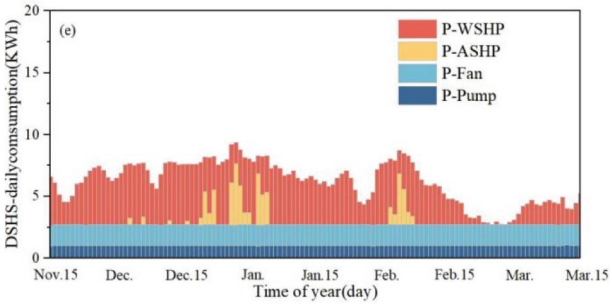


(c) The daily power consumption distribution map of SHAP.

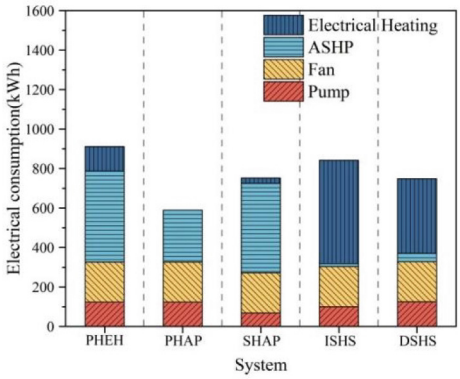
Fig. 2. Daily strategy electricity consumption and total electricity consumption.



(d) The daily power consumption distribution map of ISHS.



(e) The daily power consumption distribution map of DSHS.



(f)Total electricity consumption of each strategy during the heating season.

Fig. 2. (*continued*)

Figure 3 presents the average daily COP of the five systems during the heating season, demonstrating their energy efficiency for winter heating in Tianjin. The PHEH system maintains a moderate COP mainly in the range of 2–4, with significant January fluctuations due to higher electric heating demand under lower temperatures. In contrast, the PHAP system achieves the highest average COP mainly in the range of 4–9 by employing a direct solar heating mode that maximizes efficiency. The SHAP system (combining ASHP with indirect solar tank heating) shows a wider COP mainly in the range of 2–9 due to supplemental electric heating during extreme weather. The ISHS system exhibits the most stable COP mainly in the range of 3–4 by exclusively using solar-stored heat for the water-source heat pump. Compared to ISHS, the DSHS system integrates solar direct supply, achieving a higher COP mainly in the range of 3–9, significantly enhancing the system COP. These results highlight that systems prioritizing direct solar utilization (PHAP, DSHS) deliver superior COP performance, validating their suitability for energy-efficient heating in cold climates.

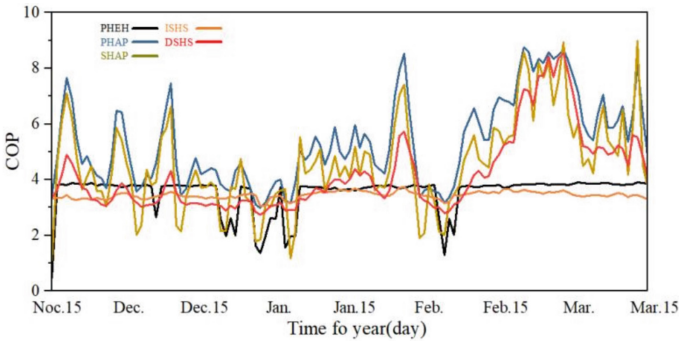


Fig. 3. Variations of daily averaged COP in five systems over a heating season.

4 Conclusion

In this paper, we propose an interactive cascade ventilation (ICV) system that combines five systems. The application of the new system and strategy will help to achieve the goals of carbon neutrality and carbon emission peak. The results show that:The comparative analysis identifies PHAP as the most efficient system, consuming just 589.7 kWh annually with a COP mainly in the range of 4–9. It outperforms PHEH at 54.7% higher consumption with a COP mainly in the range of 2–4. SHAP at 27.6% higher consumption with a COP mainly in the range of 2–9. ISHS at 42.7% higher consumption with a COP mainly in the range of 3–4 and DSHS at 27.0% higher consumption with a COP mainly in the range of 3–9. Systems utilizing direct solar heating (PHAP, DSHS) showed superior performance, with PHAP's optimized design achieving 21.3% lower consumption than DSHS. The results confirm that maximizing solar-direct integration significantly improves energy efficiency and reduces operational costs in cold climates, while electric heating dependence leads to poorer performance and higher energy penalties.

References

1. Izadi, M., Taghavi, S.F., Neshat Safavi, S.H., Afsharpanah, F., Yaïci, W.: Thermal management of shelter building walls by PCM macro-encapsulation in commercial hollow bricks. Case Stud. Therm. Eng. **47** (2023)
2. Ma, S., Guo, S., Zheng, D., Chang, S., Zhang, X.: Roadmap towards clean and low carbon heating to 2035. A provincial analysis in northern China. Energy. **225** (2021)
3. Li, Z., Wei, W., Wang, W., Sun, Y., Wang, S., Lin, Y., et al.: A method for sizing air source heat pump considering the joint effect of outdoor air temperature and relative humidity. J. Build. Eng. **65** (2023)
4. Ji, Q., Han, Z., Li, X., Yang, L.: Energy and economic evaluation of the air source hybrid heating system driven by off-peak electric thermal storage in cold regions. Renew. Energy. **182**, 69–85 (2022)
5. Liu, S., Ma, G., Lv, Y., Xu, S.: Review on heat pump energy recovery technologies and their integrated systems for building ventilation. Build. Environ. **248** (2024)
6. Liu, S., Bai, X., Zhang, L., Lin, Y., Deng, S., Wang, W., et al.: Developing condensing-frosting performance maps for a variable speed air source heat pump (ASHP) for frosting suppression. Appl. Therm. Eng. **211** (2022)
7. Amiri Rad, E., Maddah, S., Mohammadi, S.: Designing and optimizing a novel cogeneration system for an office building based on thermo-economic and environmental analyses. Renew. Energy. **151**, 342–354 (2020)
8. Han, C., Kim, J., Cho, W., Shin, H.H., Lee, H., Kim, Y.: Annual performance analysis of solar-assisted raw-water source heat pumps at low water temperatures. Energy. **291** (2024)
9. Wang, Y., Quan, Z., Zhao, Y., Wang, L., Liu, Z.: Performance and optimization of a novel solar-air source heat pump building energy supply system with energy storage. Appl. Energy. **324** (2022)
10. Sterling, S.J., Collins, M.R.: Feasibility analysis of an indirect heat pump assisted solar domestic hot water system. Appl. Energy. **93**, 11–17 (2012)
11. Li, H., Sang, T., Kong, X.F., Zheng, W., Wang, Z., Li, J., et al.: Performance analysis of interactive cascade ventilation combined with solar energy for the epidemic prevention and control. Appl. Energy. **349** (2023)
12. Kong, X.F., Wang, Z., Fan, M., Li, H.: Analysis on the performance of interactive cascade ventilation for space heating based on non-uniform indoor environment demand. Build. Environ. **219** (2022)
13. Yang, L.W., Xu, R.J., Hua, N., Xia, Y., Zhou, W.B., Yang, T., et al.: Review of the advances in solar-assisted air source heat pumps for the domestic sector. Energy Convers. Manag. **247** (2021)
14. Fraga, C., Mermoud, F., Hollmuller, P., Pampaloni, E., Lachal, B.: Large solar driven heat pump system for a multifamily building: long term in-situ monitoring. Sol. Energy. **114**, 427–439 (2015)

Construction of CO_2 Heat Pump Cycles for Space Heating in Cold Regions Using the Intelligent GraPHsep Method

Mengdi Cui and Baolong Wang(✉)

Beijing Key Laboratory of Indoor Air Quality Evaluation and Control, Department of Building Science, Tsinghua University, Beijing 100084, China
wangbl@tsinghua.edu.cn

Abstract. The global shift toward low-carbon energy underscores an urgent need for efficient heating in cold regions. CO_2 heat pumps, leveraging eco-friendly refrigerants and excellent low-ambient performance, show promise but suffer from significant throttling losses due to CO_2's low critical temperature, limiting cycle efficiency. Existing optimizations (e.g., recuperators, two-stage cycles) rely on expert-guided modifications and fail to holistically integrate refrigerant selection, cycle configuration, and heat exchange networks. To overcome this, we propose the intelligent GraPHsep method, which: (1) generates compressor/throttling valve topologies via graph theory; (2) constructs refrigerant flow structures using splits, junctions, and phase separators; (3) synthesizes heat exchangers by coupling refrigerant branches with heat sources/sinks and optimizing layouts via pinch analysis combined with a genetic algorithm. Applied to space heating at −30 °C ambient/45 °C supply water, GraPHsep designed a novel CO_2 cycle achieving a coefficient of performance of 2.17, which is 77.9% and 16.7% higher than classical single/two-stage transcritical cycles, respectively. This demonstrates its capability to develop high-efficiency heat pump systems for extreme cold climates.

Keywords: Thermodynamic Cycle · Heat Pump · CO_2

1 Introduction

The transition to low-carbon energy poses a substantial challenge for heating in cold and severe cold regions. As traditional fossil fuel-based heating methods are progressively phased out, heat pump technologies are emerging. However, heat pumps exhibit low energy efficiency at extremely low outdoor temperatures. Carbon dioxide (CO_2) heat pumps are regarded as a promising solution for heating in these regions. This phenomenon can be attributed to the thermodynamic properties of CO_2 as a low-temperature refrigerant, which operates most effectively under low ambient temperatures.

However, the low critical temperature of CO_2 necessitates its use in a transcritical cycle for space heating applications. The elevated return water temperature and the minimal temperature difference between the supply and return water result in substantial throttling losses within the CO_2 transcritical cycle. This results in a reduction

© The Author(s), under exclusive license to Springer Nature Singapore Pte Ltd. 2025
L. Ni et al. (Eds.): CCHVAC 2025, ESE, pp. 182–190, 2025.
https://doi.org/10.1007/978-981-95-3253-7_20

in the energy efficiency of the CO_2 heat pump. Consequently, numerous researchers have explored various approaches to improve its efficiency [1, 2], including modifications such as recuperators, two-stage cycles, ejectors, vortex tube, and mechanical subcooling. Recently, Dai et al. [3] proposed novel CO_2 heat pump cycles integrating refrigerant injection with mechanical subcooling, demonstrating simulated coefficient of performance (COP) enhancements of 10.61%–30.37%. Separately, Xiong et al. [4] developed a CO_2 heat pump for cold regions, achieving a tested COP of 2.10 at −12 °C ambient temperature with 35/65 °C inlet/outlet water temperatures.

At present, the proliferation of cycle configurations is predominantly attributable to manual, experience-based modifications of conventional cycles. The construction of an optimal heat pump cycle constitutes a multidimensional optimization problem, encompassing the refrigerant selection, the structure optimization, and the parameters optimization. It is particularly challenging to optimize the cycle structure quantitatively. Consequently, modifications based on experience encounter difficulties in attaining the optimal cycle configuration.

Researchers have proposed several methods to construct thermodynamic cycles that rely on computer technology or artificial intelligence. These include superstructure optimization [5], heat exchange process separation [6, 7], thermodynamic graph [8], and thermodynamic process combination [9]. These approaches have advanced the computability of thermodynamic cycle optimization significantly, thereby laying the groundwork for intelligent cycle construction. However, the prevailing computer-based methodologies are encumbered by two significant limitations. Firstly, there is an absence of comprehensive cycle structure libraries. Secondly, there are challenges inherent in integrating optimization with external heat sources and sinks. To address this, the authors previously proposed the GraPHsep method [10, 11], which utilizes graph theory and intelligent optimization algorithms to achieve integrated optimization of the vapor compression cycle and external heat exchange network.

In order to enhance the energy efficiency of heat pump heating in cold regions, this study employs the GraPHsep method to construct a novel high-efficiency CO_2 heat pump cycle. A comparative analysis of the novel cycle with classical configurations is presented in the study, demonstrating its thermodynamic advantages.

2 GraPHsep Method

The GraPHsep method has demonstrated its efficacy in the construction of efficient vapor compression cycles [10, 11]. The fundamental principle of the GraPHsep method, as illustrated in Fig. 1, is derived from the intrinsic thermodynamic configuration of vapor compression cycles. This structure consists of alternating isobaric heat exchange and adiabatic pressure manipulation processes. The sequence of these processes dictates the overall cycle configuration. It is imperative to note that the flow topology of the refrigerant is governed exclusively by the types and interconnections of the adiabatic pressure-regulating devices, independent of the placement of the heat exchangers. Consequently, the construction of a vapor compression cycle decomposes into two distinct subproblems: (1) the synthesis of the refrigerant flow path using graph theory, and (2) the optimization of the configuration of the heat exchanger network, a well-established domain employing techniques such as pinch point analysis.

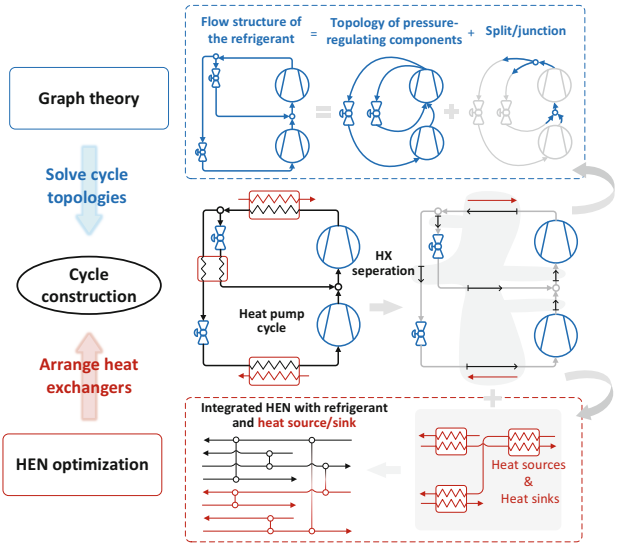


Fig. 1. Schematic of GraPHsep method.

The algorithmic implementation of the GraPHsep method was previously detailed by the authors [10]. As illustrated in Fig. 2, the workflow for efficient CO_2 heat pump cycle synthesis consists of three stages:

The initial stage of the process is the generation of cycle topologies via graph theory. Given the constraints on pressure-regulating components (two compressors and two throttle valves, reflecting typical system complexity), all viable topologies are generated via graph theory. The interconnections among components are encoded as adjacency matrices, with the topological validity of four constraints: connectivity, mass conservation, isobaric connection, and isomorphism elimination.

The subsequent stage of the process is the derivation of the refrigerant flow structure. Split/sink points are derived from the pressure-regulating topology to define refrigerant pathways. This approach is founded upon the principles of isobaric split/junction. Multi-inlet components have been demonstrated to induce junction point consolidation. Conversely, multi-outlet components necessitate split point generation. Phase separation functionality is embedded in split points, yielding all feasible flow structures.

The third stage of the process is the synthesis and optimization of the heat exchanger network (HEN). For any given flow configuration, the following steps must be taken in order to ensure the successful implementation of optimization. (1) Variable Initialization: The following parameters are considered independent: refrigerant selection, state variables upstream of pressure-regulating components and splits/junctions, and branch mass flow rates (see Table 1). For the split configuration of Refrigerant Flow Structure No. 22, two independent cycles can theoretically be charged with distinct refrigerants. This study employs R32 – commonly used in building heat pumps – as the secondary refrigerant integrated with the CO_2 cycle. (2) State Calculation: The pressure-regulating components models and the refrigerant properties model are induced to resolve downstream

states of each pressure-regulating component and split/junction. (3) HEN Integration: The heat exchange process is facilitated by a network comprising refrigerant branches, heat sources (e.g., ambient air/water), and heat sinks (e.g., space heating water/air). (4) Heat exchanger deployment: Pinch analysis with energy balance (Eq. 1) and heat transfer feasibility (Eq. 2) constraints are used to arrange heat exchangers. (5) Performance Maximization: Genetic algorithms are used to optimize parameters, thereby maximizing the COP (see Eq. 3). This process culminates in the finalization of the CO_2 heat pump cycle structure and parameters.

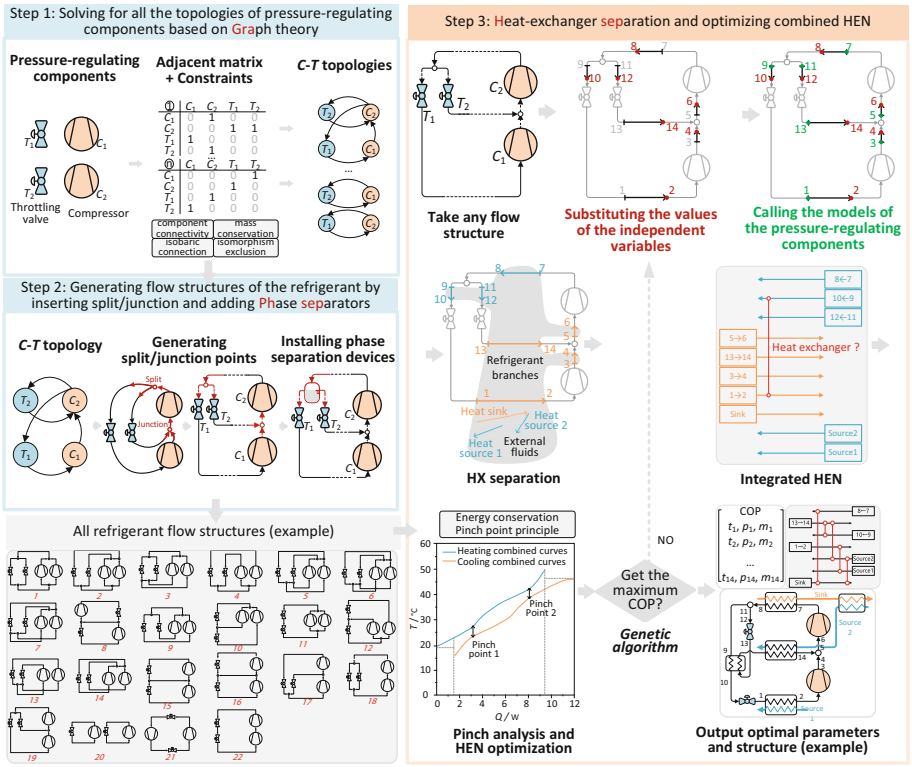


Fig. 2. Procedure of GraPHsep method.

$$\begin{cases} Q_{\mathrm{ref},i} = m_{\mathrm{ref},i}(h_{\mathrm{ref},i,\mathrm{out}} - h_{\mathrm{ref},i,\mathrm{in}}) \\ Q_{\mathrm{source},i} = m_{\mathrm{source},i}(h_{\mathrm{source},i,\mathrm{out}} - h_{\mathrm{source},i,\mathrm{in}}) \\ Q_{\mathrm{sink},i} = m_{\mathrm{sink},i}(h_{\mathrm{sink},i,\mathrm{out}} - h_{\mathrm{sink},i,\mathrm{in}}) \\ \sum_{i=1}^{n_{\mathrm{ref}}} Q_{\mathrm{ref},i} + \sum_{i=1}^{n_{\mathrm{source}}} Q_{\mathrm{source},i} + \sum_{i=1}^{n_{\mathrm{sink}}} Q_{\mathrm{sink},i} = 0 \end{cases} \tag{1}$$

where Q, $\dot{m}$, and h represent the heat flow rate, mass flow rate, and specific enthalpy, respectively; ref, source, sink, in, and out represent the refrigerant, external heat sink

Table 1. Independent variables and boundary condition.

Variables	Range
Compressor number	≤2
Compressor model	CO_2: (−0.0614·PR2 + 0.9545·PR -0.8795)/(PR-0.9294) R32: −0.000000316·PR6 + 0.000021588·PR5 –0.000578958·PR4 + 0.007712442·PR3 −0.052903324·PR2 + 0.143067335·PR + 0.527609551
Throttling valve number	≤2
Throttling valve model	The enthalpy of inlet and outlet is equal
Temperature difference of heat exchangers (K)	5
Refrigerant	CO_2 + R32
Condensing temperature (°C)	30–60
Evaporating temperature (°C)	5–30
Subcooled degree before throttling (K)	0–50
Superheated degree of the suction vapor (K)	0–30
Mass flow rate of the refrigerant ($kg \cdot s^{-1}$)	0–0.1
Rated heating capacity (W)	10000
Inlet/outlet temperature of outdoor airflow (°C)	−30/−35
Inlet/outlet temperature of supply water (°C)	40/45

fluid, external heat source fluid, inlet, and outlet, respectively; n_{ref}, n_{source}, and n_{sink} represent the numbers of the refrigerant branches, external heat source fluids, and external heat sink fluids, respectively.

$$\begin{cases} T_{\text{shift}} = T_{\text{fluid}} \pm \Delta T_{\text{pinch}} / 2 \\ T_{\text{shift}} \in \left[T_{\text{shift,min}},\ T_{\text{shift,max}} \right] \\ \delta Q_{\text{ref},i}(T_{\text{shift}}) = m_{\text{ref},i} \mathrm{d}h_{\text{ref},i}(T_{\text{shift}}) \\ \delta Q_{\text{source},i}(T_{\text{shift}}) = m_{\text{source},i} \mathrm{d}h_{\text{source},i}(T_{\text{shift}}) \\ \delta Q_{\text{sink},i}(T_{\text{shift}}) = m_{\text{sink},i} \mathrm{d}h_{\text{sink},i}(T_{\text{shift}}) \\ \delta Q_{\text{composite}}(T_{\text{shift}}) = \sum_{i=1}^{n_{\text{ref}}} \delta Q_{\text{ref},i}(T_{\text{shift}}) + \sum_{i=1}^{n_{\text{source}}} \delta Q_{\text{source},i}(T_{\text{shift}}) + \sum_{i=1}^{n_{\text{sink}}} \delta Q_{\text{sink},i}(T_{\text{shift}}) \\ Q_{\text{composite}}(T_{\text{shift}}) = \int_{T_{\text{shift,min}}}^{T_{\text{shift}}} \delta Q_{\text{composite}}(T_{\text{shift}}) > 0 \end{cases} \tag{2}$$

where T_{shift}, $T_{\text{shift,min}}$, and $T_{\text{shift,max}}$ represent the shifting temperature, its minimum, and its maximum, respectively; ΔT_{pinch} represents the minimum pinch-point temperature difference of heat exchangers; $Q_{\text{composite}}$ represents the composite heating capacity.

$$COP = \frac{Q_{\text{heat}}}{W_{\text{comp}}} \tag{3}$$

where Q_{heatl} represents the heating capacity; and W_{comp} represents the power of the compressor.

3 Results and Discussion

The configuration of the heat pump cycle for space heating in cold regions, constructed by the GraPHsep method, is illustrated in Fig. 3. On the low-temperature side, the CO_2 sub-cycle extracts heat from the cold environment and elevates its temperature grade. The higher-temperature heat in the superheated region is then used directly to heat the supply water, while the intermediate-temperature heat is absorbed by the evaporator of the high-temperature R32 sub-cycle. On the high-temperature side, the R32 sub-cycle further elevates the intermediate-temperature heat for supply water heating. Furthermore, a recuperator is incorporated between the liquid upstream of the expansion valve and the vapor downstream of the compressor suction to reduce throttling losses of the CO_2 sub-cycle. It is noteworthy that a three-stream heat exchanger is utilized in the R32 sub-cycle to facilitate concurrent heat exchange between the recuperator and evaporator. On the heat sink side, water is heated in parallel through both the R32 condenser and the CO_2 condenser. On the heat source side, outdoor air releases heat in the CO_2 evaporator.

The energy efficiency of the GraPHsep-based heat pump cycle was evaluated by comparing it to two control groups: a CO_2 single-stage transcritical cycle and a CO_2 two-stage transcritical cycle with a flash tank. The structures and parameters of the baseline cycles are illustrated in Fig. 4, while the cycle comparisons are presented in Fig. 5. The findings of the study suggest that the COP of the GraPHsep-based cycle attains 2.17, signifying a 77.8% enhancement over the single-stage cycle (COP: 1.22) and a 16.5% advancement over the two-stage cycle (COP: 1.86). Thermodynamic analysis reveals that the R32 sub-cycle efficiently diminishes the temperature of CO_2 subsequent to the condenser (i.e., subcools the CO_2). This reduction in temperature has been shown to lead to a significant decrease in substantial throttling losses. Nonetheless, both single-stage and two-stage cycles function in transcritical mode and exhibit substantial throttling losses. Furthermore, pinch analysis during the construction process optimized temperature matching in heat exchange, thereby minimizing exergy losses. For instance, the parallel water heating configuration across both condensers enhances temperature matching. Additionally, a multi-variable algorithm is employed to ensure sufficient COP optimization. For instance, the three-stream heat exchanger is employed to recuperate heat in both sub-cycles concurrently, thereby reducing throttling losses.

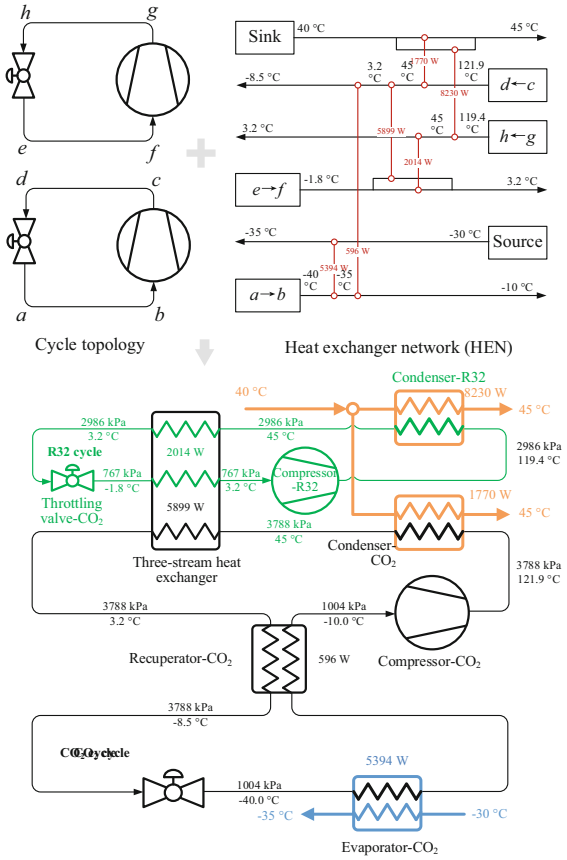
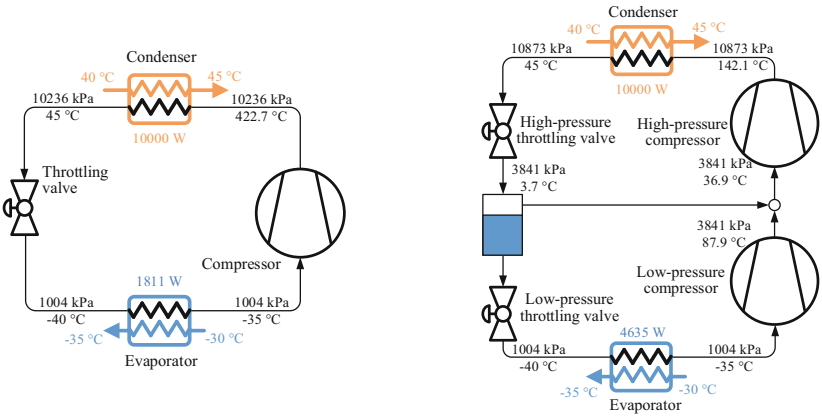


Fig. 3. Construction results of efficient heat pump for space heating in cold regions.

A primary challenge in implementing heat pump technology in cold regions is the necessity of overcoming excessively high compressor discharge temperatures. Under conditions of extremely low ambient temperatures, elevated pressure ratios result in excessively high discharge temperatures in conventional systems. As illustrated in Fig. 4, the single-stage cycle exhibits a discharge temperature of 422.7 °C, which would lead to significant deterioration of lubricant performance. Despite the reduction in pressure ratios caused by the two-stage configuration, the discharge temperature remains elevated at 142.1 °C. Conversely, the GraPHsep-based cycle demonstrates discharge temperatures of approximately 120 °C for both R32 and CO_2 sub-cycles. This is achieved through mechanical subcooling, which effectively enables subcritical operation of the CO_2 sub-cycle at reduced pressure ratios.



(a) single-stage transcritical cycle (b) two-stage transcritical cycle

Fig. 4. Baseline cycles.

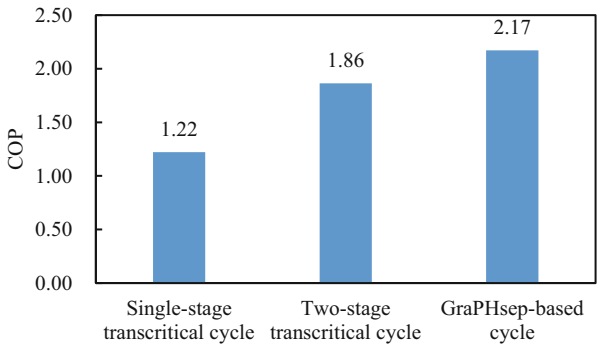


Fig. 5. COP comparison between GraPHsep-based cycle and baseline cycles.

4 Conclusion

In order to address the challenge of low energy efficiency in heat pump heating for cold regions, this study employed the intelligent GraPHsep method to construct a novel CO_2 heat pump cycle. Under the condition of an ambient temperature of −30 °C and a supply water temperature of 45 °C, the novel cycle attains a COP of 2.17. This performance exceeds that of single-stage and two-stage transcritical cycles by 77.8% and 16.5%, respectively, while concurrently achieving a substantial reduction in discharge temperatures. This outcome demonstrates the efficacy of the GraPHsep method for intelligent construction of CO_2 heat pumps and provides a viable solution for efficient heating in cold regions.

References

1. Yu, B., Yang, J., Wang, D.: An updated review of recent advances on modified technologies in transcritical CO_2 refrigeration cycle. Energy **189**, 116147 (2019)
2. Song, Y., Cui, C., Yin, X., Cao, F.: Advanced development and application of transcritical CO_2 refrigeration and heat pump technology—a review. Energy Rep. **8**, 7840–7869 (2022)
3. Dai, B., et al.: Hybrid CO_2 air source heat pump system integrating with vapor injection and mechanical subcooling technology for space heating of global application: life cycle techno-energy-enviro-economics assessment. Energy Convers. Manage. **271**, 116324 (2022)
4. Xiong, C., et al.: An efficient CO_2 air-to-water heat pump central space heating system in cold regions: a case study. Renew. Energy **242**, 122433 (2025)
5. Wallerand, A.S., Kermani, M., Kantor, I., Maréchal, F.: Optimal heat pump integration in industrial processes. Appl. Energy **219**, 68–92 (2018)
6. Toffolo, A., Lazzaretto, A., Morandin, M.: The HEATSEP method for the synthesis of thermal systems: an application to the S-Graz cycle. Energy **35**, 976–981 (2010)
7. Lazzaretto, A., Manete, G., Toffolo, A.: SYNTHSEP: a general methodology for the synthesis of energy system configurations beyond superstructures. Energy **147**, 924–949 (2018)
8. Gao, L., Hwang, Y., Radermacher, R.: Graph-based configuration optimization for S-CO_2 power generation systems. Energy Convers. Manage. **244**, 114448 (2021)
9. Zhao, D., Deng, S., Zhao, L., Xu, W., Zhao, R., Wang, W.: From 1 to N: a computer-aided case study of thermodynamic cycle construction based on thermodynamic process combination. Energy **210**, 118553 (2020)
10. Cui, M., Ying, Y., Wang, B., Wei, F.: Construction of vapor compression cycle with composite pressure-regulating components using GraPHsep method. Energy Convers. Manage. **301**, 118074 (2024)
11. Cui, M., Wang, B., Wang, C., Wei, F., Shi, W.: GraPHsep: an integrated construction method of vapor compression cycle and heat exchanger network. Energy Convers. Manage. **277**, 116576 (2023)

Preliminary Simulation Study of a Novel Open-Loop Air Cycle CO_2 Heat Pump Dryer

Jay Wang[1](✉) and Ding Mao[2]

[1] School of Engineering, Computer & Mathematical Sciences, Auckland University of Technology, Auckland, New Zealand
jay.wang@aut.ac.nz

[2] Department of Building Environment and Equipment, School of Civil Engineering, Hefei University of Technology, Hefei, China

Abstract. This study investigates the preliminary performance of a CO_2 heat pump dryer system with an open-loop air cycle, offering a simplified and energy-efficient alternative to conventional drying technologies. The open-loop cycle has been proposed in this study, with its working principles illustrated in the psychrometric chart. Through numerical analysis, the system demonstrates stable thermodynamic performance, with the gas cooler effectively heating air to 41.8–50.8 °C with the airflow 0.5–1 kg/s. The simulation results reveal that lower air mass flow rates (0.5 kg/s) optimize drying performance, yielding faster moisture removal (57.54 min for 5 kg moisture) and higher energy efficiency (SMER = 0.37 kg/kWh). In contrast, higher flow rates (1.0 kg/s) prolong drying times (102.73 min) and reduce efficiency (SMER = 0.21 kg/kWh) due to reduced dehumidification effectiveness. The open-loop system can simplify the complicated piping, making it cheaper and easier to install while still working well in various weather conditions. This research shows the potential of the system that can save energy without being overly complex, making it a competent option for eco-friendly drying solutions. With this as a baseline, future research can focus on comparative analyses between open-loops (with dry and wet outlets) and closed-loop cycle to further optimize performance and broaden applicability.

Keywords: CO_2 heat pump · Dryer · Open loop · Air cycle · SMER

1 Introduction

Heat pump dryers have emerged as a promising alternative to conventional vented dryers, consuming approximately one-third of the energy required by traditional systems. Despite this advantage, the majority of existing heat pump dryers utilize a closed-loop air cycle, drawing in either dry or wet air as the inlet. This configuration, while effective in maintaining system efficiency, often leads to higher capital costs and complex ducting requirements, which can limit broader adoption and practical deployment.

Carbon dioxide (CO_2) heat pump systems have already demonstrated their potential as a competitive technology [1], particularly in replacing traditional electric water

© The Author(s), under exclusive license to Springer Nature Singapore Pte Ltd. 2025
L. Ni et al. (Eds.): CCHVAC 2025, ESE, pp. 191–199, 2025.
https://doi.org/10.1007/978-981-95-3253-7_21

heaters [2]. However, the use of CO_2 heat pump systems in drying applications remains limited, particularly regarding the exploration of open-loop air cycle configurations. Such configurations have the potential to substantially simplify system design and lower capital costs by removing the necessity for complex return ductwork.

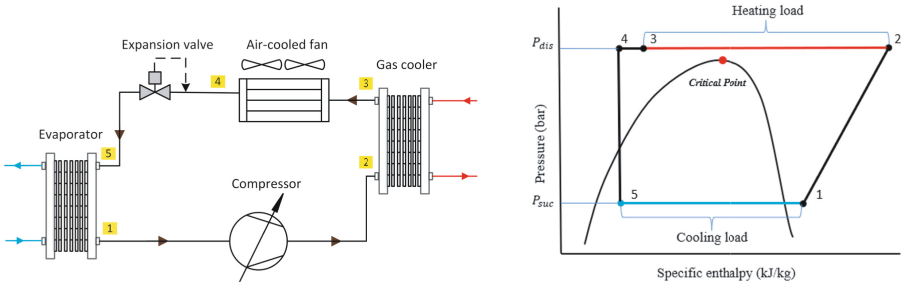
Using fresh air as the inlet in an open-loop configuration has the potential to simplify system design and reduce installation costs. Furthermore, an open-loop air cycle could offer operational flexibility, particularly under varying ambient conditions, while maintaining energy efficiency advantages over conventional drying methods. Despite these potential benefits, comparative studies evaluating the performance differences between open-loop and closed-loop air cycles in CO_2 heat pump dryers are scarce. Moreover, strategies for optimizing the operation of open-loop air cycles in such systems have not been adequately proposed or evaluated.

In this study, a preliminary simulation analysis is conducted to investigate a novel CO_2 heat pump dryer utilizing an open-loop air cycle under various fresh air inlet conditions. This research aims to address the existing knowledge gap by assessing the system performance, providing a foundational understanding for the future development of practical, energy-efficient drying systems using CO_2 heat pumps.

2 System Configuration and Cycles

2.1 CO_2 Heat Pump

The configuration of the CO_2 heat pump system, shown in Fig. 1, is employed for analysis in this conceptual study. Both the gas cooler and evaporator will function in the air cycle, that is, the air temperature will be heated up through the CO_2 gas cooler while the moisture will be removed during the cooling process inside the evaporator. Since the study is based on the theoretical analysis considering the real settings of the real-world system, the process from state 3 to 4 involves a subcooling process to ensure the heat pump system maintains the same dynamic at the outlet of the gas cooler, if there are variations in temperature and mass flow rate at the inlet.



(a) Configuration (b) *P-h* cycle

Fig. 1. Transcritical CO_2 heat pump system

2.2 Open-Looped Air Cycles

The working cycles in the air-drying process can be illustrated by physical models, where Fig. 2(a) is an open-loop cycle with a fresh air inlet and dry air outlet. In a closed-loop cycle, a drying chamber is required to get rid of the moisture from the fresh air before entering the cycle, while it is not necessarily needed in an open-loop cycle. The fresh air inlet can be positioned at either the evaporator entry or the condenser entry, with the outlet of the wet air or dry air, respectively. As shown in the figure, the process from state 1 to 2 can raise the temperature of the fresh air even further, enhancing its capacity to absorb moisture from the wet material. Moisture contained in the material will be picked up with the air passing through. During the evaporation process from state 3 to 4, the wet air will be first cooled sensibly only to its dew point, followed by the combination of cooling and dehumidifying, that is, water vapor is gradually condensed from the air. Since the air is not re-circulated in an open-loop cycle, the state at the outlet does not need to match the state at the inlet of the loop. In other words, the entire heating or cooling capacity produced on the refrigerant side can be utilized for air heating or cooling independently, only depending on the effectiveness of the heat exchanger. The drying temperature can be then unconstrained, as it is only restricted by the maximum withstand temperature of the material and the discharge temperature post-compression.

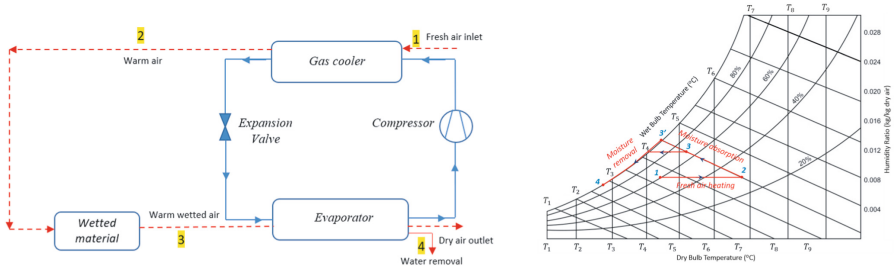


Fig. 2. The physical model of an open-loop air cycle with dry air outlet

The psychrometric diagram for the air-drying process using fresh air inlet is shown in Fig. 2(b). Each loop includes the process of air heating, moisture absorption, and moisture removal (dehumidification). The humidity ratio remains constant during the air heating process, while the moisture absorption is nearly isenthalpic: the humidity ratio increases as the air temperature drops due to evaporation. During moisture removal, the humidity ratio stays constant during sensible cooling before reaching the dew point, after which both temperature and humidity ratio decrease at 100% relative humidity. For the open-loop cycle with a dry air outlet, as shown in the figure, the fresh air can be heated to a higher temperature at state 2 after going through the heat exchanger, as its inlet temperature (state 1) is typically higher than the dry air outlet (state 4). Here, the airflow rate can be adjusted based on the desired air temperature and heating capacity, while the dehumidification process (state 3 to 4) remains necessary for continuous heat pump operation.

3 Numerical Model

This chapter focuses on a numerical model for the purposes of moisture removal, dry air heating, and moisture absorption for the air cycles. The processes between CO_2 and air in fin-and-tube heat exchangers were investigated separately during the evaporation and condensation processes. Some equations have been described in the existing study [3]. Key assumptions for this study can be made as follows:

1. The effect of the pressure drop during the heat exchange process is negligible.
2. There are no pressure drops and leakage for the flow of air in ducts.
3. There is an isenthalpic process for air during the moisture absorption process.
4. There is an isenthalpic process through an expansion valve.
5. The power consumption of the air-cooled fan is negligible.

3.1 Evaporator and Gas Cooler

The Reynolds number based on collar diameter (Re_{Dc}) can be defined as:

$$\mathrm{Re}_{Dc} = \frac{\dot{m}_{air} d_c}{u_{air} A_c} \tag{1}$$

where $\dot{m}_{air}$ is air mass flow rate, d_c is fin collar diameter, $u_{air}$is the air dynamic viscosity, and A_c is minimum flow area.

The Air Nusselt number (Nu) can be determined from [4–6]:

$$\begin{cases} Nu = 0.3 + \left(\dfrac{0.62 \mathrm{Re}_{Dc}{}^{0.5} \mathrm{Pr}_{air}{}^{\frac{1}{3}}}{1 + \left(\frac{0.4}{\mathrm{Pr}_{air}} \right)^{\frac{2}{3}}} \right)^{\frac{1}{4}} & \mathrm{Re}_{Dc} < 1000 \\ Nu = j \mathrm{Re}_{Dc} \mathrm{Pr}_{air}{}^{\frac{1}{3}} & 1000 \le \mathrm{Re}_{Dc} \le 20000 \\ Nu = 0.35 \mathrm{Re}_{Dc}{}^{0.6} \mathrm{Pr}_{air}{}^{0.36} \left(\frac{P_t}{P_l} \right)^{0.2} & \mathrm{Re}_{Dc} > 20000 \end{cases} \tag{2}$$

where j is a Colburn j-factor, Pr_{air} is air Prandtl number, P_t is transverse tube pitch, P_l is longitudinal tube pitch.

The heat transfer coefficient (h_o) in airside can be defined as:

$$h_o = \frac{Nu \times k_{air}}{d_c} \tag{3}$$

where k_{air} is air thermal conductivity.

The CO_2 Nusselt number (Nu_{CO_2}) can be calculated as:

$$\begin{cases} Nu_{CO_2} = \dfrac{\frac{f}{8} (\mathrm{Re}_{CO_2} - 1000) \mathrm{Pr}_{CO_2}}{1 + 12.7 \sqrt{\frac{f}{8}} \left(\mathrm{Pr}_{CO_2}{}^{\frac{2}{3}} - 1 \right)}, & \mathrm{Re}_{CO_2} > 3000 \\ Nu_{CO_2} = 3.66, & \mathrm{Re}_{CO_2} \le 3000 \end{cases} \tag{4}$$

where Pr_{CO_2} is CO_2 Prandtl number and f is friction factor. The CO_2 Reynolds number (Re_{CO_2}) can be described similarly by using Eq. (1), which employs CO_2 mass flow

rate ($\dot{m}_{CO_2}$), tube inner diameter (d_i), CO_2 flow area (A_i), and dynamic viscosity of CO_2 $\left(u_{CO_2}\right)$.

The fin parameter (m) can be defined as:

$$m = \sqrt{\frac{2h_o}{k_{fin}\Delta_f}} \tag{5}$$

where k_{fin} is fin thermal conductivity and Δ_f is fin thickness.

The fin efficiency (η_{fin}) can be defined as:

$$\eta_{fin} = \frac{\tanh(mL_e)}{mL_e} \tag{6}$$

where L_e is effective fin length.

The overall heat transfer coefficient (UA) can be defined as:

$$UA = \left(\frac{1}{\eta_{fin}h_oA_o} + \frac{\Delta_x}{k_{wall}A_m} + \frac{1}{h_iA_i}\right)^{-1} \tag{7}$$

Where A_o is outer surface area, k_{wall} is wall thermal conductivity, A_m is mean conduction area, A_i is CO_2 flow area, Δ_x is tube wall thickness. The heat transfer coefficient (h_i) on the CO_2 side can similarly be calculated using Eq. (3), which employs Nu_{CO_2}, k_{CO_2}, and the tube's inner diameter (d_i).

The heat transfer rate (Q) can be defined as:

$$Q = UA\left(T_{air} - T_{CO_2}\right) \tag{8}$$

Where T_{air} is CO_2 temperature, T_{CO_2} is CO_2 temperature, UA is mean conduction area, A_i is CO_2 flow area, Δ_x is tube wall thickness.

3.2 Moisture Absorption Process

The moisture absorption rate ($\dot{m}_{w\_abs}$) from the wet material can be calculated from:

$$\dot{m}_{w\_abs} = \dot{V}_{air}\overline{\rho}_{air}\left(x_{abs} - x_{con\_air}\right) \tag{9}$$

where x_{con_air} is the humidity ratio after the air heating process through the gas cooler and x_{abs} is the humidity ratio after absorbing the moisture from the wet material, of which the maximum ratio can be described as:

$$x_{abs\_\max} = x_{abs}\Big|_{RH_{max},h=h_{con\_air\_out}} \tag{10}$$

where $h_{con\_air\_out}$ is the air enthalpy at the outlet of the condenser.

If the mass of moisture containing in the material is defined as $m_{material\_w}$, hence, the time required for drying up the material can be determined from:

$$t_{material\_w} = \frac{m_{material\_w}}{\dot{m}_{w\_abs}} \tag{11}$$

The term of specific moisture of extraction rate (SMER) is employed to describe the ratio of the amount of the water removed from a material to the total energy consumed for compressor (Q_{comp}) [7]:

$$SMER = \frac{m_{material\_w}}{Q_{comp}} \tag{12}$$

4 Simulation Results

The dimensions and geometry information of the fin-and-tube heat exchangers for the evaporator and gas cooler have been included in the existing study [8, 9], and the type of the compressor selected is Bitzer 4HTE-20 K-50 Hz [10]. Table 1**.** includes initial conditions set for the numerical model.

Table 1. Initial conditions for the model

Maximum withstand temperature, $T_{material\_max}$	90 °C
Operating range for the air mass flow rate, $\dot{m}_{air}$	0.5–1.0 kg/s
Mass of the moisture contained, $m_{material\_w}$	5 kg
Ambient air temperature, T_{amb}	20 °C
Gas cooler temperature, T_{gas}	45 °C
Discharge pressure, P_{dis}	80 bar
Relative humidity of ambient air, RH_{amb}	50%
Evaporation temperature, T_{ev}	5 °C
Suction superheat, ΔT_{super}	10 K
Relative humidity of air after moisture absorption, RH_{max}	80%

4.1 Air-Heating

Figure 3 shows how the air temperature at the outlet increases as it is heated during the CO_2 gas cooling process. As a result, lower air mass flow rates lead to higher air temperatures, which range from 41.8 °C to 50.8 °C based on the air flow rate from 0.5 kg/s to 1 kg/s.

4.2 Moisture Absorption and Air-Dehumidification

Figure 4 examines the performance of a CO_2 heat pump dryer using four sub-plots. The CO_2 temperature stays constant during evaporation since only latent heat is involved and then increases to around 15 °C during the superheating stage, as illustrated in Fig. 4(a). It is observed that during the moisture absorption process (that is, an isenthalpic process),

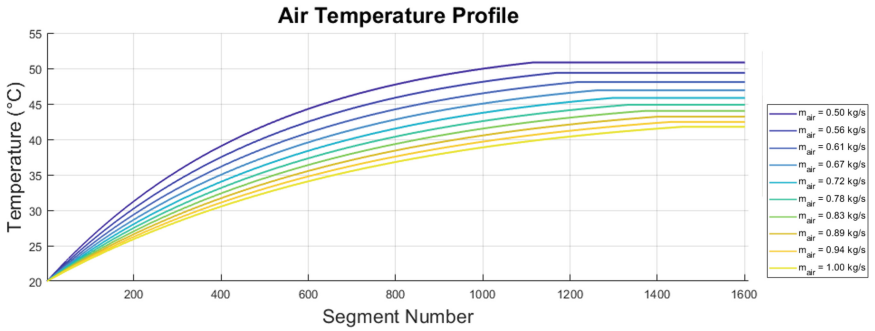


Fig. 3. Air outlet temperature after the heating process in a CO_2 gas cooler

the air temperature exiting the gas cooler decreases, leading to a lower air temperature entering the evaporator, as depicted in Fig. 4(b). Initially, the air temperature decreases quickly as a result of sensible cooling, and then it continues to fall further as the dehumidification process starts to occur alongside the ongoing temperature reduction. This can also be reflected in Fig. 4(c), where the humidity ratio first remains constant before starting to decline when the dew point temperature has been reached. In Fig. 4(d), the cooling capacity is approximately 6.5 kW and decreases as the air mass flow rate increases.

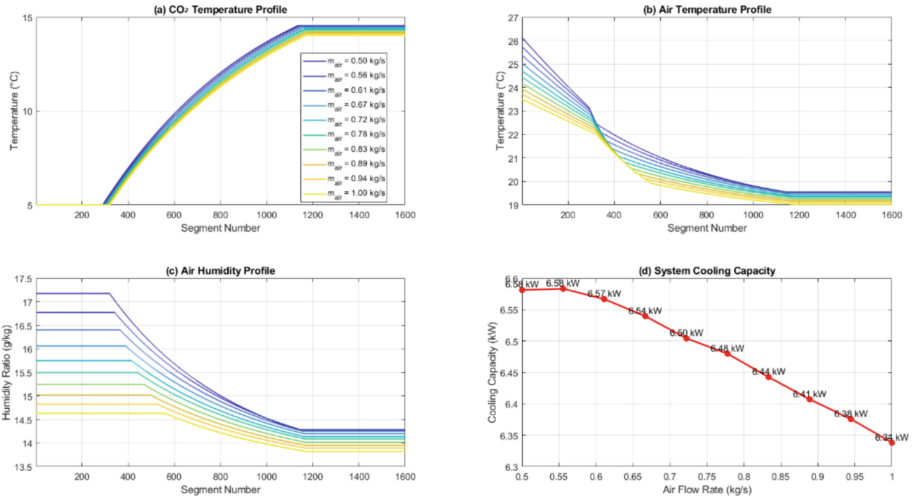


Fig. 4. Performance analysis for CO_2 and air during the evaporation process

Figure 5. illustrates that increasing the air flow rate in a CO_2 heat pump dryer leads to longer drying time and lower moisture extraction efficiency. Specifically, as shown in Fig. 5(a), since the air flow rate rises from 0.5 to 1.0 kg/s, the drying time increases from 57.54 to 102.73 min, while the SMER decreases from 0.37 to 0.21 kg/kWh, as described in Fig. 5(b). This indicates that lower air flow rates are more effective for achieving faster drying and higher energy efficiency.

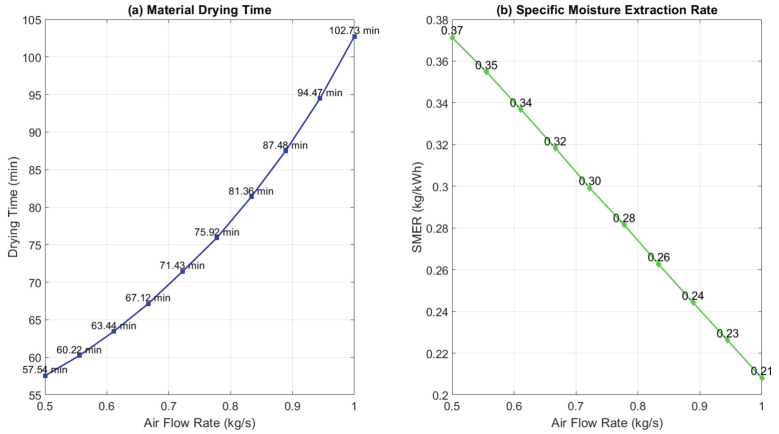


Fig. 5. Effect of air flow rate on material drying time and SMER

5 Conclusion and Future Work

This study numerically examines a CO_2 heat pump dryer employing an open-loop cycle featuring fresh air inlet and dry air outlet. By utilizing fresh air inlet (20 °C, 50% RH, and air flow rate 0.5–1 kg/s) and eliminating recirculation ductwork, the design simplifies installation while maintaining performance. Some conclusions can be drawn from this study:

1. The CO_2 heat pump system shows stable performance: air heats to 41.8–50.8 °C in the gas cooler with different airflow rates, while the evaporator effectively removes moisture when air cools below dew point.
2. Lower air mass flow rates provide a balance between drying speed and system performance, achieving faster drying, that is, 57.54 min for 5 kg moisture removal at 0.5 kg/s.
3. Higher airflows reduce dehumidification effectiveness, leading to higher drying time up to 102.73 min at 1.0 kg/s, and lower SMER at 0.21 kg/kWh.

Future studies can be focused on the parametric analysis and comparative study between the current open-loop (with dry air outlet), closed-loop, and alternative open-loop (with wet air outlet) cycles.

Nomenclature			
A	Area, m^2	UA	Overall heat transfer coefficient, W/K
d	Diameter, m	$\dot{V}$	Volumetric flow rate, m^3/s
f	Friction factor	x	Humidity ratio
h	Heat transfer coefficient, $W/m^2 \cdot K$	Δ_f	Fin thickness, m
j	Colburn j-factor	Δ_x	Tube wall thickness, m
k	Thermal conductivity, W/m·K	μ	Dynamic viscosity, Pa·s
L_e	Effective fin length, m	***Abbreviations***	
m	Fin parameter, m^{-1}	*SMER*	Specific Moisture Extraction Rate, kg/kWh
$\dot{m}$	Mass flow rate, kg/s	***Subscripts***	
Nu	Nusselt number	*abs*	After moisture absorption
P_t	Transverse tube pitch, m	*abs_max*	Maximum humidity after absorption
Pr	Prandtl number	*con_air*	After air heating through gas cooler
Q	Heat transfer rate, W	*con_air_out*	At condenser outlet
Re	Reynolds number	*comp*	compressor
t	time, s	*c*	Fin collar
T	Temperature, °C	*i*	Inner

References

1. Wang, J., Gullo, P., Ramezani, H.: Review on the trend of ultra-low-GWP working fluids for small-capacity vapour-compression systems. Sustain Energy Technol Assess. **66**, 103803 (2024)
2. Wang, J., et al.: A comprehensive review and analysis on CO2 heat pump water heaters. Energy Convers. Manag. **X**, 100277 (2022)
3. Lee, B.-H., Sian, R.A., Wang, C.-C.: A rationally based model applicable for heat pump tumble dryer. Dry. Technol. **37**(6), 691–706 (2019)
4. Churchill, S.W., Bernstein, M.: A correlating equation for forced convection from gases and liquids to a circular cylinder in crossflow. J. Heat Transfer. **99**, 300–306 (1977)
5. Wang, C.-C., Chi, K.-Y., Chang, C.-J.: Heat transfer and friction characteristics of plain fin-and-tube heat exchangers, part II: correlation. Int. J. Heat Mass Transf. **43**(15), 2693–2700 (2000)
6. Žukauskas, A.: Heat transfer from tubes in crossflow. In: Advances in Heat Transfer, pp. 93–160. Elsevier, Amsterdam (1972)
7. Sarkar, J., Souvik, B., Gopal, M.R.: Transcritical CO2 heat pump dryer: part 1. Mathematical model and simulation. Dry. Technol. **24**(12), 1583–1591 (2006)
8. Sian, R.A., Wang, C.-C.: Comparative study for CO2 and R-134a heat pump tumble dryer – a rational approach. Int. J. Refrig. **106**, 474–491 (2019)
9. Lin, K.-H., Kuo, C.-S., Hsieh, W.-D., Wang, C.-C.: Modeling and simulation of the transcritical CO2 heat pump system. Int. J. Refrig. **36**(8), 2048–2064 (2013)
10. Wang, J., Lu, W.: A Streamlined Polynomial Regression-Based Modeling of Speed-Driven Hermetic-Reciprocating Compressors. Appl. Sci. **15**(22), 12016 (2025)

Study on Field Performance Testing Methods for Air-Source Heat Pump Refrigerant-Direct Radiant Systems

Fan Xu, Gang Wang(✉), Yu Du, and Encan Jia

Qingdao University of Technology, Qingdao, China
wanggang@qut.edu.cn

Abstract. This study focuses on air-source heat pump (ASHP) refrigerant-direct radiant systems, conducting field performance testing research. An integrated field performance testing system was developed incorporating compressor performance curve method, electrically heated refrigerant enthalpy difference method, and outdoor air enthalpy difference method. Through empirical comparative analysis, the measurement accuracy and applicability of these approaches were evaluated, establishing a methodological foundation for field performance testing of ASHP refrigerant-direct radiant systems. The results demonstrate measurement accuracies of ±5.5% for the compressor performance curve method, ±11.0% for the electrically heated refrigerant enthalpy difference method, and ± 11.0% for the outdoor air enthalpy difference method. The compressor performance curve method achieves the highest accuracy but requires complete compressor operational data. The electrically heated refrigerant enthalpy difference method carries inherent system disturbance risks, the outdoor air enthalpy difference method non-intrusive nature enables more authentic characterization of actual system operating conditions. This study provides empirical validation for field performance testing research to refrigerant-direct heat pump systems. The research results establish a methodological foundation for performance evaluation of ASHP refrigerant-direct radiant systems.

Keywords: Air-source heat pump · Refrigerant-direct radiant systems · Field performance testing

1 Introduction

Driven by China's "Dual Carbon" strategy, air-source heat pump (ASHP) have emerged as critical infrastructure in northern China's clean heating systems, leveraging their high energy efficiency ratios and low-carbon attributes [1, 2]. As a novel terminal configuration, refrigerant-direct radiant systems demonstrate significant potential for building energy efficiency due to their dual advantages of enhanced heat transfer effectiveness and thermal comfort [3]. Existing field performance testing methods for evaluating the operational performance of ASHP include the water-side heat metering method, the indoor air enthalpy difference method, the outdoor air enthalpy difference method, and

© The Author(s), under exclusive license to Springer Nature Singapore Pte Ltd. 2025
L. Ni et al. (Eds.): CCHVAC 2025, ESE, pp. 200–208, 2025.
https://doi.org/10.1007/978-981-95-3253-7_22

the refrigerant enthalpy difference method [4]. For refrigerant-direct radiant terminals, their distinctive phase-change heat transfer mechanisms and terminal coupling characteristics [5] preclude application of conventional hydronic metering approaches and indoor air enthalpy difference methods. Field performance testing must consequently shift focus to the outdoor unit, encompassing the outdoor heat exchanger and compressor sections. This necessitates adopting outdoor air enthalpy difference method and refrigerant enthalpy difference method, which impose no special requirements on terminal configurations.

However, research on the applicability of these two methods to ASHP refrigerant-direct radiant systems remains relatively scarce. Existing literature has not yet established a comprehensive field-test evaluation methodology. Based on the foregoing analysis, this study focuses on exploring field performance testing methods suitable for refrigerant-based terminals. Corresponding test apparatus is developed utilizing field conditions to evaluate the system's operational performance on-site. The measurement accuracy of these methods is analyzed and compared, establishing a methodological framework for the field performance assessment of ASHP refrigerant-direct radiant systems. Furthermore, the two methods discussed not only contribute to improving the accuracy of field performance assessment for refrigerant-direct radiant terminals, but the refrigerant enthalpy difference method can also be effectively applied to evaluate the performance of pure refrigerant systems relying on direct refrigerant circulation, such as variable refrigerant flow (VRF) systems. Similarly, the outdoor air enthalpy difference method offers significant reference and insights for water-based terminal systems.

2 Principles and Testing Apparatus Development for Outdoor Air Enthalpy Difference Method

2.1 Principles for Outdoor Air Enthalpy Difference Method

The outdoor air enthalpy difference method operates on the principle of determining system performance through measurement of inlet-outlet air parameters at the outdoor heat exchanger. Conventional implementations include: the static multi-point measurement approach, external air hood method, static outlet air sampling technique, and real-time scanning sampling method. After comprehensive evaluation of the limitations and advantages inherent in existing outdoor air enthalpy difference methodologies (factoring in spatial constraints and unit installation configurations) this study employs the external air hood method for field performance testing of ASHP refrigerant-direct radiant systems.

The external air hood method [6] employs a sealed air hood to capture the entire outlet airflow from the outdoor unit, eliminating air leakage during testing. The coefficient of performance (COP) is calculated by measuring inlet-outlet air parameters at the outdoor heat exchanger, defined as the ratio of heating capacity output to electrical energy input.

2.2 Development of Testing Apparatus for External Air Hood Method

The detailed configuration of the testing apparatus is illustrated in Fig. 1. The system comprises: 1. structural frame, 2. external insulation layer, 3. weather-resistant cladding,

4. temperature/humidity sensors, 5. anemometers. Accuracy of experimental test sensors as shown in Table 1, high-accuracy instrumentation was employed, with systematic error analysis conducted in advance using relative uncertainty assessment. Moreover, computational fluid dynamics simulation was used to optimize the position of measurement points, and the number of measuring points is effectively reduced under the premise of ensuring the measurement precision.

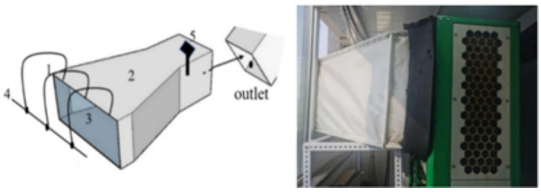


Fig. 1. Structure and physical prototype of the experimental test rig

Table 1. Detailed sensor specifications

Type	Model	Accuracy	Range	Response time
HVAC Psychrometer	SHT40	±0.2 °C 、 ± 1.8%Rh	−40 ~ 125 °C 、 0 ~ 100%Rh	4 s
Duct Airflow Sensor	EVGT30	±0.2 m/s	0 ~ 20 m/s	3 s
Refrigeration Power Meter	SPM91	±1.0%	–	–

The error analysis results indicate that under long-term operating conditions, the relative expanded uncertainties of COP and heating capacity are 4.65% and 4.86%, respectively.

3 Principles and Testing Apparatus Development for Refrigerant Enthalpy Difference Method

3.1 Principles for Refrigerant Enthalpy Difference Method

The refrigerant enthalpy difference method determines heating (or cooling) capacity and system performance by calculating the enthalpy change across the heat exchanger. This calculation requires the refrigerant mass flow rate, typically obtained via compressor testing, compressor performance maps, or energy balance methods, combined with measured condenser inlet and outlet pressures and temperatures. Accurately measuring the refrigerant circulation flow rate within the test system represents the critical challenge and core aspect of this method. Current measurement approaches include mass flow meters, compressor performance curve method, heat balance methods, and

the electrically heated refrigerant enthalpy difference method. Leverage the enthalpy difference principle while ensuring direct on-site assessment, this study employs a combined approach: compressor performance curve method alongside the electrically heated refrigerant enthalpy difference method. The latter technique is primarily employed to determine the refrigerant circulation flow rate within the operating system.

Principles for compressor performance curve method. Compressor performance curve method utilizes functional curves or relational expressions derived from compressor testing. These characterize the heating (cooling) capacity, input power, current, and refrigerant mass flow rate of a compressor under variable speeds or fixed-speed conditions as functions of evaporation temperature and condensation temperature. The compressor's heating (cooling) capacity and operational performance are calculated based on these performance curves. By adopting the ten-coefficient compressor model [7] developed by the American Society of Heating, Refrigerating and Air-Conditioning Engineers (ASHRAE), measurement refrigerant mass flow rate accuracy within ±5% can be achieved. The calculation formula is expressed as follows:

$$G_{ref} = \rho_{suc}\left(x_1 + x_2 t_e + x_3 t_c + x_4 t^2{}_e + x_5 t_e t_c + x_6 t^2{}_c + x_7 t^2{}_e + x_8 t_c t^2{}_e + x_9 t_e t^2{}_c + x_{10} t^3{}_c\right)(3.1) \quad (1)$$

where G_{ref} is the refrigerant mass flow rate (kg/h); ρ_{suc} is the refrigerant density at compressor suction port (kg/m^3); $x_1 \sim x_{10}$ is the empirically fitted coefficients derived from manufacturer's experimental data; t_e and t_c is the system evaporation temperature and condensation temperature (°C).

For variable-speed compressors, the suction and discharge parameters dynamically vary with operational conditions and system control actions during operation. Consequently, temperature compensation must be applied specifically to the compressor suction and discharge temperatures [8]. Numerous researchers have investigated the compressor performance curve method, with existing studies demonstrating its testing accuracy within ±3% [9]. However, this method exhibits significant dependence on compressor test data. Additionally, operational factors such as compressor wear and performance degradation during runtime can lead to substantial deviations from actual test conditions. To address these limitations, this paper presents a preliminary exploration of applying the electrically heated refrigerant enthalpy difference method to field performance testing.

Principles for electrically heated refrigerant enthalpy difference method. Electrically heated refrigerant enthalpy difference method [10] determines the refrigerant mass flow rate within the system through energy balance principles by measuring the input power to electric heaters and the enthalpy change of refrigerant before and after passing through the heaters. Subsequently, the unit's operational performance is calculated based on pressure and temperature measurements upstream and downstream of the condenser.

3.2 Development of Testing Apparatus for Electrically Heated Refrigerant Enthalpy Difference Method

The main assembly includes electric heaters, a voltage controller and temperature sensors. Temperature measurement employed PT1000 resistance temperature detectors (RTDs) with an operational range of −50 to 700 °C and accuracy of ±0.15 °C, where

six RTDs were strategically positioned: two at electric heater surfaces, two on outer surfaces of insulation layers, one pre-heating point, and one post-heating point; while pressure measurement utilized SENSATA 45CP2-7 transducers (range: 0–4.6 MPa, accuracy: ±0.5%) installed upstream of the electrically-heated test apparatus, with negligible pressure loss in the piping system.

4 Experimental Validation of the Test Apparatus

4.1 Laboratory Testing Platform

Laboratory validation of the test apparatus was conducted in accordance with GB/T 25127.2-2020 [11] to verify measurement accuracy. The test unit was an FRSYXZBO08ZLRS air-source heat pump with rated heating capacity of 7.5 kW and heating power consumption of 4.1 kW at −25 °C conditions. Testing commenced after system stabilization with 30-min duration. Data acquisition occurred at 6-s intervals. Ambient temperature measured −7 °C during testing. Unit outlet water temperature was set to 40 °C. Figure 2 shows the environmental chamber test schematic.

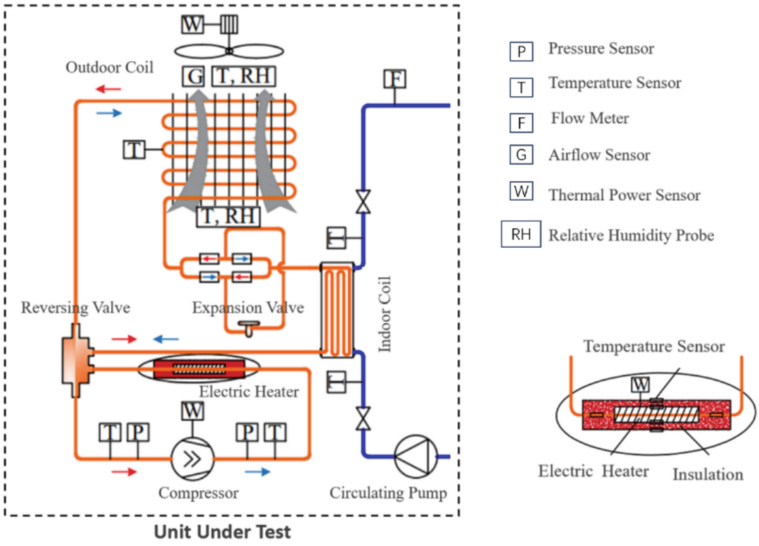


Fig. 2. Environmental chamber test schematic

4.2 Laboratory Testing Results Analysis

During stable compressor operation at an average frequency of 87.64 Hz, the benchmark heating capacity was first determined using the water-side heat metering method. (This approach is exclusively applicable to hydronic terminal systems, where the stable thermophysical properties of water ensure high measurement accuracy and comparative

methodological simplicity [12, 13]). Water-side heat metering recorded heating capacity $Q_{c\text{-}ave}$ of 12.00 kW, the water-side heat metering method $Q_{c\text{-}ave}$ serves as the benchmark for validating measurement accuracy of both the outdoor air enthalpy difference test apparatus and electrically-heated refrigerant enthalpy difference test apparatus.

Figure 3 presents a comparison of the measured heating capacities across different test methods. During laboratory validation, the outdoor air enthalpy difference method yielded an average unit heating capacity $Q_{c,coil\text{-}outdoor\text{-}ave}$ of 12.48 kW, representing a 4.0% error compared to the water-side heat metering method, with relative errors ranging from −3.3% to 11.0%. The compressor performance curve analysis measured an average unit heating capacity $Q_{c,per\text{-}cur\text{-}ave}$ of 12.1 kW, showing a smaller error of 0.84% and relative errors between −5.5% and + 5.5%. Meanwhile, the electrically heated refrigerant enthalpy difference method produced $Q_{c,heat\text{-}bal\text{-}ave}$ of 12.67 kW, corresponding to a 5.6% error and relative errors from −2.0% to 11.0%; however, the shorter duration of this test suggests potential for greater deviations in long-term measurements.

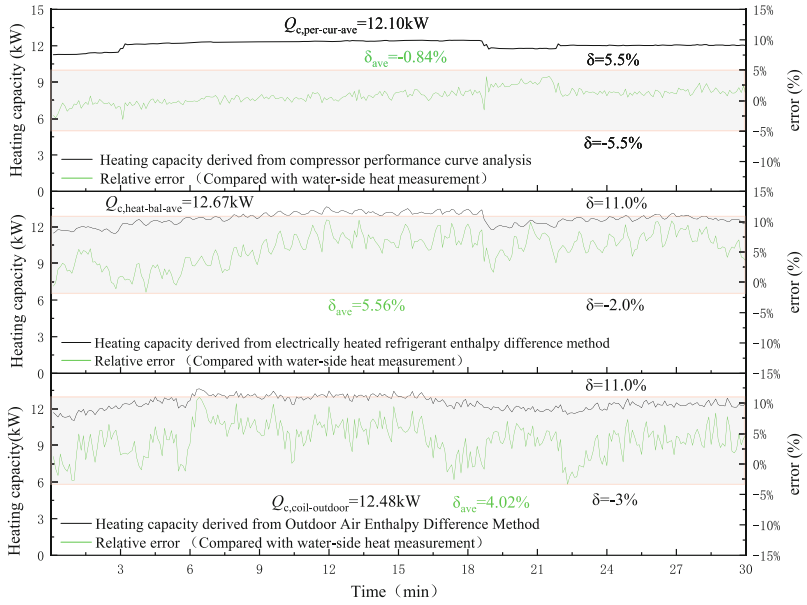


Fig. 3. Comparison of the measured heating capacities across different test methods

The compressor performance curve method exhibited an average relative error $\delta_{per\text{-}cur\text{-}ave}$ of −0.84%, while the electrically heated refrigerant enthalpy difference method yielded an average relative error $\delta_{\text{heat-bal-ave}}$ of 5.56%, and the outdoor air enthalpy difference method resulted in $\delta_{coil\text{-}outdoor} = 4.02\%$. Considering both the magnitude and fluctuation range of test errors, the compressor performance curve method demonstrates superior accuracy, followed by the electric heating refrigerant enthalpy difference method, with the outdoor air enthalpy difference method showing the lowest precision.

To enhance the measurement precision of the electrically heated refrigerant enthalpy difference method apparatus, laboratory experiments were conducted under varying electric heater input powers and operational states, with test data presented in Table 2.

Table 2. Comparison of test results during activated vs deactivated operation

Test condition	Electric heater deactivated		Electric heater activated				
	Input power	Heating capacity	Input power	Heating capacity	Electric heater power	Heating capacity	Relative error
	kW	kW	kW	kW	kW	kW	%
1	5.48	12.38	5.49	12.61	0.03	11.89	−5.7
2	5.56	12.54	5.67	12.59	0.05	13.47	6.9
3	5.42	11.87	5.49	12.05	0.07	12.76	5.9
4	5.72	12.43	5.78	12.65	0.1	12.21	−3.5
5	5.55	12.01	5.64	12.21	0.13	12.65	3.5
6	5.45	12.35	5.64	12.64	0.15	12.19	−3.6
7	5.87	12.41	6.01	12.56	0.2	12.75	1.5

Each 10-min test cycle comprised 5-min intervals with the electric heater activated and deactivated respectively, with results representing averaged values over each 5-min operational period. Table 2 demonstrates that measurement precision improves significantly with increased heater power. Concurrently, heater activation marginally elevates unit input power and heating capacity, the maximum observed increase in unit input power was limited to 3.4%, while the heating capacity exhibited a maximum increase of only 2.3%. This phenomenon is attributed to elevated superheat levels induced by the heater's thermal influence during operation, which modifies system operating conditions and consequently increases input power. Therefore, when equivalent precision is achievable between outdoor air enthalpy difference methods and electrically heated refrigerant enthalpy difference method, the former is recommended due to its reduced systemic impact, yielding test results that more accurately reflect actual operating conditions.

4.3 Multi-Condition Field Performance Testing

Field performance testing was conducted on a refrigerant-direct radiant system. Since there was no water circulation system in the setup, the water-side heat metering method cannot be used as a benchmark for comparison. As verified in the laboratory testing discussed earlier, the compressor performance curve method demonstrates high testing accuracy under conditions of compressor suction superheat. Therefore, in the field performance testing, the results obtained from the compressor performance curve method were used as the benchmark for a comparative analysis of the outdoor air enthalpy difference method and the electrically heated refrigerant enthalpy difference method.

During field performance testing, long-term measurements were conducted. To facilitate analysis, the operating conditions were categorized into three types based on test duration and characteristics: (1) Typical frosting conditions (representing a single frosting-defrosting cycle under standard frosting conditions); (2) Continuously variable conditions (where the unit experiences three consecutive frosting-defrosting cycles); and (3) Long-term operating conditions (continuous operation for 7 days).

During the typical frosting condition test, compared to the compressor performance curve method, the electrically heated refrigerant enthalpy difference method yielded an average relative error of −1.43% (range: −11.0% to 10.0%), while the outdoor air enthalpy difference method exhibited an average relative error of −3.47% (range: −10.14% to 13.95%). (Note: Data during defrosting periods were excluded due to the system operating in a non-steady-state condition.)

Under the continuously variable conditions, both measurement methods maintained accuracy within ±11.0%. The outdoor air enthalpy difference method exhibited an average relative error of −3.98%, while the electrically heated refrigerant method achieving −0.47%. During long-term operating conditions, the electrically heated refrigerant method showed an average error of 2.14% (range: −3.96% to 6.0%), compared to the outdoor air method, which had a higher average error of 4.86% (range: 1.0% to 10.0%).

5 Summary Statement

Based on laboratory test data analysis, both the outdoor air enthalpy difference method, compressor performance curve method and the electrically heated refrigerant enthalpy difference method meet the engineering accuracy requirement of ±15%, demonstrating applicability for field performance testing of ASHP refrigerant-direct radiant systems. When considering both measurement accuracy and fluctuation range of errors, the compressor performance curve method achieves the highest precision, followed by the electrically heated refrigerant enthalpy difference method, with the outdoor air enthalpy difference method exhibiting the lowest accuracy.

Although the compressor performance curve method offers superior accuracy, its reliance on compressor test data introduces limitations. Factors such as compressor wear and performance degradation during operation may lead to significant deviations from actual conditions. Conversely, the outdoor air enthalpy difference method provides a non-intrusive measurement that more authentically reflects the unit's real-world operating conditions. The electrically heated refrigerant enthalpy difference method may slightly perturb system operation due to its heating intervention. For field evaluations aiming to capture the system's true operational state, the outdoor air enthalpy difference method is recommended.

The outdoor air enthalpy difference method is highly sensitive to outdoor air conditions and evaporator heat exchange performance, making it particularly effective at detecting changes in the evaporator's operating state. During testing, this method was found to be capable of evaluating frost -induced performance losses. It can therefore be applied in future studies to quantitatively assess energy losses caused by evaporator frosting, and to optimize frosting detection strategies and defrosting logic for the unit.

References

1. Li, Z.X.: Analysis of current application and development prospects of air-source heat pump air conditioning technology. Neijiang Sci. Technol. **46**(5), 101–102 (2025)
2. Torekov, M.S., Bahnsenb, N., Qvale, B.: The relative competitive positions of the alternative means for domestic heating[J]. Energy. **32**, 627–633 (2007)
3. Li, T.B.: Research on Direct-Condensation Air-Source Heat Pump Floor Heating System Master's Thesis. Guangdong University of Technology (2016)
4. Huang, W.Y., Ding, L.R., Wang, B.L., et al.: Research progress on field performance testing techniques for air source heat pumps*[J]. Heat. Vent. Air Cond. **47**(7), 1–10 (2017)
5. Zeng, Z.C., Wei, X.L.: Energy Efficiency and Floor Heat Transfer in Direct Radiant Floor Heating Systems Using Air-Source Heat Pumps M.S. Thesis. Zhengzhou University, Zhengzhou (2010)
6. Jactard, A., Li, Z., et al.: Investigation of Methods for Evaluation of Heat Pump Performance [D]. Chalmers University of Technology, Göteborg (2011)
7. Air-Conditioning, Heating and Refrigeration Institute: Standard for Performance Rating of Positive Displacement Refrigerant Compressors and Compressor Units: ANSI/AHRI540-2004[S], pp. 3–5. Air Conditioning, Heating, and Refrigeration Institute, Arlington (2004)
8. Dabiri, A.E., Rice, C.K.: A compressor simulation model with corrections for the level of suction gas superheat. ASHRAE Trans. **87**(Part 2), 771–782 (1981)
9. Marti, J., Mauersberger, K.: A survey and new measurements of ice vapor pressure at temperatures between 170 and 250K[J]. Geophys. Res. Lett. **20**(5), 363–366 (1993)
10. Han, L., Shao, S., Wang, Z., Yang, Q., Xu, Z., Li, J., Suo, J.: A new method for field test of the heating capacity of air source heat pumps. Flow Meas. Instrum. **85**, 102168 (2022)
11. GB/T 25127.1-2020: Low Ambient Temperature Air Source Heat Pump (Chilled Water) Units—Part 1: Heat Pump (Chilled Water) Units for Industrial, Commercial and Similar Purposes[S]. China Standards Press, Beijing (2020)
12. Ai, S.H., Wu, C.B., Shi, W., et al.: Performance of low ambient temperature air source heat pump units during winter in Beijing [J]. Heat. Vent. Air Cond. **45**(3), 52–58 (2015)
13. Zhang, G., Cao, Y., Nan, S., et al.: Operational performance and problem analysis of low ambient temperature air source heat pump water heating units in winter [J]. Build. Technol. Dev. **43**(11), 158–163 (2016)

Turbulence Control Simulation Inside the Defoulant Hydrocyclone for Sewage Source Heat Pump

Tao Song, Jing Li, Xin Yang, Qisheng Yang, Changhua Hu, and Bo Wang(✉)

Rocket Force University of Engineering, Xi'an, People's Republic of China
53754924@qq.com

Abstract. The heat energy in the sewage can be recovered using a heat pump and utilized for cooling or heating. However, the problems of heat-exchanger blockage and scaling have not been adequately addressed. A defoulant hydrocyclone (DFH) has the advantages of fewer moving components, a simple structure, and high separation efficiency. The separation of particulate matter primarily depends on the external swirling flow that adheres to the wall; however, the external swirling flow is easily converted into an internal swirling flow, causing separation failure. We conducted a simulation to investigate the influence of installing a conical surface (CS) at the locus of zero vertical velocity (LZVV) on separation performance. The numerical simulation results were in good agreement with the experimental data. Simulation studies on the size of the CS revealed that longer CS resulted in a stronger suppression effect on turbulence; the turbulence caused by the transition from external to internal swirl flow was weakened, thereby reducing the system energy consumption. However, the particle trajectory and residence time indicate that a longer CS caused a stronger particle binding effect, making it difficult to separate particles in a timely manner. We changed the axial position of the fixed CS and found that turbulence was most intense at the bottom of the DFH, and the pressure and pressure loss were minimized when the inner cone was installed at a distance of −100 mm from the column cone interface.

Keywords: Defoulant hydrocyclone · Conical surface · Locus of zero vertical velocity · Heat energy · Sewage

1 Introduction

In the current era of increasing global energy consumption, 72% of global primary energy consumption is lost following conversion, with 63% of the waste heat flowing occurring below 100 °C. There exists a need to shift to less valuable energy sources for heating and cooling (reducing energy demand by a quarter) [1]. If heat pumps are used for local heat recovery in 20% of buildings, the heat demand of the buildings decreases by 4%, and the total heat loss in the network decreases by 3% [2]. The deposition of dirt on the heat-transfer surface can reduce the thermal performance of the heat exchanger and increase the pressure drop. This reduces the overall performance of the heat pump,

© The Author(s), under exclusive license to Springer Nature Singapore Pte Ltd. 2025
L. Ni et al. (Eds.): CCHVAC 2025, ESE, pp. 209–216, 2025.
https://doi.org/10.1007/978-981-95-3253-7_23

resulting in higher operating costs [3]. A effective anti-scaling technology is crucial to ensuring the efficient operation of wastewater source heat pump systems. The working of a defoulant hydrocyclone (DFH) applied to extract heat from wastewater through geometric parameter design is as follows. After passing through the grille to remove large debris, the wastewater enters the DFH. The particles were centrifuged, during which they moved toward the wall and flowed out of the underflow outlet of the DFH. The particle-free wastewater flowed upward from the overflow outlet along the center and entered the heat exchanger (evaporator) of the wastewater source heat pump system. After heat exchange, the overflow wastewater is introduced into the underflow outlet, where it absorbs and washes away the particles flowing out from the underflow outlet [4, 5]. Therefore, DFH can temporarily separate contaminants from the sewage, and subsequently extract the heat from the purified sewage without altering the nature of the sewage [6]. The primary aspect of this process is that the wastewater flowing out from the overflow port contains fewer particles and has sufficient kinetic energy to pass through the wastewater heat exchanger and rinse the underflow. A locus of zero vertical velocity (LZVV) exists in the hydrocyclone, which is considered to be the interface between the underflow and overflow [7]. The region outside the LZVV corresponds to a downward external swirl, whereas the central portion of the LZVV is characterized by an upward swirl. However, the precise location of the LZVV within the hydrocyclone and associated radial particle migration at the LZVV remain ambiguous. We have previously demonstrated that inserting a 0.5 mm-thick insert (conical surface, CS) at the midpoint radius of the DFH (a position analogous to the LZVV identified by Kelsall [8]) can effectively regulate the turbulence intensity of the DFH. The energy consumption of DFH decreased by approximately 40% due to the presence of CS, whereas the separation efficiency increased by approximately 5% [9]. However, we conducted a comprehensive study using numerical simulations due to the difficulty of changing the CS structure during the experiment. A simulation was conducted with respect to the size, position, and response of the CS at the LZVV to analyze the influence of the CS on the internal turbulence intensity, axial velocity, radial velocity, pressure field, and particle trajectory of the DFH. Based on these findings, we proposed an optimal design for the size and installation position of the CS, thereby providing a valuable reference for designing efficient wastewater heat recovery heat exchangers.

2 Simulation Methodology

2.1 Numerical Model and Mesh Strategy

The RSM employed has been extensively utilized to simulate the flow field of hydrocyclones. A numerical simulation established a model consistent with the geometric parameters of the experimental device. The detailed component names and geometric dimensions are shown in Fig. 1(a). The primary structure of the DFH consists of cylindrical, conical, and ejection sections. We employed high-quality six-sided meshes to model the DFH. The geometric model was used for grid-independence verification, and a comparison was made using the split ratio as the calculation result indicator. The results are shown in Fig. 1(b). An increase in the number of grids from approximately 800,000 to approximately 1.6 million reduced the split ratio by approximately 3%. A continuous

increase in the number of grids until reaching four million fluctuated the split ratio by no more than 1%. Therefore, considering the economic efficiency of the calculation, this study selected approximately 1.6 million as the effective number of grids for the numerical simulation calculations, which was comparable to the number of grids in other models.

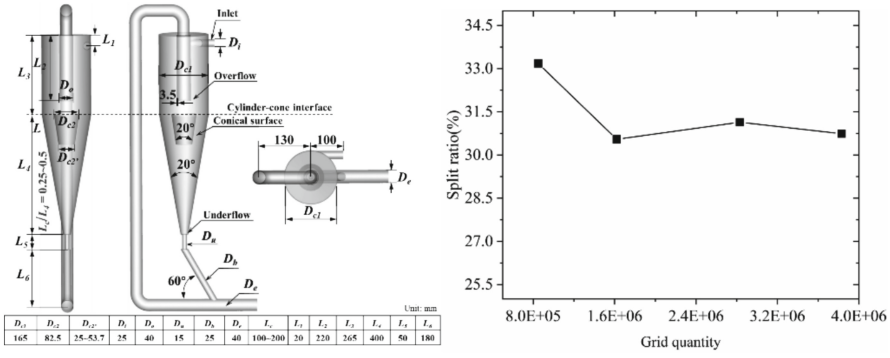


Fig. 1 Model parameters and grid-independence verification

2.2 Experiment for Model Verification

The parameters of the DFH model in this study were consistent with those of the PIV flow-field test model. However, in practice, a DFH evaluated using PIV was synthesized by firing glass as a whole, and its forming parameters may not be completely consistent with design parameters. The results of the split ratio at the same inlet speed of 4 m/s are shown in Fig. 2(a). The results differed by approximately 3%. This also proved that the difference between the CFD and experimental test results was relatively small. The axial velocity fields obtained from the PIV tests and numerical simulations are shown in Fig. 2(b). Both presented three primary types of flows in the axial velocity field (downward flow at the near-wall region, upward flow at the center, and downward flow generated at the center bottom owing to the ejector effect) in terms of the flow field structure. The maximum positive axial velocity occurred in the overflow pipe in both cases in terms of velocity distribution, and the maximum negative axial velocity was generated at the outer wall and underflow outlet, both of which demonstrated clear boundaries, with the LZVV near the wall (located in the area of the blue-to-red transition) in Fig. 2(b). A comparison of the radial velocities is presented in Fig. 2(c). Both demonstrated the rotational movement characteristics of the flow field inside the cyclone. The axial velocity alternated sequentially, sometimes to the left, and sometimes to the right. However, the intensity and number of transitions were inconsistent. As analyzed for the axial velocity, this could be attributed to the unequal lengths of the pipes connected to the overflow and underflow outlets. In the experiment, a rubber tube was used for convenient connection and was deformed under water pressure.

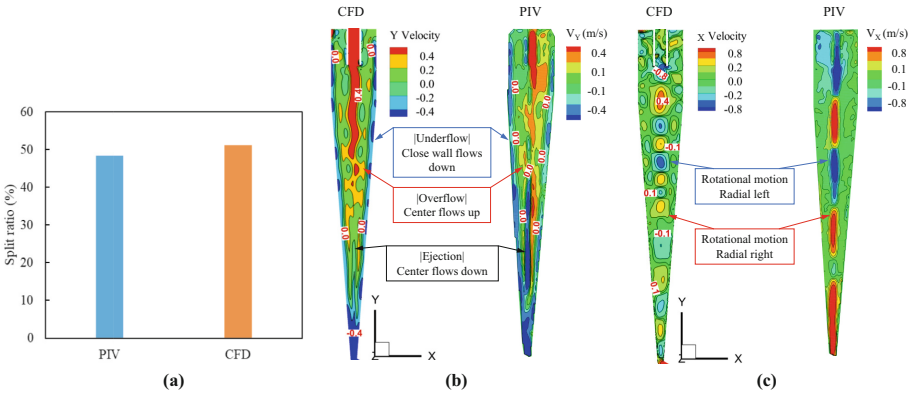


Fig. 2 The split ratio, axial velocity and radial velocity field of CFD and PIV

3 Results and Discussion

3.1 Simulation of CS Size

The CS is the solidification of LZVV. The conical part in the LZVV is CS symmetrical to the central axis. However, the position of the bottom remains unknown. We investigated the influence of the vertical length of the CS along the LZVV on separation performance. Two CS are demonstrated in Fig. 3, with length ratios to the conical component being 0.25 and 0.5. The results of simulating two different sizes of CS and comparing them with DFH without a CS are shown in Fig. 3.

The pressure distribution results are demonstrated in Fig. 3(a1–a3). When the DFH contained CS, the pressure drop decreased significantly, which was consistent with the experimental results. The CS isolated the underflow and overflow from each other, reducing the pressure loss caused by mutual interference. Moreover, larger CS caused a more significant isolation effect, as shown in Fig. 3(a2–a3), and smaller pressure. Combining the experimental results from the pressure drop analysis, at the bottom of the LZVV, after the overflow and underflow mix, the distance to the bottom was small, and the narrow space caused intense turbulence, increasing the pressure drop. However, the increase in CS caused the internal spiral flow to increase the friction on the inner wall and the external spiral flow to increase the friction on the outer wall, which was equivalent to an increase in the flow resistance inside the DFH. Therefore, longer CS caused a greater increase in ΔP_1, ΔP_2, and ΔP.The axial velocity distribution is shown in Fig. 3(b1–b3). The presence of the CS created differences in the axial velocity between the overflow and underflow. Smaller CS led to greater downward velocity of the underflow that intricately adhered to the DFH wall, and the upward velocity of the overflow also increased. The axial velocity distribution is shown in Fig. 3(c1–c3). The presence of CS restricted the radial migration of the fluid, and longer CS caused greater restriction. Reduced CS caused a significant difference between the left and right migration velocities at the bottom of the CS, as shown in Fig. 3(c3).

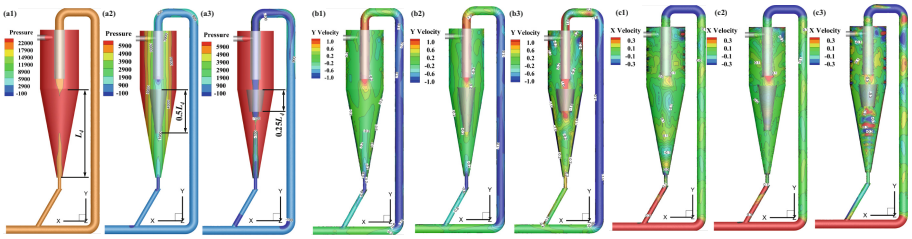


Fig. 3. Filled contour plot showing the influence of CS size on pressure, axial velocity, and radial velocity

3.2 CS Position Simulation

A study on the CS size indicated that longer CS led to a stronger turbulence suppression effect. However, it could not accurately reflect the position with the most significant impact on the turbulence. Therefore, two positive positions and four negative positions were simulated using a small CS that moved along the central axis (vertical direction) within the flow field to explore the main position where the CS affected the turbulence. The pressure field distributions at the six positions are shown in Fig. 4. As shown in **Fig. 4**(a), at the column–cone interface and above (0 to +50 mm), the pressure first decreased and subsequently increased as the CS position increased. This indicated that the turbulence intensity was stronger below a certain distance from the overflow pipe than at the bottom of the overflow pipe or the column–cone interface. Below the column–cone interface (−25 to −150 mm), the pressure first decreased as the CS position decreased, and subsequently increased. As shown in **Fig. 4**(b), the total pressure drop exhibited the same pattern. This indicated that the turbulence was more intense further below the interface, and the decrease in pressure due to the lowering of the CS position effectively suppressed the turbulence and reduced the pressure drop. The increase at −150 mm was because the CS came into contact with the inner wall of the DFH, blocking the flow channel along the wall, increasing the flow resistance and pressure. A comparison of the positive minimum pressure position +25 mm and the negative minimum pressure position −100 mm revealed that the pressure at −100 mm was the lowest. Therefore, the CS, which was most effective in suppressing turbulence, was at the bottom of the cone. In the forward position, as the distance increased, the overflow rising speed at the center gradually decreased. This is because higher CS caused turbulence constraints on the lower part (**Fig. 4**(c)). Under the centrifugal force, more fluid flowed outward, joined the outer vortex, and flowed downward. The split ratio increased (**Fig. 4**(d)). In the negative position (except for −150 mm), the overflow upward speed weakened, and the underflow downward speed strengthened as the CS moved downward. This was because the turbulence was more intense toward the bottom of the cone. The downward movement of the CS hindered the transformation of the outer vortex into the inner vortex, and more fluid flowed downward between the inner wall of the cone and the CS, eventually flowing out from the underflow port and increasing the underflow, decreasing the overflow, and increasing the split ratio. However, at −150 mm, the contact between the CS and the cone base hindered the downward flow of the outer vortex, and the fluid started vibrating under the strong centrifugal force. It climbed along the outer wall of

the CS and finally entered the center of the flow field. Under the action of the overflow, it climbed along the overflow pipe and was discharged.

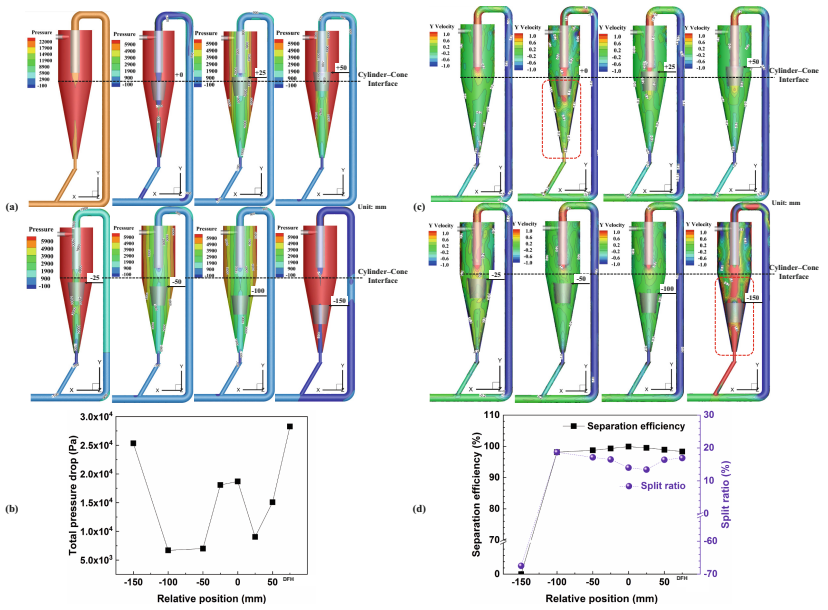


Fig. 4 Filled contour plot showing the influence of the CS position on pressure, axial velocity, separation efficiency, split ratio and at different CS positions

It is shown in Fig. 5 of the radial velocity fields at different CS positions and CS position movement on the particle movement trajectory. After the CS left the interface between the cylinder and the cone (except at −150 mm), the radial velocity decreased. When the CS increased from +25 to +50, its radial velocity remained unchanged in **Fig. 5**(a); the same was true for the negative position. This was because radial motion mainly occurred at the center. After the CS left the interface, it fixed the periphery of the inner vortex either upward or downward, thereby causing less disturbance to the inner vortex. At −150 mm, the flow field became disordered due to the blockage of the descending channel of the outer vortex, thus increasing the radial motion. The trajectory analysis revealed that the presence of CS complicated the flow of particles within the DFH. Compared to a short CS, a long CS exerted a greater restraint on the particles, and it took longer for the particles to enter the CS for separation in **Fig. 5**(b).

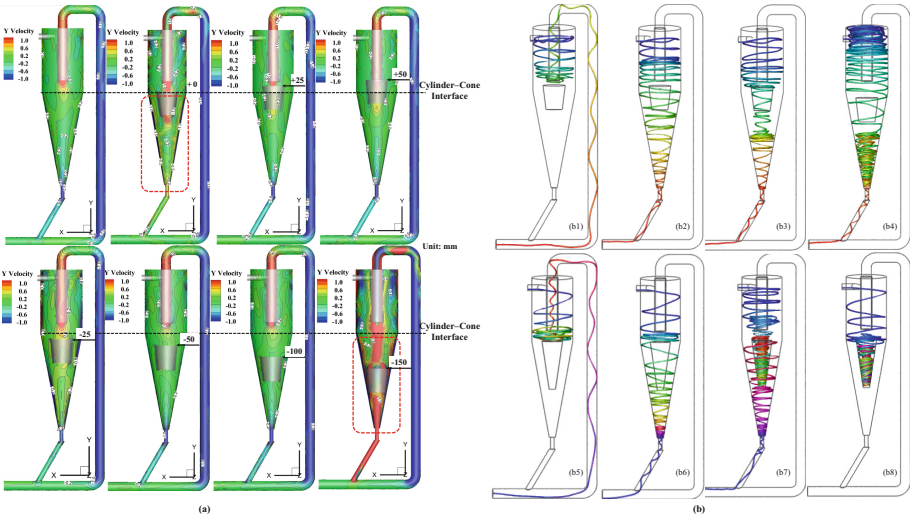


Fig. 5. Filled contour plot showing the influence of (**a**) CS position on radial velocity and (**b**) CS size on particle trajectories

4 Conclusions

We employed numerical simulation and experimental comparison. Based on the characteristics of the numerical model, such as ease of modification, ease of adjusting operating conditions, and ability to study local flow, by conducting research on the size and position of the CS at the LZVV location, the pressure field, velocity field, and particle motion trajectories within the DFH were analyzed under different CS parameters. The results demonstrated

1. The longer CS (with a length-to-length ratio of the DFH cone part being approximately 0.5) exerted a stronger inhibitory effect on turbulence. The turbulence caused by the transition from the outer swirling flow to the inner swirling flow was weakened, causing a lower pressure drop in the DFH compared with traditional hydrocyclones.
2. Installing a CS that was very high or very low caused severe turbulence in the flow field. The turbulence was the most intense at the bottom of the DFH cone. Therefore, the CS should be installed at a distance of −100 mm from the interface between the column and the cone to achieve the minimum pressure and pressure loss.Acknowledgements

This work was supported by the National Natural Science Foundation of China (No. 52308127).

References

1. Forman, C., Muritala, I.K., Pardemann, R., Meyer, B.: Estimating the global waste heat potential. Renew. Sust. Energ. Rev. **57**, 1568–1579 (2016)

2. Golzar, F., Silveira, S.: Impact of wastewater heat recovery in buildings on the performance of centralized energy recovery – a case study of Stockholm. Appl. Energy. **297**, 117141 (2021)
3. Meesenburg, W., Aguilera, J.J., Kofler, R., Markussen, W.B., Elmegaard, B.: Prediction of fouling in sewage water heat pump for predictive maintenance. In: 35th International Conference on Efficiency, Cost, Optimization, Simulation and Environmental Impact of Energy Systems. ECOS (2022)
4. Ni, L., Tian, J., Zhao, J.: Feasibility of a novel de-foulant hydrocyclone with reflux for flushing away foulant continuously. Appl. Therm. Eng. **103**, 695–704 (2016)
5. Song, T., Tian, J., Ni, L., Shen, C., Yao, Y.: Experimental study on enhanced separation of a novel de-foulant hydrocyclone with a reflux ejector. Energy. **163**, 490–500 (2018)
6. Song, T., Tian, J., Ni, L., Shen, C., Yao, Y.: Experimental study on performance of a de-foulant hydrocyclone with different reflux devices for sewage source heat pump. Appl. Therm. Eng. **149**, 354–365 (2019)
7. Bradley, D.: The Hydrocyclone. Pergamon Press, London (1965)
8. Kelsall, D.F.: A further study of the hydraulic cyclone. Chem. Eng. Sci. **2**, 254–272 (1953)
9. Song, T., Tian, J., Ni, L., Shen, C., Yao, Y.: Experimental study of de-foulant hydrocyclone performance with a conical surface. Powder Technol. **366**, 283–292 (2020)
10. Zhang, Z.-W., Li, Q., Zhang, Y.-H., Wang, H.-L.: Simulation and experimental study of effect of vortex finder structural parameters on cyclone separator performance. Sep. Purif. Technol. **286**, 120394 (2022)
11. Song, J., Wei, Y., Sun, G., Chen, J.: Experimental and CFD study of particle deposition on the outer surface of vortex finder of a cyclone separator. Chem. Eng. J. **309**, 249–262 (2017)
12. Zheng, Y., Ni, L.: Numerical study on particles separation using a cyclone enhanced by shunt device: effects of cylinder-to-cone ratio and vortex finder-to-cylinder ratio. Powder Technol. **408**, 117767 (2022)
13. Zheng, Y., Liu, X., Ni, L.: Numerical investigation on particles separation using an enhanced cyclone with shunt device: effect of vortex finder lengths. Chem. Eng. Process. Process Intensif. **181**, 109125 (2022)
14. He, F., Zhang, Y., Wang, J., Yang, Q., Wang, H., Tan, Y.: Flow patterns in mini-hydrocyclones with different vortex finder depths. Chem. Eng. Technol. **36**, 1935–1942 (2013)
15. Zhang, Y., Cai, P., Jiang, F., Dong, K., Jiang, Y., Wang, B.: Understanding the separation of particles in a hydrocyclone by force analysis. Powder Technol. **322**, 471–489 (2017)
16. Ji, L., Kuang, S., Qi, Z., Wang, Y., Chen, J., Yu, A.: Computational analysis and optimization of hydrocyclone size to mitigate adverse effect of particle density. Sep. Purif. Technol. **174**, 251–263 (2017)

Absorption Chiller Design for Liquid Cooling in Data Centers

Zixuan Peng, Haojun Duan, and Xiaoyun Xie(✉)

Building Energy Research Center, Tsinghua University, Beijing, People's Republic of China
xiexiaoyun@tsinghua.edu.cn

Abstract. With the rapid development of artificial intelligence and cloud computing, data centers are shifting towards high power density and energy efficiency. Traditional air-cooling methods are reaching their limits in cooling high-power-density IT cabinets. Liquid cooling, with its superior efficiency, is poised to become the mainstream solution for reducing energy consumption and addressing these challenges. This study focuses on liquid-cooled data centers with high single-cabinet power density and auxiliary air cooling. A liquid-cooled data center absorption chiller is de-signed. The absorption chiller uses the high-temperature water from the chip side of the liquid-cooled data center as the driving heat source for the generator and the heat from other components as the low-temperature heat source for the evaporator. The heat in the absorber and condenser is removed by circulating water and discharged via an outdoor cooling tower, enabling heat distribution and waste heat utilization in the liquid cooling system. A computational program is developed to simulate the absorption ma-chine's operation. The numerical model simulates steady-state changes in chip temperature, component temperature, cooling water temperature, and dynamic conditions such as sudden external parameter changes. The absorption chiller performs better under high supply liquid temperature, high component temperature, and low cooling temperature conditions and maintains stability across multiple operational conditions. To address server load fluctuations in data centers, a device operation strategy based on solution storage is proposed. By altering the flow direction of the solution be-tween the concentrated and diluted solution tanks and the distribution of condensate water in the refrigerant water tank, the strategy provides solutions for high/low IT load and low natural temperature conditions. The study also explores energy quality storage under high heat supply and low-temperature cooling circulating water conditions.

Keywords: Data center · Absorption chiller · Numerical simulation

1 Introduction

The rapid increase in high-performance computing, data storage, and website workloads has led to a corresponding surge in energy consumption of data centers. In 2018, the global energy consumption of data centers was estimated to be 205 TWh, accounting for approximately 1% of the world's total electricity consumption [1], and it is projected

© The Author(s), under exclusive license to Springer Nature Singapore Pte Ltd. 2025
L. Ni et al. (Eds.): CCHVAC 2025, ESE, pp. 217–228, 2025.
https://doi.org/10.1007/978-981-95-3253-7_24

to grow to more than 800 TWh by 2026 [2]. Meanwhile, the requirements for energy efficiency in data centers are continuously increasing. In China, the average Power Usage Effectiveness (PUE) of data centers should be lower than 1.5 by the end of 2025, and the PUE of newly built, reconstructed, and expanded large and ultra-large data centers should be lower than 1.25. Additionally, the power density per unit in data centers is also continuously increasing, with modern IT equipment having a power density of 20 kW or more per rack. It is expected that the scale, power consumption, and power density of data centers will continue to rise in the future. Air cooling technology, which already has disadvantages such as high mechanical energy consumption and large floor space, can no longer adapt to the development trend of data centers. Liquid cooling technology with strong heat dissipation capability and high cooling efficiency will become an important direction for future development.

Data centers equipped with liquid cooling systems can better meet the requirements of high-density cabinets. Liquids have far superior thermal conductivity compared to air. Maximum capacity of traditional data centers with air cooling air is 20 to 30 kW per station; However, liquid cooling can reach 100 kW [3]. According to the contact state of the liquid with servers and other equipment during heat exchange, liquid cooling modes can be divided into direct single-phase liquid cooling, direct two-phase liquid cooling, and indirect liquid cooling, which can be further subdivided into cold plate cooling, heat pipe cooling, immersion liquid cooling, spray liquid cooling, etc. [4]. Currently, cold plate cooling accounts for the main part of liquid cooling in data centers, and other liquid cooling methods also have a certain research foundation and have made breakthrough progress. Liquid cooling has obvious advantages in reducing the PUE of the cooling system and addressing the challenges of high-power density cabinets.

In the field of absorption and adsorption cooling, Pan et al. [5] investigated the application of a silica gel–water adsorption cooling system for waste heat utilization in data centers and found that, compared to solar cooling applications, adsorption cooling holds greater potential for waste heat utilization in data centers. The Ebrahimi team [6, 7] attempted to use absorption cooling for waste heat recovery in data centers and also designed a waste heat recovery system for data centers based on the organic Rankine cycle.

Aiming at the characteristics of high average power per cabinet in liquid-cooled data centers and that the current mainstream liquid-cooled data centers still adopt air cooling + liquid cooling for heat dissipation, this study uses an absorption chiller to utilize the waste heat of the liquid cooling system in data centers. The high-temperature hot water measured by the chip is used as the high-temperature driving heat source, the heat generated by other components is used as the low-temperature heat source, and the heat from the absorber and condenser is discharged by the cooling tower. Compared with the general architecture, integrating the two cooling systems of air cooling and liquid cooling into a liquid-cooled absorption chiller facilitates management and operation and maintenance, realizing the integration of the liquid cooling system. Meanwhile, the chiller of the air cooling module is eliminated, reducing the power consumption of the chiller. At the same time, in order to cope with the load fluctuations of servers in

data centers, energy storage and flexible deployment are achieved by setting up concentrated/dilute solution tanks and refrigerant water tanks and formulating corresponding operation strategies.

2 Equipment and Model Description

Aiming at the characteristics of traditional single-phase cold plate liquid-cooled data centers (i.e., high power density per cabinet, liquid cooling for chip heat dissipation, and air cooling for other components), the absorption chiller adopted in this study is a single-effect lithium bromide absorption refrigeration unit. Its specific configuration and connections are illustrated in Fig. 1, with heat exchange processes in each component described as follows: The generator side utilizes high-temperature hot water generated by high-heat-density components (CPUs, GPUs) as the high-temperature driving heat source, corresponding to the liquid-cooled plate heat dissipation part of traditional single-phase cold plate systems and accounting for 70% of the total heat load. Meanwhile, the evaporator side employs heat from the air-conditioning return air after exchanging heat with low-heat-density components (other components); the hot water obtained from the water-air heat exchanger using the return air enters the evaporator to provide a low-temperature heat source, corresponding to the air-cooled heat dissipation part of traditional systems and accounting for 30% of the total heat load. For the absorber side, an external cold source (e.g., an open cooling tower) is used for heat dissipation: the low-temperature cooling water from the tower cools the circulating water through a plate heat exchanger before entering the absorber for heat exchange, and the heated water then flows into the condenser. Similarly, the condenser side shares the same external cold source; the circulating water from the absorber releases heat in the condenser, then enters the plate heat exchanger to exchange heat with the tower water after being heated, completing the cooling water cycle.

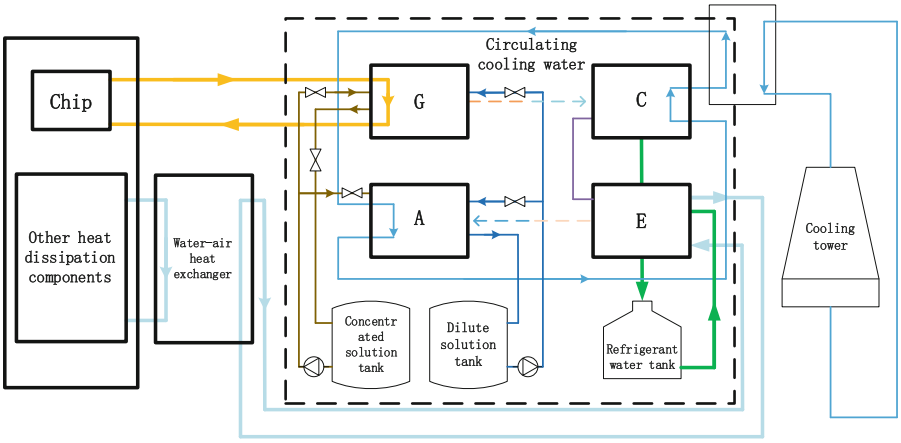


Fig. 1. Schematic diagram of absorption chiller for data center liquid cooling

To address server load fluctuations in the data center, the system incorporates concentrated solution tanks, dilute solution tanks, and refrigerant water tanks to enable energy storage and regulation. During periods of high chip power, the system initiates an energy storage process: excess heat from the generator is converted into concentrated solution stored in the concentrated tank, while excess condensate water is stored in the refrigerant tank. Conversely, during low-load periods, the system activates an energy release process by feeding concentrated solution and refrigerant water from the tanks into the absorber to compensate for reduced solution concentration and water vapor caused by insufficient server loads. Moreover, when the temperature of the circulating cooling water is low, the generator can produce a higher-concentration solution, allowing the system to convert excess energy into chemical potential energy of higher quality.

The governing equations of the system primarily include mass balance equations, energy conservation equations, and heat transfer equations for the absorber, generator, condenser, evaporator, internal plate heat exchangers, and energy storage devices. These equations form the basis for analyzing and optimizing the system's thermal performance under dynamic operating conditions. The numerical models of key components are introduced as follows.

2.1 Absorber and Generator

The solution circuit of a lithium bromide absorption chiller primarily consists of an absorber and a generator. For the internal solution circulation between these components, a counter-current heat and mass transfer grid differential model is employed for numerical simulation. Taking the generator as an example, the heat and mass transfer processes between the solution and water are discretized into multiple grids. Within each grid, the heat and mass transfer processes are assumed to satisfy Eqs. (1), (2), and (3).

In the equation, $Q_{g[i]}$ denotes the energy exchanged between the two fluids within the i-th grid, K_g represents the heat transfer coefficient of the generator, and A_g signifies the heat transfer area of each grid after discretizing the generator. $T_{wg[i]}$ and $T_{sg[i]}$ denote the hot water temperature and the dilute lithium bromide solution temperature at the i-th grid, respectively. m_{wg} denotes the mass flow rate of hot water, $T_{wg[i]}$ is the hot water temperature at the i-th grid, $h_{sg[i]}$ is the specific enthalpy of the dilute lithium bromide solution at the i-th grid, $m_{sg[i]}$ is the mass flow rate of the dilute solution at the i-th grid, $d_{mg[i]}$ is the evaporation rate of water vapor from the solution at the i-th grid, and $h_{g,steam[i]}$ is the specific enthalpy of water vapor at the i-th grid.

$$Q_{g[i]} = K_g A_g \left(T_{wg[i]} - T_{sg[i]}\right) \tag{1}$$

$$Q_{g[i]} = m_{wg} * c_{pw} * \left(T_{wg[i+1]} - T_{wg[i]}\right) \tag{2}$$

$$Q_{g[i]} = m_{sg[i+1]} * h_{sg[i+1]} - m_{sg[i]} * h_{sg[i]} + dm_{g[i]} * h_{g,steam[i]} \tag{3}$$

During the heat and mass transfer processes of the dilute lithium bromide solution, the mass of the solute remains constant. The flow rate entering a grid is equal to the sum of the flow rate exiting the grid and the evaporated water vapor, ensuring mass conservation

of the solution and solute across adjacent grids, as described by Eqs. (4) and (5). Here, $x_{g[i]}$ denotes the concentration of the dilute lithium bromide solution at the i-th grid.

$$m_{sg[i+1]} = m_{sg[i]} - dm_{g[i]} \tag{4}$$

$$m_{sg[i]} * x_{g[i]} = m_{sg[i+1]} * x_{g[i+1]} \tag{5}$$

2.2 Condenser and Evaporator

In the refrigerant circuit of a lithium bromide absorption chiller, the condenser and evaporator constitute the primary components. Taking the condenser as an example, during the refrigerant cycle within the condenser, it is assumed that the pressure *Pc* and temperature *Tc* remain constant during the heat exchange process between the water vapor (saturated condensate) and the circulating cooling water. Here, the condenser pressure *Pc* is equal to the generator pressure *Pg*, and the condensation temperature *Tc* corresponds to the saturation temperature of water vapor at *Pc*. The heat and mass transfer processes between the water vapor and cooling water are governed by the following equations:

$$Q_c = K_c * A_c * dT_c \tag{6}$$

$$Q_c = m_{wc} * C_{pw} * \left(T_{wc_{out}} - T_{wc_{in}}\right) \tag{7}$$

$$Q_c = d_{mc} * \left(h_{c,steam} - h_{c,water}\right) \tag{8}$$

$$dT_c = \frac{\left(T_{wc_{out}} - T_{wc_{in}}\right)}{\left(\ln\left(T_c - T_{wc_{in}}\right) - \ln\left(T_c - T_{wc_{out}}\right)\right)} \tag{9}$$

$$d_{mc} = d_{mg} = \sum_1^n dm_{g[i]} \tag{10}$$

In the equation, Q_c denotes the condensation heat released during the phase change of water vapor in the condenser, K_c represents the overall heat transfer coefficient of the condenser, A_c is the effective heat transfer area, and dT_c is the logarithmic mean temperature difference (LMTD) between the condensing vapor (saturated condensate) and the cooling water. m_{wc} denotes the mass flow rate of the circulating cooling water, T_{wcin} and T_{wcout} represent the inlet and outlet temperatures of the cooling water, respectively. d_{mc} denotes the mass flow rate of condensed water vapor, which is equivalent to dm_g and equals the summation of water vapor evaporation rates $dm_{g[i]}$ from all generator grids. $h_{c,steam}$ and $h_{c,water}$ denote the specific enthalpies of water vapor and saturated liquid condensate, respectively.

2.3 Energy Storage Components

In this study, the energy storage components include the concentrated solution tank, the diluted solution tank, and the refrigerant water tank. For a simulation with a time step

of 1 s, the solution in the tanks at second $\tau + 1$ is equal to the mixture of the solution in the tanks at second τ and the solution entering/leaving the tanks (with negative mass for outflow). During the charging and discharging processes, the concentrated and diluted solution tanks satisfy the mass conservation equations for both the solution and the solute:

$$m_{s_{nong[\tau+1]}} = m_{s_{nong[\tau]}} + dm_{s_{nong[t]}} \tag{11}$$

$$X_{nong[\tau+1]} * m_{s_{nong[\tau+1]}} = X_{nong[\tau]} * m_{s_{nong[\tau]}} + X_{d_{nong[t]}} * dm_{s_{nong[t]}} \tag{12}$$

$$m_{s_{xi[\tau+1]}} = m_{s_{xi[\tau]}} + dm_{s_{xi[t]}} \tag{13}$$

$$X_{xi[\tau+1]} * m_{s_{xi[\tau+1]}} = X_{xi[\tau]} * m_{s_{xi[\tau]}} + X_{d_{xi[t]}} * dm_{s_{xi[t]}} \tag{14}$$

where $m_{snong[\tau]}$ and $m_{sxi[\tau]}$ represent the mass of the solution in the concentrated and diluted solution tanks at second τ, respectively; $dm_{snong[\tau]}$ and $dm_{sxi[\tau]}$ represent the mass of the solution entering or leaving the concentrated and diluted solution tanks at second τ, respectively; $X_{nong[\tau]}$ and $X_{xi[\tau]}$ represent the concentration of the solution in the concentrated and diluted solution tanks at second τ, respectively; and $X_{d,nong[\tau]}$ and $X_{d,xi[\tau]}$ represent the concentration of the solution entering or leaving the concentrated and diluted solution tanks at second τ, respectively.

The numerical simulation of the refrigerant water tank only considers the mass conservation equation, where $m_{water[\tau]}$ represents the mass of the refrigerant water in the refrigerant water tank at second τ, and $dm_{water[\tau]}$ represents the mass of the refrigerant water entering or leaving the tank at second τ.

$$m_{water_{[\tau+1]}} = m_{water_{[\tau]}} + dm_{water[\tau]} \tag{15}$$

3 Simulation Principles and Parameters

The rated operating conditions for the absorption chiller used in data center liquid cooling are as follows: the cabinet power is 54 kW; the inlet/outlet water temperatures on the liquid-cooled side of the chips are 45 °C/50 °C; the inlet/outlet water temperatures on the air-cooled low-temperature component side are 25 °C/28 °C; the cooling tower's chilled water outlet temperature is 24 °C. The internal heat exchanger and plate heat exchanger in the absorption chiller have a heat transfer end difference of 2 °C. The inlet temperature of the circulating cooling water is 26 °C, and the inlet temperature of the cooling water to the condenser is equal to the outlet temperature of the cooling water from the absorber. The relevant parameters of the absorption chiller, including the area of the internal plate heat exchanger and the heat transfer coefficients of each component, are shown in Table 1.

Based on the established model and the initial parameters set, simulations were conducted to investigate the steady-state operation of the absorption chiller under rated load conditions, with a COP value of 0.7. The simulation results for each equipment

Table 1. Design parameters for absorption chiller used in liquid cooling

	Absorber	Generator	Condenser	Evaporator	Plate heat exchanger
Heat Exchanger Area (m^2)	7.5	6.5	5	4	1
Heat Transfer Coefficient ($kW/m^2 \cdot K$)	0.8	1.5	1.8	1.5	1.5
External Water Flow (kg/s)	3.2	2.6	3.2	2.2	–
Internal Inlet Fluid Flow (kg/s)	0.579	0.585	0.0063	0.0063	0.579 /0.585

under rated load conditions are presented in Table 2. To simulate the variations in high-temperature driving heat sources and low-temperature heat sources, the inlet and outlet water temperatures and flow rates were adjusted. The flow rate on the chip side was varied within the range of 40% to 140%, with a temperature range of 48 °C to 60 °C, while the flow rate on the low-temperature component side was varied within the range of 70% to 120%, with a temperature range of 30 °C to 36 °C. The temperature of the cooling water varies from 20 °C to 28 °C.

For the energy storage/energy use conditions, the fluctuation time, the relevant parameters of the energy storage equipment, and the server load fluctuation conditions are set. The time step is set to 1 s, and the total duration is 1 h. The volume of the concentrated/diluted solution tanks is 400 L, and the volume of the refrigerant water tank is 15 L. The initial concentration of the concentrated solution tank and the diluted solution tank is determined according to the design conditions. During energy storage, the chip power first increases rapidly from 54 kW to 63 kW within 10 min, then maintains high chip power operation (for 40 min), and finally returns to the initial conditions (recovery time 10 min). During energy use, the chip power first decreases rapidly from 54 kW to 45 kW within 10 min, then maintains low chip power operation (for 40 min), and finally returns to the initial conditions (recovery time 10 min).

Table 2. Simulation results of main equipment under rated load conditions

Fluid Name	Temperature (°C)	Pressure (kPa)	Concentration (kg/kg)	Flow rate (kg/s)
Generator inlet solution	38.09	4.305	0.4287	1.17
Generator outlet solution	46.09	4.305	0.4332	1.16
Absorber inlet solution	37.42	2.618	0.4332	1.16
Absorber outlet solution	29.50	2.618	0.4287	1.17
Refrigerant vapor at condenser inlet	30.24	4.305	–	0.0123
Refrigerant water at condenser outlet	30.24	4.305	–	0.0123
Refrigerant water at evaporator inlet	21.82	2.618	–	0.0123
Refrigerant vapor at evaporator outlet	21.82	2.618	–	0.0123
Return water on the chip side	45.17	–	–	2.6
Inlet cooling water	26	–	–	6.4
Intermediate cooling water	27.94	–	–	6.4
Return water from low-temperature component	22.78	–	–	2.2

4 Result and Discussion

Initially, we examined the operational characteristics of the system in response to alterations in temperature and water flow rate on both the chip side and the low-temperature component side. The air-side cooling capacity decreases with the augmentation of both inlet water temperature and flow rate on the chip side. Elevated inlet temperature and flow rate engender a heightened concentration of the concentrated solution exiting the generator, concurrently fostering an escalation in high-pressure water vapor generation, which amplifies the cooling capacity on the generator side. The correlation between the increase in chip-side water flow rate and chip temperature with the rise in heat absorption by the generator, which is synonymous with liquid cooling heat dissipation, is an anticipated result. Notably, the system sustains a heat dissipation of approximately 35 kW even when the chip-side inlet water temperature is 48 °C and the chip-side water flow

rate is merely 40% of the rated flow. This underscores the absorption chiller's robust performance under low-flow and low-temperature conditions in the simulation (Fig. 2).

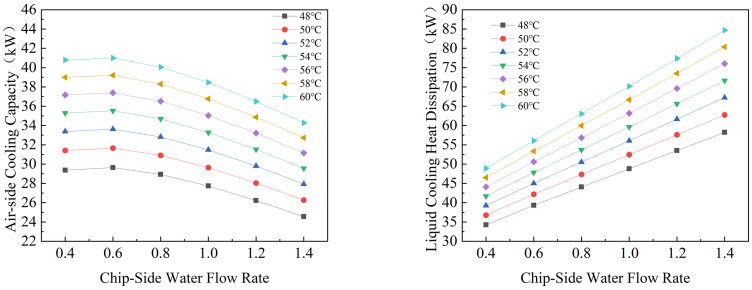


Fig. 2. Results of high-temperature heat source variations

The air-side cooling capacity increases with the rise in inlet water temperature and flow rate on the low-temperature component side. The increase in water flow rate and temperature on the low-temperature component side corresponds to an increase in liquid cooling heat dissipation. However, the magnitude of the increase in liquid cooling heat dissipation is smaller than that of the increase in air-side cooling capacity. The results demonstrate that the system exhibits good stability across multiple operating conditions and closely matches the design specifications (Fig. 3).

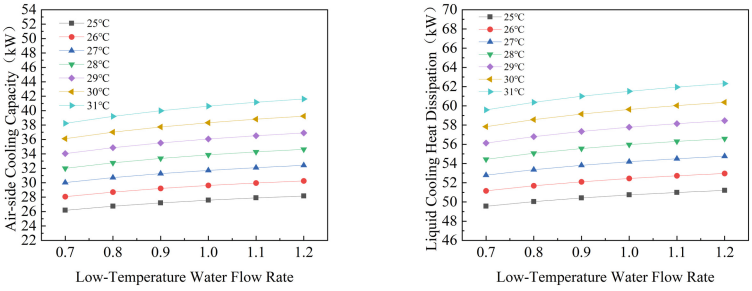


Fig. 3. Results of low-temperature heat source variations

The heat absorption and rejection of each component were investigated as the inlet temperature of the cooling water changed. When the inlet temperature of the cooling water increased from 23 °C to 29 °C, the cooling capacity decreased from 38.78 kW to 20.62 kW, and the generator load decreased from 62.25 kW to 41.58 kW. The heat absorption of the absorber remained consistent with the heat rejection of the generator, while the heat rejection of the condenser was in close agreement with the heat absorption of the evaporator. Under favorable meteorological conditions, the cooling tower can produce colder water, which lowers the inlet temperature of the circulating cooling water. This, in turn, provides more cooling capacity for the chips and low-temperature components. Conversely, when the cooling water temperature is higher, the heat dissipation to the data center is affected without a change in flow rate (Table 3).

Table 3. Impact of inlet cooling water temperature on heat absorption/rejection

Inlet cooling water temperature (°C)	Absorber heat rejection (kW)	Generator heat absorption (kW)	Condenser heat rejection (kW)	Evaporator heat absorption (kW)
23	62.25	62.99	39.36	38.75
24	58.79	59.47	36.26	35.7
25	55.33	55.95	33.17	32.66
26	51.88	52.45	30.09	29.63
27	48.44	48.95	27.03	26.61
28	45.01	45.46	23.98	23.61
29	41.58	41.98	20.94	20.62

Figure 4 illustrates the variations in heat of generation and vaporization, cooling water flow rate, and liquid volume within the energy storage components during the energy storage and energy utilization processes. During the energy storage process, the liquid volume in the concentrated solution tank gradually increases while that in the diluted solution tank decreases, with a change in liquid volume of approximately 150 L. The heat of generation and vaporization, as well as the cooling water flow rate, initially rise, then stabilize, and subsequently decline in accordance with the changes in chip power. In the refrigerant water tank, the storage process of refrigerant water is observed, with the refrigerant water volume increasing from 0 L to 8 L. During the energy utilization process, the liquid volume in the concentrated solution tank gradually decreases while that in the diluted solution tank increases, with a change in liquid volume of approximately 170 L. The heat of generation and vaporization, as well as the cooling water flow rate, initially decrease, then stabilize, and subsequently increase in accordance with the changes in chip power. In the refrigerant water tank, the utilization process of refrigerant water is observed, with the refrigerant water volume decreasing from 15 L to 7.8 L. These results demonstrate that the absorption chiller and energy storage equipment can operate effectively during the simulated low-chip-power energy utilization process, fulfilling the energy storage requirements.

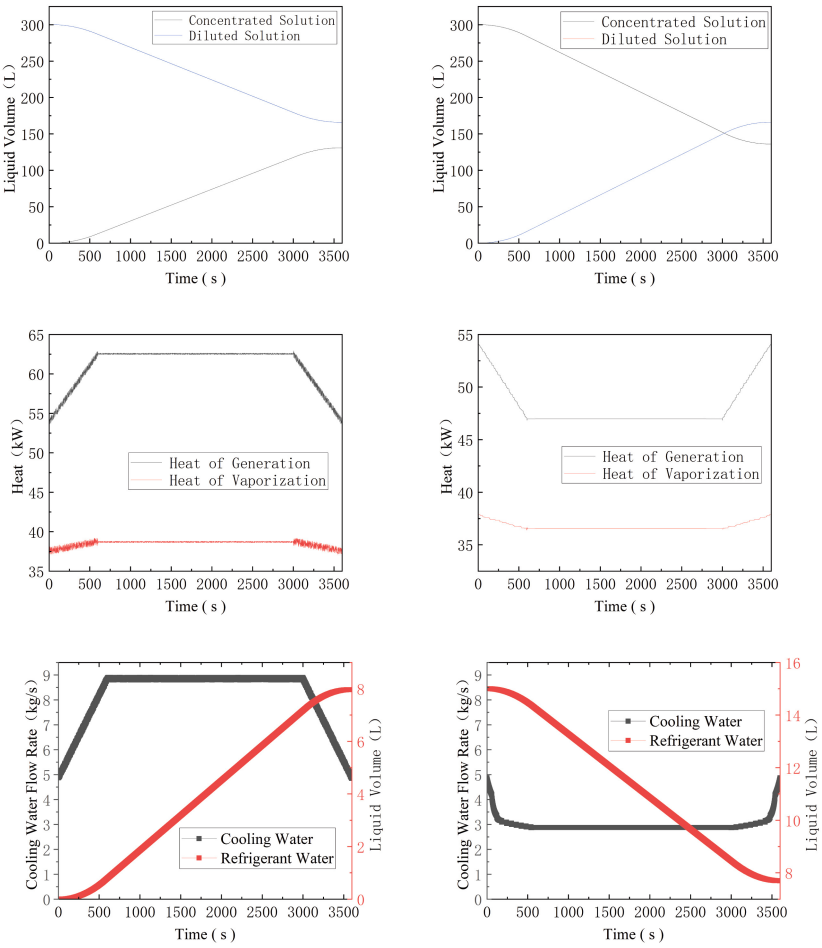


Fig. 4. Equipment parameter variations during energy storage/utilization processes

5 Conclusion

This study designed an absorption chiller for liquid cooling systems in data centers and conducted simulation analyses of its operation under multiple conditions as well as energy storage/usage processes. The main conclusions are summarized as follows:

1. The design of the absorption chiller for data center liquid cooling was completed, encompassing the relevant parameters of each component of the absorption chiller, the parameters of external cooling/heating sources, and the energy storage equipment. The interconnections and operational modes among the components were also elucidated.

2. A numerical model of an absorption chiller with an energy storage system was developed to simulate scenarios involving load fluctuations on both the liquid-cooled and air-cooled sides of a data center, as well as variations in the outlet water temperature of the cooling tower. Simulation results indicate that both the liquid-side heat dissipation and air-side cooling capacity of the system were maintained within reasonable ranges, demonstrating the system's robust stability across diverse operating conditions.
3. Based on the absorption chiller numerical model, simulations were conducted to investigate scenarios of server load fluctuations in data centers and reduced cooling tower outlet water temperatures. The simulation results indicate that the implementation of energy storage operation strategies can effectively stabilize the energy storage and usage processes within a 1-h timeframe.

References

1. Masanet, E., et al.: Recalibrating global data center energy-use estimates. Science. **367**, 984–986 (2020)
2. Eren Çam, Z.H.N.S.: Electricity 2024 – Analysis and Forecast to 2026[R]. International Energy Agency, 2024. Author, F., Author, S., Author, T.: Book title. 2nd edn. Publisher, Location (1999)
3. Yan, K.W., Lin, P.Y., Kuo, S.L.: Thermal challenges for HPC 3DFabric TM packages and systems. In: 2022 IEEE International Reliability Physics Symposium (IRPS), p. 4C-1. IEEE (2022)
4. Azarifar, M., Arik, M., Chang, J.-Y.: Liquid cooling of data centers: a necessity facing challenges. Appl. Therm. Eng. **247**(123112), 1359–4311 (2024)
5. Pan, Q.W., Peng, J.J., Wang, R.Z.: Application analysis of adsorption refrigeration system for solar and data center waste heat utilization[J]. Energy Convers. Manag. **228**, 113564 (2021)
6. Ebrahimi, K., Jones, G.F., Fleischer, A.S.: Thermo-economic analysis of steady state waste heat recovery in data centers using absorption refrigeration[J]. Appl. Energy. **139**, 384–397 (2015)
7. Ebrahimi, K., Jones, G.F., Fleischer, A.S.: The viability of ultra low temperature waste heat recovery using organic Rankine cycle in dual loop data center applications[J]. Appl. Therm. Eng. **126**, 393–406 (2017)

Smart Energy System

Decoupling Simulation of Thermal Processes with Two-Time Scale for Heated Buildings in Cold Regions

Wei Jiang[1,2] and Peng Wang[1,2(✉)]

[1] School of Architecture and Design, Harbin Institute of Technology, Harbin, China
cahnburg@hit.edu.cn

[2] Key Laboratory of Cold Region Urban and Rural Human Settlement Environment Science and Technology, Ministry of Industry and Information Technology, Harbin, China

Abstract. To accommodate the development of Internet of Things (IoT) technology and the increasing demand for automatic control in district heating systems, efficient modeling of building thermal processes is imperative. This study aims to establish a low-dimensional and physically interpretable thermal process model for residential buildings in severe cold regions, facilitating the design of simplified control systems. Based on the lumped parameter method and heat balance principles, an 8th-order state-space model is developed to characterize the building thermal dynamics. The two-time scale decoupling of this model is achieved using the regular perturbation method, decomposing it into a fast subsystem representing the indoor air thermal response and a slow subsystem representing the building envelope thermal response. Both the original and decoupled models are validated against measured data, with the error of 3.24%. During the decoupling process, the time-scale separation criterion is revised, and a new criterion: $f_1 < 10^{-1}$ and $f_2 < 10^{-6}$ is proposed specifically for buildings with heavyweight masonry external envelopes. Future work will further investigate time-scale separation criteria for other building types and lay the theoretical foundation for designing control systems based on the decoupled two-time-scale model.

Keywords: District heating system · Time-scale decoupling · Regular perturbation theory

1 Introduction

Building heating systems constitute a major energy consumption sector in severe cold regions, accounting for over 30% of total regional energy use [1]. With the increasing integration of IoT technologies and growing demand for precise automatic control, developing efficient mathematical models for building thermal processes has become essential for implementing smart heating systems [2]. These processes involve complex, nonlinear heat exchanges between indoor air and building envelopes, exhibiting distinct multi-timescale characteristics with minute-scale indoor temperature responses contrasting hour-scale envelope thermal dynamics.

© The Author(s), under exclusive license to Springer Nature Singapore Pte Ltd. 2025
L. Ni et al. (Eds.): CCHVAC 2025, ESE, pp. 231–238, 2025.
https://doi.org/10.1007/978-981-95-3253-7_25

Among existing modeling frameworks, data-driven approaches are effective in fitting operational data but suffer from limited physical interpretability and poor generalizability [3, 4]. In contrast, first-principles RC network models retain physical meaning but often lead to high-dimensional state spaces, presenting challenges in control optimization [5–7]. Perturbation methods address this by decomposing high-order differential equations into fast and slow subsystems, exploiting weak coupling identified via a small parameter ε. While these methods preserve physical interpretability and extend to nonlinear systems, their practical application is hindered by the lack of universal criteria for time-scale separation.

Nevertheless, time-scale separation has been demonstrated in established engineering applications [8, 9]. Its applicability to heating systems is rooted in physical principles: the thermal capacitance of building envelopes is typically one to two orders of magnitude higher than that of indoor air, leading to significantly different thermal time constants and forming a natural basis for time-scale separation.

Conventional building thermal models often underutilize these time-scale characteristics. Unified timescale formulations fail to reconcile the high thermal inertia of building envelopes with the rapid temperature regulation required for indoor comfort, resulting in prediction inaccuracies and control delays. Traditional state-space models require small time steps to accurately simulate slow dynamics, leading to excessive computational loads that hinder real-time control feasibility.

To address these challenges, this study proposes an 8th-order state-space model for residential buildings in severe cold region. A two-time-scale decoupling framework based on regular perturbation theory is introduced, with decoupling criteria derived from the ratio of wall-to-air thermal capacitance and their corresponding time constants. Effective separation between the fast indoor-air subsystem and the slow building-envelope subsystem is achieved. The decoupled model decomposes the original high-dimensional system into independent, low-dimensional subsystems, laying a theoretical foundation for hierarchical predictive control.

2 Methodology

2.1 State-Space Model for Heated Buildings

Based on thermal balance principles and the envelope structure of heated buildings, an 8th-order state-space model is developed to describe thermal processes. This model treats the entire building as a single unit, simplified through eight mass points: indoor air, exterior envelopes (four orientations, ground and roof), and interior envelopes (partition walls and floors). The foundational assumptions are:

- **Equivalent Air Mass Point.** Uniform indoor air temperature distribution is assumed, concentrated at a single point with mass equivalent to the building's total air mass and thermal capacity equal to the sum of all rooms' air thermal capacities.
- **Building Thermal Equilibrium.** Hydraulic imbalances between rooms are neglected, with uniform supply/return water temperatures across all radiators.
- **Equivalent Interior Envelope Mass Point.** Internal envelopes exhibit homogeneous temperature distribution with negligible inter-component heat transfer.

- **Equivalent Exterior Envelope Mass Point.** External envelopes are represented by six mass points (four orientations, ground and roof) with aggregate surface area matching actual building dimensions. Heat-storing components are modeled as non-stratified homogeneous bodies.

Thermal balance equation for the *i*-th exterior envelope component:

$$C_{ei}\frac{dt_{ei}}{d\tau} = K_{ei}A_{ei}(t_{in} - t_{ei}) + K_{oi}A_{ei}(t_{out} - t_{ei}) \tag{1}$$

where C_{ei} is the heat capacitance of the *i*-th envelope component, J/°C; t_{ei} is the temperature of the thermal mass of the *i*-th envelope component, °C; τ is sampling period, s; K_{ei} is heat transfer coefficient between the indoor air and the inner surface of the *i*-th envelope component, W/m^2 °C; K_{oi} is heat transfer coefficient between the outer surface of the *i*-th envelope component and the outdoor air, W/m^2 °C; A_{ei} is the surface area of the *i*-th envelope component, m^2; t_{in} is the temperature of indoor air, °C; t_{out} is the temperature of outdoor air, °C; *i* is the index of envelope components, including east, west, south, and north exterior walls, roof, and ground, i.e., $i = 1,2,3,4,5,6$.

Thermal balance equation for the interior envelope component:

$$C_{ie}\frac{dt_{ie}}{d\tau} = K_{ie}A_{ie}(t_{in} - t_{ie}) \tag{2}$$

where C_{ie} is the heat capacitance of the interior envelope component, J/°C; t_{ie} is the temperature of the thermal mass of the inner envelope component, °C; K_{ie} is heat transfer coefficient between the indoor air and the surface of the interior envelope component, W/m^2 °C; A_{ie} is the surface area of the interior envelope component, m^2.

The ground heat loss is calculated using the zonal division method. For residential buildings in Harbin, the ground is divided into Zone 1, Zone 2, and Zone 3, and the corresponding heat loss through the ground is calculated as follows:

$$Q_g = \sum_{j=1}^{3} K_{gj}A_{gj}(t_{out} - t_{in}) \tag{3}$$

where Q_g is the heat loss through the ground, W; K_{gj} is the heat transfer coefficient of Zone *j*, W/m^2 °C; A_{gj} is the area of Zone *j*, m^2; *j* is the index of ground zones, $j = 1,2,3$.

Thermal balance equation for indoor air:

$$\begin{aligned} c_a\rho_a V_a\frac{dt_{in}}{d\tau} &= Q + \sum_{i=1}^{6} K_{ei}A_{ei}(t_{ei} - t_{in}) + K_{ie}A_{ie}(t_{ie} - t_{in}) \\ &+ \sum_{j=1}^{3} K_{gj}A_{gj}(t_{out} - t_{in}) + c_a G_a(t_{out} - t_{in}) + K_w A_w(t_{out} - t_{in}) \end{aligned} \tag{4}$$

where c_a is the specific heat capacity of indoor air, J/kg·°C; ρ_a is the density of indoor air, kg/m^3; V_a is the volume of indoor air, m^3; Q is the heating supply, W; G_a is the ventilation rate to the outside, m^3; K_w is the transfer coefficient of doors and windows, W/m^2 °C.

By combining Eqs. (1)–(4), the state-space model of the building can be formulated:

$$\mathbf{C}\dot{\mathbf{T}} = \mathbf{A_0}\mathbf{T} + \mathbf{B_0}\mathbf{U} \tag{5}$$

where the temperature node vector $\mathbf{T} = [t_{\text{in}}\ t_{\text{e1}}\ t_{\text{e2}}\ t_{\text{e3}}\ t_{\text{e4}}\ t_{\text{e5}}\ t_{\text{e6}}\ t_{\text{ie}}]^{\text{T}}$, $\mathbf{C}$ is the heat capacity matrix; $\mathbf{A_0}$ is the matrix consists of the heat transfer coefficients; the disturbance input vector $\mathbf{U} = \left[t_{\text{out}}\ t_{\text{out}}\ t_{\text{out}}\ t_{\text{out}}\ t_{\text{out}}\ t_{\text{out}}\ t_{\text{out}}\ 1\right]^{\text{T}}$; $\mathbf{B_0}$ is the matrix consists of the corresponding coefficients of these disturbances.

2.2 Decoupling Principle for Building Thermal Process

The system matrices are partitioned into blocks as shown in Fig. 1.

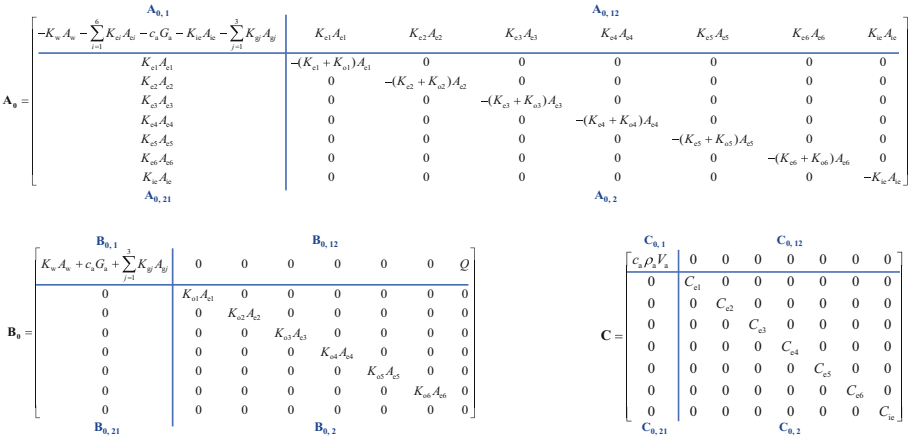


Fig. 1. Schematic diagram of the parameter matrix and its decoupled block structure

A matrix transformation is then applied to the state-space model (5), letting $\mathbf{A} = \mathbf{C}^{-1}\mathbf{A_0}$, $\mathbf{B} = \mathbf{C}^{-1}\mathbf{B_0}$, and rearranging the system into the form of Eq. (6).

$$\dot{\mathbf{T}} = \mathbf{A}\mathbf{T} + \mathbf{B}\mathbf{U} \tag{6}$$

The "weak coupling criterion" is used to assess the strength of dynamic interactions between subsystems. It is assumed that the eigenvalues of $\mathbf{A_1}$ and $\mathbf{A_2}$ are well separated in magnitude (i.e., $|\lambda_i(\mathbf{A_1})| \gg |\lambda_j(\mathbf{A_2})|$), where n is the dimension of $\mathbf{A_2}$ [10]. Let:

$$\begin{aligned} R &= \max_i |\lambda_i(\mathbf{A_1})|,\ r = \min_j \left|\lambda_j(\mathbf{A}_2)\right| \\ \delta_{12} &= \max_{i,j} \left|\{\mathbf{A}_{12}\}_{ij}\right|,\ \delta_{21} = \max_{i,j} \left|\{\mathbf{A}_{21}\}_{ij}\right| \end{aligned} \tag{7}$$

The system is considered weakly coupled when

$$\begin{aligned} f_1 &= \frac{r}{R} \ll 1 \\ f_2 &= \frac{n\delta_{12}\delta_{21}}{R^2} \ll 1 \end{aligned} \tag{8}$$

Since the criterion proposed in [7] is general and lacks specific threshold values, this study aims to define explicit time-scale separation thresholds for building thermal processes in severe cold regions and to validate them accordingly.

3 Case Study

The case building is a six-story residential structure located in Harbin, Heilongjiang Province, within China's severe cold region. Its envelope system is shown in Table 1.

Table 1. Physical parameters of envelope components

Component	Layer description	Heat capacitance ($J/m^2 \cdot °C$)	Heat transfer coefficient ($W/m \cdot °C$)
Exterior Wall	20 mm Cement Mortar + 240 mm Hollow Brick + 100 mm EPS + 20 mm Insulating Mortar	318,580	0.52
Roof	30 mm Fine Concrete + 10 mm Waterproof Layer +20 mm Cement Mortar + 150 mm Fire-Resistant EPS + 120 mm Reinforced Concrete	375,145	0.50
Ground Floor	40 mm Fine Concrete	80,960	0.20
Partition Wall	20 mm Cement Mortar + 240 mm Solid Brick + 20 mm Cement Mortar	430,080	2.02
Floor Slab	30 mm Cement Mortar + 100 mm Reinforced Concrete +10 mm Plain Cement Mortar	287,200	0.55

The measured data includes the building's heat supply, indoor air temperature, and outdoor air temperatures. The hourly outdoor temperature and heat supply data measured are presented in Fig. 2. The heating period in Harbin extends from late October to late April of the following year. During the sampling interval, the outdoor temperature reaches its lowest level of the year, corresponding to the stable heating phase in Harbin.

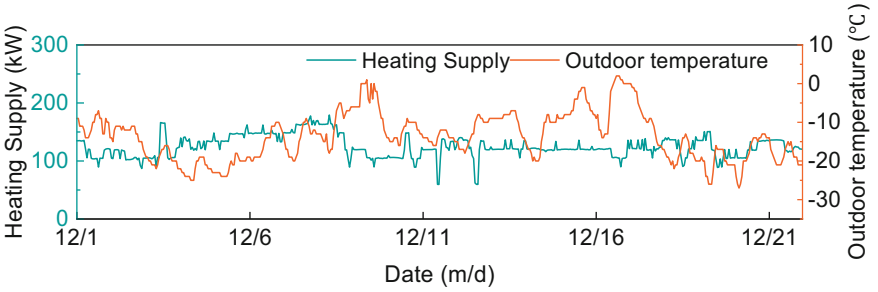


Fig. 2. Data acquisition of heating supply and outdoor temperature for a residential building in Harbin (sampling interval: 1 h; period: Dec. 1, 2023 – Dec. 21, 2023)

4 Validation for Model

4.1 8-Dimensional State-Space Model

The 8-dimensional state-space model is validated using measured data and the physical parameters of the envelope components as listed in Table 1. The simulation results show that the model reproduces indoor temperature dynamics with reasonable accuracy, yielding an average error of 3.24%, demonstrating good consistency between simulated values and measured data (Fig. 3).

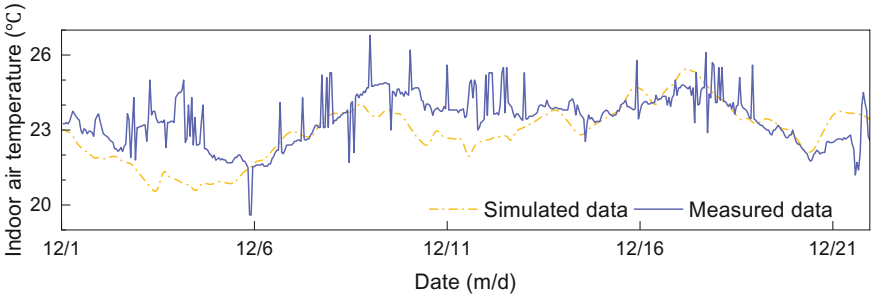


Fig. 3. Comparison between simulated and measured indoor air temperatures using the 8-dimensional state-space model

4.2 Decoupled Model and Time-Scale Separation Criteria

Based on the validated 8-dimensional model, the state-space model of the building thermal process is further decoupled. From this, the parameters in **Eq. (8)** are calculated as $f_1 = 3.80 \times 10^{-2}$ and $f_2 = 4.15 \times 10^{-7}$. As shown in Fig. 4, the fast-timescale subsystem in the decoupled model, which represents the indoor temperature dynamics, was simulated and validated against the measured temperature data. The relative error exhibits an average of 4.76%, with a maximum deviation of 14.22%.

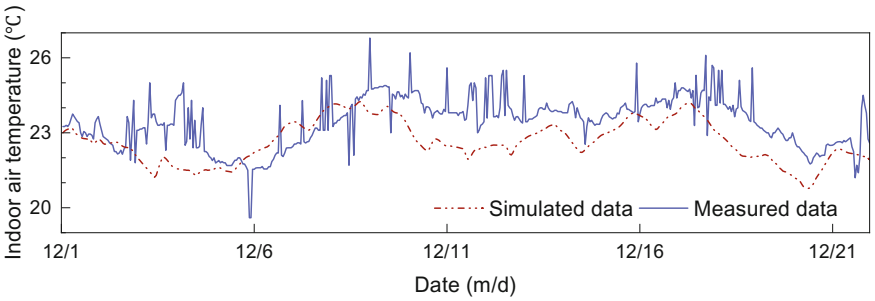


Fig. 4. Comparison between simulated and measured indoor air temperatures using the fast-response indoor air subsystem of the decoupled thermal process model

Figure 5 compares the absolute errors of indoor air temperature between the original 8-dimensional model and the decoupled model. It can be observed that the error trends of both models are consistent. For buildings with similar thermal capacitance levels, the time-scale decoupling criteria for thermal processes can thus be clearly defined as $f_1 < 10^{-1}$ and $f_2 < 10^{-6}$.

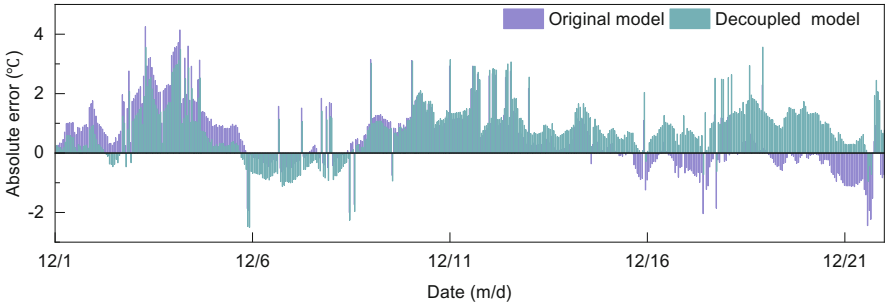


Fig. 5. Comparison of indoor air temperature simulations between the original 8-dimensional model and the decoupled model

5 Conclusion

This study presents a physically interpretable, low-dimensional thermal process model for residential buildings in severe cold regions, aimed at supporting the development of simplified control systems. The main conclusions are as follows:

- **Model Construction and Validation.** An eighth-order state-space model was developed based on lumped thermal parameters and validated using measured data. The model effectively captures indoor air dynamics, with a maximum error of 13.70% and an average error of 3.24%.

- **Time-Scale Decoupling.** Using the regular perturbation method, the model was decomposed into a fast subsystem representing indoor air dynamics and a slow subsystem representing envelope thermal behavior, reflecting their distinct thermal inertia. This decoupling significantly reduces computational complexity for control applications.
- **Separation Criterion and Fast Subsystem Accuracy.** A time-scale separation criterion was proposed based on the ratio of wall-to-air thermal capacitance and time constants. Preliminary results ($f_1 = 3.80 \times 10^{-2}$ and $f_2 = 4.15 \times 10^{-7}$) indicate that the decoupling condition is satisfied under defined thresholds. The fast subsystem maintains satisfactory accuracy after decoupling.

Further research will focus on refining the time-scale separation criteria and extending the decoupling method to other building types. This will help establish a solid theoretical foundation for the development of real-time predictive control systems based on multi-timescale models.

References

1. IEA, GlobalABC, UN Environmental Programme: 2020 global status report for buildings and construction: towards a zero-emissions, efficient and resilient buildings and construction sector – executive summary (2020). URL https://wedocs.unep.org/xmlui/handle/20.500.11822/34572. Accepted: 2020-1215T20:46:48Z
2. Zhang, K., Kummert, M.: Evaluating the impact of thermostat control strategies on the energy flexibility of residential buildings for space heating. Build. Simul. **14**, 1439–1452 (2021). https://doi.org/10.1007/s12273-020-0751-x
3. Hu, M., Xiao, F., Wang, L.: Investigation of demand response potentials of residential air conditioners in smart grids using grey-box room thermal model. Appl. Energy. **207**, 324–335 (2017). https://doi.org/10.1016/j.apenergy.2017.05.099
4. Wang, J., Jiang, Y., Tang, C.Y., Song, L.: Development and validation of a second-order thermal network model for residential buildings. Appl. Energy. **306**, 118124 (2022). https://doi.org/10.1016/j.apenergy.2021.118124
5. Wang, P., Ju, Y., Liu, S., Wang, W., Lei, C.: Reduction analysis of building thermal models for simulation of heating accidents. Build. Simul. **13**, 1249–1258 (2020). https://doi.org/10.1007/s12273-020-0654-x
6. Jiang, W., Wang, P., Ma, X., Liu, Y.: Development of a grey-box heat load prediction model by subspace identification method for heating building. Build. Environ. **280**, 113119 (2025). https://doi.org/10.1016/j.buildenv.2025.113119
7. Afram, A., Fung, A.S., Janabi-Sharifi, F., Raahemifar, K.: Development of an accurate gray-box model of ubiquitous residential HVAC system for precise performance prediction during summer and winter seasons. Energ. Buildings. **171**, 168–182 (2018). https://doi.org/10.1016/j.enbuild.2018.04.038
8. Zhu, H.Y.: Research on Normal Matrix Methodology of Attitude Control for Spacecraft Ph.D. Thesis. Harbin Institute of Technology (2009)
9. Yang, C.: Identification and Operational Optimization of Integrated Heat and Electricity Systems Ph.D. Thesis. Zhejiang University (2022)
10. Liu, Y.X.: Introduction to Dynamic Large-Scale System Methods. National Defense Industry Press, Beijing (1992)

Research on the Collaborative Benefits of Energy Conservation and Emission Reduction in the Blast Furnace Process Technology Based on the CSC Method

Yan Long[1(✉)], Qiuyan Lu[2], and Tianyi Hua[3]

[1] Huazhong University of Science and Technology, Wuhan, China
ly_hust@hust.edu.cn
[2] China-EU Institute for Clean and Renewable Energy, Huazhong University of Science and Technology, Wuhan, China
m202371668@hust.edu.cn
[3] School of Energy and Power Engineering, Huazhong University of Science and Technology, Wuhan, China

Abstract. To explore the potential for energy conservation and emission reduction in the blast furnace process technology of the steel industry, this study selected six advanced energy – saving and emission – reduction technologies for the blast furnace process in the steel industry as research subjects. An extended Conservation Supply Curve (CSC) model was constructed. In combination with the cost – benefit analysis method, three indicators, namely "unit energy-saving cost of technology-net present value – internal rate of return", were selected. Based on the TOPSIS evaluation method, the technical feasibility was analyzed from the dual perspectives of technical energy-saving potential and enterprise benefits, achieving a collaborative evaluation of the economic feasibility and environmental benefits of extreme energy-efficiency technologies and providing a quantitative basis for steel enterprises to select technological routes.

The results show that the extreme energy-efficiency technologies with higher comprehensive scores are ranked as follows: the automatic combustion and thermal equalization technology of blast furnace hot stoves, the dual pre-heating technology of air and gas for hot stoves, and the oxygen-enriched combustion technology for hot stoves.

Keywords: Blast furnace process · CSC model · Collaborative benefits

1 Introduction

The steel industry is an important pillar industry in China's national economic development. Meanwhile, it is also a major consumer of fossil energy and a large emitter of pollutants. Statistics show that the energy consumption of China's steel industry accounts for about 15% of the country's total energy consumption [1], and the energy consumption generated by blast furnace ironmaking accounts for more than 50% of the total energy

© The Author(s), under exclusive license to Springer Nature Singapore Pte Ltd. 2025
L. Ni et al. (Eds.): CCHVAC 2025, ESE, pp. 239–249, 2025.
https://doi.org/10.1007/978-981-95-3253-7_26

consumption in the entire steel production process. There is a gap between the energy consumption and carbon emissions of Chinese steel enterprises and the international standard levels [2, 3]. It can be seen that the blast furnace iron-making process is the key point for energy conservation and consumption reduction in the production of steel enterprises, and the evaluation of the energy-saving potential and economic efficiency of technologies is particularly important.

Many scholars at home and abroad have used the Conservation Supply Curve (CSC) model to conduct quantitative analyses of energy – saving technologies. Meier [4] first introduced the concept of CSC, developed an audit framework for calculating energy – saving potential, and guided the analysis of the impact of changes in predictive factors. Zhang S et al. [5] analyzed the collaborative benefits of energy – efficiency improvement and pollutant emission reduction in China's steel industry. Huang YH et al. [6] and Hasanbeigi A et al. [7, 8] evaluated the energy-saving potential and cost-effectiveness of different advanced technologies in the pulp and paper industry, the cement and steel industries in Thailand. Zhang et al. and Morrow W et al. [9, 10] analyzed 35 energy-saving technologies in the Chinese steel industry, and 22 and 25 energy-saving technologies in the Indian cement and steel industries respectively, and evaluated their technical energy-saving potential and energy-saving costs. Worrell et al. [11, 12] used the bottom-up ECSC model to evaluate the energy-saving potential, carbon emission reduction opportunities and productivity benefits of energy-efficiency investments in the US steel industry.

Wen et al. [13] further used the CSC method and the quadrant method to evaluate and compare the performance of advanced technologies. Liu Y et al. and Li et al. [14, 15] combined the CSC to evaluate the energy-saving potential and costs of the popular EST technology in the steel industry and open-pit metal mines. Wang et al. [16] took China's steel, cement and coal-fired power generation industries as examples, and used the bottom-up modeling method to quantify the energy-saving and emission-reduction potential of information and communication technologies and further analyze the economic benefits.

The above-mentioned studies have a single evaluation dimension for energy-saving technologies, and the analysis results of technical energy-saving potential are also inconsistent. Therefore, this paper combines the extended CSC model with the cost-benefit analysis method to construct a multi-dimensional comprehensive evaluation system of technology-economy-environment. Three indicators, namely "unit energy-saving cost of technology-net present value-internal rate of return", are selected to achieve a collaborative evaluation of the economic feasibility and environmental benefits of extreme energy-efficiency technologies, providing a quantitative basis for steel enterprises to select technological routes.

2 Research Methods

For various energy-saving technologies in the blast furnace process, the energy-saving and emission-reduction potential and costs of each technology are calculated respectively. The extended Conservation Supply Curve (CSC) method is combined with the cost-benefit analysis method. Considering the collaborative benefits of energy-saving, emission-reduction, and pollution-reduction of the technologies, a measurement

framework is provided from multiple perspectives of technical energy-saving potential and collaborative benefits to describe the energy-saving potential of the technologies. From the perspective of enterprise investment decision-making, the economic feasibility of energy-saving technologies in the blast furnace process is evaluated. A multi-dimensional comprehensive evaluation system of "economic-environmental benefits" for energy-saving technologies in the blast furnace process based on TOPSIS evaluation is established.

2.1 Extended Conservation Supply Curve (CSC) Model

The energy-saving, emission-reduction, and pollution-abatement potential of technologies. The CSC model integrates the parameters of an energy-saving technology and is a visual tool for analyzing the energy-saving potential and cost-effectiveness of energy-saving and low-carbon technologies. The calculation of the energy-saving, emission-reduction, and pollution-abatement potential of technologies is shown in Eqs. (1)–(2).

$$ESP_T = ECR_P \times HV_{sc} \times \mathrm{Q} \tag{1}$$

$$ER_i = ECR_P \times \mathrm{Q} \times EF_{sc}^{i} \tag{2}$$

In Eq. (1), ESP_T represents the energy-saving potential of the technology, with the unit of GJ; ECR_P is the reduction in process energy consumption of the technology, with the unit of kgce/t-iron; HV_{sc} is the calorific value of standard coal, which is 3 GJ/kg; and Q is the product output, with the unit of t.

In Eq. (2), i can be CO_2, SO_2, NO_x or inhalable particulate matter (PM_{10}). ER_i represents the emission reduction amounts of the four substances brought about by the energy-saving technology, with the unit of kg, and EF_{sc}^{i} is the standard coal emission factor of the four substances.

Comprehensive evaluation of the synergistic benefits of energy conservation, emission reduction and pollution abatement of technologies. The calculation formula for the unit energy-saving cost considering the synergistic benefits of energy conservation, emission reduction, and pollution abatement of the technology is as follows.

$$CCE_0 = \frac{C}{ESP_T} \times TA \tag{3}$$

$$CCE_a = \frac{C - \mathrm{EB}}{ESP_T} \times TA \tag{4}$$

$$CCE_b = \frac{C - \mathrm{EB} - RB_{CO_2}}{ESP_T} \times TA \tag{5}$$

$$CCE_c = \frac{C - \mathrm{EB} - RB_{CO_2} - RB_{ap}}{ESP_T} \times TA \tag{6}$$

$$C = Q \times K \times \frac{d}{\left[1 - (1+d)^{-n}\right]} + \Delta O\&M \tag{7}$$

$$EB = ECR_P \times \mathrm{Q} \times P^{sc} \tag{8}$$

$$RB_{CO_2} = ER_{CO_2} \times P^{CO_2} \tag{9}$$

$$RB_{ap} = ER_{SO_2} \times P^{SO_2} + ER_{NO_x} \times P^{NO_x} + ER_{PM_{10}} \times P^{PM_{10}} \tag{10}$$

CCE_0 represents the unit energy-saving cost without considering any benefits. CCE_a represents the unit energy-saving cost considering the energy-saving benefits. CCE_b represents the unit energy-saving cost considering the benefits of energy conservation and emission reduction. CCE_c represents the unit energy-saving cost considering the benefits of energy conservation, emission reduction, and pollution reduction, with the unit of ¥/GJ; C is the comprehensive cost of the technology, with the unit of ¥; EB is the energy-saving benefit of the technology, with the unit of ¥/year; RB_{CO_2} is the emission reduction benefit of CO_2, with the unit of ¥/year; RB_{ap} is the emission reduction benefit of air pollutants, with the unit of ¥/year; TA is the attainable rate, in percentage (%).In Eq. (7), ΔO & M is the operation and maintenance cost, with the unit of ¥/year; K is the capital cost, with the unit of ¥/t; d is the discount rate, which is 10%; n is the service life of the technology, with the unit of years.

In Eq. (8), P^{sc} is the price of standard coal. In Eq. (9), ER_{CO_2} is the emission reduction amount, and P^{CO_2} is the price of CO_2.In Eq. (10), ER_{CO_2}, ER_{SO_2}, ER_{NO_x} and $ER_{PM_{10}}$ respectively represent the emission reduction amounts of CO_2, SO_2, NO_x and PM_{10} brought about by the energy-saving technology; P^{SO_2} is the price of SO_2, P^{NO_x} is the price of NO_x, and $P^{PM_{10}}$ is the price of PM_{10}.

2.2 Cost-Benefit Analysis Method

The advantage of the cost – benefit analysis (CBA) lies in its comprehensiveness and long-term nature. In this study, dynamic evaluation indicators are selected: Net Present Value (NPV) and Internal Rate of Return (IRR).

$$NPV = \left(\sum_{i=1}^{n} \frac{CF_i}{(1+r)^i} - CF_0 \right) \times \mathrm{TRL} \tag{11}$$

$$\sum_{i=1}^{n} \frac{CF_i}{(1+IRR)^i} = CF_0 \tag{12}$$

$$CF_i = EB + RB_{CO_2} + RB_{ap} \tag{13}$$

In Eq. (11), CF_i represents the cash inflow for each year, CF_0 is the initial capital investment in ten thousand yuan, r is the discount rate at 8%, and n is the project duration, which is 20 years. TRL (Technology Readiness Level) refers to the technology readiness level. In this paper, the technology readiness level is divided into five levels within the range of 0–1. The feasibility of the scheme is evaluated based on the value of NPV. If NPV is greater than or equal to zero, the scheme is considered feasible; otherwise, it is not. In this study, the cash flow of the technology is defined as shown in Eq. (13), which is the sum of the energy-saving revenue, carbon emission reduction benefit, and air pollutant emission reduction benefit.

2.3 Construction of the Comprehensive Evaluation System

Multiple indicators are selected from both the technology and enterprise perspectives. Based on the TOPSIS method, a comprehensive evaluation system for the energy-saving technology-economic and environmental benefits of the blast furnace process is established. The selection of indicators and the definition of their weights are as follows (Table 1).

Table 1. Comprehensive evaluation indicators for technology

	Indicator selection	Indicator type	Weight
Technology dimension	CCE	quantitative	0.5
Enterprise dimension	NPV	quantitative	0.3
	IRR	quantitative	0.2

3 Case Analysis

3.1 Data Source

Brief Introductions to Six Energy-Saving Technologies for Blast Furnace Ironmaking

Gas recovery technology for top equalizing pressure of blast furnace: Recover the gas discharged during the pressure equalization of charging, increase the amount of available gas, reduce costs, and decrease pollution; Automatic combustion and thermal equalizing pressure technology for blast furnace hot blast stoves: Automatically control combustion and equalize temperature, improve efficiency, stabilize hot air temperature, and reduce energy consumption; New ignition and accompanying combustion technology for blast furnace gas flare stack: Stably ignite the dispersed gas, reduce emissions, ensure safety, and decrease pollution; High-efficiency waste heat recovery technology for blast furnace granulated slag: Recover the waste heat from granulated slag and convert it into energy, improving energy utilization efficiency and reducing costs; Oxygen-enriched firing technology for hot blast stoves: Use oxygen – enriched air for combustion to increase hot air temperature, enhance smelting intensity, and reduce coke ratio; Double preheating technology for air and gas in hot blast stoves: Pre – heat both air and gas, improve combustion efficiency, reduce consumption, and increase heat storage capacity.

The energy-saving and emission-reduction technologies in the blast furnace process and their economic parameters are shown in Table 2.

Table 2. Energy-saving and emission-reduction technical parameters

Energy-saving technology	Unit energy saving (kgce/t-iron)	Investment cost (ten thousand ¥)	Operation and maintenance cost (ten thousand ¥ per year)	Technical lifespan (years)	Technical achievement rate (%)
Gas recovery technology for top equalizing pressure of blast furnace(T1)	0.526	200	15	15	95
Automatic combustion and thermal equalizing pressure technology for blast furnace hot blast stoves(T2)	1.127	80	12	20	75
New ignition and accompanying combustion technology for blast furnace gas flare stack(T3)	0.204	240	8	20	85
High-efficiency waste heat recovery technology for blast furnace granulated slag(T4)	1.789	2400	75	20	90
Oxygen-enriched firing technology for hot blast stoves(T5)	1.400	500	30	20	70
Double preheating technology for air and gas in hot blast stoves(T6)	4.000	1500	60	20	35

3.2 Result Analysis

The energy-saving and emission-reduction potential and benefits of six blast furnace process technologies are shown in Table 3. Among the six energy-saving technologies,

the three technologies with the greatest energy-saving and emission-reduction potential are T6, T4 and T5.

Table 3. Assessment of energy-saving and emission-reduction potential and benefits

Energy-saving technology	Energy-saving potential (GJ)	Carbon emission reduction potential (kg)	Pollution reduction potential (kg)	Unit energy-saving cost (CCE_0 ¥/GJ)
Gas recovery technology for top equalizing pressure of blast furnace(T1)	91367	7678960	3311	12.65
Automatic combustion and thermal equalizing pressure technology for blast furnace hot blast stoves(T2)	195588	16438230	7088	1.69
New ignition and accompanying combustion technology for blast furnace gas flare stack(T3)	35435	2978152	1284	24.95
High-efficiency waste heat recovery technology for blast furnace granulated slag(T4)	310752	26117224	11261	29.98
Oxygen-enriched firing technology for hot blast stoves(T5)	243183	20438297	8812	6.62
Double preheating technology for air and gas in hot blast stoves(T6)	694807	58395134	25178	3.32

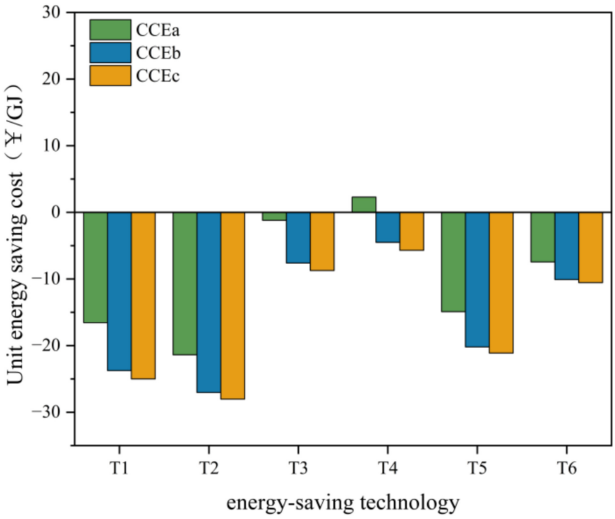


Fig. 1. Comparison of unit energy-saving costs of energy-saving technologies for blast furnace processes considering different benefits

From the perspective of the benefits of technological energy conservation and emission reduction, Fig. 1 presents a comparison of the unit energy-saving costs of six energy-saving technologies under different revenue scenarios. After taking energy-saving benefits into account, the energy-saving cost of one technology is negative. The three technologies with the lowest energy-saving costs are T2, T1, and T5, with energy-saving costs of −21.37 ¥/GJ, −16.56 ¥/GJ, and − 14.90 ¥/GJ respectively. After considering the synergistic benefits of CO_2 emission reduction, the energy-saving costs of these three technologies are −27.04 ¥/GJ, −23.75 ¥/GJ, and − 20.2 ¥/GJ respectively. After further incorporating the synergistic benefits of reducing three types of air pollutants, the energy-saving costs of these three technologies are −28.04 Yuan/GJ, −25.0 ¥/GJ, and − 21.12 ¥/GJ respectively. At this time, the energy-saving costs of all six technologies are negative. In conclusion, the automatic combustion and thermal equalization technology for blast furnace hot stoves performs best in terms of both energy-saving benefits and the synergistic benefits of emission reduction and pollution control.

Analyzed from the perspective of corporate benefits, Fig. 2 shows the Net Present Value (NPV) and Internal Rate of Return (IRR) of six energy-saving technologies after their respective implementation. NPV reflects the absolute return, while IRR reflects the relative efficiency. It can be observed that the NPVs of all six technologies are greater than zero, indicating their economic viability. The three technologies that bring relatively high absolute returns to the enterprise are T6, T5, and T2, with NPV values of 153.21 million, 71.7 million, and 60.24 million respectively. The three technologies with relatively high IRRs are T2, T1, and T5 (Table 4).

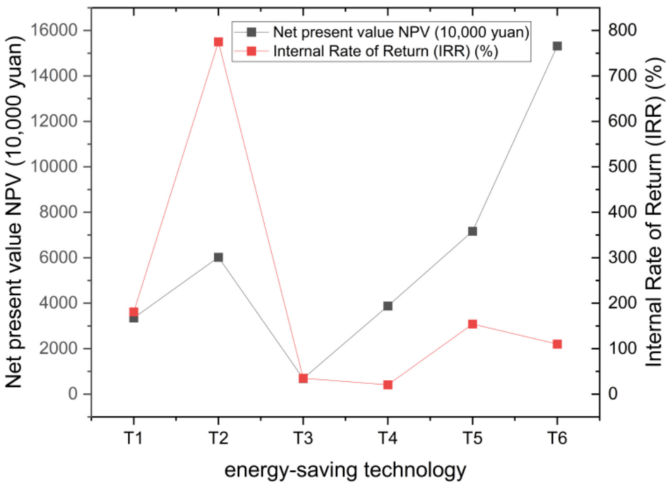


Fig. 2. Enterprise economic benefit indicators of energy-saving technologies

Table 4. Comprehensive evaluation of technological energy-saving potential and enterprise benefits

Energy-saving technology	Score	Comprehensive ranking
Gas recovery technology for top equalizing pressure of blast furnace(T1)	0.56	3
Automatic combustion and thermal equalizing pressure technology for blast furnace hot blast stoves(T2)	0.74	1
New ignition and accompanying combustion technology for blast furnace gas flare stack(T3)	0.11	5
High-efficiency waste heat recovery technology for blast furnace granulated slag(T4)	0.10	6
Oxygen-enriched firing technology for hot blast stoves(T5)	0.60	2
Double preheating technology for air and gas in hot blast stoves(T6)	0.43	4

Evaluating the technical feasibility from a single dimension, either solely from the perspective of technological energy conservation and emission reduction or solely from the perspective of enterprise benefits, is unconvincing, and the evaluation results are inconsistent. Therefore, based on the TOPSIS method, this paper comprehensively evaluates the technical feasibility from both the technological and enterprise perspectives to overcome the limitations of single-dimension evaluation. The comprehensive priority ranking of the six technologies is obtained as follows: T2, T5, T1, T6, T3, T4.

4 Results and Discussion

This study overcomes the single-dimensional limitation of energy-efficiency technology evaluation in the blast furnace process of existing technologies. It constructs a multi-dimensional comprehensive evaluation system integrating technology, economy, and environment. Three indicators, namely "unit energy-saving cost of technology, net present value, and internal rate of return", are selected. Based on the TOPSIS evaluation method, a collaborative evaluation of the economic feasibility and environmental benefits of extreme energy-efficiency technologies is realized, providing a quantitative basis for the technology route selection of iron and steel enterprises. The main conclusions are as follows:

1. From the perspective of techno-economy: After considering the synergistic benefits of energy conservation and emission reduction, among the six extreme energy-efficiency technologies in the blast furnace process, the technologies with relatively low unit energy-saving costs are T2, T1, and T5. The energy-saving costs are −28.04 ¥/GJ, − 25 ¥/GJ, and − 21.12 ¥/GJ respectively.
2. From the perspective of enterprise benefits: The three technologies that bring relatively high absolute benefits to enterprises are T6, T5, and T2. The three technologies with relatively high technology yields are T2, T1, and T5.
3. Comprehensive evaluation: Starting from both the technology and enterprise perspectives, while quantifying the potential for energy conservation and emission reduction, economic feasibility, and environmental benefits, the technologies with better comprehensive evaluation performance are T2, T6, and T5.

Acknowledgments. The authors thank the Hubei Provincial Key Research and Development Program of China (No. 2023DJC155) and Hubei Provincial Natural Science Foundation of China (No. 2023AFB1062). for funding and supporting this work.

References

1. World Steel Association. Steel Statistical Yearbook. (2015).
2. Ministry of Industry and Information Technology. Guidance on Energy Conservation in Iron and Steel Industry.
3. Wang, W.: Comments on the use of secondary energy recycling in iron and steelenterprises. China Steel. **10**, 29–31 (2013)
4. Meier, A.K.: Supply Curves of Conserved Energy Ph.D. Thesis. University of California, Lawrence Berkeley National Laboratory (1982)
5. Zhang, S., Worrell, E., Crijns Graus, W., et al.: Co-benefits of energy efficiency improvement and air pollution abatement inthe Chinese iron and steel industry. Energy. **78**, 333 (2014)
6. Huang, Y.H., Wu, J.H., Liu, T.Y.: Bottom-up analysis of energy conservation and carbon dioxide mitigation potentials by extended marginal abatement cost curves for pulp and paper industry. Energ. Strat. Rev. **42**, 100893 (2022)
7. Hasanbeigi, A., Menke, C., Therdyothin, A.: The use of conservation supply curves in energy policy and economic analysis: the case study of Thai cement industry. Energy Policy. **38**, 392–405 (2010)

8. Hasanbeigi, A., Morrow, W., Sathaye, J., et al.: A bottom–up model to estimate the energy efficiency improvement and CO2 emission reduction potentials in the Chinese iron and steel industry. Energy. **50**, 315–326 (2013)
9. Zhang, Q., Zhao, X.Y., Lu, H.Y., et al.: Waste energy recovery and energy efficiency improvement in China's iron and steel industry. Appl. Energy. **191**, 502520 (2017)
10. Morrow, W., Hasanbeigi, A., Sathaye, J., et al.: Assessment of energy efficiency improvement and CO2, emission reduction potentials in India's cement and iron & steel industries. J. Clean. Prod. **65**, 131–141 (2014)
11. Worrell, E., Price, L., Martin, N.: Energy efficiency and carbon dioxide emissions reduction opportunities in the US iron and steel sector. Energy. **26**, 513–536 (2001)
12. Worrell, E., Laitner, J.A., Ruth, M., et al.: Productivity benefits of industrial energy efficiency measures. Energy. **28**, 1081–1098 (2003)
13. Wen, Z.G., Wang, Y.H., Li, H.F., et al.: Quantitative analysis of the precise energy conservation and emission reduction path in China's iron and steel industry. J. Environ. Manag. **246**, 717–729 (2019)
14. Liu, Y., Zhang, C.R., Xu, X.C., et al.: Assessment of energy conservation potential and cost in open-pit metal mines: bottom-up approach integrated energy conservation supply curve and ultimate pit limit. Energy Policy. **163**, 112809 (2022)
15. Li, Y., Zhu, L.: Cost of energy saving and CO2 emissions reductions in China's iron and steel sector. Appl. Energy. **130**, 603–616 (2014)
16. Wang, Y.H., Wen, Z.G., Cao, X., et al.: Is information and communications technology effective for industrial energy conservation and emission reduction? Evidence from three energy-intensive industries in China. Renew. Sust. Energ. Rev. **160**, 112344 (2022)



Automatic Hourly Calibration of a Multi-Purpose Building Simulation Model in an Adaptive Framework Using IDA-Python API

Hamed Amini[1(✉)], Hang Yin[2], Kari Alanne[1], Mohamed Hamdy[2], and Risto Kosonen[1]

[1] Aalto University, Espoo, Finland
hamed.amini@aalto.fi
[2] Norwegian University of Science and Technology – NTNU, Trondheim, Norway

Abstract. Automatic calibration of building performance simulation models is essential for creating digital twins and training adaptive AI control agents. This paper introduces an automatic multi-phase calibration methodology for a simplified simulation model of a complex multi-purpose building. A multi-objective optimization framework, implemented using the IDA-Python API and based on the NSGA-II algorithm, is utilized to minimize the discrepancies between measured data and simulated outputs. The methodology contains 1) a monthly calibration stage (stage I) and 2) a continuous hourly calibration stage (stage II). First, a monthly calibration is conducted to establish baseline monthly accuracy. Then, an hourly calibration is performed on a weekly basis to refine the model further, ensuring its readiness to be used for training AI control agents and making control decisions. For each week, if the inherited schedules violate acceptable error thresholds between the simulation results and measurements (CVRMS >30% for all objectives), AHU's fan and internal heat gain schedules are automatically modified to restore hourly accuracy (recalibration). The hourly CVRMSE values for the calibrated model in the whole simulation period were 18.8% for AHU heating and 14.1% for space heating energy consumption. Hence, the model serves as a reliable environment for assessing robust control and management strategies for the real building. This automatic adaptive calibration method can effectively address building dynamics, internal heat gain variations, and sudden weather events such as heat waves or cold waves.

Keywords: Automatic calibration · Adaptability · Hourly calibration · Multi-stage · High-fidelity BPS

1 Introduction

Developing building performance simulation models that accurately capture the building dynamics while not demanding high computational cost is beneficial for many applications requiring numerous high-fidelity simulation runs [1] (e.g., providing simulation-based AI training environments [2]). However, simplifications and assumptions in the

© The Author(s), under exclusive license to Springer Nature Singapore Pte Ltd. 2025
L. Ni et al. (Eds.): CCHVAC 2025, ESE, pp. 250–259, 2025.
https://doi.org/10.1007/978-981-95-3253-7_27

simulation model result in discrepancies between the predictions and the building's actual performance [3]. In this regard, when a building performance simulation (BPS) model is ready, its fidelity needs to be improved through its calibration against measurements. The calibration process usually happens using manual (e.g., [4]) or automatic (e.g., [5]) methods, based on various calibration schemes, and in different time resolutions (annual, monthly [6], hourly [7]).

Automated calibration methods search for a good solution for inputs (calibration parameters), minimizing the errors using a computational program [6]. Optimization-based calibration is a common method for minimizing the discrepancy between simulation predictions and measurements. This involves adjusting uncertain calibration parameters within predefined ranges to reduce the error metrics like Normalized Mean Bias Error (NMBE) and Coefficient of Variation of the Root Mean Square Error (CVRMSE) [8].

In the context of real-time building management and digital twin applications, ensuring that the model remains representative of the actual building's current state, synchronization is essential. This process involves ensuring that the measured data from the building is correct, as well as continuous updating of model variables and parameters based on recent measurements. It can be achieved through automated calibration techniques [9]. So, in this study, an optimization-based calibration method is employed to automatically calibrate a simplified simulation model of a multi-purpose complex building at both monthly and hourly time resolutions. The multi-objective optimization algorithm, developed in Python, interacts with the IDA ICE simulation tool to find optimum solutions through a two-stage process (monthly and hourly calibration). For the hourly calibration stage, a sequential weekly calibration scheme is applied to adjust schedules in the monthly calibrated model. The model's accuracy is evaluated weekly to determine whether it needs to be recalibrated or not. To enhance the optimization process in hourly calibration, a schedule refinement strategy is implemented, and the optimization algorithm is initialized using the best solutions from previous weeks.

2 Methodology

2.1 Building and Simulation Model

In this study, a multi-purpose building complex located in Espoo, Finland, was selected as the case study. The target building has a 47,500 m^2 heated floor area and contains various sections, including a shopping center, metro station, and education building (including classes, office, labs, etc), which have different air handling units and occupancy patterns. The building's multi-purpose functionality and large scale make it challenging to accurately simulate the building in a way that captures the hourly energy performance and the average temperature of the building.

On the other hand, since the final calibrated simulation model will be used in iterative processes, e.g., as a training environment for AI agents, which demand low computational time and high fidelity, the building was simulated with a high level of simplification. IDA ICE 5.1, a whole-building simulation tool developed by EQUA [10], was utilized for developing the simulation model. The simplified model consists of only five thermal zones representing the whole building [11].

The calibration process aimed to minimize discrepancies between simulated and measured data in heating period for two distinct objectives: (1) the heating energy consumed by air handling units (AHUs), and (2) the energy consumption for space heating required to follow the rule-based control strategy implemented in the actual building (constant 21 °C heating temperature setpoint). The supply air temperature setpoint was defined based on the building automation system's control settings.

2.2 Multi-Phase Calibration Process

An optimization-based calibration method was developed using a multi-phase calibration scheme implemented in Python. The Non-dominated Sorting Genetic Algorithm II (NSGA-II) was utilized as the optimization algorithm. This algorithm generates a population of input parameter sets (identified by sensitivity analysis in [11]) in each generation, sends them to the simulation model, and evaluates the resulting outputs against the measured data. Over generations, the error across both objectives is minimized in two phases: monthly resolution in Phase I and hourly resolution in Phase II.

Since the simulation model and the optimization code were developed in two different environments, a two-way communication between Python and IDA ICE was required. To this end, IDA-Python API was utilized, as demonstrated in Fig. 1. The measured data included weather information and real-world values for both objectives, calculated in hourly intervals by thermal energy meters since July 2019.

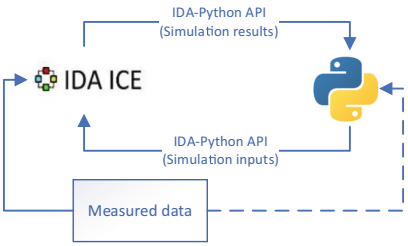


Fig. 1. Data flow between Python and simulation software

Figure 2 illustrates the two-phase automated calibration process developed to minimize the discrepancy between the simplified simulation model and the complex building.

- Phase I (Fig. 2) focuses on identifying and calibrating the model's most influential fixed parameters, which are constant over time, against monthly measured data from January to March 2022 (3 months of the heating season).

  The NSGA-II algorithm was then utilized to minimize the normalized mean biased error between simulated and measured monthly data. The output of this phase is a monthly calibrated model, which is well-suited for applications such as long-term energy consumption analysis, energy consumption estimations, etc. Also, it serves as the initial input model with constant schedules for Phase II of the automated calibration process.

- Phase II (Fig. 2) focuses on refining the simulation's time-dependent variables (schedules) using hourly measured data. The hourly calibration process was carried out in weekly segments starting from the first week of 2022 in an automatic setting. Each week (*week n*) was first simulated using the calibrated schedules from the previous week (*week n − 1*). If the model satisfied the ASHRAE guidelines for hourly accuracy (hourly CVRMSE <30% [12]), the schedules were accepted, and the process continued to the next week (*week n + 1*). Otherwise, the current week (*week n*) required recalibration because the inherited schedules failed to accurately capture that week's energy usage patterns.

  Additionally, to accelerate the convergence of the multi-objective optimization process during recalibration, previous weeks' solutions were used as the initial population for the NSGA-II algorithm. This iterative calibration-validation cycle continued until the schedules for all weeks (week 12 in this study) in the dataset were successfully calibrated or passed. The outcome is an hourly calibrated model, which is essential for applications requiring hourly/sub-hourly resolutions, e.g., real-time operation, demand response, building energy management systems (BEMS), etc.

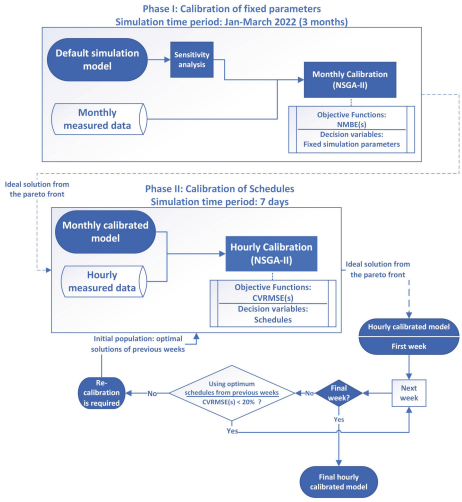


Fig. 2. Multi-stage optimization-based calibration flowchart

2.3 Optimization Problem

The NSGA-II algorithm is responsible for minimizing the error metrics (E) of both objective functions simultaneously as formulated below:

$$\min_{x \in C} \left(E_{\text{AHU heating}(x)}, E_{\text{Space heating}(x)} \right) \tag{1}$$

Subject to

$$C = \{x : x_{min} < x < x_{max}, g(x) \leq 0\} \tag{2}$$

Where for **phase I**, $x = (x_1, x_2, \ldots, x_5)$ and E is the monthly NMBE between simulation results and measured data (Eq. 3). The threshold range for monthly NMBE is ±5 [12, 13].

Decision variables (x) based on the sensitivity analysis [11]:

x_1: Effectiveness of the AHU's heat exchanger (heat recovery): (0.4, 0,8)
x_2: Supply air flow rate: (1, 3) L/(s. m^2)
x_3: Emitted heat per unit (internal heat gain) in Room 0(central zone): (50, 200)W
x_4: Emitted heat per unit in Room 1 (west) and Room 2 (east): (50, 200)W
x_5: Emitted heat per unit in Room 3 (south) and Room 4 (north): (50, 200)W

$$NMBE = \frac{1}{n}\sum_{i=1}^{n}\frac{(m_i - s_i)}{\overline{m}} \times 100 \tag{3}$$

On the other hand, for **phase II**, $x = (T_1, V_1, T_2, V_2, T_3, V_3)^{Sch_i}$ for three different schedules, including:

Sch_1: AHU fan schedule
Sch_2: Internal heat gain schedule of the central zone (Room 0)
Sch_3: Internal heat gain schedules of the perimeter zones (Rooms 1–4).

Also, E is the hourly CVRMSE between simulation results and measured data (eq. 4) and the inequality constraint function ($g(x)$) is defined as eq.5.

$$CV(RMSE) = \frac{RMSE}{\overline{m}} \times 100 = \frac{1}{\overline{m}}\sqrt{\frac{1}{n}\sum_{i=1}^{n}(m_i - s_i)^2} \times 100 \tag{4}$$

$$g(x) = \left({T_1}^{Sch_i} - {T_2}^{Sch_i}\right), \left({T_2}^{Sch_i} - {T_3}^{Sch_i}\right)\ i = 1, 2, 3 \tag{5}$$

2.4 Schedules' Refining Strategy

As mentioned before, three daily schedules were considered for hourly calibration in Phase II. Since optimizing all hourly schedule values (3*24 = 72 variables) would result in high computational time, a strategy was developed for calibrating the schedule, which reduced the number of variables to six per schedule (3*6 = 18 variables). Figure 3 demonstrates the decision variables for each schedule, containing 3 variables for the time of the day and 3 for their corresponding schedule values between 0 and 1.

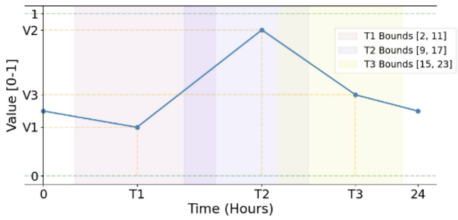


Fig. 3. Schedule's refining strategy and decision variables' bounds

3 Results

The calibration process started with the baseline simulation model and the measured data from the actual building. The following subsections demonstrate and discuss the improvements in the model's energy consumption estimation accuracy in both phases.

3.1 Phase I, Monthly Calibration

The optimization process, which minimized the monthly NMBE between the building's simulated and measured heating energy consumption, resulted in a Pareto front containing optimum solutions. Figure 4 illustrates the improvement in the monthly accuracy of the model with the calibrated fixed parameters (as listed in sect. 2.3). The figure compares the total energy consumed in AHUs and zones during the first three months of 2022 with the corresponding measured values. According to the results, the monthly NMBE for space heating and AHU heating in the monthly calibrated model are 0.12% and 0.6%, respectively. Since the resulting model is accurate enough according to all standards [14], it is used as the baseline for phase II.

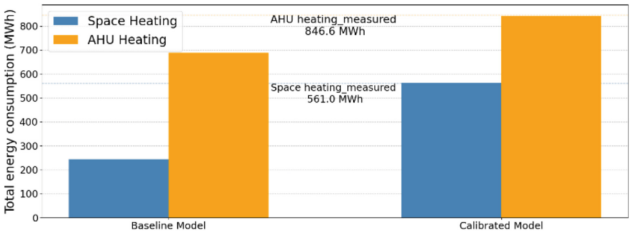


Fig. 4. Monthly calibration results

3.2 Phase II, Hourly Calibration

The hourly calibration was performed on a weekly basis to minimize the hourly CVRMSE between measured and simulated values by optimizing internal heat gain and fan schedules. Figure 5 presents the hourly accuracy of the final calibrated model (according to the schedule's refining strategy demonstrated in Fig. 3 and the example

shown in Fig. 6), plotting the hourly CVRMSE for both objective values. It demonstrates that the model could reflect the building's hourly energy performance accurately with a reasonable computational time (3 months simulation time: 65[s]).

Notably, the high and consistent accuracy in space heating estimation (less than 20%) during the simulation period indicates that the calibration process successfully captured internal heat gain patterns, containing occupancy patterns, equipment, and lighting usage. Also, the higher accuracy in space heating compared to AHU heating is because of the greater flexibility in its corresponding decision variables. In fact, twelve variables directly influenced space heating (variables related to the internal heat gain schedules of room 0 and room 1–4, according to Fig. 3), while only six were associated with AHU heating (variables related to the AHU fan schedule according to Fig. 3).

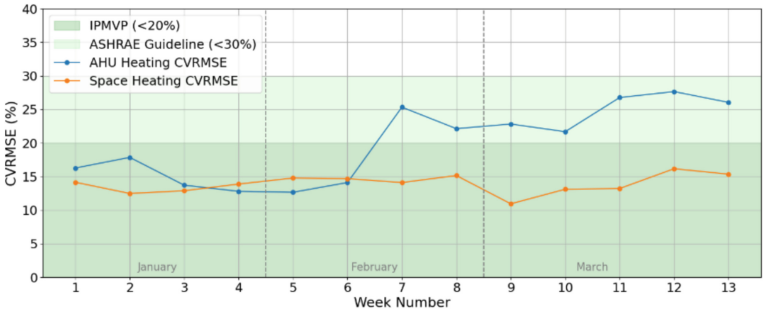


Fig. 5. Hourly CVRMSE of the calibrated model

Table 1 shows how the proposed sequential weekly calibration proceeded through the weeks. Also, Fig. 6 illustrates an example of how the AHU fan schedule was calibrated compared to the baseline for Week 1 and Week 2. After calibrating the first week, the model failed to meet the error threshold in week 2. So, minor refinements were applied to the calibrated schedules from the first week (Fig. 6). However, the updated schedules from week 2 remained valid for the following four weeks, likely because of the similar weather conditions and occupant patterns during this period. The calibration process was triggered for all subsequent weeks, mostly because the error in the AHU heating objective exceeded the thresholds when evaluating the previous week's schedules.

Table 1. The weekly process of the calibration scheme

Week	1	2	3	4	5	6	7	8	9	10	11	12	13
Weighed error (%)	15.2	15.2	13.3	13.3	13.7	14.4	19.7	18.6	16.9	17.4	19.9	21.9	20.7
Action	Calibration	Calibration	Pass[a]	Pass	Pass	Pass	Calibration	Calibration	Calibration	Calibration	Calibration	Calibration	Calibration

[a]Calibrated schedules are acceptable for this week

Finally, Fig. 7 illustrates the good agreement between measured and simulated values for both objectives over the entire simulation period. The hourly CVRMSE for the

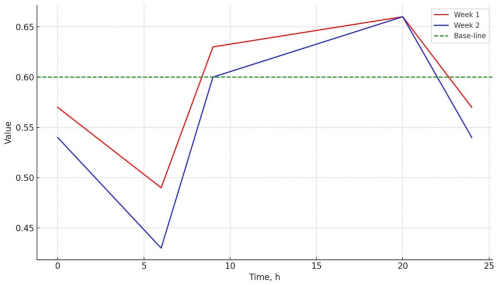


Fig. 6. Fan schedule calibration example for the first two weeks of the calibration

calibrated model's AHU heating and space heating energy consumption for the whole simulation period are 18.8% and 14.1%, respectively. Also, the hourly NMBEs for the final calibrated model are −0.5% and 3%. These results confirm that the final optimum model is accurate according to all standards for both objectives in hourly time steps [15]. Compared to another study's result, the same building's more detailed model (21-zone), calibrated using a single-stage method, resulted in a minimum CVRMSE of 37.5%, while running almost twice as slow.

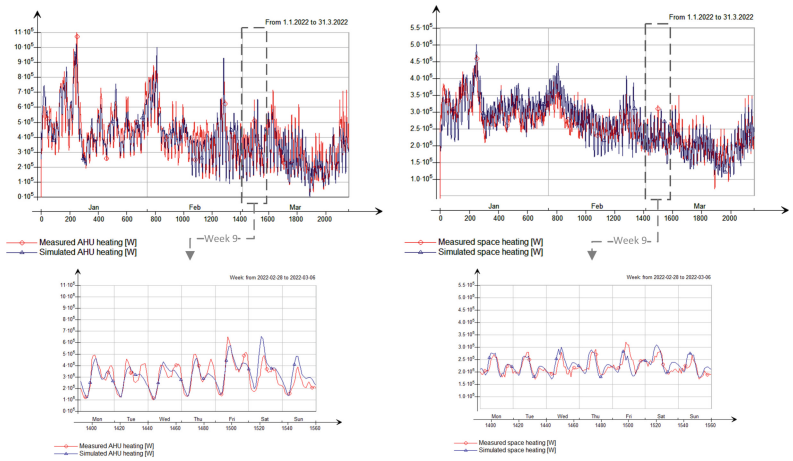


Fig. 7. Hourly calibration results

4 Conclusion

In this study, a two-phase automated calibration scheme was proposed and implemented for monthly and hourly calibration of a simplified simulation model of a multi-purpose complex building. To this end, a multi-objective optimization problem was developed

in Python to calibrate the IDA ICE model's AHU and space heating energy consumption automatically using the IDA-Python API. In phase I, the fixed calibration parameters were calibrated to form the monthly calibrated model. Then, in phase II, AHU's Fan schedule and internal heat gain schedules of the model were refined using the proposed schedule refinement strategy to minimize the hourly CVRMSE between simulated and measured values for both objectives on a weekly basis. The model's accuracy was evaluated weekly to determine whether it needed to be recalibrated or not.

As a result of the proposed calibration scheme, the model could successfully satisfy the accuracy criteria of all standards for hourly estimation of both AHU and space heating energy consumption. The hourly CVRMSE values for the calibrated model in the whole simulation period were 18.8% for AHU heating and 14.1% for space heating energy consumption, while the corresponding hourly NMBE values were − 0.5% and 3%, respectively. For future research, the proposed calibration scheme could be integrated into adaptive frameworks as a synchronization strategy to maintain model accuracy in response to real-time changes in building operations.

References

1. de Wilde, P.: Building performance simulation in the brave new world of artificial intelligence and digital twins: a systematic review. Energ. Buildings. **292**, 113171 (2023)
2. Amini, H., Alanne, K., Kosonen, R.: Building simulation in adaptive training of machine learning models. Autom. Constr. **165**, 105564 (2024)
3. Jeong, C., Byon, E.: Calibration of building energy computer models via bias-corrected iteratively reweighted least squares method. Appl. Energy. **360**, 122753 (2024)
4. Guyot, D., et al.: Building energy model calibration: a detailed case study using sub-hourly measured data. Energ. Buildings. **223**, 110189 (2020)
5. Zuhaib, S., Hajdukiewicz, M., Goggins, J.: Application of a staged automated calibration methodology to a partially-retrofitted university building energy model. J. Building Eng. **26**, 100866 (2019)
6. Yang, T., et al.: An automated optimization method for calibrating building energy simulation models with measured data: orientation and a case study. Appl. Energy. **179**, 1220–1231 (2016)
7. Chong, A., Menberg, K.: Guidelines for the Bayesian calibration of building energy models. Energ. Buildings. **174**, 527–547 (2018)
8. Martínez, S., et al.: A performance comparison of multi-objective optimization-based approaches for calibrating white-box building energy models. Energ. Buildings. **216**, 109942 (2020)
9. Eneyew, D.D., Capretz, M.A.M., Bitsuamlak, G.T.: Continuous model calibration framework for smart-building digital twin: a generative model-based approach. Appl. Energy. **375**, 124080 (2024)
10. Mazzeo, D., et al.: EnergyPlus, IDA ICE and TRNSYS predictive simulation accuracy for building thermal behaviour evaluation by using an experimental campaign in solar test boxes with and without a PCM module. Energ. Buildings. **212**, 109812 (2020)
11. Amini, H., Bjelland, D., Maria, T., Alanne, K., Hamdy, M., Kosonen, R.: Scalable and adaptive multi-stage hourly calibration of simulation models with high usage fluctuations: case studies for multi-purpose buildings. J. Build. Perform. Simul. 1–22 (2025). https://doi.org/10.1080/19401493.2025.2586513
12. Ashrae, A.: Ashrae guideline 14: measurement of energy and demand savings. Am. Soc. Heat. Refrig. Air Cond. Eng. **35**, 41–63 (2002)

13. Walker, C., Coleman, P., Voss, P.: Supplement to M&V Guidelines: Measurement and Verification for Performance-Based Contracts Version 4.0. National Renewable Energy Laboratory (NREL), Golden (2023)
14. Cowan, J.: International Performance Measurement and Verification Protocol: Concepts and Options for Determining Energy and Water Savings-Vol. I, p. 1. International Performance Measurement & Verification Protocol (2002)
15. Chong, A., Gu, Y., Jia, H.: Calibrating building energy simulation models: a review of the basics to guide future work. Energ. Buildings. **253**, 111533 (2021)

Mitigating Data Imbalance in Neural Network-Based Building Energy Prediction Using Multi-Task Learning

Chaobo Zhang[1(✉)], Feng Wang[1], and Jian Zhang[2]

[1] Department of Building Environment and Energy Engineering, The Hong Kong Polytechnic University, Hong Kong, China
chaobo.zhang@polyu.edu.hk

[2] Institute of Refrigeration and Cryogenics, Zhejiang University, Hangzhou, China

Abstract. Buildings operate under a wide range of conditions (e.g., weekdays and weekends), each associated with different energy usage patterns. The amount of data across different conditions may vary significantly, resulting in a data imbalance issue. This issue can lead to biased neural network models that perform poorly when predicting energy demand under data-scarce conditions. To address this issue, this paper proposes a building energy demand prediction method based on multi-task neural networks. This method first identifies operating conditions using the clustering decision tree algorithm. Then, a multi-task neural network model is trained. This model incorporates shared and task-specific parameters. The shared parameters are used to capture common patterns across different conditions, while the specific parameters enable the model to adapt to the unique characteristics of each condition. This method is evaluated using one-year cooling load data from a public building. Three baseline models are selected for performance evaluation, including single-model neural networks, single-model neural networks with data augmentation, and multi-model neural networks. According to the results, the multi-task neural network model shows significantly higher accuracy than the three baseline models. The R^2 and mean absolute error of the multi-task neural network model are improved by 5.2% and 24.7%, respectively, under all conditions compared to those of the single-model neural networks.

Keywords: Multi-task learning · Data imbalance · Building energy prediction

1 Introduction

Accurate prediction of building energy demand is highly valuable for the design, operation, and retrofitting of buildings, as it contributes to enhanced energy efficiency and reduced carbon emissions [1]. Data-driven methods are widely used for predicting building energy demand when large amounts of energy-related data are available [2]. Many data-driven models have been applied for building energy demand prediction, such as multiple linear regression, random forests, gradient boosting, and neural networks (NN). Among these methods, NN is the most commonly used model, adopted in more than 50%

© The Author(s), under exclusive license to Springer Nature Singapore Pte Ltd. 2025
L. Ni et al. (Eds.): CCHVAC 2025, ESE, pp. 260–267, 2025.
https://doi.org/10.1007/978-981-95-3253-7_28

of the papers related to data-driven building energy demand prediction [3]. However, Zhang et al. have demonstrated that imbalanced training data from buildings can significantly reduce the energy demand prediction accuracy of NN [4]. The data imbalance issue results from the broad diversity of operating conditions in buildings. For example, data from weekends (two days) accounts for only two-fifths of that from weekdays (five days). Even if a NN model performs relatively poorly on weekends but very well on weekdays, it will still be considered well-trained, as the loss function typically reflects an average of prediction errors. Hence, NN models tend to exhibit reduced prediction accuracy under operating conditions with significantly less available data.

Training multiple models tailored to different operating conditions is one of the most widely used methods to address the data imbalance issue in building energy demand prediction. For instance, Zhang et al. proposed a multi-model building energy demand prediction method that trained multiple models for different conditions to address the data imbalance issue [4]. The results showed that this method improved the accuracy of NN by 8.5%. Tian et al. also developed a two-phase model training methods to overcome the data imbalance issue in building energy demand prediction [5]. In the first stage, a data-driven model was trained using the entire training dataset. In the second stage, this model was fine-tuned to create multiple specialized models tailored to different operating conditions. This method improved the accuracy by approximately 12.0%. Data augmentation is another method used to address the data imbalance issue. For instance, Zhang et al. employed generative adversarial networks to generate synthetic training data for holidays, thereby mitigating the imbalance between holiday and workday data [6]. The results showed that the building load prediction accuracy of data-driven models on holiday was increased by 16.1%.

However, both of the aforementioned methods have certain limitations. The first method may be ineffective under conditions with very limited data, as training a data-driven model on such limited data often leads to overfitting. For the second method, increasing the amount of training data in data-scarce conditions may reduce the accuracy of data-driven models in data-rich conditions. Multi-task learning might be an effective solution to overcome these limitations. It can train a single NN model to perform multiple prediction tasks under different conditions simultaneously. It includes two kinds of parameters: shared parameters and task-specific parameters. The shared parameters are designed to capture common patterns across different conditions, while the specific parameters allow the model to adapt to the unique characteristics of each condition. The shared parameters help mitigate overfitting in data-scarce conditions, while the task-specific parameters improve accuracy for each condition. Moreover, it typically does not require data augmentation, so the accuracy on data-rich conditions remains unaffected.

Based on the aforementioned idea, this paper proposes a multi-task NN (MTNN)-based method for accurate prediction of building energy demand under imbalanced conditions. One-year operational data from a real public building is utilized to verify the performance of this method. The performance of MTNN is compared with three baseline models: single-model NN, single-model NN with data augmentation, and multi-model NN.

2 Methodology

Figure 1 illustrates the flowchart of the MTNN-based building energy demand prediction method. It includes two steps: condition identification and model development. Condition identification aims to identify the operating conditions of a building. Model development is designed to train a MTNN model for this building.

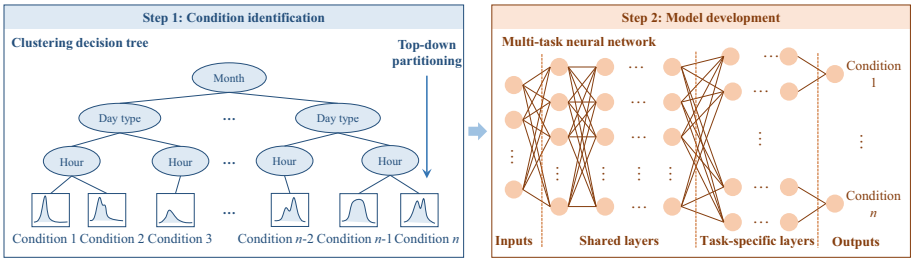


Fig. 1. Illustration of the MTNN-based building energy demand prediction method

2.1 Condition Identification

The goal of condition identification is to partition a building energy demand dataset into several sub-datasets. Data points within the same sub-dataset exhibit similar demand patterns, and data points from different sub-datasets differ significantly.

The clustering decision tree algorithm is one of the most effective methods for identifying building operating conditions based on energy demand distributions under varying conditions [4, 7]. This algorithm combines decision tree and clustering algorithms. It splits a dataset by applying a top-down partitioning strategy (see Fig. 1), starting from the root node and recursively dividing the dataset. There are multiple partitioning nodes in a clustering decision tree. Clustering is applied at each node for data partitioning through a three-step process. First, kernel density estimation is employed to get energy demand distributions that are derived based on different values (such as Jan., Feb., and Mar.) of an input variable (such as month) that has not been previously used. Second, k-means++ clustering is applied to group these distributions into several categories. The Pearson correlation coefficient is applied to quantify the similarity between these distributions, and the silhouette coefficient is utilized to determine the optimal cluster number. Third, perform the first and second steps using other available input variables. The input variable and cluster number with the maximum silhouette coefficient will be chosen for data splitting at this node. More details about this algorithm can be found in Ref. [4].

2.2 Model Development

Multi-task learning is a method where a model is trained to perform multiple tasks simultaneously, rather than training multiple models for different tasks independently [8]. As shown in Fig. 1, the MTNN model utilized in this study is composed of four

types of layers: an input layer, several shared layers, several task-specific layers, and an output layer. The input layer is responsible for receiving the input data. The shared layers are applied to extract common representations across all conditions. Sharing parameters in these layers enable the network to leverage knowledge transfer across different conditions. The task-specific layers are separate branches of the network that handle the unique characteristics of each condition. They can enhance the accuracy of the network for each condition. The output layer is used to generate the final prediction for each condition.

The loss function of this MTNN model is defined by Eq. (1). The mean squared error function is utilized to calculate the loss for a condition. In addition, this study assumes equal importance across all conditions. Thus, an equal-weighting strategy is employed, with each loss weight set to $1/N$. The Adam optimizer, a widely used algorithm for model training, is employed to train this model.

$$L_{total} = \sum_{i}^{N} w_i L_i \tag{1}$$

where, L_{total} is the total loss for all conditions, L_i is the loss for the i-th condition, w_i is the loss weight for the i-th condition, and N is the number of conditions.

3 Results

3.1 Experimental Preparation

The cooling load and outdoor weather data from 2016, collected at 10-min intervals in a real public building in Shenzhen, China, are used for performance verification. The model output is the cooling load. Three commonly used variable types are selected as the model inputs: outdoor weather, time index, and historical data [9]. The outdoor weather inputs include outdoor air temperature and outdoor air relative humidity. The time index inputs include the month, hour of the day, and day of the week. The historical data inputs include the cooling load, outdoor air temperature, and outdoor air relative humidity from one hour ago.

The dataset for each identified condition is randomly split into a training set (70%) and a test set (30%). Two widely utilized accuracy measures are applied for performance evaluation, including coefficient of determination (R^2) and mean absolute error (MAE). Three baseline models are utilized for performance comparison: single-model NN, single-model NN with data augmentation, and multi-model NN. The first baseline model is a fully-connected NN (FCNN) model. Four hyper-parameters are optimized using grid search for this model, including number of hidden layers, number of nodes in each hidden layer, activation function, and learning rate. The second baseline model uses the same NN model as the first baseline model. However, it employs an upsampling-based data augmentation technique to increase the data volume in data-scarce conditions. For each condition, if the number of its data points is fewer than that of the condition with the most data, random sampling with replacement is applied to increase the data volume until it matches the condition with the most data. After upsampling, the data volume is the same for all conditions. The last baseline model trains multiple FCNN models for different conditions. Grid search is also applied to optimize the hyper-parameters of

the MTNN model. Six hyper-parameters are optimized, i.e., number of shared layers, number of nodes in each shared layer, number of task-specific layers, number of nodes in each task-specific layer, activation function, and learning rate. The search space for hyper-parameter optimization of FCNN and MTNN is listed in Table 1.

Table 1. Search space for hyper-parameter optimization

Model	Hyper-parameter	Search space
FCNN	Number of hidden layers	1, 2, 3, 4, 5
	Number of nodes in each hidden layer	6, 8, 10
	Activation function	Sigmoid, tanh, ReLU
	Learning rate	0.1, 0.01, 0.001
MTNN	Number of shared layers	1, 2, 3, 4, 5
	Number of nodes in each shared layer	6, 8, 10
	Number of task-specific layers	1, 2, 3
	Number of nodes in each task-specific layer	6, 8, 10
	Activation function	Sigmoid, tanh, ReLU
	Learning rate	0.1, 0.01, 0.001

3.2 Condition Identification Results

Three variables are selected as input variables for condition identification, including the month, hour of the day, and day of the week. The parameters of the clustering decision tree algorithm are set to be the same as those in Ref. [4]. Five conditions are discovered by the clustering decision tree algorithm, as listed in Table 2. The results indicate that the proportion of data points under different conditions varies significantly, ranging from 7.1% to 39.3%. The average cooling demand varies significantly under different conditions, ranging from 1664.0 kW to 6533.5 kW.

Table 2. Illustration of the conditions identified by the clustering decision tree algorithm

No.	Description	Average cooling demand (kW)	Number of data points
1	May to Oct.; Weekends (0:00–7:00, 20:00–23:00) and Weekdays (0:00–7:00, 19:00–23:00)	3959.5	13611 (26.8%)
2	May to Oct.; Weekends (8:00–19:00)	5148.1	3624 (7.1%)
3	May to Oct.; Weekdays (8:00–18:00)	6533.5	8416 (16.6%)

(*continued*)

Table 2. (*continued*)

No.	Description	Average cooling demand (kW)	Number of data points
4	Jan. to Apr., Nov., Dec.; Weekdays and weekends (0:00 to 8:00, 12:00, 13:00, 16:00 to 23:00)	1664.0	19961 (39.3%)
5	Jan. to Apr., Nov., Dec.; Weekdays and weekends (9:00 to 11:00, 14:00, 15:00)	2506.7	5249 (10.3%)

3.3 Performance Comparison Results

Figure 2 shows the accuracy of three baseline models (BMs 1–3) and MTNN under various conditions on the test set. BM 1 represents the single-model NN, BM 2 is the single-model NN with data augmentation, and BM 3 is the multi-model NN.

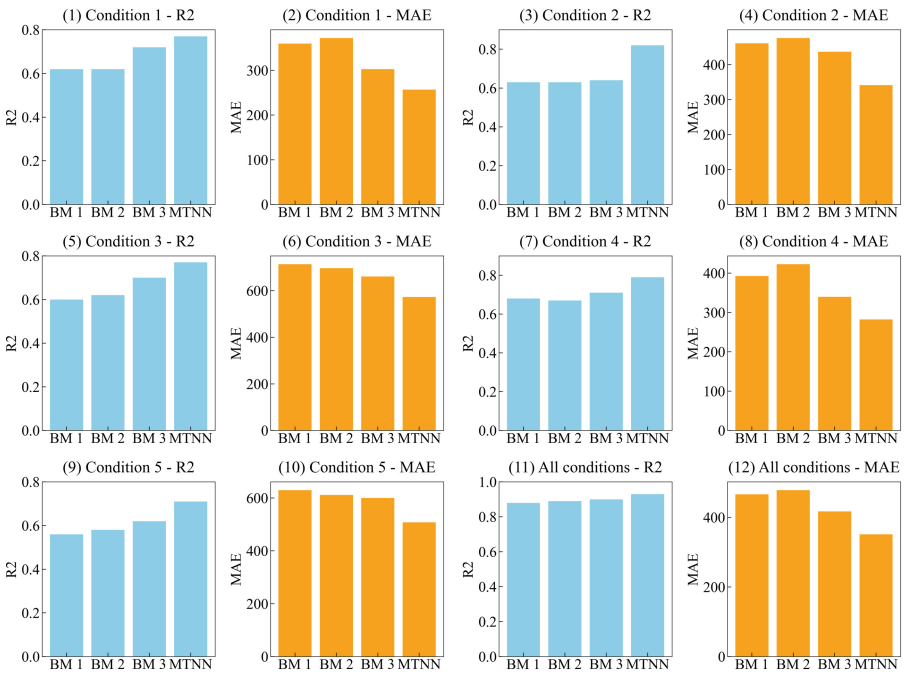


Fig. 2. Prediction accuracy of the three baseline models and MTNN on the test set

According to the accuracy of BM 1 and BM 2 under all conditions (see Fig. 2 (11) and (12)), data augmentation does not enhance the accuracy of NN. This is because data

augmentation enhances the accuracy in conditions with limited data (e.g., conditions 3 and 5), while it reduces the accuracy in conditions with sufficient data (e.g., conditions 1 and 4). As a result, the overall accuracy of NN under all conditions does not show significant improvement. It indicates that data augmentation may not be an effective solution for addressing data imbalance in NN-based building energy demand prediction.

Both BM 3 and MTNN improve the accuracy of NN under each condition. However, the improvement ratio of MTNN is significantly higher than that of BM 3. The R^2 and *MAE* of BM 3 are improved by 2.4% and 10.6%, respectively, under all conditions compared to those of BM 1. The R^2 and *MAE* of MTNN are improved by 5.2% and 24.7%, respectively, under all conditions compared to those of BM 1. It indicates that the multi-task learning strategy is more effective than the multi-model strategy at mitigating data imbalance in NN-based building energy prediction.

The R^2 and *MAE* of MTNN under all conditions are 0.93 and 351.17 kW, respectively. According to ASHRAE guidelines, R^2 for a building energy demand prediction model should exceed 0.75 to be considered suitable for practical applications [7]. The proposed model meets this criterion, indicating its suitability for real-world implementation.

4 Conclusion

Buildings operate under a wide range of conditions, and the amount of data available for each condition can vary significantly. This issue, known as data imbalance, leads to reduced accuracy of neural network models under data-scarce conditions. To address this issue, this paper proposes a building energy demand prediction method based on multi-task neural networks. The clustering decision tree is first applied to identify building operating conditions. Then, a multi-task neural network model is trained to perform multiple prediction tasks under different operating conditions simultaneously.

One-year cooling load data from a public building is applied to verify the performance of the proposed method. The clustering decision tree identifies five conditions for this building, which are highly imbalanced. The proportion of data points across these conditions varies considerably, ranging from 7.1% to 39.3%. Three baseline models are employed for performance comparison: single-model neural networks, single-model neural networks with data augmentation, and multi-model neural networks. It is discovered that data augmentation does not effectively improve the accuracy of neural networks under imbalanced conditions. Both multi-model neural networks and multi-task neural networks can enhance the accuracy of neural networks under imbalanced conditions. However, multi-task neural networks show higher accuracy than multi-model neural networks. It indicates that the multi-task learning strategy is more effective than the multi-model strategy at mitigating data imbalance in neural network-based building energy prediction. The R^2 and mean absolute error of multi-task neural networks are improved by 5.2% and 24.7%, respectively, under all conditions compared to those of single-model neural networks.

This paper demonstrates that multi-task neural networks can effectively mitigate data imbalance in building energy demand prediction. Exploring the performance of multi-task neural networks on other tasks with data imbalance, such as indoor air quality prediction and building energy system fault diagnosis, is highly valuable. Additionally,

investigating the applicability of multi-task neural networks in a wider range of buildings across different climate zones would also be of great significance.

Acknowledgements. This work is supported by the Start-up Fund for RAPs under the Strategic Hiring Scheme from the Hong Kong Polytechnic University (No. P0057944).

References

1. Pan, Y., Zhu, M., Lv, Y., Yang, Y., Liang, Y., Yin, R., et al.: Building energy simulation and its application for building performance optimization: a review of methods, tools, and case studies. Adv. Appl. Energ. **10**, 100135 (2023)
2. Zhao, Y., Zhang, C., Zhang, Y., Wang, Z., Li, J.: A review of data mining technologies in building energy systems: load prediction, pattern identification, fault detection and diagnosis. Energ. Built Environ. **1**, 149–164 (2020)
3. Fathi, S., Srinivasan, R., Fenner, A., Fathi, S.: Machine learning applications in urban building energy performance forecasting: a systematic review. Renew. Sust. Energ. Rev. **133**, 110287 (2020)
4. Zhang, C., Li, J., Zhao, Y., Li, T., Chen, Q., Zhang, X., Qiu, W.: Problem of data imbalance in building energy load prediction: concept, influence, and solution. Appl. Energy. **297**, 117139 (2021)
5. Tian, Z., Lin, X., Lu, Y., Song, W., Niu, J.: Imbalanced data-oriented model learning method for ultra-short-term air conditioning load prediction. Energ. Buildings. **286**, 112931 (2023)
6. Zhang, Y., Wang, J., Yin, Z., Shao, Y., Kang, J., Ma, Z.: Mitigation imbalance distribution: data augmentation of local small sample for building electricity load in time-series generative adversarial network. J. Build. Eng. **99**, 111549 (2025)
7. Zhang, C., Hoes, P.J., Wang, S., Zhao, Y.: Intrinsically interpretable machine learning-based building energy load prediction method with high accuracy and strong interpretability. Energ. Built Environ. (2024)
8. Zhang, Y., Yang, Q.: A survey on multi-task learning. IEEE Trans. Knowl. Data Eng. **34**, 5586–5609 (2022)
9. Sun, Y., Haghighat, F., Fung, B.C.M.: A review of the-state-of-the-art in data-driven approaches for building energy prediction. Energ. Buildings. **221**, 110022 (2020)

A City-Level Carbon Emissions Prediction Method Based on Open-Source Data and LLMs: A Case Study of 65 Winter Cities Worldwide

Biaoqing Tao[1,2], Cheng Sun[1,2], Xiran Cui[1,2], Jingrong Ma[1,2], and Yunsong Han[1,2(✉)]

[1] School of Architecture and Design, Harbin Institute of Technology, Harbin, China
hanyunsong@hit.edu.cn

[2] Key Laboratory of Cold Region Urban and Rural Human Settlement Environment Science and Technology, Ministry of Industry and Information Technology, Harbin, China

Abstract. Winter cities, characterized by severe weather conditions, contribute significantly to global carbon emissions. The carbon emissions reduction of winter cities directly relates to the possibility of achieving the Paris Agreement's temperature control target (1.5 °C). Accurate daily predictions of city-level carbon emissions can help us better understand the carbon emissions mechanism of cities, as well as the impact of urban operation on carbon emissions, and thus better guide low-carbon operation in cities. Through analysis of long-term series carbon emissions data, this study reveals that winter cities globally exhibit typical weekly cyclical fluctuations. By leveraging the analytical capabilities of large language models (LLMs), we propose a new prediction workflow that uses an STL-decomposition-based in-context learning method to guide LLMs in predicting winter city carbon emissions. The method utilizes cities' historical daily carbon emissions data to provide accurate future predictions in a natural language conversational format without additional training. The results suggest that compared with the Multi-layer Perceptron (MLP) and Naive Bayes models (NBM), the LLMs combined with in-context learning improves the prediction accuracy of daily winter city carbon emissions.

Keywords: Carbon emissions prediction · Open-source data · Large language model

1 Introduction

The IEA report highlights that space heating is the largest end-use of global building energy consumption, taking up over 30% of final energy use in buildings [1]. District heating is a major source for this demand, predominantly serving winter cities [2]. In recent years, increasing extreme weather events have led to irregular fluctuations in winter city carbon emissions. Refined prediction is crucial for precise energy management, effective policy formulation, and achieving carbon neutrality.

© The Author(s), under exclusive license to Springer Nature Singapore Pte Ltd. 2025
L. Ni et al. (Eds.): CCHVAC 2025, ESE, pp. 268–276, 2025.
https://doi.org/10.1007/978-981-95-3253-7_29

However, traditional carbon emissions prediction relies on annual or quarterly city-level carbon emissions data for training, lacking high-quality and high-resolution data sources. The coarse temporal resolution of these data leads to a significant time lag effect in city-level carbon emissions prediction. It fails to fully capture the impact of sudden extreme weather events, which cannot meet the requirements of high-frequency and high-precision prediction for refined carbon emissions management. Therefore, there is an urgent need to develop city-level carbon emissions prediction methods based on high-quality and high-resolution data sources. This will enable managers to shift from post-analysis to proactive prediction and real-time regulation, supporting decarbonization planning for winter cities and low-carbon design for buildings.

With the explosive growth of multi-source data and the rise of artificial intelligence, breakthroughs have been achieved in constructing high-resolution carbon emissions databases. Liu, Z. et al. created Carbon Monitor [3, 4], the first public data-base offering near-real-time and daily resolution estimates of global carbon emissions. Despite this progress, further research is needed to effectively use such data-bases for granular forecasting and to capture the uncertainty impacts of sudden events at daily resolution.

In recent years, Large Language Models (LLMs) have shown great potential in handling heterogeneous data and time-series forecasting. TIME-LLM enhances LLMs' reasoning abilities for temporal sequences by reprogramming time-series data [5]. Tempo improves comprehension by decomposing data and dynamically selecting prompts [6]. In the carbon emissions field, Feng et al. explored fine-tuned T5 models for provincial-level industrial carbon emissions forecasting, demonstrating their potential in carbon emissions prediction and complex data integration [7]. How-ever, these methods, which often involve parameter tuning or fine-tuning, require training costs and computational resources, limiting their ability for rapid prediction and flexible deployment.

This study proposes an STL-decomposition-based in-context learning method for LLMs to predict carbon emissions. It leverages LLMs' learning and reasoning capabilities while preserving their natural language interaction and generalization abilities. This approach supports zero-shot training and instant deployment, offering robust support for refined low-carbon strategies in winter cities.

2 Methodology

2.1 Study Area

This study targets winter cities in D category of the Köppen climate classification. The climate classification is defined as having the warmest month's average temperature greater than 10 °C, while the coldest month's average temperature is less than or equal to 0 °C [8]. These cities are mostly between 40°N and the Arctic Circle.

We selected 65 cities from 13 countries (see Fig. 1), including 8 capital cities, 29 provincial capital cities and 28 cities. Their populations range from 50 thousand to over 10 million, based on census data (2019–2021), urban statistical yearbooks, and relevant websites. Despite the limited sample size, these cities are also representative.

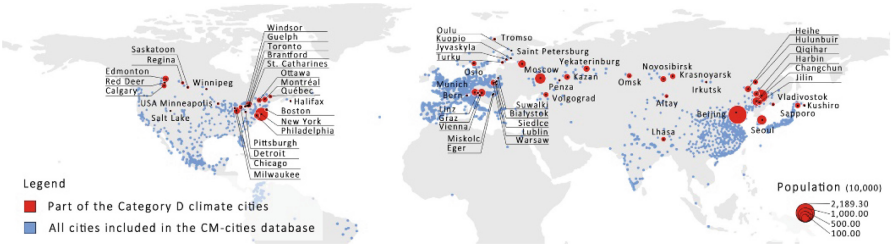


Fig. 1. The geographical location distribution of 65 winter cities selected worldwide

2.2 Winter City Carbon Emissions Prediction Method

This study expounds the process of winter city carbon emissions prediction method from three steps, and the workflow is shown in Fig. 2.

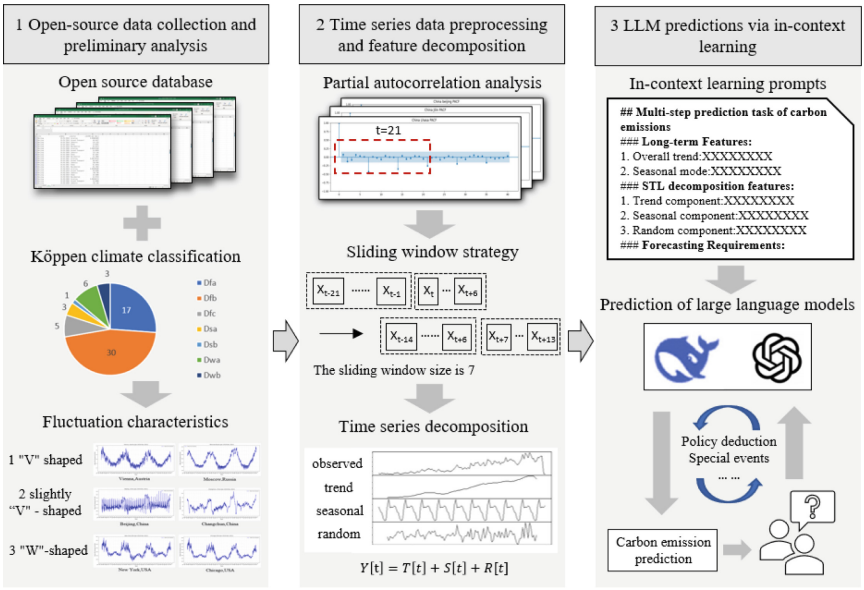


Fig. 2. Workflow of the STL-decomposition-based in-context learning method for LLMs to predict carbon emissions

2.3 Open-Source Data Collection and Preliminary Analysis

In this study, Python 3.12 was used to analyze the daily carbon emissions data of 65 winter cities. Data integration was carried out using Pandas, and carbon emissions sequences were extracted from city-specific Excel files. Descriptive statistics calculated using NumPy include extreme values, central tendency and dispersion measurements. The time trend analysis was visually expressed using Matplotlib, and the fluctuation pattern of carbon emissions was revealed through superimposed observations.

2.4 Time Series Data Preprocessing and Feature Decomposition

In the preprocessing stage, we utilize the Partial Autocorrelation Function (PACF) to analyze the intrinsic relationship of winter city carbon emissions, guiding the formulation of the sliding time window strategy in the prediction. PACF is used to measure the direct correlation between the current value y_t of the time series and the value y_{t-k} in the past lag period, and its calculation method is solved through the following model.

$$y_t = \Phi_1 y_{t-1} + \Phi_2 y_{t-2} + \cdots + \Phi_k y_{t-k} + \epsilon_t \tag{1}$$

Among them, Φ_k is the partial autocorrelation coefficient with a lag of k periods.

Based on the above analysis, we selected 21 days of historical carbon emissions data to predict the carbon emissions for the next 7 days. The multi-step prediction strategy of the sliding time window is shown in Fig. 3. The input of the model requires training data with a time window length of k to predict the values of n future time steps. After the prediction is completed, slide n time steps to predict the value of the next time step.

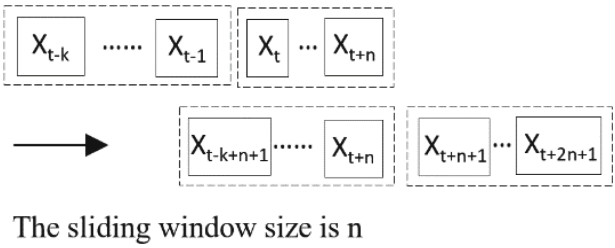


Fig. 3. The multi-step prediction strategy of the sliding time window

Finally, to construct the prompts, we choose seasonal and trend decomposition using Loess (STL) procedure to disaggregate the complex time series information $Y[t]$ into meaningful components for representation, which is helpful for LLMs to understand the time series information. Among them, $T[t]$ represents the trend and can capture the potential long-term patterns in the data; $S[t]$ is the seasonal component that contains repetitive short-term cycles; $R[t]$ is the residual component, which is usually an unpredictable noise with a mean of 0.

$$Y[t] = T[t] + S[t] + R[t] \tag{2}$$

2.5 LLM Predictions through in-Context Learning

In this study, we combine in-context learning with the inherent learning and reasoning abilities of LLMs. This method can enhance the semantic understanding of the model without changing the underlying parameters of the model. It performs exceptionally well especially in scenarios with scarce data and changing demands, featuring real-time performance and zero training costs. It addresses the limitations of traditional carbon emissions prediction models, namely the need for cumbersome construction and retraining due to the changes in data distribution during unexpected events.

3 Results and Discussion

3.1 Descriptive Analysis of Winter City Carbon Emissions Data

Comparison of per capita carbon emissions in 65 winter cities. In Fig. 4, cities in the United States, such as Salt Lake City and Detroit, are in the first echelon, with high annually per capita carbon emissions of 80.73 tons and 71.60 tons respectively. It can be attributed to the energy structure of the old industrial bases and the inefficient infrastructure under the low population density. Most cities in Russia and Canada form the second echelon, with average carbon emissions that are 23% of those cities in the United States. In China, cities show regional differences. Those in Northeast China tend to have relatively high carbon emissions, whereas cities in Northwest China, such as Altay, hold significant low-carbon potential. However, the per capita carbon emissions in cities in European countries are 3.16 tons, achieving high energy efficiency and low carbon emissions through compact urban forms, especially Eger and Siedlce.

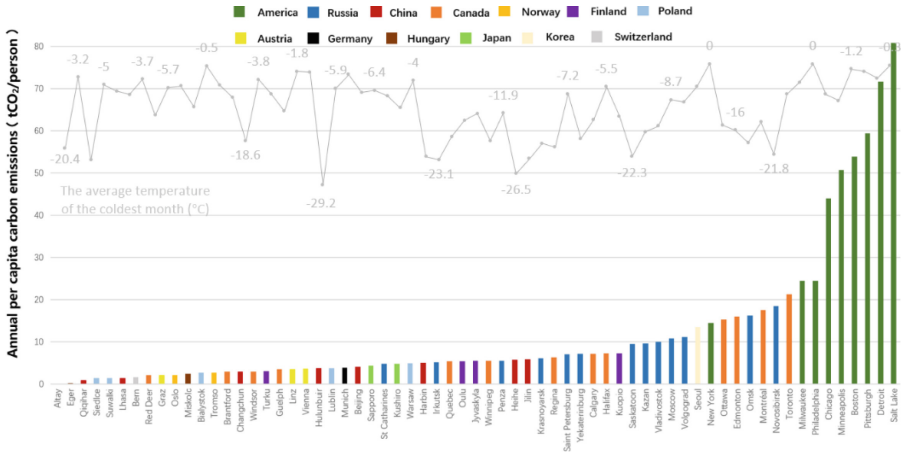


Fig. 4. Analysis of annual per capita carbon emissions in 65 winter cities worldwide

This three-level pattern identifies different carbon emissions reduction paths and highlights the need for precise city-level carbon control policies. Cities in the United States with high carbon emissions require reform their energy systems and infrastructure and establish an upper limit on per capita carbon emissions. Most cities in Canada and Russia are required to promote industrial and technological upgrading. Most cities in European countries provide a global example for compact and low-carbon cities.

It is worth noting that there is a counterintuitive correlation between the severity of cold weather and carbon emissions intensity. The average carbon emissions of cities with an average temperature of the coldest month below −20 °C are lower than those of cities with a temperature above −5 °C. This finding contributes to understanding the complex relationship between climate change and carbon emissions, and providing valuable experience for other regions to addressing severe cold climates.

Comparison of overall fluctuation characteristics of carbon emissions in 65 winter cities. The trend analysis of carbon emissions in 65 winter cities reveals three typical fluctuation characteristics, reflecting the interaction between regional climate and human activities (see Fig. 5). In some cities in European countries, a "V"-shaped pattern prevails, marked by a deep summer trough from June to September and a winter peak from October to March. For example, the winter peak of carbon emissions in Vienna reached 34.22 thousand tons, which was 4.5 times the summer trough of 7.53 thousand tons per day. This significant difference can be attributed to the mild summer climate, which results in lower cooling demands, and district heating during the winter.

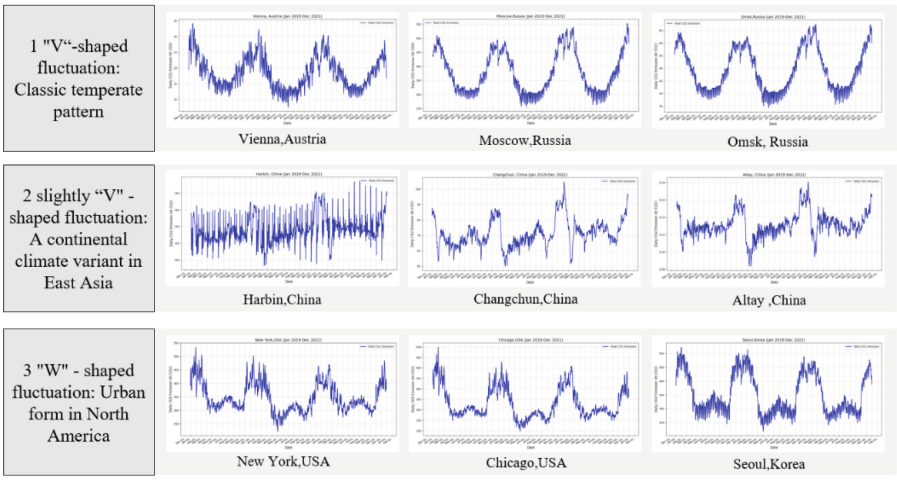


Fig. 5. Three typical fluctuation characteristics of winter city carbon emissions

Most cities in China show a slightly "V"-shaped fluctuation. A spring trough was formed after the heating ended in March, a median platform for industrial activities was formed from June to September, and carbon emissions began to increase sharply from October. The typical curve of Harbin shows that there was an eight-week period from the trough in April (93.6 thousand tons) to the peak in December (194.3 thousand tons), with a month-on-month growth rate of 80–120%, showing the superimposed interference of "late spring cold snap" and industrial production under the continental climate.

Cities in the United States, as well as Seoul, display a "W"-shaped, with the main winter peak and the secondary summer peak forming the double high points. The main peak of carbon emissions in Chicago in January exceeded 450 thousand tons, the secondary peak in August was over 300 thousand tons, and it dropped to around 200 thousand tons in spring and autumn. This structure stems from the dual demands for cooling in summer and heating in winter.

In future, a response model between fluctuation characteristics and carbon emission factors needs to be established to guide different low-carbon strategies.

3.2 Time Series Analysis of Winter City Carbon Emissions

PACF analysis was conducted on the carbon emissions time series of the above-mentioned 65 winter cities from 2019 to 2021, with a sample size of n = 1095 for each city. The approximate statistics of the PACF analysis results are as follows (see Fig. 6).

The analysis results show that the PACF of these cities all present a truncation phenomenon. Most of the data fluctuate around 21 timesteps, indicating a direct linear dependence between the current carbon emissions values of each city and the historical carbon emissions values of the past 21 days. The results show that the carbon emissions cycles of cities in winter share certain similarities. This also helps us determine the prediction strategy and thereby determine the prompts for the LLM prediction task.

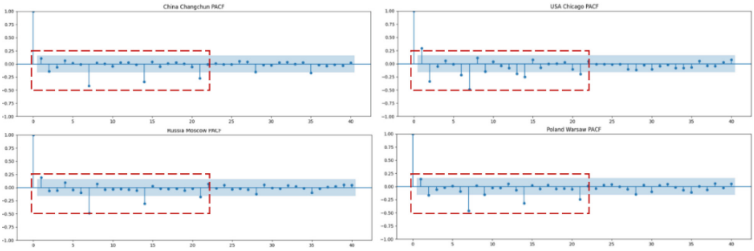


Fig. 6. PACF analysis of some cities (Changchun; Chicago; Moscow; Warsaw)

3.3 LLMs' Carbon Emissions Prediction through in-Context Learning

This study employs two open-source LLMs, DeepSeek and Qwen, using STL-based in-context learning to conduct multi-step prediction experiments. LLMs is not trained and is called directly using the API. The Multi-layer Perceptron (MLP) and Naive Bayes models (NBM) were used as the control group, which were trained on a dataset spanning 33 months and then tested over a subsequent 3-month period. This study also compares the performance of Deepseek with and without in-context learning. The specific prompts used in each case are detailed in Fig. 7.

a. In-context learning prompt words	b. multi-step prediction prompt words
## Multi-step prediction task of carbon emissions **### Long-term characteristics** 1. **Overall trend**: XXXXXX 2. **Seasonal mode**:XXXXXX **### STL decomposition features** 1. **Trend component**:XXXXXX 2. **Seasonal component**:XXXXXX 3. **Residual component**:XXXXXX **### Reasoning steps:XXXXXX** **### Forecasting Requirements:XXXXXX**	## Multi-step prediction task of carbon emissions **Prediction range**:YY/MM/DD- YY/MM/DD **### Historical data (date: value)** 1.(YY/MM/DD:X) 2.(YY/MM/DD:X) 3.(YY/MM/DD:X) . . 21.(YY/MM/DD:X) **### Forecasting Requirements:XXXXXX**

Fig. 7. The comparison of two examples of prompts

Given the number of winter city more, considering the time cost and workload, this study selected 4 cities for each of the 3 fluctuation types based on the fluctuation characteristics, and a total of 12 cities were selected for comparative experiments. Factors such as population size and the average temperature of the coldest month were also taken into account. The mean absolute percentage error (MAPE) and the coefficient of determination (R^2) are used to evaluate the predictive performance of the model.

The results show that Deepseek with in-context learning performs the best (referred to as Deepseek* in Fig. 8), with an average MAPE of 0.0630 and R^2 of 0.6006. Qwen with in-context learning follows closely with an MAPE of 0.0635 and R^2 of 0.5831(referred to as Qwen* in Fig. 8). The MLP has an MAPE of 0.0645 and R^2 of 0.5746. The NBM and Deepseek without in-context learning lag behind, with MAPEs of 0.0740 and 0.0770, and R^2 values of 0.4610 and 0.4047, respectively.

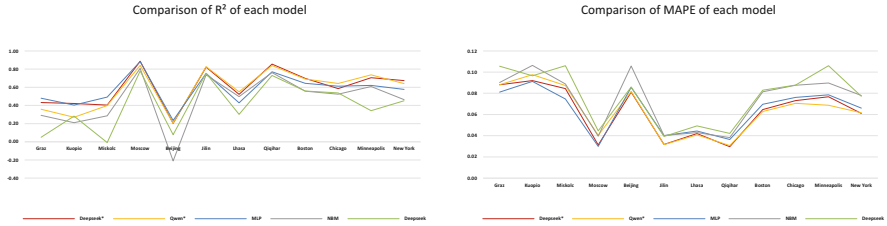


Fig. 8. Comparison of carbon emissions prediction results among different models

These findings indicate that in-context learning significantly enhance LLMs' understanding of time series prediction tasks, improving their performance. Deepseek with in-context learning shows an 18.2% lower MAPE and a 48.4% higher R^2 compared to the non-prompt version. This highlights the potential of LLMs in time series prediction, outperforming traditional models like MLP and NBM.

3.4 Limitations and Prospects

Based on open-source databases, this study utilizes the analytical capabilities of LLMs, combines time series decomposition and context learning, and proposes a new city-level daily carbon emissions prediction workflow. This study also has limitations. Firstly, the spatio-temporal range of the database used in this study is limited, which restricts the application of this method to carbon emission prediction in cities outside the database's scope. Furthermore, the comparative tests of the models are not comprehensive enough. Closed-source LLMs and more machine learning models should be widely considered. Future work will focus on integrating richer data sources, supplementing extreme event modeling and further verifying the robustness and universality of the workflow in a wider range of cities and environments.

4 Conclusion

This study developed and verified a new prediction workflow that uses an STL-decomposition-based in-context learning method to guide LLMs in predicting winter city carbon emissions. Our main conclusions are:

1. **LLMs' potential for carbon emissions prediction through in-context learning:** When providing decomposed time series components (trends, seasons, residuals) as context learning prompts, compared with traditional MLP and NBM, LLMs achieve a lower MAPE and a higher R^2 in predicting daily carbon emissions. Furthermore, in-context learning enables LLMs to adapt to carbon emissions prediction with zero-shot constructed, thereby eliminating the need for expensive fine-tuning, which further demonstrates the importance of context learning.
2. **Distinct carbon emissions patterns in winter cities:** Winter cities exhibit heterogeneous carbon emissions levels with characteristic "V", slightly "V" and "W" fluctuation patterns. These patterns are driven by regional climate, energy, and activities. Notably, extreme cold does not equate to the highest per capita carbon emissions, which further underscores the dominance of energy systems and the form and scale of cities.
3. **Practical advantages for urban management:** This method offers zero training costs for carbon emissions prediction in new cities and can be deployed immediately. It supports natural language interaction and can be used as a decision-making tool for policy simulation and emergency impact assessment.

Acknowledgments. This study was funded by the National Natural Science Foundation of China (Grant No. 52394222), and National Natural Science Foundation of China (Grant No. 52422801).

References

1. Net Zero by 2050: A Roadmap for the Global Energy Sector. https://www.iea.org/reports/net-zero-by-2050. Last accessed 21.06.2025
2. An Energy Sector Roadmap to Carbon Neutrality in China. https://www.iea.org/events/an-energy-sector-roadmap-to-carbon-neutrality-in-china. Last accessed 21.06.2025
3. Huo, D., et al.: Carbon monitor cities near-real-time daily estimates of CO_2 emissions from 1500 cities worldwide. Sci. Data. **9**, 533 (2022)
4. Near-real-time daily estimates of CO_2 emissions from 1500 cities worldwide. https://figshare.com/articles/dataset/Near-real-time_daily_estimates_of_CO2_emissions_from_1500_cities_worldwide/19425665?file=34515194. Last accessed 03.06.2025
5. Jin, M. et al.: Time-LLM: Time Series Forecasting by Reprogramming Large Language Models. arXiv:2310.01728 [cs.LG] (2024)
6. Cao, D. et al.: Tempo: Prompt-Based Generative Pre-Trained Transformer for Time Series Forecasting. arXiv:2310.04948 [cs.LG] (2023)
7. Feng, Z., et al.: Implementing a provincial-level universal daily industrial carbon emissions prediction by fine-tuning the large language model. Appl. Energy. **383**, 125372 (2025)
8. Beck, H., et al.: Present and future Köppen-Geiger climate classification maps at 1-km resolution. Sci. Data. **5**, 180214 (2018)

A Two-Stage Optimal Design Framework for Improving the Energy Flexibility of District Energy System

Chenxin Feng[1], Jiayu Xu[1], Yang Zhao[1(✉)], and Xiao Peng[2]

[1] Zhejiang University, Hangzhou Zhejiang 310000, China
youngzhao@zju.edu.cn
[2] Utrecht University of Applied Sciences, Padualaan 101, 3584 CH Utrecht, The Netherlands

Abstract. Enhancing the flexibility of district energy systems (DES) helps reduce peak load and improve grid stability under high renewable energy penetration. However, existing methods often evaluate flexibility using baseline-free indicators, which lack accuracy in quantifying the benefits of demand response strategies. To address this problem, a two-stage optimal design framework that integrates baseline-required flexibility index is proposed. In the first stage, the operating strategies under baseline scenario and demand response scenario are determined. Then, the energy flexibility is calculated as the deviation between the energy demand under baseline scenario and demand response scenario. In the second stage, a multi-objective optimization approach is employed to minimize economic cost and maximize energy flexibility. The Entropy Weight – Technique for Order Preference by Similarity to Ideal Solution (EW-TOPSIS) method is applied to determine the optimal design solution. Results show that, compared with the conventional single-objective optimization-based design scheme, the proposed method can increase flexibility by 12%. The proposed framework provides a guideline to promote the energy flexibility of DES in the planning and design phases.

Keywords: District Energy System · Energy Flexibility · Optimal Design

1 Introduction

With the increasing integration of renewable energy, the electricity grid is facing the challenge of imbalance between supply side and demand side [1]. By participating in demand response (DR) programs, district energy systems (DES) demonstrate significant potential to adjust energy demand, due to their multi-energy complementary characteristics and the aggregation of numerous flexibility resources. The ability of a system to manage its energy demand and generation in DR programs is defined as flexibility [2]. However, the flexibility potential of DES is often overlooked in the design stage, which limits its exploitation during operation. Improving the energy flexibility at the design stage helps reduce peak energy demand and remit stress on electricity grid.

© The Author(s), under exclusive license to Springer Nature Singapore Pte Ltd. 2025
L. Ni et al. (Eds.): CCHVAC 2025, ESE, pp. 277–286, 2025.
https://doi.org/10.1007/978-981-95-3253-7_30

In the context of optimal design under DR programs, current research can be divided into single-objective and multi-objective optimization approaches. Single-objective optimization typically minimize the annual total cost. The flexibility of system is calculated as a part of objective function in forms of DR penalty [3] or subsidy [4]. Essentially, the objective function of single-objective optimization is a combination of economic indicators and flexibility indicators via specific weighing factor. However, economic indicators often contradict with flexibility indicators. It is difficult to achieve the optimal value for both indicators simultaneously. To achieve the trade-off, multi-objective optimization is essential. For instance, Sun [5] developed a heuristic algorithm for grid-interactive design of net zero energy buildings (NZEB). The mismatch rate between energy supply and demand is considered as one of the objective functions. Notably, the flexibility indicators employed in these studies are baseline-free, meaning their calculation does not depend on a reference scenario without DR control strategies. These indicators are easy to calculate, and reflect the interaction level with electricity grid. However, as noted in [6], approximately 81% of existing flexibility indexes are baseline-required, such as energy shedding [7], peak power shedding [8], cost savings [9] and so on. Baseline-required indexes can evaluate benefits from DR control strategies more accurately, providing a broader applicability than baseline-free indexes. How to integrate the baseline-required flexibility indices into optimal design frameworks remains an open research question.

This paper proposes a two-stage optimal design framework to enhance the energy flexibility of DES. The proposed framework enables the integration of baseline-required flexibility indexes during the design stage, thereby improving the system's flexibility.

2 Methods

The flowchart of proposed two-stage optimal design framework is shown in Fig. 1. It composed of the inner optimization in the operation stage and the outer optimization in the design stage. In the operation stage, model under baseline scenario and the DR scenario are considered.

2.1 Optimization at the Operation Stage

At the beginning of the flowchart, the design parameters of the DES are initialized. These parameters provide initial values for the following operation optimization.

The structure of the DES model is shown in Fig. 2. The electricity load is supplied by photovoltaic panels (PV), electric energy storage (EES) and electricity purchased from external electricity grid. The cooling load is supplied by electricity chillers (EC), heat pumps (HP) and cooling energy storage (CES). The heating load is supplied by the HP, the electric boilers (EB) and the heating energy storage (HES). The cooling and heating loads are modeled by the five-resistances, one-capacitance (5R1C) building thermal model [10]. The detailed equations of the PV, EC, HP, EB, EES, CES, HES and 5R1C models are provided in Eqs. (1)–(5).

For PV models [11]:

$$P_{PV}(t) = f_{PV}[1 + \delta(T_{cell}(t) - T_{stc})]P_{PV}^{rated} I(t)/I_{stc} \tag{1}$$

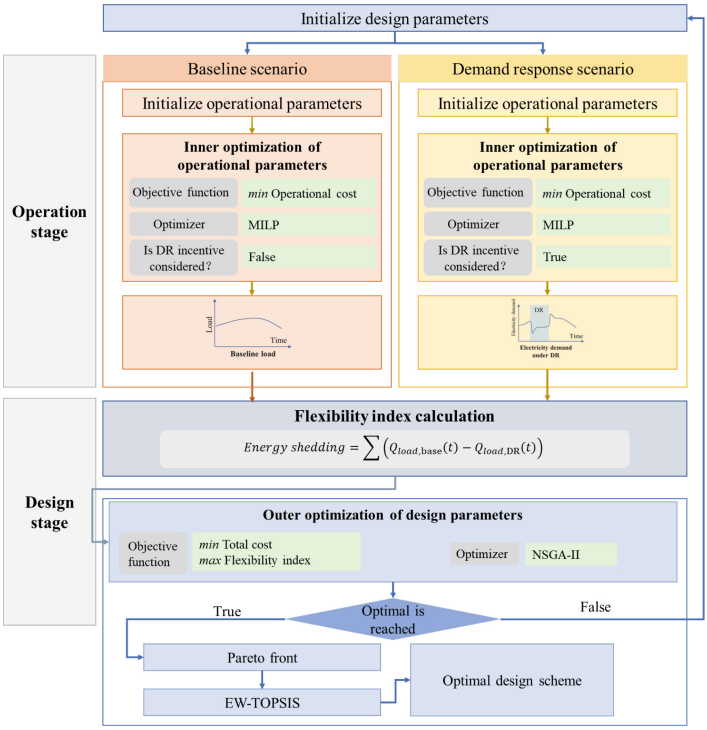


Fig. 1. The schematic of proposed two-stage optimal design framework.

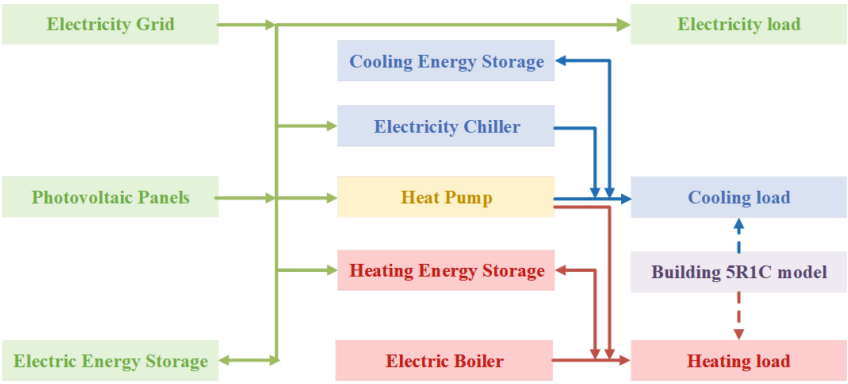


Fig. 2. The model structure of DES.

$$T_{cell}(t) = T_0(t) + 0.03I(t) \tag{2}$$

where $P_{PV}(t)$ is the generating power of the PV device at time t; f_{PV} is the power derating factor of the PV device; P_{PV}^{rated} is the rated capacity of the PV device; $I(t)$ is the solar radiation intensity at time t; I_{stc} is the solar radiation intensity under standard

test conditions; $T_{cell}(t)$ is the surface temperature of the PV cell during actual operation; T_{stc} is the temperature of the PV battery under standard test conditions; δ is the power temperature coefficient of the PV device.

For energy transition equipment:

$$Q_X^c(t) = \eta_X P_X(t) \tag{3}$$

where $Q_X^c(t)$ is the cooling or heating power of the energy transition equipment at time t; η_X is the cooling or heating efficiency of the equipment X; and $Px(t)$ is the electrical input power of the equipment X at time t, equipment X denotes EC, HP and EB.

For energy storage equipment:

$$SOC(t+1) = SOC(t) + \left(\eta_{cha} x_{cha} P_{te,cha}(t) - x_{te,dis} P_{te,dis}(t)/\eta_{te,dis}\right)\Delta t / V_{te} \tag{4}$$

where $SOC(t+1)$ and $SOC(t)$ are the charge state of the ES at time $t+1$ and t, respectively; $\eta_{te,cha}$ is the charging efficiency of the ES, respectively; $P_{cha}(t)$ is the charging power of the ES at time t; x_{cha} is variables indicating the state of charging and discharging energy, ranging from –1 to 1; V_{te} is the rated capacity of the ES.

For RC model:

$$C_i \frac{dT_i(t)}{dt} = \sum_j \frac{T_j(t) - T_i(t)}{R_{ij}} + Q_r(t) + Q_i(t) + Q_{load}(t) \tag{5}$$

where C_i is the thermal capacitance at node i; $T_i(t)$ and $T_j(t)$ are the temperature at node i and j at time t; R_{ij} is the thermal resistance between node i and node j, $Q_r(t)$, $Q_i(t)$ *and* $Q_{load}(t)$ are the heat gains from solar radiation, internal gains and HVAC system.

The equations of electricity balance, cooling energy balance and heating energy balance are provided in Eqs. (6)–(8).

Electric power balance:

$$P_{PV}(t) + P_{ele,buy}(t) = P_{load}(t) + P_{EB}(t) + P_{EC}(t) + P_{HP}(t) + P_{ees,charge}(t) \tag{6}$$

Heating power balance:

$$Q_{EC}(t) + Q_{HP}^c(t) = Q_{load}^c(t) + Q_{ces,charge}(t) \tag{7}$$

Cooling power balance:

$$Q_{EB}(t) + Q_{HP}^h(t) = Q_{load}^h(t) + Q_{hes,charge}(t) \tag{8}$$

In the DR scenario, the control strategy is optimized to minimize the operational cost. The operational cost is composed of cost of purchasing electricity, the cost of equipment maintenance, the penalty of users' thermal comfort sacrifice and the DR incentives, as Eqs. (9)–(13) shows. The linear operational optimization is solved by Gurobi solver. The decision variables are operational outputs of each equipment and the indoor temperature setpoints of buildings. Equipment capacity constraints are represented in Eq. (14). The constraint of indoor temperature setpoint is represented in Eq. (15).

$$C_{ope,DR} = C_{ele} + C_{main} + C_{com} - C_{inc} \tag{9}$$

$$C_{ele} = \sum_{d=1}^{365} \sum_{t=1}^{24} c_{ele,buy} P_{ele,buy,DR}(t) \tag{10}$$

$$C_{main} = \sum_{d=1}^{365} \sum_{t=1}^{24} \sum_{j} c_{main,j} \cdot X_j \tag{11}$$

$$C_{com} = \alpha \cdot \sum_{d=0}^{n_{DR}} \sum_{t=t_{DR,start}}^{t_{DR,end}} \max\left(Q_{load,DR}(t) - Q_{load,base}(t), 0\right) \tag{12}$$

$$C_{inc} = \lambda \sum_{d=0}^{n_{DR}} \sum_{t=t_{DR,start}}^{t_{DR,end}} \left(P_{ele,buy,base}(t) - P_{ele,buy,DR}(t)\right) \tag{13}$$

where C_{ope} is the annual operational cost, C_{ele} is the cost of purchasing electricity, C_{main} is the cost of equipment maintenance, C_{com} is the sacrifice of users' thermal comfort, C_{inc} is the incentive from DR events, $c_{ele,\,buy}$ is the unit prices for electricity purchase, $c_{main,\,j}$ is the maintenance cost of equipment j , X_j is the capacity of equipment j, α is the penalty factor, n_{DR} is the number of DR events in one year, $t_{DR,\,start}$ and $t_{DR,\,end}$ is the start time and end time of DR period; $Q_{load,\,DR}$ and $Q_{load,\,base}$ are the cooling/heating load under DR scenario and baseline scenario;, λ is the incentive price per response amount.

Constraints of equipment capacity:

$$0 \leqslant P_j(t) \leqslant X_j \tag{14}$$

where $P_j(t)$ is the electrical input power of the EB, HP, EC and PV. The X_j is the designed capacity of EB, HP, EC and PV.

Constraint of indoor air temperature:

$$T_{set}(t) = \begin{cases} [T_{low}, T_{up}] if t_{DR,start} \leqslant t \leqslant t_{DR,end} \\ T_{base} \qquad\qquad otherwise \end{cases} \tag{15}$$

where T_{low} and T_{up} is the lower bound and upper bound of the adjustable band of temperature setpoint.

In the baseline scenario, it is assumed that no incentive-based DR events occur. The indoor temperature setpoint is set at constant value T_{base}, and the equipment operation is optimized.

2.2 Optimization at the Design Stage

The comparative experiment is conducted to evaluate the impact of integrating flexibility-related index during the design stage. Three cases are: (1) the proposed flexibility-integrated multi-objectives design optimization (MOO), (2) single-objective design optimization considering DR events (SOO+DR) and (3) single-objective design optimization without consideration of DR events (SOO).

In the flexibility-integrated design, the objective is to maximize flexibility index and minimize the total cost. Depending on the dimension of interest—such as power, time,

or cost—the flexibility can be quantified using different metrics. In this study, *Energy shedding,* one of the most popular flexibility index is selected, which measures the system's ability to shift energy use from DR period to non-DR period [6]. The equations of Energy shedding are provided in Eqs. (16)–(17).

$$Energy\ shedding = \sum_{t=t_{DR,start}}^{t=t_{DR,end}} \left(Q_{load,\mathrm{base}}(t) - Q_{load,\mathrm{DR}}(t)\right) \tag{16}$$

$$C_{ope,base} = C_{ele,buy} \tag{17}$$

The annual total cost is calculated using Eqs. (18)–(19). The decision variables are the configuration of each equipment. Nondominated sorting genetic algorithm II (NGSA-II) is adopted to solve the multi-objective optimization problem. If the design parameters fail to meet operational demands, the objective function returns extremely high costs and minimal flexibility value. Upon completion of NSGA-II process, a pareto solution set is obtained. The entropy weight technique for order preference by similarity to an ideal solution (EW-TOPSIS) method is applied to select final design scheme.

$$C_{tot} = C_{inv} + C_{ope} \tag{18}$$

$$C_{inv} = \sum_{j} c_{epu,j} X_j \frac{r(1+r)^Y}{(1+r)^Y - 1} \tag{19}$$

where C_{tot} is the annual total cost, C_{inv} is the annual equipment investment cost, $c_{epu,j}$ is the unit price of equipment j, r is the discount rate, Y is the lifespan of equipment.

For the SOO+DR based design scheme, the only difference from the MOO design scheme is that in the design stage, the optimization object is to minimize the total cost. For the SOO based design scheme, the demand response incentive is not considered.

3 Case Study

A region in Hangzhou is selected as the study area. Typical days of summer, winter and transitional seasons are selected to represent the weather conditions throughout the year. The electricity pricing takes the time-of-use pricing in Hangzhou. The parameters used in this study are summarized in Tables 1 and 2 [10].

Table 1. The economic and technical parameters for the energy equipment.

Type	Efficiency	Initial investment (¥/kW)	Maintenance cost (¥/kWh)
PV		8000	0.060
GB	0.85	670	0.010
EC	4.00	900	0.030

(*continued*)

Table 1. (*continued*)

Type	Efficiency	Initial investment (¥/kW)	Maintenance cost (¥/kWh)
HP	Cooling:5.00 Heating:4.00	1300	0.020
TES	0.90	1000	0.05
HES	0.88	500	0.02
CES	0.88	600	0.02

Table 2. Other parameters used in the case study.

Parameters	Value	Parameters	Value
f_{PV}	0.95	I_{stc}	1 kW/m^2
n_{DR}	30	T_{base}	26 °C
T_{low}	24 °C	T_{stc}	25 °C
T_{up}	28 °C	$t_{DR,\,start}$	12:00
$t_{DR,\,end}$	14:00	α	0.8 CNY/kWh
δ	-0.005 %/°C	λ	3.5 CNY/kWh

4 Results

4.1 Capacity Configuration Results

The pareto front is illustrated in Fig. 3. Flexibility increases with rising total cost. The increasing rate gradually decrease, and eventually the flexibility reaches a plateau. This indicates that these two objectives have contract relationship and cannot reach the optimum simultaneously. According to the result of EW-TOPSIS, Table 3 summarizes the optimal equipment capacity configuration and objective results.

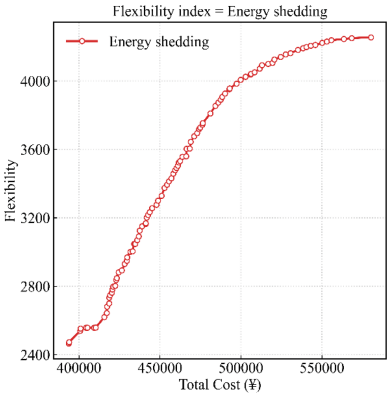


Fig. 3. Pareto fronts for multi-objective optimization.

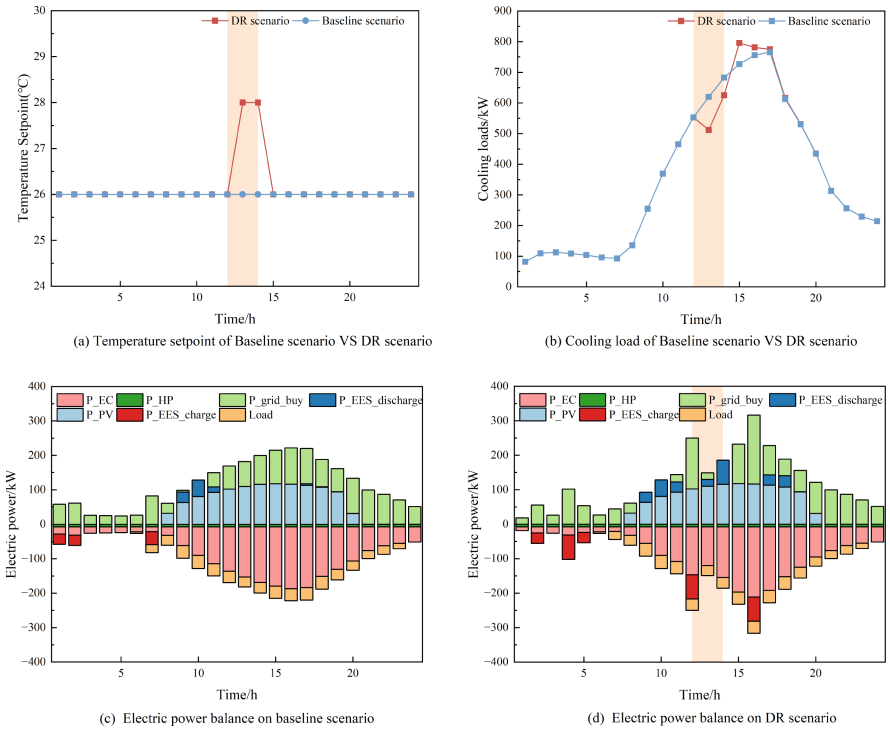
Table 3. The optimized equipment capacity and objective results.

	MOO	SOO+DR	SOO
PV/kW	113	123	108
HP/kW	74	160	153
EC/kW	172	0	0
EB/kW	0	0	0
CES/kW	31	0	0
HES/kW	50	10	0
EES/kW	48	50	0
C_{inv}/CNY	100071	100547	85421
C_{ope}/CNY	292887	285939	315197
C_{tot}/CNY	392958	386486	400618
Energy shedding/kWh	7583	6721	0

It is evident that compared with SOO, design schemes of MOO and SOO+DR equip with more energy storage equipment, leading to a significant increase in flexibility index—from 0 kWh to 6721 ~7583 kWh. Comparing the design schemes between MOO and SOO+DR, MOO scheme provides more flexibility (increasing from 6721 kWh to 7583 kWh, increasing by 12%). This increase comes at the expense of higher annual total cost, which also increases from 386486 CNY to 392958 CNY. Specifically, the MOO design scheme invests less on high-efficiency HP, contributing to higher operational costs. This trade-off enables the system to access greater flexibility during DR periods.

4.2 Operational Results

Based on the optimal capacity configuration, the operational strategies of building and energy equipment on summer typical day is depicted in Fig. 4.



(a) Temperature setpoint of Baseline scenario VS DR scenario

(b) Cooling load of Baseline scenario VS DR scenario

(c) Electric power balance on baseline scenario

(d) Electric power balance on DR scenario

Fig. 4. Operating strategy in typical summer day.

As shown in Fig. 4 (a) and (b), in typical summer day, the indoor temperature setpoint is set at the maximum value at the beginning of DR period. In response, the cooling load suffer a sudden drop. After the DR period, the temperature setpoint is reset at the baseline value, and the cooling load suffer a rebound period before returning stability. For the electric power demand of the whole system, compared with the baseline scenario in Fig. 4 (c), in DR scenario, more electricity will be purchased from grid before the DR period to store the electricity, and more electricity will be purchased after the DR period to compensate for the rebound effect. While during the DR period, the electricity purchased from grid decreases sharply, from 155 kWh in baseline scenario to 19 kWh in DR scenario.

5 Conclusion

This study proposes a two-stage optimal design framework to enhance the flexibility of DES. First, design parameters are initialized, and operating strategies are determined under both baseline and DR scenario. Then, the flexibility index is calculated. Finally,

the design parameters are optimized under the dual objectives of minimizing the annual cost and maximizing the flexibility.

The capacity configuration results show that, by using MOO, the flexibility can increase by 12% compared with SOO+DR design scheme, coming with an increase in annual total cost. Operational results show that, under DR scenario, temperature setpoints and energy storage usage are adjusted to reduce the energy demand during DR period. The proposed method provides a structured framework to integrate baseline-required flexibility index into the design process. Further work can extend the framework by incorporating the impacts of weather-related uncertainty and extremity on capacity configurations.

6 Acknowledgements

This work was supported by the National Natural Science Foundation of China (No. 52161135202) and the Merian Fund by the Dutch Research Council (482.20.608).

References

1. Marouani, I.: Contribution of renewable energy technologies in combating phenomenon of global warming and minimizing GHG emissions. Clean Energy Sci. Technol. **2**, 164 (2024). https://doi.org/10.18686/cest.v2i2.164
2. Jensen, S.Ø., Marszal-Pomianowska, A., Lollini, R., Pasut, W., Knotzer, A., Engelmann, P., et al.: IEA EBC Annex 67 Energy Flexible Buildings. Energy Build. **155**, 25–34 (2017). https://doi.org/10.1016/j.enbuild.2017.08.044
3. Shivanaganna, N., Shivamurthy, K.P., Boddapati, V.: Optimal strategy for transition into nearly zero energy residential buildings: a case study. Energy. **307**, 132742 (2024). https://doi.org/10.1016/j.energy.2024.132742
4. Stochastic peak shaving scenario generation for grid-friendly building energy system design. Energy. **324**, 135925 (2025). https://doi.org/10.1016/j.energy.2025.135925
5. Sun, Y., Ma, R., Chen, J., Xu, T.: Heuristic optimization for grid-interactive net-zero energy building design through the glowworm swarm algorithm. Energy Build. **208**, 109644 (2020). https://doi.org/10.1016/j.enbuild.2019.109644
6. Li, H., Johra, H., de Andrade, P.F., Hong, T., Le Dréau, J., Maturo, A., et al.: Data-driven key performance indicators and datasets for building energy flexibility: a review and perspectives. Appl. Energy. **343**, 121217 (2023). https://doi.org/10.1016/j.apenergy.2023.121217
7. Johra, H., Heiselberg, P., Dréau, J.L.: Influence of envelope, structural thermal mass and indoor content on the building heating energy flexibility. Energy Build. **183**, 325–339 (2019). https://doi.org/10.1016/j.enbuild.2018.11.012
8. Reynders, G., Diriken, J., Saelens, D.: Generic characterization method for energy flexibility: applied to structural thermal storage in residential buildings. Appl. Energy. **198**, 192–202 (2017). https://doi.org/10.1016/j.apenergy.2017.04.061
9. Junker, R.G., Azar, A.G., Lopes, R.A., Lindberg, K.B., Reynders, G., Relan, R., et al.: Characterizing the energy flexibility of buildings and districts. Appl. Energy. **225**, 175–182 (2018). https://doi.org/10.1016/j.apenergy.2018.05.037
10. Tian, Z.: A bi-level optimization method for regional integrated energy system considering uncertainty and load prediction under climate change. J. Build. Eng. **84**, 108527 (2024). https://doi.org/10.1016/j.jobe.2024.108527

Centralized Demand Response Control for a Finnish Apartment Building Considering Indoor Air Conditions

Yuchen Ju(✉), Perttu Karjalainen, Juha Jokisalo, and Risto Kosonen

Department of Energy and Mechanical Engineering, Aalto University, Espoo 00076, Finland
yuchen.ju@aalto.fi

Abstract. Achieving climate neutrality increasingly relies on integrating renewable energy sources into existing energy infrastructures. Demand response techniques may enable the incorporation of variable renewable energy within district heating networks. Therefore, this paper analyzed the benefits of a rule-based centralized demand response control applied to a Finnish district heated apartment building. It was simulated by the validated dynamic building simulation software, IDA ICE. The control strategy was developed considering the changing trends of Finnish hourly dynamic district heat prices to adjust inlet water temperature setpoints of water radiators. Indoor air conditions were taken into account to maintain the temperatures at least 20 °C when designing the control strategy. What is more, setpoint smoothing was utilized to minimize rebound effects. The results indicate that the implementation of the centralized demand response control can save the district heat energy costs of the apartment building by 3.8% during the heating season. In addition, thermal comfort was preserved, with the living space's minimum indoor air temperature maintained at 20 °C. These findings demonstrate that demand response can contribute to economic goals without compromising thermal comfort.

Keywords: Demand Response · District Heating · Thermal Comfort

1 Introduction

District heating remains the dominant approach to space heating in Finland. As of 2020, it supplied approximately 45% of the heating demand across residential, public, and commercial sectors. By 2021, this heating method had been adopted by 54% of residential properties, 84% of public buildings, and 58% of commercial buildings [1]. Because of the aim to achieving carbon neutrality by 2035 in Finland [1], it is imperative to implement decarbonization approaches to energy sector in parallel with improving the energy efficiency of buildings.

One key strategy is demand side management, which involves changing consumer energy consumption patterns to better align with variable energy production [2]. Typically, demand response (DR) offers financial incentives to users to increase energy

© The Author(s), under exclusive license to Springer Nature Singapore Pte Ltd. 2025
L. Ni et al. (Eds.): CCHVAC 2025, ESE, pp. 287–295, 2025.
https://doi.org/10.1007/978-981-95-3253-7_31

consumption during periods of low pricing, enabling them to realize economic benefits through demand response. This encourages further exploration of the possibility for adjusting building energy consumption using demand response to align supply and reduce energy costs.

A practical application of demand response has been developed in building energy systems via utilizing the thermal mass of buildings. By adjusting temperature setpoints of indoor air or space heating inlet in response to fluctuating energy prices, heat can be charged in thermal mass when prices are low and discharged when prices rise. This means higher setpoints are set during low-price periods to store heat, and lower setpoints are implemented to reduce consumption when prices are high [3, 4]. Recently, there has been a growing focus on how demand response can be employed in buildings connected to district heating systems [5, 6].

This study investigated the potential advantages of a centralized demand response control strategy for an apartment building in Finland. It also assesses the effects by the strategy on indoor air temperatures were analyzed in the results.

2 Methods

2.1 Building Parameters

The studied apartment building locates at Kisakylä, Helsinki, Finland. Table 1 lists the building parameters. The dimensioning heating power demand is the power for district heating at design outdoor temperature, –26 °C, calculated excluding internal heat gains. There is natural ventilation for the building.

Table 1. Apartment building properties.

Properties		Apartment Building
Heated net floor area (m^2)		3402
Floor number		4
U-Value ($W/m^2 \cdot K$)	External walls	0.73
	Roof	0.70
	Ground slab	1.37
	Windows	2.9
Air leakage rate at 50 Pa pressure difference($m^3/h \cdot m^2$)		4
Indoor air temperature setpoint of for heating (°C)	Living area:	21
	Bathroom:	23
	Cellar and staircase:	17
Dimensioning heating power demand (kW)		367

The apartment building was equipped with water radiators. Figure 1 shows the district heating and space heating radiators inlet water temperatures changed with outdoor temperatures.

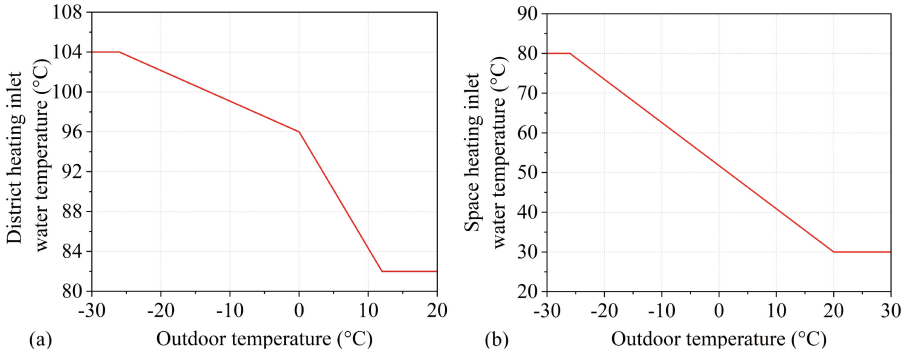


Fig. 1. Control curves of inlet water temperatures for district heating (**a**) and space heating (**b**) as a function of outdoor temperatures.

2.2 Weather Data and Simulation Software

Figure 2 shows the outdoor temperatures during the heating season in Helsinki, Finland are shown [7]. The minimum outdoor temperature is −22.1 °C in January.

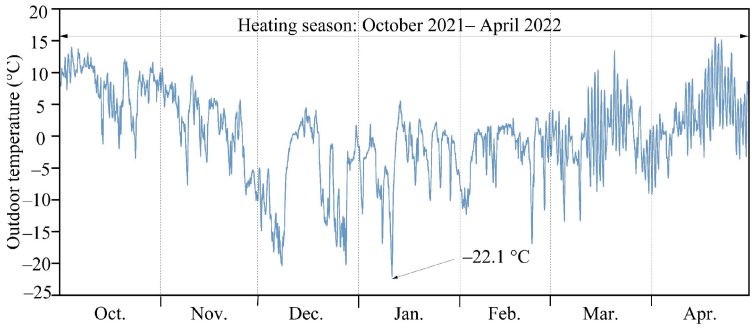


Fig. 2. Outdoor temperatures of Helsinki, Finland during the heating season.

The software IDA Indoor Climate and Energy (IDA ICE) was selected for the demand response simulation. Investigations have provided substantial justification conducted using IDA ICE in this research for the simulation [8–10].

2.3 Hourly District Heat Prices

The dynamic hourly district heat prices were calculated according to the conditions of an actual plant in Espoo which includes three combined heat and power units, several heat-only boilers, heat pumps (HP) using sewage water waste heat, and a centralized short-term storage. To make sure that the annual revenues by selling heat utilizing the hourly prices are realistic, the prices were adjusted thus the annual weighted average price was equal to the one of a local district heating company [11]. Figure 3 shows the hourly district heat prices during heating season. More details of the price calculation and configuration can be found in the study by Ju et al. [12].

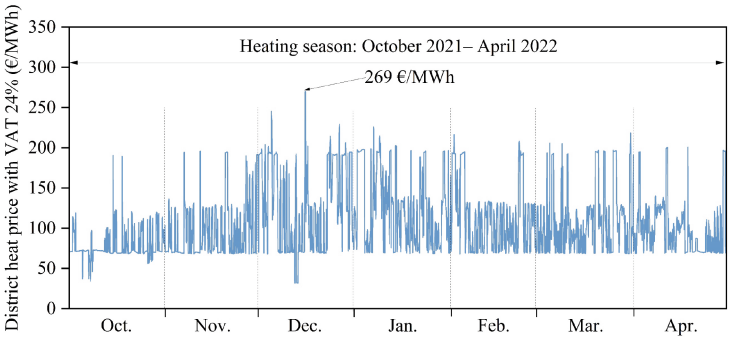


Fig. 3. Hourly district heat prices during heating season.

2.4 Centralized Demand Response Control Strategy

This study made the assumption that the moving future 24-h district heat prices were known. The control signals (CS) of demand response were determined based on the method from Behrang-Sirén [13] as shown in Eq. (1). The price trend was categorized with signals as –1 and 0. The value –1 means the price trend is decreasing, and the current price is high. The idea of the centralized demand response control is to reduce the inlet water temperature of water radiators when the district heat price is high.

$$\begin{aligned} &If\ \ HEP > HEP_{avr}^{+1,+24},\ Then\ CS = -1 \\ &Else\ CS = 0 \\ &End\ If \end{aligned} \tag{1}$$

where *HEP* is the hourly district heat energy price, €/MWh; *HEP+1+24 avr* is the future average district heat price from hour 1 to 24, €/MWh.

Figure 4 shows the rule-based centralized demand response (DR) control algorithm.

The space heating system in the building controlled the inlet water temperatures. The inlet water temperature setpoints of radiator network decreased in a way that heating power output of radiators cut by 80% if living area temperatures were 20 °C or higher and CS=–1. Figure 5 presents the inlet water temperature setpoints of water radiators changed with the outdoor temperatures after reducing heating power output by 80%. Setpoint smoothing technique was implemented to these inlet water temperatures to mitigate rebound effects [12].

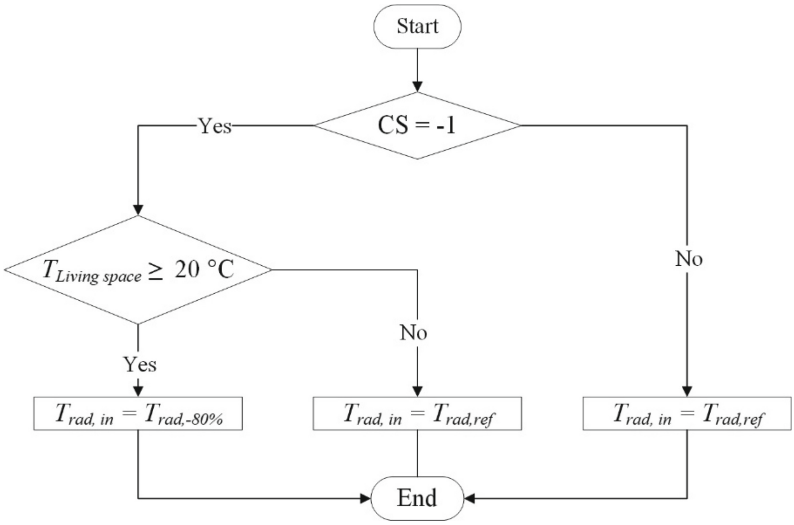


Fig. 4. Algorithm for centralized demand response control.

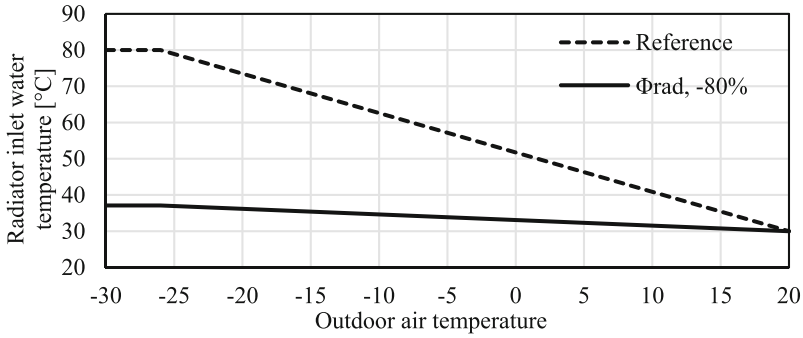


Fig. 5. Inlet water temperature of radiators for demand response.

3 Results

3.1 District Heating Consumption and Energy Costs

Figure 6 presents the district heating consumption and the district heat energy costs of the apartment building with and without the centralized demand response control during the heating season. The results indicate that the space heating consumption cuts by 11 MWh, which leads to a 2.4% of saving for the total consumption. The control strategy saves the district heat energy cost by 2156 € which is 3.8%.

3.2 Indoor Air Temperatures

Figures 7, 8, 9, 10 show the indoor air temperatures' duration curves during the heating season (from 1st of Oct. to 30th of Apr.) for coldest and warmest living spaces, bathrooms,

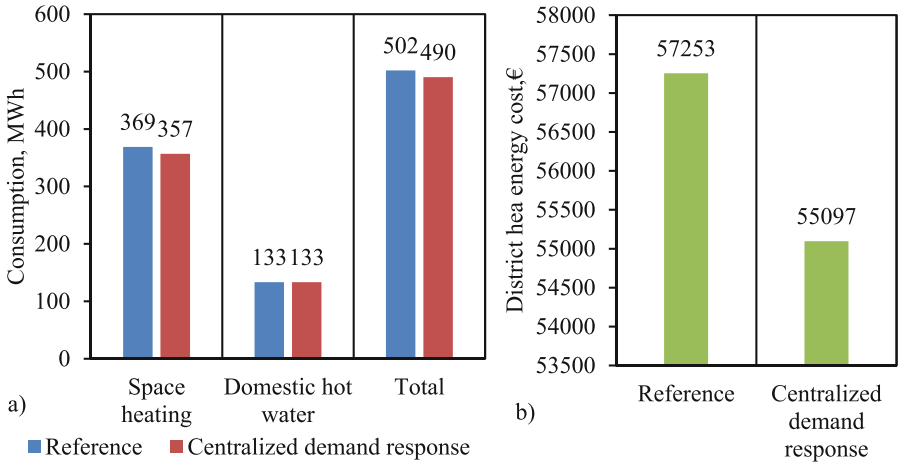


Fig. 6. District heating consumption a) and district energy costs b) during the heating season.

cellars and staircases separately. Since there was the feedback control to stop decreasing inter water temperatures of water radiators when the living area temperatures were lower than 20 °C, it can be seen in Fig. 7, the thermal comfort can be guaranteed for the coldest living space with the centralized demand response control. When the control was employed, there was only small temperature difference for the warmest living space with the reference case. The coldest living space's minimum indoor air temperature had 1 °C temperature difference compared with the reference one after demand response utilization.

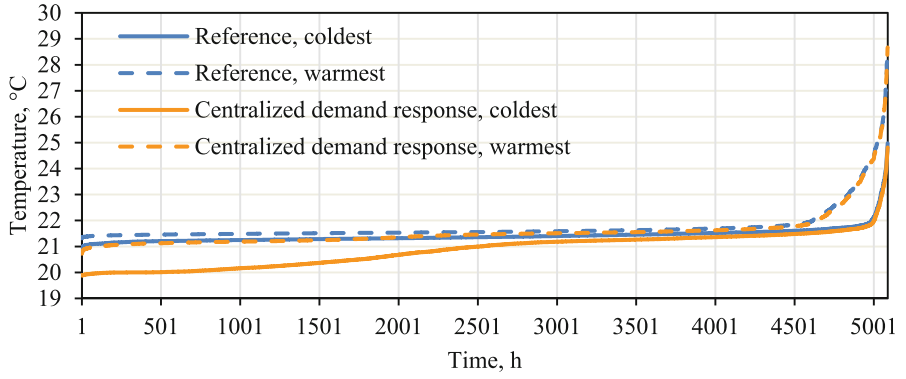


Fig. 7. Indoor air temperatures' duration curves for living spaces during the heating season.

Different with living spaces, there was no feedback control to maintain a minimum indoor air temperature for bathrooms, cellars and staircases.

Therefore, compared with the reference cases, there is an obvious reduction of the indoor air temperatures, especially for these coldest rooms. Among these four room

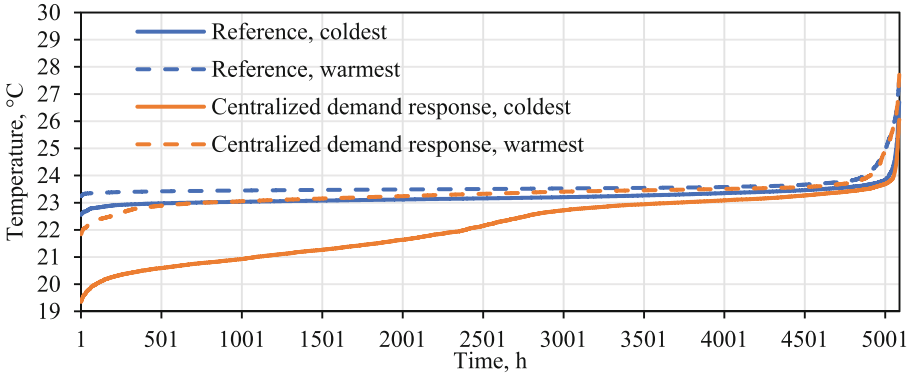


Fig. 8. Indoor air temperatures' duration curves for bathrooms during the heating season.

types, the bathroom's indoor air temperatures were the most affected by the centralized demand response control. The coldest bathroom's minimum indoor air temperature had 3.2 °C temperature difference compared with the reference one after demand response application. In addition to no feedback control, another reason is that the apartment building is not well-insulated and water radiators are installed for heating in the bathrooms, which leads to a quicker response and faster temperature drop than floor heating.

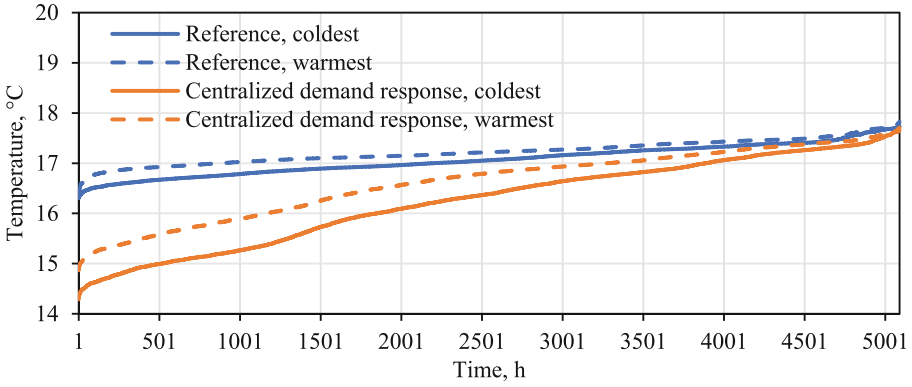


Fig. 9. Indoor air temperatures' duration curves for cellars during the heating season.

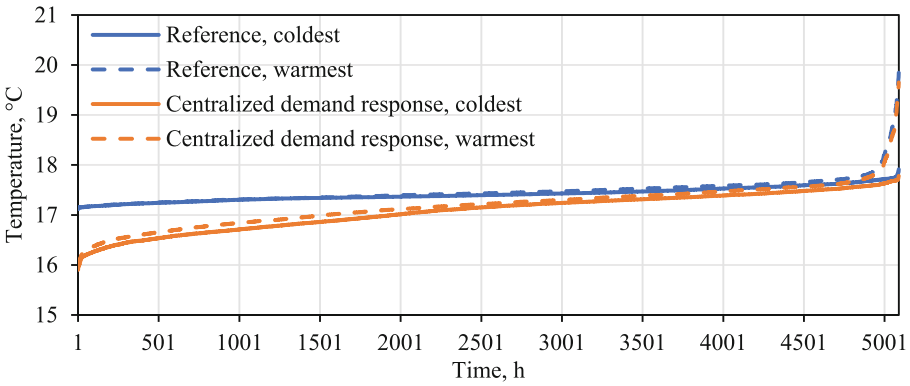


Fig. 10. Indoor air temperatures' duration curves for staircases during the heating season.

4 Conclusions

This study investigated the effectiveness of a centralized demand response control strategy in a Finnish apartment building. The findings indicate that the implementation of this control approach resulted in a cost saving of 2156 €, which is 3.8% for heating season all while maintaining thermal comfort within the living areas in the apartment building. Among these four room types, living spaces, bathrooms, cellars and staircases, the bathrooms exhibited the most notable sensitivity to the demand response control. Specifically, the coldest bathroom experienced a maximum indoor air temperature reduction of 3.2 °C compared with the reference one after demand response application.

Acknowledgement. This study is supported by the "BLOCKCC- energy communities" project funded by European Regional Development Fund (ERDF), grant number: A80246 and "B2RECoM" project, intelligent use and storage of renewable electricity and heat production in buildings, Business Finland, grant number: 10785/31/2022.

References

1. Finnish Government. Programme of Prime Minister Sanna Marin's Government 10 December 2019: Inclusive and Competent Finland—A Socially, Economically and Ecologically Sustainable Society, http://urn.fi/URN:ISBN:978-952-287-811-3. Last accessed 2021/11/21.
2. Gelazanskas, L., & Gamage, K. A. Demand side management in smart grid: a review and proposals for future direction. Sustain. Cities Soc. 11, 22–30 (2014)
3. Le Dréau, J., Heiselberg, P.: Energy flexibility of residential buildings using short term heat storage in the thermal mass. Energy. **111**, 991–1002 (2016)
4. Reynders, G., Diriken, J., Saelens, D.: Generic characterization method for energy flexibility: applied to structural thermal storage in residential buildings. Appl. Energy. **198**, 192–202 (2017)
5. Hedegaard, R.E., Kristensen, M.H., Pedersen, T.H., Brun, A., Petersen, S.: Bottom-up modelling methodology for urban-scale analysis of residential space heating demand response. Appl. Energy. **242**, 181–204 (2019)

6. Dominković, D.F., Gianniou, P., Münster, M., Heller, A., Rode, C.: Utilizing thermal building mass for storage in district heating systems: combined building level simulations and system level optimization. Energy. **153**, 949–966 (2018)
7. Finnish Meteorological Institute. Weather and sea—Download Observations, https://en.ilmatieteenlaitos.fi/download-observations. Last accessed 28 Jan 2023
8. Bring, A., Sahlin, P., Vuolle, M.: Models for Building Indoor Climate and Energy Simulation–A Report of IEA SHC Task 22: Building Energy Analysis Tools. IEA, Stockholm, Sweden (1999)
9. Equa Simulation, A.B. Validation of IDA Indoor Climate and Energy 4.0 build 4 with Respect to ANSI/ASHRAE Standard 140-2004; EQAU Simulation Technology Group: http://www.equaonline.com/iceuser/validation/ASHRAE140-2004.pdf (2010).. Last accessed 11 Feb. 2023
10. Moosberger, S.: IDA ICE CIBSE-Validation: Test of IDA Indoor Climate and Energy version 4.0 according to CIBSE TM33, issue 3. HTA LUZRN/ZIG. http://www.equaonline.com/iceuser/validation/ICE-Validation-CIBSE_TM33.pdf (2017). Last accessed 2023/02/11.
11. Helen. Kiinteähintainen Kaukolämpö (Fixed-price District Heating), https://www.helen.fi/yritykset/lampoa-yrityksille/kaukolampo-yrityksille/kiinteahintainen-kaukolampo. Last accessed 3 May 2025
12. Ju, Y., Hiltunen, P., Jokisalo, J., Kosonen, R., Syri, S.: Benefits through space heating and thermal storage with demand response control for a district-heated office building. Buildings. **13**(10), 2670 (2023)
13. Martin, K. Demand Response of Heating and Ventilation within Educational Office Buildings. Master's Thesis. Aalto University (2017)

Performance Investigation and Design Principles of PEMFC Integrated Energy Supply Systems Based on Flexible Load Regulation

Ruyi Zhang[1], Xu Li[1], Jintao Wu[2], and Shanshan Cai[1,2(✉)]

[1] China-EU Institute for Clean and Renewable Energy, Huazhong University of Science and Technology, Wuhan, Hubei 430074, China
shanshc@hust.edu.cn

[2] School of Energy and Power Engineering, Huazhong University of Science and Technology, Wuhan, Hubei 430074, China

Abstract. Combined cooling, heating, and power (CCHP) systems, with high efficiency and low pollutant emissions, are ideal for addressing these issues. Proton exchange membrane fuel cells (PEMFCs) exhibit high energy conversion efficiency, good stability, and concurrent heat production, which makes them suitable for powering residential cooling and thermal supply systems. For a PEMFC integrated energy supply system, flexible loads can realize the "interaction" between the supply and demand sides by changing their own energy consumption time or load size. This study introduces three systems under flexible load regulation. A comprehensive evaluation explores flexible regulation impacts. The results indicated that with flexible regulation, the energy efficiency of most systems in summer was improved, the exergy efficiency and CO_2 emission reduction rate of all systems increased, and the average daily cost decreased. This study further analyzed the changes in energy efficiency, exergy efficiency, environmental benefit, and economic benefit of each cogeneration system under variable loads and formed the design principle. The CCHPH-VCC (CCHP with humidity control and vapor compression cycle) system had the best overall performance in the studied cooling/power ratio range; however, the CCHP system can be selected at a cooling/power ratio less than 0.69 for summer operation if the focus of the system selection is on environmental and economic benefits.

Keywords: PEMFC Integrated Energy Supply System · Flexible load Regulation · Heating/power Ratio

1 Introduction

Proton exchange membrane fuel cells (PEMFCs) exhibit high efficiency, good stability, and high power density, and can generate a large amount of heat energy while generating electricity [1], which is suitable for driving the cogeneration systems of residential buildings [2].

A common type of combined cooling, heating and power (CCHP) system for PEMFCs integrates PEMFCs with waste heat utilization technologies, such as absorption

© The Author(s), under exclusive license to Springer Nature Singapore Pte Ltd. 2025
L. Ni et al. (Eds.): CCHVAC 2025, ESE, pp. 296–306, 2025.
https://doi.org/10.1007/978-981-95-3253-7_32

chiller or adsorption chiller, among which absorption chiller are more widely adopted. The temperature application range of the adsorption chiller system is wide, ranging from 50 to 600 °C, and it is suitable for cooling with low-temperature waste heat generated by PEMFCs [3]. Several studies have combined PEMFC with other cooling/heating cycles. Chang et al. [4, 5] combined a PEMFC with an organic Rankine cycle system and a vapor compression cycle (VCC) subsystem and found that the system had high efficiency, high stability, low noise, and low emissions and exhibited good prospects for residential applications.

Recent studies have shown that selecting an appropriate system type for different thermal and electrical load requirements is important. Changes in load characteristics can also affect system control strategies [6]. Xia et al. [7] proposed an adiabatic compressed-air energy storage system that optimizes the energy supply by matching the cold and hot electricity outputs of the system with district demand loads. Economic analysis showed a 23.1% reduction in annual energy supply costs compared to conventional systems.

Compared with traditional rigid loads, flexible loads can realize the "interaction" between the supply and demand sides by altering their own load size or energy consumption time. Resetting the temperature setpoint and preheating/precooling treatments are currently the commonly used flexible adjustment methods. By utilizing the thermal inertia of buildings and transferring loads through precooling or preheating to reduce peak values [8], adaptable control of refrigeration and air conditioning equipment can be achieved while meeting human thermal comfort, reducing energy use by 40–87% [9].

Comprehensive research shows that existing studies have not considered the comprehensive performance of systems under different load demands. The impact mechanism of flexible load regulation on different types of integrated energy systems remains unclear. To address this, this study proposes three types of PEMFC-driven integrated energy supply systems and compares their operational performance with and without a flexible load regulation strategy. For the first time, the influence of load characteristics is considered to clarify the applicability of multiple PEMFC-integrated energy systems under different heating/power and cooling/power load ratios. The research aims to provide a theoretical foundation for the design principles of PEMFC-integrated energy supply systems under diversified load demand characteristics.

2 PEMFC Integrated Energy Supply Systems

The CCHP system used a PEMFC as the main energy supply unit to provide electrical and thermal energy to the building, and a silica gel-water adsorption chiller used the PEMFC waste heat for cooling. The CCHPH-AD system was based on the CCHP system, and dehumidification wheel equipment was added to form a CCHP system with a humidity control system. Based on the CCHPH-AD system, the CCHPH-VCC system replaced the adsorption chiller with a VCC system. The thermal storage tank in each system was used to store excess heat, and a gas boiler was used for auxiliary heating, which was turned on when the heating was insufficient. A flexible load refers to a load that can vary within a specified range or shift between different periods. Compared with traditional rigid loads, a flexible load enables interaction between the supply and demand sides by changing the energy usage time or load size. The flexible regulation strategies were designed in detail in the previous work [10, 11].

2.1 Modeling Method

PEMFC Stack Model. The voltage of a single cell is shown in Eq. (1):

$$V_{cell} = V_0 - V_{act} - V_{ohm} - V_{conc} \tag{1}$$

where V_0 represents the energy-state voltage of the monolithic cell in the standard state (298.15 K, 1 atm), V_{act} represents the activation loss, V_{ohm} represents the ohmic loss, and V_{conc} represents the concentration loss. The output electrical power P_{el}, heating power P_{th}, and stack heat output P_f are shown in Eqs. (2)–(4).

$$P_{el} = V_{st} \cdot I \tag{2}$$

$$P_{th} = N \cdot I \cdot \left(\frac{LHV}{2F} - V_{cell} \right) \tag{3}$$

$$P_f = P_{th} - P_{O_2} - P_{N_2} - P_{H_2O} \tag{4}$$

Where V_{st} is the voltage of the PEMFC stack; I is the total current; LHV is the low heating value of hydrogen; P_{O_2}, P_{N_2} and P_{H_2O} represent the heat carried away by excess oxygen, nitrogen, and water vapor, respectively.

Adsorption Chiller Model. In this study, a silica gel-water adsorption chiller is used. This study uses the data learning method to obtain the empirical relationship of COP of adsorption chiller, as given in Eq. (5).

$$COP = a_1 \cdot T_{COW}^4 + a_2 \cdot T_{COW}^3 + a_3 \cdot T_{COW}^2 + a_4 \cdot T_{COW} + a_5 \tag{5}$$

Where T_{COW} is the temperatures of the cooling water.

Desiccant Wheel Model. The mass and heat balances of air and desiccant are shown in Eqs. (6)–(9):

$$\frac{\mathrm{d}Y}{\mathrm{d}t} + \frac{U}{L}(Y_{out} - Y_{in}) + \omega_1 \frac{\mathrm{d}W}{\mathrm{d}t} = 0 \tag{6}$$

$$\frac{\mathrm{d}W}{\mathrm{d}t} + \omega_2 (Y_d - Y) = 0 \tag{7}$$

$$\frac{\mathrm{d}T}{\mathrm{d}t} + \frac{U}{L}(T_{out} - T_{in}) + \omega_3 \frac{\mathrm{d}T_d}{\mathrm{d}t} = \omega_4 (Y - Y_d) \tag{8}$$

$$\frac{\mathrm{d}T_d}{\mathrm{d}t} + \omega_5 (T_d - T) + \omega_6 (Y_d - Y) + \omega_7 (Y_d - Y)(T - T_d) = 0 \tag{9}$$

where Y is air moisture content (kg/kg); Y_d is the mass transfer between air and desiccant to achieve the equilibrium moisture content (kg/kg); U is the airflow velocity (m/s); L is the width of the desiccant wheel (m); W is desiccant moisture content (kg/kg); T is the absolute temperature of air (K); T_d is the absolute temperature of desiccant (K); and ω_i ($i = 1, 2, 3, 4, 5, 6, 7$) are relevant parameters.

SMER is the specific moisture extraction rate. It reflects the comprehensive performance of the drying system.

$$SMER = \frac{\dot{m}_{air} \bullet (Y_{in} - Y_{out})}{P_{re}} \tag{10}$$

Where P_{re} is the dehumidification energy consumption (kW), and $\dot{m}_{air}$ is the mass flow rate of dehumidification air (kg/h).

Vapor Compression Cycle System Model. The CCHPH-VCC system uses a single-stage vapor compression cycle system for heating and cooling. The modeling approach used is the pressure-enthalpy diagram method [4], and R22 is selected as the refrigerant.

During the winter heat pump cycle, the capacity for heating is equivalent to the heating load, which can be obtained as:

$$P_{HC} = P_{Heating} = \dot{m}_{VCC}\left(h_{in,cond} - h_{out,cond}\right) \tag{11}$$

where $h_{in,\ cond}$ is the enthalpy of the refrigerant at the condenser inlet, and $h_{out,\ cond}$ is the enthalpy of the refrigerant at the condenser outlet.

During the summer refrigeration cycle, the capacity for cooling is equivalent to the cooling load. which can also be obtained as:

$$P_{RC} = P_{Cooling} = \dot{m}_{VCC}\left(h_{out,evap} - h_{in,evap}\right) \tag{12}$$

where $h_{out,\ evap}$ is the enthalpy of the refrigerant at the evaporator outlet and $h_{in,\ evap}$ is the enthalpy of the refrigerant at the evaporator inlet.

The power consumption for the compressor can be calculated by:

$$W_{comp} = \dot{m}_{VCC}\left(h_{is,comp} - h_{in,comp}\right)/\eta_{is,comp} \tag{13}$$

where $h_{is,\ comp}$ and $h_{in,\ comp}$ represent the enthalpies at the outlet and inlet of the compressor under isentropic compression, respectively, and $\eta_{is,\ c}$ represents the isentropic efficiency of the compressor.

Gas Boiler Model. The gas boiler is used as an auxiliary heating equipment, and the heat provided by the gas boiler can be calculated by Eq. (14).

$$H_{gas} = \eta_{gas} \times F_{gas} \tag{14}$$

Where $\eta_{gas} = 0.93$ is the heat efficiency of the gas boiler, and F_{gas} represents the natural gas consumption of the gas boiler.

Thermal Storage Tank Model.

$$Q_{tst}^{t+1} = Q_{tst}^{t} \cdot \left(1 - \eta_{tst,loss}\right) + \left[\left(\varepsilon \cdot Q_{tst,ch}^{t+1} \cdot \eta_{tst,ch} - (1-\varepsilon) \cdot \frac{Q_{tst,disch}^{t+1}}{\eta_{tst,disch}}\right)\right] \cdot t \tag{15}$$

Where Q_{tst}^{t} denotes heat stored in the TST at time t; $Q_{tst,ch}^{t+1}$ and $Q_{tst,disch}^{t+1}$ are the TST charge and discharge heat at time t+1; $\eta_{tst,\ loss} = 0.99$, $\eta_{tst,\ ch} = 0.85$ and $\eta_{tst,\ disch} = 0.85$ represent self-discharging rate, heat charge efficiency and heat discharge efficiency of

the TST. ε represents the working state of the TST, where ε=1 indicates an endothermic state, and ε=0 indicates an exothermic state.

The maximum heat storage capacity can be determined using Eq. (16):

$$Q_{max} = c_{pl} \cdot (85 - 30) \cdot \rho_w \cdot M_{TST} \tag{16}$$

where ρ_w is the density of the water (kg L^{-1}), and M_{TST} is the TST maximum capacity (L), c_{pl} is the heat capacity of the water ($J \cdot kg^{-1} \cdot K^{-1}$).

System Energy Efficiency. The overall energy efficiency of the cogeneration system was calculated using Eq. (17).

$$\eta_{en} = \frac{Q_{DHW} + Q_{cool} + P_{el} + Q_{heat} + Q_{wheel}}{Q_{in}} \tag{17}$$

Where P_{el} is the electricity produced by the PEMFC stack (W), Q_{DHW} denotes the thermal energy utilized for domestic hot water purposes (W), Q_{in} is the total energy consumption of hydrogen and natural gas (W), Q_{cool} is the cooling load (W), Q_{heat} is the heating load (W), and Q_{wheel} is the heat used for dehumidification (W).

System Exergy Efficiency. In this system, the exergy efficiency was calculated using Eq. (18).

$$\eta_{ex} = \frac{Ex_{cool} + Ex_{el} + Ex_{HW}}{Ex_{CHfuel} + Ex_{PHfuel}} \tag{18}$$

Where Ex_{cool} is the refrigeration exergy; Ex_{HW} is the thermal exergy. Ex_{CHfuel} and Ex_{PHfuel} separately denote the chemical exergy and physical exergy consumed within the system.

System Environmental Benefit. This study assumed that hydrogen is produced by natural gas steam reforming. The relationship between hydrogen production and each pollutant emission is obtained from Literature [12]. The daily GHG emissions from the PEMFC cogeneration system can be calculated using Eq. (19):

$$M_{CS,GHG} = GHG_{H_2} \times n_{H_2} \times LHV_{H_2} + GHG_{gas} \times n_{gas} \times LHV_{gas} \tag{19}$$

where GHG_{H_2} is the greenhouse gas produced during hydrogen production, compression, and transportation, and GHG_{gas} is the greenhouse gas produced by natural gas combustion; n_{H_2} and n_{gas} are the amount of hydrogen and natural gas moles (mol) consumed by the system per day.

System Economic. In this study, the average daily cost was employed as a metric for assessing the economic viability of the cogeneration system.

$$C_{average} = \frac{C_{invest} + C_{maint} \times T_{LP}}{365 \times T_{LP}} + C_{run} \tag{20}$$

$$C_{run} = \frac{\left(C_{H_2} + C_{gas}\right)_{Winter} + \left(C_{H_2} + C_{gas}\right)_{Summer}}{2} \tag{21}$$

Where C_{invest} is the initial investment cost of the system, C_{maint} is the annual maintenance expense of the system taken as 5% of the initial cost, and T_{LP} is the service life (20 years) of the PEMFC cogeneration system. C_{H_2} and C_{gas} are the daily costs associated with hydrogen and natural gas consumption, respectively.

Priority Index. To comprehensively evaluate the performance of each system, a priority index K was introduced, which was calculated using (22)–(25):

$$K_{en,i} = \frac{\eta_{en,i}}{\eta_{en,\min}} \tag{22}$$

$$K_{en,i} = \frac{\eta_{en,i}}{\eta_{en,\min}} \tag{23}$$

$$K_{GHG,i} = \frac{m_{GHG,\max}}{m_{GHG,i}} \tag{24}$$

$$K_{C,i} = \frac{C_{run,\max}}{C_{run,i}} \tag{25}$$

where C_{run}, m_{GHG}, η_{ex}, η_{en} are the average daily cost, the CO_2 emission, the exergy efficiency, and the energy efficiency, respectively; *min* and *max* are the minimum and maximum values of the corresponding indexes, respectively; i characterizes CCHP, CCHPH-AD, and CCHPH-VCC.

2.2 Model Validation

The TST, VCC system, and gas boiler are based on empirical equations adopted from the literature [4, 13]. The validation of the adsorption chiller has been presented in our previous study [11]. The PEMFC model was validated using experimental data [11]. The simulation results are in good agreement with the experimental data (see Table 1). The validation of the desiccant wheel model is presented in this section. Under the same conditions, the predicted values of temperature and humidity ratio of the mixed process air agree well with the experimental data [14]. The average error is 2.87%, which predicts heat and mass transfer inside the desiccant wheel by the one-dimensional model have great credibility.

Table 1. Error data in PEMFC model validations.

	The average error	The maximum error
Cell voltage	4.03%	6.07%
Power density	3.65%	6.54%

3 Results and Analysis

3.1 Building Loads and Related Operational Parameters

Situated in Shanghai, China, this single-story residence boasted a total built-up area of 256 m^2. To evaluate the energy requirements of the villa, both cooling and heating loads were simulated using the method detailed in Ref. [15]. Furthermore, data on the electrical and domestic hot water (DHW) loads were sourced from Ref. [16]. The building heat load was flexibly adjusted using a fuzzy logic controller. Additionally, the operational performance of these systems has been investigated in prior work [10, 11]. The following analysis will reference the operational parameters obtained from that study for further calculations.

3.2 Comprehensive Performance Analysis under Flexible Load Regulation

Energy Efficiency. Figure 1(a) compares the energy efficiencies of various cogeneration systems. After flexible regulation, the energy efficiency of the CCHP system during winter operation decreased slightly from 90.17% to 89.73%. This is because there was no need to use a gas furnace for reheating, and the heat production efficiency of the gas furnace is higher than that of the PEMFC. The CCHPH-VCC system showed a similar trend in winter. There was no need to activate the vapor compression cycle, resulting in a reduction in energy efficiency from 93.17% to 89.73%. In summer, the CCHP and CCHPH-AD systems originally had relatively low energy efficiencies due to the low COP of the adsorption chiller, at 51.33% and 66.23% respectively. Flexible adjustment reduces the heat required for cooling, resulting in a 7.3% and 1.7% increase in the summer energy efficiency of the CCHP and CCHPH-AD systems, respectively. Overall, the energy efficiencies in descending order are: the CCHPH-VCC system, the CCHPH-AD system, and the CCHP system.

Exergy Efficiency. Figure 1(b) shows a comparison of the exergy efficiency of various cogeneration systems. It can be seen from the figure that with the implementation of flexible regulation, the exergy efficiency of each system has been improved. This is because flexible regulation reduces mainly the cold and heat demands. During winter operation, the exergy efficiency of the CCHP system was similar to that of the CCHPH-VCC system. After both systems adopted flexible regulation, their exergy efficiencies increased from approximately 58–59.09%. Owing to the higher exergy efficiency of the steam compression refrigeration cycle compared to that of the adsorption chiller, the exergy efficiency of the CCHPH-VCC system during summer operation was higher than that of the CCHP system. After flexible adjustment, the summer energy efficiency of the CCHPH-VCC system and the CCHP system increased by 7.7% and 25% respectively. The exergy efficiency of the CCHPH-AD system was the lowest. This is because the added desiccant wheel had a relatively low exergy efficiency.

Environmental Benefit. Figure 1(c) presents a comparison of CO_2 emissions. The CCHPH-VCC system has the lowest CO_2 emissions, and after adopting flexible regulation, its CO_2 emissions have been reduced by approximately 5.47%. The CCHP system, which used a gas furnace to supply heat to the adsorption chiller, had relatively

higher CO_2 emissions. The CCHPH-AD system has the highest CO_2 emissions, mainly because of the high heat demand of its adsorption chiller and desiccant wheel as well as the high reheating demand of the gas furnace. After adopting flexible regulation, the carbon dioxide emissions of the CCHPH-AD system decreased by approximately 25.54%.

Economic. Figure 1(d) presents an economic analysis of the PEMFC cogeneration system. After implementing adaptable regulation, the average daily cost of the CCHPH-AD system decreased to $75.57, a reduction of 8.28%. The CCHPH-AD system achieved the highest cost reduction rate. Followed by the CCHPH-VCC system with a reduction of approximately 4.84%. And the CCHP system with the lowest cost reduction rate of 4.68%.

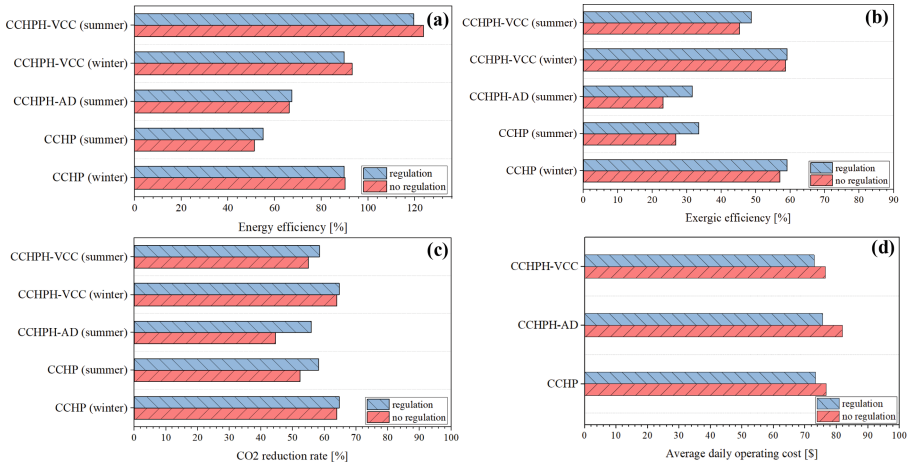


Fig. 1. The influence of flexible regulation on the comprehensive performance of the PEMFC cogeneration system.

3.3 Performance Assessment under Variable Loads

Load demands may vary across different regions; hence the ratios of heating/power and cooling/power may differ. The heating/power ratio represents the ratio of the building's heating load to its electrical load over the course of a day. The cooling/power ratio is the ratio of the building's cooling load to its electrical load over the course of a day. The following analysis will examine the performance of multiple PEMFC-integrated energy supply systems under varying loads. A priority index K is introduced to comprehensively evaluate the performance of each system. The analyzed heating/power ratios are 0.5, 0.73, 1, 1.5, and 2, with corresponding cooling/power ratios of 0.69, 1.02, 1.39, 2.08, and 2.77, respectively.

Table 2 shows a comprehensive comparison of each PEMFC cogeneration system under different cooling/power ratio conditions in summer. When the cooling/power ratio

was greater than or equal to 1.39, the CCHPH-VCC system had the highest priority for all indicators and therefore had the best overall performance. When the cooling/power ratio was less than 0.69, the priority of the CCHPH-VCC system was slightly lower than that of the CCHP and CCHPH-AD systems in terms of environmental and economic benefits, but the comprehensive performance was still the highest. Therefore, if the selection of the cogeneration system focuses on environmental and economic benefits, the CCHP system can be considered. The sum of the priority of the CCHP system was slightly lower than that of the CCHPH-AD system. Therefore, the CCHPH-AD system had better overall performance. If the selection of the cogeneration system focuses on environmental and economic benefits, the CCHP system is preferred over the CCHPH-AD system. Appropriate selection can be made according to different requirements. Table 3 shows a comprehensive comparison of each system under different heating/power ratio conditions in winter. In winter, the CCHPH-VCC system had the best overall performance, followed by the CCHP system, and the CCHPH-AD system had the lowest priority.

For winter, the CCHPH-VCC system was the highest under different heating/power ratio conditions, and for summer, the reference of the PEMFC cogeneration system design under different cooling/power ratio conditions is shown in Fig. 2.

Table 2. Comprehensive comparison of each PEMFC cogeneration system under different cooling/power ratio conditions in summer.

$\sum K_i$	CCHP	CCHPH-AD	CCHPH-VCC
Cooling/power ratio=0.69	4.211	4.263	4.942
Cooling/power ratio=1.02	4.165	4.223	5.8
Cooling/power ratio=1.39	4.166	4.265	6.544
Cooling/power ratio=2.08	4.182	4.323	7.801
Cooling/power ratio=2.77	4.201	4.383	8.509

Table 3. Comprehensive comparison of each PEMFC cogeneration system under different heating/power ratio conditions in winter.

$\sum K_i$	CCHP	CCHPH-AD	CCHPH-VCC
Heating/power ratio=0.73	4.017	4.000	4.06
Heating/power ratio=1.5	4.033	4.000	4.131
Heating/power ratio=2	4.042	4.000	4.178

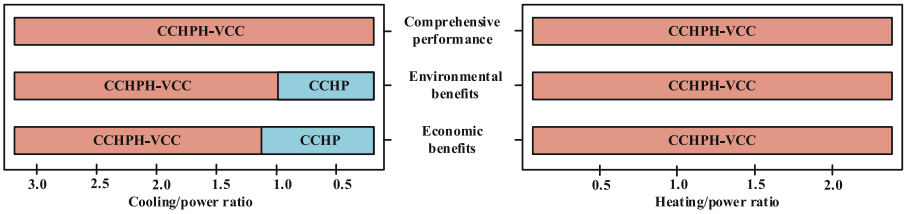


Fig. 2. Design reference of PEMFC cogeneration system

4 Conclusion

In this study, three types of PEMFC-integrated power supply systems based on flexible regulation were proposed and investigated. A "4E" comprehensive evaluation system was used to explore the influence of flexible regulation on system performance. The variations of system performance were also evaluated under different load ranges to form a recommended design principle. The main conclusions are as follows:

1. After adopting flexible regulation, the exergy efficiency and CO_2 emission reduction rate of all PEMFC co-supply systems increased, and the average daily costs decreased. The energy efficiency of the CCHP and CCHPH-AD systems increased by 7.3% and 1.7% respectively in summer, whereas that of the CCHP system in winter and the CCHPH-VCC system in winter and summer decreased.
2. The CCHPH-VCC system had the best overall performance in the studied cooling/power ratio range; however, the CCHP system can be selected at a cooling/power ratio less than 0.69 for summer operation if the focus of the system selection is on environmental and economic benefits.

Acknowledgments. The authors thank the National Natural Science Foundation of China (Grant No. 827 52476199) for funding and supporting this work.

References

1. Cai, S., Wang, W., Zou, Y., Li, S., Tu, Z.: Performance and sustainability assessment of PEMFC/solar-driven CCP systems with different energy storage devices. Energy. **278**, 127863 (2023)
2. Arsalis, A.: A comprehensive review of fuel cell-based micro-combined-heat-and-power systems. Renew. Sustain. Energy Rev. **105**, 391–414 (2019)
3. Oro, M.V., de Oliveira, R.G., Bazzo, E.: An integrated solution for waste heat recovery from fuel cells applied to adsorption systems. Appl. Therm. Eng. **136**, 747–754 (2018)
4. H. Chang, et al.: Energy analysis of a hybrid PEMFC–solar energy residential micro-CCHP system combined with an organic Rankine cycle and vapor compression cycle. Energ. Convers. Manage. 142, 374-384 (2017).

5. Chang, H., Wan, Z., Zheng, Y., Chen, X., Shu, S., Tu, Z., Chan, S.H., Chen, R., Wang, X.: Energy and exergy-based working fluid selection and performance analysis of a high-temperature PEMFC-based micro combined cooling heating and power system. Appl Energ. **204**, 446–458 (2017)
6. Wang, J., Hao, J., Liu, C., Zhuo, J., Ren, X., Yao, Q.: Enlargement of heat-electricity ratio for flexibility operation in a large-scale extraction condensing turbine system. Thermal Power Generation. **12**, 41–50 (2020)
7. Xia, Q., He, Y., Xv, Y., Chen, H., Deng, J.: Matching performance between the trigeneration of an adiabatic compressed air energy storage system and load. Energy Storage Sci. Technol. **5**, 1494–1502 (2021)
8. Troitzsch, S., Sreepathi, B.K., Huynh, T.P., Moine, A., Hanif, S., Fonseca, J., Hamacher, T.: Optimal electric-distribution-grid planning considering the demand-side flexibility of thermal building systems for a test case in Singapore. Appl. Energ. **273**, 114917 (2020)
9. Foteinaki, K., Li, R., Péan, T., Rode, C., Salom, J.: Evaluation of energy flexibility of low-energy residential buildings connected to district heating. Energy Build. **213**, 109804 (2020)
10. Li, X., Li, R., Cai, S., Luo, X., Tu, Z.: Impact of flexible regulation on combined cooling, heating, power and humidity system driven by fuel cell. J. Eng. Thermophys. **45**(05), 1290–1299 (2024)
11. Cai, S., Li, X., Li, S., Luo, X., Tu, Z.: Flexible load regulation method for a residential energy supply system based on proton exchange membrane fuel cell. Energy Convers. Manage. **258**, 115527 (2022)
12. Feng, W., Wang, S., Ni, W., Chen, C., Zheng, X.: Environmental, economic and energy assessment of hydrogen energy systems for fuel cell vehicles. Acta Energy Sol. Sin. **24**(03), 394–400 (2003)
13. Zhou, Y., Wang, J., Liu, Y., Yan, R., Ma, Y.: Incorporating deep learning of load predictions to enhance the optimal active energy management of combined cooling, heating and power system. Energy. **233**, 121134 (2021)
14. Zhang, X.J., Dai, Y.J., Wang, R.Z.: A simulation study of heat and mass transfer in a honeycombed rotary desiccant dehumidifier. Appl. Therm. Eng. **23**, 989–1003 (2003)
15. Ahamed, M.S., Guo, H., Tanino, K.: Modeling heating demands in a Chinese-style solar greenhouse using the transient building energy simulation model TRNSYS. J. Build. Eng. **29**, 101114 (2020)
16. Wu, Q., Ren, H., Gao, W.: Economic assessment of micro-CHP system for residential application in Shanghai, China. Energy Proc. **88**, 732–737 (2016)

Study on Thermal Environment and Energy-Saving Control of Radiant Terminals in Winter Based on Operative Temperature

Haiying Wang(✉), Hang Meng, Junli Sun, and Renjie Yan

Qingdao University of Technology, No. 777 Jialingjiang East Road in Huangdao District, Qingdao, Shandong Province, China
wanghaiying@qut.edu.cn

Abstract. This study focuses on a south-facing room in an office building at a university in Qingdao, where a floor radiant air-conditioning system is employed. The thermal environment of the interior and perimeter zones, as well as the system's energy consumption, are investigated. A simulation model of the room and its HVAC system was developed using TRNSYS software, and the model's accuracy was validated using measured data. Based on the differences between air temperature and operative temperature within the room, the space was divided into interior and perimeter zones. Different control strategies using air temperature and operative temperature as control signals were proposed accordingly. After verifying the model's accuracy, TRNSYS was used to simulate various control modes, analyzing thermal comfort and energy consumption in each zone. A comparison of indoor comfort and energy use under each control strategy was conducted to identify the control mode that minimizes energy consumption while meeting basic thermal comfort requirements.

Keywords: Operative temperature · Radiant terminal · Energy consumption

1 Introduction

Globally, buildings account for approximately 40% of total energy consumption [1], and in China, this proportion has risen to 46.5%. Reducing building energy consumption has thus become an essential pathway toward achieving energy conservation goals.

Currently, the operation and regulation of building air-conditioning systems primarily rely on the setpoint of indoor air temperature. This control strategy proves effective when indoor air temperature closely aligns with the mean radiant temperature. However, in certain specific conditions, such as when rooms contain radiative surfaces that significantly differ in temperature from the ambient air, including seasonally affected exterior walls and windows or radiant heating/cooling surfaces—air temperature-based control alone may fail to achieve optimal thermal comfort.

© The Author(s), under exclusive license to Springer Nature Singapore Pte Ltd. 2025
L. Ni et al. (Eds.): CCHVAC 2025, ESE, pp. 307–314, 2025.
https://doi.org/10.1007/978-981-95-3253-7_33

Operative temperature, which incorporates both air temperature and mean radiant temperature, two key parameters influencing human thermal comfort—has been recognized as a more appropriate index for evaluating indoor thermal environments [2, 3]. Compared with using air temperature as the sole control signal, operative temperature is more suitable for regulating indoor thermal conditions in spaces with large envelope structures or significant surface temperature variation, making it easier to meet thermal comfort requirements.

The operative temperature can be defined as follows [4, 5]:

$$t_{op} = \frac{h_c t_a + h_r t_r}{h_c + h_r} (1)$$

Where:

- t_{op} is the operative temperature, °C;
- h_c is the convective heat transfer coefficient at the human body surface, W/(m^2·K);
- h_r is the radiative heat transfer coefficient at the human body surface based on linear temperature difference, W/(m^2·K);
- t_a is the indoor air temperature, °C.
- t_r is the mean radiant temperature, °C.

Recent studies have investigated the impact of operative temperature control versus air temperature control on thermal comfort and energy consumption. Wang et al. [6, 7] evaluated thermal comfort and energy performance of different terminal units under both control strategies in three climatic zones. Their findings revealed that for convective terminals, operative temperature control improved thermal comfort but increased energy consumption, whereas for radiant terminals, it reduced energy use at the expense of a slight decline in comfort. Li Jiankai [8] examined spatial variations of air and operative temperatures in a university library in a cold region and proposed tailored control strategies for convective terminals. Results indicated that operative temperature control enhanced thermal comfort, albeit with an associated rise in energy consumption.

Given their notable advantages in both energy efficiency and thermal comfort, radiant terminal systems are receiving growing attention and are being widely implemented in large-scale public buildings and renewable energy applications [9, 10]. Consequently, understanding how operative temperature distributes spatially under such systems, and how to design rational control strategies that ensure comfort while minimizing energy use, remains an important subject for further research and exploration.

2 Research Methods and Model Construction.

In this study, SketchUp was used to construct the geometric model of the room,and TRNSYS was employed to develop the thermal and system simulation models. This modeling work lays the foundation for simulating indoor air temperature and system energy consumption under different control strategies.

The research focuses on a south-facing room equipped with a floor radiant air-conditioning system. The room is located on the fifth floor of an office building at a university in Qingdao. The actual interior view of the room is shown in Fig. 1. The total



Fig. 1. Actual Interior View of the Room.

room area is 124.2 m^2, including an 8 m^2 equipment room, resulting in an effective heated area of 116.2 m^2.

The composition and thermal performance parameters of the room's envelope in the model were determined based on the actual building, as detailed in Table 1. The room adopts a combined system consisting of a radiant floor system and a fresh air system. Two variable-frequency air source heat pump units are used to provide cooling and heating separately for the radiant floor and the fresh air system. In the room model, the air-conditioning terminals and air source heat pump units were configured in accordance with the actual system setup. The schematic diagram of the system model is shown in Fig. 2.

Table 1. Thermal Performance Parameters of the Room Envelope.

Structure name	Structure compusition	Heat transfer coefficient [W/(m^2·K)]
Exterior Wall	20 mm Exterior Finish + 50 mm Concrete Hollow Block + 50 mm EPS Board + 100 mm Concrete Hollow Block + 20 mm Plaster Finish	0.37
Exterior Window	6 mm Standard Low-E + 13 mm Air Layer + 6 mm Standard CLE	1.7
Interior Wall	50 mm Concrete Hollow Block + 100 mm Air Layer + 20 mm Gypsum Board	1.4
Floor Slab	20 mm Granite Slab + 30 mm Cement Mortar + 100 mm Reinforced Concrete Floor Slab	1.2

To maintain the target air temperature/operative temperature, a bypass pipe and control valve are installed on the supply and return lines of the terminal units in the

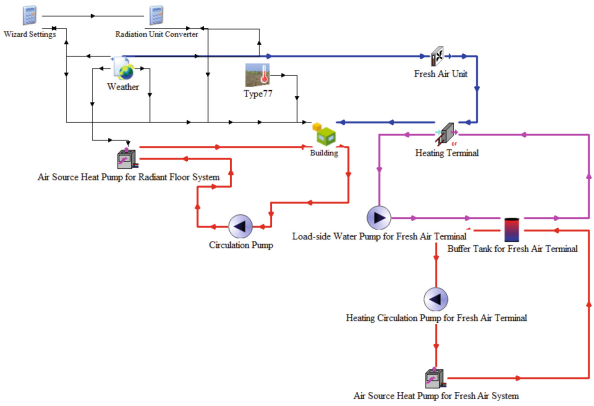


Fig. 2. TRNSYS system model for air source heat pump.

room's interior and perimeter zones. During operation, the bypass stays closed and hot or chilled water is supplied directly to the coils. When the room temperature reaches the upper limit, the supply valve closes and the bypass opens; when the temperature drops near the lower limit, the supply resumes and the bypass closes. Thanks to the heat storage of the floor radiant system, the floor continues to release heat after supply stops, helping to keep the temperature stable. The target temperature is set at 20 °C ± 1 °C.

Field measurements were carried out from February 26 to March 1, 2024, to capture a typical winter week. Based on the measured indoor air and envelope surface temperatures, the operative temperatures for the interior and perimeter zones were calculated. Results showed the interior zone had a higher operative temperature than the perimeter zone, with a maximum difference of 2.48 °C and an average of 1.94 °C, indicating non-uniform temperature distribution. Thus, the area within 4 m of the exterior envelope was defined as the perimeter zone, and the rest as the interior zone.

The hourly HVAC power consumption—including the air source heat pump and pumps—was compared with simulated values, showing an average deviation below 10%, confirming the model's accuracy. Measured indoor air temperatures and outdoor dry-bulb temperatures were used to simulate heating output, yielding an average deviation below 10% and mean error within 5%, verifying the model's reliability.

3 Simulation and Results Analysis

Based on the differences between the interior and perimeter zones, various control signals can be selected, including the air temperature or operative temperature of either zone. It is also feasible to implement separate control strategies for the interior and perimeter zones by using their respective temperatures as individual control signals.

In all control strategies, the target air temperature or operative temperature is set to 20°C. The specific names of the control strategies and their corresponding control temperature types are listed in Table 2.

Since the parameter names frequently recur in this paper, simplified names defined in Table 2 are used to replace the full names of each control method, and the parameter

Table 2. Naming of Room Control Strategies.

Abbreviated Names of Control Strategies	Type of Control Temperature
C-Tair	The interior and perimeter zones of the room are using its own air temperature as the control signal.
C-Top	The interior and perimeter zones of the room are using its own operative temperature as the control signal.
C-outTair	The entire room is controlled based on the air temperature of the perimeter zone.
C-inTair	The entire room is controlled based on the air temperature of the interior zone.
C-outTop	The entire room is controlled based on the operative temperature of the perimeter zone.
C-inTop	The entire room is controlled based on the operative temperature of the interior zone.

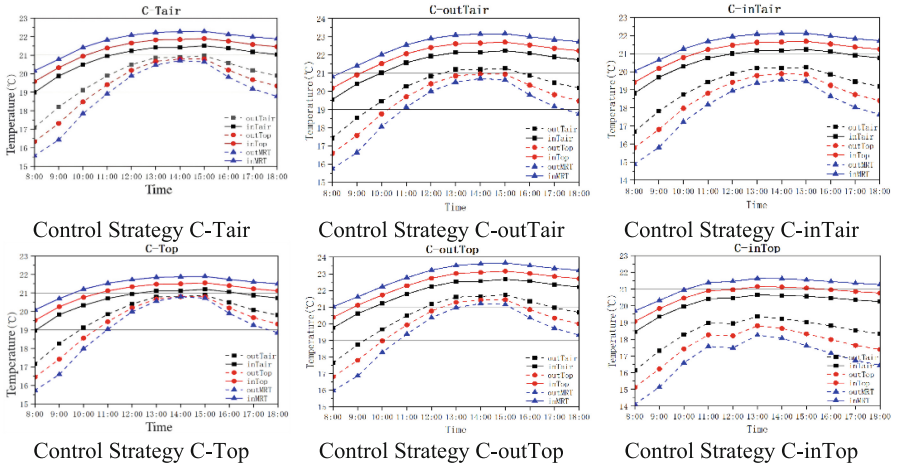
names are simplified into symbols. The corresponding definitions of these symbols are shown in Table 3.

Table 3. Explanation of parameters for interior and exterior zones under each control method.

Simplified symbol names	Meaning represented by the parameter
outTair	the air temperature of the perimeter zone
inTair	the air temperature of the interior zone
outTop	the operative temperature of the perimeter zone
inTop	the operative temperature of the interior zone
outMRT	the air temperature of the perimeter zone
inMRT	the air temperature of the interior zone

3.1 Typical Day Temperature Distribution

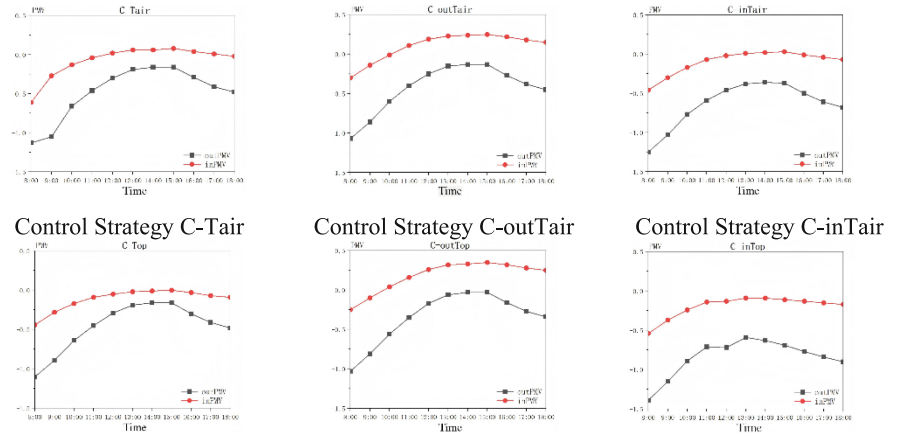
The variations of temperature parameters and PMV in the inner and outer zones are shown in Figs. 3 and 4. As seen, due to the influence of the envelope, the inner zone temperature is higher than that of the outer zone. With radiant terminals, the inner zone's mean radiant temperature is higher than its operative and air temperatures, while in the outer zone, the air temperature is higher than the operative temperature, which in turn is higher than the mean radiant temperature. The floor radiant heating cannot fully offset the cold radiation from the envelope surfaces.



Control Strategy C-Tair | Control Strategy C-outTair | Control Strategy C-inTair

Control Strategy C-Top | Control Strategy C-outTop | Control Strategy C-inTop

Fig. 3. Temperature Parameters of the Interior and Exterior Zones under Different Conditions.



Control Strategy C-Tair | Control Strategy C-outTair | Control Strategy C-inTair

Control Strategy C-Top | Control Strategy C-outTop | Control Strategy C-inTop

Fig. 4. PMV of the Interior and Exterior Zones under Different Conditions.

Compared to C-Tair, under the C-Top control, the minimum values of all three temperatures in the exterior zone slightly increase and their ranges narrow. The interior air temperature range narrows to 18.96–21.2 °C, keeping both zones closer to the 19–21 °C target range. Meanwhile, the air temperature difference (Tair) between zones shrinks to 0.31–1.79 °C, the operative temperature (Top) difference to 0.7–3.07 °C, and the mean radiant temperature (MRT) difference to 1.09–4.36 °C.

Because the exterior zone's operative temperature is lower than its air temperature, using Top as the control signal takes longer to reach the setpoint, extending floor heating operation and slightly raising exterior temperatures. In contrast, in the interior zone, Top is higher than the air temperature, so the system reaches the setpoint earlier, shortening

operation time and slightly lowering the interior temperature. This narrows the thermal differences between zones.

For PMV, the C-Top trend is similar to C-Tair. Interior PMV (inPMV) is higher in the morning, but the PMV gap between zones slightly decreases overall, though not significantly different from C-Tair.

For C-outTair and C-outTop, which use exterior zone temperatures as control signals, all temperatures rise compared to C-Tair. Since the exterior zone temperatures are lower, heating runs longer, raising temperatures in both zones but widening the zone differences. Under C-outTop, exterior PMV ranges from –1.03 to –0.23 and interior PMV from –0.25 to 0.65; under C-outTair, they range from –1.07 to –0.33 (exterior) and –0.3 to 0.55 (interior). At times, these deviate from the comfort range, worsening thermal comfort consistency.

For C-inTair and C-inTop, temperatures drop compared to C-Tair. The Tair gap is 0.9–2.1 °C, Top 1.7–3.6 °C, and MRT 2.4–5.1 °C. Since the interior zone reaches the setpoint first, floor heating shuts off sooner, lowering exterior temperatures and increasing zone differences. Overall, room temperatures drop by 0.5–1 °C compared to C-Tair, and exterior PMV more frequently falls outside the comfort range.

3.2 Cumulative Heating Supply per Unit Area During the Winter Season

Figure 5 presents the simulated results of cumulative heating supply per unit area for the six control strategies during the winter season.

Comparing C-Tair and C-Top, the C-Top strategy reduces the cumulative heating supply per unit area by 8.24% compared to C-Tair, highlighting the energy-saving advantage of using operative temperature as the control signal. Specifically, the cumulative heating under C-Tair is 52.08 kWh/m^2, while under C-Top it is 47.79 kWh/m^2.

For the strategies using exterior zone temperature as the control signal,C-outTair results in 58.64 kWh/m^2,C-outTop results in 62.74 kWh/m^2,which are 12.60% and 20.47% higher than C-Tair, respectively.

In contrast, for the strategies using interior zone temperature as the control signal,C-inTair results in 46.63 kWh/m^2,C-inTop results in 41.90 kWh/m^2,representing reductions of 10.46% and 19.55% compared to C-Tair, respectively.

4 Conclusion

This paper takes a south-facing office room with a radiant floor air-conditioning system as an example. Field measurements of the indoor thermal environment and energy use were conducted during actual operation. A simulation model of the room and system was developed and validated. Based on this, six control strategies using different zone air and operative temperatures were proposed and analyzed through simulation.

The results show that under the same setpoint, using the operative temperatures of the interior and exterior zones as control signals (C-Top) provides similar overall comfort to air temperature control (C-Tair) but reduces the comfort difference between zones. The operative temperature gap between zones decreases by 0.2–0.5 °C, allowing

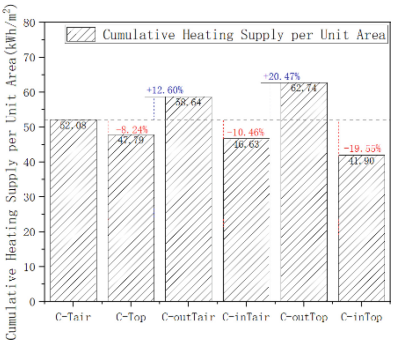


Fig. 5. Winter Cumulative Heating Supply per Unit Area Under Different Control Strategies.

occupants to feel more uniform comfort. C-Top also reduces overheating and lowers energy consumption by 8.24%.

Further analysis shows that using only the interior zone temperature (C-inTair, C-inTop) for the whole room saves the most energy but results in poor comfort and large temperature differences between zones. Using the exterior zone temperature (C-outTair, C-outTop) increases energy use and causes overheating in the interior zone in winter, degrading comfort.

References

1. Buildings Performance Institute Europe: Europe's Buildings Under the Microscope. Belgium, Brussels (2011)
2. Wu, Z., et al.: Adaptive thermal comfort in naturally ventilated dormitory buildings in Changsha, China. Energy Build. **186**, 56–70 (2019)
3. Becchio, C., et al.: Toward NZEB by optimizing HVAC system configuration in different climates. Energy Proc. **140**, 115–126 (2017)
4. ASHRAE: ANSI/ASHRAE Standard 55: Thermal Environmental Conditions for Human Occupancy. ASHRAE, Atlanta (2020)
5. European Committee for Standardization: EN 15251: Indoor Environmental Input Parameters for Design and Assessment of Energy Performance of Buildings Addressing Indoor Air Quality, Thermal Environment, Lighting and Acoustics, Brussels, Belgium (2007).
6. Wang, H., Olesen, B.W., Kazanci, O.B.: Using thermostats for indoor climate control in offices: the effect on thermal comfort and heating/cooling energy use. Energy Build. **188**, 71–83 (2019)
7. Wang, H, Olesen, B.W., Kazanci, O.B.: Effect of glazing ratio on thermal comfort and heating/cooling energy use. In: The International Symposium on Heating, Ventilation and Air Conditioning (ISHVAC), Harbin, China (2019)
8. Li, J.: Operation and analysis of air source heat pump floor heating system in cold regions. Build. Sci. **39**, 105–112 (2023)
9. Hu, R., Niu, J.L.: A review of the application of radiant cooling & heating systems in Mainland China. Energy Build. **52**, 11–19 (2012)
10. Yeom, D., Roche, P.L.: Investigation on the cooling performance of green roof with a radiant cooling system. Energy Build. **149**, 26–37 (2017)

Automatic Wiring Method of Fire Alarm System in Metro Station Based on BIM and Ant Colony Algorithm

Ruiying Jin[1], Peng Xu[1(✉)], Junjie Li[1], Hongxin Wang[2], and Jiefan Gu[3]

[1] School of Mechanical Engineering, Tongji University, Shanghai 201804, China
xupeng@tongji.edu.cn
[2] Midea Building Technologies, Shanghai 201702, China
[3] College of Architecture and Urban Planning, Tongji University, Shanghai 200092,, China

Abstract. With the rapid advancement of metro construction in China, the design process of fire alarm systems (FAS) still relies on manual operation, which is cumbersome and inefficient. Metro FAS design is gradually moving from two-dimensional computer-aided design (CAD) to three-dimensional building information model (BIM) to improve design accuracy and cross-disciplinary collaboration efficiency. In this paper, we propose a framework for the automatic wiring design of FAS in metro stations based on BIM. First, a wide variety of FAS devices and cable tray information is obtained through BIM to determine information about the layout, and loops are divided based on predefined rules. Second, since ring loops involve numerous devices, the Ant Colony Algorithm (ACA) optimizes connection sequences. For tree loops, devices are classified based on the presence of cable trays: if cable tray exist, devices connect to the nearest cable tray to minimize wiring usage; otherwise, the Minimum Spanning Tree algorithm determines the connection sequence. Then, the connectivity between the devices will be through an obstacle avoidance algorithm. Third, the study validates the feasibility of the proposed method through a real-world case study of a metro station in Fujian Province. The results indicate that the automatic design methodology can reduce wire length by 11.2% to 24.7%. This not only demonstrates the advantages of applying BIM in FAS design but also highlights its potential for enhancing intelligent design processes. Furthermore, the findings provide a solid research foundation for future advancements in this field.

Keywords: Building information model · Fire alarm system · Design optimization

1 Introduction

The rapidly growing demand for metro construction in China has led to a steadily increasing need for metro station design [1]. With the development of computer technology, design methods have evolved from the most traditional approach of manual drafting to computer-aided design (CAD). Currently, the most advanced design method involves

© The Author(s), under exclusive license to Springer Nature Singapore Pte Ltd. 2025
L. Ni et al. (Eds.): CCHVAC 2025, ESE, pp. 315–325, 2025.
https://doi.org/10.1007/978-981-95-3253-7_34

using building information modeling (BIM) to integrate the design outcomes of multiple disciplines, enabling multi-disciplinary collaborative design. The emergence of BIM has improved design efficiency and accelerated the automation process within the industry. As a result, the Architecture, Engineering, and Construction (AEC) industry has increasingly embraced BIM to enhance design and management efficiency [2]. Unlike traditional two-dimensional techniques, BIM helps to reduce clashes during the design and construction phases and supports more effective communication among stakeholders [3]. This methodology contributes to lowering labor costs, decreasing the need for rework, and increasing the use of prefabrication [4].

To enable early fire detection, safeguard personnel and property, and facilitate firefighting and rescue efforts, a comprehensive automatic fire alarm system (FAS) is required across the entire metro project. However, FAS design involves over 30 categories of devices and nearly 10 types of wiring, rendering the design process highly time-consuming, labor-intensive, and often constrained by insufficient specialized expertise [5]. How to abstract the FAS system design into a problem that can be understood by computers, and leverage intelligent algorithms to improve design efficiency and reduce labor costs, has become an urgent issue to be addressed.

The structure of this paper is as follows: Sect. 2 reviews the applications of BIM, ant colony algorithms, and related approaches in building system design; Sect. 3 details the proposed automatic wiring framework and design workflow for the FAS system; Sect. 4 validates the proposed method through a practical case study; and the final chapter concludes the paper with a summary and future perspectives.

2 Related Works

2.1 BIM in MEP System Design

The mechanical, electrical, and plumbing (MEP) system refers to a building's non-structural systems, including plumbing, HVAC, electricity, energy conservation, and elevator maintenance, etc [6]. It is essential for meeting people's daily needs and plays a vital role in ensuring a comfortable and safe environment for occupants. BIM has seen widespread application in MEP system design, especially in the areas of heating, ventilation, and air conditioning (HVAC) [7, 8] and system operation and maintenance [9, 10]. In the field of building fire protection, Zhou et al. [11] addressed the challenges of private fire data sharing and the alignment of fire sensors with BIM models, enabling the visualization of sensor status at appropriate locations within the three-dimensional BIM environment. Tang et al. [12] integrated design for safety (DFS) with BIM in metro station projects, achieving applications such as the identification of DFS control facilities and the evaluation of evacuation design effectiveness. Huang et al. [13] extended the Industry Foundation Classes (IFC) to promote the application of BIM in the design, construction, and management of underground infrastructure, and introduced multiple levels of detail (LOD) to represent the geometric information required for different application scenarios. It can be seen that the primary role of BIM models is often to automatically extract building information and automatically present design outcomes.

2.2 Ant Colony Algorithm in MEP System Design

The ant colony algorithm (ACA) was first proposed by Marco Dorigo in his 1992 doctoral dissertation [14]. Inspired by the behavior of ants in finding food, it is an optimization algorithm designed to find the optimal path in a graph. As ants travel, they deposit a chemical substance called pheromone on their paths. The ants in the colony can sense the pheromone, whose concentration is inversely proportional to the path length, and tend to follow paths with higher pheromone concentrations. Over time, the entire colony converges to the shortest path to the food source. The ACA has been applied to shortest path planning problems in fields such as aviation [15, 16], navigation [17, 18], and HVAC systems [19]. Jiang et al. [20] combined a co-evolution mechanism with the ACA to address the design of branched pipelines. Yang et al. [21] modified the search rules and pheromone update rules of the basic ACA to control the output scattering light field after incident light passes through a turbid medium. Pu et al. [22] proposed an improved ACA that simultaneously considers local and global optimal searches to solve single-robot and multi-robot multi-target path planning problems. Huang et al. [23] proposed an improvement to the ACA by incorporating the density peak clustering algorithm for local optimization, addressing the issue of the traditional algorithm's relatively random strategy selection and slow convergence speed. It can be seen that as a bio-inspired optimization algorithm, the ACA offers advantages such as robustness, parallelism, and ease of combination, making it widely applicable in solving path planning problems.

2.3 Research Gaps

Although there has been extensive research on both BIM and the ACA, there remain three key research gaps worth attention: (1) The application of BIM in FAS system design is still limited, how to link multidisciplinary information within BIM and realize automatic FAS system design based on BIM is an important direction for future research. (2) While ACA has become increasingly mature, how to appropriately apply this method to the path planning problem in FAS systems is another key area for future exploration. (3) The proposed methods should be validated through real-world engineering case studies.

3 Methodology

The process framework proposed in this paper is divided into four main parts: information acquisition and preprocessing, determination of the wiring sequence, optimization of the obstacle avoidance wiring algorithm, and post-processing results. The detailed technical roadmap is shown in Fig. 1.

3.1 Information Acquisition and Preprocessing

The acquisition of information includes two parts: building layout information and device position information. BIM models are typically created using Autodesk's Revit software. The information acquisition process can be implemented using Revit's secondary development based on C# programming, utilizing the Revit API documentation to extract

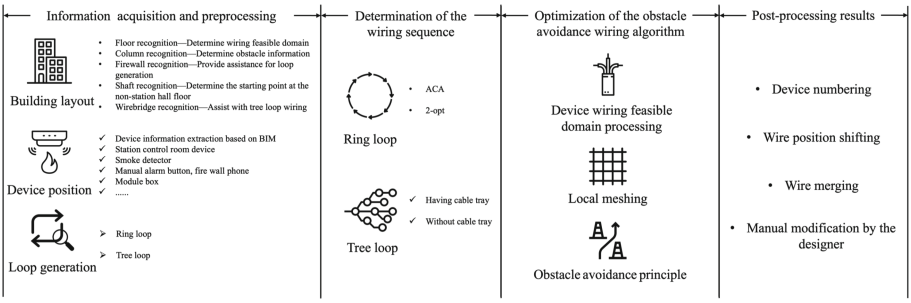


Fig. 1. FAS device automatic wiring logic.

various family information contained in the model, and then using Python for post-processing of this information. The acquisition of building layout information primarily includes five aspects: (1) Floor recognition: By identifying the "Floors" family information, geometric details of the floors are obtained. Due to the complexity of the building structure and the thickness of solid walls, each floor in the model typically contains multiple floor structures with gaps. Therefore, the Shapely library can be used to scale and merge the geometric information, thus obtaining the complete feasible wiring domain information for each floor in the metro station. (2) Column recognition: By identifying the “StructuralColumns” family information, geometric details of the obstacles are obtained. (3) Firewall recognition: By identifying the properties of the "Walls" family information, the location information of the firewalls is retrieved to assist in generating the system loops. (4) Shaft recognition: By identifying the "Rooms" family information, rooms with the name of the shaft are determined, allowing for the geometric location of the room to be obtained. This helps determine the starting points for wiring in non-station-floor layers, since the loop starting point for non-station floors is connected vertically via shafts from the station floor. (5) Cable tray recognition: By identifying the “CableTray” family information, the geometric information of cable trays is obtained to assist in subsequent tree loop wiring. The acquisition of device position information mainly involves obtaining device position data from the BIM models in HVAC, plumbing, and electrical systems, as well as devices such as station control room device and smoke detectors, etc.

Before determining the device wiring sequence, preparation work also includes automatic loop generation. Based on the shape of the FAS wiring, the loops are categorized into ring-shaped and tree-shaped connections. Since metro stations typically have a large floor area, and in line with fire protection regulations and design practices, firewalls on each metro station floor are often used as dividing lines, splitting the wiring on each floor into three loops.

3.2 Determination of the Wiring Sequence

Ring Loop Wiring Sequence. Each ring loop in the system typically involves connecting 80 to 100 devices, making the task of quickly determining the shortest and non-intersecting wiring sequence a critical problem to address. This paper combines the ACA with secondary optimization to achieve satisfactory wiring sequence results.

The subsequent wiring process (Sect. 3.3) is based on a grid layout, so the ACA also needs to be adapted to graph-based forms. In this paper, the relationship between vertices and edges is established using the networkx library in Python. The wiring sequence obtained through the ACA may often result in intersecting wires or fail to find the optimal solution, so a 2-opt algorithm is applied for local secondary optimization of the results. By reversing the subpath between two non-adjacent vertices in the path, the algorithm attempts to reduce the total path length. The algorithm continuously performs this 2-exchange operation until no shorter path can be found, thus achieving a local optimum. This method is typically used to further optimize the initial solutions generated by the ACA or other heuristic methods, improving the overall solution quality.

Tree Loop Wiring Sequence. Tree-shaped wiring involves multiple types of connections, and during the design process, cable trays are often installed to keep the wiring layout as neat and centralized as possible. Therefore, the tree loop wiring must take into account both cases: having cable tray and without cable tray.

Having Cable Tray. At this stage, the wiring principle is to connect devices vertically to the nearest cable tray whenever possible. To accelerate the wiring sequence process, a clustering method is first applied to classify devices based on their associated cable trays. Specifically, the Python Shapely library is used to determine whether the connection line between each pair of devices intersects with any cable tray. If no intersection is detected, the pair of devices is considered to belong to the same cluster. Then, by iterating over the distances from each cluster to the cable trays, the closest cable tray for each group of devices can be identified.

No Cable Tray At this stage, the wiring principle is to determine the wiring sequence that forms the shortest tree-shaped connection among the devices in the tree loop. This paper applies the Minimum Spanning Tree (MST) method to obtain an effective wiring sequence. By calculating the Manhattan distances between devices and implementing Prim algorithm using the Python Scipy library, the shortest connection scheme between devices is identified.

3.3 Optimization of the Obstacle Avoidance Wiring Algorithm

Traditional obstacle avoidance algorithms, such as A* and Dijkstra [24], often suffer from excessively long traversal times. This paper proposes three optimization strategies for the A* algorithm: device wiring feasible domain processing, local meshing, and the obstacle avoidance principle.

Device Wiring Feasible Domain Processing. Since FAS wiring consists of orthogonal line segments, this paper stores the feasible domain of the metro station floor plan in the form of an orthogonal graph. FAS devices are typically represented as quadrilateral shapes in the planar layout, so when performing grid partitioning, the grid spacing should be carefully selected (specifically, the grid size should be smaller than half the width of a device) to ensure that the grid can segment at least the edges of each device (see Fig. 2 (a)).

Local Meshing. Compared to the overall feasible domain on each metro station floor, the devices occupy relatively small areas in the drawings. This leads to a large number of redundant planar vertices during the A* algorithm's feasible vertex exploration, significantly increasing computational time. To improve algorithm efficiency, this paper adopts a local meshing approach for obstacle-avoiding wiring between pairs of devices. Specifically, a rectangular region is defined by enlarging the bounding box formed by the diagonal line between the two devices, and this enlarged area is used as the exploration domain for the A* algorithm (see Fig. 2 (b)).

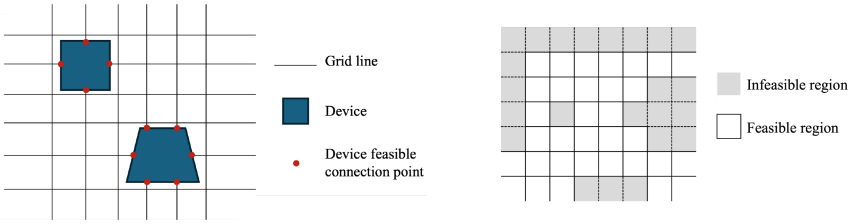


Fig. 2. Optimization methods for obstacle avoidance algorithms.

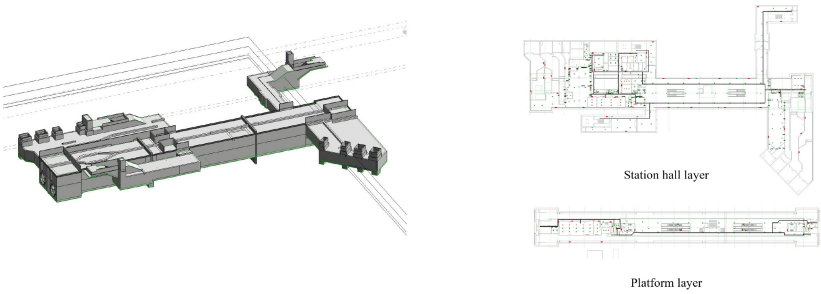
Obstacle Avoidance Principle. In this paper, the vertices covered by obstacles in the orthogonal graph are removed to ensure that the wiring paths do not cross devices, columns, or already connected regions, thereby guaranteeing the rationality of the wiring layout. For tree-shaped wiring involving cable tray information, additional vertex attributes are assigned within the regions covered by the cable trays to record their locations.

3.4 Post-processing of Results

After the automatic FAS system wiring is completed, post-processing is applied to make the results better aligned with practical engineering design. This typically involves the following four steps: (1) Device numbering: Using regular expressions in Python, devices in both ring and tree wiring are numbered according to their determined wiring sequences. (2) Wiring position shifting: Given the large variety of FAS wiring types, the final wiring results inevitably contain overlapping segments. These overlapping sections are locally offset to ensure clarity and separation. (3) Wire merging: Since the wiring paths are generated based on grid structures, there are often many continuous, parallel, and consecutive short wire segments. To accelerate the final generation of wiring layouts, these segments are merged where possible. (4) Manual modification by the designer: The automatic wiring process is primarily intended to assist designers. In particularly complex scenarios, manual fine-tuning of the results by designers is still necessary to achieve optimal layout quality.

4 Case Study

This paper uses a metro station located in Fuzhou, Fujian Province, China, as a case study to validate the feasibility of the proposed automatic design method. The building includes a concourse level and a platform level. A schematic diagram of the BIM model is shown in Fig. 3, which clearly indicates the presence of cable trays in the model.



(a) (b)

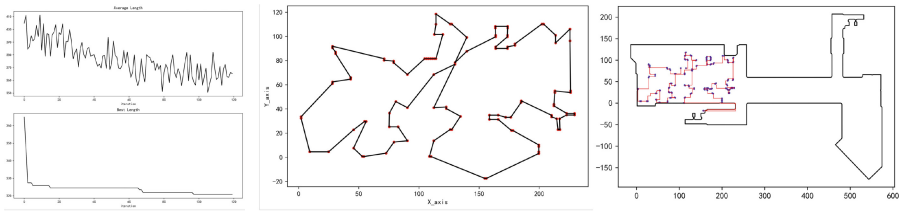
Fig. 3. The metro station BIM model in case study.

After acquiring the building layout information, device position data, and automatically dividing the system loops, the results are presented in Table 1. The ring wiring results are shown in Fig. 4 and Fig. 5, and the tree wiring results are shown in Fig. 6. The final statistical results of the design are provided in Table 1, and the design savings can be calculated using Formula 1. It can be observed that the automatic design results typically result in significant savings in wire and accessory usage compared to traditional design approaches. However, it is important to note that the automatic design results require careful inspection by designers.

$$I_{saving} = \frac{L_{algorithm} - L_{convention}}{L_{convention}} \times 100\% \tag{1}$$

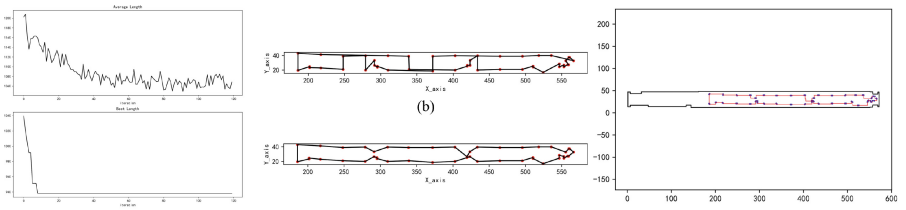
Table 1. Loop generation results in the case study.

Loop type	Loop name	Location of devices	Device number	Wire length (Algorithm)	Wire length (Convention)	Wire savings
Ring loop	Ring bus	Station hall floor	111	1627.9 m	1849 m	12%
		Platform floor	48	921.7 m	1135 m	18.8%
Tree loop	Telephone line	Station hall floor	78	1075.6 m	1429 m	24.7%
	Power line	Station hall floor	4	86.3 m	96 m	11.2%



(a) (b) (c)

Fig. 4. Ring loop wiring result for station hall floor, where (a) shows the average length and the best length of wiring sequence during the iterations of ACA, (b) shows the direct wiring result after ACA and 2-opt algorithm, and (c) represents the final wiring result after using optimal obstacle avoidance wiring algorithm.



(a) (b) (c) (d)

Fig. 5. Ring loop wiring result for platform floor, where (a) shows the average length and the best length of wiring sequence during the iterations of ACA, (b) shows the direct wiring result after ACA, (c) shows the final direct wiring result after ACA and 2-opt algorithm, and (d) represents the final wiring result after using optimal obstacle avoidance wiring algorithm.

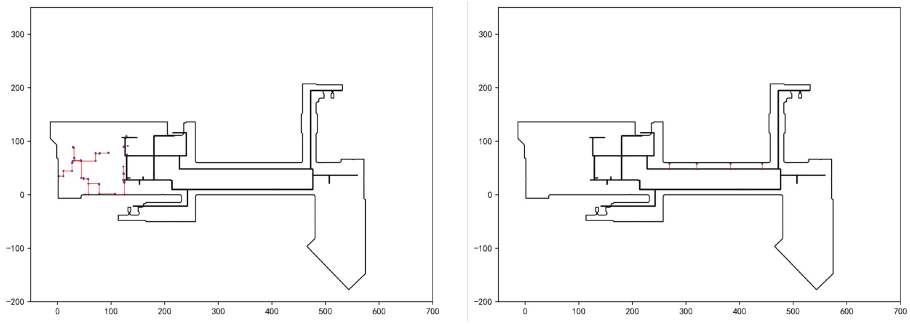


Fig. 6. Tree loop wiring result (telephone line and power line) for the station hall floor when cable trays exist.

5 Conclusions

This paper proposes an innovative automatic wiring method for FAS in metro stations based on BIM and ACA. Compared to traditional manual design, the proposed automatic design method improves design efficiency and reduces the engineering workload while ensuring design accuracy, leading to cost savings in the design process. The main contributions of this paper are as follows: (1) The FAS wiring problem is abstracted as a path planning problem, and an automatic wiring framework for FAS systems based on BIM and algorithms is proposed. (2) The ACA is successfully applied to the automatic wiring process of the FAS system, and the algorithm is optimized to save computational time. (3) The proposed method is validated through a real metro station case study, and the results show that the automatic design method can save 11.2% to 24.7% of the engineering workload.

However, this paper inevitably has some limitations. For instance, when determining the optimal wiring sequence for the ring loop, the results of orthogonal wiring were not considered simultaneously, which may lead to some device wiring results intersecting to a certain extent. Additionally, the current automatic design results generate only two-dimensional wiring layouts, without considering the three-dimensional wiring scenarios when connecting wires to devices. Therefore, the authors will continue to optimize the automatic wiring process for FAS systems to enhance the robustness and practicality of the method.

Acknowledgement. This research is funded by the National Natural Science Foundation of China (No.52161135202).

References

1. Smith, R.A., Zhou, J.: Background of recent developments of passenger railways in China, the UK and other European countries. J. Zhejiang Univ. Sci. A. **15**, 925–935 (2014). https://doi.org/10.1631/jzus.A1400295

2. Sacks, R., Eastman, C., Lee, G., Teicholz, P.: BIM Handbook: A Guide to Building Information Modeling for Owners, Designers, Engineers, Contractors, and Facility Managers (2018). https://doi.org/10.1002/9781119287568
3. Park, S., Shin, M., Jang, J.Y., Koo, B., Kim, T.W.: Automated process for generating an air conditioning duct model using the CAD-to-BIM approach. J. Build. Eng. **91**, 109529 (2024). https://doi.org/10.1016/j.jobe.2024.109529
4. Wang, Y., Zhang, L., Yu, H., Tiong, R.L.K.: Detecting logical relationships in mechanical, electrical, and plumbing (MEP) systems with BIM using graph matching. Adv. Eng. Inform. **54**, 101770 (2022)
5. Jin, R., et al.: Automatic device arrangement and wiring for fire alarm systems in metro stations: a case study. J. Build. Eng. **97**, 110617 (2024)
6. Hu, Z.-Z., Tian, P.-L., Li, S.-W., Zhang, J.-P.: BIM-based integrated delivery technologies for intelligent MEP management in the operation and maintenance phase. Adv. Eng. Softw. **115**, 1–16 (2018)
7. Qi, Z., Jin, R., Li, J., Guan, H., Xu, P.: BIM-based automated multi-air distribution layout generation for office buildings: a case study. Buildings. **13** (2023)
8. Jin, R., et al.: A framework for HVAC system auto-zoning based on BIM. Building Simulation Conference Proceedings (2023)
9. Palha, R.P., Hüttl, R.M.C., Da Costa, E., Silva, A.J.: BIM interoperability for small residential construction integrating warranty and maintenance management. Autom. Constr. **166**, 105639 (2024)
10. El Hamshary, O., Abouhamad, M., Marzouk, M.: Maintenance framework for subway network systems using BIM. J. Perform. Constr. Facil. **36**, 04022045 (2022)
11. Zhou, X., et al.: CloudFAS: cloud-based building fire alarm system using Building Information Modelling. J. Build. Eng. **53**, 104571 (2022)
12. Tang, Y., Xia, N., Lu, Y., Varga, L., Li, Q., Chen, G., Luo, J.: BIM-based safety design for emergency evacuation of metro stations. Autom. Constr. **123**, 103511 (2021)
13. Huang, M.Q., Zhu, H.M., Ninić, J., Zhang, Q.B.: Multi-LOD BIM for underground metro station: interoperability and design-to-design enhancement. Tunn. Undergr. Space Technol. **119**, 104232 (2022)
14. Dorigo, M., Birattari, M., Stutzle, T.: Ant colony optimization. IEEE Comput. Intell. Mag. **1**, 28–39 (2006)
15. Yu, Z., Si, Z., Li, X., Wang, D., Song, H.: A novel hybrid particle swarm optimization algorithm for path planning of UAVs. IEEE Internet Things J. **9**, 22547–22558 (2022)
16. Tang, J., Chen, X., Zhu, X., Zhu, F.: Dynamic reallocation model of multiple unmanned aerial vehicle tasks in emergent adjustment scenarios. IEEE Trans. Aerosp. Electron. Syst. **1–43** (2022)
17. Ding, Y., Li, R., Shen, H., Li, J., Cao, L.: A novel energy-saving route planning algorithm for marine vehicles. Appl. Sci. **12**, 5971 (2022)
18. Zheng, Y., Lv, X., Qian, L., Liu, X.: An optimal BP neural network track prediction method based on a GA–ACO hybrid algorithm. J. Mar. Sci. Eng. **10**, 1399 (2022)
19. Dong, L., Lin, B., Jiang, Y., Wang, W., Zhang, Y., Gu, J., Xu, P.: Automatic generation of pipe routing for variable refrigerant flow air conditioning system. J. Build. Eng. **100**, 111755 (2025)
20. Jiang, W.-Y., Lin, Y., Chen, M., Yu, Y.-Y.: A co-evolutionary improved multi-ant colony optimization for ship multiple and branch pipe route design. Ocean Eng. **102**, 63–70 (2015)
21. Yang, Z., Fang, L., Zhang, X., Zuo, H.: Controlling a scattered field output of light passing through turbid medium using an improved ant colony optimization algorithm. Opt. Lasers Eng. **144**, 106646 (2021)
22. Pu, X., Song, X., Tan, L., Zhang, Y.: Improved ant colony algorithm in path planning of a single robot and multi-robots with multi-objective. Evol. Intell. **17**, 1313–1326 (2024)

23. Huang, R., Ning, J., Mei, Z., Fang, X., Yi, X., Gao, Y., Hui, G.: Study of delivery path optimization solution based on improved ant colony model. Multimed. Tools Appl. **80**, 28975–28987 (2021)
24. Soltani, A.R., Tawfik, H., Goulermas, J.Y., Fernando, T.: Path planning in construction sites: Performance evaluation of the dijkstra, a∗, and GA search algorithms. Adv. Eng. Inform. **16**, 291–303 (2002)

EfficientWiPose: A Lightweight and High-Accuracy WiFi-Based Human Pose Estimation System for Energy-Efficient Smart Buildings

Weili Wang[1], Weixiong Zhang[1], Linjun Zhao[2], Benying Tan[3], Huijun Wu[4], and Huakun Huang[1](✉)

[1] School of Computer Science and Cyber Engineering, Guangzhou University, Guangzhou 510006, China
huanghuakun@gzhu.edu.cn
[2] School of Electronics and Information, Guangdong Polytechnic Normal University, Guangzhou 510665, China
[3] School of Artificial Intelligence, Guilin University of Electronic Technology, Guilin Guangxi Zhuang Autonomous Region, 541004, China
[4] School of Civil Engineering and Transportation, Guangzhou University, Guangzhou 510006, China

Abstract. WiFi-based human pose estimation offers a privacy-preserving and cost-effective solution for human motion monitoring, with significant implications for enhancing energy efficiency in smart buildings. In the context of smart energy systems, the use of low-power WiFi devices is crucial for sustainable energy management. However, deploying WiFi-based human pose estimation on these resource-constrained devices presents challenges due to computational limitations. To address this, we propose EfficientWiPose, a model specifically designed for commercial low-power WiFi devices. EfficientWiPose achieves low model complexity and hardware-friendliness, facilitating the integration of human motion monitoring into smart energy systems. Our experiments show EfficientWiPose achieves an impressive mPCK@0.05 of 78.67%, outperforming other WiFi-based methods. Its hardware-friendly and energy-efficient design provides a robust solution for accurate pose estimation and paves the way for real-time WiFi sensing in various practical applications, especially in smart buildings where reducing energy consumption is paramount.

Keywords: WiFi-based Human Pose Estimation · EfficientWiPose · Smart Energy Buildings

This work was supported by the Natural Science Foundation of Guangdong Province, China (No. 2025A1515011755), and in part by the Key Laboratory of Cognitive Radio and Information Processing, Ministry of Education (No. CRKL240204).

© The Author(s), under exclusive license to Springer Nature Singapore Pte Ltd. 2025
L. Ni et al. (Eds.): CCHVAC 2025, ESE, pp. 326–333, 2025.
https://doi.org/10.1007/978-981-95-3253-7_35

1 Introduction

Human pose estimation underpins a wide range of building-automation tasks that directly affect energy efficiency and occupant comfort. Accurate knowledge of occupants' body configurations allows Heating, Ventilation and Air-Conditioning (HVAC) systems to switch from coarse presence detection to fine-grained activity-aware control—for example, distinguishing between a person who is sedentary at a desk and one who is exercising, thereby modulating airflow and temperature set-points in real time. Similarly, lighting controllers can dim or redirect luminaires when fine-grained pose cues indicate that occupants are looking away from work surfaces. Beyond environmental control, pose estimation is routinely employed in gesture-based interfaces for smart appliances, fall-detection systems for elderly care, and automated ergonomic assessments in office spaces. Traditional camera-based solutions, while accurate, raise privacy concerns, perform poorly under low illumination, and require line-of-sight that is often obstructed by furniture or walls. These limitations are compounded by their substantial power consumption, which conflicts with the stringent energy budgets of sustainable smart buildings. WiFi-based pose estimation offers a promising solution that not only addresses privacy and usability but also contributes to a more energy-efficient building infrastructure. By leveraging existing WiFi networks, this approach minimizes the need for additional hardware and reduces the overall energy footprint of sensing systems.

To overcome these limitations, recent research has explored ambient radio-frequency sensing, particularly WiFi Channel State Information (CSI). CSI measures amplitude and phase changes of OFDM packets as they interact with moving bodies, inherently encoding fine-grained motion cues even through walls or in darkness [1]. Crucially, these signal measurements do not capture identifiable imagery, offering a privacy-preserving alternative. Given the pervasive nature of WiFi access points indoors and the ability to process CSI on resource-constrained edge devices, this modality promises low-cost, continuous monitoring without specialized cameras or powerful GPUs.

Alternative human pose estimation methods include: (i) Wearable device-based HPE, which requires users to purchase and carry specific devices [2, 3]. (ii) Computer vision-based HPE, which offers high precision but raises privacy concerns, making it unsuitable for private spaces. (iii) Radio frequency-based human posture estimation, utilizing devices like radar [4, 5] and WiFi. Radar is often too expensive for common use. Fortunately, WiFi sensing-based methods such as, MetaFi [6] address these issues. WiFi signals, including Received Signal Strength (RSS) and Channel State Information (CSI), enable operation in dark or obstructed environments without high device costs.

WiFi-based pose estimation, particularly using CSI, offers a powerful alternative to RSS-only approaches due to its ability to capture richer, fine-grained details of signal propagation. By tracking amplitude and phase variations of OFDM packets as they scatter off moving bodies, CSI inherently encodes subtle motion cues, even through walls or in total darkness, without recording identifiable images. Since most indoor spaces already have WiFi access points and CSI processing can run on low-power edge devices, this method provides a low-cost, privacy-preserving way to monitor human posture without specialized cameras or GPUs.

While existing works demonstrate the feasibility of recovering body silhouettes or joint heatmaps from CSI, most rely on heavy networks or offline processing. To achieve

real-time WiFi human pose estimation on off-the-shelf routers and embedded platforms, computationally frugal and highly accurate models are needed.

In this work, we introduce EfficientWiPose, a streamlined neural network tailored for real-time pose estimation from WiFi CSI under commercial hardware constraints. EfficientWiPose is designed to be hardware-friendly, ensuring energy efficiency and suitability for real-time applications on commercial WiFi hardware with limited compute capacity. It builds upon a MobileNetV3-Small [7] backbone and integrates depthwise-separable convolutions [8], spatial attention modules, and feature normalization layers. These components selectively amplify human-motion signals while suppressing static and multipath artifacts, enabling the network to focus its limited parameters on salient pose cues.

Our contributions are summarized as follows:

1) We introduce EfficientWiPose, a lightweight yet powerful architecture combining MobileNetV3-Small with custom attention and normalization modules. This fusion achieves an optimal balance between fast inference speeds and high joint localization accuracy, making it hardware-friendly for deployment on resource-constrained devices.
2) We establish a real-time WiFi sensing system to evaluate the performance of state-of-the-art WiFi sensing-based methods.

By delivering accurate, privacy-respecting pose estimates at frame rates compatible with real-world applications, EfficientWiPose paves the way for unobtrusive human-motion monitoring in homes, offices, healthcare facilities, and beyond, significantly contributing to smart energy management in buildings.

2 System Design

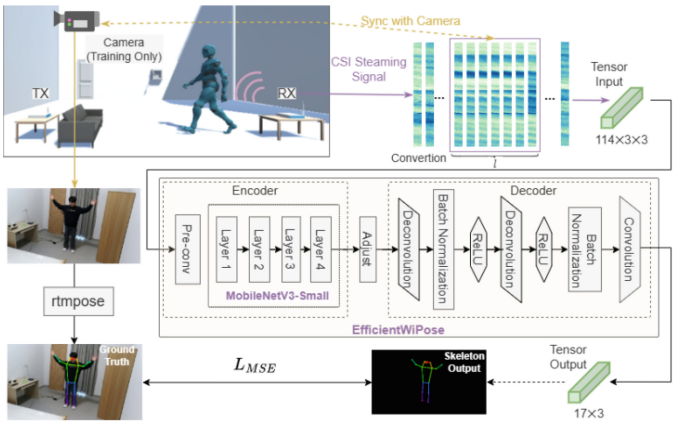


Fig. 1. Architecture of our proposed method

As depicted in Fig. 1, the architecture of our proposed method encompasses data collection & preprocessing, model architecture, and camera support for data association and model training. In the context of smart energy buildings, the system design prioritizes efficiency and low power consumption. The core idea is to leverage the precise human pose estimation capabilities of EfficientWiPose to inform and optimize building energy management systems.

Data collection & preprocessing involves 500 Hz CSI sampling with interpolation, synchronized to 60 Hz video (1 frame $\approx$ 16 CSI samples). For ground truth, RTMPose [9] extracts 2D keypoints from video, excluding the visualization branch during training. The model architecture utilizes MobileNetV3-Small for Encoder/Decoder. CSI signals are converted to tensor inputs and processed to output a 17×3 tensor. The system employs a skeletal output module to enable human skeleton keypoint detection/regression (Skeleton Output). The lightweight nature of our model ensures that it can run on low-power WiFi devices, directly contributing to reduced energy consumption within the building infrastructure. By accurately detecting human presence and activity, the system can dynamically adjust environmental controls, leading to significant energy savings without compromising occupant comfort.

2.1 Labeling Design

We generate ground truth 2D joint annotations by processing each video frame through the MMPoseInferencer from the MMPose library, configured with pose2d="human". This setup employs RTMPose, a real-time multi-person pose estimation model, which utilizes a top-down approach with a high-resolution network backbone pretrained on the COCO keypoint dataset. RTMPose first detects human bounding boxes and then predicts precise keypoint heatmaps for each detected person. For every frame, we extract the final joint coordinates and confidence scores, which serve as our "true" labels for both training and evaluation purposes.

2.2 Model Design

Our proposed method, EfficientWiPose, is meticulously designed to achieve high accuracy in WiFi-based human pose estimation while maintaining a lightweight architecture suitable for resource-constrained environments, particularly in smart energy buildings. The design adheres to three core principles: efficient adaptation of WiFi CSI data for convolutional processing, utilization of a highly optimized backbone for hierarchical feature extraction, and a compact decoding pipeline for precise joint coordinate reconstruction with minimal computational overhead. This approach directly supports the goal of reducing energy consumption by enabling deployment on low-power edge devices.

First, the raw CSI tensor, which captures rich information about human movement through multiple time-subcarrier frames across transmit-receive antenna pairs, is efficiently transformed. It is linearly projected into a three-channel feature map. This initial adaptation layer is designed to be lightweight, preserving the statistical properties of the data while reshaping the input to match the dimensionality expected by the backbone. By aligning the number of channels with the first convolution's input, we leverage the

benefits of large-scale pretraining without incurring significant upfront processing costs, thus contributing to the overall energy efficiency of the system.

At the heart of EfficientWiPose is a streamlined version of MobileNetV3-Small. This choice is driven by its proven superior trade-off between accuracy and computational cost, making it ideal for deployment in energy-sensitive smart building applications. Instead of standard convolutions, we employ depthwise-separable operations. These operations decompose each 3×3 filter into a lightweight depthwise pass (one filter per input channel) followed by a pointwise 1×1 projection. This decomposition drastically reduces both the parameter count and multiply-accumulate operations by approximately an order of magnitude. This efficiency is crucial for minimizing the computational load and the energy consumption on edge devices, while still effectively learning complex spatial correlations within the CSI data. The network is structured into four successive blocks, progressively extracting features from fine-grained, low-level patterns (like subtle phase shifts) to higher-order human-motion features.

Following the final backbone stage, a narrow 1×1 convolution is applied to compress hundreds of feature channels into a compact set of 128. It also compels the network to prioritize the most discriminative features for pose estimation. A subsequent batch normalization and lightweight non-linearity stabilize these representations, ensuring optimal performance for subsequent upsampling operations.

Our decoder is designed for maximum parsimony and efficiency. It consists of two small transposed-convolution layers that progressively restore spatial resolution. Each layer is followed by normalization and activation functions to prevent feature degradation. A final 1×1 projection generates three values per keypoint (confidence, horizontal offset, and vertical offset) across the output grid. Global average pooling then collapses the spatial dimensions into per-joint predictions, eliminating the need for computationally expensive fully connected layers. This lean decoding pipeline further reduces the model's complexity and computational demands, making it highly suitable for real-time applications in energy-constrained smart building environments.

By integrating this minimal adaptation layer, an energy-efficient depthwise-separable backbone, aggressive channel reduction, and a lean upsampling path, EfficientWiPose achieves real-time performance on off-the-shelf WiFi routers and embedded processors. This carefully balanced architecture ensures that every parameter contributes to either isolating human-motion cues from multipath clutter or precisely localizing body joints. The result is a lightweight yet highly accurate solution for live WiFi-based pose estimation, directly supporting the development of intelligent energy management systems in smart buildings by providing accurate occupancy and activity data with minimal energy overhead.

3 Experiment Results

We evaluate the performance of our model on our own collected dataset. The hardware running experiments has 24 core CPUs of Intel i9-13900@5.20 GHz, NVIDIA RTX4090 GPU, and 64 GB of memory. The operating system is Ubuntu 22.04. We implemented the model using PyTorch 2.5.1 with Python 3.9.20.

3.1 Experiment Configurations

Experimental Setup and Dataset
To build our dataset, two mini-PCs—each equipped with a Qualcomm Atheros AR9380 wireless card and three identical external antennas—served as WiFi transmitter (TX) and receiver (RX), placed at opposite ends of a furnished apartment. CSI was captured at 5.68 GHz carrier frequency, 40 dBm transmit power, and a 500 Hz sampling rate. A separate camera (60 Hz) recorded the scene solely for offline labeling. Its timestamps were synchronized so that one video frame aligned with exactly sixteen CSI samples. Over two collection sessions (29281 and 19568 video frames), we amassed 781584 CSI snapshots covering everyday actions—hand waving, slow walking, sitting, standing, and more—under realistic lighting and furniture layouts.

Data Preprocessing
Before putting the CSI and video frames into our model, we performed some necessary preprocessing on them. First, we set the sampling rate of the WiFi device to 500 Hz to prevent packet loss due to hardware imperfections, where the RX fails to receive a packet or the TX fails to send it. Although this reduces the probability of packet loss, we linearly interpolated the CSI to fill in the gaps to make it more complete. The recording frequency of our camera was set to 60 Hz. To synchronize the two, we synchronized the timestamps of the two, so that each video frame corresponded to 16 CSI.

Parameter Settings
Our network was trained for 150 epochs using the AdamW optimizer, which decouples weight decay from gradient updates and handles sparse gradients effectively. The initial learning rate was set to 0.01 based on preliminary tuning. To smooth convergence and prevent oscillations in keypoint-accuracy curves, we employed a ReduceLROnPlateau scheduler: whenever the validation loss failed to improve for five consecutive epochs, the learning rate was halved.

Evaluation Metrics
We evaluate pose-estimation accuracy using the Mean Percentage of Correct Keypoints (mPCK). Let N denote the total number of annotated keypoints, $\hat{p}_n$ the predicted coordinates and p_n the ground-truth coordinates of keypoint n. For a single normalized threshold θ, the Percentage of Correct Keypoints (PCK) is defined as

$$PCK(\theta) = (1/N) * \sum_{n=1}^{N} \left[\|\hat{p}_n - p_n\|_2 \leq \theta * S \right] \tag{1}$$

where S is the diagonal length of the ground-truth bounding box and $[\cdot]$ is the indicator function. An alternative but incorrect formulation, sometimes found in the literature, is

$$PCK_{alt}(\theta) = (1/N) * \sum_{n=1}^{N} \left[\left(\|\hat{p}_n - p_n\|_2^2 \right)/S \leq \theta \right] \tag{2}$$

which uses squared error inside the indicator and divides by a length rather than comparing lengths directly. To obtain a single aggregate measure, we compute mPCK as the

average of PCK(θ) over a sequence of thresholds $\sigma_k{}_{k=1}^{10} = 0.05, 0.10, \ldots, 0.50$:

$$mPCK = (1/|\sigma|) \sum_{\theta \in \sigma} PCK(\theta) \tag{3}$$

3.2 Results Analysis

Our experimental results unequivocally demonstrate the superior performance of EfficientWiPose across key evaluation criteria: pose-estimation accuracy, model complexity, and inference latency. These findings underscore its significant potential for real-world applications, particularly in the context of smart energy buildings.

Pose-Estimation Accuracy
EfficientWiPose achieved an impressive mPCK@0.05 of 78.67%, significantly outperforming existing state-of-the-art WiFi-based pose estimation methods. For instance, accurate pose estimation can differentiate between a person standing and sitting, allowing for more nuanced adjustments to environmental controls, thereby optimizing energy usage without compromising occupant comfort.

Model Complexity
One of the most compelling advantages of EfficientWiPose is its remarkably low model complexity. With only 2.78 million parameters and a mere 0.01 GFLOPs. This lightweight design is paramount for deployment on resource-constrained, low-power WiFi devices commonly found in smart building infrastructures. By minimizing computational demands, EfficientWiPose directly contributes to reducing the overall energy footprint of the sensing system, aligning perfectly with the objectives of smart energy management. This efficiency allows for widespread deployment without the need for expensive, high-power computing hardware, making it a cost-effective and sustainable solution (Table 1).

Table 1. Performance comparison of WiFi-based pose estimation methods.

Model	mPCK@0.05 (%)	Params (M)	FLOPs (G)
MetaFi	30.53	9.40	35.65
EfficientWiPose (Ours)	**78.67**	**2.78**	**0.01**

4 Conclusion

In this paper, we introduced EfficientWiPose, a lightweight and high-accuracy method for WiFi-based human pose estimation. EfficientWiPose combines a MobileNetV3-Small backbone with custom attention and normalization modules, achieving an optimal balance between fast inference speeds and high joint localization accuracy. We demonstrated

its superior performance through extensive experiments on our collected dataset, where it achieved the highest mPCK@0.05 (78.67%), outperforming other WiFi-based methods. The hardware-friendly design of EfficientWiPose makes it energy-efficient and suitable for deployment on devices with limited computational resources. This enables real-time human motion monitoring in various applications such as homes, offices, and healthcare facilities, significantly contributing to smart energy management in buildings. The results of our study highlight the potential of EfficientWiPose to pave the way for unobtrusive and energy-efficient human pose estimation in real-world scenarios, particularly in the context of smart energy buildings.

References

1. Adib, F., Katabi, D.: See through walls with WiFi! In: Proceedings of the ACM SIGCOMM 2013 conference on SIGCOMM, pp. 75–86 (2013)
2. Liu, L., Liu, J., Qiu, S., et al.: Kinematics analysis of arms in synchronized canoeing with wearable inertial measurement unit. IEEE Sens. J. **23**(5), 4983–4993 (2023)
3. Li, T., Yu, H.: Upper body pose estimation using a visual–inertial sensor system with automatic sensor-to-segment calibration. IEEE Sens. J. **23**(6), 6292–6302 (2023)
4. Adib, F., Hsu, C.Y., Mao, H., et al.: Capturing the human figure through a wall. ACM Trans. Graph. **34**(6), 1–13 (2015)
5. Zhao, M., Li, T., Abu Alsheikh, M., et al.: Through-wall human pose estimation using radio signals. In: Proceedings of the IEEE Conference on Computer Vision and Pattern Recognition, pp. 7356–7365 (2018)
6. Yang, J., et al.: MetaFi: device-free pose estimation via commodity WiFi for metaverse avatar simulation. In: IEEE 8th World Forum on Internet of Things (WF-IoT), pp. 1–6. IEEE (2022)
7. Howard, A., Sandler, M., Chu, G., et al.: Searching for mobilenetv3. In: Proceedings of the IEEE/CVF International Conference on Computer Vision, pp. 1314–1324 (2019)
8. Chollet F. Xception: deep learning with depthwise separable convolutions. In: Proceedings of the IEEE Conference on Computer Vision and Pattern Recognition, pp. 1251–1258 (2017)
9. Jiang, T., Lu, P., Zhang, L., et al.: Rtmpose: real-time multi-person pose estimation based on mmpose. arxiv preprint arxiv:2303.07399 (2023)

A Mean Room Temperature Prediction LSTM Model for Heating Buildings

Yongjie Wang[1], Yangming Liu[2], Guanjing Lin[1(✉)], and Changhong Zhan[3]

[1] Tsinghua Shenzhen International Graduate School, Tsinghua University, Shenzhen, Guangdong 518055, China
linguanjing@sz.tsinghua.edu.cn

[2] School of Computer Science and Technology, Harbin Institute of Technology, Shenzhen, Guangdong 518055, China

[3] School of Architecture and Design, Harbin Institute of Technology; Key Laboratory of Cold Region Urban and Rural Human Settlement Environment Science and Technology, Ministry of Industry and Information Technology, Harbin, Heilongjiang 150000, China

Abstract. The thermal process of buildings is characterized by nonlinear and long time lag. Accurately predicting the mean room temperature of buildings is crucial for regulating heating systems. However, the current black box model determines inputs mainly through theoretical analysis without conducting correlation analysis. Moreover, the inputs do not sufficiently cover various factors influencing the mean room temperature, such as heating system operation parameters, outdoor meteorological conditions, time, and building physical parameters. To address these challenges, this study employs Spearman correlation index to select inputs for the mean room temperature long short-term memory (LSTM) prediction model. A composite indicator (the product of the building exterior surface area on different orientations with corresponding solar radiation on different orientations) is proposed and it is set as an input index. The results indicate that the proposed composite indicator improves prediction accuracy compared to using solar radiation alone, with errors decreasing 0.45%. The order of correlation strength between influencing factors and mean room temperature, from highest to lowest, is as follows: historical mean room temperature, water flow rate, supply water temperature, outdoor air temperature, solar radiation, return water temperature, wind velocity. These findings are essential for achieving predictive control and smart solutions in heating systems.

Keywords: Mean room temperature · LSTM · Heating buildings

1 Introduction

1.1 Background

The world is facing energy shortages and climate change challenges. As highlighted in [1, 2], building operations accounted for 30% of global energy consumption and 28% of global CO_2 emissions in 2021. In China, the situation is similarly concerning. Heating

© The Author(s), under exclusive license to Springer Nature Singapore Pte Ltd. 2025
L. Ni et al. (Eds.): CCHVAC 2025, ESE, pp. 334–341, 2025.
https://doi.org/10.1007/978-981-95-3253-7_36

in northern urban areas consumed 217 million tce and emitted 490 million tons of CO_2. Given the substantial scale of building operations in northern urban areas, optimizing energy efficiency and implementing low-carbon operations are crucial for achieving energy strategies and mitigating climate change impacts.

Precise regulation of heating systems is one of the most effective strategies for energy conservation and emission reduction. At the core of this strategy lies the prediction of mean room temperature. Mean room temperature prediction captures the variation patterns of indoor temperatures in response to changes in the operational state of the heating system and outdoor meteorological parameters. Based on the results of the prediction, tailored regulation strategies can be formulated, ultimately achieving the goal of maintaining stable indoor temperatures and avoiding over- or under-supply. The prediction fundamentally addresses current challenges in heating buildings, including excessive energy consumption and poor regulation accuracy. It enables precise heating, advancing the achievement of smart buildings.

1.2 Literature Review

The white box model, black box model, and gray box model are commonly adopted for the mean room temperature prediction. The white box model, based on the physical mechanism, can only solve a few physical problems with simple boundary conditions. The black box model, relying on the data-driven methods, exhibits ease of realization and high prediction accuracy. Thus, the black box model is adopted here to predict the mean room temperature. The gray box model combines physical laws with data-driven characteristics. Currently, machine learning-based gray box models are in their early stages of development.

The black box algorithms include LSTM, artificial neural networks (ANNs), ExtraTrees, etc. Palmer Real J et al. [3] proposed a black box model to predict mean room temperatures, achieving a prediction error of 5%. Briga-Sá A et al. [4] compare the prediction accuracy of the ANNs and support vector machine for mean room temperature, showing that ANNs outperform support vector machines. Elmaz F et al. [5] construct several mean room temperature forecasting models. The results show that the convolutional neural network - LSTM achieves an R^2 value exceeding 0.9. Alawadi S et al. [6] compared 36 types prediction algorithms, and concluded that LSTM and ExtraTrees exhibited strong performance. In conclusion, mean room temperature black-box prediction models ultilize a variety of algorithms. Most studies adopt LSTM for handling mean room temperature series data. Thus, LSTM is a more suitable algorithm for predicting mean room temperature.

The inputs of the mean room temperature black box model mainly contain heating system operation parameters, ambient meteorological parameters, time, historical mean room temperature, etc. Afroz Z et al. [7] announced that feature engineering is crucial for enhancing the mean room temperature prediction accuracy. Kalidindi S V et al. [8] demonstrate that integrating building height into the inputs of the mean room temperature prediction model significantly improves forecasting accuracy. Jiang B et al. [9] adopt outdoor temperature, historical room temperature, and building surface temperature to forecast mean room temperature, without considering heating system operation parameters and building physical information. Sulzer M et al. [10] announced that time

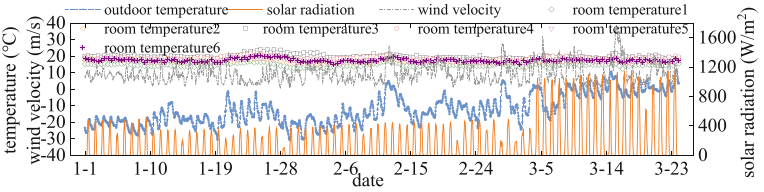
and solar radiation should be set as the inputs. The study overlooked the impact of heating system operation conditions on mean room temperature. Tzuc O M et al. [11] selected solar radiation, wind velocity, and ambient temperature as inputs for the prediction model, indicating that the effects of solar radiation and wind velocity on mean room temperature should not be ignored. Attoue N et al. [12] compared the effects of different combinations of inputs on the prediction accuracy ignoring the physical parameters of the building. Mba L et al. [13] predicted the mean room temperature by outdoor temperature and the historical mean room temperature from the past 6 h. In summary, the input variables for black box prediction models are not unified. Most studies merely select partial influencing factors, particularly neglecting the physical parameters (like surface area) of the building. While those physical parameters are the critical elements affecting the mean room temperature. Since the physical parameters are fixed values, how to incorporate them into the model inputs remains an issue to be addressed.

To address the aforementioned gaps, the correlations between influencing factors and mean room temperature were calculated. Then the inputs for the prediction model were selected according to the calculation results. The building's physical information was also be incorporated into the model inputs. Finally, LSTM is employed to construct the prediction model.

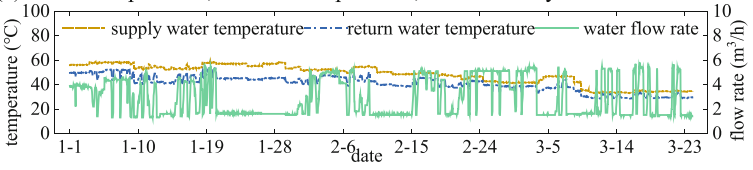
2 Methodology

2.1 Data Collection

Field tests were conducted on an office building, and the data can be found in [14] (Fig. 1).



(a) Room temperature, outdoor temperature, wind velocity and solar radiation.



(b) Heating system supply water temperature, return water temperature and water flow rate.

Fig. 1. Tested data.

The construction area of the office building is 614.2 m^2. Its exterior surface area is 729.3 m^2. Data were collected hourly from January 1 to March 23, 2021, yielding 2065 samples. The mean room temperature was calculated by clause 4.0.2 of the "Standard

for energy efficiency test of public buildings (JGJ/T 177-2009)". During the test, room temperature, heating system operation parameters, and outdoor meteorological parameters were collected. However, considering data availability and the ease of developing a prediction model, internal heat gains/occupancy, ventilation airflow rates, and occupancy schedules in the space were not tested.

2.2 LSTM Model

LSTM Architecture and Parameter Setting. LSTM shows strong learning capabilities and high adaptability to sequential data. Fig. 2 gives the structure of an LSTM network. Multiple gates are used in the network to control and select the information flowing through the sequence. The hidden layer nodes are configured to 12. Each training round consists of 100 epochs with a learning rate of 0.01.

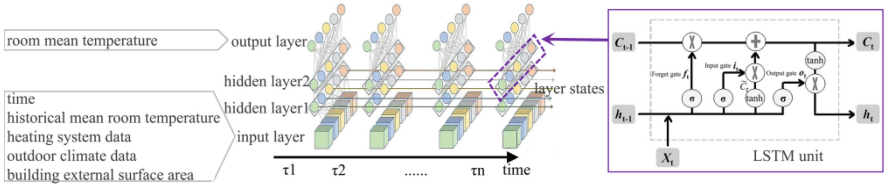


Fig. 2. Structure of an LSTM network.

Dataset Partitioning. The dataset is divided into a training set and a testing set. The last seven days of the dataset are set as the testing set, while the remaining data form the training set. Fig. 3 illustrates the test set. The training dataset is exclusively utilized for feature engineering and model training, while the testing dataset is only used for evaluating the well-trained LSTM model.

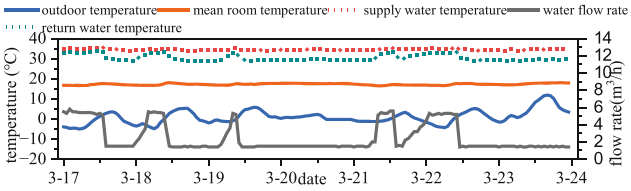


Fig. 3. The testing dataset.

Feature Engineering. To comprehensively consider all factors affecting the mean room temperature and ensure data availability, the following parameters are selected as inputs for the prediction model: heating system operation parameters (supply and return water temperature, water flow rate), outdoor meteorological parameters (air temperature, wind velocity, and solar radiation), time, and building exterior surface area. The supply water temperature, return water temperature, and flow rate data are historical data during the

training. In the testing phase, these parameters represent the target operating conditions of the heating system. The Spearman correlation r_s [14] between the current mean room temperature and its influencing factors is calculated.

Solar radiation is a key factors influencing the mean room temperature. The solar radiation heat gain on the outer surfaces of the building's exterior envelope in different orientations is closely related to the exterior envelope's surface area. Thus, two models were constructed to compare the impact of combining the exterior surface area with solar radiation on the prediction accuracy, as is shown in Table 1.

Table 1. LSTM model description.

ID	model descriptions
Model 1	using horizontal solar radiation density
Model 2	using the combination of the building exterior surface area and corresponding solar radiation on different orientations as an input

2.3 Evaluation Index

Percent error (*PE*), mean average percent error (*MAPE*), mean absolute error (*MAE*), and root mean square error (*RMSE*) are adopted to evaluate the prediction accuracy. t_τ is the predicted value at time τ, $t_{\text{target},\tau}$ is the target value at time τ.

$$PE_\tau = \frac{t_\tau - t_{\text{target},\tau}}{t_{\text{target},\tau}} \times 100\%, \quad \tau = 1, 2, 3, \ldots, \text{n} \tag{1}$$

$$MAPE = \frac{1}{n}\left(\sum_{\tau=1}^{n}\left|\frac{t_\tau - t_{\text{target},\tau}}{t_{\text{target},\tau}}\right| \times 100\%\right), \quad \tau = 1, 2, 3, \ldots, \text{n} \tag{2}$$

$$MAE = \frac{1}{n}\sum_{\tau=1}^{n}\left|t_\tau - t_{\text{target},\tau}\right|, \quad \tau = 1, 2, 3, \ldots, \text{n} \tag{3}$$

$$RMSE = \sqrt{\frac{1}{n}\sum_{\tau=1}^{n}\left(t_\tau - t_{\text{target},\tau}\right)^2}, \quad \tau = 1, 2, 3, \ldots, \text{n} \tag{4}$$

3 Results and Discussion

3.1 Correlation Calculation and Input Parameters Selection Results

Figure 4 shows the calculated Spearman index values. Figure 4 demonstrates that the correlation among outdoor air temperature, solar radiation, and wind velocity with the mean room temperature gradually weakens. The maximum Spearman index values for these three factors are 0.27, 0.23, and 0.14, respectively. The maximum Spearman index

value for the heating system's water flow rate, supply water temperature, and return water temperature are 0.68, 0.34, and 0.22, respectively. Clearly, the overall impact of the heating system's status on the mean room temperature is stronger than that of outdoor meteorological parameters. The reason is that the heating system directly acts on the indoor air, while outdoor influencing factors must pass through the building envelope, whose thermal insulation reduces their impacts. When considering only the maximum values of the index, the order of correlation strength, from highest to lowest, is as follows: historical mean room temperature, heating system water flow rate, supply water temperature, outdoor air temperature, solar radiation, return water temperature, and wind velocity.

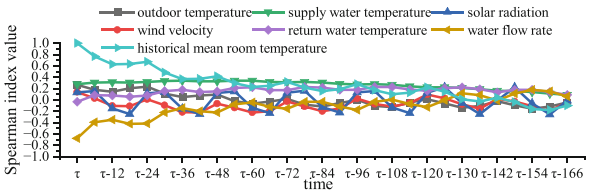


Fig. 4. Correlation calculation results.

A 72-h historical data window is used as the input, considering the building's dynamic heat transfer process. Data with relatively high correlation are set as the final inputs. Table 2 shows the selected input results. τ is time (h).

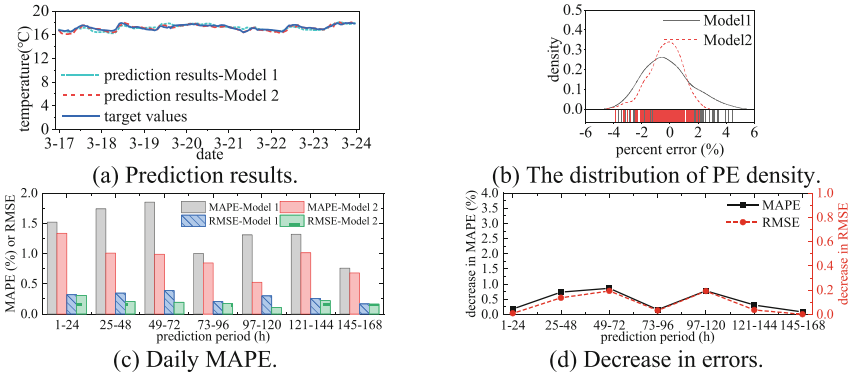
Table 2. Selected input variables for the prediction model.

variables	time
time	τ
outdoor temperature	τ, τ-1, τ-22, τ-46, τ-71
wind velocity	τ, τ-1, τ-16, τ-39, τ-63
solar radiation	τ-3, τ-17, τ-27, τ-41, τ-51, τ-65
supply water temperature	τ, τ-1, τ-5, τ-10, τ-37, τ-57
return water temperature	τ, τ-1, τ-8, τ-36, τ-58
water flow rate	τ, τ-1, τ-5, τ-21, τ-46, τ-70
historical mean room temperature	τ-1, τ-2, τ-3, τ-22, τ-47, τ-72

3.2 Comparison of Prediction Results Between the Two Models

Figure 5 presents the prediction results and the corresponding errors of the two models. Figure 5 shows that on each day of the prediction, Model 2 consistently outperforms Model 1 in accuracy. Specifically, the MAPE for the 24-hour forecast of Model 2 and Model 1 are 1.34% and 1.52%, respectively, and the corresponding MAEs are 0.22 °C

and 0.26 °C. Model 2, which takes building external surface area and solar radiation into account, provides a more comprehensive solar radiation profile and a detailed building physical characteristic, thereby better elucidating the impact of those factors on the indoor temperature.



(a) Prediction results. (b) The distribution of PE density.

(c) Daily MAPE. (d) Decrease in errors.

Fig. 5. Forecasting results and the corresponding errors of mean room temperature.

Combining the building exterior surface area and corresponding solar radiation on different orientations as an input variable enhances the prediction accuracy of mean room temperature across different forecast periods. The prediction accuracy improves significantly during the 49–72 h forecast window, with a 0.86% decrease in MAPE and a 0.15°C decrease in MAE. The MAPE and MAE for Model 2 and Model 1's 7-day prediction results are 0.91% and 1.36%, 0.16°C and 0.23 °C.

4 Conclusion

A mean room temperature LSTM prediction model was established to support heating system regulation. Spearman index were calculated between the mean room temperature and its effectors. The inputs for the LSTM were selected. The impact of combining the building external surface area with solar radiation on the prediction accuracy is demonstrated.

(1) The Spearman correlation between influencing factors and mean room temperature, from highest to lowest, is as follows: historical mean room temperature, water flow rate, supply water temperature, outdoor air temperature, solar radiation, return water temperature, and wind velocity. Those variables and the building exterior surface area should be set as the inputs for the prediction model.
(2) Combining the building exterior surface area and corresponding solar radiation on different orientations as an input improves prediction accuracy compared to using solar radiation alone. The MAPE for Model 2 and Model 1's prediction results are 0.91% and 1.36%.

The research findings contribute to energy-efficient operation of building heating systems. The application of the proposed methods in other machine learning algorithms will be explored in future work.

Acknowledgements. The authors would like to acknowledge that this research has been funded by the Scientific Research Start-up Funds Grant QD2024005C from the Tsinghua Shenzhen International Graduate School, Tsinghua University, China.

References

1. International Energy Agency: Global Status Report for Buildings and Construction (2021)
2. Research Center for Building Energy Efficiency, Tsinghua University, Annual development and research report on building energy efficiency in China 2024 (Rural housing special topic). China Construction Industry Press (2024)
3. Palmer Real, J., Rasmussen, C., Li, R., et al.: Characterisation of thermal energy dynamics of residential buildings with scarce data. Energy Build. **230** (2021)
4. Briga-Sá, A., Leitão, D., Boaventura-Cunha, J., et al.: Trombe wall thermal performance: data mining techniques for indoor temperatures and heat flux forecasting. Energy Build. **252**, 111407 (2021)
5. Elmaz, F., Eyckerman, R., Casteels, W., et al.: CNN-LSTM architecture for predictive indoor temperature modeling. Build. Environ. **206**, 108327 (2021)
6. Alawadi, S., Mera, D., Fernández-Delgado, M., et al.: A comparison of machine learning algorithms for forecasting indoor temperature in smart buildings. Energy Syst. **13**(3), 689–705 (2022)
7. Afroz, Z., Shafiullah, G.M., Urmee, T., et al.: Prediction of indoor temperature in an institutional building. Energy Proc. **142**, 1860–1866 (2017)
8. Kalidindi, S.S.V., Banaee, H., Karlsson, H., et al.: Indoor temperature prediction with context-aware models in residential buildings. Build. Environ. **244**, 110772 (2023)
9. Jiang, B., Gong, H., Qin, H., et al.: Attention-LSTM architecture combined with Bayesian hyperparameter optimization for indoor temperature prediction. Build. Environ. **224**, 109536 (2022)
10. Sulzer, M., Christen, A., Matzarakis, A.: Predicting indoor air temperature and thermal comfort in occupational settings using weather forecasts, indoor sensors, and artificial neural networks. Build. Environ. **234**, 110077 (2023)
11. Tzuc, O.M., Livas-García, A., Torres, M.J., et al.: Artificial intelligence techniques for modeling indoor building temperature under tropical climate using outdoor environmental monitoring. J. Energy Eng. **146**(2) (2020)
12. Attoue, N., Shahrour, I., Younes, R.: Smart building: use of the artificial neural network approach for indoor temperature forecasting. Energies (Basel). **11**(2), 395 (2018)
13. Mba, L., Meukam, P., Kemajou, A.: Application of artificial neural network for predicting hourly indoor air temperature and relative humidity in modern building in humid region. Energy Build. **121**, 32–42 (2016)
14. Wang, Y., Zhan, C., Li, G., et al.: Physics-guided LSTM model for heat load prediction of buildings. Energy Build. **113169** (2023)

Zero Energy Buildings

Feasibility Study on Low-temperature Transformation of Air Conditioning Heating in Existing Buildings: A Case Study of Industrial Parks

Siqi Wu[1,2] and Peng Wang[1,2](✉)

[1] School of Architecture and Design, Harbin Institute of Technology, Harbin 150090, China
cahnburg@hit.edu.cn

[2] Key Laboratory of Cold Region Urban and Rural Human Settlement Environment Science and Technology, Ministry of Industry and Information Technology, Harbin 150001, Heilongjiang, China

Abstract. The heat sources for heating in existing buildings are transitioning from traditional high-temperature systems to medium- and low-temperature sources. While lowering the water supply temperature can reduce heat loss during distribution and improve energy efficiency, it may also introduce potential challenges such as insufficient heat supply and lower indoor temperatures. This study investigates the factors influencing the performance of low-temperature heating and explores methods for evaluating its feasibility. Focusing on existing buildings in industrial parks located in severe cold area, combines experimental testing with numerical simulation to examine the effect of supply air parameters (i.e., temperature and volume) on heating performance. Furthermore, a dimensionless effective draft temperature is proposed as an evaluation index. The concepts of "low-temperature disturbance zones" and "heating stability zones" are introduced, enabling the assessment of heating effectiveness based on the area proportion of the former. The results indicate that when the water supply temperature is reduced from 80 °C to 60 °C, the supply air temperature decreases by 1.9 °C, and the areas of the low-temperature disturbance zones in the horizontal and vertical directions decrease by 4.75% and 19.14%, respectively. These findings provide a reference for evaluating the feasibility of low-temperature heating retrofits in existing buildings.

Keywords: Existing buildings · Low-temperature operation · Effective draft temperature

1 Introduction

Driven by energy conservation and carbon reduction objectives, district heating is evolving towards 5th generation systems that integrate low-temperature sources, such as renewable energy and industrial waste heat. This strategy reduces fossil fuel consumption, minimizes thermal losses in distribution networks and enhances the economic benefits of energy transformation [1, 2]. However, most existing building heating systems

© The Author(s), under exclusive license to Springer Nature Singapore Pte Ltd. 2025
L. Ni et al. (Eds.): CCHVAC 2025, ESE, pp. 345–353, 2025.
https://doi.org/10.1007/978-981-95-3253-7_37

were designed and constructed for high-temperature heat sources. Directly utilizing low-temperature heat sources for heating may result in insufficient heat supply and decreased indoor temperatures, making it challenging to meet heating demands [3]. Therefore, a comprehensive feasibility assessment is essential before transitioning to low-temperature heat sources. This assessment must consider the feasibility of low-temperature heating in terms of heat source capacity and transmission networks, while also accounting for the existing heating systems and building types, in order to formulate an appropriate retrofit plan.

The feasibility of low-temperature heating retrofits is critically dependent on indoor heating performance, which may be compromised by lower air supply temperatures, resulting in significant thermal stratification and non-uniform temperature fields. Consequently, a robust evaluation must analyze the relationship between supply air parameters and indoor airflow patterns, and ultimately quantify heating efficacy through thermal comfort indices.

Numerous scholars have conducted research on the effects of air supply of air conditioning systems. Houghten and Yaglou [4] studied human responses to variations in temperature, wind speed, and airflow conditions. Fanger et al. [5] proposed a model for quantifying the draught risk in spaces. Chen et al. [6] demonstrated that supply air temperature and velocity strongly influence air diffusion and supply efficiency. These studies form the foundation for indoor thermal comfort research. Additionally, scholars have conducted quantitative analyses of indoor thermal comfort using various evaluation indicators. Liu et al. [7, 8] updated the Air Diffusion Performance Index (ADPI) for both cooling and heating modes. Wang et al. [9] proposed the effective coefficient of operating temperature and the effective coefficient of local heating and assessed the spatial range of the heat source's effect. Operating temperature, radiant temperature [10], inhomogeneity coefficients (Kt and Ku), the Predicted Mean Vote (PMV) model and the Predicted Percentage Dissatisfaction (PPD) index [11], are also widely used in the quantitative evaluation of indoor thermal environments.

To investigate the impact of reduced water supply temperature on indoor heating performance, this study established the relationship between water supply temperature and supply air temperature of various air handling units (AHUs) through experiments. Analyzed the characteristics of the indoor thermal environment under different operating conditions using numerical simulations. Proposed a dimensionless effective draft temperature index to evaluate indoor heating effectiveness, providing a reference for assessing the feasibility of low-temperature heating retrofits in existing buildings.

2 Indoor Thermal Environment Experiments and Simulation Exploration

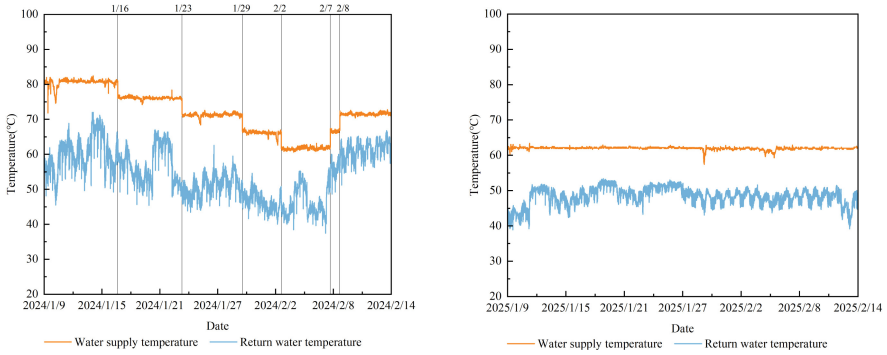
2.1 Research on Heat Exchange Characteristics of AHU Coil

This study takes the foundry workshop of a certain automobile factory as the re-search object to investigate the relationship between the supply air temperature and the supply water temperature under winter heating conditions. During a constant air volume treatment process, the supply air temperature is related to the supply water temperature.

Based on heat transfer theory and experimental data, a mathematical model is developed to characterize the variation of supply air temperature under different supply water temperatures.

Test on Heat Exchange Characteristics of Coil.

Design of Water Supply Temperature Regulation Scheme. The heat exchange performance of the coil was experimentally investigated during two consecutive heating seasons, 2023–2024 and 2024–2025. The water supply temperature regulation schemes for both seasons are presented in Fig. 1.



(a) Supply and return water temperature regulation curves for the 2023-2024.

(b) Supply and return water temperature regulation curves for the 2024-2025.

Fig. 1. Water supply temperature regulation curve.

Data record for AHU. Temperature dataloggers were placed upstream and downstream of the AHU heating section to monitor the air temperatures before and after heat exchange. Patched thermocouples were installed at the supply and return water pipes to document the supply and return water temperatures of the AHU, while an ultrasonic flowmeter was used at the return water pipe to measure the water flow rate. The experiments were conducted from January 9, 2024 to February 14, 2024 and from January 9, 2025 to February 14, 2025, with data recorded at 1-minute intervals.

Establishment of Mathematical Models. The heat exchanger primarily facilitates the heat exchange between the air side and the water side, and its mathematical model represented primarily by the following heat transfer equation.

$$KF\Delta t_m = G_a c_{p,a}(t_{a2} - t_{a1}) = G_w c_{p,w}(t_{w1} - t_{w2}) \tag{1}$$

where K is heat transfer coefficient, W/(m^2·°C); F is heat exchange area, m^2; Δt_m is logarithmic mean temperature difference (LMTD), °C; G_a is air flow, kg/s; $c_{p,a}$ is specific heat capacity at constant pressure of air, kJ/(kg·°C); t_{a1}, t_{a2} represent the inlet air temperature and outlet air temperature respectively, °C; G_w is mass flow rate of water, kg/s; $c_{p,w}$ is specific heat capacity at constant pressure of water, kJ/(kg·°C); t_{w1}, t_{w2} represent the water supply temperature and return water temperature respectively, °C.

Relationship Between Water Supply Temperature and Air Supply Temperature. In a typical constant-air-volume AHU, the supply air volume remains constant, while the inlet air temperature is affected by outdoor conditions. Therefore, with the supply air volume and inlet air parameters fixed, the variation curves of supply air temperature under different supply water temperatures are presented in Fig. 2.

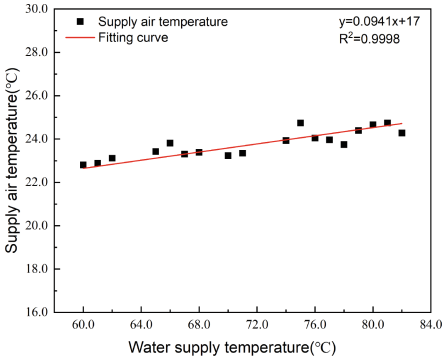


Fig. 2. The relationship between the variation of water supply temperature and supply air temperature.

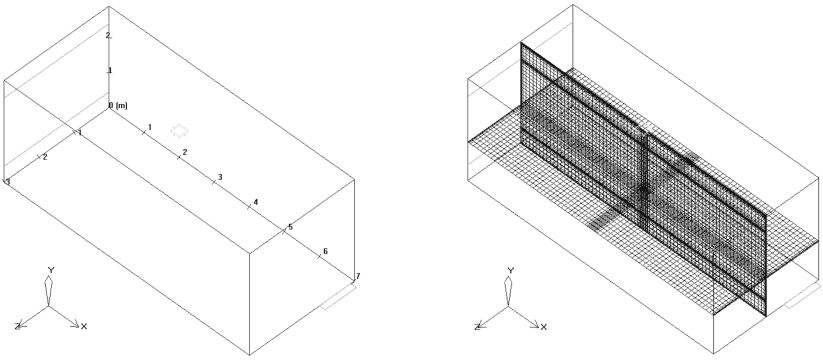
2.2 Model Establishment and Experimental Validation

Physical Model. A consultation room in an automobile manufacturing plant in Shenyang was selected for testing, and a simplified physical model was established, as shown in Fig. 3. The room measures 7.0 m × 3.0 m × 2.9 m. The north wall is exterior, while the remaining walls are interior partitions. A window on the north-facing wall measures 3.0 m × 2.0 m. Cross-sectional planes at Y = 1.1 m and Z = 1.5 m were selected to analyze indoor air temperature and velocity distributions.

Mathematical Model. *Boundary Conditions.* The outdoor and indoor design temperatures for winter are −20.7 °C and 18.0 °C, respectively [12]. The room's supply air temperature is 22.6 °C, with a supply air volume of 490.68 m^3/h. Adjacent rooms are assumed to maintain the same temperature, and the ceiling, floor, and interior walls are insulated.

Solution of Equation. The simulation analyzes airflow distribution in a mechanically ventilated room using the k-ε turbulence model. To improve the agreement between simulation and measured results, the following assumptions are adopted:

1. The indoor air is modeled as an incompressible fluid, under the Boussinesq approximation [13], the flow is assumed to be steady.
2. The indoor air is treated as a transparent medium, neglecting its heat storage and radiative properties.
3. A no-slip boundary condition is applied to the indoor air at all room surfaces.



(a) Physical model. (b) The positions of sections Y and Z.

Fig. 3. The physical model and cross-sectional distribution of the test room.

Based on these assumptions, a mathematical model of indoor airflow and heat transfer is established. The governing equations are discretized using the finite volume method (FVM) with a first-order upwind scheme.

Experimental Testing and Model Validation. *Experimental Scheme Design.* The experiment was conducted from December 11 to December 18, 2024, with a constant water supply temperature of 60 °C. Inner wall surface temperatures, indoor air temperatures, supply air temperatures and velocities in the consultation room were recorded at 1-minute intervals.

Experimental Validation. To verify the model's accuracy, simulated and measured temperature data along the room's horizontal direction were compared, as shown in Fig. 4. The temperature differences are within 1 °C, with relative errors below 5%, indicating good agreement and suitability for subsequent simulations.

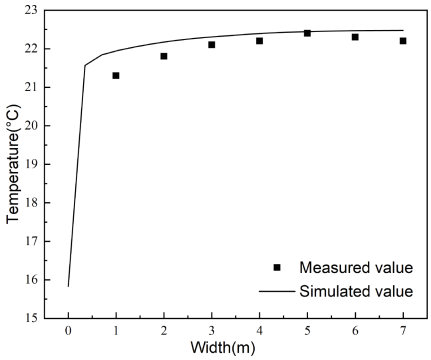


Fig. 4. Simulation Validation Results.

Simulation Working Condition Analysis. The calculated heating load of the consulting room is 757.32 W. Based on the fitted relationship between supply water temperature

and supply air temperature as shown in Fig. 2, the supply air parameters at various water supply temperatures were determined as shown in Table 1. Numerical simulations were performed to evaluate indoor temperature and airflow variations under different operating conditions, thereby evaluating heating performance.

Table 1. Summary Table of Simulation Working Conditions.

	Case 1	Case 2	Case 3	Case 4	Case 5
Water Supply Temperature (°C)	60	65	70	75	80
Supply Air Temperature (°C)	22.6	23.1	23.6	24.1	24.5
Air Supply Volume (m^3/h)	490.68	443.16	403.56	370.08	348.12

Indicators for Assessing Indoor Thermal Comfort in Air-Conditioning Heating Systems. Combining the influence of air flow organization on the heating performance, a dimensionless effective draft temperature evaluation index is proposed. Through dimensionless processing, the heating effect of the room is quantified, which can effectively evaluate the heating performance of indoor air conditioners.

Effective Draft Temperature (EDT). The EDT is a calculated temperature that combines air temperature difference and measured air speed. The EDT at heating mode can be written according to the ASHRAE Standard [14]:

$$\theta_n = t_{acn} - t_{\mathrm{ac}} - 9.1(v_{an} - 0.15)^{\circ}\mathrm{C} \tag{2}$$

where t_{acn} is corrected temperature at test point n, °C; t_{ac} is average test zone temperature, °C; v_{an} is time-averaged speed at test point n, m/s. Based on the thermal comfort range defined by PMV, the thermal comfort boundary of the EDT at heating model is fitted to be –2.2 °C to 2 °C.

Dimensionless Effective Draft Temperature The dimensionless EDT is used to analyze the relative differences and variation trends of the EDT in the studied area. The dimensionless EDT in the range of 0–0.5 corresponds to the low-temperature disturbance area, while in the range of 0.5–1.0 corresponds to the stable heating area. The dimensionless EDT at heating mode can be written as following:

$$\varphi_n = \frac{\theta_n - \theta_{\min}}{\theta_{\max} - \theta_{\min}} \tag{3}$$

where $\theta_{\min}$ and $\theta_{\max}$ are respectively the minimum and maximum value of the dimensionless EDT in this area, °C.

3 Result and Discussion

This section presents a detailed analysis of simulation results under five operating conditions to investigate the impact of supply air parameters on the indoor thermal environment. Figure 5 shows the regional distribution proportion of dimensionless EDT in

the consultation room under five supply air conditions. As shown in Fig. 5 (f), the Y section is discretized into 441 (21 × 21) points, and the dimensionless EDT of each measurement point is calculated to obtain the distribution of data point proportions at different levels (Fig. 5 (a)–(e)). Compared with the other four working conditions, the heating effect of working Case 1 (Fig. 5 (a)) is the best, and the proportion of dimensionless EDT ranging from 0.9 to 1.0 is the highest. In working Case 5, the proportion of measurement points from 0.9 to 1.0 is 65.8%, while in working case 1, the proportion of measurement points is 80.5%, an increase of 14.7%. This is because the air supply volume increases, the air supply speed rises, the fresh air can be delivered over a longer distance, and the influence range is wider, promoting the movement of indoor air flow and making the indoor air distribution more uniform.

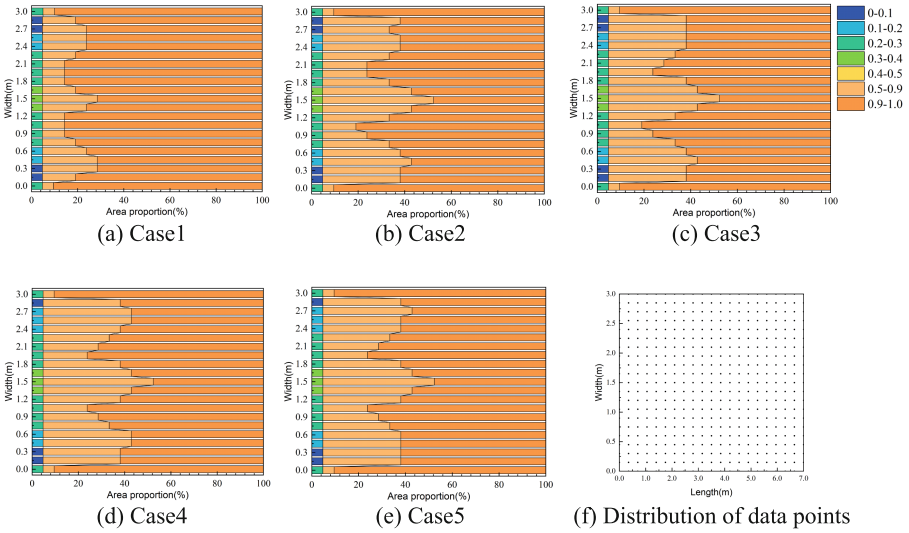


Fig. 5. The proportion of dimensionless EDT zones with a Y=1.1m cross-section in the consultation room under different operating conditions

Figure 6 compares the areas of the low-temperature disturbance zone across different operating conditions at cross-sections Y = 1.1 m and Z = 1.5 m. Case 1 serves as the reference, and the relative change rates of the low-temperature disturbance areas for the remaining four cases were calculated accordingly. When the supply air temperature varies, the area of the low-temperature disturbance zone exhibits slight fluctuations in the Y cross-section, with growth rates ranging from 4.3% to 5.0%. In contrast, fluctuations are more pronounced in the Z cross-section, with growth rates ranging from 15.2% to 23.7%. This discrepancy is attributed to the higher window-to-wall ratio at the Z = 1.5 m cross-section and the variations in supply air parameters.

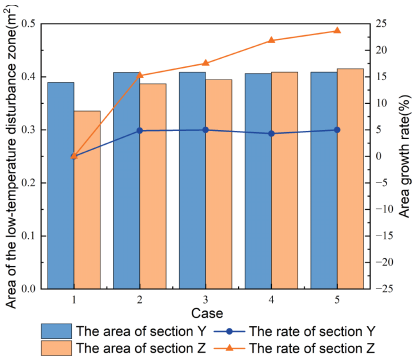


Fig. 6. Comparison of areas of low-temperature disturbance zones in Y and Z cross-sections of the consulting room under different operating conditions.

Lower supply air velocities reduce the air volume reaching the external wall, thereby weakening its resistance to cold air intrusion through external windows. While maintaining indoor comfort, higher supply air velocities enhance indoor air mixing and mitigate temperature non-uniformity. As the supply air temperature decreases, the low-temperature disturbance zone area in the Z cross-section gradually decreases from 0.41 m^2 in Case 5 to 0.33 m^2 in Case 1, whereas the corresponding area in the Y cross-section decreases from 0.053 m^2 to 0.003 m^2.

4 Conclusion

To evaluate the feasibility of low-temperature heating retrofits in existing buildings, this study proposes a novel evaluation index for heating performance. The proposed index was applied to a real room case study to evaluate heating performance. The main conclusions of this study are summarized as follows:

1. A reduction in supply water temperature from 80 °C to 60 °C leads to a 1.9 °C decrease in supply air temperature.
2. A moderate reduction in supply air temperature, combined with an increase in supply air velocity, improves the uniformity of the temperature field and enhances heating performance.
3. The proposed evaluation indicators can be used to assess the air conditioning heating performance. After reducing the water supply temperature, the area of the low-temperature disturbance zone in the room is 0.33 m^2, which is 23.7% smaller compared with high-temperature heating. This room meets the criteria for low-temperature heating.

References

1. Tunzi, M., Yang, Q., Olesen, J.B., Diget, T., Fournel, L.C.: Economic viability and scalability of a novel domestic hot water substation for 4th generation district heating: a case study of temperature optimization in the Viborg district heating network. Energy. **313**, 134010 (2024)

2. Yao, S., Wu, J., Qadrdan, M.: A state-of-the-art analysis and perspectives on the 4th /5th generation district heating and cooling systems. Renew. Sustain. Energy Rev. **202**, 114729 (2024)
3. Østergaard, D.S., Smith, K.M., Tunzi, M., Svendsen, S.: Low-temperature operation of heating systems to enable 4th generation district heating: a review. Energy. **248**, 123529 (2022)
4. Houghten, F.C., Yaglou, C.P.: Cooling effect on human beings produced by various air velocities. J. ASHVE. **30**, 169–184 (1924)
5. Fanger, P.O., Melikov, A.K., Hanzawa, H., et al.: Air turbulence and sensation of draught. Energy Build. **12**(1), 21–39 (1988)
6. Chen, Q., Suter, P., Moser, A.: Influence of air supply parameters on indoor air diffusion. Build. Environ. **26**(4), 417–431 (1991)
7. Liu, S., Novoselac, A.: Air Diffusion Performance Index (ADPI) of diffusers for heating mode. Build. Environ. **87**, 215–223 (2015)
8. Liu, S., Clark, J., Novoselac, A.: Air diffusion performance index (ADPI) of overhead-air-distribution at low cooling loads. Energy Build. **134**, 271–284 (2017)
9. Wang, D., Li, W., Liu, Y., et al.: Non-uniform operative temperature distribution characteristics and heat-source-controlled core-area range of local heating radiators. Build. Simul. **16**, 87–103 (2023)
10. Kalmár, T., Bodó, B., Han, S., Li, B., Kalmár, F.: Comparative analysis of energy demand at an equal operative temperature in the case of radiator and low-temperature radiant heating. J. Build. Eng. **100**, 111792 (2025)
11. He, J., Chen, Y., He, D.: Piston effect of subway trains under different operating conditions and its influence on passenger thermal comfort. J. Build. Eng. **78**, 107610 (2023)
12. GB: Design Code for Heating Ventilation and Air Conditioning of Civil Buildings, GB 50736 – 2012. Ministry of Housing and Urban-Rural Development of the People's Republic of China, Beijing (2012)
13. ANSYS: ANSYS Fluent Theory Guide, Version 19.0. ANSYS, Canonsburg, PA (2018)
14. ASHRAE: Method of Testing for Room Air Diffusion, ANSI/ASHRAE Standard 113-2022. ASHRAE, Atlanta, GA (2022)

A Study on the Optical and Thermal Performance and Energy Efficiency Analysis of a Novel Adjustable Wall-Like Window

Huiyan Tang and Zhengrong Li(✉)

School of Mechanical Engineering, Tongji University,
No. 4800 Caoan Highway, Jiading District, Shanghai 201804, China
lizhengrong@tongji.edu.cn

Abstract. Windows are the weakest component of a building's thermal performance. While existing optimizations have significantly improved the heat transfer coefficient (U-value) and solar heat gain coefficient (SHGC) of windows, most of these technologies are only suitable for a single season. The adoption of adjustable wall-like windows has emerged as one of the most effective strategies to address this issue. In this work, a novel adjustable wall-like window (WLW) is designed to balance insulation and shading effects, based on the requirements for summer shading, winter insulation, and the construction forms of composite windows. It consists of a double-glazed window filled with argon gas and a layer of aerogel board. Experimental testing and numerical simulations are conducted to analyze the heat transfer process of the wall-like window. Additionally, the effects of cavity thickness (D1), aerogel thickness (D2), and surface emissivity (ε) on its optical and thermal performance are investigated. The results indicate that when the cavity thickness (D1) is less than 20 mm, heat conduction dominates within the cavity, significantly affecting the U-value of the wall-like window, while its influence on the SHGC is relatively minor. The aerogel thickness (D2) shows a nonlinear inverse relationship with the U-value. As the surface emissivity (ε) increases, both the U-value and SHGC of the wall-like window rise. However, ε has a more pronounced effect on the U-value than on SHGC. The visible transmittance declines steadily with aerogel thickness but is unaffected by D1 and ε. In cold regions, the proposed adjustable wall-like window can further reduce energy consumption beyond the baseline of ultra-low energy public buildings, with an energy-saving rate of approximately 13%.

Keywords: Dynamic building envelope · Heat transfer process · Solar heat gain coefficient (SHGC)

1 Introduction

Windows are the weakest part of the building envelope in terms of thermal insulation. They account for about 40% to 50% of the envelope's total energy use. At the same time, windows strongly affect both the thermal and optical performance of buildings [1].

© The Author(s), under exclusive license to Springer Nature Singapore Pte Ltd. 2025
L. Ni et al. (Eds.): CCHVAC 2025, ESE, pp. 354–363, 2025.
https://doi.org/10.1007/978-981-95-3253-7_38

Since outdoor climate conditions change throughout the year, windows should ideally respond to these changes. In winter, they should allow solar heat in and reduce heat loss. In summer, they should block sunlight and reduce cooling loads. This seasonal adaptability is essential for improving energy efficiency in buildings [2]. Two key window performance metrics are the heat transfer coefficient (U-value) and the solar heat gain coefficient (SHGC). A lower U-value means less heat loss, especially in winter. SHGC shows how much solar energy enters through the glass [3]. Some advanced windows, such as those filled with vacuum or aerogel, can achieve very low U-values—down to 0.28–0.30 W/(m^2·K) [4]. However, these windows are static. A window that reduces heat loss in winter may also block useful sunlight. A design based on fixed properties must compromise between summer and winter needs [5].

To solve this issue, researchers have proposed the Adaptive Building Envelope (ABE) [6]. ABE allows building components to respond to outdoor changes automatically and continuously, improving energy efficiency while maintaining comfort [1]. As part of this concept, many dynamic window technologies have been developed. These systems can adjust their optical and thermal properties to meet seasonal needs.

Most existing studies focus on dynamic shading. Luo Daina studied windows with internal blinds and showed that adjusting the blind angles could reduce the U-value and solar transmittance in winter, lowering heating demand [7]. Similarly, Kunwar et al. tested honeycomb shades. Their results showed that the cellular structure helped improve comfort and saved up to 9% of annual heating and cooling energy [8]. Zuo Chunlei and colleagues combined blinds with honeycomb shades into a single device. This system reduced the U-value to between 1.15 and 1.49 W/(m^2·K), offering improved insulation [9].

Other researchers have explored dynamic glazing technologies. These include systems using phase-change materials (PCMs) [10, 11], thermochromic [12, 13], photochromic [14], and electrochromic glass [15–18]. DeForest et al. studied near-infrared switching electrochromic (NEC) windows. Their results showed that NEC systems can vary U-value from 1.625 to 1.804 W/(m^2·K) and SHGC from 0.297 to 0.646, saving up to 10% in energy use across different climate zones [19]. A review by Michael et al. found that thermochromic glass offers limited U-value adjustability but a wider range of SHGC (0.17–0.37) and visible light transmittance (0.13–0.60) [20]. However, due to their cost and complexity, many of these technologies remain difficult to apply on a large scale [10, 21].

In summary, existing solutions like adjustable blinds, honeycomb shades, and smart glass can improve window performance to some extent. But their limited adjustability and high complexity prevent widespread use. Building on these studies, this paper analyzes the principles of shading and insulation in traditional building composite windows and designs a novel U-value adjustable wall-like window (WLW). Under extreme weather, it can perform like an insulated wall, limiting outdoor temperature impact. It can also switch between heat gain and heat block modes as needed, helping reduce building energy use. Based on this proposed system, experimental measurements and numerical simulations were conducted to validate its heat transfer performance. The effects of cavity thickness (D1), aerogel thickness (D2), and surface emissivity (ε) on the

optical and thermal Performance were investigated. Furthermore, the potential energy-saving benefits of this adjustable WLW system in office buildings located in cold regions were analyzed, providing a feasible approach for the development of high-performance, thermally adaptable window systems.

2 Methodology and System Design

2.1 Design of the Wall-Like Window (WLW) System

Building on the typical design of exterior windows and shading systems, this study developed a new wall-like window (WLW) with an adjustable U-value. As shown in Fig. 1, the system has two main parts. The glazing is the same as that in a standard window. An extra insulation layer is added on the outside. This layer can switch between two states: open and closed. When the insulation is open, the window works like a normal window. When it is closed, the system acts like an insulated wall. It blocks most heat transfer and solar radiation. This dual-mode setup allows the window to stay closed when heat retention is needed and open when solar gain is useful. By switching between these states, the WLW helps reduce energy use and makes better use of natural heat and light.

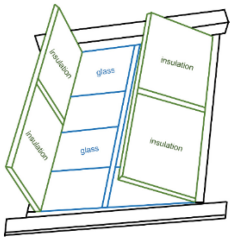


Fig. 1. Wall-like window (WLW) system

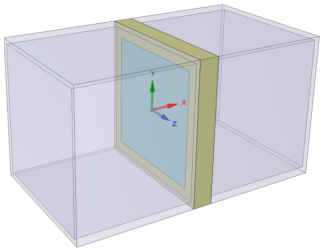


Fig. 2. Experimental setup diagram

2.2 Heat Transfer Performance Analysis

Experimental Testing. The experiment used a window-wall heat transfer test device based on the steady-state heat transfer method. The U-value of the wall-like window was measured using the calibrated hot-box technique. The setup included a cold chamber and a hot chamber. This allowed for accurate measurement of heat transfer through both windows and wall-like components. The experimental setup is shown in Fig. 2. The opening in the window frame measured 1200 mm × 1200 mm. The glazing used a typical configuration: 6 mm low-emissivity (low-e) glass, a 12 mm argon-filled air gap, and 6 mm clear glass.

T-type thermocouples and heat flux sensors were installed on both sides of the sample to measure surface temperatures and heat flux accurately. The measurement layout and test setup are shown in Fig. 3 and Fig. 4. Before testing, all instruments were calibrated to ensure reliable data. Details of the equipment are listed in Table 1.

The experiment followed the Chinese national standard GB/T 8484–2020 [22], which defines the test method for evaluating the thermal insulation of building doors and windows. This standard ensures consistent testing conditions, equipment requirements, measurement steps and data analysis methods.

Table 1. List of Experimental Instruments

Instrument	Model	Measured Parameter	Measurement Range	Accuracy
T-type Thermocouple	TT-T-24	Temperature	-200 to 260 °C	±0.5 °C
Heat Flux Sensor	JZRL-2	Heat Flux Density	-500 to 500 W/m^2	±3%
Data Logger	HIOKI-30-LR8400	Temperature	-200 to 400 °C	±0.05 °C
		Voltage	-20 to 20 mV	±0.05%



Fig. 3. Photograph of the experimental site.

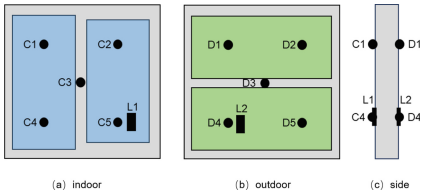


Fig. 4. Schematic layout of measurement points.

About six hours after starting the experiment, the temperatures on the hot side (indoor) and cold side (outdoor) reached a steady state. During this time, sensor readings gradually stabilized, creating a suitable thermal environment for accurate measurement.

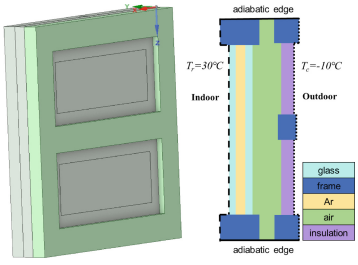


Fig. 5. Simulation Setup

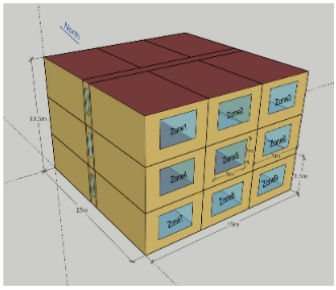


Fig. 6. 3D model of the office building.

Simulation Setup. The numerical simulation model was developed based on the physical test specimen, as shown in Fig. 5. The glazing measured 1200 mm × 1200 mm, with a cavity thickness of 60 mm. All other dimensions matched the experimental setup to ensure consistency between simulation and testing. The simulation was conducted using ANSYS Fluent, a computational fluid dynamics (CFD) software. The RNG (Re-Normalization Group) k–ε turbulence model was selected for its effectiveness in handling high strain rate flows and curved streamlines [23]. Enhanced wall treatment was applied to better resolve near-wall flow behaviors.

Validation and Comparative Analysis. To further validate the accuracy of the simulation model, a representative case from the experiment was selected for comparison. The test condition involved a temperature difference of $\Delta T = 40°C$ between the indoor and outdoor environments. The simulation results were compared with the measured data in terms of surface temperatures on both sides of the specimen and the heat flux.

The heat flux from the simulation was 31.09 W/m^2, while the experimental result was 28.77 W/m^2. The relative error between the two results was 8.06%, which is within the commonly accepted engineering tolerance of ±10%. The absolute error between the temperatures predicted by Fluent and those recorded at the measurement points did not exceed ±1.5 °C. This indicates that the relative error remained low across the tested area. The simulation results are considered reasonably accurate and reliable.

2.3 Annual Energy Performance Simulation

In this study, a three-story office building located in Beijing was selected as the simulation model. The building is oriented along the north–south axis. Each floor contains six office units, with a total floor area of 225 m^2 per floor. The 3D building model used for the simulation is shown in Fig. 6.

Both the baseline and WLW scenarios were equipped with smart lighting systems. The simulation was conducted using typical office building parameters for cold-climate regions, as summarized in Table 2. The building envelope and operational schedules comply with Beijing's local standard DB11/T 687–2024 [24].

The building energy simulations were performed using EnergyPlus version 24.1, a whole-building energy modeling tool developed by the U.S. Department of Energy's Building Technologies Office (BTO). The dynamic control of the WLW system was implemented using the Energy Management System (EMS) module in EnergyPlus. The simulation covered a full year with an hourly timestep, totaling 8,760 h.

3 Results and Discussion

This study investigates the impact of D1, D2, and ε on the optical and thermal performance of the WLW system. The results demonstrate that all three parameters play critical roles in regulating thermal behavior, offering a theoretical foundation for optimizing the performance of adjustable window systems.

Table 2. Design parameters for building energy simulation.

Parameter	Baseline	WLW
Heating setpoint temperature (°C)	20 (day)/5 (night)	
Cooling setpoint temperature (°C)	26	
HVAC operation period	Jun.1–Aug.31 (cooling) Nov.15–Mar.15 (heating) Weekdays 7:00–18:00	
Exterior wall U-value (W/(m^2·K))	0.438	0.438
Roof U-value (W/(m^2·K))	0.346	0.346
Window U-value (W/(m^2·K))	1.78	2.33 (open)/0.42 (close)
SHGC of windows	0.38	0.63 (open)/0.21 (close)
Visible transmittance of windows	0.61	0.71 (open)/0.11 (close)
Window-to-wall ratio	0.35	
Outdoor air ventilation rate	8.333 L/(s·person)	
Occupant density	0.1 person/m^2	
Lighting power	300 lx; 6.8 W/m^2 (smart lighting)	
Equipment power	15 W/m^2	
Usage schedules for occupancy, lighting, HVAC, and equipment	As per local standard: DB11/T 687-2024 (Design Standard for Energy Efficiency of Public Buildings, Beijing)	

3.1 Influence of Cavity Thickness (D_1)

Figure 7 shows the effect of cavity thickness D1 on the optical and thermal performance of the WLW system. When D1 increases from 0 to 20 mm, the U-value drops significantly. However, beyond 20 mm, further increases have little impact. This trend reflects the heat transfer mechanisms in sealed cavities: at small thicknesses, conduction dominates and thermal resistance rises with thickness. Once D1 exceeds 20 mm, natural convection becomes significant, stabilizing the U-value. The visible transmittance (VT) remains constant as the cavity thickens. Since the cavity contains transparent gas and no optical materials, it has minimal influence on light transmission. VT is primarily determined by the glazing itself. These results indicate that the cavity mainly serves as a thermal buffer, not an optical modulator.

3.2 Influence of Aerogel Layer Thickness (D_2)

The relationship between the WLW system's optical and thermal performance and aerogel thickness D2 is shown in Fig. 8. As D2 increases, the overall U-value decreases, indicating improved insulation. Similarly, the SHGC decreases with increasing D2, as the thicker insulation acts as a stronger barrier to solar radiation. Aerogel thickness has a

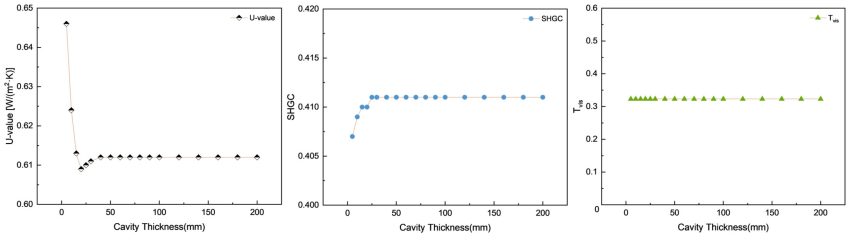


Fig. 7. Influence of cavity thickness (D_1) on the overall U-value, SHGC, and visible transmittance (VT).

more pronounced impact on U-value than SHGC. VT decreases as D2 increases, but the decline slows with further thickness. Designers should balance insulation and lighting needs by selecting an optimal D2 that maximizes energy performance without overly reducing indoor daylight levels.

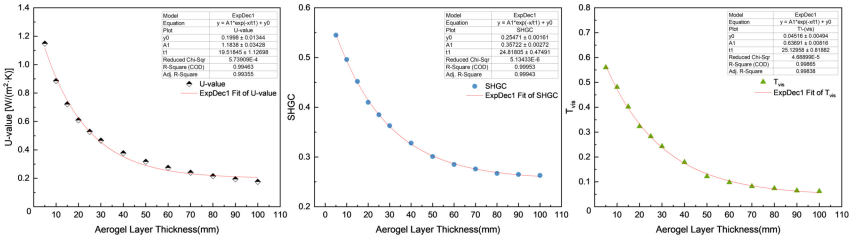


Fig. 8. Influence of Aerogel Layer Thickness (D_2) on the overall U-value, SHGC, and visible transmittance (VT).

3.3 Influence of Surface Emissivity (ε)

As shown in Fig. 9, the U-value rose by about 0.05 W/(m^2·K) with increasing surface emissivity, with the rate of change gradually decreasing. The SHGC also increased by approximately 0.025, showing a similar diminishing trend. In contrast, VT remained nearly constant across the full range of emissivity values. It is particularly useful in optimizing composite window systems where both thermal insulation and natural lighting must be considered.

3.4 Energy-Saving Potential of the WLW System

Figure 10 presents a monthly comparison of energy consumption between the Baseline configuration and the dynamically regulated WLW system. The results clearly indicate that the WLW system significantly reduces heating energy consumption during the winter months. In February, the system achieves the greatest benefit, with a maximum monthly energy savings of 34%. During the summer cooling season, the WLW system also

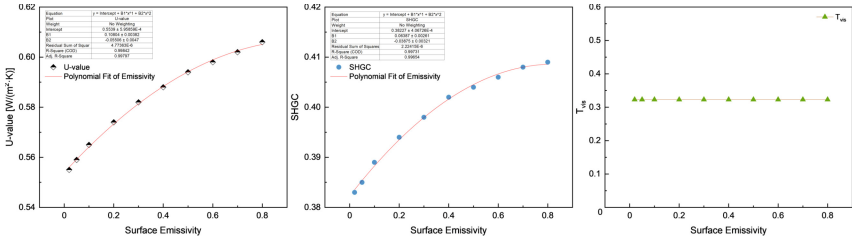


Fig. 9. Influence of Surface Emissivity (ε) on the overall U-value, SHGC, and visible transmittance (VT).

contributes to modest reductions in cooling energy use. Among the summer months, August shows the highest reduction, with a total monthly savings of 6%.

On an annual basis, compared to the Baseline, the WLW system reduces cooling energy consumption by 4.6%, heating energy consumption by 32.2%, and increases lighting energy consumption by 20.4%. Despite the increase in lighting demand, the total annual energy consumption is reduced by 12.9%, demonstrating the strong energy-saving potential of the WLW system under dynamic regulation.

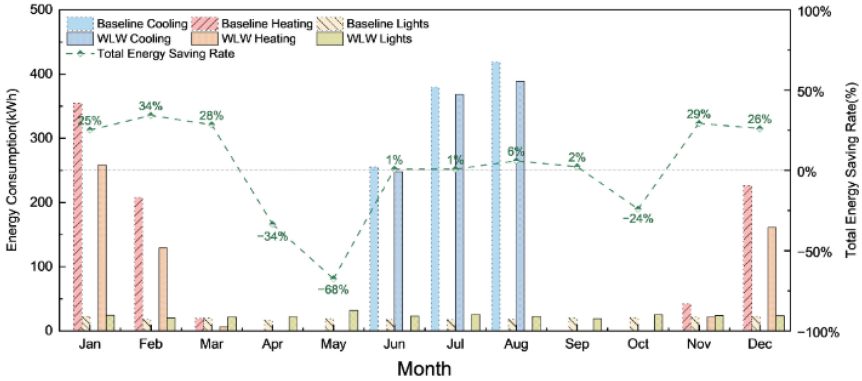


Fig. 10. Monthly comparison of energy consumption between the Baseline configuration and the dynamically controlled WLW system.

4 Conclusion

This study investigates the optical and thermal performance of a novel wall-like window (WLW) system with adjustable aerogel insulation. Experimental and simulation results identify cavity thickness (D1), aerogel thickness (D2), and surface emissivity (ε) as the key factors influencing thermal transmittance and solar gain.

An increase in cavity thickness up to 20 mm significantly reduces the U-value by limiting conduction. Beyond 20 mm, further reductions are minimal due to natural convection. Aerogel thickness has a strong impact on thermal resistance, but improvement

slows as thickness increases. SHGC decreases with thicker insulation and higher emissivity, while visible transmittance declines steadily with aerogel thickness but is unaffected by emissivity. Dynamic simulations show that the WLW system reduces heating demand by 32.2% and cooling demand by 4.6%, with an overall annual energy savings of 12.9%, despite a 20.4% rise in lighting energy. It also improves thermal comfort, especially during transitional seasons. Compared to the Baseline, WLW system reduces the total annual hours of thermal discomfort by 9.0%.

These results highlight the WLW system's effectiveness in reducing energy use and enhancing comfort in cold climates. Integrating adjustable insulation and emissivity control offers a promising strategy for future energy-efficient building envelopes.

References

1. Casini, M.: Active dynamic windows for buildings: a review. Renew. Energy. **119**, 923–934 (2018)
2. Khaled, K., Berardi, U.: Current and future coating technologies for architectural glazing applications. Energy Build. **244** (2021)
3. Meller, B.J., Marinoski, D.L., Güths, S., Ghisi, E.: Comparison of methods to determine the solar heat gain coefficient of glazing. Ambiente Construído. **24**, e138257–e138257 (2024)
4. Jelle, B.P., Hynd, A., Gustavsen, A., Arasteh, D., Goudey, H., Hart, R.: Fenestration of today and tomorrow: a state-of-the-art review and future research opportunities. Sol. Energy Mater. Sol. Cells. **96**, 1–28 (2012)
5. Zeng, Z., Chen, J., Augenbroe, G.: Movable window insulation as an instantiation of the adaptive building envelope: an investigation of its cost-effectiveness in the U.S. Energy Build. **247** (2021)
6. Loonen, R.C.G.M., Trcka, M., Costla, D., Hensen, J.L.M.: Climate adaptive building shells: state-of-the-art and future challenges. Renew. Sustain. Energy Rev. **25**, 483–493 (2013)
7. Luo Daina, Y., Jikang, Y.G.: Experimental study on shading and heat transfer performance of built-in louver hollow glass windows. Build. Sci. **37**, 78–84 (2021)
8. Kunwar, N., Bhandari, M., Curcija, D.C.: National energy savings potential of cellular shades: a measurement and simulation study. Build. Environ. **225** (2022)
9. Zuo, C., Ge, J., Zhao, K., Jie, S.: Research on the integrated shading and thermal insulation window system and thermal performance. Build. Sci. **38**, 121–127 (2022)
10. Li, D., Wu, Y., Wang, B., Liu, C., Arici, M.: Optical and thermal performance of glazing units containing PCM in buildings: a review. Constr. Build. Mater. **233** (2020)
11. Zheng, X., Liang, Y., Yang, H., Zeng, Y., Cui, H.: Collaborative optimized design of glazing parameters and PCM utilization for energy-efficient glass curtain wall buildings. Buildings. **14** (2024)
12. Giovannini, L., Favoino, F., Pellegrino, A., Lo Verso, V., Serra, V., Zinzi, M.: Thermochromic glazing performance: from component experimental characterisation to whole building performance evaluation. Appl. Energy. **251** (2019)
13. Khaled, K., Berardi, U.: Energy modelling and saving potential of polymeric solar-responsive thermochromic window films. Sol. Energy. **244**, 84–103 (2022)
14. Khaled, K., Berardi, U.: A cross-climate assessment of the visual and energy performance of flexible photochromic films for in-situ window retrofits. Energy Build. **300** (2023)
15. Granqvist, C.G., Azens, A., Heszler, P., Kish, L.B., Osterlund, L.: Nanomaterials for benign indoor environments: electrochromics for "smart windows", sensors for air quality, and photocatalysts for air cleaning. Sol. Energy Mater. Sol. Cells. **91**, 355–365 (2007)

16. Kheybari, A., Alwalidi, M., Hepf, C., Auer, T., Hoffmann, S.: A multi-objective evaluation for envelope refurbishments with electrochromic glazing. Results Eng. **14** (2022)
17. Wu, S., et al.: Applications of thermochromic and electrochromic smart windows: materials to buildings. Cell Rep. Phys. Sci. **4** (2023)
18. Shao, Z., et al.: Tri-band electrochromic smart window for energy savings in buildings. Nat. Sustain. **7** (2024)
19. DeForest, N., Shehabi, A., Garcia, G., Greenblatt, J., Masanet, E., Lee, E.S., Selkowitz, S., Milliron, D.J.: Regional performance targets for transparent near-infrared switching electrochromic window glazings. Build. Environ. **61**, 160–168 (2013)
20. Michael, M., Favoino, F., Jin, Q., Luna-Navarro, A., Overend, M.: A systematic review and classification of glazing technologies for building facades. Energies. **16** (2023)
21. Kim, J.-H., Hong, J., Han, S.-H.: Optimized physical properties of electrochromic smart windows to reduce cooling and heating loads of office buildings. Sustainability. **13** (2021)
22. Standardization Administration of China: Test Method for Thermal Insulating Performance for Building Exterior Doors and Windows (GB/T 8484–2020). Standardization Administration of China, Beijing (2020)
23. Stolarski, T., Nakasone, Y., Yoshimoto, S.: 5 – Analysis for fluid dynamics. In: Stolarski, T., Nakasone, Y., Yoshimoto, S. (eds.) Engineering Analysis with ANSYS Software, 2nd edn, pp. 235–281. Butterworth-Heinemann (2018)
24. Beijing Municipal Commission of Planning and Natural Resources: Design Standard for Energy Efficiency of Public Buildings (DB11/T 687–2024). Beijing Municipal Commission of Planning and Natural Resources, Beijing (2024)

Design and Application of a Novel Intelligent Building Envelope with Adjustable Window-to-Wall Ratio

Shijun Ni and Cui Li(✉)

Tongji University, Shanghai 200092, People's Republic of China
licui20140718@tongji.edu.cn

Abstract. To address the conflict between high energy consumption in large WWR designs and poor thermal-visual comfort in small WWR designs, an adaptive variable WWR intelligent envelope system was developed. A cost-effective guided sliding mechanism enables dynamic WWR adjustment via motor-driven insulation panels. Modified phenolic foam (MPF) and extruded polystyrene (XPS) were selected for insulation based on thermal performance, market availability, and cost, achieving a U-value as low as 0.31 W/(m^2·K). Reflective layers with different optical properties enhance seasonal adaptability. Intelligent control is realized through sensor-microprocessor integration and machine learning. Simulations and field tests demonstrate up to 35.7% energy savings, reduced indoor temperature fluctuations, and strong potential for application in ultra-low energy buildings.

Keywords: Variable glazing ratio · Adjustable performance · Building envelope

1 Introduction

Transparent building envelopes significantly affect heat transfer and cooling loads due to their high thermal transmittance compared to opaque walls. Increased window-to-wall ratios (WWR) enhance occupant comfort but substantially increase energy consumption, creating a fundamental trade-off [1, 2]. Dynamic WWR systems, which adjust thermal, ventilation, and lighting characteristics in response to environmental conditions and occupancy, offer a promising approach to optimize this balance [3].

Relevant researches primarily focus on improving shading or ventilation performance of transparent building envelope using active devices or passive materials, but lack focus on improving insulation performance and integration of comprehensive control strategies [4, 5, 6, 7, 8, 9, 10, 11].

This study accordingly develops a novel intelligent variable WWR building envelope system, aiming to improve thermal performance of transparent envelope. Compatible with existing transparent envelopes, this system can be installed indoors or outdoors. Python was employed for the development of control programs and the implementation of optimization algorithms. The energy-saving potential will be evaluated through both DesignBuilder energy simulations and on-site field testing.

© The Author(s), under exclusive license to Springer Nature Singapore Pte Ltd. 2025
L. Ni et al. (Eds.): CCHVAC 2025, ESE, pp. 364–373, 2025.
https://doi.org/10.1007/978-981-95-3253-7_39

2 System Design

To enhance the thermal performance of transparent building envelopes, the variable WWR system (hereafter referred to as *the system*) is designed with two core components: the mechanical subsystem (hereafter referred to as *the device*) and the software subsystem. The device consists of insulation panels and guiding & driving system. The software subsystem consists of a program based on control logic and decision threshold optimization algorithm.

2.1 Insulation Materials

For the thermal insulation layer, modified phenolic foam (MPF) and extruded polystyrene (XPS) were selected.

When the unit is in the fully closed position, the cross-section from exterior to interior includes an insulation panel, an air layer, and a double-glazed Low-E window composed of 6 mm Low-E glass, a 9 mm air gap, and 5.7 mm clear glass. The combined layering of the insulation panel and the original window glazing is illustrated in Fig. 1:

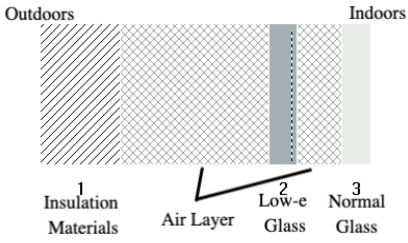


Fig. 1. Layering of materials.

Thermal simulation using Window7 indicates that in the fully closed state, the system achieves a heat transfer coefficient (U-value) of 0.31 W/(m^2·K), satisfying stringent public building insulation standards.[12, 13]错误!未找到引用源。.

The simulation result was verified by a field test. 30 mm XPS insulation panels were attached to the windows to simulate the system in fully-closed position. Two NH211WS temperature sensors were positioned to monitor ambient temperature variations, and two heat flow sensors were installed on the interior surface of the XPS panels to measure heat flow.

According to the experimental data, the actual U-value of the insulation panel is 0.624 W/(m^2·K). The discrepancy from the theoretical value is mainly due to the use of 5 mm Low-E glass in the test room window instead of 6 mm type, which leads to higher measured results.

In order to optimize the performance of the system for the specific demands of different seasons, panels are coated on opposing sides with high-reflectivity (90%) PET film and low-reflectivity (20%) black velvet, facilitating seasonal switching to reduce cooling loads in summer and enhance heat gain in winter.

2.2 Mechanical Structure Design

The device comprises insulation panels, their respective frames, a set of upper guide rails, as illustrated in Fig. 2. Each panel frame is mounted on sliders that travel along the guide rails (Fig. 3), allowing the panels to perform a range of motions, including full closure, half opening, full opening, outward tilting at 45° to reduce glare, and surface orientation adjustments.

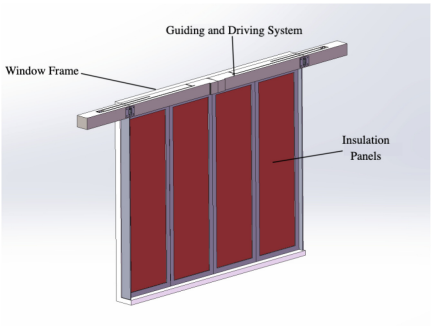


Fig. 2. Main structure diagram.

The system adopts motor-driven screw mechanisms, a differentiated guiding rail structure, a reversible insulation panel design, and a tiltable rail assembly to achieve precise multi-mode movement, enhanced airtightness, seasonal thermal-optical adaptability, and improved visual comfort. Specifically, screw rods work in concert with motors installed on both sides of the frame, enabling accurate positioning and alignment of the panels; the combination of "L"-shaped and straight linear rails ensures coplanarity of all four panels in the fully closed state, ensuring airtightness. Continuous gaskets around each panel and the frame effectively reduce air infiltration and thermal bridging. A guiding system divided into a fixed wall-embedded segment and a hinged movable segment facilitates a 45° outward tilting mode actuated by integrated motors and constrained by hydraulic cylinders to optimize glare control in winter. Additionally, each insulation panel is coated with reflective materials on opposing sides and can rotate 180° around its central axis in the tilted position, enabling seasonal adjustment of surface properties without disassembly, thereby saving space and simplifying maintenance.

2.3 Control Strategy

The system adopts a multi-layer control strategy consisting of a common strategy, special strategy, and optimization algorithm. The common strategy divides operation into occupied (6:00–22:00) and unoccupied (22:00–6:00) periods. During occupied periods, the seasonal control logics are applied. In summer (June 1 to August 31) the system adjusts its positions based on the ratio of window heat transfer to the building's design cooling load. When this ratio falls below 11%, the system remains fully open; between 11% and 22%, it switches to half-open position; and above 22%, it closes completely. In

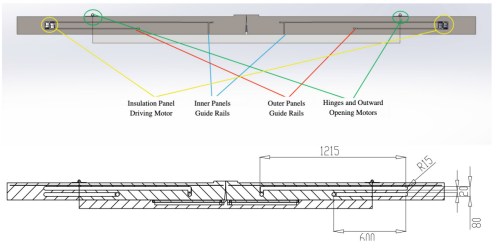


Fig. 3. Guiding and driving system diagram.

winter (December 1 to February 28) the system maintains fully open status when solar gains exceed window heat losses, otherwise closing completely. In transitional seasons the device automatically defaults to natural ventilation mode when outdoor conditions permit, significantly reducing mechanical system operation time.

However, limitations exist: in summer, while solar gain is reduced, limited ventilation can hinder heat dissipation; in winter, solar heating reduces load but low-angle sunlight may cause glare; and in transitional seasons, comfort can be compromised by large temperature swings despite acceptable energy performance.

To address these issues, special strategies are added during occupied periods. In summer, when the wet-bulb temperature is below 26 °C and wind pressure exceeds 0.5 Pa, the system temporarily increases its opening level (e.g., from fully closed to half-open) to enhance natural ventilation and cooling. Once conditions change, it reverts to its original state. In winter, during early morning and late afternoon hours, the system switches from fully open to a fully closed mode with a 45° outward tilt to reduce glare while preserving daylight and thermal performance. For transitional seasons, hybrid control is applied, using summer logic when temperatures exceed 22 °C and winter logic when below 10 °C to adapt to fluctuating conditions.

The system updates all parameters every minute for rapid response and includes a manual mode for maintenance or emergencies, allowing users to directly set the panel position.

2.4 Decision Threshold Optimization

To improve system adaptability and enhance energy-saving performance, this study applies a random forest machine learning algorithm to optimize the decision thresholds within the control program. While the original control strategy is based on fixed thresholds such as work schedules, heat flux, solar irradiance, and indoor temperature setpoints, these predefined values often fail to balance energy efficiency with occupant comfort, and lack the flexibility to adapt to varying climates and building orientations.

To address these limitations, the proposed algorithm evaluates four key parameters: occupancy count, lighting satisfaction (light_score), thermal comfort (thermal_score), and energy consumption (energy_usage). It employs multi-output regression to model the complex, nonlinear relationships between dynamic occupancy patterns, energy usage, user feedback, and the optimal control thresholds for building envelope operation.

The random forest model offers strong robustness against sensor noise and outliers, ensuring stable training outcomes even in the presence of imperfect data. Furthermore, it enables quantitative analysis of parameter influence through feature importance evaluation (using model.feature_importances_), which supports model refinement and guides optimization of control logic [15].

By incorporating this algorithm, the control system evolves from a static, reactive model to a dynamic, predictive framework. It adjusts decision thresholds in real time based on actual building performance metrics and subjective comfort feedback, allowing for automated optimization of system responses. This data-driven approach not only improves control accuracy and energy efficiency, but also enhances adaptability across different building configurations and climatic conditions, while providing transparent, interpretable decision support through ranked feature contributions. The machine learning algorithm execution flow is shown in Fig. 4:

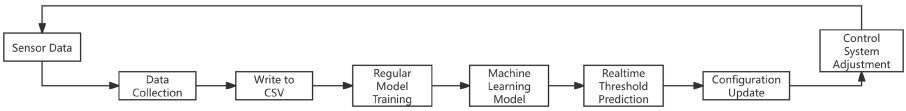


Fig. 4. Flowchart of machine learning algorithm

3 Performance Evaluation

The system's energy-saving performance was evaluated through a two-step approach combining simulation and a field test. First, energy performance was simulated using DesignBuilder software; then, on-site field tests were conducted under real climatic and architectural conditions.

3.1 Building Energy Simulation and Analysis

Building Model Parameters Settings. The building model was created using DesignBuilder, representing a four-story structure in Shanghai with a total floor area of 10,084.65 m^2 and a floor height of 5 m. Windows are 3.5 m high with a 0.5 m sill, and a building of equal height was placed to the south to simulate actual shading.

To simulate the variable WWR system, a shading model with a U-value of 0.35 W/(m^2·K) (see Sect. 2) was created. The module was controlled by operational strategies simplified from Sect. 2.3, including "Cooling" in summer, "Night heating" in winter, and "Night heating + day cooling" with "Block beam solar" in spring and autumn, aiming to reduce HVAC loads and enhance natural ventilation.

Two control groups were established for comparison: one without shading, and another using DesignBuilder's built-in intelligent shading model under the same seasonal logic.

The building followed the Shanghai Ultra-Low Energy Building Standard, setting the external wall U-value at 0.3 W/(m^2·K). Windows used a 6 mm Low-E + 9 mm

air gap + 5.7 mm regular glass configuration. Occupant behavior was modeled using predefined templates, and HVAC performance was evaluated using the "Ideal Loads" system to balance accuracy and computational efficiency.

Building Energy Consumption Simulation Data Analysis. For three scenarios, cooling and heating load simulations were carried out. The results are shown in Figs. 5, 6, and 7, respectively.

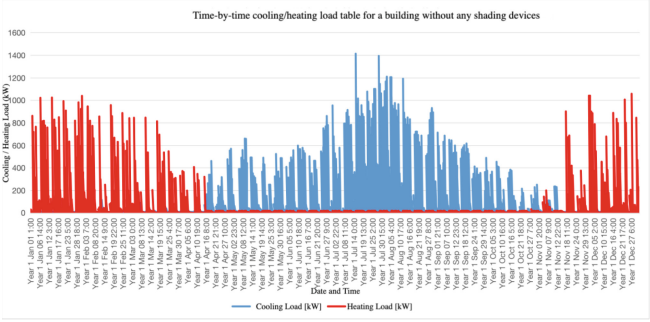


Fig. 5. Time-by-time cooling/heating load table for a building without any shading devices

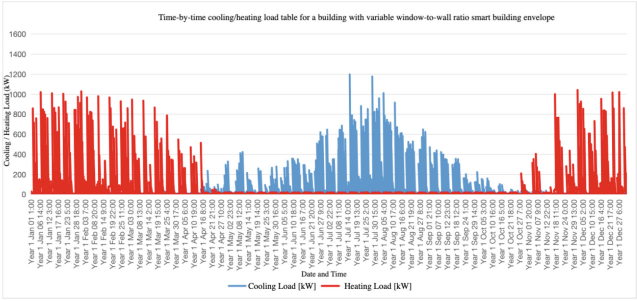


Fig. 6. Time-by-time cooling/heating load table for a building with intelligent shading

The cooling/heating coefficient of performance (COP) is set to 3. The results of the energy consumption simulation are shown in Table 1.

The energy consumption simulation data demonstrate that the implementation of the variable WWR intelligent building envelope achieves significant energy savings. Compared to the scenario without any shading devices, the system achieves a 35.7% reduction in cooling energy consumption, while maintaining only a 12% increase in heating energy consumption. Compared to the scenario with conventional intelligent shading systems, it provides 13.3% cooling energy savings with merely a 2.3% increase in heating demand. At the whole-building level, the system delivers an annual electricity savings of 83,467.29 kWh, representing a 22% energy usage reduction compared to the no-shading baseline, and a 24,572.93 kWh saving compared to conventional intelligent

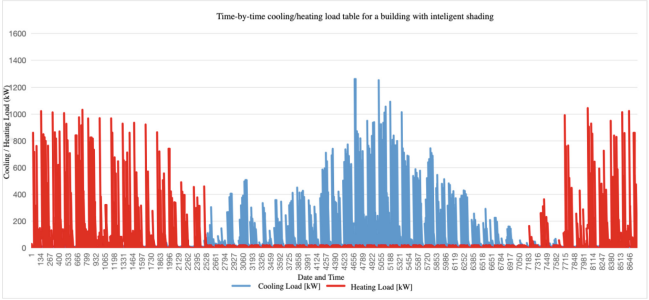


Fig. 7. Time-by-time cooling/heating load table for a building with variable WWR intelligent building envelope

Table 1. Table of energy consumption simulation results

programmatic	COP	cooling intensity (kWh/m^2)	Refrigeration energy consumption (kWh)	Heating intensity (kWh/m^2)	Heating energy consumption (kWh)	Annual energy consumption (kWh)
No shading measures applied	3	81.98	275579.87	29.34	98627.88	374207.75
Intelligent shading implemented		60.80	204382.24	33.00	110931.15	315313.39
Variable WWR intelligent building envelope implemented		52.70	177153.69	33.79	113586.77	290740.46

shading systems, representing a 7.79% energy usage reduction. These results substantiate the superior energy saving performance of the adaptive WWR enclosure system across different operational seasons.

3.2 Analysis of the Impact on Air-Conditioning Use

Furthermore, this study conducted a detailed analysis of the hourly cooling load heatmaps (Figs. 8, 9, and 10) for three comparative scenarios.

The heatmap analysis demonstrates that the variable WWR intelligent building envelope achieves energy savings primarily through two mechanisms: significantly reducing air conditioning runtime in transitional seasons, and lowering peak cooling loads during summer. On May 10th, for example, the system delayed air conditioning activation

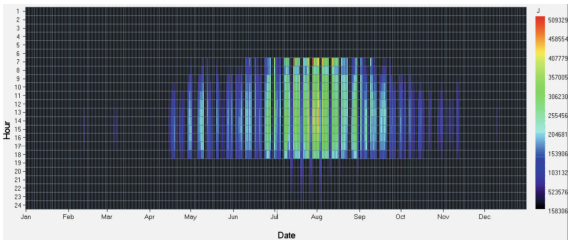


Fig. 8. Time-by-time heat map of working condition cooling load for a building without any shading device

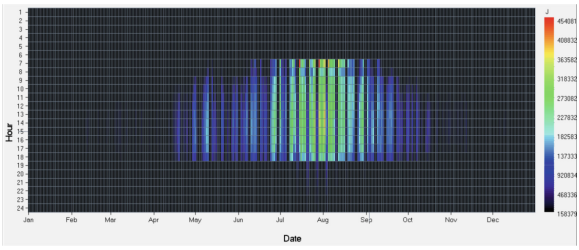


Fig. 9. Time-by-time heat map of cooling loads for a building general smart shading conditions only

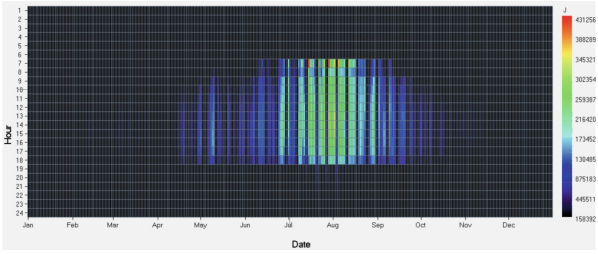


Fig. 10. Time-by-time heat map of cooling loads for a building with variable WWR intelligent building envelope

by 1–2 h compared to conventional shading and no-shading cases, while maintaining a similar end time around 18:00, indicating reduced operational duration. On August 2nd, it achieved a peak load reduction of 20.26% compared to no shading and 9.06% compared to conventional intelligent shading, highlighting its effectiveness in managing peak demand and enhancing overall thermal performance.

3.3 Field Test

To verify the system's thermal performance and its impact on indoor conditions, a field test was conducted in a third-floor office of the prototype building. The room was divided into three equal sections using partitions with thermal properties matching the

walls. The innermost and middle compartments (same dimensions) served as test zones. From November 17, 2024, the innermost compartment simulated the fully closed state by sealing the windows with 30 mm XPS insulation panels (see Section 2), while the middle compartment remained unaltered. Each was equipped with two NH211WS temperature sensors.

Experimental results showed that after applying the insulation panels, the test room had consistently smaller temperature fluctuations than the control room. Between December 15–20, the temperature variation in the test room was only 57.14% of that in the control room, aligning well with simulation results. During a sharp temperature rise from February 28 to March 2, 2025, the final temperature increase in the test room was 62.5% of the control, and its fluctuation range was just 50%. Comparative indoor and outdoor trends are shown in Fig. 11.

These results confirm that the fully closed configuration effectively reduces indoor temperature fluctuations, improving thermal comfort and lowering energy use for cooling and heating.

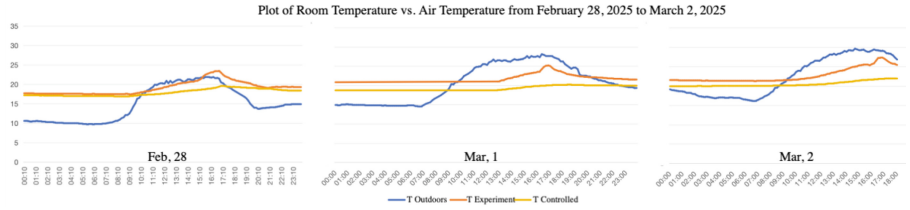


Fig. 11. Plot of Room Temperature vs. Air Temperature from February 28, 2025 to March 2, 2025

4 Conclusions and Outlook

The system envelope developed in this study integrates program controlled insulation panels with existing window-wall structures to enable intelligent variable WWR.

The use of modified phenolic foam (MPF) and extruded polystyrene (XPS) lowers the heat transfer coefficient down to 0.31 W/(m^2·K), approaching wall-level insulation and minimizing unwanted heat exchange while providing shading. Mechanical design enabling the system to shift between fully closed, half-open, fully open, or anti-glare modes to regulate daylight and solar gains. Each insulation panel has a dual-surface design with reflective PET film and low-reflectivity black velvet on each side respectively, reversible seasonally to further reduce heating and cooling loads.

A two-layer control strategy adjusts WWR based on temperature, humidity, irradiance, and heat flux was developed, while machine learning algorithm was utilized to optimize decision thresholds by evaluating indoor comfort metrics, occupancy, and energy performance.

DesignBuilder simulation and field test validated that the system reduces annual energy use by 35.7% while maintaining high occupant comfort in lighting and thermal conditions.

Funding. This research was funded by the National Key Research and Development Program of China during the 14th Five-Year Plan, "Research and Application of High-Efficiency Intelligent Building Envelopes". Grant number 2023YFC3806300.

References

1. Wriske, J. (2005). Bedarfsorientierte Raumwärmeversorgung durch dynamische Elektroflächenheizsysteme (Doctoral dissertation, Aachen, Techn. Hochsch., Diss., 2005).
2. Jiang, D.: Influence of window-to-wall ratio on energy consumption of residential buildings. Build. Technol. **40**(12), 1099–1102 (2009)
3. Wu, Y., Sun, H., Duan, M., Lin, B.: Overview of international development and application considerations of performance-adjustable building envelopes. Archit. Sci. **37**(10), 186–192 (2021). https://doi.org/10.13614/j.cnki.11-1962/tu.2021.10.25
4. Shi, F., Huang, J.: The impact of variable building skin on building energy consumption and indoor environment: a case study of the net-zero energy residence "Between Nature". South. Archit. **06**, 48–54 (2020)
5. Chen, S., Lyu, Y., Li, C., Li, X., Yang, W., Wang, T.: Liquid flow glazing contributes to energy-efficient buildings: a review. Renew. Sustain. Energy Rev. **191**, 114087 (2024)
6. Ke, Y., et al.: Smart windows: electro-, thermo-, mechano-, photochromics, and beyond. Adv. Energy Mater. **9**(39), 1970153 (2019)
7. Raimundo, A.M., Sousa, A.M., Oliveira, A.V.M.: Assessment of energy, environmental and economic costs of buildings' thermal insulation–influence of type of use and climate. Buildings. **13**(2), 279 (2023)
8. Formentini, M., Lenci, S.: An innovative building envelope (kinetic façade) with Shape Memory Alloys used as actuators and sensors. Autom. Constr. **85**, 220–231 (2018)
9. Boreyko, J.B., Zhao, Y., Chen, C.H.: Planar jumping-drop thermal diodes. Appl. Phys. Lett. **99**(23) (2011)
10. Tsinghua University: (2021-01-05). CN212295381U.
11. Košir, M.: Adaptive building envelope: an integral approach to indoor environment control in buildings. In: Automation and Control Trends. IntechOpen (2016)
12. GB 50189-2005: General Administration of Quality Supervision, Inspection and Quarantine of China (2005)
13. GB/T51350-2019: General Administration of Quality Supervision, Inspection and Quarantine of China (2019)
14. DG/TJ08-2466-2025: Shanghai Municipal Housing and Urban-Rural Construction Management Committee (2025)
15. Jose, J., Varshini, P.: Integrating technical indicators and ensemble learning for predicting the opening stock price. Int. J. Inf. Technol. Res. Appl. **3**(2), 1–15 (2024)

Effects of Surface Painting on Indoor Hygrothermal Performance and Energy Consumption in Pile-Dwellings

Yin Ying-de(✉), Li Yuan-yu, Shi Heng-lin, Li Hou-ying, Qin Xin-ping, Tan Shu-hao, and Lu Da-ji

School of Architecture and Transportation Engineering, Guilin University of Electronic Technology, Guilin 541004, China
yinyingde@guet.edu.cn

Abstract. The moisture buffering capacity of wooden building envelopes plays a significant role in regulating indoor humidity and influencing energy consumption, particularly in hot-humid climates. This study examines the hygrothermal performance of traditional pile-dwelling structures in northern Guangxi, comparing two surface finishing conditions: painted and unpainted walls. Using the dynamic simulation tool WUFI Plus, a representative building model was developed and evaluated under both natural ventilation and HVAC-controlled scenarios. The results indicate that surface painting substantially diminishes the moisture buffering capacity of walls, leading to greater fluctuations in indoor relative humidity. While painted walls slightly reduce dehumidification loads by limiting vapor transmission, they also increase cooling energy demand by 6.96%. Seasonal variations in moisture transfer were also observed, with buffering effects more pronounced in summer than in winter. These findings highlight the importance of carefully considering wall surface treatments to enhance indoor comfort and optimize energy efficiency in wooden buildings exposed to hot-humid conditions.

Keywords: Wooden · Hygrothermal · Paint

1 Introduction

According to the International Energy Agency (IEA), building operations account for approximately 30% of global final energy consumption and 26% of global carbon emissions [1]. As the energy crisis and climate change intensify, the development of green buildings and sustainable materials has become a critical priority for the construction industry. Wooden structures, in particular, are increasingly regarded as a low-carbon building solution due to their carbon sequestration potential, low embodied energy, and renewability [2]. Wood is a hygroscopic material that passively regulates indoor hygrothermal conditions through moisture absorption and release. However, improper design can lead to durability issues, such as decay and mold growth, highlighting the need for accurate assessment of the hygrothermal performance of wooden structures to optimize energy efficiency and environmental adaptability.

© The Author(s), under exclusive license to Springer Nature Singapore Pte Ltd. 2025
L. Ni et al. (Eds.): CCHVAC 2025, ESE, pp. 374–384, 2025.
https://doi.org/10.1007/978-981-95-3253-7_40

Heat, Air, and Moisture Transfer (HAMT) models have advanced from steady-state to dynamic coupling approaches, becoming a standard tool for evaluating building envelope performance [3–8]. Studies suggest that the moisture buffering capacity of hygroscopic materials can reduce building energy consumption, either directly or indirectly. In buildings with HVAC systems, such materials typically decrease heating demand by 2–3% and cooling demand by 5–30% [9]. Furthermore, their moisture storage and release properties can help stabilize indoor humidity levels, improving thermal comfort and air quality [10].

Wall surface treatments significantly influence hygrothermal behavior. Fang et al. [11] simulated five interior finishes across 15 Chinese cities and found that moisture-buffering materials generally enhance humidity control and reduce HVAC loads, particularly in temperate climates, though their effectiveness diminishes in humid regions. Seasonal variations also affect buffering performance, sometimes exacerbating indoor humidity conditions. In temperate and semi-arid climates, optimal use of hygroscopic materials can reduce building energy consumption by 25–30% [12]. Dobrosława et al. [13] examined four wall finishes under different occupancy scenarios, concluding that interior paint restricts moisture buffering, leading to greater indoor relative humidity fluctuations.

The influence of HAMT on building performance varies across climate zones, with particularly pronounced effects in hot-humid regions [14]. Traditional pile-dwellings, prevalent in the mountainous areas of northern Guangxi, exemplify climate-responsive design through their elevated, ventilated structures and the inherent moisture-regulating properties of wood. These features enhance adaptability to the local climate, which experiences hot, humid summers and cold, damp winters. However, prior research has predominantly focused on thermal conditions and ventilation performance, with limited systematic investigation into the hygrothermal behavior of walls—especially the role of surface treatments.

This study employs WUFI Plus to simulate the hygrothermal performance of typical wooden walls in northern Guangxi under two surface conditions:

1. Painted walls (Sd-value = 1 m)
2. Unpainted walls (Sd-value = 0 m)

Simulations are conducted for both natural ventilation and HVAC-controlled scenarios. The objective is to evaluate how surface treatments affect indoor environmental and building energy consumption, thereby providing insights for optimizing the hygrothermal performance and energy efficiency of traditional pile-dwellings.

2 Methods

2.1 Simulation Method

In this study, hygrothermal simulations were performed using WUFI Plus. The software is based on the HAMT model proposed by Künzel [6], which enables the simulation of the hygrothermal behavior of building materials under real climate. The governing

equations for HAMT are as follows:

$$\frac{\partial H}{\partial T \partial t} = \frac{\partial}{\partial x}\left(\lambda \cdot \frac{\partial T}{\partial x}\right) + h_v \cdot \frac{\partial}{\partial x}\left(\frac{\delta}{\mu} \cdot \frac{\partial(\varphi \cdot P_{sat})}{\partial x}\right) \tag{1}$$

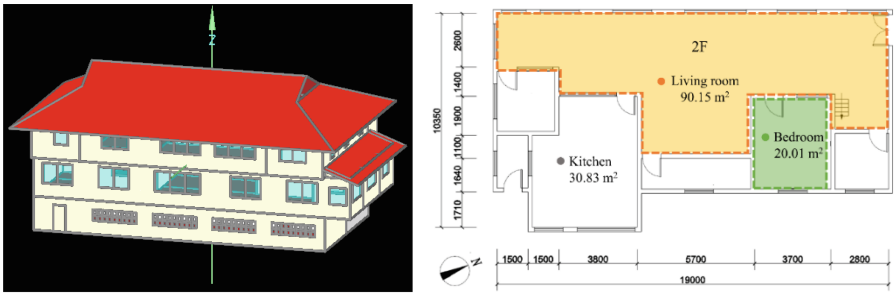
$$\frac{\partial w}{\partial \varphi}\frac{\partial \varphi}{\partial t} = \frac{\partial}{\partial x}\left(D_w \cdot \frac{\partial w}{\partial \varphi}\frac{\partial \varphi}{\partial x}\right) + \frac{\partial}{\partial x}\left(\frac{\delta}{\mu} \cdot \frac{\partial(\varphi \cdot P_{sat})}{\partial x}\right) \tag{2}$$

Where H, λ, T, φ, w, and t denote total enthalpy, thermal conductivity, temperature, relative humidity, moisture content, and time, respectively. P_{sat}, D_{w}, δ, μ, h_{v} represent saturation vapor pressure, liquid diffusivity, water vapor diffusion coefficient in air, water vapor diffusion resistance of the dry material, and evaporation enthalpy of the water, respectively.

The accuracy of WUFI Plus in simulating hygrothermal performance in building envelopes has been fully validated in the literature [9, 15, 16], confirming its effectiveness for predicting indoor thermal environments and energy consumption under hot-humid conditions.

2.2 Study Cases

The traditional pile-dwellings typically comprise three levels: a raised ground floor for storage, a primary living space on the second floor (containing kitchen, bedrooms, and living area), and an upper floor for additional habitation or storage. Following this architectural configuration, we established a representative building model, with the overall structure and second-floor layout illustrated in Fig. 1. The building envelope's construction details, material specifications, and corresponding hygrothermal properties are comprehensively presented in Tables. 1 and 2, with key material parameters derived from the WUFI database. Table. 3 details the internal heat and moisture sources along with the occupancy schedule.



(a) (b)

Fig. 1. Geometry and layout of the selected building model, (**a**) 3D view of the pile-dwellings, (**b**) Floor plan of the second floor with room divisions.

Given that most occupant activities concentrate on the second floor, we selected the bedroom and living room as focal points for analysis. The study examines two

operational scenarios: natural ventilation and HVAC-controlled conditions maintaining winter (18 °C/30% RH) and summer (26 °C/60% RH) setpoints. For each scenario, we evaluated both indoor thermal conditions and HVAC energy consumption under two wall treatments: fully painted surfaces (interior and exterior, Sd-value = 1 m) and unpainted walls (Sd-value = 0 m).

In WUFI, the effect of surface coatings is typically represented by assigning a vapor diffusion-equivalent air layer thickness (Sd-value) at the material surface. A higher Sd-value corresponds to a more vapor-tight finish, effectively reducing moisture exchange between the indoor/outdoor environment and the wall assembly. A higher Sd-value corresponds to a more vapor-tight finish, effectively reducing moisture exchange between the indoor/outdoor environment and the wall assembly. It is calculated as:

$$Sd = \mu \cdot d \tag{3}$$

where μ is the water vapor diffusion resistance factor of the material, and d is the thickness of the material.

The natural ventilation simulation covered the entire year; seasonal natural ventilation time settings were shown in Table. 4, while specific periods were designated for cooling and heating season analysis. The cooling season was defined from June 1st to September 30th, and the heating season was divided into two phases: January 1st to March 31st and November 10th to December 31st. Infiltration rates were set at 0.5 air changes per hour (ACH) for the living room and 0.3 ACH for the bedroom.

Meteorological data from the Typical Meteorological Year (TMY) of Guilin were adopted as the outdoor boundary condition, with a simulation timestep of 1 hour. A two-year *simulation* was performed, with the first year used to eliminate the influence of inaccurate initial conditions and moisture content; thus, the analysis was based on the second-year simulation results.

Table 1. Enclosure structure information.

Structure	Material	Specification (mm)	Heat transfer coefficient (W/m^2·K)	SHGC [−]
wall	Spruce	30	2.797(Exterior wall) 2.235(Interior wall)	–
Roof	Tile +air+ spruce	15 + 5 + 10	3.249	–
Window	Wood-framed single-glazed window	1400 × 1000, 1000 × 1000	5.74	0.87

Table 2. Hygrothermal performance of the envelope material.

Physical property parameters	Spruce	Concrete brick	Cement Lime Plaster	Tile
Bulk density (kg/m^3)	600	2315	1900	2800
Porosity (−)	0.2	0.5	0.24	–

(*continued*)

Table 2. (*continued*)

Physical property parameters	Spruce	Concrete brick	Cement Lime Plaster	Tile
Specific heat capacity (J/kg● K)	2000	800	85	920
Thermal conductivity, dry. (W/m● K)	0.16	0.73	0.8	0.43
Water vapor diffusion resistance factor (−)	132.6	200	19	–

Table 3. Occupants in-room rate, and hourly heat and moisture caused by occupant activity.

Time (h)	Indoor heat convective (W)		Indoor heat radiant (W)		Indoor moisture source (g/h)		In-room rate	
	Living room	Bedroom	Living room	Bedroom	Living room	Bedroom	Living room	Bedroom
0	0	132	0	88	0	76	0	1
8	164	0	109	0	138	0	1	0
18	209	0	159	0	138	0	1	0
22	0	132	0	88	0	76	0	1

Table 4. Seasonal Natural Ventilation Time Settings

Season	Room	Natural ventilation (1/h)		
		0:00–8:00	8:00–22:00	22:00–24:00
Summer	Living room	3	5	3
	Bedroom	1.5	2	1.5
Winter	Living room	0.5	3.5	0.5
	Bedroom	0.3	1.5	0.3
Spring& Autumn	Living room	3	3.5	3
	Bedroom	1.5	2	1.5

3 Results

3.1 Impact of Paint on the Indoor Environment

3.1.1 Summer

Figure 2 presents box plots of indoor air temperature and relative humidity in the living room and bedroom under summer natural ventilation conditions, comparing painted walls with unpainted walls.

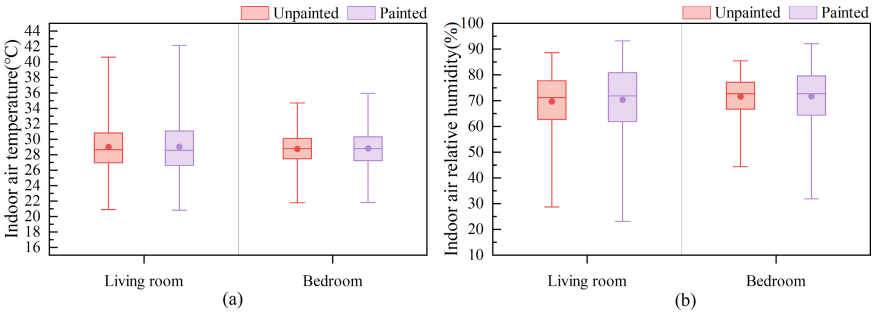


Fig. 2. Distribution of indoor air temperature and relative humidity during summer.

Analysis results demonstrate that painted walls lead to greater fluctuations in both temperature and relative humidity compared to unpainted walls. In the living room, the interquartile range (IQR) for temperature was 26.6–31.1 °C (painted) versus 27.0–30.8 °C (unpainted), while the humidity IQR spanned 61.9–80.9% (painted) compared to 62.8–77.8% (unpainted). The bedroom exhibited similar patterns, though with smaller temperature variations due to its single east-facing exterior wall and reduced solar exposure. These findings suggest that paint layers inhibit moisture transfer across walls, diminishing their moisture buffering capacity and consequently amplifying indoor humidity variations.

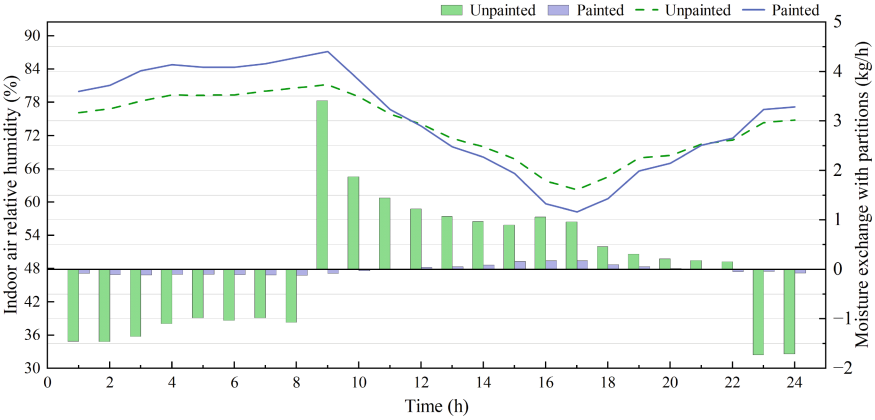


Fig. 3. Indoor relative humidity and moisture exchange with partitions in the living room on a typical summer day (July 14).

Figure 3 shows the 24-hour variation in indoor relative humidity (left axis) and wall moisture flux (right axis) in the living room on a typical summer day (July 14). Compared to the painted wall, the unpainted wall exhibits significant moisture absorption/desorption capability. During the simulation period, the indoor relative humidity fluctuation range for the painted wall (58.3%–87.2%) was significantly larger than that for the unpainted wall. Between 08:00 and 10:00, enhanced ventilation caused

the unpainted wall to shift from desorption to absorption, with a peak absorption rate at 3.41 kg/h, resulting in a subsequent decrease in indoor relative humidity. In contrast, the painted wall, due to its increased vapor diffusion resistance, showed only a weak absorption tendency (moisture flux consistently below ±0.2 kg/h), leading to more pronounced fluctuations in its indoor relative humidity. From 18:00 to 08:00 the next day, reduced ventilation frequency prompted a recovery in relative humidity. The above results demonstrate that the wall finish layer has a decisive influence on moisture buffering performance.

3.1.2 Winter

Figure 4 presents box plots comparing indoor air temperature and relative humidity in the living room and bedroom during winter natural ventilation conditions. While wall finish treatment (painted versus unpainted) showed minimal influence on temperature regulation, it significantly affected humidity control. The living room exhibited an interquartile range (IQR) for relative humidity was 31.41–88.05% for unpainted walls compared to 20.94–98.28% for painted walls, with similar patterns observed in the bedroom. These results demonstrate that unpainted walls provide superior humidity stability through enhanced moisture buffering capacity.

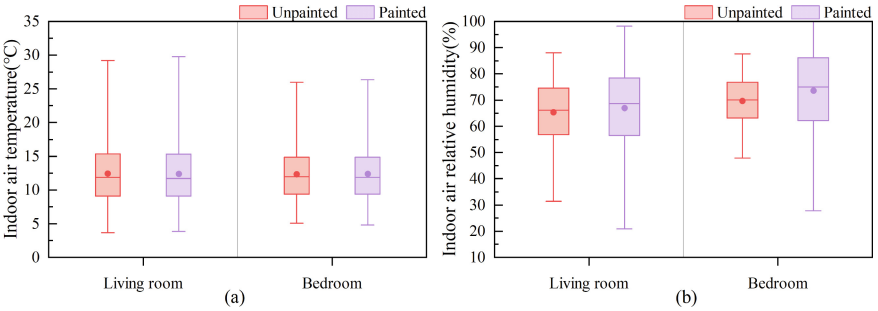


Fig. 4. Distribution of indoor air temperature and relative humidity during winter: (a) indoor air temperature; (b) indoor air relative humidity.

Figure 5 shows variations in indoor relative humidity and wall moisture flux in the living room on a typical winter day (January 6). Overall, the painted wall exhibited a larger relative humidity fluctuation range (33.8%–70.8%) than the unpainted wall (41.7%–64.2%). The absorption/desorption intensity of the painted wall was significantly lower, with a peak flux of only ~0.13 kg/h, which is far below the peak flux of the unpainted wall at 0.63 kg/h. After 10:00, increased ventilation (0.5 h^{-1} to 3.5 h^{-1}) caused a gradual decrease in relative humidity, during which the unpainted wall continuously absorbed moisture. After ventilation decreased post-18:00, humidity rose, and the unpainted wall shifted from absorption to desorption.

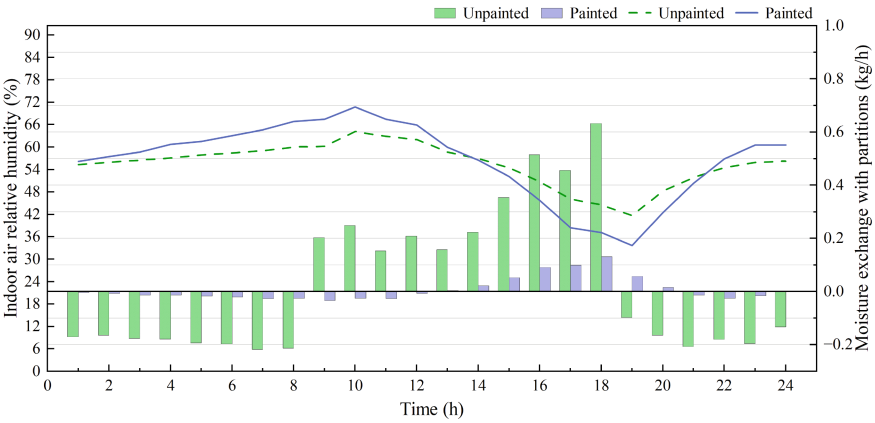


Fig. 5. Indoor relative humidity and moisture exchange with partitions in the living room on a typical winter day (January 6).

Seasonal analysis revealed significant differences in moisture behavior. Unpainted walls demonstrated markedly higher peak moisture flux in summer (3.41 kg/h) than winter (0.63 kg/h), attributable to seasonal variations in outdoor humidity and vapor pressure gradients. Painted walls maintained consistently low moisture flux ($<\pm 0.2$ kg/h) year-round, indicating that surface coatings persistently restrict moisture transfer. Consequently, painted finishes compromise the wall's ability to absorb summer humidity and release winter moisture, ultimately diminishing its humidity-stabilizing function.

3.2 Impact of Paint on Energy Consumption

Figure 6 presents a comparative analysis of annual energy consumption and humidity control loads between painted and unpainted wall conditions. The results demonstrate that wall finish treatment had minimal impact on heating requirements, with the living room showing nearly identical consumption between unpainted (106.09 kWh/m^2) and painted (105.99 kWh/m^2) walls. The bedroom exhibited marginally higher consumption with painted walls (76.26 vs. 74.96 kWh/m^2), attributable to the living room's three west-facing exterior walls that increase envelope heat transfer compared to the bedroom's single east-facing wall.

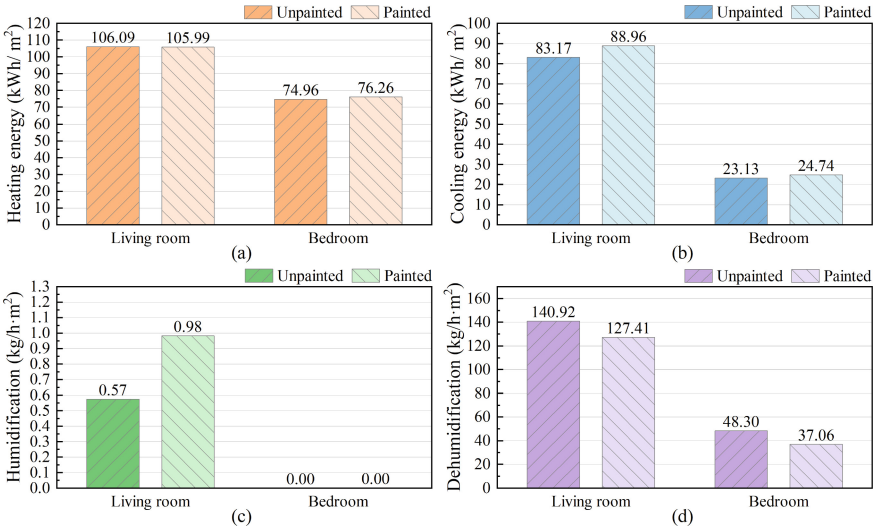


Fig. 6. Annual energy and humidity control loads under different wall finish conditions: (**a**) heating energy; (**b**) cooling energy; (**c**) humidification; (**d**) dehumidification.

In contrast, surface treatment significantly affected cooling performance, with painted walls increasing consumption by 6.96% in both spaces. This difference stems from unpainted walls' superior moisture exchange capacity during summer, where their latent heat effect reduces sensible cooling demands. Humidity control loads revealed important trade-offs: while painted walls increased living room humidification demand by 72% due to their vapor resistance compared with unpainted walls, creating excessively dry winter conditions, they reduced dehumidification requirements by 9.6% (living room) and 23.3% (bedroom). This reduction occurs because unpainted walls' lower vapor resistance permits greater moisture ingress during humid periods, despite their moisture buffering capacity. The bedroom maintained adequate humidity without supplemental humidification, benefiting from better airtightness and occupant-generated moisture.

4 Conclusions

This study investigated the effects of surface painting on indoor environmental conditions and energy performance in traditional pile-dwellings in northern Guangxi's hot-humid climate using WUFI Plus simulations. Comparative analysis of painted and unpainted wall conditions under both natural ventilation and HVAC-controlled scenarios yielded three principal findings:

First, surface painting substantially diminishes the moisture buffering capacity of wooden walls. The painted walls demonstrated markedly lower peak moisture flux values (summer: 0.17 kg/h vs. unpainted 3.41 kg/h; winter: 0.13 kg/h vs. 0.63 kg/h), resulting in greater indoor relative humidity fluctuations.

Second, the energy implications of painting are particularly significant during cooling seasons. While painted walls increased cooling energy consumption by 6.96% in both

living and bedroom spaces, they reduced dehumidification loads by 9.6% and 23.3%, respectively, due to decreased vapor transmission.

Third, moisture buffering performance displays distinct seasonal variation, with the potential to occasionally exacerbate indoor humidity conditions. This underscores the need for judicious selection and implementation of surface finishes.

These findings highlight that the moisture buffering performance of wooden walls depends strongly on surface treatment and room function. In hot-humid climates, surface coatings should be applied with caution to preserve adequate moisture buffering performance and enhance hygrothermal comfort and energy efficiency. However, the potential long-term durability risks posed by repeated moisture transfer—such as biological degradation and structural damage—should also be considered. Therefore, surface treatments should be selected with a balanced consideration of energy performance, indoor comfort, and material durability.

References

1. International Energy Agency. https://www.iea.org/energy-system/building, 2023/09/30
2. Ayanleye, S., Udele, K., Nasir, V., Zhang, X., Militz, H.: Durability and protection of mass timber structures: a review. J. Build. Eng. **46**, 103731 (2022)
3. Glaser, H.: Vereinfachte Berechnung der Dampfdiffusion durch geschichtete Wände bei Ausscheidung von Wasser und Eis. Kältetechnik. **10**(11), 358–364 (1958)
4. Philip, J.R., Vries, D.D.: Moisture movement in porous materials under temperature gradients. EOS Trans. Am. Geophys. Union. **38**(2), 222–232 (1957)
5. Luikov, A.V.: Advances in Heat Transfer. Elsevier (1966)
6. Künzel, H.M.: Simultaneous Heat and Moisture Transport in Building Components. IRB Verlag, Stuttgart (1995)
7. Hagentoft, C.-E., et al.: Assessment method of numerical prediction models for combined heat, air and moisture transfer in building components: benchmarks for one-dimensional cases. J. Therm. Envel. Build. Sci. **27**(4), 327–352 (2004)
8. Fang, A.M., Chen, Y.M., Wu, L.: Modeling and numerical investigation for hygrothermal behavior of porous building envelope subjected to the wind driven rain. Energ. Buildings. **231**, 110572 (2021)
9. Osanyintola, O.F., Simonson, C.J.: Moisture buffering capacity of hygroscopic building materials: experimental facilities and energy impact. Energ. Buildings. **38**(10), 1270–1282 (2006)
10. Woloszyn, M., Kalamees, T., Olivier Abadie, M., Steeman, M., Sasic Kalagasidis, A.: The effect of combining a relative-humidity-sensitive ventilation system with the moisture-buffering capacity of materials on indoor climate and energy efficiency of buildings. Build. Environ. **44**(3), 515–524 (2009)
11. Fang, J.Z., Zhang, H.B., Ren, P., He, B.-J., Tang, M.F., Feng, C.: Influence of climates and materials on the moisture buffering in office buildings: a comprehensive numerical study in China. Environ. Sci. Pollut. Res. **29**(10), 14158–14175 (2022)
12. Zhang, M.J., Qin, M.H., Rode, C., Chen, Z.: Moisture buffering phenomenon and its impact on building energy consumption. Appl. Therm. Eng. **124**, 337–345 (2017)
13. Kaczorek, D., Basińska, M., Koczyk, H.: Hygrothermal behaviour of a room with different occupancy scenarios. J. Build. Eng. **66**, 105928 (2023)
14. Wang, Y.Y., Tian, Y., Zhao, Z.J., Wang, D.J., Liu, Y.F., Liu, J.P.: Effect of moisture transfer on heat transfer through exterior corners of cooled buildings in hot and humid areas. J. Build. Eng. **43**, 103160 (2021)

15. Kang, Y.J., Jo, H.H., Kim, S.: Enhancing indoor comfort and building energy efficiency with cross-laminated timber (CLT) in hygrothermal environments. J. Buid. Eng. **84**, 108582 (2024)
16. Xia, D.W., et al.: Impact of coupled heat and moisture transfer on indoor comfort and energy demand for residential buildings in hot-humid regions. Energ. Buildings. **288**, 113029 (2023)

Impact of Hygrothermal Transfer in Pile-Dwellings' Walls on Indoor Hot-Humid Environments and Energy Consumption

Yin Ying-de(✉), Shi Heng-lin, Li Yuan-yu, Li Hou-ying, Lin Fei, Chen Guan-yu, and Pan Li-rong

School of Architecture and Transportation Engineering, Guilin University of Electronic Technology, Guilin 541004, China
yinyingde@guet.edu.cn

Abstract. To investigate the impact of Heat-Air-Moisture Transfer (HAMT) in walls on the indoor thermal environment and energy consumption of pile-dwellings in northern Guangxi, this study establishes a model of a typical pile-dwelling using WUFI Plus software. The indoor temperature, humidity, and air-conditioning energy consumption are simulated and analyzed for both summer and winter under three scenarios: thermal, hygrothermal, and WDR. The results show that the hygrothermal model significantly enhances indoor environmental stability. In summer, it reduces the maximum temperatures in the living room and bedroom by 2.08 °C and 1.68 °C, respectively, and decreases the humidity fluctuation range by 19.1%–38.1% compared to the thermal model. In winter, humidity fluctuations are reduced by 29.7%–47.4%. This improvement leads to a reduction in summer cooling energy consumption by 4.3%–6.6%, although it increases the dehumidification load by 12.55%–35.2%. The influence of WDR is minimal (temperature reductions≤0.08 °C, humidity changes<0.2%, and fluctuations in cooling and dehumidification energy consumption<2%). These findings underscore the importance of incorporating HAMT into the thermal optimization and energy-efficient design of pile-dwellings to improve environmental comfort, reduce energy use, and guarantee simulation accuracy.

Keywords: Wooden · Hygrothermal · Wind-driven Rain

1 Introduction

According to the International Energy Agency (IEA), building operations account for approximately 30% of global final energy consumption and 26% of global carbon emissions [1]. In light of the escalating global energy crisis and climate change, the development of green buildings and sustainable materials has become a critical focus within the construction industry. Wooden buildings are increasingly recognized as a model of low-carbon construction due to their high carbon storage capacity, low energy consumption during manufacturing, and strong renewability [2]. However, as a hygroscopic material,

© The Author(s), under exclusive license to Springer Nature Singapore Pte Ltd. 2025
L. Ni et al. (Eds.): CCHVAC 2025, ESE, pp. 385–395, 2025.
https://doi.org/10.1007/978-981-95-3253-7_41

wood absorbs and releases moisture in response to environmental conditions. This characteristic can lead to issues such as mold growth and decay during both construction and long-term use. Therefore, the HAMT properties of wood must be carefully considered when designing and evaluating the performance of wooden buildings.

The HAMT model is a key tool for describing heat and moisture transfer in building envelopes. It has evolved from early steady-state models to transient coupled models, with numerous equations proposed by researchers over time [3, 4]. Commonly used simulation tools for modeling HAMT in buildings include software such as Delphin, WUFI, and MATCH. Kang et al. [5] analyzed indoor thermal and humidity conditions, as well as energy consumption, under scenarios involving both passive and active building elements (e.g., exterior walls and indoor temperature control) in buildings with CLT walls. Their results demonstrated that CLT walls offer improved indoor comfort compared to traditional concrete walls. Brambilla A et al. [6] found through dynamic hygrothermal simulation analysis that composite structures made of composite materials and wood are generally superior to lightweight wooden structures in terms of moisture and mold resistance, but their performance is greatly affected by indoor climate conditions. Fedorik F et al. [7] investigated the hygrothermal performance and risk of mold growth within wooden building assemblies from both steady-state and dynamic perspectives, taking into account the effects of factors including material properties, climatic variations, initial conditions, and diffusion characteristics. Libralato M et al. [8] simulated three types of wooden walls in seven locations around the world to assess the risk of wood decay. The results showed that the humidity lag effect was significant and that the choice of adsorption curve had a significant impact on the simulation results. Chen Y et al. [9] studied a split-type insulated wall composed of straw bricks and an EPS insulation layer, with the aim of reducing wall thickness. The results showed that this structure has higher thermal inertia and better moisture regulation capabilities than traditional glass fiber walls, and that the humidity at the jacket-insulation layer interface is highest. Reich B Z et al. [10] used WUFI simulation to analyze the effect of vapor diffusion ports (VDPs) on the drying performance of wood walls. The results showed that VDPs can increase the drying rate of walls and significantly reduce the risk of mold growth under high humidity loads, but have little effect under moderate humidity conditions.

Conventional thermal load calculations for building envelopes generally account solely for heat transfer processes, while overlooking the coupled heat and moisture transfer (HAMT) phenomena. In reality, building materials possess substantial moisture storage capacity and transport characteristics, resulting in continuous moisture exchange between wall assemblies and their surrounding environment. This exchange becomes particularly pronounced under wind-driven rain (WDR, which represents the combined action of wind and precipitation that results in oblique water deposition on building surfaces) [11] conditions. The traditional pile-dwellings prevalent in northern Guangxi, southern China, exemplify effective passive climate adaptation through their elevated ventilation design and the inherent hygrothermal properties of wood construction. Although previous studies have extensively investigated these structures' ventilation efficiency and thermal performance, their HAMT characteristics remain insufficiently explored. Considering both the hygroscopic nature of wood materials and the region's

consistently high humidity levels, a comprehensive understanding of HAMT dynamics is essential for enhancing indoor environmental quality and ensuring structural longevity.

Based on WUFI Plus software, this paper simulates the indoor hygrothermal environment changes of typical pile-dwellings in northern Guangxi under summer and winter conditions. It compares the impacts of different models : (1) a pure conductive heat transfer model (thermal model), (2) a coupled heat and moisture transfer model incorporating temperature and humidity differentials (hygrothermal model), and (3) an advanced wind-driven rain model that accounts for precipitation effects on building exteriors (WDR model). The investigation focused on elucidating the specific impacts of moisture transfer on indoor thermal environments and energy consumption in timber structures, while assessing the feasibility of simplifying moisture transfer considerations. The findings aim to provide theoretical foundations for optimizing hygrothermal performance and energy-efficient design in such buildings.

2 Methods

2.1 Simulation Method

In this study, WUFI Plus was used to evaluate the effects of HAMT on the indoor environment and energy consumption of pile-dwellings. WUFI Plus is based on the HAMT model developed by Künzel [4], which enables the simulation of hygrothermal behavior in building materials under real climatic conditions. It has been widely applied in both architectural design and research [12]. The governing equation for HAMT is as follows:

$$\frac{\partial H}{\partial T \partial t} = \frac{\partial}{\partial x}\left(\lambda \cdot \frac{\partial T}{\partial x}\right) + h_v \cdot \frac{\partial}{\partial x}\left(\frac{\delta}{\mu} \cdot \frac{\partial(\varphi \cdot P_{sat})}{\partial x}\right) \tag{1}$$

$$\frac{\partial w}{\partial \varphi}\frac{\partial \varphi}{\partial t} = \frac{\partial}{\partial x}\left(D_w \cdot \frac{\partial w}{\partial \varphi}\frac{\partial \varphi}{\partial x}\right) + \frac{\partial}{\partial x}\left(\frac{\delta}{\mu} \cdot \frac{\partial(\varphi \cdot P_{sat})}{\partial x}\right) \tag{2}$$

Where H, λ, T, φ, w, and t denote total enthalpy, thermal conductivity, temperature, relative humidity, moisture content, and time, respectively. P_sat, D_w, δ, μ, h_v represent saturation vapor pressure, liquid diffusivity, water vapor diffusion coefficient in air, water vapor diffusion resistance of the dry material, and evaporation enthalpy of the water, respectively. Eqs. (1), (2) represent the laws of energy and mass conservation, respectively. The left-hand sides of both equations comprise the storage terms, and the fluxes on the right-hand side vary according to local climate conditions.

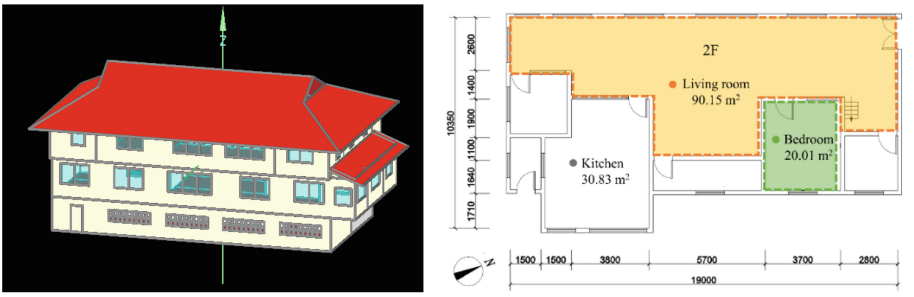
The accuracy of WUFI Plus in simulating HAMT in building envelopes has been effectively validated in previous studies [5]. It is capable of accurately modeling the indoor thermal environment and energy consumption, particularly in hot-humid climates.

2.2 Description of the Case

The typical pile-dwelling consists of three floors: the ground floor is elevated and used for storage; the second floor serves as the main living area, including the kitchen, bedroom, and living room; the top floor is used for additional occupancy or storage. The

architectural model in this study is developed based on this typical structure, with the model diagram and second-floor plan shown in Fig. 1. The envelope components and hygrothermal parameters of materials are presented in Tables 1 and 2, with the primary material data sourced from the WUFI database. As the primary living spaces are located on the second floor, this study focuses on the bedroom and living room as the main areas of analysis (Table 3). Two operational scenarios are studied: one with natural ventilation, and the other using an HVAC system to control indoor temperature to 18°C/30% (winter) and 26°C/60% (summer), to assess indoor thermal environment and HVAC system energy demand.

Natural ventilation was simulated year-round, with seasonal settings detailed in Table 4 and designated periods for cooling and heating analyses. The cooling season spanned June 1 to September 30; heating included January 1 to March 31 and November 10 to December 31. Infiltration rates were 0.5 ACH (living room) and 0.3 ACH (bedroom).



(a) (b)

Fig. 1. Geometry and layout of the selected building model, (**a**) 3D view of the pile-dwellings, (**b**) Floor plan of the second floor with room divisions.

Table 1. Enclosed information.

Structure	Material	Specification (mm)	Heat transfer coefficient ($W/m^2 \cdot K$)	SHGC [-]
Wall	Spruce	30	2.797(Exterior wall) 2.235(Interior wall)	-
Roof	Tile +air+ spruce	15+5+10	3.249	-
Window	Wood-framed Single-glazed Window	1400×1000, 1000×1000	5.74	0.87

Table 2. Hygrothermal physical property parameters of materials.

Physical property parameters	Spruce	Concrete brick	Cement Lime Plaster	Small grayish-green tiles
Bulk density(kg/m^3)	600	2315	1900	2800
Porosity(-)	0.2	0.5	0.24	-
Specific heat csapacity(J/kg• K)	2000	800	85	920
Thermal conductivity, dry.(W/m• K)	0.16	0.73	0.8	0.43
Water vapor diffusion resistance factor(-)	132.6	200	19	-

Table 3. Occupants' in-room rate, and hourly heat and moisture caused by occupant activity.

–Time (h)	Indoor heat convective (W)		Indoor heat radiant (W)		Indoor moisture source (g/h)		In-room rate	
	Living room	Bedroom	Living room	Bedroom	Living room	Bedroom	Living room	Bedroom
0	0	132	0	88	0	76	0	1
8	164.4	0	109.6	0	138	0	1	0
18	209.4	0	159.6	0	138	0	1	0
22	0	132	0	88	0	76	0	1

Table 4. Seasonal natural ventilation time settings.

Season	Room	Natural ventilation (1/h)		
		0:00–8:00	8:00–22:00	22:00–24:00
Summer	Living room	3	5	3
	Bedroom	1.5	2	1.5
Winter	Living room	0.5	3.5	0.5
	Bedroom	0.3	1.5	0.3
Spring& Autumn	Living room	3	3.5	3
	Bedroom	1.5	2	1.5

2.3 Outdoor Boundary Conditions

Typical annual meteorological data for Guilin were used as the outdoor boundary conditions, with a simulation time step of one hour. The total simulation period was two

years: the first year served to minimize the influence of uncertain initial conditions and initial moisture content, while data from the second year were used for analysis.

3 Results

3.1 Effect of HAMT on Indoor Thermal Environment

3.1.1 Summer

Fig. 2 presents box plots illustrating the distribution of indoor air temperature (Fig. 2a) and relative humidity (Fig. 2b) in the living room and bedroom of the pile-dwellings in northern Guangxi during summer, under three simulation models: thermal, hygrothermal, and WDR.

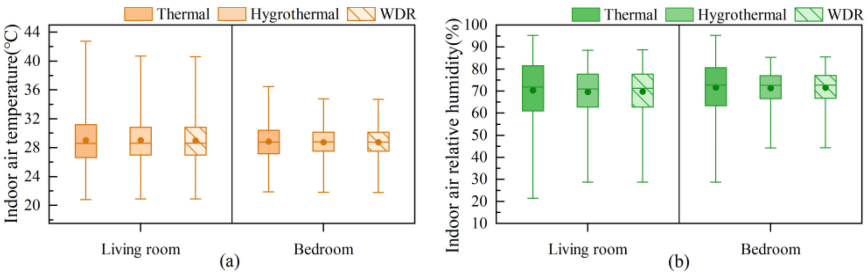


Fig. 2. Distribution of indoor air temperature and relative humidity during summer

As shown in Fig. 2a, the living room shows higher IQR, extremes, and mean temperatures than the bedroom. This difference is primarily due to the living room's greater exposure to solar radiation, as it has three west-facing walls and a larger envelope surface area for heat transfer, whereas the bedroom has only one east-facing wall. In the thermal model, maximum temperatures reach 42.77 °C (living room) and 36.45 °C (bedroom). With the inclusion of HAM, the maximum temperatures decrease significantly to 40.69 °C (living room) and 34.77 °C (bedroom) —reductions of 2.08 °C and 1.68 °C, respectively. Increases in WDR reduced living room temperatures and bedroom temperatures by 0.08 °C and 0.06 °C, respectively. These results indicate that HAMT effectively suppresses temperature peaks via moisture evaporation and heat absorption in walls under high external temperatures, reducing heat transfer indoors.

As shown in Fig. 2b, the living room's average relative humidity (RH) is 70.43% (thermal), 69.72% (hygrothermal), and 69.79% (WDR); the bedroom's RH is some-what higher at 71.69%, 71.44%, and 71.59%, respectively, mostly as a result of resi-dents' increased moisture emission per unit area. In the living room, the RH range decreases by 19.1% from 21.41%–95.31% (thermal) to 28.75%–88.52% (hygrothermal); in the bedroom, it decreases by 38.1% from 28.75%–95.31% to 44.22%–85.43%. The RH range displayed by the hygrothermal model and the WDR model is comparable. The substantial reduction in humidity variation suggests that wooden walls effectively moderate indoor humidity fluctuations. This performance is attributed to wood's capacity to absorb

and release moisture, as well as the vapor pressure differential between indoor and outdoor environments, which drives moisture transfer through the walls. Consequently, the hygrothermal and WDR models exhibit a smaller range of humidity changes compared to the thermal model.

Comprehensive summer results demonstrate that the HAMT greatly lowers the range of humidity variations and the peak indoor temperature, demonstrating the wood structure's superior hygrothermal regulation capabilities and enhancing the stability of the interior thermal environment.

3.1.2 Winter

Fig. 3 compares the indoor air temperature (Fig. 3a) and relative humidity (Fig. 3b) distributions in the living room and bedroom under winter conditions for the three models of thermal, hygrothermal, and WDR.

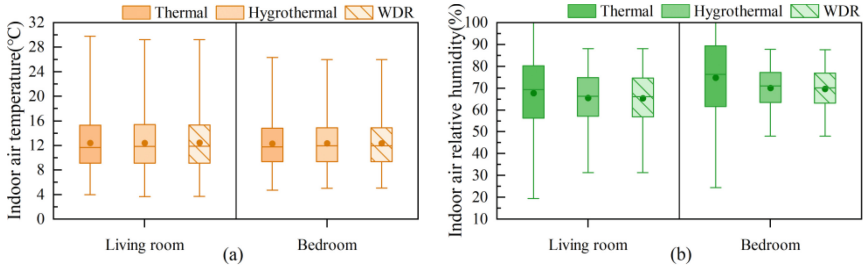


Fig. 3. Distribution of indoor air temperature and relative humidity during winter

Fig. 3a shows average temperatures of the living room as 12.39°C (thermal), 12.44°C (hygrothermal), and 12.44°C (WDR), and the bedroom as 12.32°C (thermal), 12.37°C (hygrothermal), and 12.37°C (WDR). The hygrothermal model yields negligible temperature increases of about 0.04% compared to the thermal model. Both the hygro-thermal and WDR models have minimal impact on average indoor temperatures during winter, with the WDR model showing no significant fluctuations. In contrast, Fig. 3b shows that the differences in relative humidity between different models are more significant, with the average relative humidity in the living room and bedroom under the thermal model being 67.74% and 74.75%, respectively. The hygrothermal model decreases the average humidity to 65.52% in the living room (a decrease of 3.3%) and 70.12% in the bedroom (a decrease of 6.2%). With humidity variations of 0.2% in the living room and 0.6% in the bedroom, the WDR model exhibits smaller changes than the hygrothermal model. In the living room, the RH range decreases by 29.7% from 19.38%–100% (thermal) to 31.41%–88.05% (hygrothermal); similarly, the RH range decreases by 47.4% from 24.38%–100.0% (thermal) to 47.97%–87.73% (hygrothermal) in the bedroom. The WDR model exhibits a range comparable to that of the hygrothermal model, indicating that HAMT of walls significantly moderates indoor humidity. Specifically, the wall releases stored water vapor to increase indoor humidity when external humidity is high, and adsorbs excess vapor for storage in its pore structure when external humidity is high.

3.2 Impact of HAMT on Indoor Humidification/Dehumidification and Energy Consumption

As shown in Fig. 4a, with a variance of less than 0.1%, the three models' estimates of the heating energy consumption in the living room are 106.22 kWh/m2 (thermal), 106.09 kWh/m2 (hygrothermal), and 106.09 kWh/m2 (WDR). For the thermal model, the bedroom's heating energy consumption is 76.37 kWh/m2, for the hygrothermal model, it is 74.86 kWh/m2 (down 2.0%), and for the WDR model, it is 74.96 kWh/m2 (up 0.1% from the hygrothermal). Because the living room is more impacted by the outside temperature than the bedroom, it uses a lot more energy for heating. There is no significant difference between the heating energy consumption of the living room and the bedroom under all three model calculations. Combined with the indoor temperature and humidity under natural ventilation in Fig. 3, it can be seen that the HAMT does not have a significant effect in winter.

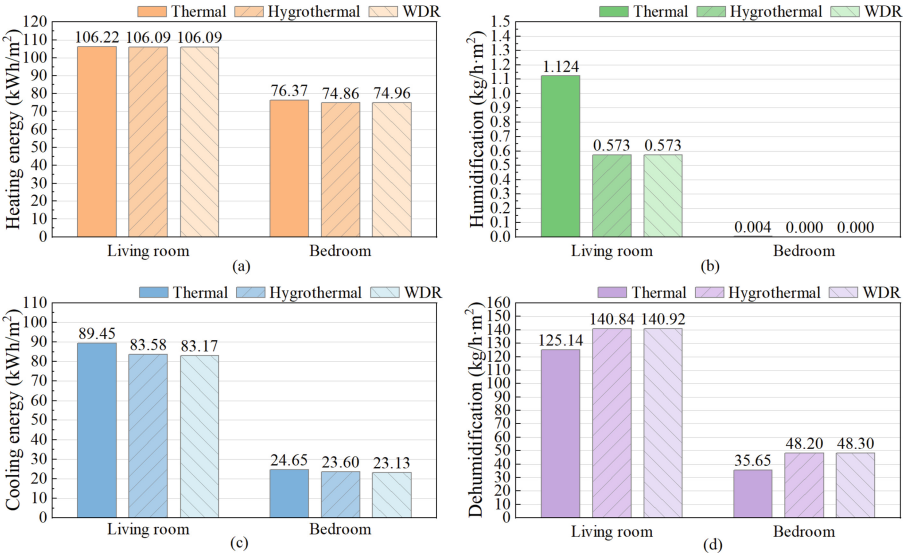


Fig. 4. Annual energy and humidity control loads under different wall finish conditions: (**a**) heating energy; (**b**) cooling energy; (**c**) humidification; (**d**) dehumidification.

As shown in Fig. 4b, the bedroom only has a slight humidification requirement (0.004 kg/h·m^2) under the thermal model, while the humidification amount under the hygrothermal and WDR models is 0 kg/h·m^2. The humidification capacity of the living room is 1.124 kg/h·m^2 (thermal), 0.573 kg/h·m^2 (hygrothermal), and 0.573 kg/h·m^2 (WDR). The hygrothermal model reduced it by 49.0% compared with the thermal model. The WDR model remains unchanged compared with the hygrothermal model. Although the humidification capacity in the living room is significantly higher than that in the bedroom, the overall humidification demand is lower. This is attributed to the long-term high-humidity outdoor environment in northern Guangxi. Moreover, in the hygrothermal

and WDR models, the moisture absorption and release characteristics of wood further reduce the indoor humidification demand to a negligible level.

As shown in Fig. 4c, the cooling energy consumption in the living room is 89.45 kWh/m^2 (thermal), 83.58 kWh/m^2 (hygrothermal, 6.6% less than thermal), and 83.17 kWh/m^2 (WDR, 0.5% less than hygrothermal). The cooling energy consumption in the bedroom is 24.65 kWh/m^2 (thermal), 23.60 kWh/m^2 (hygrothermal, 4.3% less than thermal), and 23.13 kWh/m^2 (WDR, 2.0% less than hygrothermal). The evaporation and heat absorption of the internal moisture in the wood during the HAMT are the main reasons why the living room and bedroom of the hygrothermal model have lower cooling energy consumption than the thermal model. In contrast, the WDR model's residual moisture from WDR on the building façade enhances the evaporative cooling effect, which results in a further slight reduction in energy consumption.

As shown in Fig. 4d, the dehumidification capacity in the living room is 125.14 kWh/m^2 for the thermal model, 140.84 kWh/m^2 for the hygrothermal model (increasing by 12.55% compared to thermal), and 140.92 kWh/m^2 for the WDR model (increasing by 0.07% compared to hygrothermal). The dehumidification capacity in the bedroom is 35.65 kWh/m^2 for the thermal model, 48.20 kWh/m^2 for the hygrothermal model(increasing by 35.2% compared to thermal), and 48.30 kWh/m^2 for the WDR model (increasing by 0.2% compared to hygrothermal). The living room has a higher dehumidification demand than the bedroom, primarily due to greater ventilation introducing more humid outdoor air. When heat and moisture transfer are considered (Hygrothermal/WDR models), additional moisture from vapor pressure-driven wall migration and rainwater absorption (WDR) further increases the indoor moisture load, resulting in a significantly higher dehumidification demand compared to the thermal model.

Overall, the HAMT model has a slight impact on heating energy consumption, whereas it significantly reduces summer cooling energy consumption; meanwhile, although it eliminates low levels of winter humidification demand, it significantly increases summer dehumidification demand.

4 Conclusions

This study simulates and compares the indoor temperature and humidity characteristics of pile-dwellings, as well as the differences in annual air-conditioning energy consumption under typical summer and winter conditions, using three numerical models: thermal, hygrothermal, and WDR. The main conclusions are as follows:

(1) Under natural ventilation conditions, pile-dwellings in hot-humid regions effectively stabilize indoor thermal conditions through HAMT within the building envelope. In summer, compared to the thermal model, the hygrothermal model reduces the maximum indoor temperature by 2.08 °C (living room) and 1.68 °C (bedroom), and decreases the relative humidity fluctuation range by 19.1% and 38.1%, respectively. In winter, the humidity fluctuation ranges in the living room and bedroom are reduced by 29.7% and 47.4%, respectively, demonstrating strong humidity buffering capacity.

(2) The HAMT enhances the building's thermal performance and contributes to a more efficient energy use structure. In summer, the hygrothermal model reduces cooling energy consumption by 6.6% (living room) and 4.3% (bedroom). In winter, humidification demand decreases significantly, with the rate dropping from 1.124 to 0.573 kg/h·m^2 (living room) and reaching 0 kg/h·m^2 (bedroom). However, the moisture adsorption and release processes lead to a substantial increase in dehumidification load during summer, by 12.55% (living room) and 35.2% (bedroom).
(3) The WDR has a limited impact on temperature, humidity regulation, and energy consumption in hot-humid climates, but provides minor refinements in simulation accuracy. Compared to the hygrothermal model, the WDR model yields negligible temperature differences (maximum decrease of 0.06°C–0.08 °C) and humidity changes (<0.2%). Cooling loads are slightly reduced (0.5%–2.0%), while dehumidification loads show marginal increases (0.07%–0.2%).

Although the differences in indoor environmental outcomes between the hygrothermal and WDR models are limited, they differ in terms of modeling complexity. The WDR model requires more detailed surface boundary parameters and significantly longer computational time. The simpler hygrothermal model is sufficient to capture the dominant moisture effects for most simulation purposes, making it more practical in typical building assessments.

However, considering Guilin's hot-humid climate characterized by frequent rainfall events, timber structures face exacerbated risks of microbial growth and durability degradation under elevated moisture conditions. Thus, further investigation remains imperative to elucidate the WDR impacts on wooden wall assemblies.

References

1. International Energy Agency. https://www.iea.org/energy-system/building, 2023/09/30
2. Ayanleye, S., Udele, K., Nasir, V., Zhang, X., Militz, H.: Durability and protection of mass timber structures: a review. J Build Eng. **46**, 103731 (2022)
3. Glaser, H.: Vereinfachte Berechnung der Dampfdiffusion durch geschichtete Wände bei Ausscheidung von Wasser und Eis. Kältetechnik. **10**(11), 358–364 (1958)
4. Künzel, H.M.: Simultaneous heat and moisture transport in building components. IRB Verlag, Stuttgart (1995)
5. Kang, Y.J., Jo, H.H., Kim, S.: Enhancing indoor comfort and building energy efficiency with cross-laminated timber (CLT) in hygrothermal environments. J Build Eng. **84**, 108582 (2024)
6. Brambilla, A., Gasparri, E.: Hygrothermal behaviour of emerging timber-based envelope technologies in Australia: a preliminary investigation on condensation and mould growth risk. J Cleaner Prod. **276**, 124129 (2020)
7. Fedorik, F., Niemi, A.H.: Hygrothermal assessment and design models for mass timber building envelopes in northern conditions. Eng Struct. **305**, 117714 (2024)
8. Libralato, M., De Angelis, A., Saro, O., Qin, M.H., Rode, C.: Effects of considering moisture hysteresis on wood decay risk simulations of building envelopes. J. Build. Eng. **42**, 102444 (2021)
9. Chen, Y.C., Wang, X.A., Li, D.H., Rodrigue, D., Gosselin, L.: Hygrothermal performance of straw bales split-insulation wall assembly in cold and humid climates. Energy Build. **307**, 113974 (2024)

10. Reich, B.Z., Ge, H., Wang, J.Y.: Effect of vapor diffusion port on the hygrothermal performance of wood-frame walls. J Build Eng. **39**, 102280 (2021)
11. Yu, S., Liu, X.Y., Li, Y.Z., He, S., Yao, Y.F., Sun, S.K.: Experiment and numerical simulation study on hygrothermal migration of damaged envelope walls during wind-driven rain. Build Environ. **243**, 110653 (2023)
12. Akhavan Shams, S., Ge, H., Wang, L.: Hygrothermal modeling in mass timber constructions: recent advances and machine learning prospects. J Build Eng. **96**, 110500 (2024)

Optimization of Architectural Design to Improve Thermal Performance in Standard Housing in Daqing, China

Samanta López Salazar[1], Dong Li[1(✉)], Ruitong Yang[1], E. Simá[2], and Zhe Yuan[1]

[1] Heilongjiang Provincial Key Laboratory of Thermal Utilization and Disaster Reduction of New Energy in Cold Regions, Northeast Petroleum University, Daqing 163318, China
lidonglvyan@126.com

[2] Tecnológico Nacional de México/CENIDET, Morelos 62490, Mexico

Abstract. The orientation of envelope elements defines thermal load distribution and directly influences energy demand and indoor conditions. This study analyzes the relationship between orientation and thermal load in a standard 9 m^2 room in Daqing, China, under winter and summer conditions. A hybrid model based on differential and global approaches quantified heat transfer and identified the elements with the highest thermal demand. The distribution of thermal loads varied by orientation and surface type. East–west façades concentrated the highest cooling loads during summer, while the roof and glazing contributed most to heat loss in winter. In response to these variations, orientation optimization reduced heating demand by up to 40%. Proper opening placement and high-performance materials lowered energy use by 46%. Wall and roof insulation achieved 70.3% energy savings with a six-year payback. Low-emissivity glazing and external shading preserved thermal stability and reduced operational costs. These results support passive strategies with thermal and economic value.

Keywords: Passive architectural design · Thermal performance optimization · Energy efficient housing

1 Introduction

Architectural design determines thermal efficiency, especially in cold climates where heating dominates energy use [1]. In extreme winters, envelope heat transfer affects indoor comfort and HVAC reliance [2, 5]. The construction sector holds potential to lower energy demand and preserve indoor quality [3]. Several studies confirm the effectiveness of passive solutions. Energy use dropped by 14.6% after insulation upgrades [6], and heating demand decreased when insulation thickness was adjusted [7]. In Daqing, aerogel glazing with PCM reduced heat loss by 11.4% [8], while solariums and aerogel windows lowered heating needs by 14% [9]. Window placement and insulation achieved thermal load reductions of 4–8%, with payback periods between 2.4 and 9.3 years [10].

© The Author(s), under exclusive license to Springer Nature Singapore Pte Ltd. 2025
L. Ni et al. (Eds.): CCHVAC 2025, ESE, pp. 396–405, 2025.
https://doi.org/10.1007/978-981-95-3253-7_42

Thermal insulation and high-performance glazing improve energy efficiency [11]. Integrated into passive design, they offer accessible solutions [12]. Orientation and glazing placement help regulate indoor conditions and reduce energy use [13, 14]. Passive strategies reduce thermal loads and preserve thermal stability without extra systems [15]. Orientation also plays a decisive role in energy performance. Lower thermal loads were obtained when façade orientation followed solar exposure patterns [16]. Energy use decreased by up to 46% in cold climates through orientation and opening adjustments [17]. A 20° east-of-south orientation combined with optimized openings increased thermal efficiency [18], and strategic planning of both variables improved lighting and energy indicators without additional cost [19].

Further studies confirmed the need to evaluate orientation and openings together. Energy savings reached 9% when optimizing orientation based on climate [20], and geometric optimization with evolutionary algorithms reduced consumption by 11% [21]. Adjusting insulation thickness according to façade exposure led to reductions of up to 70.3% [22].

Studies on architectural design demonstrate its impact on thermal and environmental efficiency. Research on traditional housing in Xuzhou proposed principles to guide low-energy buildings [23]. A parametric model for early-stage design identified high-demand typologies and reduced construction costs [24]. Architectural optimization enhanced thermal performance, lowered emissions, and improved economic outcomes. Energy demand decreased by 34.5%, with CO_2 emissions reduced to 57.6 kg/m^2·year through design strategies and building management systems [25].

Alternative materials such as sand and rice husk ash in concrete reduced thermal resistance cost by 20.3–39.1% and emissions by 20.2–38.9% [26]. Advanced envelope materials also decreased energy use and environmental impact [27]. However, their application remains limited due to high cost and performance uncertainty. In contrast, passive low-cost strategies continue to offer effective solutions in cold-climate housing. Passive measures reduced thermal exposure by 69–91% and consumed up to 100 times less energy than HVAC systems [28]. These results highlight the importance of integrating multiple architectural variables. Although orientation and glazing have been widely analyzed, few studies address their combined influence on thermal performance.

This study evaluates the impact of envelope orientation on the thermal performance of a standard room. It identifies the orientations with the highest thermal loads and proposes optimized configurations of materials, thicknesses, and glazing types tailored to climates with significant seasonal variations.

2 Model Description and Thermal Considerations

The simulation used thermal properties reported in previous studies [4, 31]. The multilayer envelope incorporated reinforced concrete, clay brick, and concrete to adjust thermal behavior. Indoor temperature was fixed at seasonal comfort levels under constant HVAC operation [32]. Internal loads, occupancy schedules, and ventilation rates were excluded to isolate the envelope's thermal response. These assumptions defined uniform boundary conditions and ensured valid comparison across scenarios.

2.1 Heat Transfer Model and Solar Radiation Variability

The model resolves heat transfer through two analysis levels. The differential approach solves conduction, convection, and radiation in the glazing using the finite volume method (FVM), which provides detailed profiles and layer interactions. The global approach applies an energy balance to estimate heat exchanges between the room and the environment, considering material properties and outdoor conditions. Each envelope surface receives solar radiation based on orientation and seasonal solar paths, defining winter gains and summer loads.

The modular subroutine structure allows insertion of passive systems in walls or roofs. Each subsystem resolves heat transfer through FVM, and feeds results into the global energy balance. This configuration supports orientation-based evaluation of passive strategies.

2.2 Simulation and Thermal Evaluation

Figure 1 illustrates the schematic of the simulation model used to evaluate the thermal performance of a room based on orientation and glazing type. The model includes three sections: (1) input data, which define climatic conditions, thermal properties, and room configuration; (2) simulation, based on a global energy balance and a differential model that uses the finite volume method and allows the integration of subroutines for passive systems; and (3) results, which report surface temperatures, thermal loads, and recommendations to improve thermal comfort. This study applied only the subroutines related to glazing. The model can incorporate other passive strategies in future analyses.

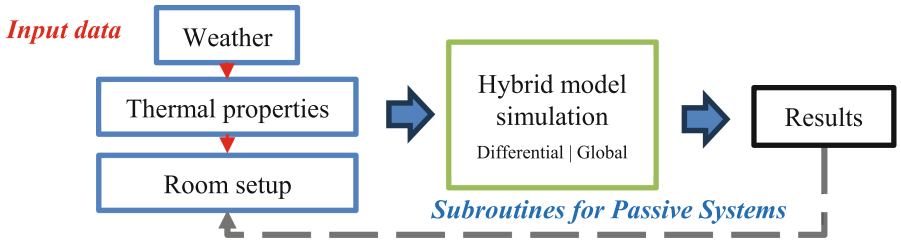


Fig. 1. Scheme of the simulation and thermal assessment model.

This study focused on glazing and room orientation; therefore, only the subroutine for glazing thermal resolution was applied. Other subroutines will be included in future work, selected based on thermal patterns in the envelope to evaluate the impact of passive systems such as advanced insulating materials.

Daqing, China, has a humid continental climate (Dwa, Köppen), with large seasonal temperature differences. Winter temperatures drop below −30 °C and summer temperatures exceed 30 °C, with high humidity [29]. Figure 2 shows strong seasonal temperature variation in Daqing. Siberian winds increase winter heat loss; high solar radiation and humidity raise summer cooling loads. Peak radiation on exposed façades emphasizes the need for proper glazing and passive strategies in variable climates.

The thermal properties were based on previous studies [4, 30, 31]. The simulation included reinforced concrete slab, clay brick, and concrete, with multilayer configurations. Indoor temperature followed seasonal comfort levels [32], assuming constant HVAC control. This allowed estimation of energy savings and CO_2 reduction. Envelope adjustments were made through iterative simulation and redesign.

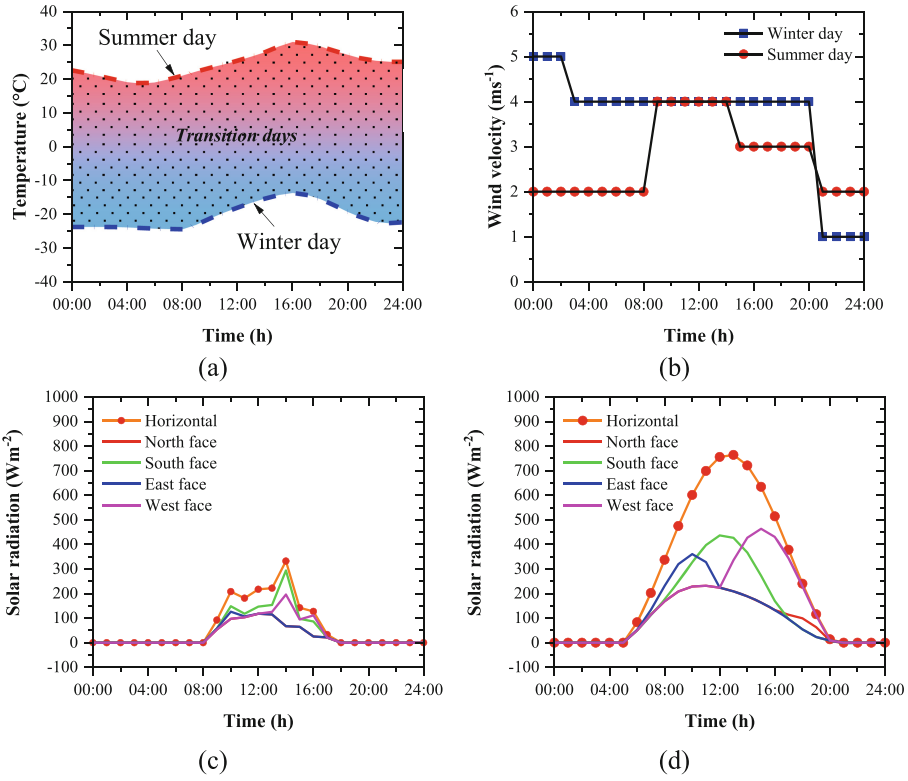


Fig. 2. Representative climatic conditions in Daqing, China. (**a**) Temperature variation in winter, summer, and transition days. (**b**) Wind velocity on representative days. (**c**) and (**d**) Incident solar radiation on different orientations.

3 Results

This section evaluates thermal load by orientation to identify surfaces with highest demand and define passive strategies. Insulation, PCM, or other solutions are recommended for exposed elements, based on results, without the need for further simulations.

3.1 Passive Strategies for Thermal Optimization

Figure 3 shows the thermal load distribution in winter (a) and summer (b). The vertical axis represents the energy required to maintain indoor comfort: heating in winter and cooling in summer. Glazing and the roof show the highest demands in winter, while glazing, the roof, and east–west façades present the largest loads in summer. These patterns demonstrate that both seasonal extremes must be addressed through tailored passive strategies.

Glazing registers the highest thermal exchange year-round. Low-emissivity glass with solar control reduces winter heat loss and summer gains and preserves daylight. The roof benefits from insulation and reflective coatings to minimize losses and solar absorption. East and west walls require shading and high-inertia materials to stabilize indoor temperature. Although the floor has a minor role, slab insulation improves performance in extreme cold. Tailored strategies for each surface ensure year-round efficiency.

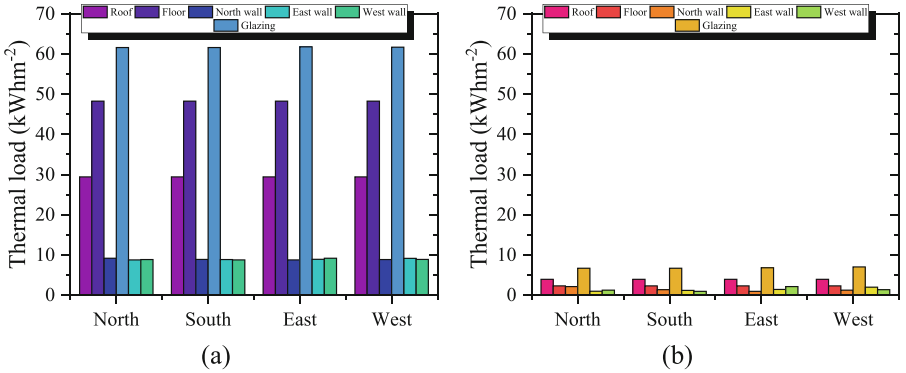


Fig. 3. Thermal load by envelope element: (**a**) winter, (**b**) summer.

4 Discussion

This section compares the results with previous studies, analyzes thermal, economic, and environmental implications, and identifies study limitations. It also validates the proposed strategies and outlines potential model improvements through configuration and code adjustments.

Table 1 presents passive strategies for climates with strong seasonal variation, evaluated through this study. It includes orientation, glazing, insulation, shading, nighttime ventilation, and thermal mass. Each strategy is classified by feasibility and impact, with associated limitations and recommendations for similar contexts.

Daqing, in northeastern China, has a continental climate (Dwa) with cold winters and warm summers. This study evaluates passive strategies—insulation, orientation, thermal mass, shading, and nighttime ventilation—by cost (USD), thermal impact (%), CO_2 reduction, durability, and long-term return over periods of at least ten years.

4.1 Thermal Insulation and Envelope Sealing

Envelope orientation influences energy demand and guides passive design. In cold climates like Daqing, insulation and triple glazing reduce energy use by 66% and CO_2 emissions by 43% [34]. Each kilowatt-hour saved avoids 0.5–0.8 kg of CO_2. Full retrofits lower heating needs by up to 70% [33].

Initial costs rise by 20%–50% ($50–$100 USD/m^2), but payback occurs in 12 years. Optimized designs reduce demand to 115 kWh/m^2·year and cut operating costs. Materials such as XPS, mineral wool, and triple glazing preserve efficiency. Airtight envelopes with vapor barriers and sealed joints prevent infiltration and ensure comfort. Long-term savings and emission reductions are proven in passive buildings [35].

Table 1. Comparison of passive measures in Daqing and similar regions.

Reference	Proposed solution	Feasibility	Impacts	Limitations	Recommendation
Habibi (2020)	Optimize building orientation	High	Up to 40% heating reduction	Depending on climate and location	Areas with strong seasonal variation
Zheng et al. (2019)	Adjust orientation and openings	High	Up to 46% energy savings	Limited to cold climates	Passive designs in cold regions
Zhang et al. (2021)	20° east of south orientation	Medium	Improved thermal balance	Not suitable for all climates	Traditional houses (e.g., Xuzhou)
González et al. (2018)	Window layout for daylighting	High	Energy and visual comfort gains	Requires early-stage planning	Cold/temperate climates
Cherier et al. (2020)	Orientation + envelope optimization	High	9% energy savings	Requires cost validation	Low-energy design goals
Wang et al. (2021)	Parametric design (size, orientation)	Medium	11% annual reduction	Needs simulation tools	Early design optimization
Canbolat (2019)	Wall insulation by orientation	High	70.3% savings; 6-year ROI	High upfront cost	High-performance envelopes
Sun et al. (2020)	Predictive model for thermal design	Medium	Guides early decisions	Depends on input accuracy	Sustainable housing design
Shi et al. (2022)	Material selection	High	20–39% cost reduction, less CO_2	Access to innovative materials	Extreme climates

(*continued*)

Table 1. (*continued*)

Reference	Proposed solution	Feasibility	Impacts	Limitations	Recommendation
Lian & Wang (2021)	Passive + BMS integration	High	34.5% less energy, 57.6 kg $CO_2/m^2 \cdot yr$	High initial investment	Smart low-energy buildings

4.2 Optimal Orientation and Passive Solar Utilization

Orientation modifies thermal load at no additional cost [33]. South-oriented glazing with shading improves seasonal efficiency. This strategy requires no maintenance and reduces CO_2 emissions, though land or zoning constraints may limit its use.

4.3 Thermal Mass and Heat Storage

Thermal mass regulates indoor temperature in climates with strong daily fluctuations like Daqing. South-facing façades and high-inertia materials lower heating and cooling demand. Trombe walls reduce heating needs by up to 30%, while PCM-enhanced walls cut fuel use by 43% [33]. This solution requires minimal investment.

Fuel and CO_2 reductions match the thermal load decrease. In Daqing, thermal storage walls paired with conventional systems cut fuel use by nearly 50% [34]. In summer, night ventilation and thermal mass evacuate heat passively. PCMs and massive walls retain performance for decades and require no major maintenance [35].

4.4 Passive Shading and Efficient Windows

Shading limits summer gains and permits winter solar access. Overhangs, blinds, and louvers reduce cooling demand by 5%–15%; extended overhangs reach 12%. Double glazing increases efficiency by 50% compared to single-pane glass, reduces losses, and preserves daylight [35].

Costs vary. Overhangs and blinds require moderate investment; vegetation offers free seasonal shading. Triple glazing raises cost but improves thermal balance. These systems offer long durability with minimal maintenance. Shading and glazing reduce electricity use, lower CO_2 emissions, and improve comfort.

4.5 Nighttime Ventilation and Natural Cooling

Night ventilation reduces heat buildup and lowers cooling demand in Daqing. This widespread practice in northern China takes advantage of cooler nights. Studies indicate 15–30% less cooling demand; in high-inertia homes, air conditioning use fell by 27% [36]. Some cases reported full elimination of active cooling.

Costs remain low with operable windows. Manual systems suffice, while automation improves performance. Maintenance is minimal. A 1.5 kW unit turned off for several hours per day saves hundreds of kilowatt-hours per season. One study reported a 15% reduction per day maintained over ten summers [36]. A 200 kWh decrease prevents approximately 140 kg of CO_2. The integration of this measure with thermal mass and shading increases overall efficiency.

4.6 Long-Term Costs, Accumulated Savings, and Return on Investment (ROI)

Passive strategies in cold climates reduce energy use and emissions with long-term benefits. Although costs rise by 20–30%, savings recover the investment within 10–12 years [33]. In Daqing, passive measures cut thermal load by 70%, cooling demand by 30%, and energy use by up to 90%. These improvements also enhance comfort and property value. Annual CO_2 emissions decrease by 5 tons and reach a total reduction of 50 tons over 10 years. In Tongchuan, retrofits reduced emissions in 3–4 years [34].

Insulation, thermal mass, and orientation adjustments reduce heating demand by over 60% in Daqing. These strategies improve performance through durable materials and minimal maintenance. Due to strong seasonal contrasts, a multi-objective optimization process defines the best passive combination under thermal and economic constraints.

4.7 Limitations of the Study

This study excluded internal heat gains and ventilation to isolate the thermal behavior of the envelope. Although this simplification assumes ideal conditions, it does not affect the consistency of the comparison among design alternatives.

5 Conclusions

This study confirms that envelope orientation affects energy demand and introduces a hybrid approach that captures both local and global thermal behavior. Results show higher summer gains on east and west façades, and major winter losses through the roof and glazing. Passive strategies reduce thermal load by up to 70% and cooling demand by 30%. The hybrid model defines criteria to optimize insulation, glazing, and shading per orientation and addresses the limitations of uniform-envelope analyses. Thermal mass, nighttime ventilation, and shading enhance performance and maintain low cost. The investment recovers within 10–12 years and confirms feasibility. Orientation-based optimization increases energy efficiency in climates with strong thermal variation.

References

1. Toroxel, J.L., Silva, S.M.: A review of passive solar heating and cooling technologies based on bioclimatic and vernacular architecture. Energies. **17**(5), 1006 (2024)
2. Al-Shatnawi, Z., Hachem-Vermette, C., Lacasse, M., Ziaeemehr, B.: Advances in cold-climate-responsive building envelope design: a comprehensive review. Buildings. **14**(11), 3486 (2024)

3. Almusaed, A., Yitmen, I., Myhren, J.A., Almssad, A.: Assessing the impact of recycled building materials on environmental sustainability and energy efficiency: a comprehensive framework for reducing greenhouse gas emissions. Buildings. **14**(6), 1566 (2024)
4. Wang, H., Liu, B., Wu, W.: Optimizing the integration of building materials, energy consumption, and economic factors in rural houses of cold regions: a pathway. Buildings. **14**(9), 2760 (2024)
5. Yin, P., et al.: Winter indoor thermal environment and heating demand of low-quality centrally heated houses in cold climates. Appl. Energy. **331**, 120480 (2022)
6. Zhang, X., Xiao, F., Li, Y., Ran, Y., Gao, W.: Energy flexibility and resilience analysis of demand-side energy efficiency measures within existing residential houses during cold wave event. Build. Simul. **17**(7), 1043–1063 (2024)
7. Aktemur, C., Çakır, M.T., Çakır, M.F.: Optimising of thermal insulation thickness based on wall orientations and solar radiation using heating-degree hour method. Case Stud Thermal Eng. **60**, 104725 (2024)
8. Li, D., Ma, Y., Zhang, S., Yang, R., Zhang, C., Liu, C.: Photothermal and energy performance of an innovative roof based on silica aerogel-PCM glazing systems. Energy Convers. Manag. **262**, 115567 (2022)
9. Ma, L., et al.: Energy performance of a rural residential building with PCM-silica aerogel sunspace in severe cold regions. Energ. Buildings. **280**, 112719 (2022)
10. Delarami, A., Mohammadbeigi, A., Gharib, M.R.: The influence of the climate, the materials of the walls, and the gas effects of double and triple-glazed windows in terms of energy evaluation and economic expenses. Results Eng. **23**, 102793 (2024)
11. Mujeebu, M.A., Ashraf, N.: Energy-saving benefits of thermal insulation and glazing in code-compliant office building in cooling-dominated climates. Renew. Sust. Energ. Rev. **199**, 114532 (2024)
12. Zong, C., Chen, X., Deghim, F., Staudt, J., Geyer, P., Lang, W.: A holistic two-stage decision-making methodology for passive and active building design strategies under uncertainty. Build. Environ. **251**, 111211 (2024)
13. Harshalatha, N., Patil, S., Kini, P.G.: A review on simulation based multi-objective optimization of space layout design parameters on building energy performance. J. Build. Pathol. Rehabil. **9**(1) (2024)
14. Ratmia, F.Z.B., et al.: Street design strategies based on spatial configurations and building external envelopes in relation to outdoor thermal comfort in arid climates. Sustainability. **16**(1), 221 (2023)
15. Jayalath, A., Vaz-Serra, P., Hui, F.K.P., Aye, L.: Thermally comfortable energy efficient affordable houses: a review. Build. Environ. **256**, 111495 (2024)
16. Habibi, S.: The effect of building orientation on energy efficiency. Clean Techn. Environ. Policy. **26**(4), 1315–1330 (2023)
17. Zheng, C., Xu, W., Wang, L., Cao, X., Li, M., Zhang, A.: Multi-objective optimization of energy, thermal and visual comfort for dormitory buildings in the cold climate of China. Indoor Built Environ. **33**(2), 250–268 (2023)
18. Zhang, M., Fang, Z., Liu, Q., Zhang, F.: Simulation and analysis of factors influencing climate adaptability and strategic application in traditional courtyard residences in hot-summer and cold-winter regions: a case study of Xuzhou, China. Sustainability. **16**(19), 8676 (2024)
19. González, J., Da Costa, B.B.F., Tam, V.W.Y., Haddad, A.: Effects of latitude and building orientation in indoor-illuminance levels towards energy efficiency. Int. J. Constr. Manag. **24**(7), 784–798 (2023)
20. Cherier, M.K., et al.: Impact of glazing type, window-to-wall ratio, and orientation on building energy savings quality: a parametric analysis in Algerian climatic conditions. Case Stud Thermal Eng. **61**, 104902 (2024)

21. Wang, M., Xu, Y., Shen, R., Wu, Y.: Performance-oriented parametric optimization design for energy efficiency of rural residential buildings: a case study from China's hot summer and cold winter zone. Sustainability. **16**(19), 8330 (2024)
22. Canbolat, A.S.: Comprehensive cost–energy evaluation of wall insulation for diverse orientations and seasonal usages. Appl. Sci. **14**(18), 8239 (2024)
23. Zhang, M., Liu, F., Liu, Q., Zhang, F., Li, T.: Climate adaptation analysis and comfort optimization strategies for traditional residential buildings in hot-summer, cold-winter regions: a case study in Xuzhou, China. Sustainability. **16**(8), 3411 (2024)
24. Sun, M., Xue, Y., Wang, L.: Research on optimized design of rural housing in cold regions based on parametrization and machine learning. Sustainability. **16**(2), 667 (2024)
25. Liang, R., Wang, P.: Enhancing energy efficiency in buildings, optimization method and building management systems application for lower CO_2 emissions. Energy. **134054** (2024)
26. Shi, J., Zhang, M., Zhu, X., Yalçınkaya, Ç., Çopuroğlu, O., Liu, Y.: Evaluation of thermal insulation capacity and mechanical performance of a novel low-carbon thermal insulating foam concrete. Energ. Buildings. **323**, 114744 (2024)
27. Ghazwani, K., Beach, T., Rezgui, Y.: Energy retrofitting using advanced building envelope materials for sustainable housing: a review. Build. Environ. **112243** (2024)
28. Aijazi, A., Parkinson, T., Zhang, H., Schiavon, S.: Passive and low-energy strategies to improve sleep thermal comfort and energy resilience during heat waves and cold snaps. Sci. Rep. **14**(1) (2024)
29. Liu, J., Gao, X., Ruan, Z., Yuan, Y., Dong, S.: Analysis of spatial and temporal distribution and influencing factors of fine particles in Heilongjiang Province. Urban Clim. **41**, 101070 (2021)
30. Salazar, S.L., Simá, E., Vargas-López, R., Yang, R., Li, D., Hernández-López, I.: Assessing different glazing types for energy savings and CO_2 reduction in a tropical climate: a comparative study. J Build Eng. **82**, 108188 (2023)
31. Salazar, S.L., Yang, R., Li, D., Chagolla-Aranda, M., Chávez-Chena, Y., Simá, E.: Advanced hybrid assessment of glazing systems: a comparative analysis using differential and global methods for precise thermal optimization and energy efficiency in building. J Build Eng. **111711** (2024)
32. Sánchez-García, D., Rubio-Bellido, C., Pulido-Arcas, J.A., Guevara-García, F.J., Canivell, J.: Adaptive comfort models applied to existing dwellings in Mediterranean climate considering global warming. Sustainability. **10**(10), 3507 (2018)
33. Cao, P., Wang, J., Huang, D., Cao, Z., Li, D.: Evaluation and analysis of passive energy saving renovation measures for rural residential buildings in cold regions: a case study in Tongchuan, China. Sustainability. **17**(2), 540 (2025)
34. Pan, W., Mei, H.: A design strategy for energy-efficient rural houses in severe cold regions. Int. J. Environ. Res. Public Health. **17**(18), 6481 (2020)
35. Mohammed, A., et al.: Reducing the cooling loads of buildings using shading devices: a case study in Darwin. Sustainability. **14**(7), 3775 (2022)
36. Darmanis, M., Çakan, M., Moustris, K.P., Kavadias, K.A., Nikas, K.P.: Utilisation of mass and night ventilation in decreasing cooling load demand. Sustainability. **12**(18), 7826 (2020)

Carbon Emission Index System and Effectiveness Evaluation of Carbon Reduction Measures in Substation Operational Phase

Yanfeng Wang[1], Can Fang[2], Huijun Wu[2(✉)], Jia Liu[2], Yanchen Liu[2], and Zhuwei Xie[2]

[1] Guangdong Power Grid Corporation Limited, Guangzhou, Guangdong 511400, China
[2] School of Civil Engineering and Transportation, Guangzhou University, Guangzhou, Guangdong 510004, China
wuhuijun@tsinghua.org.cn

Abstract. As critical energy hubs in power systems, substations face significant challenges in achieving net-zero operation due to the substantial carbon emissions associated with their infrastructure and operational processes. This study establishes a comprehensive carbon emission index system to evaluate and optimize the operational phase carbon footprint of substation facilities. Four functional categories were established based on the carbon emission composition of substations, and 12 key variables were identified. The analytic hierarchy process was used to determine variable weighting coefficients, while process based on life-cycle assessment combined with grey relational analysis enabled quantitative calculation of carbon indices across four representative substations. Implement carbon reduction measures for the two key variables of main transformers and air conditioning, and assess the carbon reduction effectiveness of substations based on sensitivity analysis. The results indicate that the proposed carbon index effectively characterizes operational emissions, achieving 89.7% evaluation accuracy. Deployment of high-efficiency transformers and advanced HVAC technologies demonstrated carbon intensity reductions of 28.2% and 4.4%, respectively. The developed indicator system provides dual functionality: facilitating emission diagnostics for existing facilities and guiding low-carbon design strategies for new substations. This methodology advances the development of quantitative assessment frameworks for achieving carbon-neutral substation operations in alignment with zero-energy building standards.

Keywords: Substation · Carbon Emission Index · Carbon Reduction

1 Introduction

The latest data show that global carbon emissions, driven by economic recovery in the post epidemic era, show a significant growth of 5.4% in 2021, with the growth rate narrowing to 1.9% in the following year [1]. Notably, the year-on-year increase

© The Author(s), under exclusive license to Springer Nature Singapore Pte Ltd. 2025
L. Ni et al. (Eds.): CCHVAC 2025, ESE, pp. 406–413, 2025.
https://doi.org/10.1007/978-981-95-3253-7_43

in global CO_2 emissions plummets to 0.1% in 2023 [2], As an energy-intensive basic industry, the power sector's carbon emission intensity and scale effect have significant leverage on the global carbon budget [3]. As the key energy hub of the transmission and distribution network of the modern power system, the sum of the building body energy consumption and equipment operation energy consumption of the substation group accounts for about 50% of the total energy consumption of the power grid system [4], and this energy efficiency feature illustrates the importance of energy saving and carbon reduction in substations.

At present, a multi-dimensional research framework has been formed for the operational efficiency evaluation system of substation buildings and equipment, mainly focusing on two major directions: energy consumption analysis and energy efficiency optimization. Oliveira et al. proposed a system-level loss assessment method that adopts a macroscopic perspective to analyze the characteristics of the overall energy consumption [5, 6], It is worth noting that the comprehensive evaluation index model established by Luo et al. by introducing grey correlation analysis effectively integrates the equipment operating parameters and environmental influences [7–9].

In terms of carbon reduction measures in substations, Dennice et al used adaptive control algorithms to improve the performance of distributed reactive power control of photovoltaic (PV) cells to reduce carbon emissions [10]; Park et al used a load shifting strategy that employs the concept of emerging locational marginal emissions to analyze carbon reduction in a more granular manner. of load shifting strategy to analyze the reduction of carbon emissions in a more refined way [11]. In the context of dual-carbon goals and strategies, there is an urgent need for research on evaluation methods that shift from energy consumption as a goal to carbon emissions as an indicator.

2 Carbon Emission Indicators and Assessment Methods for Substation Operation

2.1 Establishment of Carbon Emission System for Substation Operation Stage

In this study, a three-level dynamic assessment model integrating gray correlation analysis and hierarchical analysis is constructed (shown in Fig. 1), which divides the carbon emission index system of the substation operation phase into three hierarchical structures, namely, the target layer focuses on the carbon footprint accounting of the substation during the operation phase of the whole life-cycle, and the guideline layer is divided into four core dimensions based on the sources of carbon emission, and 12 key indexes are dynamically correlated by gray correlation analysis. Dynamic correlation analysis of 15 key indicators through gray correlation analysis.

2.2 Calculation of Carbon Emissions from Substation Operation

Primary Equipment (*A*). The operational losses of the high-voltage equipment in the substation (main transformers, reactors, capacitors) are the main factor affecting the carbon emissions of the substation, so the scenario layer of type A is the product of the losses of the high-voltage equipment and the carbon emission factor of the electricity per unit of time.

Secondary Equipment (*B*). The energy efficiency of secondary equipment (air conditioning equipment, lighting equipment, ventilation equipment, green energy equipment) in substations is one of the factors affecting carbon emissions from substations. Carbon emissions from secondary equipment are the product of equipment energy efficiency and the carbon emission factor of electricity.

Operational Status (*C*). The degree of aging of substation equipment and the extent of greenhouse gas leakage from equipment during operation also affect the carbon emissions of substations. The carbon emissions of operational status are calculated as the product of equipment operation and the carbon emission factor of electricity.

Greening Factors (*D*). The green space vegetation in the substation station area absorbs carbon dioxide through photosynthesis, thus achieving carbon reduction, so type D is the amount of carbon dioxide absorbed by the green space vegetation in the substation.

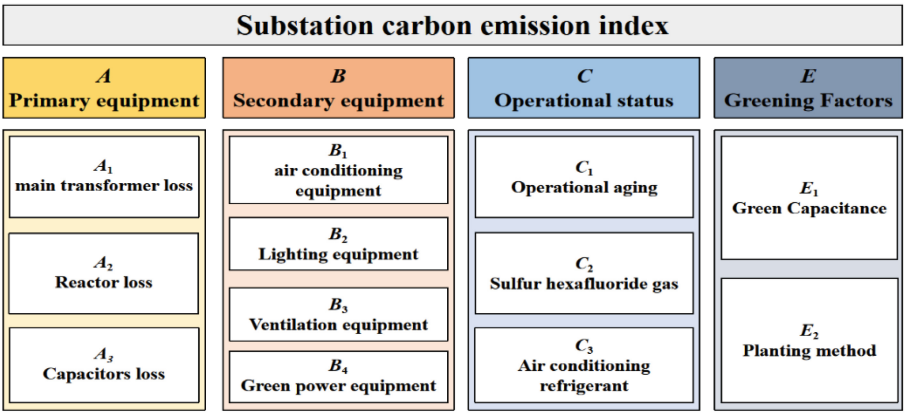


Fig. 1. Evaluation system model of substation carbon emission indicator.

2.3 Calculation of Carbon Emissions from Substation Operation

Gray correlation is a measure of the degree of correlation between the internal factors of an incomplete information system by serializing them and quantifying the degree of similarity and difference in the development trend between the factors. The degree of correlation of the carbon emission index of each substation is calculated as the carbon emission index of each substation. The correlation coefficient β_i is calculated based on the maximum value of the maximum difference and the minimum value of the minimum difference and the discrimination coefficient ρ calculated above, as calculated in Eq. (1):

$$CE = \sum_{i=1}^{n} \beta_i \times W_{\mathrm{i}} \tag{1}$$

where β_i is the correlation coefficient of the ith carbon emission. W_i is the weight value of the carbon emission composition of the ith substation.

3 Calculation of Carbon Emission Index for a Typical Substation

3.1 Typical Substations are Selected as Calculation Cases

Taking Guangdong area as an example, four substations of the same type were selected, and the basic engineering data of buildings and equipment were researched and collected to calculate and obtain the annual carbon emissions of each substation in the operation stage, as shown in Table 1.

Table 1. 4 typical examples of substations.

Substation	I	II	III	IV
Annual carbon emissions (t CO_2e)	527	574	532	585

3.2 Calculation Results of Key Factors of Carbon Emissions of Typical Substations

The process analysis method was used to calculate the composition of each carbon emission of the four substations, and the results are shown in Table 2; the gray correlation analysis method was used to calculate the carbon emission indexes in the operation stage of each substation, and the results are shown in Figure 4.

From the results of Fig. 2 and 3, it can be seen that the degree of influence of each key factor on the carbon emissions of the substation operation stage, in which the main transformer has the greatest influence on the carbon emissions of the substation, and the carbon emission value of the main transformer of the four typical substations is higher than that of the carbon emission value of other key factors.

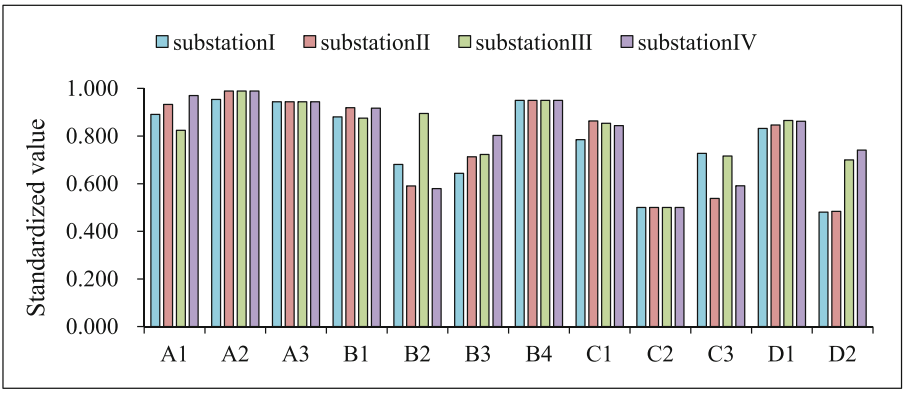


Fig. 2. Sequence of key factors after standardization of 4 substations.

Table 2. Calculated values of key factor indicators for 4 typical substations.

Substation	I	II	III	IV
A_1	44.545	46.629	41.213	48.513
A_2	3.815	3.956	3.956	3.956
A_3	0.189	0.189	0.189	0.189
B_1	0.132	0.138	0.131	0.138
B_2	0.613	0.531	0.805	0.522
B_3	0.644	0.713	0.723	0.803
B_4	0.475	0.475	0.475	0.475
C_1	0.471	0.518	0.512	0.506
Substation	I	II	III	IV
C_2	0.005	0.005	0.005	0.005
C_3	0.291	0.215	0.286	0.237
D_1	0.832	0.847	0.866	0.862
D_2	0.144	0.145	0.210	0.222

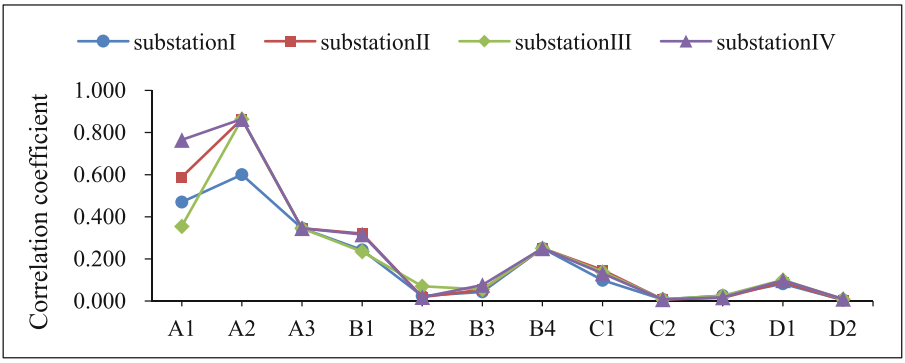


Fig. 3. Gray correlation values for each key factor at the 4 substations.

3.3 Calculation results of carbon emission index for typical substation

As can be seen from Fig. 4, the carbon emission index values of the four substations vary in the range of 0.2-0.5, with substation IV having the largest carbon emission index (0.404) and substation I having the smallest carbon emission index (0.284). Combined with the engineering data of the substations (Table 1), the commissioning time of substation IV and I shows that there is a large difference between the two commissioning times, and substation IV has a more serious aging of equipment, which corresponds to a larger carbon emission index; whereas the commissioning time of substation II and IV is $\geq$6 years, and the aging rate of equipment is higher, and the carbon emission index of

the substation is larger than that of substation I and III, and it can be seen that the newer substations have a smaller carbon emission index.

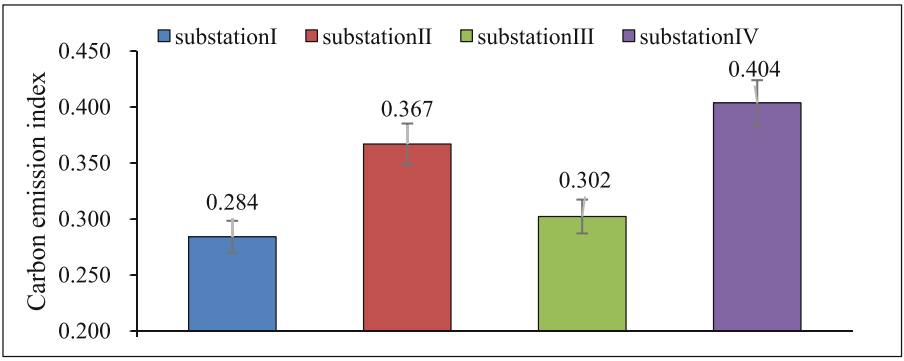


Fig. 4. Carbon emission target values for 4 substations.

4 Evaluation of Carbon Reduction Effects Based on Carbon Emission Indicators

4.1 Carbon Reduction Methodology Based on Carbon Emission Targets

Carbon emission indicators are used to study the carbon reduction effect of each major carbon reduction measure. Two major carbon reduction measures (main transformer carbon reduction and air-conditioning equipment carbon reduction) were selected and the carbon emission indexes were calculated after the changes.

4.2 Analysis of the Carbon Reduction Effect of Key Factors

Carbon Reduction Effect of Main Transformer. If the transformer losses are reduced, the carbon emission index calculation method is used to obtain the carbon reduction effect as shown in Figure 5. When the loss of the main transformer is reduced by 18.75kW, the carbon emission index in the operation phase of substation IV is reduced from 0.404 to 0.290, which is 28.2% lower. Substation II is reduced from 0.367 to 0.286, a reduction of 22.4%.

Carbon Reduction Effect of Air-Conditioning Equipment. If the energy efficiency ratio of the air conditioner is increased, the carbon reduction effect is obtained as shown in Fig. 6. When the air conditioning energy efficiency ratio is increased by 0.65, the carbon emission index in the operation phase of substation IV is reduced from 0.404 to 0.386, which is a reduction of 4.4%. Substation III, on the other hand, decreased from 0.302 to 0.290, a reduction of only 3.9%.

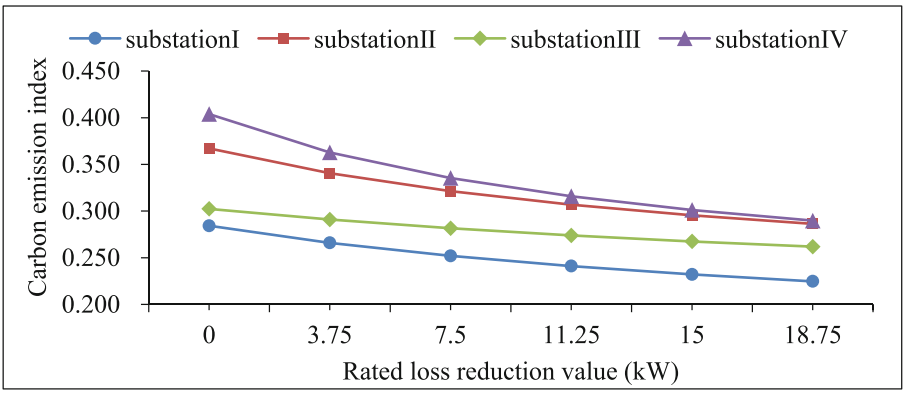


Fig. 5. Carbon reduction effect of main transformers in 4 substations.

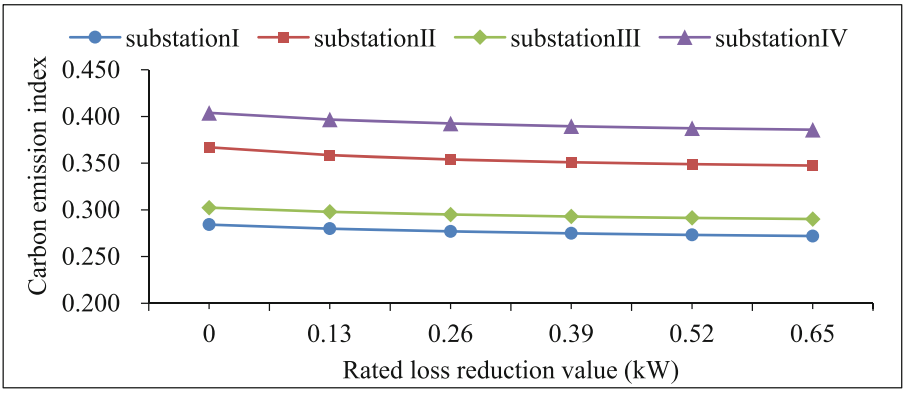


Fig. 6. Carbon reduction effect of air-conditioning equipment at 4 substations.

5 Conclusion

This paper proposes an evaluation system of operational carbon emission indicators for substations to assess the level of carbon emissions from substations. The main conclusions are as follows:

1. The annual carbon emissions of the substation are positively related to the carbon emission index, so the carbon emission index can effectively reflect the carbon emission level of the substation in the operation stage.
2. The main equipment of the substation, such as the main transformer loss, has the greatest impact on the carbon emission of the substation. When the loss of the main transformer is reduced by 18.25kW, the carbon emission index of the substation in the operation stage can be reduced by 28.2%.

3. The effect of improving the energy efficiency of building air-conditioning equipment in substations on carbon reduction in substation operation is 4.4%.

Acknowledgement. This work was sponsored by the "Funding for Technical Advisory Projects of China Southern Power Grid" (CG0300022001911736) and National Natural Science Foundation of China (Grant numbers: 52378092).

References

1. Friedlingstein, P., et al.: Global carbon budget 2024. Earth Syst Sci Data. **17**(3), 965–1039 (2025)
2. Liu, Z., et al.: Global carbon emissions in 2023[J]. Nat Rev Earth Environ. **5**(4), 253–254 (2024)
3. Calvin K, et al.: IPCC, 2023: Climate change 2023: synthesis report. Contribution of working groups I, II and III to the sixth assessment report of the intergovernmental panel on climate change [core writing team, H. Lee and J. Romero (eds.)]. IPCC, geneva, switzerland. First. Intergovernmental Panel on Climate Change (IPCC) (2023)
4. Wei, W., et al.: Embodied greenhouse gas emissions from building China's large-scale power transmission infrastructure. Nat Sustainaby. **4**(8), 739–747 (2021)
5. Oliveira, M.E., Padilha-Feltrin, A.: A Top-Down approach for distribution loss evaluation. IEEE Trans Power Delivery. **24**(4) (2029)
6. Yuan, J., et al.: Analysis and evaluation of the operation data for achieving an on-demand heating consumption prediction model of district heating substation. Energy. **214**, 118872 (2021)
7. Zhikun, L., et al.: Energy efficiency evaluation index system and modeling method of substations. Electric Power Automat Equip. **37**(3), 132–138 (2017)
8. Tanaka, H., et al.: Multiple criteria assessment of substation conditions by pair-wise comparison of analytic hierarchy process. IEEE Trans Power Delivery. **25**(4) (2010)
9. Farsani, E.A., et al.: A novel policy for LMP calculation in distribution networks based on loss and emission reduction allocation using nucleolus theory. IEEE Trans Power Syst. **31**(1), 143–152 (2016)
10. Yeh, H.G.: Adaptive VAR control for distribution circuits with photovoltaic generators. IEEE Trans Power Syst. **27**(3) (2012)
11. Park, B., et al.: Decarbonizing the grid: utilizing demand-side flexibility for carbon emission reduction through locational marginal emissions in distribution networks. Appl Energy. **330**, 120303 (2023)

Study on a Simplified Heat Transfer Model for the Roof Ventilated Desiccant Bed

Sheng Liu and Xinhua Xu(✉)

Huazhong University of Science and Technology, 430074 Wuhan, China
bexhxu@hust.edu.cn

Abstract. The roof ventilated desiccant bed is a passive building energy-saving device that directly utilizes solar energy for building insulation and indoor dehumidification. Its operation involves significant thermal-moisture coupling effects, with complex heat and moisture transfer mechanisms and computational processes. This study analyzes the heat transfer process of the roof-integrated passive regenerative drying bed under direct solar radiation. A simplified heat transfer model was established based on the lumped parameter method and energy conservation principles, with model parameter identification accomplished through COMSOL simulation data and the differential evolution algorithm. Further comparative analysis of computational results between this simplified heat transfer model and the numerical model under multi-cycle dynamic boundary conditions indicates: The simplified model demonstrates excellent agreement with numerical simulations, where the mean absolute error (MAE) of temperatures at characteristic nodes remains below 1.2 °C; the MAE of heat flux density at the inner surface is 1.71 W/m^2, with a mean absolute percentage error (MAPE) of 2.9% during the 10:00–16:00 period. Furthermore, its computational efficiency far surpasses that of the numerical model: the numerical model required approximately 48 minutes to complete the aforementioned case study, while the simplified model completed the same computation in merely 2.9 seconds on the same computer.

Keywords: Ventilated desiccant bed · Heat transfer characteristics · Simplified heat transfer model

1 Introduction

Humans spend approximately 80% of their time indoors [1], where relative humidity levels directly impact occupant comfort, health conditions, and building envelope durability. According to ASHRAE standards, residential indoor relative humidity should be maintained between 40% and 65% [2]. However, in China's hot summer and cold winter (HSCW) regions, summers are sweltering while winters are damp and cold, with substantial annual precipitation [3]. The average annual relative humidity ranges from 70% to 80%, reaching as high as 95% during transition seasons [4]. Conventional HVAC systems achieve dehumidification by cooling air below its dew point—an energy-intensive process accounting for 30%–50% of total air-conditioning energy consumption [5]. Therefore, reducing indoor latent heat loads or adopting higher-efficiency dehumidification systems is crucial for improving building energy efficiency.

© The Author(s), under exclusive license to Springer Nature Singapore Pte Ltd. 2025
L. Ni et al. (Eds.): CCHVAC 2025, ESE, pp. 414–423, 2025.
https://doi.org/10.1007/978-981-95-3253-7_44

Compared to the high energy consumption of traditional refrigeration-based dehumidification, solid desiccant technology uses porous materials to adsorb water vapor, offering lower regeneration temperatures and the ability to harness low-grade energy sources such as waste heat or solar energy [6]. Ref. [7] designed a solar-regenerated solid desiccant bed with a maximum hourly moisture removal capacity of 4.3 g/kg. Ref. [8] developed a solar-driven desiccant window that regenerates silica gel within the window assembly, achieving an average capacity of 2.6 g/kg.

Building on this research, the present study proposes a roof ventilated desiccant bed—a passive energy-saving system utilizing solar energy for insulation and indoor dehumidification. However, its operation involves strong thermal-moisture coupling, leading to complex heat and mass transfer processes and increased computational difficulty. Current studies primarily rely on numerical simulations (e.g., Ansys Fluent, COMSOL Multiphysics), which, despite high precision, are computationally intensive and time-consuming, limiting their suitability for rapid, multi-cycle dynamic analysis.

In contrast, the lumped parameter method has shown promise in simplifying heat transfer modeling in buildings. By discretizing continuous temperature fields into uniform-temperature nodes and representing their interactions via thermal resistance-capacitance (RC) networks [9], it enables efficient analysis. Ref. [10] applied this approach to a phase change material (PCM) wall, achieving temperature prediction errors below 0.5 °C and requiring only 0.4% of the computation time compared to Fluent [11]. Ref. [12] used a simplified 2D steady-state model for radiant concrete cooling panels, with prediction errors under 6%. Ref. [13] developed an RC model for embedded-tube radiant floors, which showed strong agreement with a frequency-domain finite difference model, validating its accuracy.

This study focuses on the roof ventilated desiccant bed, analyzing its heat transfer process and developing a simplified heat transfer model based on the lumped parameter method. Using multi-operational-point simulation data from COMSOL, global optimization of the model's equivalent thermal resistance parameters was achieved via the differential evolution algorithm. The computational accuracy and efficiency of this simplified model were further evaluated through comparison with COMSOL simulation data under multi-cycle dynamic boundary conditions.

2 The Roof Ventilated Desiccant Bed

2.1 Physical Parameters

The roof ventilated desiccant bed is a passive energy-saving system that directly utilizes solar energy for building insulation and indoor dehumidification. Installed on rooftops at a fixed inclination, it operates in two distinct modes: nocturnal adsorption and daytime regeneration.

During the nocturnal adsorption phase, with both end valves closed, fans circulate warm, humid indoor air through the desiccant bed. The silica gel adsorbs moisture from the air, returning cool, dry air indoors for continuous dehumidification. The heat generated during adsorption is dissipated via natural convection and nocturnal sky radiation. During the daytime regeneration phase, the indoor air valve closes while both end

valves open. Solar radiation heats the collector plate, transferring energy to the desiccant layer and initiating moisture desorption. The resulting temperature rise, combined with the stack effect, drives upward airflow, expelling water vapor and completing the regeneration cycle. The operating principle is illustrated in Fig. 1(a).

The desiccant bed comprises multiple adsorption units, each consisting of a metal frame with internally coated desiccant. Each unit measures 1.5 m in length with a cross-section of 50 mm × 50 mm. The metal frame has a thickness of 1.5 mm, while the silica gel desiccant coating is 3 mm thick. A schematic cross-sectional view is provided in Fig. 1(b). Material properties of each component are listed in Table 1**.**

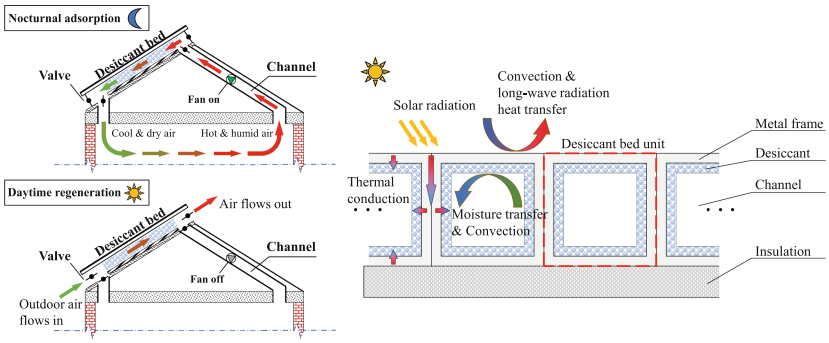


Fig. 1. Schematic diagram of the ventilated desiccant bed (**a**) and its cross-sectional view (**b**).

Table 1. Material properties of desiccant bed components.

Component	Material	Thickness mm	Density kg/m^3	Specific heat J/(kg·°C)	Thermal conductivity W/(m·°C)
Metal Frame	Aluminum Alloy 6063-T5	1.5	2700	900	210
Desiccant	Silica Gel	3.0	770	0.92	0.165

2.2 Heat Transfer Processes

To simplify the investigation, a single desiccant bed unit was selected as the research object, focusing on four key heat transfer processes: heat exchange between the metal frame and external environment, conductive heat transfer between the metal frame and desiccant, natural convective heat transfer within the air channel, and coupled heat-moisture transfer between the desiccant and air. Emphasizing the heat-moisture transfer

in silica gel desiccant, heat transfer is categorized into external and internal components, while moisture transfer occurs internally.

External heat transfer primarily involves solar radiation and natural convection with outdoor air. Given the high thermal conductivity and minimal thickness of the metal frame, the upper layer (solar collector plate) is reasonably assumed to have uniform temperature distribution. External heat gain (q_{out}) enters the silica gel desiccant via conduction as expressed in Eq. 错误!未找到引用源。.

$$q_{out} = \alpha_d E + h_{out}(T_{amb} - T_{d1}) + \varepsilon_d \sigma \left((T_{sky} + 273.15)^4 - (T_{p1} + 273.15)^4 \right) \quad (1)$$

Where, h_{out} is the convective heat transfer coefficient at the solar collector plate's upper surface, W/(m^2·°C); T_{amb} is the outdoor air temperature, °C; T_{p1} is the solar collector plate temperature, °C; T_{sky} is the sky temperature, °C; α_d and ε_d is the solar absorptivity and emissivity of the solar collector plate surface; E is the solar radiation intensity, W/m^2; σ is the Stefan-Boltzmann constant.

Internal heat transfer encompasses convective heat exchange between air and desiccant surfaces within the air channel, along with thermal effects from vapor desorption, calculated via Eq. 错误!未找到引用源。.

$$q_{in} = h_{in}(T_a - T_d) + k_m q_{ads}(Y_a - Y_d) \quad (2)$$

Where, h_{in} is the convective heat transfer coefficient at the desiccant surface, W/(m^2·°C); T_a is the air temperature within the channel, °C; T_d is the desiccant temperature, °C; k_m is the mass transfer coefficient at the desiccant-air interface, kg/(m^2·s); Y_a is the air humidity ratio in the channel, kg/kg; Y_d is the humidity ratio at the desiccant surface, kg/kg; q_{ads} is the adsorption heat of water, J/kg.

The energy conservation equation for silica gel desiccant is thus derived as Eq. 错误!未找到引用源。.

$$\frac{\partial T_d}{\partial \tau} = \frac{A_{out} q_{out} + A_{in} q_{in}}{M_d \left(C_{p,d} + W C_{p,w} \right)} \quad (3)$$

Where, τ is the time, s; A_{in} is the internal heat transfer area, m^2; A_{out} is the external heat transfer area at the metal frame, m^2; M_d is the total mass of desiccant and contained water, kg; $C_{p,d}$ is the specific heat capacity of desiccant, J/(kg·°C); $C_{p,w}$ is the specific heat capacity of liquid water, J/(kg·°C); W is the moisture content of desiccant, kg/kg; Other parameters retain their previously defined meanings.

3 Simplified Heat Transfer Model and Parameter Identification

3.1 Simplified Heat Transfer Model

This study employs the lumped parameter method to model heat transfer in the desiccant bed unit, temporarily disregarding thermal effects during moisture adsorption/desorption of silica gel desiccant. The unit is discretized into subregions, with the average temperature of each subregion represented by characteristic temperature nodes interconnected via an equivalent thermal resistance network. The schematic of the simplified heat transfer model is shown in Fig. 2(a), while actual dimensions of the desiccant bed are provided in Fig. 2(b).

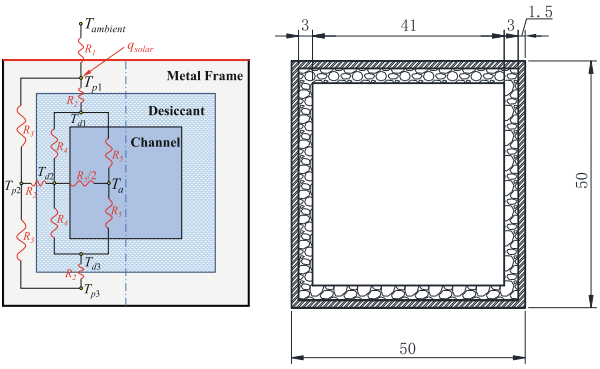


Fig. 2. Schematic diagram of the simplified heat transfer model (a) and actual dimensions of the desiccant bed (b).

The upper surface of the unit receives direct solar radiation. Adiabatic boundary conditions are applied to lateral interfaces contacting adjacent units, consistent with negligible lateral heat transfer in actual operation. Since the bottom of the desiccant bed is equipped with an insulation layer, it is also set as an adiabatic boundary condition. Given the unit's low thermal capacity and significant daytime temperature fluctuations induced by solar radiation, thermal inertia effects are neglected (i.e., thermal capacitances omitted). Based on energy conservation principles, the heat balance equations for each temperature node are expressed as Eq. 错误!未找到引用源。

$$\begin{aligned}
&\frac{T_{amb}-T_{p1}}{R_1}+\frac{T_{d1}-T_{p1}}{R_2}+\frac{T_{p2}-T_{p1}}{R_3}+Q_{solar}=0\\
&\frac{T_{p1}-T_{p2}}{R_3}+\frac{T_{p3}-T_{p2}}{R_3}+\frac{T_{d2}-T_{p2}}{R_2}=0\\
&\frac{T_{p2}-T_{p3}}{R_3}+\frac{T_{d3}-T_{p3}}{R_2}=0\\
&\frac{T_{p1}-T_{d1}}{R_2}+\frac{T_{d2}-T_{d1}}{R_4}+\frac{T_a-T_{d1}}{R_5}=0\\
&\frac{T_{d1}-T_{d2}}{R_4}+\frac{T_{p2}-T_{d2}}{R_2}+\frac{T_{d3}-T_{d2}}{R_4}+\frac{T_a-T_{d2}}{R_5/2}=0\\
&\frac{T_{d2}-T_{d3}}{R_4}+\frac{T_{p3}-T_{d3}}{R_2}+\frac{T_a-T_{d3}}{R_5}=0\\
&\frac{T_{d1}-T_a}{R_5}+\frac{T_{d2}-T_a}{R_5/2}+\frac{T_{d3}-T_a}{R_5}=Q_a
\end{aligned} \tag{4}$$

Where, T_{amb} is the ambient air temperature, °C; T_{p1}, T_{p2} and T_{p3} are the temperature nodes of metal frame subregions, °C; T_{d1}, T_{d2} and T_{d3} are the temperature nodes of desiccant subregions °C; T_a is the air temperature node in the channel °C; $R_1 \sim R_5$ are the equivalent thermal resistances between nodes, W/°C; Q_{solar} is the solar heat gain, W; Q_a is the heat transfer from the internal surface to air, W, calculated by Eq. 错误!未找到引用源。:

$$Q_a = \dot{m}c_p(T_{out} - T_{amb}) \tag{5}$$

Where, $\dot{m}$ is the air mass flow rate in the channel, kg/s; c_p is the specific heat capacity of air at constant pressure, J/(kg·°C); T_{out} is the outlet air temperature, °C; T_{amb} is the ambient air temperature (identical to inlet air temperature), °C.

The internal surface heat transfer area A_{in} is calculated as 0.123 m^2. The internal surface heat flux density is defined as $q_a = Q_a/A_{\text{in}}$, W/m^2.

3.2 Parameter Identification Method and Procedure

In the aforementioned simplified heat transfer model, Q_{solar} and T_{amb} serve as boundary conditions. To solve for nodal temperatures and heat transfer Q_a from the internal surface to air—and subsequently determine outlet air temperature T_{out}—the equivalent thermal resistances R_1 to R_5 require parameter identification.

This study employs the Differential Evolution (DE) algorithm for global optimization of thermal resistance parameters. DE is a population-based stochastic optimizer that efficiently explores continuous parameter spaces using differential mutation and competitive selection. Its mutation strategy, based on difference vectors, enhances global search capability and avoids local optima. Additionally, adaptive parameter tuning reduces reliance on initial population quality. The identification workflow is illustrated in Fig. 3.

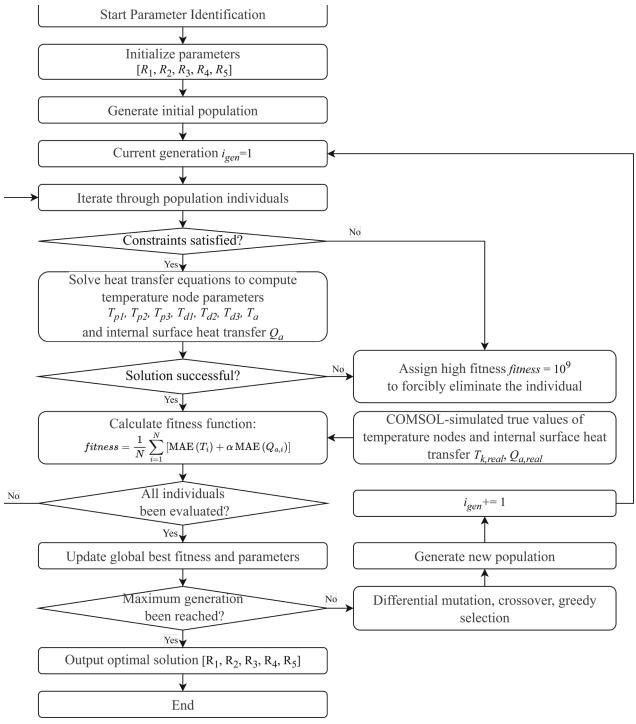


Fig. 3. Parameter identification flowchart for the simplified heat transfer model.

The DE algorithm evaluates individual fitness at each iteration, updating the population by comparing trial vectors against original individuals. The fitness function is

defined as Eq. 错误!未找到引用源。.

$$f(\mathbf{R}) = \frac{1}{N}\sum_{i=1}^{N}\left[\sum_{k=1}^{7}\left|T_{k,\text{real}}^{(i)} - T_{k,\text{pred}}^{(i)}(\mathbf{R})\right| + \alpha\left|Q_{\text{a,real}}^{(i)} - Q_{\text{a,pred}}^{(i)}(\mathbf{R})\right|\right] \tag{6}$$

Where, $\mathbf{R}$ is the optimization variable matrix $[R_1, R_2, R_3, R_4, R_5]$; N is the number of validation data points from numerical/experimental results; $T_{k,real}$ and $T_{k,pred}$ is the reference and predicted temperatures at the k-th node, °C; $Q_{a,real}$ and $Q_{a,pred}$ is the reference and predicted internal surface heat flux, W; α is the dimensional scaling factor ($\alpha = 1/\dot{m}c_p$), °C/W.

4 Parameter Identification Results and Model Validation

4.1 Parameter Identification Results

This study compares the simplified heat transfer model against numerical simulations conducted in COMSOL Multiphysics, utilizing simulation results to compute the fitness function for parameter identification. COMSOL—a finite element method-based multiphysics simulation platform—is widely employed for modeling and simulating complex systems. Its reliability and accuracy have been extensively validated through experiments, establishing its credibility in both academic research and industrial applications.

Hourly meteorological data for ten consecutive days in late July from Wuhan, China (totaling $N = 241$ operational points), served as boundary conditions (错误!未找到引用源。). Within COMSOL, the Non-Isothermal Flow coupling interface was activated, integrating laminar flow, solid heat transfer, and fluid heat transfer physics. Mesh independence verification confirmed an optimal computational grid of 415,000 elements. With an inlet velocity of 0.2 m/s, temperature distributions and internal surface heat flux density were solved (错误!未找到引用源。). These simulation results served as benchmark references for the identification procedure. The fitness function defined in Eq. 错误!未找到引用源。quantified the comprehensive deviation between the simplified model's predictions and simulation data, driving the parameter identification process (Figs. 4 and 5).

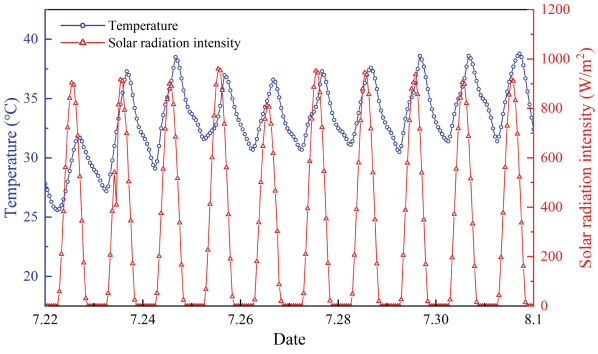


Fig. 4. Boundary conditions for numerical simulation.

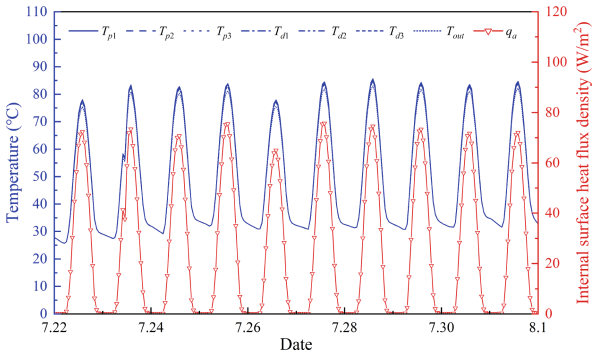


Fig. 5. Numerical simulation results.

The DE algorithm was configured as follows: (1) Mutation strategy: "best/current vector" approach, where the current population's best individual served as the base vector, augmented by a pair of random difference vectors (scaling factor F = 0.5). (2) Crossover strategy: Binomial crossover with probability CR = 0.9 to balance global exploration and local exploitation. (3) Population size: Fixed at 500 individuals to ensure comprehensive search space coverage.

The identification process converged to a stable solution at the 9th generation, yielding the following thermal resistance values: R_1 = 1.96 °C/W, R_2 = 0.15 °C/W, R_3 = 0.05 °C/W, R_4 = 28.00 °C/W, R_5 = 10.91 °C/W.

4.2 Model Validation

Using typical summer day meteorological data from Wuhan as boundary conditions, comparative calculations were performed between the simplified heat transfer model and COMSOL simulations. To eliminate initial condition effects in transient COMSOL calculations, seven full cycles (168 hours) were simulated, with the seventh cycle selected for error analysis.

As shown in 错误!未找到引用源。, temperatures across the desiccant bed nodes exhibit close alignment. 错误!未找到引用源。consequently focuses on comparative results for temperature node T_{p1} and internal surface heat flux q_a. The simplified model demonstrates strong agreement with COMSOL simulations, yielding mean absolute errors (MAE) of 1.14 °C for T_{p1} and 1.71 W/m^2 for q_a. Notably, during peak solar radiation hours (10:00–16:00), the mean absolute percentage error (MAPE) for q_a is merely 2.9%. All computational errors are summarized in 错误!未找到引用源。, with MAE values for characteristic node temperatures consistently below 1.2 °C. Given significant system temperature fluctuations ($\Delta T \approx 55$ °C), this accuracy satisfies engineering requirements (Fig. 6 and Table 2).

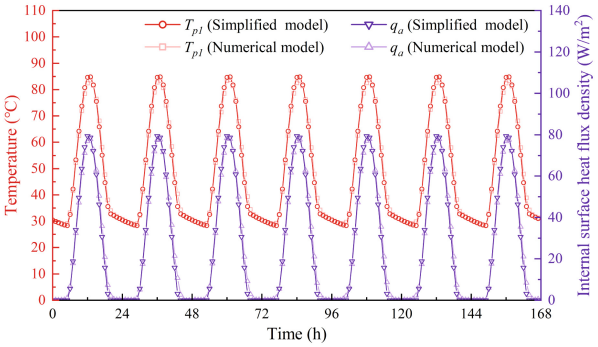


Fig. 6. Comparison of computational results between the simplified heat transfer model and numerical model.

Table 2. Computational errors of the simplified heat transfer model.

Parameters	T_{p1}	T_{p2}	T_{p3}	T_{d1}	T_{d2}	T_{d3}	T_{out}	q_a
MAE	1.10 °C	1.15 °C	1.18 °C	1.16 °C	1.12 °C	1.19 °C	1.04 °C	1.71 W/m^2

Regarding computational efficiency, on identical hardware (CPU i5-12490F), the COMSOL numerical model required approximately 48 minutes to complete the 168-hour simulation, while the simplified model accomplished equivalent calculations in merely 2.9 seconds—representing a 1000-fold efficiency improvement.

5 Conclusions

This study systematically analyzes heat transfer processes in roof ventilated desiccant beds under solar radiation, establishing a simplified heat transfer model based on lumped parameter methodology and energy conservation principles. Precise parameter identification was achieved through COMSOL simulations and differential evolution algorithms. Model validation under multi-cycle dynamic boundary conditions using Wuhan summer meteorological data yielded the following key findings. In terms of accuracy, the simplified model shows excellent agreement with numerical simulations. MAE values for all characteristic temperature nodes remain below 1.2 °C, while MAE for internal surface heat flux density is 1.71 W/m^2. During peak solar radiation (10:00–16:00), MAPE for heat flux is as low as 2.9%, confirming high computational precision. When the efficiency is of concern, under identical hardware configurations, the simplified model completed benchmark calculations in 2.9 seconds—approximately 1000 times faster than the 48-minute requirement of the numerical model—while maintaining accuracy. The developed model balances computational accuracy and efficiency, establishing a foundational analytical approach for subsequent studies on coupled heat-moisture transfer in desiccant beds.

References

1. Klepeis, N.E., et al.: The National Human Activity Pattern Survey (NHAPS): a resource for assessing exposure to environmental pollutants. J. Expo. Sci. Environ. Epidemiol. **11**(3), 231–252 (2001)
2. Qin, M., et al.: Precise humidity control materials for autonomous regulation of indoor moisture. Build. Environ. **169**, 106581 (2020)
3. Jing, L.J., Wang, J.: A study on the characteristics of energy consumption index of office buildings in hot-summer and cold-winter zone. Refrigeration Air Condition. **36**(2), 263–268 (2022) (in Chinese)
4. Ge, F., et al.: Energy savings potential of a desiccant assisted hybrid air source heat pump system for residential building in hot summer and cold winter zone in China. Energ. Build. **43**(12), 3521–3527 (2011)
5. Li, Z., et al.: Energy efficiency of dehumidification process from buildings. Heat Ventilat Air Condition. **35**(1), 90–96 (2005) (in Chinese)
6. Jeong, J., et al.: Performance analysis of desiccant dehumidification systems driven by low-grade heat source. Int. J. Refrig. **34**(4), 928–945 (2011)
7. Yang, W., et al.: Dehumidifying property testing of a solar directly regenerated solid dehumidification bed. Renew Energy Res. **34**(03), 332–338 (2016) (in Chinese)
8. Huang, H.P.: Structure Optimization and Experimental Investigation for the Solar Powered Dehumidification Window. Guangdong University of Technology, Guangzhou (2020) (in Chinese)
9. Tao, W.Q.: Heat Transfer. Higher Education Press, Beijing (2019) (in Chinese)
10. Yan, T., et al.: Dynamic simplified PCM models for the pipe-encapsulated PCM wall system for self-activated heat removal. Int. J. Therm. Sci. **144**, 27–41 (2019)
11. Yan, T.: Study on the Thermal Characteristics of the Pipe-Encapsulated Phase Change Material Wall System with the Self-Activated Heat Transfer. Huazhong University of Science and Technology, Wuhan (2021) (in Chinese)
12. Li, N., et al.: Research on heat transfer and cooling capacities of concrete radiant ceiling based on simplified RC-network model. J Hunan Univ (Natural Sciences). **44**(3), 143–150 (2017) (in Chinese)
13. Li, A.B., Xu, X.H.: Study on simplified RC heat transfer model of pipe-embedded radiant floors. J Huazhong Univ Sci Technol (Natural Science Edition). **42**(12), 16–20 (2014) (in Chinese)

Performance Simulation Study of Air Compression System Applied to Residential Air Conditioning

Rong Weilai, Ma Guoyuan(✉), Sun Shangyu, Xu Shuxue, and Nie Junrui

Beijing University of Technology, Beijing 100124, China
magy@bjut.edu.cn

Abstract. Research and technological innovation in the field of environmentally friendly refrigerants can effectively solve the problem of ozone layer depletion and help slow down the process of global warming. An air compression system suitable for residential air conditioning was proposed, which uses environmentally friendly refrigerant air as the working medium and studies its application effect in residential air conditioning. Through theoretical analysis of the heating and cooling performance of the system, its overall efficiency was evaluated. Using DeST and MATLAB tools, a simulation study was conducted on typical representative urban buildings in China's five major climate zones, and energy-saving operation strategies were proposed. The simulation results show that the air compression system performs well in low-temperature heating scenarios and with an average heating COP of 1.35 in severe cold regions and the highest annual performance coefficient APF in severe cold regions. This study has offers a key theoretical foundation for the subsequent engineering practice and product development of air compression systems.

Keywords: Air compression · Operation strategies · Residential air conditioning

1 Introduction

In recent years, China's urbanization process has been accelerating, and residents' pursuit of quality of life has been increasing, which has led to a significant increase in the market demand for household air conditioning. At present, household air conditioning equipment generally adopts vapor compression refrigeration systems, and the refrigerant used is mostly Freon. However, fluorocarbons have obvious drawbacks, not only causing damage to the atmospheric ozone layer, but also having a relatively high global warming index. According to the relevant provisions of the Montreal Protocol, some fluorocarbon refrigerants with high global warming potential (GWP) have been banned, and some will also be gradually reduced [1]. Although the GWP value of R290 refrigerant is relatively low, it has the characteristic of being flammable and explosive, which to some extent limits its wide application in the field of household air conditioning.

The air compression reverse Brayton cycle uses air as a refrigerant, which has the characteristics of safety, environmental protection, simple structure, and no pollution. In

© The Author(s), under exclusive license to Springer Nature Singapore Pte Ltd. 2025
L. Ni et al. (Eds.): CCHVAC 2025, ESE, pp. 424–431, 2025.
https://doi.org/10.1007/978-981-95-3253-7_45

recent years, air compression refrigeration systems have received increasing attention, but compared with traditional vapor compression refrigeration systems, air refrigeration systems have lower efficiency. Scholars have researched its performance improvement to enhance the system's performance. Sui et al. [2] proposed an air compression refrigeration system for data center cooling, established a thermodynamic model of the system, and calculated the impact of different indoor and outdoor temperatures and changes in component efficiency on system performance. Lin et al. [3] explored the application of air cooling systems in aircraft air conditioning, systematically elaborating on the system's cyclic operation mode and the technological evolution of turbo coolers. At the same time, they pointed out the future development direction of air cooling technology. Wang [4] studied an open reverse boost cycle system and built a new experimental platform for household air cooling systems, obtaining cooling capacity and air supply parameters. He believed that air cooling can directly supply air to the room and the air supply temperature can be adjusted.

At present, it has been applied in the aviation industry, military transportation, food freezing, and other fields [5–7]. The system adopts an open cycle and can provide fresh air for indoor use in residential buildings, ensuring the cleanliness of indoor air. It is a potential alternative to traditional vapor compression systems. This article proposes an air compression system suitable for residential air conditioning based on a compression expansion integrated compressor and analyzes the operational performance of the system. Based on the load characteristics of residential buildings, the system heating and cooling load was matched with the building load to study the applicability of typical representative urban buildings in China's five major climate zones, providing a theoretical basis for future applications.

2 System Principle

The air compression system applied to residential air conditioning is divided into refrigeration and heating modes. The schematic diagram of the refrigeration mode is shown in Fig. 1. The system consists of electrical machinery, a compression expander, a heat exchanger, valves, and pipelines. The electrical machinery is started to drive the compression expander for compression and expansion. The expansion work generated during the expansion process of the expander can be transmitted to the compressor through the shaft, reducing the system's power consumption. The compressor draws in air from the atmosphere and compresses it to produce high-temperature gas, which enters the heat exchanger for cooling. The cooled gas then enters the expander for expansion and cooling, and the expanded low-temperature air is sent into the space to cool the room. The room exhaust is sent to the heat exchanger and then discharged into the atmosphere to recover the cooling capacity of the room. Air compression systems can directly discharge low-temperature air into the room, eliminating the need for indoor heat exchangers and reducing heat transfer losses.

The schematic diagram of the heating mode is shown in Fig. 2. The compressor sucks in air from the room, compresses it, and discharges high-temperature gas, which enters the heat exchanger for cooling. The cooled gas enters the expander for expansion and pressure reduction, and the expanded low-temperature air is discharged into the

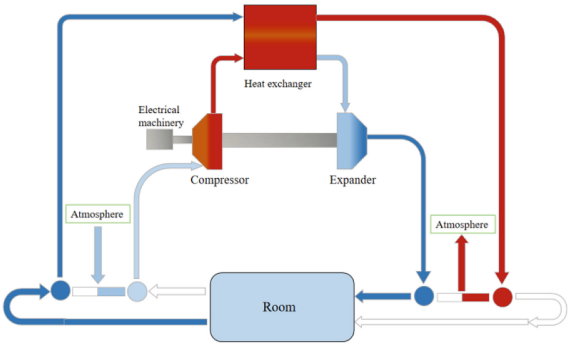


Fig. 1. Schematic diagram of refrigeration mode.

atmosphere; Inhale fresh air from the atmosphere, heat it up through a heat exchanger, and send it into the room to provide heating.

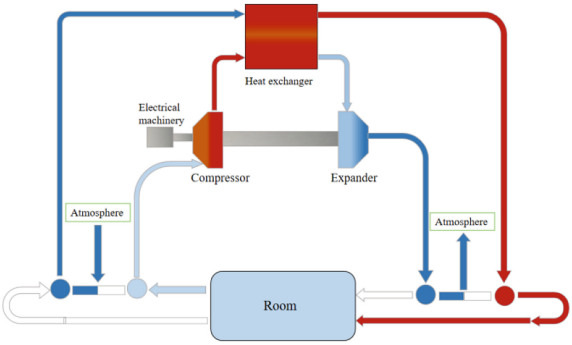


Fig. 2. Schematic diagram of heating mode.

3 System Performance

3.1 Winter Operational Performance

Figure 3 shows the heating capacity of the winter air compression system under different pressure ratios and air flow rates. According to Fig. 3, as the outdoor temperature increases, the heating capacity of the air compression system gradually increases. The higher the outdoor temperature, the higher the temperature in the room after heat exchange through the heat exchanger, increasing heating capacity. When the outdoor temperature and air flow rate are the same, the heating capacity of the system increases with the increase in pressure ratio. The higher the pressure ratio, the higher the exhaust temperature and the higher the room air supply temperature. Under the same outdoor temperature and pressure ratio, the larger the air flow rate, the greater the heating capacity. The air compression system has good heating performance at low temperatures.

When the outdoor temperature is −15 °C, the air flow rate is 0.3 kg/s, and the pressure ratio is 1.4, 1.5, and 1.6, the corresponding heating capacity can reach 8.12 kW, 9.95 kW, and 11.59 kW. With the increase in pressure ratio, heating capacity increased by 22.5% and 16.5%, respectively.

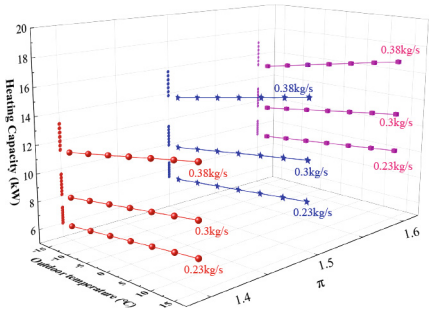


Fig. 3. Heating capacity of winter system under different pressure ratios and air flow rates.

Figure 4 shows the heating COP of the winter air compression system under different pressure ratios and air flow rates. According to Fig. 4, as the outdoor temperature increases, the COP of the air compression system gradually increases. As the outdoor temperature increases, the heating capacity of the system gradually increases and the power consumption of the system decreases, so the COP will gradually increase. When the outdoor temperature and air flow rate are the same, the heating COP of the system increases with the increase of pressure ratio. When the outdoor temperature is −15 °C and the air flow rate is 0.3 kg/s, the corresponding heating COP for pressure ratios of 1.4, 1.5, and 1.6 are 1.06, 1.14, and 1.20, respectively. With the increase of pressure ratio, heating COP increased by 7.5% and 5.2% respectively. The outdoor temperature ranges from −15 °C to 15 °C, and the COP range for system heating is 1.03–1.43.

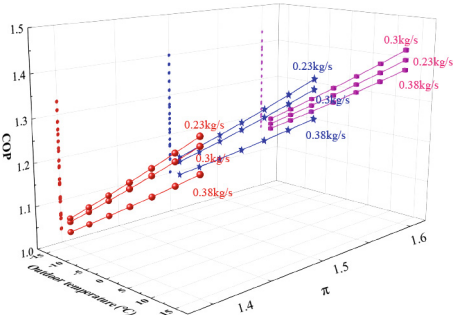


Fig. 4. Heating COP of winter system under different pressure ratios and air flow rates.

3.2 Summer Operational Performance

Figure 5 shows the cooling capacity of the summer air compression system under different pressure ratios and air flow rates. According to Fig. 5, as the outdoor temperature increases, the cooling capacity of the air compression system gradually decreases. The higher the outdoor temperature, the higher the temperature after heat exchange in the heat exchanger before being sent to the expansion machine, and the higher the outlet temperature of the expansion machine, resulting in a decrease in cooling capacity. When the outdoor temperature and air flow rate are the same, the cooling capacity of the system increases with the increase of pressure ratio, the expansion ratio increases, the exhaust temperature decreases, and the room air supply temperature decreases. Under the same outdoor temperature and pressure ratio, the larger the air flow rate, the greater the cooling capacity.

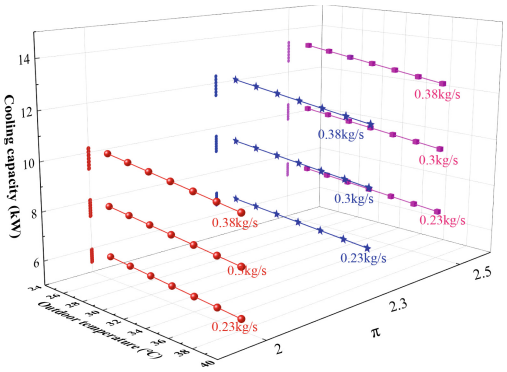


Fig. 5. Cooling capacity of summer system under different pressure ratios and air flow rates.

Figure 6 shows the cooling COP of the summer air compression system under different pressure ratios and air flow rates. From Fig. 6, it can be seen that as the outdoor temperature increases, the cooling COP of the air compression system gradually decreases. As the outdoor temperature increases, the cooling capacity of the system gradually increases, and the power consumption of the system increases, so the COP will gradually decrease. When the outdoor temperature and air flow rate are the same, the cooling COP of the system decreases with the increase of pressure ratio, because as the pressure ratio increases, the operating efficiency of the turbocharger decreases, so the cooling COP gradually decreases. When the outdoor temperature is 38 °C and the air flow rate is 0.3 kg/s, the corresponding refrigeration COP for pressure ratios of 2, 2.3, and 2.5 are 0.473, 0.47, and 0.439, respectively. With the increase of pressure ratio, the cooling COP decreased by 0.6% and 6.6%, respectively. The outdoor temperature ranges from 26 °C to 38 °C, and the refrigeration COP range is 0.35 ~ 0.58.

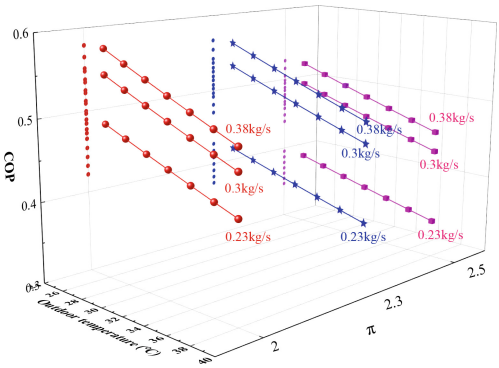


Fig. 6. Cooling COP of summer system under different pressure ratios and air flow rates.

4 Applicability Analysis of Air Compression System in Residential Buildings

Select five representative cities of climate zones, Harbin, Beijing, Shanghai, Guangzhou, and Kunming, and simulate the load characteristic values of the five representative cities under traditional buildings. The performance parameters of building maintenance structures, materials, and different room parameters are set according to the corresponding standards (designed according to the 2015 "Design Standard for Energy Efficiency of Public Buildings GB 50189-2015" [8], with indoor temperature of 20 °C in winter and 26 °C in summer, and humidity range of 30% −60%).

Figure 7 shows the building load and air compression system heating/cooling capacity of traditional buildings in five climate zones, with negative values representing building cooling load and cooling capacity. According to Fig. 7, the heating time in Harbin is longer than the cooling time throughout the year. The annual heating/cooling loads in Harbin, Beijing, Shanghai, Guangzhou, and Kunming are 0 ~ 13.73 kW/0 ~ 7.65 kW、0 ~ 9.69 kW/0 ~ 13.74 kW、0 ~ 7.69 kW/0 ~ 11.43 kW、0 ~ 5.2 kW/0 ~ 13.58 kW、0 ~ 6.25 kW/0 ~ 2.08 kW. The annual heat load demand of buildings is affected by regions and decreases in the order of Harbin, Beijing, Shanghai, Kunming, and Guangzhou. The heat load demand is highest in cold regions and lowest in hot summer and warm winter regions. The Kunming area has the lowest annual demand for building cooling load.

To meet the building load requirements of different regions, air compression systems can achieve different heating and cooling capacities by adjusting the pressure ratio. The pressure ratios under heating conditions in Harbin, Beijing, Shanghai, Guangzhou, and Kunming are 1.71, 1.41, 1.31, 1.21, and 1.21, respectively. Under heating conditions, the system pressure ratio decreases sequentially in Harbin, Beijing, and Shanghai, while the system pressure ratio remains the same in Kunming and Guangzhou. The pressure ratios under refrigeration conditions in Harbin, Beijing, Shanghai, Guangzhou, and Kunming are 1.71, 2.11, 2.21, 2.61, and 1.21, respectively. Under refrigeration conditions, the system pressure ratio increases in order along Kunming, Harbin, Beijing, Shanghai, and Guangzhou. The cooling load demand of buildings in Kunming is small, and the system

pressure ratio is the smallest. The pressure ratio of winter heating and summer cooling systems in Kunming and Harbin regions is the same, while the operating pressure ratio of summer systems in other regions is higher than that of winter systems.

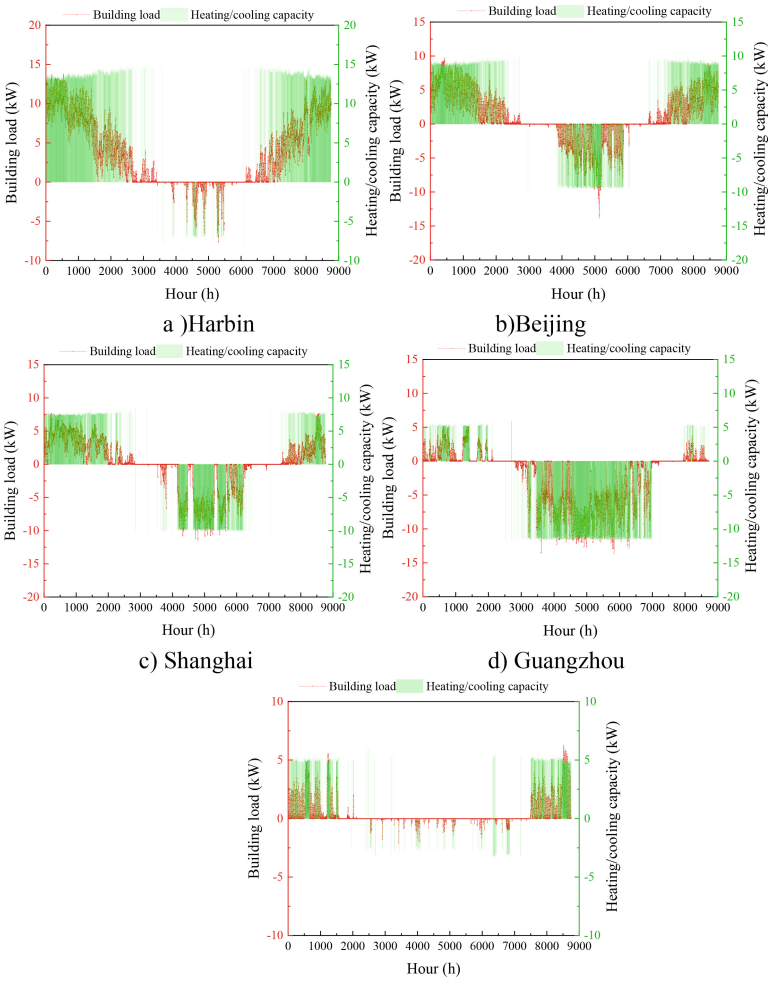


Fig. 7. Building Load and System Heating/Cooling Capacity.

Table 1 shows the annual operating conditions and performance coefficients of air compression systems applied to traditional buildings in representative cities in five major climate zones. Among them, the calculation of the annual performance factor (APF) of the air compression system adopts the following formula:

$$APF = \sum_{i=1}^{i=k} \frac{1}{k} COP_i H_i \tag{1}$$

In the formula, COP_i is the system COP at time i; H is the hour, h。

Table 1. The air compression system is applied to the annual operation and APF of representative cities in the five major climate zones.

Cities	Ventilation(h)	Ventilation+heating(h)	Ventilation+cooling(h)	Heating does not meet the required hours(h)	Cooling does not meet the required hours(h)	Heating/cooling ratio is not met in the year	APF
Harbin	6218	2388	154	32	5	0.42%	1.31
Beijing	6362	1732	666	49	43	1.05%	1.16
Shanghai	6263	1419	1078	31	53	0.96%	1.04
Guangzhou	6221	535	2004	8	112	1.37%	0.71
Kunming	7945	719	96	61	0	0.69%	1.28

According to Table 1, the applicability of air compression systems in traditional buildings in five cities is evaluated based on the standard of HVAC systems not meeting 3% annually. The air compression systems can meet the annual usage needs of traditional buildings in Harbin, Beijing, Shanghai, Guangzhou, and Kunming, with the proportion of annual heating/cooling time not meeting the requirements being 0.42%, 1.05%, 0.96%, 1.37%, and 0.69%, respectively.

References

1. Zhang, C.H., Chen, J.L., Gao, Y.: Analysis of the impact of the Kigali amendment to the Montreal protocol on the refrigeration and air conditioning industry. Refrigerat Air Condition. **17** (2017) (In Chinese)
2. Sui, Q.Y., et al.: Performance analysis of an air cooling cycle system applied to data center cooling. J Refrigerat. **43**(5), 16–23 (2022) (In Chinese)
3. Lin, S.N., et al.: The application of air cooler in aircraft air conditioning system. Fluid Mech. **10**, 46–49 (2004) (In Chinese)
4. Wang, Z.F., et al.: Performance testing of all-fresh air domestic air cooling systems. J Refrigerat. **42**(06), 15–20 (2021) (In Chinese)
5. Sheng, C.C., Yang, Y., Xie, H.T.: Analysis and experimental study of airborne pod environmental control air refrigeration system. Low Temp Superconduct. **48**(1), 80–85 (2020) (In Chinese)
6. Lin, S.N., Xia, K., Li, J.: Application of air refrigerators in aircraft air conditioning systems. Fluid Machinery. **32**(10), 46–49 (2004) (In Chinese)
7. Spence, S.W.T., John Doran, W., Artt, D.W.: Performance analysis of a feasible air-cycle refrigeration system for road transport. Int. J. Refrig. **28**(3), 381–388 (2005)
8. Energy saving design standards for public buildings: GB 50189–2015.2015 (In Chinese)

Research on the Influence of Curtain Settings on the Indoor Thermal Environment of Heated Dormitories

Kaiyue Liu[1](✉), Chenyu Ma[2], Donghai Zhang[1], Shuang Ma[1], and Zhe Liu[1]

[1] Changchun Institute of Technology, Changchun, Jilin 130012, China
liukaiyue199601@163.com
[2] Zhejiang University, Hangzhou, Zhejiang 310028, China

Abstract. Article focuses on the heating environment of dormitory rooms. Numerical simulation methods are applied, and the FLUENT software is utilized to study the impact of curtain settings on the comfort level of dormitory rooms. By establishing a detailed dormitory model, setting multiple working conditions, and conducting simulation analysis of the temperature distribution in the dormitory under different curtain settings (such as length, opening and closing degree), as well as outdoor air infiltration speed, outdoor temperature, and radiator temperature, and obtains the influence law of curtain settings on dormitory comfort. Simulation results show that during dormitory heating, the vertical temperature difference between upper and lower bunks reaches 0.2–1 °C, while the horizontal temperature distribution is relatively uniform; higher radiator temperature significantly increases indoor temperature; curtain settings affect indoor temperature distribution, with curtain length having a greater impact. These results provide a reference for optimizing the dormitory thermal environment.

Keywords: FLUENT · Curtain settings · Heated dormitory rooms

1 Introduction

In building energy consumption, the heat loss through windows accounts for a large proportion. In cold regions, the heat dissipated through windows in winter can account for 20%-50% of the total building heat loss. As an auxiliary facility of windows, the setting of curtains has a non-negligible impact on the indoor thermal environment. On the one hand, curtains can block part of the cold air infiltration from the outer windows and reduce heat loss; on the other hand, they also block the heat transfer from the radiator under the window to the indoor space. For student dormitories, the personnel density is relatively high, and students stay in the dormitory for a long time. The thermal environment of the dormitory is directly related to the students' living comfort and learning efficiency. Therefore, in-depth research on the influence of curtain settings on the comfort of heated dormitories has important practical significance.

© The Author(s), under exclusive license to Springer Nature Singapore Pte Ltd. 2025
L. Ni et al. (Eds.): CCHVAC 2025, ESE, pp. 432–440, 2025.
https://doi.org/10.1007/978-981-95-3253-7_46

Scholars have studied curtains' impact on building thermal environments. Y. Shu [1] measured Dalian residences, noting south—facing rooms with day—opened, night—closed curtains and north—facing rooms with all—day—closed curtains have higher daily average temps. Z. Wu [2] used CFD to study a room's insulation curtains, finding installing them aids heating, with best insulation at 0.05 m from windows. G. Cao [3] built a heat—transfer—based model for curtain—added window thermal resistance, showing curtains improve window heat transfer; field tests saw 1–3 °C indoor temp rise vs. no—curtain conditions, enhancing thermal environment and temp stability.

With the continuous development of CFD technology, it has shown unique advantages in the study of indoor thermal environment. FLUENT software is widely used in solving fluid and heat transfer problems. In this study, this software is used to simulate and analyze the thermal environment of the dormitory, and study the influence of curtain settings under different lengths and opening degrees on the indoor thermal environment of the heated dormitory.

2 Model Establishment

2.1 Physical Model

Taking a student dormitory of a university in Harbin as the prototype, its layout is consistent with that of most university student dormitories, featuring typicality. It's simplified to a 5 m (length) × 3.4 m (width) × 3.2 m (height) rectangular cuboid. The west wall of the dormitory is an external wall, on which an external window of 1.5 m × 1.5 m is installed, while the other three walls are internal walls. A 1 m × 2 m door is set on the east wall, leading to the corridor, with a 1 m × 0.6 m glass panel above the door. Gaps are taken into account for both the door and window, with the gap size set to 3 mm.The room is furnished with three bunk beds of 0.85 m × 1.8 m, a cabinet of 0.75 m × 1.6 m × 1.6 m, a table of 1.2 m × 0.6 m × 1.2 m, and a set of four-column 813-type radiators is arranged below the external window. In accordance with actual specifications, the radiator has dimensions of 0.696 m (length) × 0.161 m (width) × 0.813 m (height). Curtains are placed on the inner side of the external window, with a distance of 10 mm from the radiator surface. The physical model of the student dormitory and the physical model of the radiator are shown in Figs. 1 and 2 respectively**.**

In order to systematically study the influence of curtain settings on the comfort of the dormitory, different curtain length and opening degree models are established respectively. For curtain length, five curtain length models are constructed: no radiator coverage, 1/4, 2/4, 3/4, and full coverage. The curtain has a width of 2.2 m and a thickness of 0.005 m, and the partial model of the curtain is shown in Fig. 3.

When studying the influence of curtain opening degree, five models are established with curtain opening degrees of 5 cm, 15 cm, 25 cm, 35 cm, and 45 cm. Each curtain side is 1.1 m wide, 0.005 m thick and 2.83 m long, covering half of the radiator's height. The partial model of the curtain is shown in Fig. 4.

2.2 Calculation Model

The structured grid is established by using ICEM CFD, as shown in Fig. 5, and validated for independence, with simulations run in Fluent. Fluid density depends on pressure and

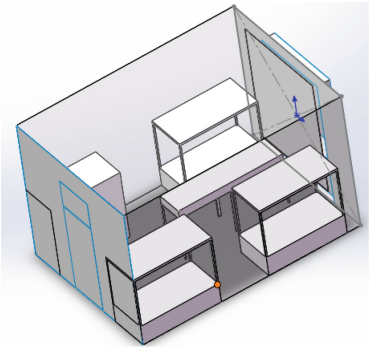


Fig. 1. Physical model of student dormitory.

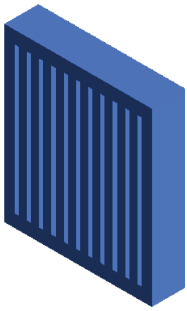


Fig. 2. Physical model of radiator.

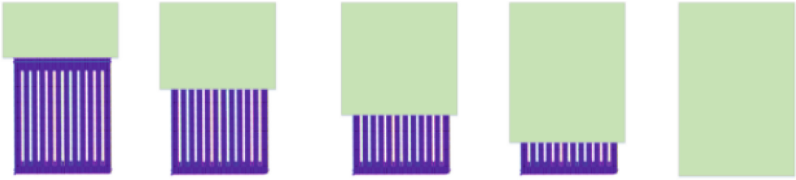


Fig. 3. Local models of different curtain lengths.
(Note: From left to right, the five models are curtain lengths with 0/4 (no), 1/4, 2/4, 3/4 and 4/4 (full) radiator coverage.)



Fig. 4. Local models of different curtain opening degrees.
Note: From left to right, the five models are curtain middle opening degrees of 5 cm, 15 cm, 25 cm, 35 cm, and 45 cm respectively

temperature. In the heated dormitory room, the air pressure change is not large, and the density change is mainly caused by the change of the air temperature. Therefore, the Boussinesq model is used for temperature-related density variations, and the k-omega model for air turbulence. The curtain is set as a porous material, and the curtain material is considered as cotton. Its density is 200 kg/m^3, the thermal conductivity is 0.05 W/(m·K), the specific heat capacity is 1000 J/(g·K), and the porosity is 0.08. The radiator material is set as an aluminum radiator.

2.3 Boundary Conditions

The surrounding area is considered as a heated room, the inner wall is set as a constant wall temperature boundary condition, and the wall temperature is set to 20 °C; the outdoor temperature and the radiator surface are set as constant wall temperature boundary

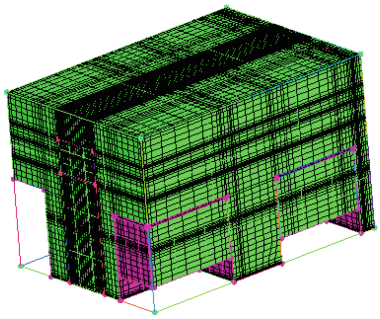


Fig. 5. Established structured grid.

conditions, and the temperature is set to different working conditions according to the research content; the outer window is set as a natural convection boundary condition, the surface temperature of the outer window is the same as the outdoor temperature, and the convective heat transfer coefficient is 5 W/(m^2·K); the gap of the outer window is set as a velocity inlet boundary condition; the gap of the door and the gap of the window above the door are set as free outflow boundary conditions.

3 Simulation Results and Analysis

3.1 Influence of Curtain Length

The surface temperature of radiators generally ranges from 40 °C to 60 °C, and the average outdoor temperature during the heating period in centralized heating areas is between −15 °C and 5 °C. Considering most scenarios, intermediate values are adopted for setting: the surface temperature of the radiator is set to 50 °C, the outdoor temperature is −5 °C, and the air infiltration speed of the outer window is 0.05 m/s. Based on this setting, the influence of curtain length on the indoor temperature distribution is studied.

Average temperature simulation data of each plane (per Fig. 6 positions) were sorted to generate Figs. 7 and 8, which study how room vertical and horizontal temperature distributions vary with curtain length. Results show 0/4 length (no radiator coverage) best facilitates radiator heat dissipation, followed by 2/4; full coverage leads to the lowest indoor temperature.

The vertical temperature distribution in the room is relatively obvious. Because the density of hot air is smaller than that of cold air, a steady-state temperature field with upper heat and lower cold is presented. The temperature difference between the floor and the ceiling of the room can reach 0.2–2 °C, and the temperature difference between the upper and lower bunks can reach 0.2–1 °C. The horizontal temperature distribution of the room changes little, and the change value is within 0.3 °C, that is, the horizontal temperature distribution of the room is uniform.

Figures 9 and 10 respectively show the temperature distribution nephograms of the vertical section of the room when the curtain length does not cover the radiator and covers 1/2 of the radiator. When the curtain length does not cover the radiator, it is conducive to the heating of the radiator, and the indoor temperature is relatively high. However,

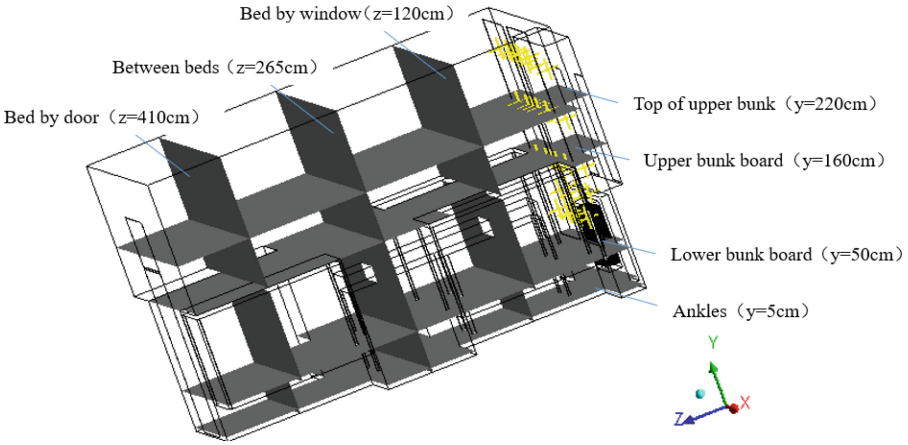


Fig. 6. Position indication diagram of the room model.

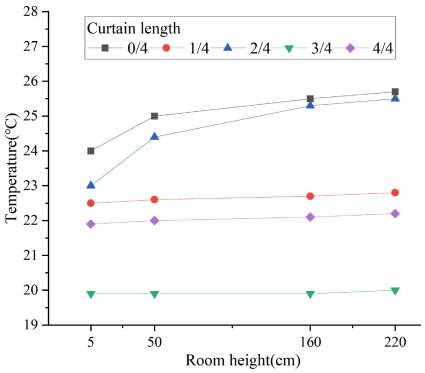


Fig. 7. Temperature vertical distribution with varying curtain lengths.

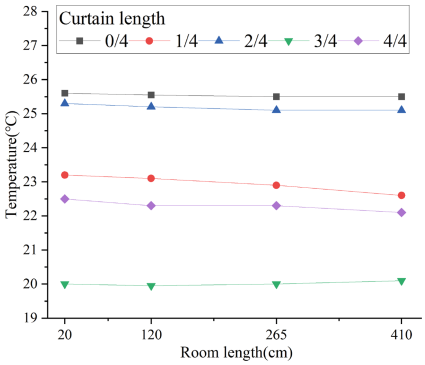


Fig. 8. Temperature horizontal distribution with varying curtain lengths.

because the curtain blocks the heat dissipation of the radiator, relatively low-temperature areas are prone to appear inside and at the bottom of the room, and the temperature is relatively low.

3.2 Influence of Curtain Opening Degree

Similarly, the surface temperature of the radiator is set to 50 °C, the outdoor temperature is −5 °C, and the air infiltration speed of the outer window is 0.05 m/s. Based on this setting, the influence of curtain opening degree on the indoor temperature distribution is studied, and the simulation results are shown in Figure 11 and 12. The average temperature of the room under different curtain opening degrees varies little, and the maximum temperature difference is about 0.2–0.5 °C. As shown in Fig. 11, the vertical temperature distribution in the room is relatively obvious, and the temperature difference between the upper and lower bunks reaches 0.2–1 °C. When the curtain opening degrees are 15 cm and

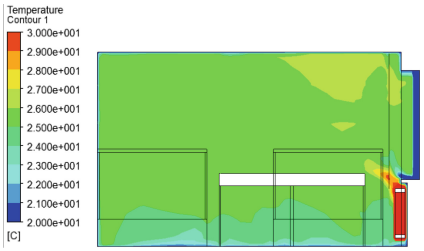


Fig. 9. Vertical section temperature nephogram (Curtain Not Covering Radiator).

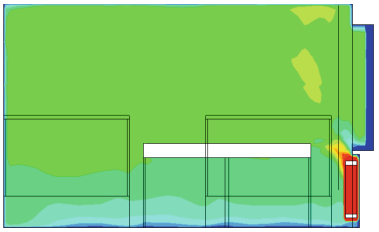


Fig. 10. Vertical section temperature nephogram (Curtain Covering 1/2 Radiator).

35 cm, the temperature difference in the height direction of the room is relatively large; while when the opening degrees are 25 cm and 45 cm, the temperature difference in the height direction of the room is relatively small. As shown in Fig. 12, the horizontal temperature distribution of the room changes little, and the temperature difference is about 0.1–0.4 °C, which is smaller than the temperature difference change in the height direction of the room.

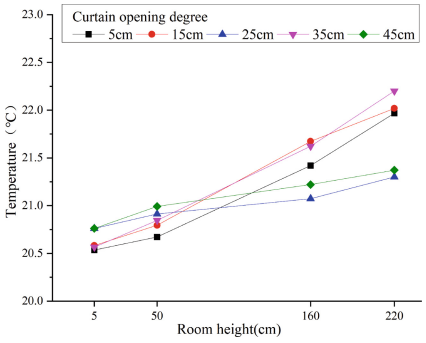


Fig. 11. Temperature vertical distribution distribution with varying curtain opening degrees.

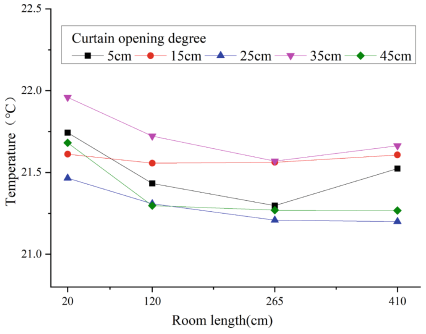


Fig. 12. Temperature horizontal with varying curtain opening degrees.

3.3 Influence of Air Infiltration Speed

The outdoor wind speed affects the air infiltration speed of the window gap through the wind pressure. To study how infiltration speed impacts heated indoor temperature, infiltration speed is set to 0.025–0.1 m/s; the curtain length is to cover 1/2 of the radiator, and the curtain opening degree is 25 cm; other parameters are set as:

(seam1:tw = −5 °C.ts = 50 °C; seam2:tw = −15 °C.ts = 50 °C; seam3:tw = 5 °C.ts = 50 °C; seam4:tw = −5 °C.ts = 45 °C; Seam5:tw = −5 °C.ts = 40 °C.)

The simulation results are shown in Fig. 13. When the air infiltration speed of the outer window gap increases, the overall temperature of the room decreases, but the

change is small. When the air infiltration speed increases from 0.025 m/s to 0.1 m/s, the overall temperature of the room decreases by about 0.3 °C. Curtains can block infiltration to some extent.

3.4 Influence of Outdoor Temperature

To study how outdoor temperature affects heated indoor temperature, outdoor temperature is set to range from −20 °C to 5 °C; curtain length covers 1/2 of the radiator, with opening degree at 25 cm. Other parameters are set as follows:

(Temp1:ts = 45 °C.v = 0.075 m/s; Temp2:ts = 55 °C.v = 0.075 m/s; Temp3:ts = 50 °C.v = 0.025 m/s; Temp4:ts = 50 °C.v = 0.1 m/s.)

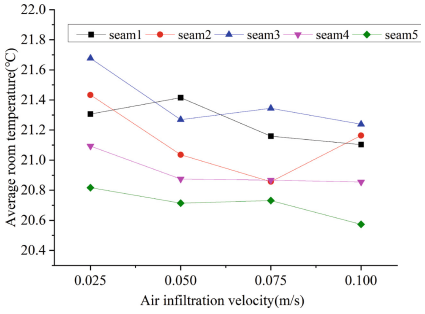


Fig. 13. Average room temperature variation with different air infiltration velocities.

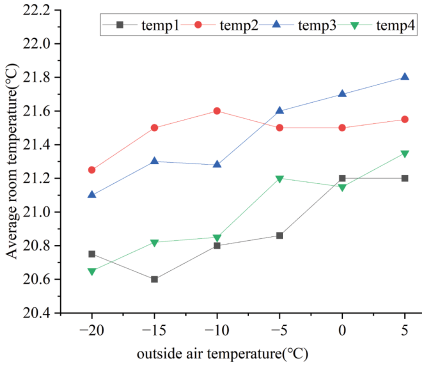


Fig. 14. Average room temperature variation with different outdoor temperatures.

Simulation results (see Fig. 14) show that higher outdoor temperature increases indoor overall temperature, but it does not change in direct proportion. When the outdoor temperature increases by 5 °C, the overall temperature of the room increases by about 0.1–0.3 °C. Outdoor temperature changes transfer heat with indoor air via the window and affect cold air infiltration temperature.

3.5 Influence of Radiator Temperature

To study how radiator temperature affects heated indoor temperature, radiator temperatures are set to 40, 45, 50 and 55 °C; curtain length covers 1/2 of the radiator, with opening degree at 25 cm. Other parameters are set as follows:

(heating1:tw = −5 °C.v = 0.075 m/s; heating2:tw = −15 °C.v = 0.075 m/s; heating3:tw = −5 °C.v = 0.025 m/s; heating4:tw = −5 °C.v = 0.05 m/s; heating5:tw = −5 °C.v = 0.1 m/s.)

Simulation results (see Fig. 15) show that higher radiator temperature significantly increases indoor overall temperature. For every 5 °C increase in the radiator temperature, the overall temperature of the room increases by about 0.3 °C. Meanwhile, the vertical

temperature difference in the room grows. This indicates radiator temperature significantly influences the indoor thermal environment and is a key factor affecting dorm temperature.

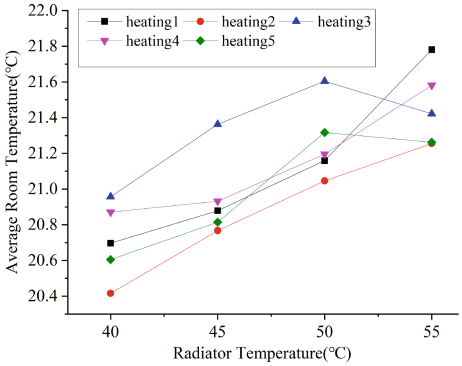


Fig. 15. Average room temperature variation with different radiator temperatures.

4 Introduction

Based on the comprehensive simulation results, the following conclusions are drawn:

The vertical temperature distribution in the heated dormitory is relatively obvious, showing a steady-state temperature field with upper heat and lower cold, and the temperature difference between the upper and lower bunks reaches 0.2–1 °C. The temperature distribution in the horizontal direction of the room is uniform.

The increase of the air infiltration speed of the outer window gap will reduce the overall temperature of the room, but the change is small. When the air infiltration speed increases from 0.025 m/s to 0.1 m/s, the overall temperature of the room decreases by about 0.3 °C.

When the outdoor temperature increases, the overall temperature of the room increases, but it is not in direct proportion. When the outdoor temperature increases by 5 °C, the overall temperature of the room increases by about 0.1–0.3 °C.

Higher radiator temperature significantly affects indoor temperature. For every 5 °C increase, the overall temperature of the room increases by about 0.3 °C.

The curtain setting has an influence on the temperature distribution of the dormitory. In actual life, for the heated dormitory, the curtain setting should be reasonably adjusted according to the outdoor temperature and the indoor personnel needs. In cold weather and when the outdoor temperature is low, the curtain length of not covering the radiator or covering 1/2 of the radiator can be selected to facilitate the heat dissipation of the radiator to the room, block the cold air infiltration of the window gap, and improve the indoor temperature; different curtain opening degrees have little influence on the average room temperature, and the maximum temperature difference is about 0.2–0.5 °C. At the same time, the sealing performance of the window can be improved, the air infiltration

speed can be reduced, the adverse impact of cold air on the indoor thermal environment can be reduced, and the comfort of the dormitory can be improved.

In the future research, the influence of various curtain materials, more complex dormitory layouts, and personnel activities on the indoor thermal environment can be further considered to more comprehensively optimize the dormitory thermal environment.

References

1. Shu, Y.: Research on the Influence of Daily Curtain Opening and Closing on the Thermal Performance of Buildings in Heating Season. Dalian University of Technology (2016)
2. Wu, Z., Wang, J.: Simulation study on improving the thermal insulation performance of a room's thermal insulation curtain based on CFD. Sci Technol Eco Guide. **28**, 62 (2017)
3. Cao, G.: Research on the Influence of Building Curtain Regulation on the Thermal Effect of Heating Rooms in Western Sichuan Region. Chongqing University (2019)

Are Heating Electrification and Mechanical Ventilation Viable Approaches for Cold Climate Rural Buildings?

Xinyi Hu[1(✉)], Juha Jokisalo[2], Risto Kosonen[2], and Matti Lehtonen[1]

[1] Department of Electrical Engineering and Automation, Aalto University, 02150 Espoo, Finland
xinyi.hu@aalto.fi

[2] Department of Mechanical Engineering, Aalto University, 02150 Espoo, Finland

Abstract. The renovation of rural buildings, especially in cold climate areas with high heating demand, is an important but often overlooked aspect in decarbonization pathway. The viability of adopting mechanical ventilation and heating electrification in such contexts remains uncertain. This study evaluated the economic and environmental performance of standard-based and customized renovation strategies for a typical rural house in Harbin. Renovation scenarios with varying intervention levels were examined, ranging from individual ventilation upgrades to holistic packages integrating envelope, ventilation, and electrified heating. Building energy performance was simulated using IDA ICE, and optimal solutions were identified through multi-objective optimization targeting life-cycle costs and CO_2 emissions. Results indicate that mechanical ventilation increases heating demand if not paired with envelope upgrades, while customized renovations outperform standard ones. The optimal case, which combines an air-to-water heat pump, PV, envelope and ventilation upgrades, reduces life-cycle costs by 11% and emissions by 80% compared to pre-renovation baseline. These findings offer simulation-based insights to guide cost-effective, low-carbon rural renovations in cold areas.

Keywords: Building renovation · multi-objective optimization · cold climate

1 Introduction

China has committed to peaking carbon emissions by 2030 and achieving carbon neutrality by 2060, positioning building energy efficiency as a key decarbonization strategy. In 2020, rural buildings accounted for 34% of national floor area and 22% of total building energy use [1], highlighting their relevance in the low-carbon transition. However, renovation efforts in cold-climate rural areas remain limited, particularly for ventilation and heating systems. Harsh winters, high heating demand, and limited household income often hinder their implementation.

Ventilation is especially problematic. To retain heat, occupants often prioritize thermal comfort over indoor air quality and avoid window opening during winter [2]. Insufficient air exchange, combined with indoor combustion of coal or biomass, causes elevated

© The Author(s), under exclusive license to Springer Nature Singapore Pte Ltd. 2025
L. Ni et al. (Eds.): CCHVAC 2025, ESE, pp. 441–448, 2025.
https://doi.org/10.1007/978-981-95-3253-7_47

indoor pollution, posing health risks that are often poorly understood. Electrified heating also faces barriers. Reports indicate that up to 14% of newly installed systems in northern China were later abandoned due to high operational costs [3]. Renewable-based options like rooftop photovoltaics (PV) offer long-term returns, but high initial investments remain a key challenge.

Therefore, the viability of adopting mechanical ventilation and heating electrification in cold-climate rural areas remain uncertain. Many stakeholders view these strategies as costly or impractical, often based on their experience rather than simulation-based analysis. Existing assessments also focus on short-term economic metrics, overlooking long-term considerations or environmental impacts.

This study aims to evaluate the economic and environmental viability of adopting mechanical ventilation and heating electrification in cold-climate rural buildings. It compares standard-based renovation scenarios with performance-driven customized strategies. Different levels of intervention were examined, including individual mechanical ventilation system installation and holistic packages including envelope, mechanical ventilation and electrified heating. Customized solutions were identified using a simulation-based multi-objective optimization approach.

2 Methods

2.1 Case Building Description and Modeling

This study examined a typical rural house located in rural Harbin, northeast China. Built in the 1990s, this single-story detached house reflects the common characteristics of local rural housing, including its spatial layout, envelope properties, system configuration, energy usage patterns, and ventilation strategies. A three-dimensional simulation model of case building is shown in Fig. 1a, and Table 1 details the original envelope properties before renovation.

Table 1. Original U-values of case building envelope and corresponding requirements from national standard [4].

Envelope component	Original envelope	Standard envelope renovation
External wall	0.92 W/(m^2 K)	0.5 W/(m^2 K)
Ground floor	3.15 W/(m^2 K) (bedrooms); 3.88 W/(m^2 K) (other rooms)	–
Roof	0.42 W/(m^2 K)	0.45 W/(m^2 K)
External windows	2.3 W/(m^2 K)	2.2 W/(m^2 K) (southern); 2.0 W/(m^2 K) (other orientations)

Figure 1b shows the floor plan, original heating system configuration and natural ventilation strategy before renovation. Space heating was provided by a coal-fired boiler in the kitchen, which distributed hot water to radiators in two bedrooms. In addition,

bedroom 1 used a traditional Kang, a thermally massive structure heated by flue gases. The heating setpoint temperatures in two bedrooms were set at 17 °C, reflecting the local thermal comfort preferences. The other three auxiliary rooms were unheated under the original system configuration.

Natural ventilation was applied in the case building, occurring through building envelope infiltration and manual window operation. Based on field measurements in comparable rural buildings in [5], the air leakage rate of the building at 50 Pa pressure difference was set at 7 air changes per hour (ACH).

Harbin experiences a six-month heating season, typically from October 20 to April 20, with an average outdoor temperature of −7 °C. The coldest month, January, could reach the lowest temperature of −31 °C. Hourly weather data was obtained from the IWEC 2 dataset and applied in the annual dynamic energy simulations.

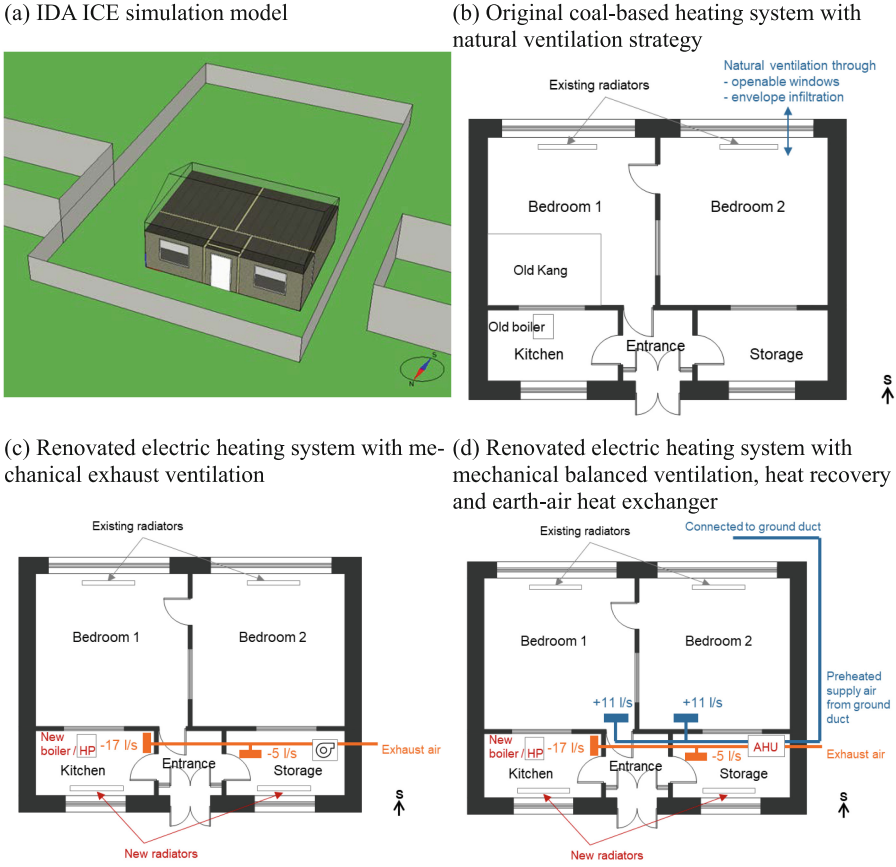


Fig. 1. Case building modeling and floor layout: (**a**) IDA ICE simulation model of case building and surroundings, (**b**) layout with original ventilation strategy and heating system, and (**c**-**d**) layouts with renovated electric heating systems and proposed mechanical ventilation options.

2.2 Simulation Cases

Figure 2 illustrates the structure of the proposed renovation packages, which were categorized into standard and customized packages. The standard renovation cases represented three levels of intervention: (1) individual ventilation upgrades, (2) combined ventilation and envelope improvements, and (3) multi-system upgrades that integrated heating electrification.

The standard ventilation renovation was designed to meet the regulatory air exchange rate of 0.5/h by installing a basic mechanical exhaust ventilation system (EX). The standard envelope upgrade (std env) complied with the thermal performance requirements in the national standard (see Table 1). Heating electrification involved replacing the original coal-based heating with an electric boiler (EB), and adding radiators in auxiliary rooms, with a setpoint temperature of 14 °C (see Fig. 1c).

The customized renovation packages adopted a holistic approach by simultaneously optimizing envelope, ventilation, and heating systems. In addition to exhaust ventilation, they included a mechanical balanced ventilation system integrating both heat recovery and an earth-air heat exchanger, as shown in Fig. 1d. Detailed configurations of the ventilation options are provided in [6]. Heating system alternatives included electric boiler and air-to-water heat pump (A2WHP). In addition, selected scenarios incorporated rooftop photovoltaic (PV) systems to explore the potential of renewable-powered electrification.

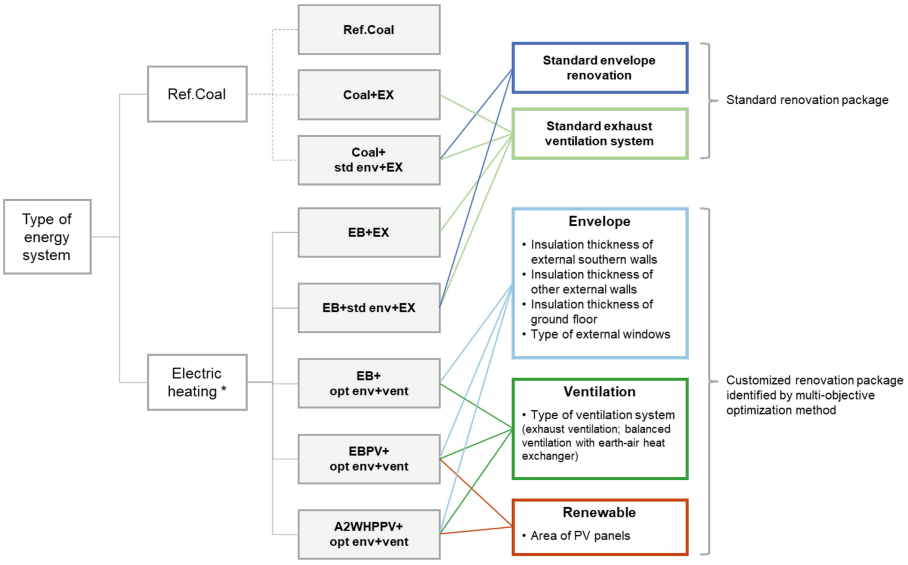


Fig. 2. Standard and customized renovation packages with decision variables.

2.3 Simulation-Based Multi-Objective Optimization

The customized renovation solutions were obtained through a simulation-based multi-objective optimization process. To capture the trade-off between economic and environmental priorities, two conflicting objectives were defined: (1) minimizing net present value of life cycle cost (NPV of LCC) of renovation measures over a 20-year period, and (2) minimizing annual CO_2 emissions associated with delivered energy use. The objective equations were detailed in [7]. The decision variables involved in the optimization process, as well as their respective ranges and types, are summarized in Table 2.

The case building was built and simulated by IDA Indoor Climate and Energy simulation program (IDA ICE). The multi-objective optimization process was conducted with the integrated AutoMOO tool in IDA ICE, which generated sets of non-dominated solutions forming the Pareto fronts. The decision-making method, technique for order of preference by similarity to ideal solution (TOPSIS), was applied to select an optimal solution from each Pareto solution set for further analysis.

Table 2. Decision variables of customized renovation packages considered in optimization process.

	Decision variable	Range	Type
1	Additional expanded polystyrene (EPS) insulation thickness for external southern walls (mm)	[0, 200]	Continuous
2	Additional EPS insulation thickness for other external walls (mm)	[0, 200]	Continuous
3	Additional extruded polystyrene (XPS) insulation thickness of ground floor (mm)	[0, 200]	Continuous
4	Type of external windows	Win1. Original windows, 2.3 W/(m^2 K). Win2–7. Renovated windows, 1.0–2.1 W/(m^2 K).	Discrete
5	Type of ventilation systems	Vent1. Exhaust ventilation. Vent2. Balanced ventilation with EAHE and heat recovery.	Discrete
6	Capacity of A2WHP (7/45 °C) (kW)	[4,9]	Continuous
7	Area of PV panels (m^2)	[0, 60]	Continuous

3 Results and Discussion

Figures 3 and 4 compare standard and customized renovation strategies in terms of CO_2 emissions and LCCs. Figure 3 presents the absolute performance based on Pareto-optimal solutions, while Fig. 4 shows the percentage changes of TOPSIS-selected optimal solutions in customized renovation packages relative to the pre-renovation baseline (Ref. Coal).

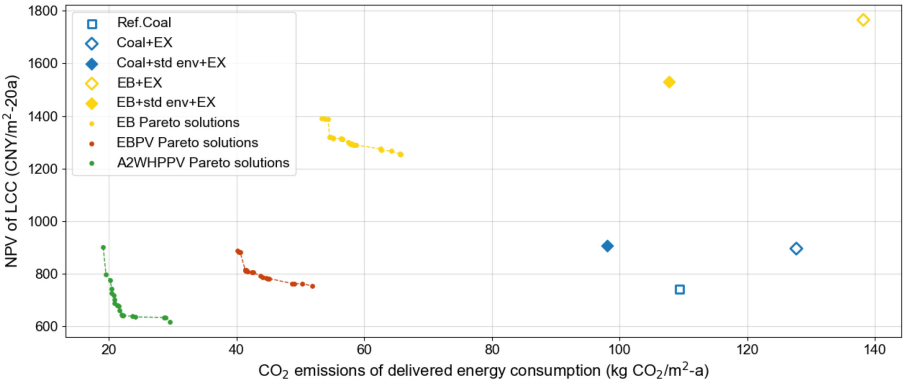


Fig. 3. Standard and customized renovation solutions compared with pre-renovation reference case in CO_2 emission and LCC levels.

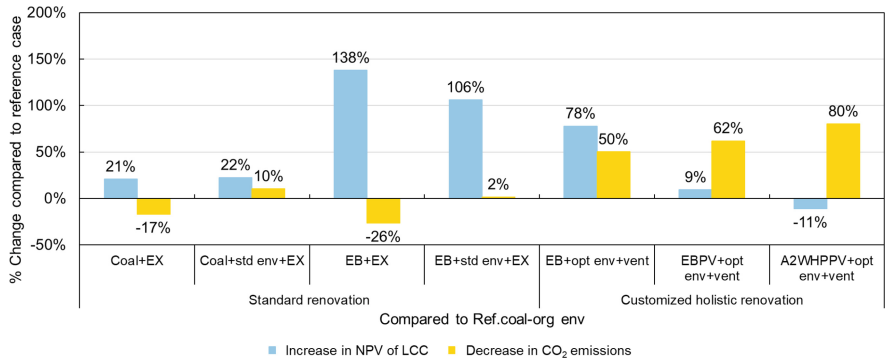


Fig. 4. Percentage changes in LCC and CO_2 emissions of renovation solutions compared to pre-renovation reference case.

Systems with exhaust ventilation only (Coal+EX, EB + EX) show performance deterioration, with LCCs increasing by 21–138% and CO_2 emissions rising by 17–26%, primarily due to increased heating demand from unconditioned outdoor air. Applying standard envelope upgrades (std env) leads to modest emission reductions (22–23%) and moderate LCC increase (1–13%).

In contrast, customized renovation strategies consistently offer substantial improvements. Optimized combinations of envelope and ventilation upgrades with an electric boiler (EB Pareto) achieve 53–66 kg CO_2/m^2 and 1253–1391 CNY/m^2 of LCC. Adding rooftop PV (EBPV) further reduces CO_2 emissions to 40–52 kg CO_2/m^2 while maintaining LCC level similar to the pre-renovation baseline (Ref.Coal). The best outcome is observed in the scenario combining an air-to-water heat pump and PV (A2WHPPV), which achieves an 11% reduction in LCC and an 80% cut in emissions compared to the pre-renovation baseline. TOPSIS-selected optimal solutions in Fig. 4 confirmed these patterns, reinforcing the advantage of performance-driven, holistic renovations over standard-based approaches.

Figure 5 compares total investments and annual energy costs across the pre-renovation baseline, standard renovations, and TOPSIS-optimal customized solutions. Exhaust ventilated electric boiler case (EB + EX) has relatively low investment (82 CNY/m^2) but incurs the highest annual energy cost (121 CNY/m^2). Adding standard envelope renovation (EB + std. env + EX) reduces energy cost to 88 CNY/m^2 at 340 CNY/m^2 investment. In contrast, the customized solution (EB + opt env + vent) achieves similar energy cost levels to the coal-based standard case (Coal+std. env + EX), while 513 CNY/m^2 higher investment eliminates on-site coal use, offering health and environmental benefits. PV-integrated solutions (EBPV+opt env + vent, A2WHPPV + opt env + vent) require significantly higher investments (1566–1606 CNY/m^2) but delivers negative annual energy costs (−55 to −72 CNY/m^2). This demonstrates the long-term economic viability of integrating rooftop PV in deep renovations.

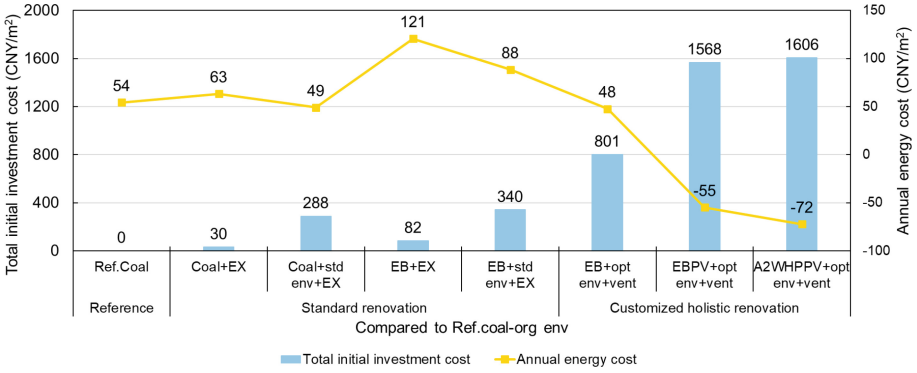


Fig. 5. Initial investment costs and annual energy costs of reference case and renovation solutions.

Customized renovation strategies significantly outperform standard approaches using the same heating systems. While standard upgrades are easier to implement, they offer limited potential for deep decarbonization. In contrast, customized solutions identified through multi-objective optimization achieve greater LCC savings and emission reductions. Results also show that mechanical ventilation should not be applied as a standalone measure, as it increases heating demand without insulation upgrades. Instead, a holistic approach combing envelope upgrades, mechanical ventilation, and electrified heating, particularly the PV-combined heat pump system, provides the most substantial

benefits in emissions costs and indoor air quality. These advantages are expected to grow over time, driven by ongoing grid decarbonization. However, high investments hinder PV adoptions in rural areas. Financial supports, such as subsidies, feed-in tariffs, or energy performance contracting (EPC), is needed to fill affordability gaps. Eliminating on-site coal use brings health and environmental benefits, providing additional justification for investing in mechanical ventilation and heating electrification in rural contexts.

4 Conclusions

This study assessed the economic and environmental viability of adopting mechanical ventilation and heating electrification in cold-climate rural buildings by comparing standard-based renovation scenarios with performance-driven customized strategies. Key findings are as follows:

- Mechanical ventilation alone increases heating demand if not paired with envelope improvements.
- Customized renovation strategies outperform standard approaches equipped with the same heating system, achieving greater CO_2 emission reductions and LCC savings.
- The most favorable outcome is achieved by integrating an air-to-water heat pump and rooftop PV with optimized envelope and ventilation upgrades, results in an 11% reduction in LCC and an 80% decrease in CO_2 emissions compared to the pre-renovation baseline.

By quantifying the trade-offs among various interventions, this study provides simulation-based evidence to inform cost-effective and low-carbon renovation pathways in rural housing.

References

1. Hu, S., Zhang, Y., Yang, Z., Yan, D., Jiang, Y.: Challenges and opportunities for carbon neutrality in China's building sector—modelling and data. Build. Simul. **15**, 1899–1921 (2022)
2. Lai, D., Qi, Y., Liu, J., Dai, X., Zhao, L., Wei, S.: Ventilation behavior in residential buildings with mechanical ventilation systems across different climate zones in China. Build. Environ. **143**, 679–690 (2018)
3. China Urban Energy Weekly: The focus of clean heating in northern China becomes clearer in the 14th Five-Year Plan, http://paper.people.com.cn/zgnyb/html/2021-02/01/content_2032628.htm. Last accessed 2024/09/24
4. MOHURD: GB/T 50824–2013 Design Standard for Energy Efficiency in Rural Residential Buildings. China Architecture & Building Press, Beijing (2013)
5. Zhang, H., et al.: Winter thermal environment and thermal performance of rural elderly housing in severe cold regions of China. Sustainability. **12**, 4543 (2020)
6. Hu, X., Jokisalo, J., Kosonen, R., Lehtonen, M.: Economic and environmental impacts of different ventilation systems in detached rural houses in severe cold climate. J Build Eng. **99**, 111689 (2025)
7. Hu, X., Jokisalo, J., Kosonen, R., Lehtonen, M.: Cost-effective and low-carbon solutions for holistic rural building renovation in severe cold climate. Energ. Buildings. **336**, 115609 (2025)

A Boundary Heat Transfer Model for CFD Simulation of Floor Radiant Heating Systems

Guiqiang Wang(✉) and Guixin Huang

Shenyang Jianzhu University, Shenyang 110168, China
guiq.wang@sjzu.edu.cn

Abstract. As an energy-efficient and comfortable heating method, radiant floor heating systems have been extensively studied for household and zonal control, with CFD simulation being a widely used approach. However, most existing CFD models adopt fixed wall temperatures or constant heat flux densities, which fail to accurately reflect the effects of water-side regulation and non-heated surfaces on radiant heat transfer. In this study we proposed a novel boundary heat transfer model for radiant floor heating that incorporates supply water temperature, flow rate, and non-heated surfaces into floor heat transfer calculations. Based on data from the JGJ142 standard, the model derives fitted values for upward and downward heat flux. A comparison was made between two flow distribution strategies: zonal control (Scenario 1) and uniform distribution (Scenario 2). Thermal comfort was shown to be maintained with a 15–20% reduction in flow demand achieved through selective 50% flow reduction in non-critical zones, when compared to uniform distribution. The proposed zonal control strategy achieves faster heating rates and improved temperature stability in bedrooms, despite exhibiting slight thermal lag in common areas, thus providing an effective solution for energy-efficient personalized thermal comfort.

Keywords: Radiant floor heating · Thermal comfort · Building energy efficiency

1 Introduction

With the advancement of heating technologies, radiant floor heating systems demonstrate superior comfort and energy efficiency compared to other heating methods [1]. Research on radiant floor heating has gradually evolved from meeting basic user requirements to addressing personalized demands while maintaining energy efficiency, making demand-side regulation of heating systems an inevitable trend in their development [2–4]. However, most current studies employ constant-temperature or constant-heat-flux boundary conditions for floors, which fail to accurately reflect real operating conditions during user-side adjustments. Consequently, a dynamically responsive boundary condition becomes essential to address this is-sue.

In practical applications, the surface temperature of radiant floor heating systems exhibits significant spatiotemporal variations due to multiple influencing factors, including supply water temperature, flow rate, indoor and outdoor thermal environments,

© The Author(s), under exclusive license to Springer Nature Singapore Pte Ltd. 2025
L. Ni et al. (Eds.): CCHVAC 2025, ESE, pp. 449–457, 2025.
https://doi.org/10.1007/978-981-95-3253-7_48

and heat transfer through building envelopes. Consequently, maintaining uniform and constant floor surface temperatures remains challenging [5]. Although the constant-temperature and constant-heat-flux methods simplifies calculations, it introduces substantial deviations from actual operating conditions, leading to simulation results that diverge from real-world performance. For instance, Peng's research on correlation models for predicting wall surface heat transfer has shown certain limitations, mainly due to its insufficient consideration of actual operating conditions in floor heating systems, particularly regarding the thermal non-uniformity along floor edges [6]. In Zhang et al.'s study, a fixed heat flux boundary condition was adopted for the floor without adequately accounting for the influence of unheated surfaces on indoor temperature variations [7]. With the increasing adoption of heat metering technology, adjustable floor boundary conditions have become critically important for studying thermal comfort and energy efficiency in radiant floor heating systems. Therefore, the primary objective of this study is to develop a zoned control model for radiant floor heating systems that enables independent regulation of different floor areas, thereby providing more accurate and reliable boundary condition configurations for demand side regulation research.

2 Building Overview

The investigated residential building, located in Cangzhou, China, with one representative unit selected for analysis. The unit was divided into seven functional zones as illustrated in Fig. 1. Located in China's cold climate zone B, the building envelope's thermal performance was evaluated according to local energy efficiency standards. Detailed material specifications and heat transfer coefficients of the building envelope are provided in Table 1.

Table 1. Envelope materials and heat transfer coefficients.

Envelope	The building envelope material	Thickness (mm)	Heat transfer coefficient W/(m2*K)
Exterior wall	concrete block (EPS) board cement mortar	280	0.45
Interior wall	cement mortar concrete block cement mortar	220	2.61
Inter-unit Partition wall	cement mortar reinforced concrete EPS board cement mortar	240	1.50
Roof	reinforced concrete EPS board cement mortar	300	0.30
Windows	-	40	2.20

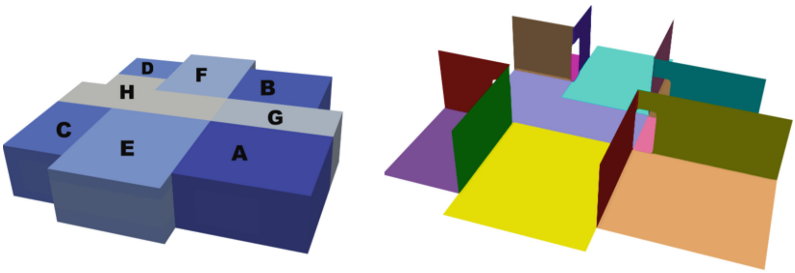


Fig. 1. Building zoning diagram.

3 Numerical Simulation

3.1 Numerical Model and Governing Equations

The building physical model is divided into solid domains and fluid domains. Each residential unit consists of one solid domain and eight fluid domains, totaling 12 units. For the fluid domains, the continuity, momentum and energy conservation equations are solved to capture the physical characteristics of the flow field, as shown in Eq. 1.

$$\frac{\partial(\rho\phi)}{\partial t} + \nabla \cdot (\rho u\phi) = \nabla \cdot \left(\Gamma_\phi \nabla\phi\right) + S_\phi \tag{1}$$

The governing equations are solved using a general variable ϕ, where ϕ represents the velocity components, pressure, turbulent kinetic energy, turbulent dissipation rate, and enthalpy, respectively. The buoyancy effects are modeled through the Boussinesq approximation, where density variations are only applied to the buoyancy term in the momentum equation. For turbulence modeling, the fluid domains utilize the RNG k-ε model with standard wall functions.

3.2 Radiation Model

In this study, we employed the view Factor radiation model to calculate radiative heat transfer between surfaces. The view factor $F_{ij}$from surface i to surface j is determined through geometric integration:

$$F_{ij} = \frac{1}{A_i}\int_{A_i}\int_{A_j} \frac{\cos\theta_i \cos\theta_j}{\pi r^2} dA_j dA_i \tag{2}$$

Here, A_i and A_j denote the areas of surfaces i and j respectively, θ_i and θ_j represent the angles between the radiation direction and surface normal vector, while r indicates the distance between the two surfaces.

The net radiative heat flux Q_i of surface i is given by:

$$Q_i = \epsilon_i A_i \sigma T_i^4 - \sum_{j=1}^{N} F_{ji}\epsilon_j A_j \sigma T_j^4 \tag{3}$$

In the formula, ϵ is the surface emissivity, σ is the Stefan-Boltzmann constant, T_i is the absolute surface temperature (K), and N is the total number of surfaces participating in the radiative exchange.

The ASHRAE solar radiation model is implemented in this work to compute direct normal irradiance (DNI) and diffuse horizontal irradiance (DHI), with subsequent mapping onto building surfaces.

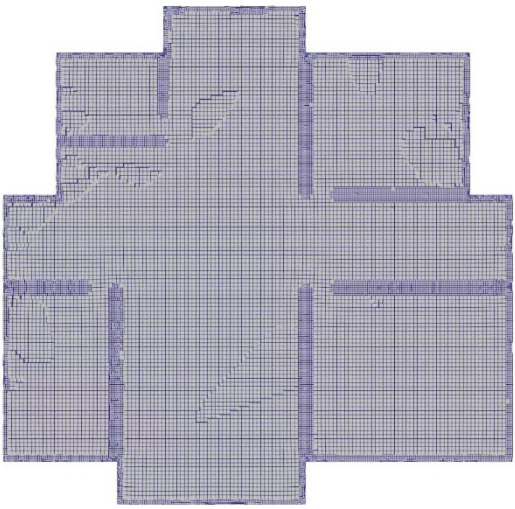


Fig. 2. Internal domain mesh visualization.

3.3 Meshing

Figures 2 and 3 shows the meshing of the building, with a total of 1.36 million grids. During the meshing process, grid refinement was carried out at the contact surfaces between different domains.

3.4 Boundary Conditions

The research employs multi-scale heat transfer boundary conditions for high-resolution building envelope modeling. Interior walls utilize baffle boundary conditions to simulate partition heat transfer characteristics, and party walls apply Mix boundary conditions with thickness effects. Floors incorporate asymmetric heat flux boundaries (40 W/m^2 upward, 20 W/m^2 downward), while roofs and exterior walls implement heat flux boundaries derived from convective heat transfer coefficients and outdoor temperatures, including wall conduction effects. Window thermal boundaries combine solar radiation transmission models, and air-floor interfaces employ coupled boundary conditions integrating thermophysical properties and interfacial heat transfer mechanisms for accurate surface temperature resolution. This approach systematically accounts for building component heat transfer behaviors, establishing a high-fidelity numerical basis for indoor thermal environment simulations.

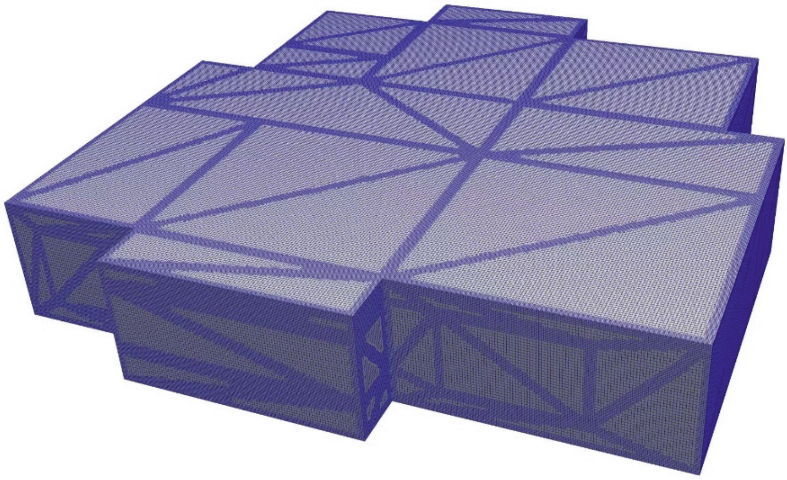


Fig. 3. Computational mesh schematic.

Regarding radiation boundary conditions, the total radiative flux at surfaces comprises both emitted and reflected radiation components.

According to the data provided by the Technical Specification for Radiant Floor Heating (JGJ 142-2012), a bivariate nonlinear regression model for floor heat output is established. The heat output is primarily influenced by the average temperature of the piping loops and the mean indoor air temperature, where the latter is calculated as the area-weighted average temperature of non-heated surfaces [8–10].Using nonlinear least squares fitting, the heat output regression formula is obtained as follows:

$$y = a_1 x_1 + a_2 x_2 + c \,(4)$$

Where y represents the heat transfer rate, x_1 denotes the average water temperature, and x_2 signifies the air temperature. The upward heat flux and the downward heat flux are shown in Fig. 4.

First obtain the grid and temperature field information of the current calculation area, and calculate the weighted average temperature of non-heated surfaces. According to the floor position and type, different calculation strategies are adopted. For intermediate floor slabs, it is necessary to simultaneously consider upward and downward heat transfer, consider the coupling effect of upward and downward heat transfer, and iteratively solve the return water temperature through the energy balance equation. Intermediate ceiling calculation: directly use the average water temperature of the adjacent floor area to calculate downward heat transfer. Ground floor treatment: only upward heat transfer needs to be considered, and the iterative method is used to solve the return water temperature through the energy balance equation.

The calculated heat flux density is subsequently combined with radiative heat flux to establish boundary conditions. To ensure computational stability, the following convergence control strategies are employed. Set tolerance as convergence criterion Introduce

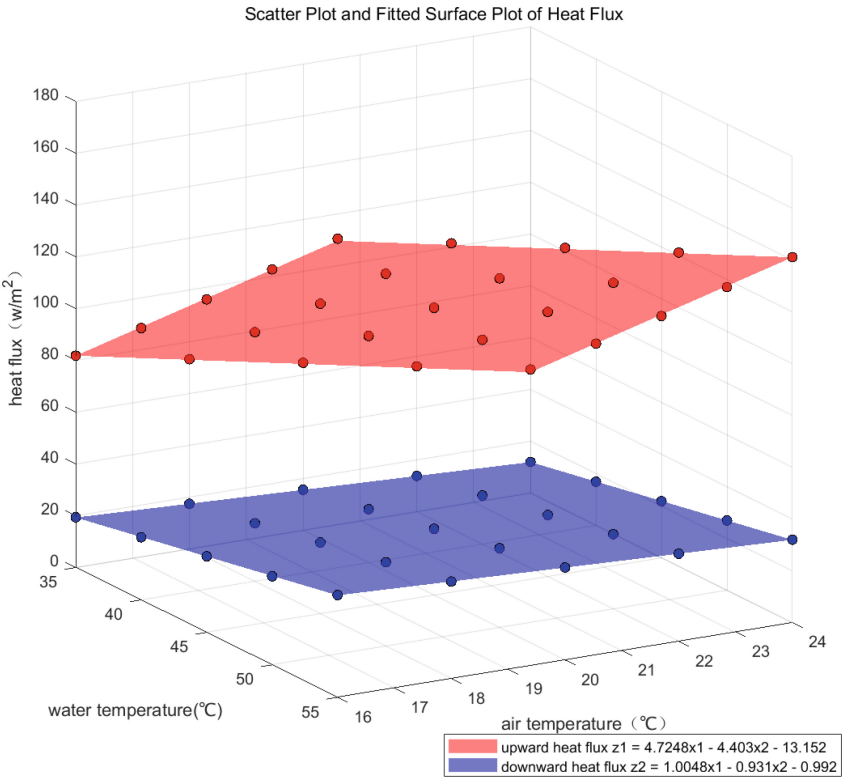


Fig. 4. Scatter Plot and Fitted Surface Plot of Heat Flux.

relaxation factor to control the variation range of return water temperature Set maximum iteration count to 1000 to prevent infinite loops.

4 Results and Discussion

The influence of different flow distribution strategies on indoor temperature and airflow distribution is analyzed through numerical simulations in this study, with a focus on the applicability of zonal control in personalized thermal environment regulation. To validate the model's effectiveness, we selected one residential unit for flow adjustment simulations. In Scenario 1, the flow rates in the bedrooms (Zones A, B, and C) remain unchanged, while those in other areas (such as the living room and kitchen) are reduced. In Scenario 2, the flow rates are evenly distributed across all zones.

As shown in the temperature trend graph in Fig. 5, the overall heating rates un-der both scenarios exhibit minimal differences, particularly in the bedroom zones. In other zones, a slight temperature decrease occurs when the flow rate is reduced, but it remains within acceptable limits.

Figure 6 provides a more intuitive comparison of temperature variations across zones. The less pronounced temperature drop in Zone C compared to Zones A and B is primarily

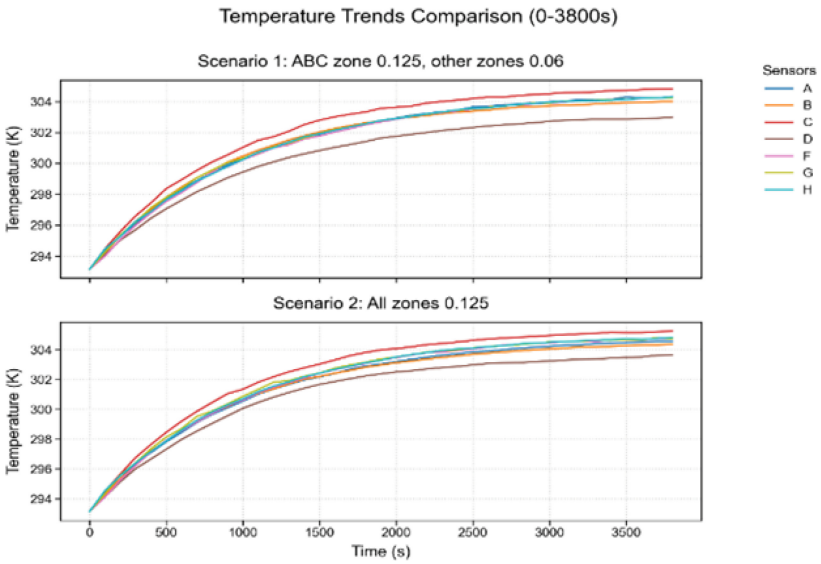
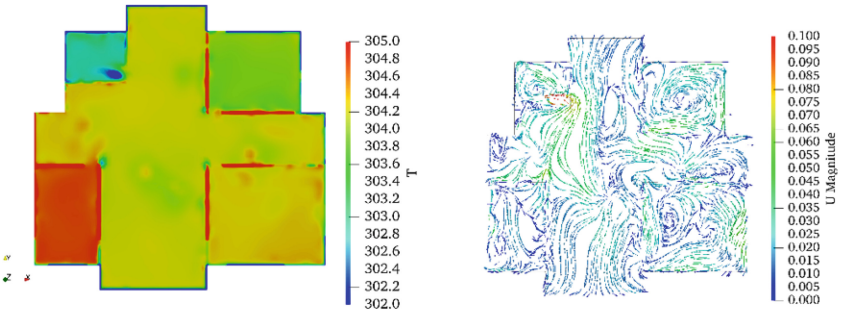


Fig. 5. Temperature trend comparison chart between Scenario 1 and Scenario 2.

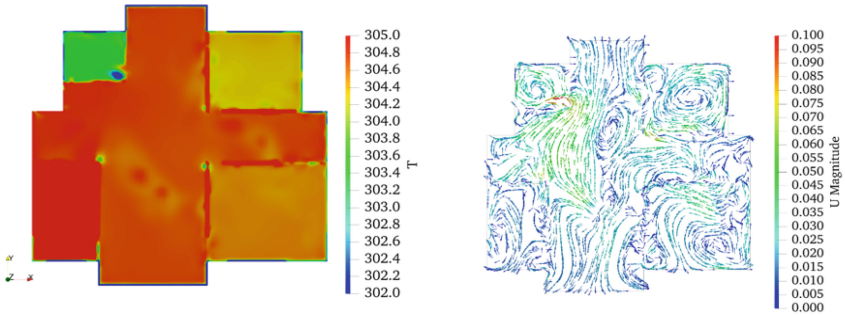
due to solar radiation effects. In Scenario 1, the indoor air velocity is lower than in Scenario 2, mainly because of the reduced temperature difference between Zone H and Zone D. These results demonstrate that appropriately reducing flow rates in non-critical zones not only prevents overheating but also helps mitigate draft discomfort.

In summary, Scenario 1 and Scenario 2 demonstrate differences in dynamic response. Scenario 1 shows significant performance advantages in bedroom areas (Points A-C), exhibiting faster initial heating rates and better temperature stability. However, this advantage comes at the cost of temperature lag and greater temperature differences in common areas (particularly at measurement Point D in the kitchen).

Although Scenario 2 achieves better spatial uniformity, this uniformity is accompanied by higher energy costs. During the system startup phase, the overall heating rate in Scenario 2 is 8.4% lower than that in the bedroom areas of Scenario 1. While Scenario 1 shows temperature fluctuations in common areas, its performance advantages in core bedroom areas and overall energy efficiency are of significant value. Especially in residential environments with well-defined living schedules, these common area temperature fluctuations can be compensated for by optimizing control algorithms.



(a)Scenario 1



(b) Scenario 2

Fig. 6. Temperature and flow field distributions at 1.5 m.

5 Conclusions

To accurately reflect the effects of water-side regulation and unheated interior sur-faces on radiant heat transfer in floor heating systems, this study establishes a CFD model that comprehensively considers the combined effects of supply water temperature, flow rate, and unheated surfaces. The developed model demonstrates multi-zone coupling capability, enabling the handling of coupled heat transfer between upper and lower surfaces of intermediate floor slabs, with numerical stability achieved through relaxation iteration methods. Comparative studies were conducted on indoor temperature variations under both zonal variable flow and constant flow conditions.

The model exhibits zonal regulation capability. By adjusting the flow rate in each zone, temperature stability in critical zones can be maintained while optimizing flow distribution in non-critical zones. In the sleep scenario (Scenario 1) simulation, temperature fluctuations in the bedroom zone remained below 0.5 °C, whereas other zones with a 50% flow reduction experienced only a 1.2–1.8° C temperature decrease, without compromising overall thermal comfort.

The zonal regulation strategy significantly enhances energy efficiency. Compared to uniform flow distribution, the differentiated control scheme reduces flow demand by 15–20% while meeting thermal environment requirements in primary functional zones, providing a feasible solution for energy-efficient building operation.

Funding. This research was funded by the National Key Research and Development Program of China through grant number 2021YFE0116200 and the Fundamental Research Program of the Education Department of Liaoning Province through grant numbers JYTZD2023166 and JYTMS20231594.

References

1. Hesaraki, A., Holmberg, S.: Energy performance of low temperature heating systems in five new-built swedish dwellings: a case study using simulations and on-site measurements. Build Environ. **64**, 85–93 (2013)
2. Yan, D., Zhe, T., Yong, W., Neng, Z.: Achievements and suggestions of heat metering and energy efficiency retrofit for existing residential buildings in northern heating regions of China. Energy Policy. **39**, 4675–4682 (2011)
3. Yuan, S., Xu, W.: Establishment and validation of a sustainable evaluation model for heat metering technology in China. Energy Build. **99**, 153–161 (2015)
4. Luo, A., Xia, J.: Policy on energy consumption of district heating in northern China: historical evidence, stages, and measures. J Cleaner Product. **256**, 120265 (2020)
5. Fu, S., Pan, Y., Wan, X., Wang, J., Jia, X., Luo, X., Ma, H.: Numerical simulation of heat transfer characteristics of capillary radiant heating floor. KSCE J. Civ. Eng. **28**, 546–556 (2024)
6. Peng, Z., Carrigan, S., Kornadt, O.: Investigation of the influence of different room geometries and wall thermal transmittances on the heat transfer in rooms with floor heating. Energy Build. **317**, 114391 (2024)
7. Zhang, Y., Zhang, M., Gao, F., Li, J.: Experimental study on internal heat transfer among adjacent rooms for building energy efficiency with housing vacancy consideration. Case Stud Thermal Eng. **62**, 105188 (2024)
8. Ministry of Housing and Urban-Rural Development: Technical Specification for Radiant Floor Heating (JGJ 142-2012). China Architecture & Building Press, Beijing (2012)
9. ASHRAE: HVAC Systems and Equipment. American Society of Heating, Refrigerating and Air-Conditioning Engineers, Atlanta (2024)
10. Lu, L., Luo, L., Chen, J., Wen, J.: Study on energy-saving potential of lowering the emissivity of unheated surfaces for floor radiant heating. Energy. **286**, 129592 (2024)

Energy Performance Comparison of Diffuse Ceiling Ventilation and Mixing Ventilation Strategies in Heating Conditions

Rui Guo[1(✉)] and Shady Attia[2]

[1] School of Environmental Science and Engineering, Huazhong University of Science and Technology, Wuhan 430074, China
guorui@hust.edu.cn

[2] Sustainable Building Design Lab, Department UEE, Faculty of Applied Sciences, Université de Liège, Liège, Belgium

Abstract. Diffuse ceiling ventilation (DCV) represents an innovative air distribution strategy that supplies air to a plenum before diffusion through suspended ceiling panels into occupied zones, offering potential advantages over conventional mixing ventilation (MV) in heating conditions. This study presents a comprehensive building energy simulation analysis comparing DCV and MV heating performance using EnergyPlus for an office room in Copenhagen. Five convective heat transfer coefficient (CHTC) algorithms and three thermal mass levels were considered. Multiple regression analysis quantified the relative importance of thermal mass levels and CHTC algorithms on system performance. Results demonstrate that DCV consistently outperforms MV across all scenarios, achieving energy savings of 1.3–2.1 kWh/m^2 (5–9% reduction) and providing better thermal comfort, with a lower average predicted percentage of dissatisfied values during occupied hours (7.4% vs 8.9%). The analysis reveals that the thermal mass level primarily influences HVAC energy use in both systems, while the selection of the CHTC algorithm mainly affects peak heating demand and thermal comfort predictions. This research establishes DCV as a viable energy-efficient alternative to conventional MV systems in heating-dominated climates.

Keywords: Diffuse ceiling ventilation · Heating energy performance · Convective heat transfer coefficient

1 Introduction

Diffuse ceiling ventilation (DCV) is an innovative air distribution concept with three main components: an air plenum, suspended ceiling panels, and the ventilated room. In this system, conditioned air is first supplied to the plenum and then diffuses uniformly into the occupied zone through perforated ceiling panels [1]. This configuration enables the supply of low-temperature air with minimal draught risk due to the low-momentum flow characteristics, offering potential advantages over conventional mixing ventilation (MV) systems that supply conditioned air with high momentum to achieve uniform air

© The Author(s), under exclusive license to Springer Nature Singapore Pte Ltd. 2025
L. Ni et al. (Eds.): CCHVAC 2025, ESE, pp. 458–466, 2025.
https://doi.org/10.1007/978-981-95-3253-7_49

mixing. Previous research on DCV has primarily focused on cooling conditions and thermal comfort performance. Numerous studies have investigated the convective heat transfer coefficient (CHTC) correlations and ventilation effectiveness for DCV systems [2], while some research has examined DCV performance in heating mode [3]. A study compared the cooling performance of night cooling with DCV and MV in summer [4]. Limited attention has been given to the systematic comparison of energy performance between DCV and MV under heating conditions, which represents a research gap.

This study aims to address this knowledge gap by conducting a comprehensive comparison of heating energy performance between DCV and MV systems in a cold climate. The research employs building energy simulation to evaluate the heating energy consumption, considering various CHTC algorithms and thermal mass levels. The performance comparison encompasses multiple evaluation metrics, including HVAC energy use, peak heating demand, and thermal comfort. This study contributes to the advancement of energy-efficient HVAC system design.

2 Methodology

An intermediate-floor office room (29.4 m^2) with a north-facing exterior wall was chosen as the case room [5]. To simplify the thermal analysis, adiabatic boundary conditions were applied to the internal partitions, assuming uniform thermal environments in adjacent spaces. The exterior wall featured a high-performance glazing system consisting of double-pane windows with 3 mm glass panels separated by a 13 mm argon-filled cavity. The fenestration specifications included a window area of 1.44 m^2, an overall U-value of 1.06 $W/m^2 \cdot K$, solar heat gain coefficient of 0.58, and a visible light transmittance of 0.70. Internal heat sources comprised two occupants generating 120 W each, with clothing resistance of 0.50 clo, lighting systems at 6 W/m^2, and electrical equipment at 8 W/m^2 [6]. These internal loads operated at full capacity during occupied hours (08:00–17:00) on weekdays, with zero operation during unoccupied hours. The infiltration rate was 0.25 h^{-1}. Weather boundary conditions were based on typical meteorological year (TMY3) data for Copenhagen (station 061800, IWEC format), specifically focusing on the heating season from January 1 to March 31 and from November 1 to December 31. The VAV air-conditioning (AC) system was also equipped for the case room. The AC operated during working hours with a heating setpoint of 22 °C and an outdoor airflow of 30 $m^3/(h \cdot person)$ [7]. The DCV and MV systems were configured to compare the heating performance, as shown in Fig. 1.

It should be noted that typical supply air change rates for HVAC systems in occupied rooms range from 4 to 6 h^{-1} [8], which corresponds to mean air velocities in the occupied zone of approximately 0.08 m/s for DCV and 0.2 m/s for MV [9]. The VAV fan specifications were based on Ref. [4]. Since DCV systems exhibit lower pressure drops compared to conventional ventilation systems [1], the fan design pressure rises were set at 80 Pa for DCV and 600 Pa for MV, respectively. Identical thermal mass (i.e., fiber plasterboards) distribution schemes were applied to both DCV and MV systems for comparative analysis. Three configurations were examined: 'Not installed', 'Floor', and 'Floor+Wall', representing scenarios where thermal mass was absent from the case room, installed only on the floor, or installed on both the floor and one interior

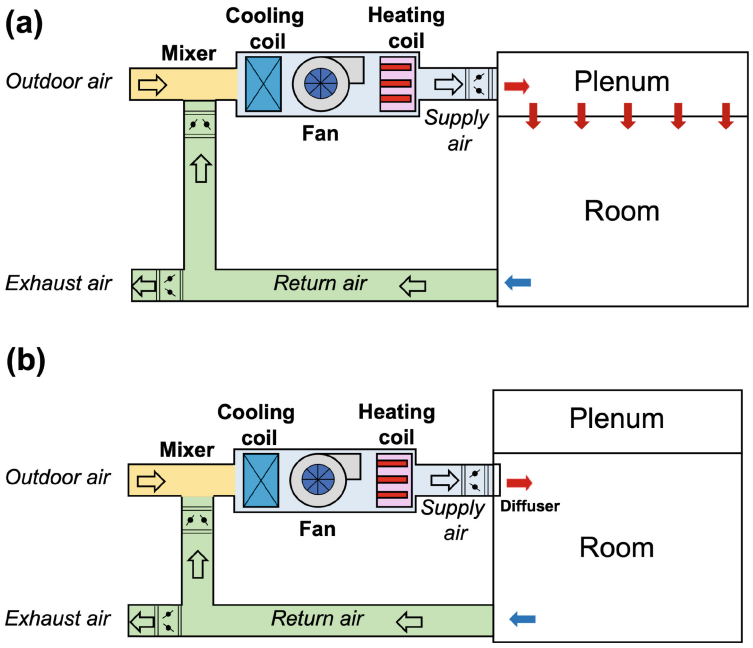


Fig. 1. VAV AC systems for the (**a**) DCV and (**b**) MV concepts.

wall, respectively. The corresponding total dynamic heat capacity per unit floor area ranges from 37.8 to 67 kJ/m^2·K. To evaluate the impact of different CHTC algorithms on the heating performance of both ventilation concepts, five algorithms were selected: Simple, TARP, Ceiling Diffuser, Adaptive Convection [10], and User-defined [4]. The user-defined algorithms have been previously validated for night cooling applications [4]. The HVAC (i.e., AC + Fan) energy use per unit floor area, peak heating demand per unit floor area, and the average predicted percentage of dissatisfied during occupied hours were selected as the simulation outputs to evaluate the heating performance.

3 Results

3.1 Impact of Thermal Mass Levels and Ventilation Concepts on Heating Performance

Figure 2 compares the HVAC energy use as a function of thermal mass levels and ventilation concepts. The thermal mass configuration has a significant influence on energy performance under both ventilation strategies. For DCV systems, buildings with floor and wall thermal mass demonstrate the highest average HVAC energy use, at 23.2 kWh/m^2, followed by buildings with floor thermal mass at 22.8 kWh/m^2. Buildings without thermal mass show the lowest energy consumption, at 22.1 kWh/m^2. Similarly, MV systems exhibit the same trend, with buildings with floor and wall thermal mass showing the highest average HVAC energy use at 25.3 kWh/m^2, buildings with floor thermal mass

at 24.7 kWh/m^2, and buildings without thermal mass demonstrating the lowest consumption at 23.4 kWh/m^2. DCV consistently outperforms MV across all thermal mass scenarios, achieving energy savings of 2.1, 1.9, and 1.3 kWh/m^2 for floor and wall thermal mass, floor thermal mass, and no thermal mass cases, respectively. The results reveal that increased thermal mass leads to higher HVAC energy consumption, with a more pronounced impact in MV systems (a 1.9 kWh/m^2 increase from no thermal mass to floor and wall thermal mass) compared to DCV systems (a 1.1 kWh/m^2 increase). This phenomenon can be attributed to the higher thermal capacity requiring additional heating energy to warm up the building envelope during the heating season, while the superior air distribution characteristics of DCV systems help mitigate this penalty through lower pressure drop (i.e., fan energy use).

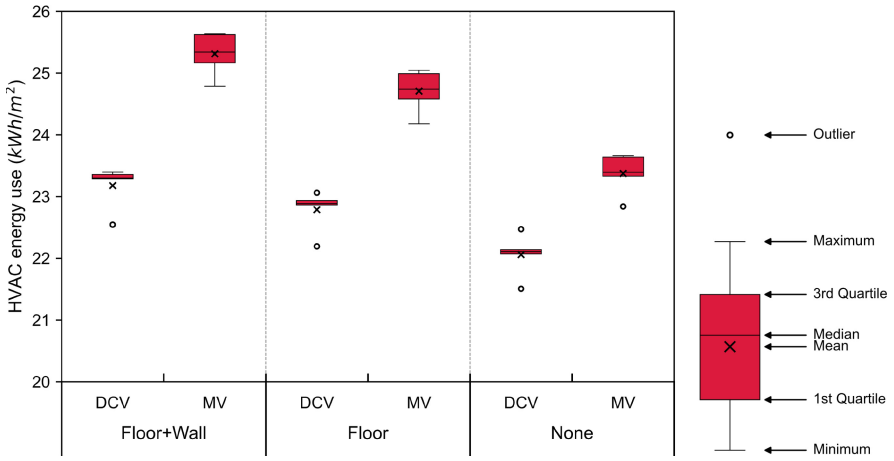


Fig. 2. HVAC energy use comparison for thermal mass levels and ventilation concepts. Floor+Wall: the floor and right wall have gypsum fiberboards. Floor: the floor has gypsum fiberboards. None: no thermal mass.

Figure 3 compares the peak heating demand as a function of thermal mass levels and ventilation concepts. The results reveal that the thermal mass tends to reduce the peak heating demand by absorbing and storing excess heat during occupied hours and gradually releasing it during unoccupied hours, thereby mitigating diurnal temperature fluctuations and minimizing the instantaneous heating load required to maintain thermal comfort. For buildings with floor and wall thermal mass, DCV systems show an average peak heating demand of 108.6 W/m^2, marginally higher than MV systems. Buildings with floor thermal mass demonstrate nearly identical performance between both strategies. Interestingly, buildings without thermal mass exhibit a reversal in this trend, where DCV systems require slightly lower peak demand (109.2 W/m^2) compared to MV systems (109.7 W/m^2). Moreover, the range of peak heating demand values for MV becomes larger than the scenarios with thermal mass.

Figure 4 shows that DCV systems consistently demonstrate superior thermal comfort performance across all thermal mass configurations, maintaining average PPD values of 7.4% regardless of the presence of thermal mass. In contrast, MV systems exhibit

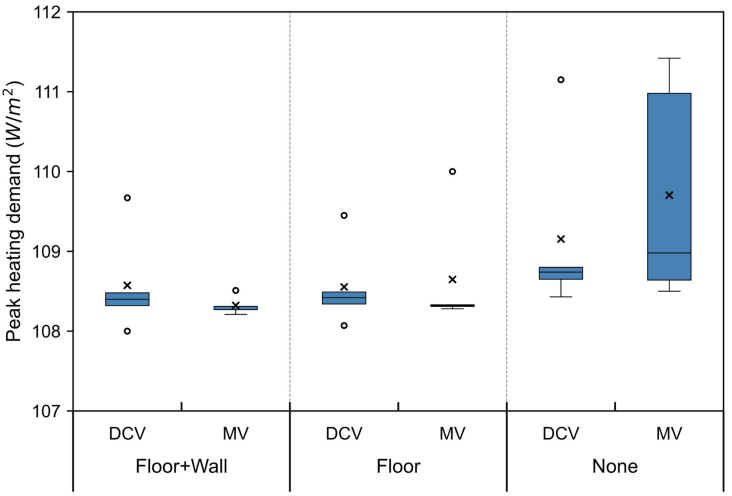


Fig. 3. Peak heating demand comparison for different thermal mass and ventilation concepts.

higher discomfort levels, with average PPD values of 8.9% across all thermal mass scenarios. This results in a consistent thermal comfort advantage of approximately 1.4–1.5 percentage points for DCV systems compared to MV systems. Notably, thermal mass configuration shows a negligible impact on PPD for both ventilation strategies. The superior comfort performance of DCV systems can be attributed to the gentler air movement compared to the direct air supply typical of MV systems.

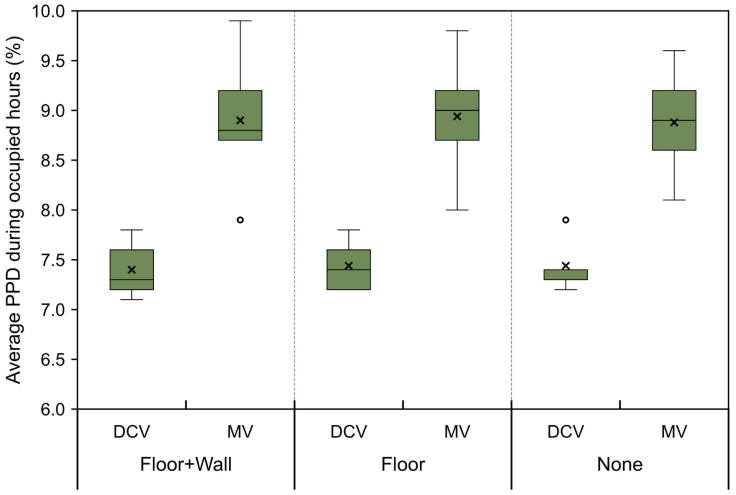


Fig. 4. Average PPD comparison for thermal mass levels and ventilation concepts.

3.2 Impact of inside Surface CHTC Algorithms and Ventilation Concepts on Heating Performance

Figure 5 compares the HVAC energy use as a function of inside surface CHTC algorithms and ventilation concepts. The choice of the CHTC algorithm has some impact on HVAC energy consumption. Among them, the user-defined algorithm exhibits the lowest HVAC energy consumption under both ventilation strategies, while the CeilingDiffuser algorithm results in the highest energy use. DCV systems exhibit an average energy use of 22.1 kWh/m^2–23.0 kWh/m^2, while MV systems show higher consumption, ranging from 23.9 kWh/m^2 to 24.8 kWh/m^2. Both ventilation strategies demonstrate similar sensitivity to CHTC algorithm selection, with comparable ranges of 0.9 kWh/m^2. DCV consistently outperforms MV across all CHTC algorithms, with energy savings ranging from 1.6 kWh/m^2 to 2.0 kWh/m^2. The user-defined algorithm yields the lowest results for both systems, likely due to its lower CHTC prediction, which reduces convective heat loss between the interior surfaces and air, thereby decreasing the heating load required to maintain thermal balance in the zone.

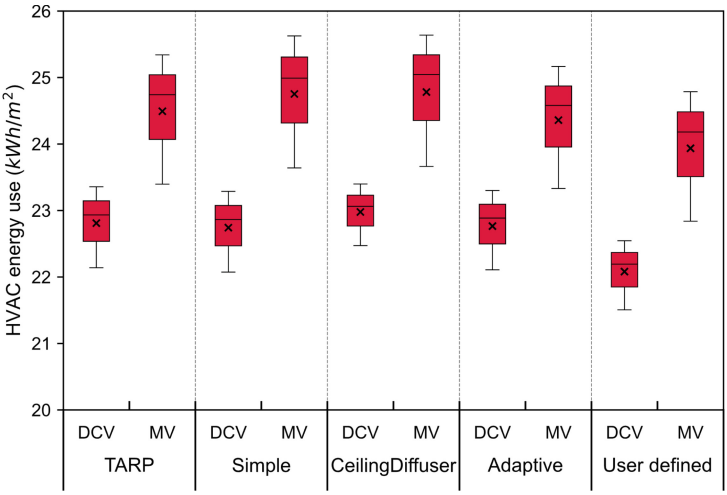


Fig. 5. HVAC energy use comparison for inside CHTC algorithms and ventilation concepts.

Figure 6 compares the peak heating demand as a function of inside surface CHTC algorithms and ventilation concepts. The CHTC algorithm selection has a noticeable impact on peak demand predictions, particularly for certain algorithms. The user-defined algorithm results in the highest peak demands for both ventilation strategies, with DCV systems averaging 110.1 W/m^2 and MV systems 109.3 W/m^2. In contrast, the CeilingDiffuser algorithm demonstrates the lowest peak demands, with DCV systems at 108.2 W/m^2 and MV systems at 108.4 W/m^2. DCV systems show slightly larger variability (1.9 W/m^2) compared to MV systems (1.5 W/m^2) across different algorithms, suggesting that the DCV system is more sensitive to convection modelling assumptions in peak demand predictions.

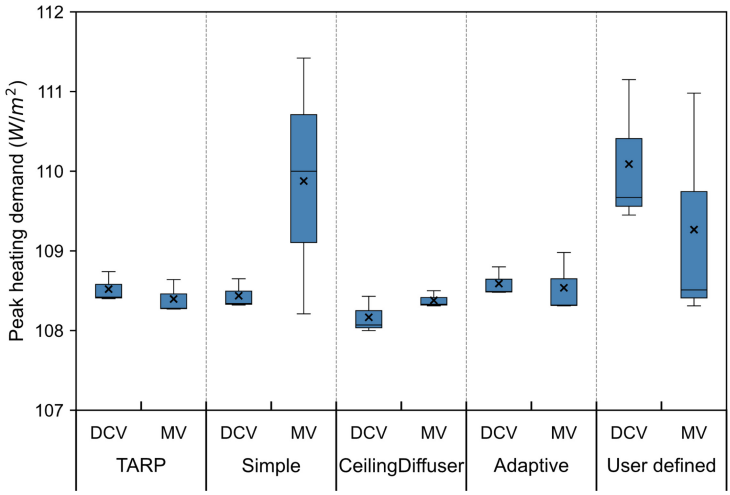


Fig. 6. Peak heating demand comparison for inside CHTC algorithms and ventilation concepts.

Figure 7 indicates that the CHTC algorithm selection can impact the thermal comfort predictions, with DCV systems consistently maintaining lower PPD values across all algorithms due to the lower velocity. The CeilingDiffuser algorithm provides the best comfort performance for both strategies, achieving 7.2% PPD for DCV and 8.0% PPD for MV systems. Notably, MV systems exhibit significantly larger variability in PPD predictions (1.6 percentage points) compared to DCV systems (0.6 percentage points), indicating that mixing ventilation comfort calculations are more sensitive to convection modeling assumptions due to the more turbulent and variable airflow patterns that characterize direct-convective ventilation systems.

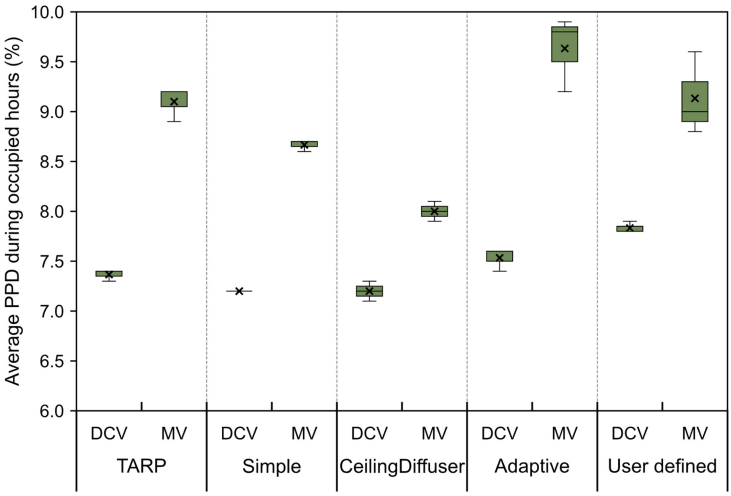


Fig. 7. Average PPD during comparison for inside CHTC algorithms and ventilation concepts.

3.3 Quantitative Impact Analysis

To quantify the relative importance of thermal mass level and CHTC algorithm on heating performance within each ventilation system, separate multiple regression analyses were conducted for DCV and MV systems following the variance decomposition methodology described by Ref. [11]. The R^2 values represent the proportion of variance in each performance indicator that is explained by individual factors, with higher values indicating a greater influence on system performance. The results in Table 1 reveal distinct sensitivity patterns between the two ventilation strategies. For DCV systems, thermal mass level dominates HVAC energy use (68.8% variance explained), while the CHTC algorithm governs peak heating demand (77.4%) and thermal comfort (93.4%). MV systems show heightened thermal mass sensitivity for energy consumption (87.3%), but balanced factor influences for peak demand (34.3% each). Notably, both systems demonstrate minimal impact on thermal mass and comfort performance (<1%). The exceptionally high R^2 values (0.686-0.999) confirm that these two design factors comprehensively explain the observed performance variations, providing crucial guidance for system-specific optimization strategies.

Table 1. Multiple regression analysis results for the impact of thermal mass levels and inside CHTC algorithms on heating performance.

Ventilation concepts	Performance indicators	Thermal mass R^2	CHTC R^2	Total R^2
DCV	HVAC energy use (kWh/m^2)	0.6881	0.3043	0.9924
	Peak heating demand (W/m^2)	0.1296	0.7741	0.9038
	PPD (%)	0.0059	0.934	0.9399
MV	HVAC energy use (kWh/m^2)	0.8727	0.1266	0.9992
	Peak heating demand (W/m^2)	0.3426	0.3434	0.6859
	PPD (%)	0.0018	0.8618	0.8636

4 Conclusions

This study conducted a comprehensive comparison of heating energy performance between diffuse ceiling ventilation (DCV) and mixing ventilation (MV) systems under cold climate conditions, examining the influence of thermal mass levels and convective heat transfer coefficient (CHTC) algorithms on system performance.

The results demonstrate that DCV systems consistently outperform MV systems across all evaluated scenarios, achieving energy savings ranging from 1.3 to 2.1 kWh/m^2

(5–9% reduction) and maintaining superior thermal comfort with lower predicted average percentage of dissatisfied values during occupied hours (7.4% vs 8.9%). Both systems show comparable peak heating demand performance, with thermal mass effectively reducing peak loads through thermal storage capacity.

The analysis reveals that the thermal mass level primarily influences HVAC energy consumption in both systems. Additionally, the selection of the CHTC algorithm significantly affects peak heating demand and thermal comfort predictions. Increased thermal mass leads to higher HVAC energy consumption, with MV systems showing greater sensitivity to this effect.

These results offer valuable insights for selecting HVAC systems in heating-dominated climates, demonstrating that DCV represents a viable alternative to conventional MV systems, with enhanced energy efficiency and improved thermal comfort.

References

1. Zhang, C., Heiselberg, P., Nielsen, P.V.: Diffuse ceiling ventilation—a review. Int. J. Vent. **13**, 49–63 (2014)
2. Guo, R., et al.: Experimental investigation of convective heat transfer for night cooling with diffuse ceiling ventilation. Build. Environ. **193**, 107665 (2021)
3. Peng, P., et al.: Experimental investigation on the ventilation performance of diffuse ceiling ventilation in heating conditions. Build. Environ. **205**, 108262 (2021)
4. Guo, R., Hu, Y., Heiselberg, P., Johra, H., Zhang, C., Peng, P.: Simulation and optimization of night cooling with diffuse ceiling ventilation and mixing ventilation in a cold climate. Renew. Energy. **179**, 488–501 (2021)
5. Guo, R., Hu, Y., Liu, M., Heiselberg, P.: Influence of design parameters on the night ventilation performance in office buildings based on sensitivity analysis. Sustain. Cities Soc. **50**, 101661 (2019)
6. ISO 7730:2005—Ergonomics of the thermal environment—Analytical determination and interpretation of thermal comfort using calculation of the PMV and PPD indices and local thermal comfort criteria (2005)
7. EN 15251. Indoor environmental input parameters for design and assessment of energy performance of buildings addressing indoor air quality, thermal environment, lighting and acoustics (2007)
8. O'Donnavan, A., et al.: Ventilative Cooling Design Guide. Aalborg University, Department of Civil Engineering (2018)
9. Petersen, S., Christensen, N.U., Heinsen, C., Hansen, A.S.: Investigation of the displacement effect of a diffuse ceiling ventilation system. Energ. Buildings. **85**, 265–274 (2014)
10. U.S. Department of Energy. EnergyPlus 9.3 Input Output Reference 2020. https://bigladdersoftware.com/epx/docs/9-3/input-output-reference/
11. Ciulla, G., D'Amico, A.: Building energy performance forecasting: a multiple linear regression approach. Appl. Energy. **253**, 113500 (2019)

Research on Ice Restaurant Form Design Based on Indoor Thermal Environment Simulation

Xianglu Ding, Peng Luo(✉), Yongxin Liu, and Tianshuo Ren

School of Architecture and Design, Harbin Institute of Technology; Key Laboratory of Cold Region Urban and Rural Human Settlement Environment Science and Technology, Ministry of Industry and Information Technology, Harbin, Heilongjiang 150090, China
pengluo@hit.edu.cn

Abstract. In recent years, China's ice and snow industry has entered a fast—growing phase, boosting the ice and snow tourism market. Amid the flourishing ice and snow tourism, ice shell buildings have gained more attention. As tourists demand better travel experiences, the thermal comfort inside ice shell buildings is crucial for their spatial use efficiency. This study focuses on ice restaurants, a typical ice shell building. Using the Grasshopper platform, it sets up a parametric modeling and performance simulation workflow to explore the indoor thermal conditions of different—shaped ice restaurant models.

Keywords: Ice Restaurants · Indoor Thermal Environment Simulation · Thermal Comfort

1 Introduction

In March 2016, General Secretary Xi Jinping emphasized when attending the deliberation of the delegation of Heilongjiang Province during the "Two Sessions" that "the ice and snow in Heilongjiang is also a golden mountain."In recent years, ice and snow tourism, a key branch of the ice and snow industry, has grown quickly. Ice and snow buildings, which focus on both landscape and function, are often key parts of ice and snow tourism attractions. Ice and snow buildings can provide short—term protection against wind and cold and serve decorative purposes. Seen mostly in cold climates, ice and snow buildings have a long history [1]. As an emerging type of ice and snow building, ice shell buildings hold significant potential for the sustainable development of the ice and snow industry. Over time, ice shell buildings have evolved into structures that blend functionality and artistic design [2]. Ice shell buildings attract tourists worldwide who often lack experience living in extremely cold regions and may struggle to tolerate the cold inside ice and snow buildings. Accordingly, there is an urgent need to upgrade the indoor thermal environment of ice shell buildings.

Currently, there are limited studies on the thermal environment of ice shell buildings. Most research on indoor thermal environments in cold regions focuses on conventional structures such as houses, office buildings, gymnasiums, and classrooms. The research methods primarily combine on-site measurements with questionnaires. Some scholars

© The Author(s), under exclusive license to Springer Nature Singapore Pte Ltd. 2025
L. Ni et al. (Eds.): CCHVAC 2025, ESE, pp. 467–475, 2025.
https://doi.org/10.1007/978-981-95-3253-7_50

also use numerical simulations and the establishment of thermal comfort evaluation systems as supplementary research methods [3]. This study uses the "Ice Shell" Ice Restaurant, "Snowy Dreamland" Ice Restaurant, and "Sky Dance" Ice Restaurant as prototypes. Based on analyzing and summarizing the development history of ice shell buildings, it extracts typical ice restaurant forms. Using the Grasshopper platform, it builds a parametric modeling and performance simulation workflow. The indoor thermal environments of ice restaurants with different forms are analyzed, and design strategies for ice restaurant forms are proposed.

2 Ice Restaurant Overview

2.1 Ice Restaurant Case Study

The "Ice Shell" ice restaurant was built in December 2019 at the 21st Ice and Snow World Park in Harbin, Heilongjiang Province. It has a total floor area of 554 m^2, a height of 7 m, a span of 13 m, a height-to-span ratio of 0.54, and can accommodate 40 people dining simultaneously [4]. The "Snowy Dreamland" ice restaurant was built in December 2020 at the 22nd Ice and Snow World Park in Harbin, Heilongjiang Province. It has a total floor area of 1,834 m^2. The main ice shell featured a span of 30 m, with a maximum height of 13 m, resulting in a height-to-span ratio of 0.43. The interior can accommodate 76 people dining simultaneously. The "Sky Dance" ice restaurant was built in December 2023 at the 25th Ice and Snow World Park in Harbin, Heilongjiang Province. It has a total floor area of 490 m^2, a span of 24 m, a maximum height of 10 m, a height-to-span ratio of 0.42, and can accommodate 40 people dining simultaneously [5]. Aerial photographs of these three ice restaurants are presented in Fig. 1.



Fig. 1. Aerial photographs of the ice restaurants "Ice Shell", "Snowy Dreamland" and "Sky Dance".

A comprehensive comparison and analysis of the plan shape, height-to-span ratio, and vent location parameters of the three case studies—the "Ice Shell" ice restaurant, "Snowy Dreamland" ice restaurant, and "Sky Dance" ice restaurant—were conducted. As summarized in Table 1, it was found that in all three cases, the vents near the lower side are arranged in combination with the entrances and exits. The top vents, on the other hand, are distributed in two forms: centralized and uniformly spread.

Table 1. Comparative analysis of three ice restaurant cases.

Ice shell buildings	Plan shape	Height, span, and height-to-span ratio	Vent location
"Ice Shell" ice restaurant		Height: 7 m, span: 13 m, height - to - span ratio: 0.54	Concentrated at the lower side and dispersed at the top
"Snowy Dream-land" ice restaurant		Height: 13 m, span: 30 m, height - to - span ratio: 0.43	Concentrated at the lower side and concentrated at the top
"Sky Dance" ice restaurant		Height: 10 m, span: 24 m, height - to - span ratio: 0.42	Concentrated at the lower side and concentrated at the top

2.2 Modeling of Ice Restaurants with Different Forms

Based on existing ice shell building cases, it can be concluded that functional ice shells predominantly feature circular or circular-like planar shapes. The height of ice shell buildings varies primarily between 3 m and 30 m, spans between 8.6 m and 30 m, and height-to-span ratios between 0.18 and 1.05. In consideration of practical conditions, the typical ice restaurant model is designed with a height of 12 m and a span of 24 m, resulting in a height-to-span ratio of 0.5. The total building area is 453 m^2, and the vent area is 22 m^2, located at the top with a centralized distribution. Additionally, two door openings are set on the lower side, with a total area of 8 m^2. These parameters—height, span, and height-to-span ratio—are within the reasonable range for ice shell structures. They ensure the structural safety of the ice restaurant building and facilitate the construction and assembly. Furthermore, they maintain the openness of the interior space within the ice restaurant. The axonometric and top views of a typical ice restaurant model are shown in Figs. 2 and 3. Based on this model, deformations in plane shape and height yield two groups of models, A and B. For group A, the variable is the plane shape, which includes four types: square circle, oval, semi-ellipse, and doughnut. The axonometric and elevation views for group A are presented in Table 2. For group B, the variable is the height, which ranges from 6 m to 18 m in increments of 3 m. The axonometric and top views for group B models are shown in Table 3.



Fig. 2. Axonometric drawing of the typical ice restaurant model.

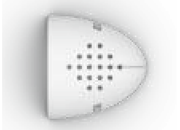


Fig. 3. Top view of the typical ice restaurant model.

Table 2. Group A model details.

No.	A1 (6m high)	A2 (9m high)	A3 (12m high)	A4 (15m high)	A5 (18m high)
Axonometric view					
Elevation					

Table 3. Group B model details.

No.	B1 (square circle)	B2 (oval)	B3 (semi-ellipse)	B4 (doughnut)
Axonometric view				
Top view				

3 Ice Restaurant Indoor Thermal Environment Simulation

3.1 Numerical Simulation Software Overview

This study uses the Rhino (Rhinoceros 3D) parametric design platform as the modeling foundation. It integrates Grasshopper's visual programming tools and professional plugins like Ladybug Tools [6], Ironbug, and Karamba3D. This creates a comprehensive digital workflow for modeling, simulation, and analysis. Ladybug Tools serves as the core module for simulating the thermal environment of ice restaurants. The Ladybug Tools suite in Grasshopper includes multiple plugins: Ladybug, Honeybee, Dragonfly, and Butterfly. This study primarily uses Ladybug and Honeybee for thermal environment simulations [7], as they can access two simulation engines: EnergyPlus and OpenStudio [8].

3.2 Indoor Thermal Environment Simulation Process

Before simulating the indoor thermal environment of the ice restaurant, the different morphological models of the ice restaurant need to be meshed and converted into a Honeybee-recognizable format [9]. Next the non-morphological parameters of the model need to be set. The first is the setting of the model envelope material parameters. The model roof, floor, and holes are assigned the corresponding materials,. The roof is made of composite ice with 2% concentration, the ground is made of compacted snow, and the hole is made of air wall. Specifically, the composite ice has a thickness of 0.2 m, a thermal conductivity of 1.586 W/(m·°C), a density of 1030 kg/m^3, and a specific heat capacity of 1960 J/(kg·°C). The compacted snow has a thickness of 0.2 m, a thermal conductivity of 0.551 W/(m·°C), a density of 550 kg/m^3, and a specific heat capacity of 1675 J/(kg·°C). Input these values into the panel cell block, then connect the panel containing the envelope material parameters to the _thickness, _conductivity, _density, and _spec_heat interfaces of the HB Opaque Material cell, respectively. At this point, it means that the materials of the roof, floor and holes of the ice restaurant model have been set up.

Next, schedule settings are performed to clarify the building type and define the load for the ice restaurant. As shown in Fig. 4, the building model type is designated as a full—service restaurant, with a staff density of 0.09 persons/m^2. To adhere to the single—variable principle, weekday and non—weekday staff activity schedules are standardized. During the simulation period (January 1–31, 17:00–22:00 daily), the staff presence rate is set to 100%. This is reflected in the Gene Pool cell block, where values are 1.0 from 17:00 to 22:00 and 0.0 otherwise. To more accurately replicate the interior equipment of the ice restaurant, the heat output from the fondue pots must be considered. In this study, the fondue pots are replaced with an HVAC system configuration. This ensures the total heat output matches that of the fondue pots at 17,600 W. The HVAC system's operation schedules align with the staff activity schedules.

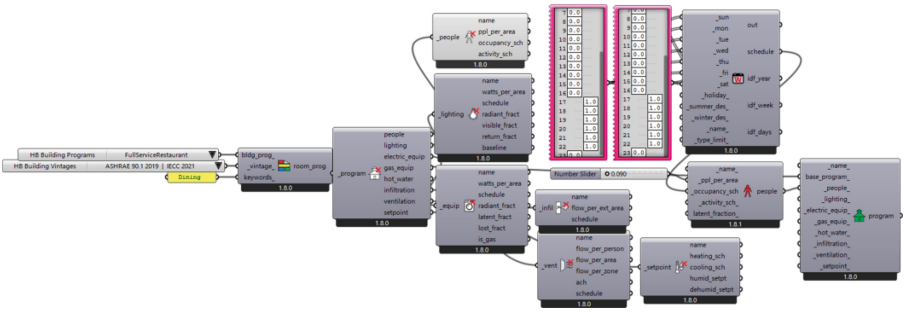


Fig. 4. Schedule and building type setup.

Obtain detailed meteorological data for Harbin from the EnergyPlus website and save it locally. Connect the saved files to the _epw and _ddy interfaces of the HB PMV Comfort Map block. This inputs time—based data on Harbin's outdoor temperature, humidity, and wind speed into the simulation system. Link the HB Model, which includes material parameters, to the _model interface and set the simulation period from 17:00 on January 1 to 22:00 on January 31 in the LB Analysis Period block. The time period of Harbin's outdoor dry—bulb temperature map is shown in Fig. 5. During this period, the lowest outdoor temperature is −24.5 °C, and the highest is −4.9 °C. At this point, the simulation system for the ice restaurant's internal temperature is initially set up. The output port temperature of the HB PMV Comfort Map block is connected to the HB Read Thermal Matrix block for result reading. Then, the result visualization block HB Visualize Thermal Map is connected to the comf_mtx output of the HB Read Thermal Matrix block. The entire internal environment temperature simulation setup is shown in Fig. 6, and the indoor thermal environment simulation process of the ice restaurant is established.

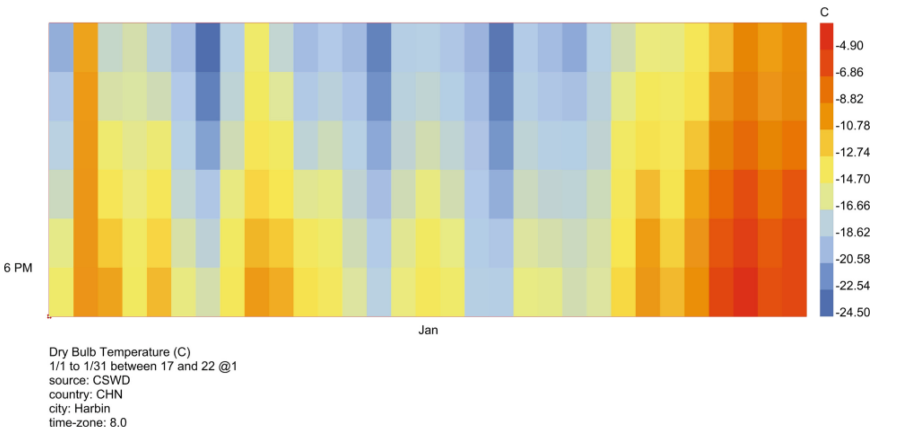


Fig. 5. Harbin's outdoor dry—bulb temperature map.

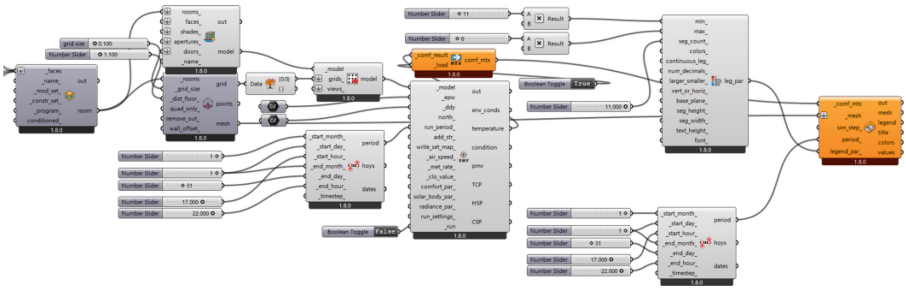


Fig. 6. The internal environment temperature simulation setup.

3.3 Indoor Thermal Environment Simulation Results

This study conducts indoor thermal environment simulations for the ice restaurant models in groups A and B. Temperature field distribution maps at a height of 1.1 m and the average temperature at this height are obtained. The simulation results for group A models are presented in Table 4, and those for group B models in Table 5. Analysis of Table 4 shows minimal variation in the average temperature at 1.1 m across different heights of the ice restaurant. From Table 5, it is evident that there are certain differences in the average temperature at 1.1 m among ice shell buildings with varying plan shapes. The highest temperature of −8.55 °C occurs when the plan shape is a square circle.

Table 4. Group A model simulation results.

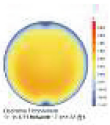
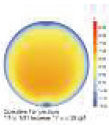
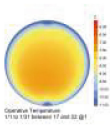
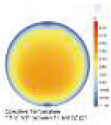
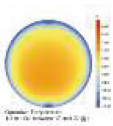
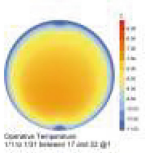
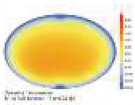
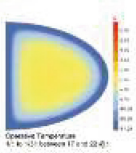
No.	A1 (6m high)	A2 (9m high)	A3 (12m high)	A4 (15m high)	A5 (18m high)
Temperature field distribution at 1.1m height					
Averaged temperature	-8.57℃	-8.54℃	-8.55℃	-8.56℃	-8.59℃

Table 5. Group B model simulation results.

No.	B1 (square circle)	B2 (oval)	B3 (semi-ellipse)	B4 (doughnut)
Temperature field distribution at 1.1m height				
Averaged temperature	-8.55℃	-8.72℃	-10.01℃	-10.07℃

4 Ice Restaurant Form Design Strategy

Simulations of indoor thermal environments for ice restaurant models with varying heights and plan shapes reveal that the height of the ice restaurant has minimal impact on the average temperature at 1.1 m above the floor. In contrast, the plan shape significantly affects the average temperature at this height, with circular or near-circular plan shapes yielding relatively comfortable indoor thermal conditions. For future ice restaurant construction projects, prioritizing circular or near-circular layouts is recommended to enhance indoor thermal comfort. Additionally, parametric tools can be used to dynamically adjust the aspect ratio of the plan shape, balancing thermal performance and structural feasibility.

Acknowledgments. This work was supported by the National Natural Science Foundation of China (grant number 52378015).

References

1. Wu, Y., Chen, B., Liu, X., et al.: Development and exploration of ice and snow buildings. In: Chinese Academy of Building Research, China Civil Engineering Society Bridge and Structural Engineering Branch Space Structure Committee. Proceedings of the 16th Space Structure Academic Conference. Harbin Institute of Technology, China (2016)
2. Zhang, Y., et al.: Tests of thermophysical properties of composite ice and investigation on solar radiation and heat transfer process of composite ice structure. Build. Environ. **2025**, 112725 (2025)
3. Ren, H., Li, G.: Experimental study on winter indoor design temperature of rural residential buildings in severe cold regions. J Arch. **S1**, 18–21 (2014)
4. Luo, P., Yang, S.: Contemporary ice and snow building innovation based on natural wisdom. Epoch Arch. **06**, 31–37 (2021). https://doi.org/10.13717/j.cnki.ta.2021.06.008
5. Luo, P., Wang, X., Yang, S.: Technical logic and artistic expression: exploration of contemporary ice and snow building innovation. Contemp Arch. **10**, 63–67 (2021)
6. Chu, Y., Li, J., Zhao, P.: Multi-objective optimization of envelope structures for rural dwellings in Qianbei region, China. Buildings. **15**(8), 1367 (2025)
7. Zhuang, Y., Liu, X., Wang, J.: Parametric simulation and field measurement of outdoor thermal comfort in urban residential areas based on grasshopper. Construct Technol. **15**, 26–30+34 (2022). https://doi.org/10.16116/j.cnki.jskj.2022.15.005
8. Tian, Y., Huang, Q., Wang, T.: Experimental and simulation study on the effect of window area on indoor thermal comfort. Build. Sci. **38**(10), 84–91 (2022). https://doi.org/10.13614/j.cnki.11-1962/tu.2022.10.11
9. Lu, J., Sui, J.: Optimal design of existing farmhouses' envelope in Yantai based on multi-objective optimization. Energy Conserv. **44**(03), 5–9 (2025)

Percentage of Dissatisfied Model of Thermal Environment Based on Beta Distribution

Yongxin Liu[1,2] and Peng Wang[1,2(✉)]

[1] School of Architecture and Design, Harbin Institute of Technology, Harbin, Heilongjiang 150090, China
cahnburg@hit.edu.cn

[2] Key Laboratory of Cold Region Urban and Rural Human Settlement Environment Science and Technology, Ministry of Industry and Information Technology, Harbin, Heilongjiang 150090, China

Abstract. Human thermal comfort is one of the important contents of environmental health. Thermal environment predicted percentage of dissatisfied (PPD) is a key index of thermal comfort evaluation. Predicted mean vote (PMV) is obtained by measuring environmental and body factors. Then, a prior distribution (pre-estimation results) of PPD forms by introducing the PMV-PPD model. Considering the characteristic of field survey data, beta distribution is introduced to express a likelihood function and a posterior distribution in Bayesian thermal comfort model. The posterior distribution of PPD can be calculated according to characteristics of beta distribution. Prediction results are expressed by a mathematical expectation of the corresponding probability distribution, which is called Bayesian percentage of dissatisfied (BPD). The results of the case study can verify the BPD model. The main results are concluded as follows. Both a variance of a prior distribution and the size of survey samples will affect prediction results. With the increasing of size of survey samples, the affection of the prior distribution on the prediction results will gradually weaken. Considering objective factors of a thermal environment, the model can be applied by fewer field survey samples, and can be applied to design and analysis of building thermal environment.

Keywords: Thermal comfort prediction · Bayesian theory · PMV-PPD · Beta distribution

1 Introduction

Rapid urbanization is an important feature of modern society. By 2050, 70% of the world's population will live in cities [1], and people will spend 80% to 90% of the whole time in buildings [2]. Designing and maintaining comfortable indoor environment becomes more indispensable. However, maintaining a comfortable indoor environment may increase building energy consumption, since energy consumption of HVAC and lighting system accounts for about 70% of the total energy consumption of buildings [3]. The main causes of energy waste of HVAC systems include not only a lower indoor temperature, but also a fixed temperature, which is not adjusted according to outdoor

© The Author(s), under exclusive license to Springer Nature Singapore Pte Ltd. 2025
L. Ni et al. (Eds.): CCHVAC 2025, ESE, pp. 476–485, 2025.
https://doi.org/10.1007/978-981-95-3253-7_51

temperatures. The study shows that a strict setting value of indoor temperature is not a necessary condition to ensure human thermal comfort, and other objective and subjective factors also affect thermal comfort and percentage of dissatisfied (PD) of thermal environment [4]. Therefore, only using temperature or other objective environmental factors to describe PPD is not in line with actual situations.

In order to analyze indoor thermal environment quantitatively, researchers have established many thermal comfort prediction and evaluation models. Predicted mean vote (PMV) takes air temperature, humidity, wind speed, average radiation temperature, clothing condition and metabolic rate as input variables. Further, PPD is used to express the predicted results of PD [4]. The PMV-PPD model has been successfully applied to air-conditioned environment, especially when a range of PMV is (−2, 2). Then, Fanger and Toftum proposed an extended predicted mean vote (ePMV) for the thermal comfort study of non-air-conditioned environment in hot and humid zones, including correction of expected factors, to make the prediction results closer to an actual thermal sensation [5]. However, there are still many studies presenting that deviations exist between predicted results and actual evaluation results, which makes the predicted results failed to reflect the actual situation. To analyze the effects of psychological adaptation, physiological adaptation and behavioral adjustment on thermal comfort, scholars have proposed an adaptive predicted mean vote (aPMV) model based on a large number of research results to reflect the thermal sensation of the human body to the environment under thermal adaptation. The results are expressed by neutral temperature, acceptable temperature range and the linear relationship between a neutral temperature and an outdoor temperature. Yao et al. establishes a quantitative relationship between aPMV and PMV by introducing an adaptive factor. Selecting different adaptation factors for different environmental conditions makes aPMV close to actual mean vote (AMV) [6]. Researchers also try to extend the PMV-PPD model from artificial climate chambers or air conditioning rooms. According to the theory of thermal adaptation, a PMV value is modified by using environmental parameters to form a new predicted mean vote (nPMV) model, which makes the predicted results closer to actual thermal sensation [7].

Thermal comfort evaluation is mainly based on survey of thermal sensation and percentage of dissatisfied, such as using AMV to express an actual evaluation result of thermal environment. The voting was based on the 7-point scale of ASHRAE-1992 [8]. Thermal sensation vote (TSV) is the most widely used evaluation model to express evaluation results. Actual percentage of dissatisfied (APD) is defined in BS EN ISO 7730-2005. The quantitative relationship between TSV and APD is established. However, TSV and AMV are mostly used in tropical areas (hot and humid environment). There is less quantitative relationship between survey results and PD under other environmental conditions.

PMV is an objective factor to describe environmental and human conditions. The PMV-PPD is often used to express prediction results of PD. In fact, there are many subjective factors, whose influences to thermal comfort have been confirmed [9]. Therefore, we try to establish an evaluation model of PD which depends on both environmental/human factors and subjective evaluation results.

2 Mathematical Models

Based on Bayesian theory, a model for calculating PD of thermal environment based on PMV is established. A prior distribution and a likelihood function are expressed by beta distribution and binomial distribution, respectively. The prior distribution (pre-estimated results) is mainly computed by a value of PMV, while the likelihood function is derived from survey results. The calculation model is described as follows.

2.1 PD of Beta Distribution

Although people's PD (also probability of dissatisfied between 0 and 1) is mainly affected by environmental and human factors, there are obviously other random influence factors. These request us to consider PD conforming to a certain probability distribution. Since PD consists of "satisfactory" or "unsatisfactory" votes, the PD is subjected to multiple Bernoulli tests. Therefore, beta distribution is chosen to express prediction results of PD. Beta distribution is a continuous distribution defined in (0,1) with two parameters. A probability density function of beta distribution is:

$$f(x; a, b) = 1/B(a, b) \cdot x^{a-1} \cdot (1 - x)^{b-1} \tag{1}$$

where x is a random variable; $B(\cdot, \cdot)$ is a beta function with model parameters a and b. In this study, model parameters a and b need to be determined according to an expectation and a variance of survey samples. The expectation and variance of beta distribution are:

$$f(x; a, b) = 1/B(a, b) \cdot x^{a-1} \cdot (1 - x)^{b-1} \tag{2}$$

where $E(X)$ and $Var(X)$ represent the expectation and variance of the sample X, respectively. The expectation of the sample should be determined according to a PMV-PPD model.

$$\overline{\varphi} = 1 - 0.95 \exp\left(-0.03353 \cdot PMV^4 - 0.2179 \cdot PMV^2\right) \tag{3}$$

where $\overline{\varphi}$ is an expectation of the sample X. Considering a variance the sample X can not be reflected in the PMV-PPD model, the variance is pre-set according to the indoor thermal environment studied. (The effects of different setting values of variances will be discussed later.) When the expectation and variance are determined, the parameters a and b can be solved uniquely. Then, the prior distribution of PPD is known.

2.2 Expression of Posterior Distribution

Bayesian method is a probability analysis method which synthesizes prior estimation and survey sample information to obtain posterior estimation. If φ is called as a predicted result or a PD in an investigation, a probability density function $g(\varphi)$ is used to express estimation of the probability of each event, which is called a prior probability. If surveys are carried out on those events, a survey sample reflects the probability of observed result y, which is expressed by density function $p(y|\ \varphi)$ and called a likelihood function. Bayesian method establishes a new method for evaluating prior estimates based on an

occurrence probability of observed result y. Density function $h(\varphi|\ y)$ is used to express a probability of possible event φ under the condition of observed result y, and it is considered that $h(\varphi|\ y)$ is a re-understanding of possible event with survey samples, and called posterior distribution (density function).

Generally, the survey results of PD belong to a binomial distribution. In a certain thermal environment, we assume that the total number of survey samples is n, the number of dissatisfied samples is y, and a probability density function of PD can be expressed as follows.

$$p(y|\varphi) = \binom{n}{y}\varphi^{y}(1-\varphi)^{n-y} \tag{4}$$

where n is the number of survey samples; and y is the number of dissatisfied samples.

According to Bayesian theory, a posterior distribution density function $h(\varphi|\ y)$ is used to express a prior estimation of PD and the information of field survey [10]. The posterior distribution is expressed as follows:

$$h(\varphi|y) = g(\varphi)\cdot p(y|\varphi)/\int_0^1 g(\varphi)p(y|\varphi)d\varphi \tag{5}$$

Equation (5) is an objective data determined by combining environmental and human factors, and obtains people's subjective evaluation through field survey. This paper will introduce a Bayesian percentage of dissatisfied (BPD) based on a posterior distribution of PD, in order to obtain the PD of both subjective and objective factors.

2.3 Prediction Results of Beta Distribution

The posterior distribution should be calculated by Eq. (5). However, since the complexity of the distribution, an analytical expression of posterior distribution can not be obtained. Numerical simulation methods (such as Markov chain Monte Carlo method) can be introduced to calculate a probability distribution. Numerical simulation methods use a large number of random numbers which satisfy the distribution conditions to calculate an expectation and a variance of the probability distribution. Considering the time consumption, we also hope to find an efficient and accurate posterior distribution calculation method. Bayesian theory and principle of statistics point out that if prior distribution of a problem is beta distribution, and the likelihood function is binomial distribution, the posterior distribution is still beta distribution [10]. This conclusion is suitable for the analysis of PD. The posterior distribution is shown as:

$$f(\varphi|y) = 1/B(a+y, b+n-y)\cdot\varphi^{a+y-1}\cdot(1-\varphi)^{b+n-y-1} \tag{6}$$

Comparing with Eqs. (1, 6) is a beta distribution of updated parameters, which is equivalent to n Bernoulli tests on the basis of prior distribution (there are y dissatisfied samples) to form a posterior distribution. Under the condition that beta distribution parameters ($a+\ y$ and $b+\ n-\ y$) are determined, a probability density function $f(\varphi|\ y)$ can be calculated directly by using software such as Scilab. Comparing with numerical simulation, this direct calculation will consume less time. Calculation processes of this model are shown in Fig. 1.

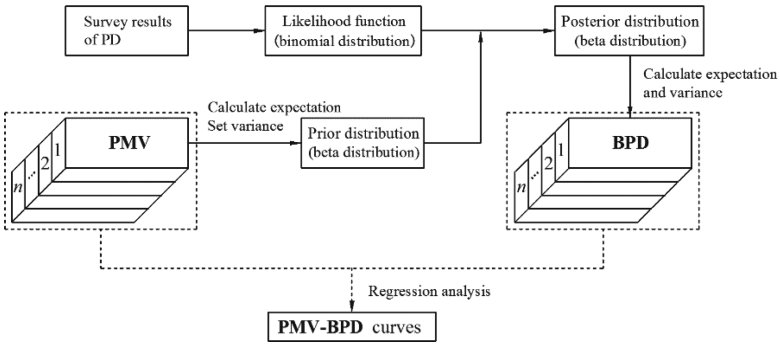


Fig. 1. Flow chart of calculating BPD.

3 Case Study

Some cases are discussed below, and calculation results are summarized and analyzed. Different conditions are set to analyze influences of prior distribution parameter selection and sample size on posterior distribution results. Then, existing data in a literature are used to verify the feasibility of this model.

3.1 Prior Distribution Characteristics

A BPD analysis model describes a prior distribution (pre-estimated results) by beta distribution. An expectation and a variance of beta distribution will determine the "shape" of a probability distribution. In this paper, PMV= ± 1.0, ± 1.5 and ± 2.0 are selected to express different environment and human states, respectively. Each group of states corresponds to a same expectation (calculated by Eq. (3)), and variances are set as 0.01, 0.02 and 0.04, respectively. Then, Scilab is used to draw the corresponding beta distribution curves. The results are shown in Fig. 2.

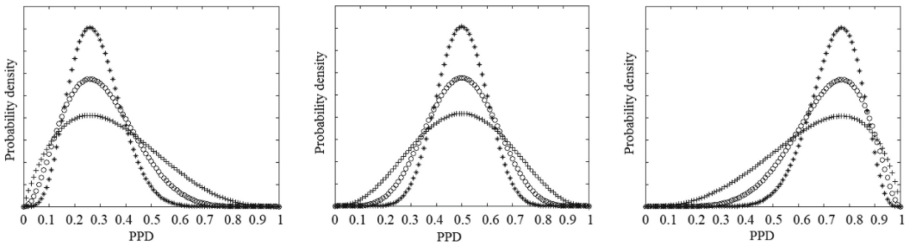
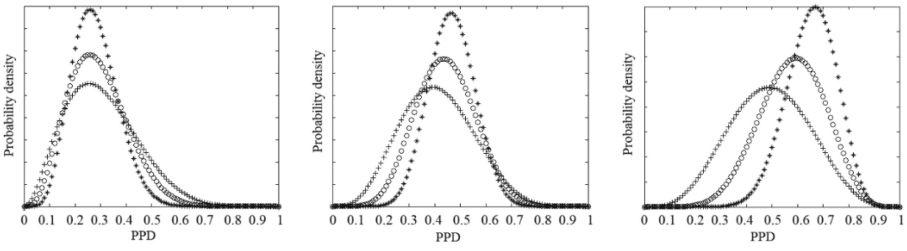


Fig. 2. Prior distribution characteristics of PD. The variances (0.01, 0.02 and 0.04) of prior distribution are expressed by "*", "o" and "+" shape lines, respectively.

In Fig. 2, a value of PMV will determine the position of the highest location on the curves. This characteristic is more obvious when a variance is smaller (such as 0.01). With the increase of the variance, a prior distribution will be more uniform, and the frequency difference in the prior distribution tends insignificant.

3.2 Distribution Variance Characteristics

A prior distribution may also affect the corresponding posterior distribution. This section will analyze this effection by calculating posterior distributions according to Eq. (6). We will express prior distributions with different PMV values (PMV= ±1, ±1.5 and ±2) and variances (0.01, 0.02 and 0.04). Moreover, PD of a survey is assumed to be 25% (1/4). Then, posterior distribution results are shown in Fig. 3.



(a) PMV=±1.0 (b) PMV=±1.5 (c) PMV=±2.0

Fig. 3. Influence of a prior distribution on the posterior distribution. The variances (0.01, 0.02 and 0.04) of prior distribution are expressed by "*", "o" and "+" shape lines, respectively.

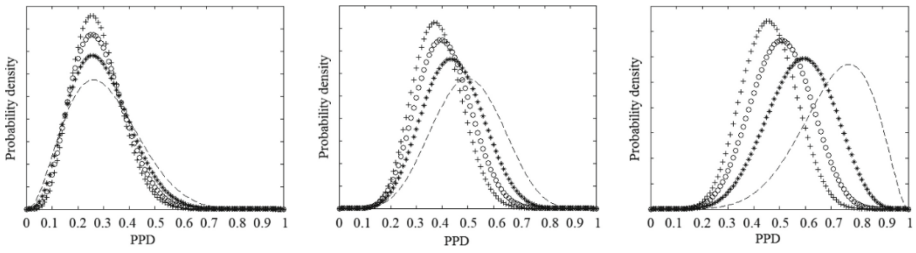
As adding survey samples, the results of PD will change. An expectation of the posterior distribution will be between the PPD and the PD of survey results, which shows that a variance of prior distribution is one of the factors affecting prediction results. If the variance is small, the posterior distribution is closed to PPD; otherwise, the posterior distribution is closed to the PD of survey results. In actual application, if we consider the prediction results are more reliable, we can choose a smaller variance; if we consider the prediction results are not accurate, we can make the posterior distribution results more easily reflect the PD of survey results by setting a larger variance.

3.3 Impact Analysis of Sample Size

In this part, we still assume the PD of survey results is 25%, and a variance of prior distribution is 0.02. The values of PMV are ±1, ±1.5 and ±2, respectively. The curves of posterior distribution with different sizes of survey samples ($n = 4$, 8 or 12) are shown in Fig. 4.

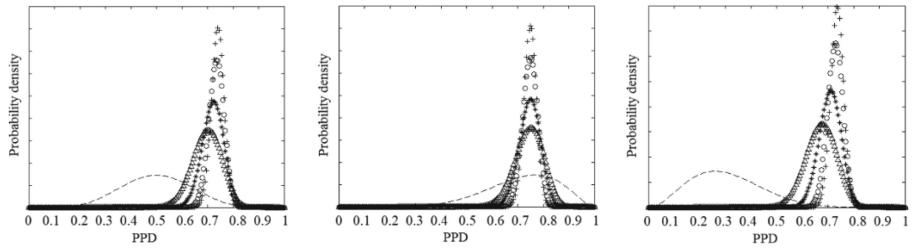
The results show that if the size of survey samples is larger; the posterior distribution is more concentrated. The prediction results are closed to the PD of survey results, which is in accordance with the law of large numbers. Then, if the size of survey samples is further increased, how does the posterior distribution change? We consider that the PD is 75% and variance of the prior distribution is 0.02 as an example to analyze the prediction results corresponding to a large number of survey samples ($n = 50$, 100, 200 and 300) with PMV values of ±1, ±1.5 and ±2, respectively. Study results are shown in Fig. 5.

The PD will gradually concentrate near survey results with the size of survey samples increasing, and if the prediction results are close to the survey results, the prediction results tend to approach the survey results easily. The influence of prior distribution on



(a) PMV=±1.0 (b) PMV=±1.5 (c) PMV=±2.0

Fig. 4. Influence of survey sample sizes on the posterior distribution. The prior distribution is expressed by "--", and the PD of the number of samples 4, 8 and 12 are expressed by "*", "o" and "+" shape lines, respectively.



(a) PMV=±1.0 (b) PMV=±1.5 (c) PMV=±2.0

Fig. 5. Posterior distribution of different sample sizes. The prior distribution is expressed by "--", and the PD of the number of samples 50, 100, 200 and 300 are expressed by "^", "*", "o" and "+" shape lines, respectively.

prediction results decreases with the size of survey samples increasing. Under the above conditions, the deviation between prior information and survey results with the size of samples increasing is shown in Table 1.

If the number of survey samples reaches 100, the deviation between prediction and survey results is generally less than 5%. When the number reaches 200, the deviation is less than 3%. At this time, the influence of prior distribution characteristics (the expectation and variance) on the posterior distribution results can be neglected.

3.4 Regression Analysis of PMV-BPD

The BPD model is further verified by PD data in the reference [11]. Survey results are shown in Table 2.

The sizes of winter and summer samples are 189 and 205, respectively [11]. In this paper, an expectation of posterior distribution is used to express a prediction result—BPD. A quadratic curve regression method is introduced to fit the survey results. To analyze BPD for different sizes of survey samples, it is assumed that the size of samples selected is 30, 60 and 120, respectively. The results are as shown in Fig. 6.

Table 1. Comparison of prediction and survey results

PMV	Expectation of prior distribution	Size of samples	Expectation of beta distribution	Deviation between prediction and survey (%)
±1	0.26	50	0.678	9.60
		100	0.711	5.20
		200	0.730	2.67
		300	0.736	1.87
±1.5	0.50	50	0.703	6.27
		100	0.724	3.47
		200	0.736	1.87
		300	0.741	1.20
±2	0.77	50	0.753	0.40
		100	0.751	0.13
		200	0.751	0.13
		300	0.751	0.13

Table 2. Prediction and survey results of PD [11]

PMV	−3	−2	−1	0	1	2	3
PPD	99%	77%	26%	5%	26%	77%	99%
APD (Winter)	99%	63%	52%	9%	18%	13%	14%
APD (Summer)	--	33%	37%	18%	85%	83%	99%

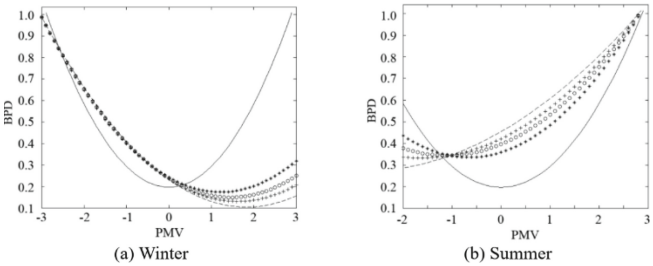


Fig. 6. Fitting results of BPD. PPD results were expressed by "—", and the BPD of the number of samples 30, 60 and 120 are expressed by "*", "o" and "+" shape line, respectively. The survey results in the literature were expressed by "--".

A large size of survey samples have been provided to obtain the results in the literature. Otherwise, the results may not be accurate enough. As shown in Fig. 6, BPD

presented in our manuscript is used to express the prediction results. The trend of prediction results is basically consistent with that of the survey results when the size of samples is large. In particular, when the size of survey samples is more than 100, the maximum deviation between the prediction and survey results is less than 5%.

4 Conclusion

This paper proposes a BPD model based on factors of thermal environment and human body and survey data of PD. The model can reflect the objective and subjective factors affecting human thermal comfort. Beta distribution is introduced to express a likelihood function and a posterior distribution in Bayesian thermal comfort model. Thus, the calculation process is simplified and calculation efficiency is improved. The analysis results in case studies show that besides PMV, a variance of prior distribution and the size of survey samples will affect a posterior distribution, and also affect a BPD. Whether the prediction results are close to the prediction or survey results will be affected by selection of the variance of prior distribution and the size of samples. When the size of samples reaches 100–200, the influence of prior distribution on the results of BPD could be neglected.

Considering the advantages of dealing with the prediction of PD by using a small number of survey samples, this BPD model based on beta distribution can also be applied in other situations, such as unsteady thermal environment, indoor thermal environment in transition seasons and thermal comfort evaluation prediction of specific population.

Acknowledgments. This study was supported by the National Natural Science Foundation of China [grant number 52378015].

References

1. de Dear, R., Akimoto, T., Arens, E., et al.: Progress in thermal comfort research over the last twenty years. Indoor Air. **23**(6), 442–461 (2013)
2. Parsons, K.: Environmental ergonomics: a review of principles, methods and models. Appl. Ergon. **31**(6), 581–594 (2000)
3. Yang, R., Wang, L.: Multi-objective optimization for decision-making of energy and comfort management in building automation and control. Sustain Cities Soc. **2**(1), 1–7 (2012)
4. Fanger, P.: Thermal Comfort: Analysis and Applications in Environmental Engineering. McGraw-Hill, New York USA (1972)
5. Fanger, P., Toftum, J.: Extension of the PMV model to non-air-conditioned buildings in warm climates. Energy Build. **34**(6), 533–536 (2002)
6. Yao, R., Li, B., Liu, J.: A theoretical adaptive model of thermal comfort – adaptive Predicted Mean Vote (aPMV). Build. Environ. **44**(10), 2089–2096 (2009)
7. Humphreys, M., Nicol, J.: The validity of ISO – PMV for predicting comfort votes in everyday thermal environments. Energy Build. **34**(6), 667–684 (2002)
8. Chen, L., Ng, E.: Outdoor thermal comfort and outdoor activities: a review of research in the past decade. Cities. **29**(2), 118–125 (2012)
9. Djongyang, N., Tchinda, R., Njomo, D.: Thermal comfort: a review paper. Renew. Sust. Energ. Rev. **14**, 2626–2640 (2010)

10. Thomas, L., John, S.J.: Bayesian Methods: An Analysis for Statisticians and Interdisciplinary Researchers. Cambridge University Press, London UK (1999)
11. Becker, R., Paciuk, M.: Thermal comfort in residential buildings – failure to predict by Standard model. Build. Environ. **44**(5), 948–960 (2009)

Energy Efficient Thermal Comfort in Temporarily Occupied Space for Winter Heating Mode: A Case Study of Ceiling Fan Aided Diffuse Ceiling Ventilation System

Bin Yang[1,2], Xinrou Han[1,2], Bin Zhou[3], and Zhe Li[1,2(✉)]

[1] School of Energy and Safety Engineering, Tianjin Chengjian University, Tianjin 300384, China
lizhe24@tcu.edu.cn

[2] Lab of Human Factors Engineering for Urban Construction, Tianjin Chengjian University, Tianjin 300384, China

[3] School of Building Services Science and Engineering, Xi'an University of Architecture and Technology, Xi'an 710055, China

Abstract. Temporarily occupied space (TOS) is defined as a thermally conditioned space where the majority of people stay for a short period of time (less than 40 min). However, traditional heating in TOS often leads to energy waste (e.g., overheating) or thermal discomfort (e.g., large vertical air temperature difference between head and ankle levels). Therefore, one solution of using ceiling fan in reverse mode is introduced to drive warm air from room high level to occupied zone to enhance heating effect of occupied zone in energy efficient mode. In this study, parameter optimization study of a ceiling fan reversing combined with a diffuse ceiling ventilation (DCV) system is based on the applicability of the system in the TOS heating mode, aiming at balancing short term thermal comfort and energy efficiency. The effects of ceiling fan speed (40–80 rpm), supply air change rates (4–8 times/h), and supply air temperature (26–30 °C) on predicted mean vote (PMV), vertical air temperature difference between head and ankle levels (ΔT), draught rate (DR), and temperature effectiveness (TE) were analyzed by validated CFD model and experimental data, and combined with the characteristics of the TOS to propose a simplified operation strategy.

Keywords: Temporarily occupied space · Ceiling fan · Diffuse ceiling ventilation

1 Introduction

Temporarily occupied space (TOS) is defined as a thermally conditioned space where the majority of people stay for a short period of time (less than 40 min), such as waiting areas of banks, post offices, railway stations [1]. Diffuse ceiling ventilation (DCV) system achieves thermal comfort and energy saving by supplying air uniform-ly at low velocity to avoid draught and reducing fan energy consumption through the low resistance of the ceiling inlets. It is widely used in public buildings [2].

© The Author(s), under exclusive license to Springer Nature Singapore Pte Ltd. 2025
L. Ni et al. (Eds.): CCHVAC 2025, ESE, pp. 486–493, 2025.
https://doi.org/10.1007/978-981-95-3253-7_52

However, DCV systems are prone to thermal buoyancy effects due to their large supply area and low momentum. During heating, warm air accumulates near the ceiling, creating vertical temperature gradients [3, 4]. To mitigate this, ceiling fans have been introduced to enhance air mixing and downward heat distribution [5]. Study shows both forward and reverse fan rotation can reduce stratification in heating-mode DCV systems, with reverse rotation offering better airspeed acceptability [6].

Although these studies have explored the impact of different speeds and rotation directions on the indoor thermal environment, there are still the following shortcomings: (1) applicability to TOS with actual occupancy is unverified; (2) sensitivity of reverse-rotation fan parameters (speed: 40–80 rpm, ACH: 4–8 times/h, supply temp: 26–30 °C) to PMV, ΔT, DR, and TE is unclear. This study addresses these gaps via validated CFD simulations and proposes a simplified TOS operation strategy.

2 Methods

2.1 Physical

This study takes the TOS in Tianjin during winter as the research object. As shown in Fig. 1, the physical model is determined according to the climate chamber, with dimensions of 3.8 m × 3.8 m × 2.6 m. The DCV system delivers warm air via a 0.17 m × 0.13 m plenum inlet through 0.6 m × 0.6 m perforated panels (6 mm holes, 0.4% perforation rate), with four 6 mm floor exhausts. A central 1.24 m-diameter ceiling fan (0.2 m below ceiling) and two thermal manikins (33.0 ± 1.5 °C, 95 W) simulate occupants.

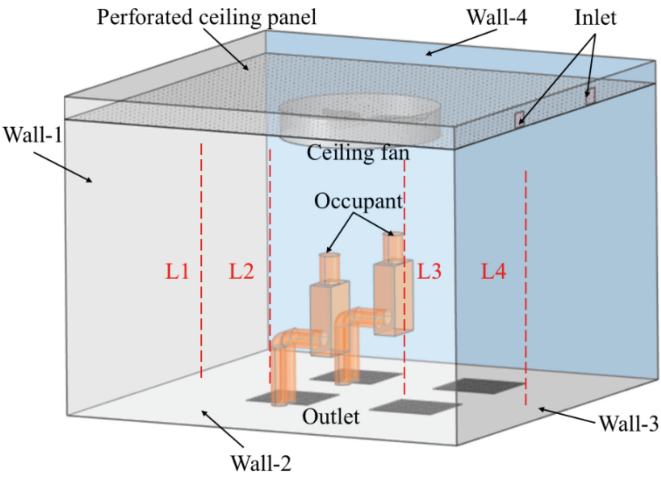


Fig. 1. Layout of the physical model.

2.2 Numerical Details and Boundary Conditions

The study modeled the room in SOLIDWORKS and simulated airflow using ANSYS FLUENT 2022 R1. The analysis assumed three-dimensional, steady-state, incompressible turbulent flow with Boussinesq approximation for density variation [7]. The turbulent airflow is investigated using the Realizable k-ε model [8]. Due to the complex geometry of the ceiling fan, directly using the moving mesh method to simulate the rotating ceiling fan is too costly [9]. Instead, the multiple reference frame (MRF) method is used [10]. The SIMPLE algorithm coupled pressure and velocity fields, with second-order upwind discretization for all equations. Solutions were considered converged when the residual levels dropped to 1×10^{-6} for all eqs. (1×10^{-3} for continuity). Since the light's heat dissipation (15 W) is negligible, the primary internal heat source is the occupants, modeled as solid boundaries with constant temperature. The inlet on the plenum sidewall is defined as a supply air vent with uniform velocity, while the outlet is specified as a pressure outlet boundary condition. Table 1 summarizes the boundary conditions.

Table 1. Boundary conditions of CFD simulations.

Boundary	Conditions
Inlet	Velocity-inlet boundary; supply air parameters are modified for different cases
Outlet	Pressure outlet with zero gauge pressure
Occupants	Wall boundary; constant temperature: 34 °C
Wall-4	Constant wall temperature; wall temperatures are modified for different cases
Other room walls	Adiabatic wall, no slip

2.3 Mesh Generation and Independency

The simulation performance depends on mesh quality. The domain was divided into plenum, rotating region, and room space. Poly-Hexcore meshing was used with global size 0.003–0.1. All meshes maintained quality >0.7 and skewness <0.7. Three mesh configurations were generated: coarse (1,504,267 cells), medium (2,590,675 cells), and fine (5,402,180 cells). Grid independence verification showed medium mesh results closely matched fine mesh (velocity RMS error 1.47%, temperature 0.03%), while coarse mesh showed larger deviations. The medium mesh was selected for optimal balance of accuracy and cost.

2.4 Model Validation

In this experiment, thermal manikins were placed directly beneath the ceiling fan, and four groups of SWEMA 03+ (as shown in Fig. 1) were arranged at four different height positions (L1-L4) to measure the indoor temperature and velocity distribution. The supply air temperature was set at 28 °C, ACH was 6 times/h, and the rotation speed of

the ceiling fan was 60 rpm. CFD predictions for lines L1-L4 were validated against measurements. Results showed good agreement, with mean absolute differences of 0.04 m/s (velocity) and 0.17 °C (temperature). Pearson coefficients reached 0.97 (velocity) and 0.91 (temperature). These validation results conclusively demonstrate that the established CFD model can reliably simulate both airflow patterns and temperature distributions in ceiling fan aided DCV systems operating in heating mode (Fig. 2).

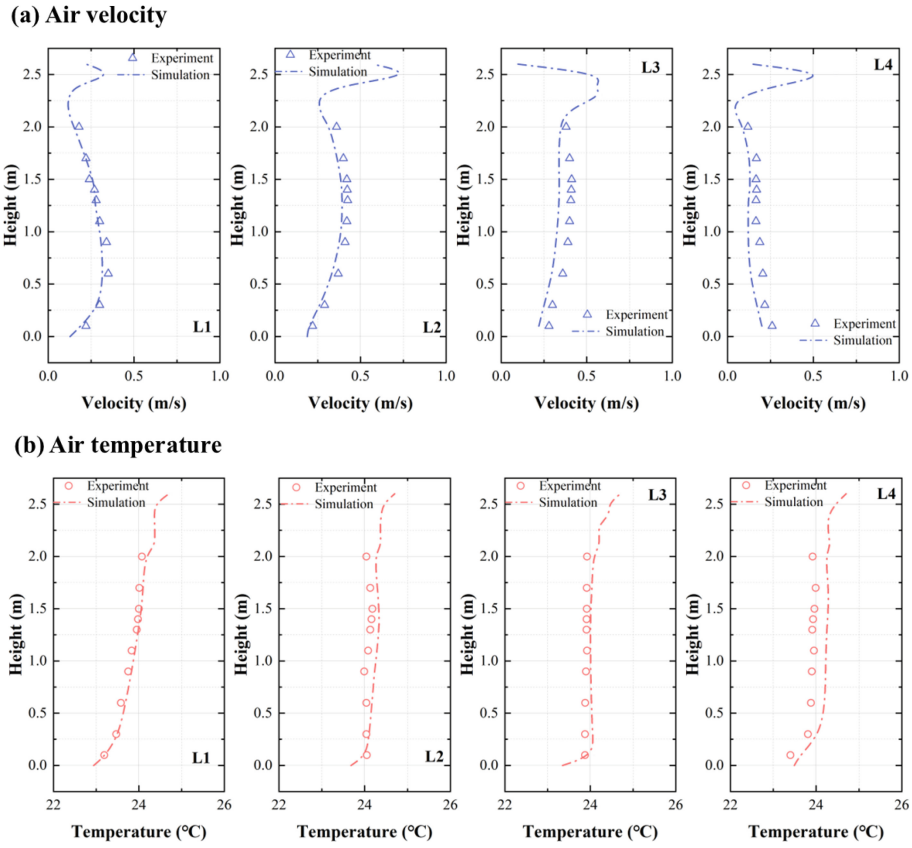


Fig. 2. Comparisons between CFD simulations and experiments: (**a**) Air velocity; (**b**) Air temperature.

2.5 Studied Cases

Based on practical conditions, the rotational speed is set at 45 rpm, 60 rpm, and 80 rpm. The air change rate (ACH) and supply air temperature (T_S) are set at 4 times/h, 6 times/h, and 8 times/h, and 26 °C, 28 °C, and 30 °C, respectively. Case 1, where all operating parameters are at the intermediate level, is marked as the baseline condition (Table 2).

Table 2. CFD simulation conditions.

Case	Rotational speed (rpm)	ACH (times/h)	T_s (°C)
1	60	6	28
2	**45**	6	28
3	**80**	6	28
4	60	**4**	28
5	60	**8**	28
6	60	6	**26**
7	60	6	**30**

2.6 Evaluating Index

The PMV is calculated for thermal comfort evaluation. ΔT is the air temperature difference between heights of 1.1 m and 0.1 m above the floor (for a seated person). The expression is described as:

$$\Delta T = T1.1 - T0.1 \tag{1}$$

where, $T_{1.1}$ is the temperature at the head level; $T_{0.1}$ is the temperature at the ankle level.

The DR is the proportion of occupants dissatisfied with the air movement, calculated at 1.1 m (head level) based on air temperature, velocity and turbulence intensity (Eq. 2).

$$DR_{\mathrm{i}} = (34 - T_i)(v_i - 0.05)^{0.62}(0.37 \times v_i \times TI + 3.14) \tag{2}$$

where, DR_i is the draught rate of the i-th measuring point; v_i and T_i represent the mean air speed and temperature measured at each measurement point.

TE indicates the heating system's energy efficiency, with higher values denoting better performance (Eq. 3).

$$TE = \frac{t_s - t_e}{t_s - t_i} \tag{3}$$

where, t_s (°C) is the supply air temperature, t_e (°C) is the exhaust air temperature and t_i (°C) is the mean air temperature at a certain height in the occupied zone.

3 Results

3.1 Indoor Temperature Distribution

Figure 3 shows three cases, i.e., case 1 with the ceiling fan off and on, and case 2, where the ceiling fan speed is 0 rpm, 60 rpm, and 45 rpm, with an air change rate of 6 times/h and a supply air temperature of 28 °C. The figure shows the vertical temperature and

velocity distribution on the central cross-section of the room. The results indicate that in winter heating conditions, the temporarily occupied space (TOS) exhibits distinct stratification, with a significant vertical air temperature difference between head and ankle levels. After turning on the reversed ceiling fan, in all cases, the air temperature in the upper part of the room decreases, while the air temperature in the lower part increases, resulting in a more uniform airflow distribution in the occupied zone.

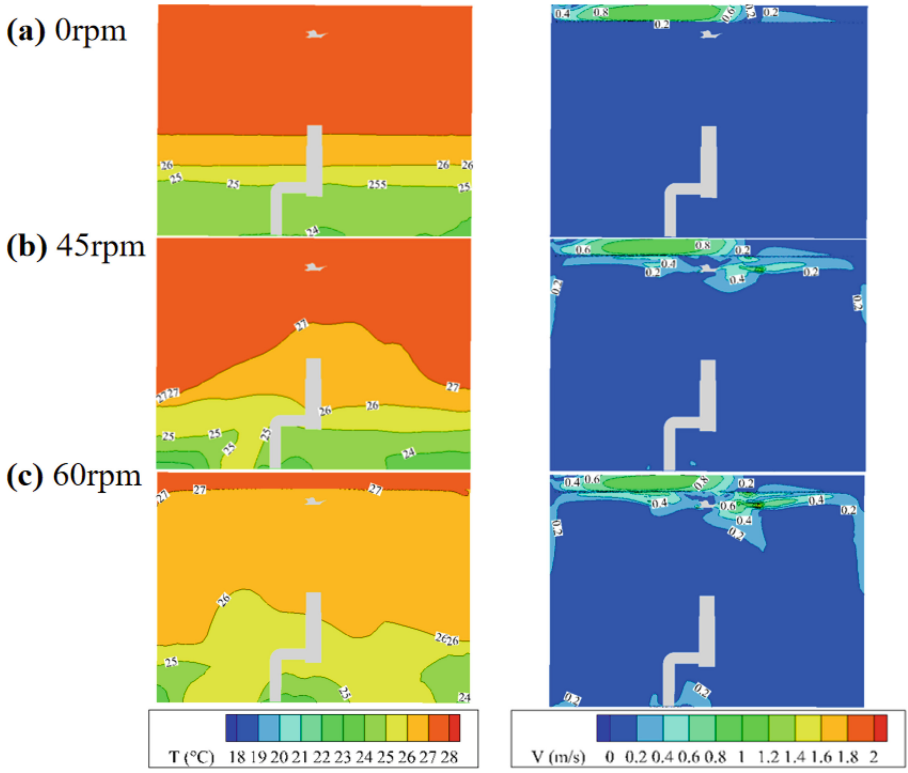


Fig. 3. Vertical temperature and velocity profile at the central section: (**a**) Case1 (fan off), (**b**) Case2 (45 rpm), (**c**) Case1 (60 rpm).

3.2 Effects of Operation Parameters on Indoor Thermal Environment

All parameters were normalized to 0–1 for comparison. Fig. 4(a) shows PMV initially rises then falls with increasing fan speed, as the reversed fan first delivers warm air to occupants but then enhances convective cooling at higher speeds. Higher supply temperature and ACH increase PMV. Fig. 4(b) demonstrates improved temperature uniformity with fan speed, reducing ΔT between 1.1 m and 0.1 m. ΔT initially increases then decreases with ACH due to shifting dominance from thermal buoyancy to air mixing effects. Figure 4(c) indicates fan speed most significantly affects DR, maintaining

acceptable levels (<10%). Figure 4(d) shows TE improves with higher fan speed and ACH.

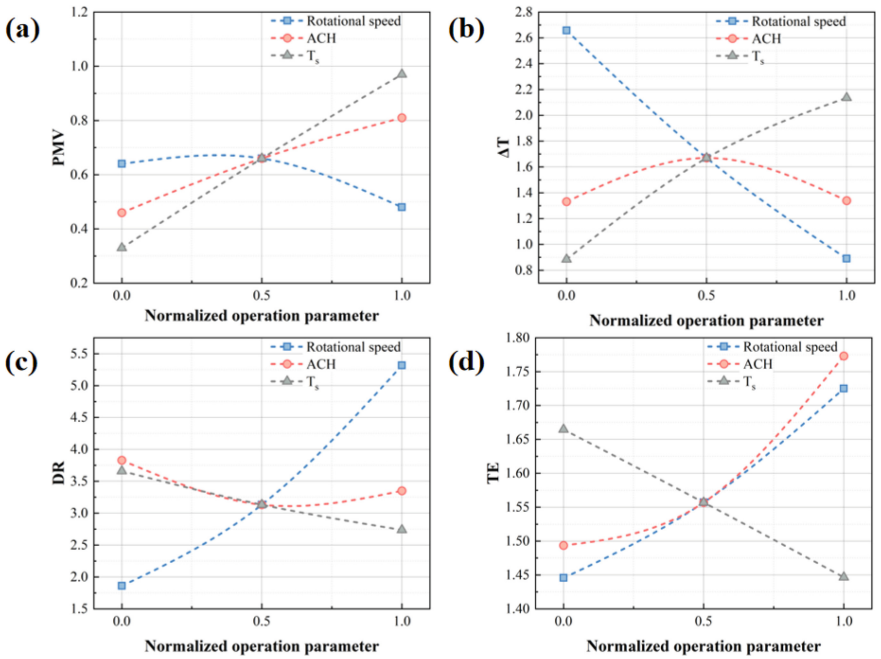


Fig. 4. Variations of (**a**) PMV, (**b**) ΔT, (**c**) DR, (**d**) TE with operation parameters.

4 Discussion and Limitation

According to the analysis results in Fig. 4, the rotational speed of the ceiling fan is the most significant factor affecting the indoor thermal environment. To optimize the performance of the ceiling fan-assisted diffuse ceiling ventilation system in the temporarily occupied space (TOS), it is recommended to fix the ceiling fan speed at 80 rpm to make the indoor air distribution more uniform, and set the supply air temperature and ACH at 26 °C and 4 times/h, respectively, to keep PMV within a comfortable level and reduce energy consumption.

In the system design and operation parameter selection of this paper, TOS is simplified as parameters under steady-state thermal environment. However, in practical applications, the people stay time in the TOS area is usually less than 40 min. Due to the short stay time, the human body's thermal state has not yet reached stability. This steady-state assumption may lead to deviations between the research results of this paper and practical applications. Therefore, it is suggested that future research should consider the transient occupancy characteristics of TOS and conduct thermal environment research under ceiling fan aided diffuse ceiling ventilation system for the time non-steady-state and spatial non-uniform temporarily occupied space.

5 Conclusions

This paper presents a numerical study of diffuse ceiling ventilation system aided by ceiling fan for heating mode in TOS. The results show that the reversed ceiling fan can make the air distribution more uniform and significantly reduce the vertical air temperature difference between head and ankle levels. Supply air temperature has the most significant impact on PMV, while ceiling fan speed has the most significant impact on ΔT and DR. An increase in ceiling fan speed and air change rate (ACH) both lead to a reduction in energy consumption. In practical applications, it is recommended to fix the ceiling fan speed at 80 rpm to make the indoor air distribution more uniform, and set the supply air temperature and ACH at 26 °C and 4 times/h, respectively.

References

1. Li, Z., Yang, B., Zhou, B., et al.: Thermal responses in temporarily occupied space in the summer: spatial-temporal synergetic alliesthesia using a ceiling fan. J. Build. Eng. **93**, 27–33 (2015)
2. Wu, W., Yoon, N., Tong, Z., et al.: Diffuse ceiling ventilation for buildings: a review of fundamental theories and research methodologies. J. Clean. Prod. **211**, 1600–1619 (2019)
3. Yang, B., Melikov, A.K., Kabanshi, A., et al.: A review of advanced air distribution methods – theory, practice, limitations and solutions. Energ. Buildings. **202**, 109359 (2019)
4. Peng, P., Pomianowski, M., Zhang, C., et al.: Experimental investigation on the ventilation performance of diffuse ceiling ventilation in heating conditions. Build. Environ. **205**, 108262 (2021)
5. Ashoori, M., Sheikhzadeh, G., Sadripour, S.: The effects of using ceiling fans on human thermal comfort in a three-dimensional room with centralized heating including an occupant. Int. J. Numer. Methods Heat Fluid Flow. **29**(10), 3976–3993 (2019)
6. Yang, B., Li, H., Zhou, B., et al.: Airflow and temperature characteristics of diffuse ceiling ventilation with ceiling fan under heating mode: an experimental study. Energ. Buildings. **329**, 115258 (2025)
7. ANSYS Inc, ANSYS Fluent Theory Guide, Canonsburg, PA (2013)
8. Li, L., He, Y., Chen, W., et al.: An integrated experimental and CFD analysis of ceiling-fan-integrated air conditioning system: indoor air quality and air velocity. Build. Environ. **258**, 111633 (2024)
9. Guo, X., Wan, S., Chen, W., et al.: Numerical simulation of cooling performance of radiant ceiling system interacting with a ceiling fan. Energ. Buildings. **297**, 113492 (2023)
10. Li, J., Hou, Y., Liu, J., et al.: Window purifying ventilator using a cross-flow fan: simulation and optimization. Build. Simul. **9**(4), 481–488 (2016)

A Nodal Model for Predicting Vertical Air Temperature Difference in a Radiant Floor Cooling Room with Mechanical Ventilation

Xiaozhou Wu(✉), Zhaoyi Liu, Diqi Yu, and Hao Gao

Department of Civil Engineering, Dalian University of Technology, Dalian, China
fonen519@dlut.edu.cn

Abstract. Radiant floor cooling (FC) systems show strong potential in large modern buildings and are typically combined with mechanical ventilation (MV) to provide fresh air and remove humidity. However, this combination often leads to large vertical air temperature differences, causing local discomfort. This paper analyzes vertical temperature distribution in simulated office and residential rooms with FC + MV using a validated numerical model with a revised wall Prandtl number. Results showed that vertical temperature difference was sensitive to supply air and floor surface temperatures, with floor temperature having a greater impact. The influence of indoor heat sources and envelope loads was minor. Finally, The two-node model was obtained by using the fitting formulas of the vertical air temperature and the absolute errors of internal wall surface temperature and indoor air temperature were within 0.4–1 °C.The research findings may provide guidance for the optimal design and prediction of a hybrid system with a floor cooling system and a mixing ventilation system, and minimize the issue of excessive vertical temperature differences.

Keywords: Floor cooling · Vertical air temperature difference · Nodal model

1 Introduction

1.1 A Subsection Sample

Radiant heating and cooling systems have gradually replaced traditional air conditioning due to their high energy efficiency and comfort [1, 2]. Among these, radiant floor cooling systems offer a high view factor to occupants, maximizing efficiency, and when combined with mechanical ventilation, they can effectively improve indoor humidity and air quality [3–6].

Although floor cooling is energy-efficient, it often causes significant vertical temperature differences. The existing research on vertical temperature difference (a key parameter for thermal comfort) is limited [7, 8].

This paper employs CFD simulation and orthogonal experiments to analyze factors influencing vertical temperature difference. A regression formula and an energy balance-based temperature prediction model are developed to accurately simulate indoor

© The Author(s), under exclusive license to Springer Nature Singapore Pte Ltd. 2025
L. Ni et al. (Eds.): CCHVAC 2025, ESE, pp. 494–505, 2025.
https://doi.org/10.1007/978-981-95-3253-7_53

temperature distribution and address challenges in predicting vertical stratification. The proposed model provides a valuable reference for the design and operation of radiant floor cooling systems and promotes their broader application.

2 Methodology

2.1 Geometric Model

A numerical model of a radiant floor cooling room with mechanical ventilation was based on Stefano Zarpellon's experimental chamber (4.2 m × 4.0 m × 2.4 m, Fig. 1) [9]. Indoor heat sources included seated dummies, computers, and lamps, simplified as rectangular or square heat sources. The air supply inlet was a 500 mm × 500 mm square diffuser divided into 9 sections, with a 45° angle airflow. The exhaust vent (440 mm × 420 mm) was located on the internal wall opposite the external wall.

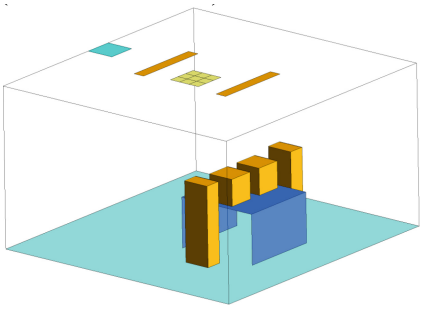


Fig. 1. The simulated room with FC + MV.

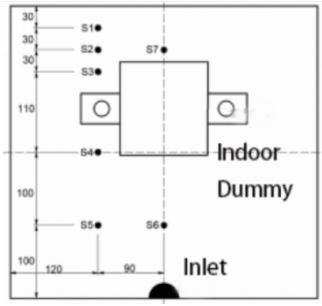


Fig. 2. Locations of measuring lines (mm).

During simulation, air velocity and temperature were recorded along seven lines (S1–S7) inside the room, matching experimental positions (Fig. 2). Lines S6 and S7 near the room center reflected overall air distribution, while S3 and S4 near the human body captured local temperature and velocity.

2.2 Turbulence Model

Indoor airflow is turbulent and complex, requiring turbulence models. This paper compares RNG, standard, and Realizable models. The standard model assumes isotropic turbulence and suits fully turbulent flows, limiting its accuracy for mechanical ventilation and swirling flows. The RNG model improves dissipation rate equations, handles rotation and curvature better, and suits this study. The Realizable model simulates various flows but less effectively predicts vertical temperature differences than RNG. Most studies favor RNG for higher accuracy, so it was chosen here [10, 11].

2.3 Radiation Model

Radiant heat transfer exceeds 50% in radiant cooling rooms, so choosing the right radiation model is crucial. FLUENT offers six models: DTRM, P-1, Roseland, DO, S2S, and Monte Carlo. The DO model is most used; it handles all optical thicknesses and both gray and non-gray radiation, covering surface and local heat source radiation as needed here. Thus, DO was selected for this study.

2.4 Convection Heat Transfer Calculation

Floor radiant cooling often causes large vertical temperature differences, hard to simulate accurately. Indoor airflow is mainly natural convection, where conduction is key when natural dominates forced convection. The wall Prandtl number (momentum to thermal diffusivity ratio) is crucial [12]. Adjusting it and turbulence models improves simulation of vertical gradients.Wall Prandtl number can be found by trial-and-error or iterative methods. Due to high cost, this study uses Tim et al.'s iterative approach (Eqs. 1 and 2) to find realistic values.

$$\mathrm{Pr}_t = \frac{q^{'}}{T_W - T_{ref}} \times \frac{0.85 \times (T_W - T_P) \times \left[1/k \ln(Ey^*) + P^{'}\right]}{h \times \left(T_W - T_P{}^{'}\right) \times \left[1/k \ln(Ey^*) + P\right]} \tag{1}$$

$$P = 9.24\left[\left(\frac{\mathrm{Pr}}{\mathrm{Pr}_t}\right)^{3/4} - 1\right]\left[1 + 0.28e^{-0.007\,\mathrm{Pr}/\mathrm{Pr}_t}\right] \tag{2}$$

where the $q^{'}$ is the heat flux density of the floor surface, the T_{ref} is the reference temperature,and the air temperature at 1.1 m is taken as the indoor reference temperature, the T_p is the temperature of the first layer of the grid near the wall and the y^* is the ystar value of the simulated wall.

Initially, the floor heat flux density, y* value, and temperature at the first grid layer near the wall are calculated using the default wall Prandtl number. Then, the convective heat transfer coefficient h and temperature at the same height under experimental conditions are determined. The iteration continues, updating through Eqs. 1 and 2, inputting into Fluent for simulation, until the difference between the simulated and experimental convective heat transfer coefficient is within 10%. Finally, a value of $\mathrm{Pr}_t = 10^{-3}$ is achieved for subsequent simulations.

2.5 Boundary Conditions

Due to complex airflow in the radiant floor cooling room with mechanical ventilation, the model is reasonably simplified. Indoor air is treated as an incompressible viscous fluid with buoyancy modeled by the Boussinesq approximation to simulate heat plume effects. The PRESTO scheme is used for pressure, SIMPLE algorithm for calculations, second-order upwind for other terms, and standard wall functions near walls.

Boundary conditions greatly affect simulation results and are set based on experiments. Three vertical walls are insulated internal envelopes, the external wall with

heating film is set as constant heat flux. The radiant floor surface has a constant temperature from thermocouple data. Air supply is a velocity inlet, exhaust is free outflow, and other heat sources have constant heat flux. Details in Table. 1.

Table 1. Boundary conditions.

Serial number	Name of boundary	Quantity	Type	Boundary condition	Internal emissivity
1	Dummy	2	wall	Constant heat flux	0.975
2	Computer	2	wall	Constant heat flux	0.9
3	Lamp	2	wall	Constant heat flux	0.9
4	Radiant floor	1	wall	Constant temperature	0.9
5	External building envelope	1	Wall	Constant heat flux	0.95
6	Internal building envelope	4	Wall	adiabatic	0.95
7	Supply terminal	1	Inlet	Velocity inlet	–
8	Exhaust terminal	1	Outlet	Outflow	–

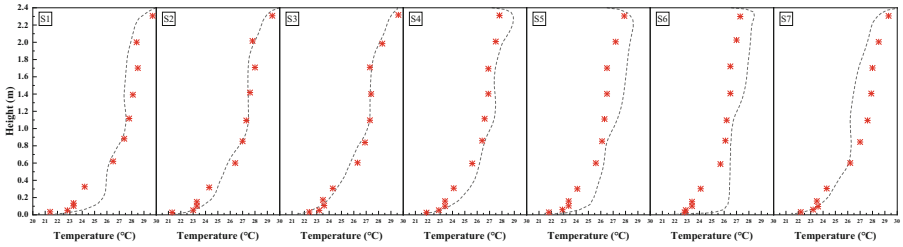
2.6 Validation of Numerical Simulation

Numerical simulations may have some deviation from the actual situation. Therefore, it is necessary to validate the established CFD model with experimental data., as certain assumptions and boundary conditions may introduce discrepancies compared to real conditions. For instance, in the numerical setup, the interior walls were modeled as adiabatic surfaces, while the ceiling was assigned a constant wall temperature. Experimental validation was therefore conducted in a controlled test chamber with dimensions of 4.2 m (length) $\times$ 4.0 m (width) $\times$ 2.4 m (height). To replicate the external sensible cooling load, electric heating films were installed on the exterior walls. Internal sensible loads were emulated using ceiling-mounted lamps, computers equipped with internal light bulbs, and thermal manikins. By adjusting the power input to the heating films and bulbs, both external and internal loads could be flexibly controlled. According to the reference, cases 1.2 and 2.2 were selected from the experimental cases as validation conditions, and the specific conditions are shown in Table. 2.

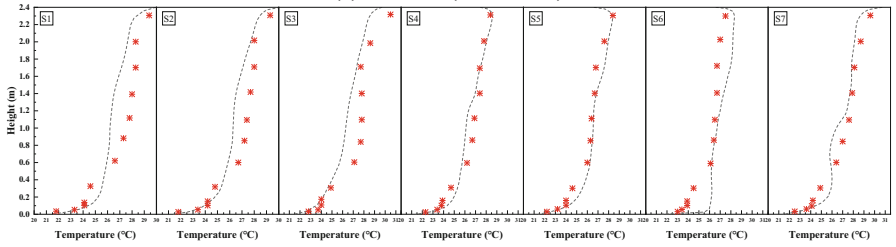
Table 2. Experimental cases.

Room type	Case	Supply air temperature /°C	Air change rate /h	Indoor heat source intensity /(W/m^2)	Envelope cooling load /(W/m^2)	Floor surface temperature /°C
Residential	1.1	18.1	0.5	5.95	28.15	21.0
	1.2	17.8	1.0	5.95	28.15	21.2
Office	2.1	17.9	1.0	11.90	28.15	20.7
	2.2	20.0	2.0	11.90	28.15	21.4
	2.3	16.1	2.0	11.90	28.15	22.6

Figure 3 and 4 show air temperature and velocity in the radiant floor cooling room with mechanical ventilation, comparing experimental and simulated results. Red stars indicate experiments, dotted lines indicate simulations.

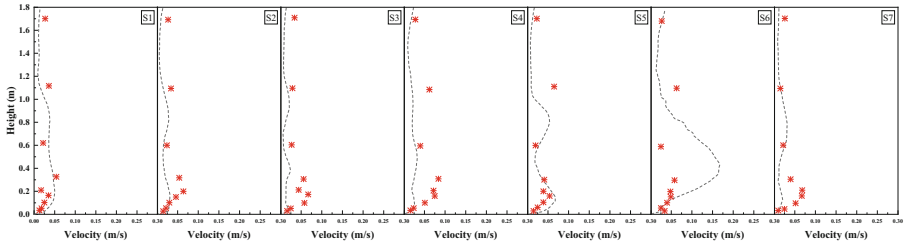


(a) 1.2 case (residential)

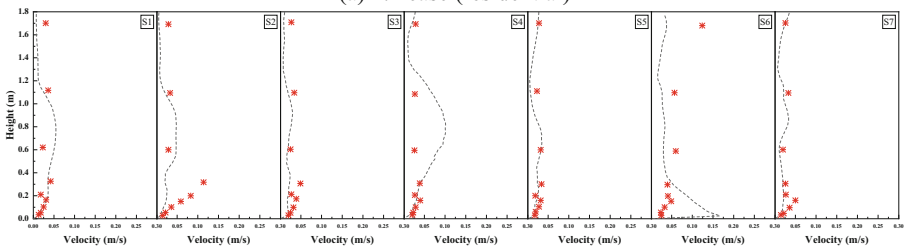


(b) 2.2 case (office)

Fig. 3. Vertical air temperature profiles for FC + MV (line-CFD simulation, star-measurement results).



(a) 1.2 case (residential)



(b) 2.2 case (office)

Fig. 4. Vertical air velocity profiles for FC + MV (line-CFD simulation, star-measurement results).

Comparison shows differences in temperature and velocity along S6 line due to model limits and experimental errors. However, most measurement lines' simulated trends match experiments well, with small errors within acceptable range. Thus, the model effectively represents airflow in the FC + MV room and suits further numerical studies.

3 Analysis of Influencing Factors and Calculation of VATD

3.1 Simulation Condition

The vertical temperature difference (VATD) expresses the temperature difference between the head and feet of a seated human body and is calculated as the difference between the air temperature at 1.1 m and 0.1 m. The first paragraphs that follows:

(1) Supply air temperature

For rooms with a height of lower than 5 m at the air supply terminal, the supply air temperature difference for comfort air conditioning typically ranges from 5 to 10 °C, with the indoor temperature set between 24.5 and 25.5 °C. The supply air temperature should not be too low to prevent people from feeling cold and windy. Consequently, the minimum supply air temperature for the floor cooling system combined with mechanical ventilation is set at 16 °C, with levels of 16, 18, and 20 °C increasing by 2 °C increments.

(2) Indoor heat source intensity

In most office spaces, the total load from personnel, equipment, and lighting typically ranges from 20 to 60 W/m^2, with specific values of 20 W/m^2, 40 W/m^2, and 60 W/m^2 often used [13]. For residential buildings,it was usually set at 10 W/m^2, 20 W/m^2, and 30 W/m^2.

(3) Envelope cooling load

Outdoor temperature changes and solar radiation can have influence on the heat transfer to the external wall. According to the heat gain of the summer envelope structure and the convective heat transfer coefficient of the external wall in general areas of China, the corresponding heat transfer levels of the exterior wall are 25 W/m^2, 35 W/m^2 and 45 W/m^2.

(4) Floor surface temperature

The surface temperature of the floor should not be too low, as it may cause discomfort to the feet and discomfort due to local thermal imbalance. Thus, with 21 °C being the minimum acceptable value. Temperature levels of 21 °C, 22 °C, and 23 °C were considered for the experiment.

The orthogonal experimental scheme is shown in Table. 3. A represented supply air temperature (°C), B represented floor surface temperature(°C), C represented indoor heat source intensity (W/m^2), D represented envelope cooling load (W/m^2). It should be pointed out that in practical applications, the above parameters may experience significant fluctuations due to differences in building types, usage modes, and climatic conditions.

Table 3. Orthogonal experiment scheme for FC + MV (Residential).

Experiment code(Residential)	Factors				Experiment code(Office)	Factors			
	A	B	C	D		A	B	C	D
1-1	16	21	10	25	2-1	16	21	20	25
1-2	16	22	20	35	2-2	16	22	40	35
1-3	16	23	30	45	2-3	16	23	60	45
1-4	18	21	20	45	2-4	18	21	40	45
1-5	18	22	30	25	2-5	18	22	60	25
1-6	18	23	10	35	2-6	18	23	20	35
1-7	20	21	30	35	2-7	20	21	60	35
1-8	20	22	10	45	2-8	20	22	20	45
1-9	20	23	20	25	2-9	20	23	40	25

3.2 Analysis of Influencing Factors of Vertical Temperature Difference

Figure 5 illustrates the influence of each factor on the vertical temperature difference in residential working conditions. It is clear from the figure that the floor surface temperature has the most significant impact on the vertical temperature difference, with a notable decrease in the vertical temperature difference observed as the floor surface temperature increases. Furthermore, when the supply air temperature also affects the vertical temperature difference, the indoor heat source intensity and the envelope cooling load have minimal influence.

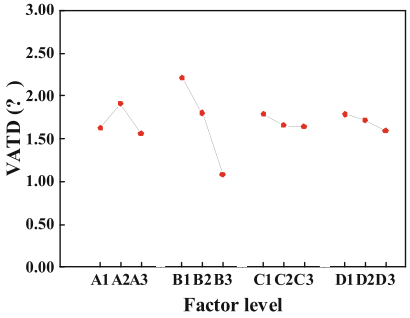


Fig. 5. Variation of factors with residential.

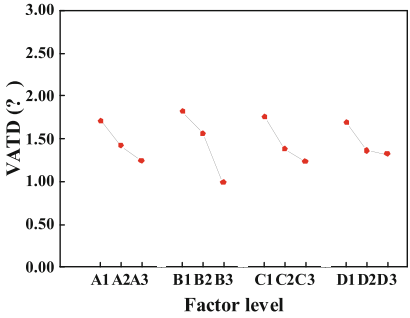


Fig. 6. Variation of factors with office.

Figure 6 illustrates the influence of various factors on the vertical temperature difference in office working conditions. Similar to residential settings, the floor surface temperature exerts the greatest influence on the vertical temperature difference, with a significant reduce observed as the floor surface temperature increases. Additionally, both the indoor heat source intensity and the supply air temperature have a noticeable effect, with the vertical temperature difference slightly decreasing as either the supply air temperature or indoor heat source intensity rises. In contrast, the envelope cooling load has the smallest impact on the vertical temperature difference.

To better understand the impact of the aforementioned factors, a multiple regression analysis was performed on the experimental results, leading to the derivation of a multiple regression equation. The relationship derived from the simulation results of vertical temperature difference is given in Eqs. 3 and 4.

$$\Delta T_{residential} = 0.1104S_A - 0.996S_B - 0.0717S_D + 24.485, \quad R^2 = 0.816 \tag{3}$$

$$\Delta T_{office} = -0.061S_A - 0.607S_B - 0.024S_C + 17.374, \quad R^2 = 0.846 \tag{4}$$

4 Indoor Air Vertical Temperature Difference Prediction Node Model

4.1 Establishment of the Node Model

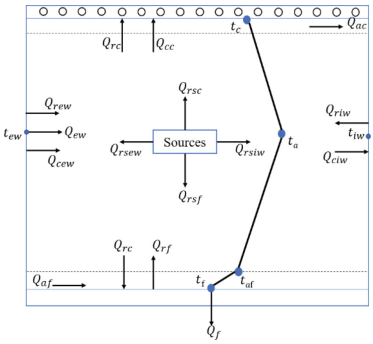


Fig. 7. Two node model.

We established energy balance equations for each part of the floor cooling room with mechanical ventilation and solved the thermal and mass balance system to find temperatures at each node. Due to notable vertical temperature differences, a two-node indoor air temperature model was created (Fig. 7) [14].

4.2 Node Model Validation

The temperature prediction node model for the floor cooling room was compared and validated against experimental measurements and predicted values. This analysis included the ceiling surface temperature, internal wall surface temperature, indoor air temperature at heights of 1.1 m and 0.1 m, as well as the vertical temperature difference between these two heights. Detailed verification results are showed in Figs. 8 and 9.

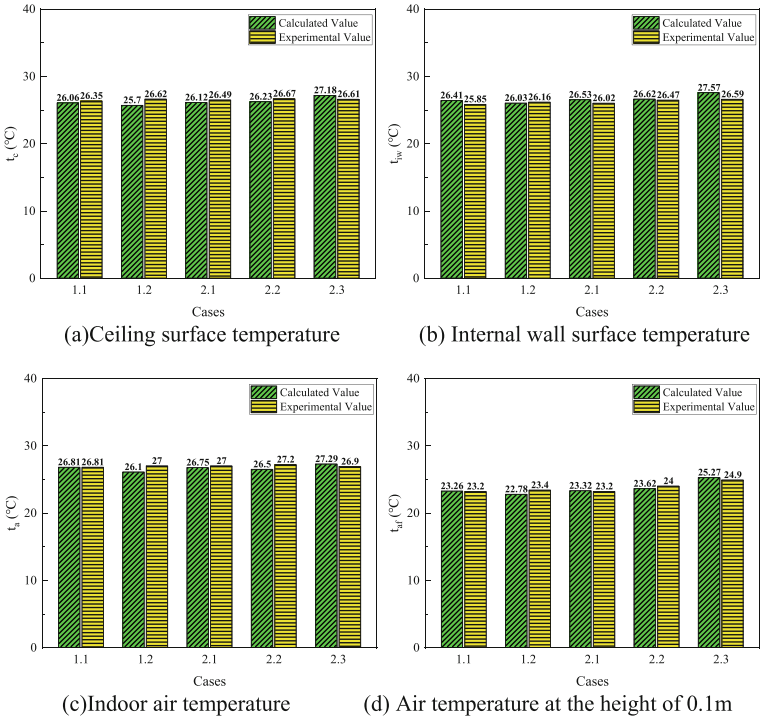


Fig. 8. Temperature verification results.

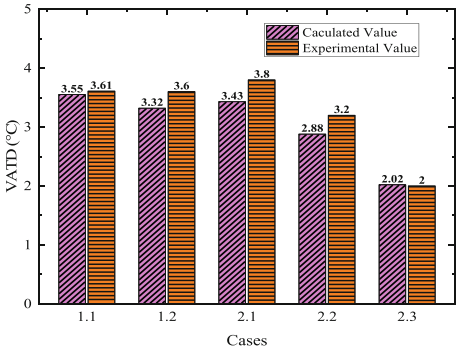


Fig. 9. Vertical temperature difference verification results.

According to Fig. 8, it can be seen that the absolute errors of the node model for the ceiling surface temperature, internal wall surface temperature, indoor air temperature (air temperature at a height of 1.1 m), and air temperature at a height of 0.1 m above the floor under various working conditions of residential and office types were maintained within 1 °C. As can be seen from Fig. 9, the absolute value of the prediction error of

the node model for each condition of vertical air temperature difference was within 0.4 °C, indicating high prediction accuracy. This is because the convective heat transfer coefficient of the model took into account the indoor airflow characteristics of the floor cooling room, making it more consistent with the actual airflow of the room. Thus, within the acceptable error range of this study, the two-node model of the floor cooling room demonstrated good predictability.

5 Conclusion

The main conclusions of this study are as follows: (1) In CF + MV systems, floor surface temperature significantly influenced vertical air temperature differences in both office and residential rooms, while supply air temperature had a much smaller effect. Indoor heat source intensity and envelope cooling load had minimal impact, with the former negligible in offices and the latter in residences (2). A two-node model based on energy balance equations was developed to predict vertical air temperature distributions. Incorporating the wall Prandtl number improved the accuracy of natural convection calculations. The predictive model exhibitted high reliability.

Acknowledgement. This study was funded by the National Natural Science Foundation of China (Grant No. 52278091).

References

1. Si, Q., Zhang, X.: Performance evaluation and experimental study of the induction radiant air-conditioning system. Procedia Eng. **121**, 1795–1804 (2015)
2. Guo, S., Tian, Y., Fan, D., et al.: A novel operating strategy to avoid dew condensation for displacement ventilation and chilled ceiling system. Appl Thermal Eng. **176**, 115344 (2020)
3. Zhou, X., Liu, Y., Zhang, J., Ye, L., M.: Luo radiant asymmetric thermal comfort evaluation for floor cooling system – a field study in office building. Energ. Buildings. **260**, 111917 (2022)
4. Bizzarri, M., Conti, P., Glicksman, L.R., Schito, E., Testi, D.: Radiant floor cooling systems: a critical review of modeling methods. Energies. **16**(17), 6160 (2023)
5. Moftakhari, A., Bourne, S., Novoselac, A.: All-air vs. radiant cooling systems: analysis of design and operation factors that impact building cooling loads (ASHRAE RP 1729). Sci Tech. Built Environ. **29**, 381–401 (2023)
6. Koca, A.: Experimental examination of heat transfer coefficients in hydronic radiant wall cooling systems. J. Build. Eng. **60**, 105209 (2022)
7. Dogan, A., et al.: An experimental comparison of radiant wall and ceiling cooling system integrated with ground source heat pump and direct expansion fan coil system in a highly glazed office room. Energ. Buildings. **273**, 16 (2022)
8. Du, H., Lian, Z., Lai, D., Duanmu, L., Zhai, Y., Cao, B., Zhang, Y., Zhou, X., Wang, Z., X.: Zhang comparison of thermal comfort between radiant and convective systems using field test data from the Chinese thermal comfort database. Build. Environ. **209**, 108685 (2022)
9. Zarpellon, S.: Experimental Study of Air Flow Patterns in a Space with Radiant and Convective Heating/Cooling Systems. Technical University of Denmark (2009)

10. Liu, X., Deng, B., Han, X., S.: PengNumerical simulation of temperature and carbon dioxide distribution in indoor environment using two-equation turbulence models Iran. J. Sci. Technol.Trans Civ. Eng. **47**, 1893–1907 (2023)
11. Wang, C., Hu, K., Liu, Y.: A novel ventilation method: experimental measurement and numerical simulation of vertical single-row inclined slit ventilation energy. Buildings. **324**, 114944 (2024)
12. Chaour, M., Boudebous, S.: Prandtl and Richardson number effects on mixed convection in a vented enclosure on application to the cooling of the fins. Defect Diffus Forum. **406**, 78–86 (2020)
13. Bean, R., Olesen, B., Kim, K.: History of radiant heating and cooling-part 2. ASHRAE J. **52**, 50–55 (2010)
14. Xiaozhou, W., Gao, H., Diqi, Y., Liu, J., Gao, J., Tian, Z., Li, X.: Sensitivity analysis of indoor air distribution performances in an office room with ceiling cooling and mechanical ventilation. Sci. Technol. Built En. **29**(8), 823–841 (2023) (SCI: 001060811400001, EI: 20233614694405, IF: 1.9)

Comparison of Air Quality Between Mechanical Ventilation Systems and Portable Air Cleaners with Research on Synergistic Integration Mechanisms

Mingqi Liu, Yiqun Li, and Wei Ye(✉)

School of Mechanical Engineering, Tongji University, Shanghai 201804, P. R. China
weiye@tongji.edu.cn

Abstract. In recent years, growing public concern over indoor air quality (IAQ) and building energy efficiency has placed greater demands on more cost-effective ventilation strategies. Currently, mechanical ventilation (MV) is widely applied in public buildings. However, the continued practice of minimum ventilation rate (VR)-based MV accounts for over 40% of the building's total energy consumption, posing a challenge to carbon emission reduction. This study proposes an energy-efficient new ventilation mode integrating MV with portable air cleaners (PACs). The investigation methodology is as follows: First, targeting typical indoor air pollutants (IAPs, i.e., $PM_{0.3–10}$, O_3, TVOC, CO_2, and UFPs), we established the dynamic models under three ventilation modes of MV alone, PAC alone, and MV combined with PAC. Second, we conducted a twin-chamber study to measure IAP concentrations under three ventilation modes. Subsequently, the cleaning efficiencies for different IAPs were obtained and compared using the Levenberg-Marquardt algorithm, while the factors impacting the efficiency were discussed. Finally, the accuracy of the prediction model for the MV-PAC combined system was validated, and the energy consumption advantage was analyzed. Our study demonstrates that integrating MV with PACs can reduce IAP concentrations with lower energy consumption.

Keywords: Indoor air quality · Twin-chamber · Cleaning efficiency

1 Introduction

1.1 A Subsection Sample

Modern lifestyles lead to individuals spending nearly 90% of their time indoors, making indoor air quality (IAQ) critical for health [1, 2]. Mechanical Ventilation (MV), mandated globally via minimum ventilation rates (VRs), dilutes indoor air pollutants (IAPs) using conditioned outdoor air but consumes over 40% of building energy [3–6]. Addressing the demand for clean air generated during the COVID-19 pandemic and the goal of achieving low energy consumption in buildings, standards like ASHRAE 241–2023 address pandemic-driven clean air demand and energy goals through the "Equivalent Clean Air" (ECAi) concept, recognizing clean air from outdoor air or purified recirculated air [7–9].

© The Author(s), under exclusive license to Springer Nature Singapore Pte Ltd. 2025
L. Ni et al. (Eds.): CCHVAC 2025, ESE, pp. 506–515, 2025.
https://doi.org/10.1007/978-981-95-3253-7_54

Portable air cleaners (PACs) offer a complementary solution, recirculating and purifying indoor air with low energy consumption [10, 14, 15]. They effectively reduce particulate matter (PM) via HEPA filtration, aiding disease control [11], and can adsorb VOCs with appropriate sorbents [12, 13]. However, PACs cannot remove CO_2, compromising their use as an indicator for ventilation adequacy, though high concentrations pose minimal direct risk [16]. Some PACs may generate by-products such as ozone [17, 18], though formaldehyde emissions are typically low [19]. MV effectively dilutes all IAPs, including CO_2, at high energy cost, while PACs efficiently remove PM and specific gases without reducing CO_2 [20, 21]. Integrating MV and PAC promises more sustainable IAQ management, particularly for infection control, but requires optimized system design and characterization.

Therefore, this study developed a novel approach integrating MV with PAC for targeted IAP control. First, characterization models for individual IAPs were proposed for three scenarios: MV only, PAC only, and MV-PAC combined. Second, IAP concentrations were measured using a twin-chamber comparative method, varying ventilation schemes, air supply/return modes, and air changes per hour (ACHs). Subsequently, purification efficiencies for all target IAPs were calculated and compared using the Levenberg-Marquardt (L-M) algorithm, while the impacts of airflow distribution design and ACHs on efficiency were investigated. Finally, the accuracy of the prediction model for the MV-PAC combined system was validated, and the energy consumption advantage was analyzed.

2 Methods

2.1 Dynamic Models for Scenarios

The first step is to identify several categories of target IAPs. Based on pollutant sources and purification principles, this study primarily selects PM (including $PM_{0.3–10}$ and understudied ultrafine particles, UFP), O_3 (a common IAPs generating secondaries), CO_2 (diluted by MV but not removable by PAC), and TVOC (inefficiently diluted by MV but removable by PAC, though with potential by-products), analyzing the purification efficiencies and overall removal rates for these IAPs.

Surrounding the sources and purification principles of different IAPs, and based on air dynamics and mass balance principles, the dynamic concentrations of MV and PAC can be expressed as Eqs. (1, 2).

$$C_i^{in}(t+\Delta t) = \frac{[(1-\eta_i)\cdot Q_{MV}]\bullet C_i^{out}(t)+S_i(t)}{\eta_i \bullet Q_{MV}+K_i \bullet V}\left[1-e^{-\left(\frac{\eta_i \bullet Q_{MV}}{V}+K_i\right)\bullet \Delta t}\right] + C_i^{in}(t)\bullet e^{-\left(\frac{\eta_i \bullet Q_{MV}}{V}+K_i\right)\bullet \Delta t} \tag{1}$$

$$C_i^{in}(t+\Delta t) = \frac{S_i(t)}{\gamma_i \bullet Q_{PAC}+K_i \bullet V}\left[1-e^{-\left(\frac{\gamma_i \cdot Q_{PAC}}{V}+K_i\right)\bullet \Delta t}\right] + C_i^{in}(t)\bullet e^{-\left(\frac{\gamma_i \bullet Q_{PAC}}{V}+K_i\right)\bullet \Delta t} \tag{2}$$

where V is the volume of the office, m^3; t is the operation time, h; $C_i^{in}(t)$ and $C_i^{out}(t)$ are the mass concentration of the i-th IAP indoors and outdoors at time t, respectively, $\mu g/m^3$;

i is an index representing different IAPs. Specifically, i = 1 corresponds to $PM_{0.3–10}$, i = 2 to UFPs, i = 3 to O_3, i =4 to VOCs, and i = 5 to CO_2; Q_f is the volumetric flowrate of the infiltration air, m^3/h; P_i is the penetration factor of the i-th IAP, which is ignored in this study, dimensionless; η_i and γ_i is the cleaning efficiency of the MV and PAC for the i-th IAP, dimensionless; Q_{MV} and Q_{PAC} is the volumetric flow rate of the MV and PAC, m^3/h; $C_i^{out}(t)$ K_i is the loss rate (including condensation, deposition, etc.) of the i-th IAP, h^{-1}; $S_i(t)$ is the total emission of the i-th pollutant indoor sources at time t, including both first and second emission, μg/h; Δt is the time step, h, which is set to 1 min (1/60 h) and proven to be sufficient in this study.

Under the assumption that the purification and loss efficiencies of MV and PAC remain unchanged, the indoor IAP concentration under the combined MV and PAC system can be derived from Eqs. (1, 2), as shown in Eq. (3).

$$C_i^{in}(t+\Delta t) = \frac{[(1-\eta_i)\cdot Q_{MV}]\bullet C_i^{out}(t)+S_i(t)}{(\gamma_i\cdot Q_{PAC}+\eta_i\bullet Q_{MV}+K_i\cdot V)}\cdot\left[1-e^{-\left(\frac{\gamma_i\cdot Q_{PAC}+\eta_i\bullet Q_{MV}}{V}+K_i\right)\bullet\Delta t}\right] + C_i^{in}(t)\bullet e^{-\left(\frac{\gamma_i\cdot Q_{PAC}+\eta_i\bullet Q_{MV}}{V}+K_i\right)\bullet\Delta t} \quad (3)$$

2.2 Experiment Design

Experiments occurred in a sealed twin-chamber facility (Fig. 1): outer chamber (7.0 m × 7.0 m × 3.5 m) housing two inner chambers (each 4.8 m × 2.6 m × 2.3 m), where all doors and windows were sealed to ensure optimal airtightness. The structure is shown as Fig. 1. Air handling units (AHUs) precondition chambers to steady-state (20 °C, 55% RH). Three configurations were tested (AD-1:Two diffusers at the top and a return air outlet positioned lower on the side wall; AD-2: An air exchange vent and a return air outlet positioned at the top; AD-3: a slot diffuser at the top and a return air outlet positioned lower on the side wall), with AD-1 as default due to superior diffuser mixing. Particle loss solely from AHU operation was calculated and subtracted from clean air system removal quantities during analysis.

Besides the AHUs, three ventilation scenarios with eight configurations were implemented (Summarized in Table 1): 1) MVs using three ventilators; 2) PAC systems with three corner-placed units (IAM Inc.: 780 m^3/h CADR; Flory: 600 m^3/h CADR); and 3) NV baseline.

Experiments comprised 25 cases (Table 2): Cases 1–7 tested MV and PAC air supply methods at constant airflow without emissions. Cases 8–14 assessed indoor emission impacts on IAP levels at a fixed ACH. Cases 15–22 compared supply and return modes and ACH variations. Cases 23–25 evaluated MV-PAC integrated cleaning efficiencies, with key cases repeated twice to reduce experimental uncertainty.

Measurement devices and sensors used identical models to minimize discrepancies: TSI Models 986/3330 for temperature, RH, CO_2, TVOC, $PM_{0.3–10}$; TSI SMPS (3938 L56) for UFPs; two 2B Tech models (106 L/205) for O_3 with their generator (306); TSI Model 8380 capture hoods for airflow; outdoor PM combined TSI 8543 and Jiading Fangtai station data. IAP emissions used TSI 9306A (PM) and 2B Tech 306 (O_3). Pollutants were extracted from chamber centers under well-mixed assumptions. An energy recording system tracked consumption—instruments logged at 10 s intervals, except UFP (2 min). Fig. 1 shows the chamber structure and instrument arrangement.

Table 1. Types of supplied air in the study.

Types	Configurations	Technologies
NV	Vent	–
MV1-PC	AHU-integrated	Physical-chemical technologies
MV2-H	Household ventilator-based	H11 filter
MV3-EC	Household ventilator-based	A filter with electrostatic and catalytic effects
PV1-EC	AHU-integrated (full recirculation)	Electrostatic and catalytic effects
PV2-H	PAC	A H12 filter
PV2-H-I	PAC	A H12 filter, negative ions technology

2.3 Parameter Fitting

The study applied the L-M algorithm [22] to fit cleaning performance metrics. This second-order optimization method combines the steepest descent and linear approaches for rapid convergence, effectively solving nonlinear least squares problems. During fitting, parameters were constrained: γ_i and η_i within 0–1, while deposition rate k was constrained to 0–1 h^{-1} for PM and 0–10 h^{-1} for O_3 based on preliminary experiments and literature [23, 24]. Resulting parameters were substituted into dynamic models to obtain IAP concentration profiles, with algorithm performance evaluated using the coefficient of determination R^2 (Eq. 4).

$$R^2 = \left\{ \sum_{j=1}^{n} \left[\left(C_{i,j}^{E} - \overline{C_i^E} \right) \left(C_{i,j}^{P} - \overline{C_i^P} \right) \right] \right\}^2 / \left[\sum_{j=1}^{n} \left(C_{i,j}^{E} - \overline{C_i^E} \right)^2 \sum_{j=1}^{n} \left(C_{i,j}^{P} - \overline{C_i^P} \right)^2 \right] \tag{4}$$

where $C_{i,j}^{\mathrm{E}}$ and $C_{i,j}^{\mathrm{P}}$ are the j-th measured and the corresponding predicted concentrations of the i-th IAP, μg/m^3; $\overline{C_i^{\mathrm{E}}}$ and $\overline{C_i^{\mathrm{P}}}$ are the mean value of $C_{i,j}^{\mathrm{E}}$ and $C_{i,j}^{\mathrm{P}}$, respectively, μg/m^3; j is an index representing different data, dimensionless; and n is the size of the data set, dimensionless.

For Cases 1–14, Chamber 2 served as a control to eliminate outdoor-influenced IAP fluctuations in Chamber 1, ensuring changes reflected purification and loss only. Moreover, temporal averaging was applied except for UFPs (6-point averaged).

Table 2. Case design.

No.	Chamber 1				Chamber 2			
	Clean air	Air pattern	ACH (h-1)	Source	Clean air	Air pattern	ACH (h-1)	Source
1	MV1-PC	AD-1	5.2	0	NV	AD-1	5.2	0
2	MV2-H							
3	MV3-EC							
4	PV1-EC							
5	PV2-H							
6	PV2-H-I							
7	PV2-H-I-EC							
8	MV1-PC	AD-1	5.2	60	NV	AD-1	5.2	0
9	MV2-H							
10	MV3-EC							
11	PV1-EC							
12	PV2-H							
13	PV2-H-I							
14	PV2-H-I-EC							
15	MV1-PC	AD-2	5.2	60	MV1-PC	AD-1	5.2	0
16	MV1-PC	AD-3			MV1-PC			
17	MV1-PC	AD-1			MV1-PC		3.8	
18	MV2-H				MV2-H			
19	MV3-EC				MV3-EC			
20	PV1-EC				PV1-EC			
21	PV2-H				PV2-H		12.4	
22	PV2-H-I				PV2-H-I			
23	MV1-PC and PV2-H	AD-1	7.0	0	MV1-PC	AD-1	7.0	0
24	MV2-H and PV1-EC	AD-1	10.4	0	PV2-H	AD-1	10.4	0
25	MV3-EC and PV2-H	AD-1	7.0	60	MV3-EC	AD-1	7.0	0

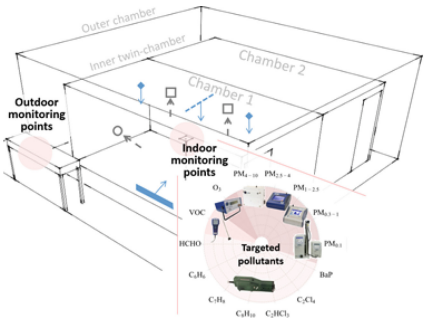


Fig. 1. Schematic diagram of test chamber structure and instrument layout.

3 Results and Discussions

3.1 Cleaning Performance of Single Clean Air

L-M algorithm fitting yielded parameters η_i and γ_i for target IAPs across MV and PAC technologies [22]. Most R^2 values exceeded 90%, confirming strong model-experiment agreement and reliability. TVOC and CO_2 analysis was excluded due to their low, stable concentrations. MV demonstrated more stable purification than PAC at the default ACH, especially for PM. MV with H11 filters achieved the highest η_i for PM, while MV integrated into AHU systems showed lower α values. For PAC, three standalone models exhibited high, comparable γ_i values for PM, demonstrating the efficacy of PAC filter technology. Both systems showed similar UFP purification patterns to other particle sizes (see Fig. 2). For O_3, η_i, γ_i and k varied considerably. PAC exhibited superior efficiency overall compared to MV. Among MVs, those with electrostatic and catalytic effects showed the best η_i, while in PACs, negative ions technology delivered the best purification (see Fig. 3).

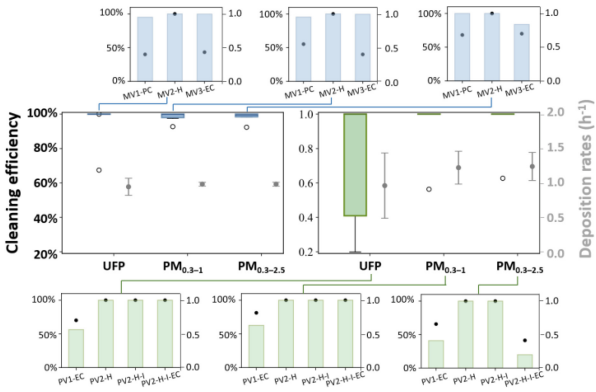


Fig. 2. Comparison regarding PM.

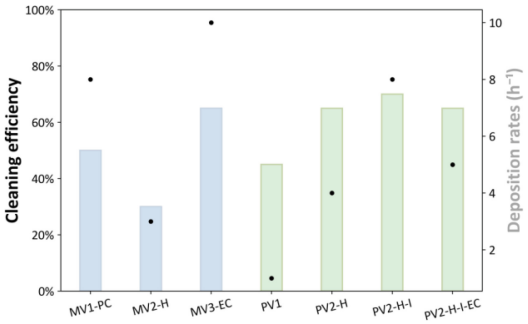


Fig. 3. Comparison regarding O_3.

3.2 Factors

Case 15–22 tested emission presence, airflow distribution, and ACH impacts on η_i and γ_i values. For PM under MV without emissions, factors affected $PM_1 > PM_{2.5}$; the absence of emissions had the most substantial effect. MV showed minimal variation in MV2-H, highest in MV3-EC. η_i of PM remained stable under AD-1 and 3 but decreased under AD-2 (ceiling>floor supply). PACs showed greater sensitivity than MV without emissions, particularly to ACH. η_i of PV2 surged 50%–100% with a 30% airflow increase (notably PV2-H-I). For O_3, η_i increased under AD-2. MV showed slight η_i increases as ACH decreased (higher ACH is ineffective), but PACs are inconsistent (see Fig. 4).

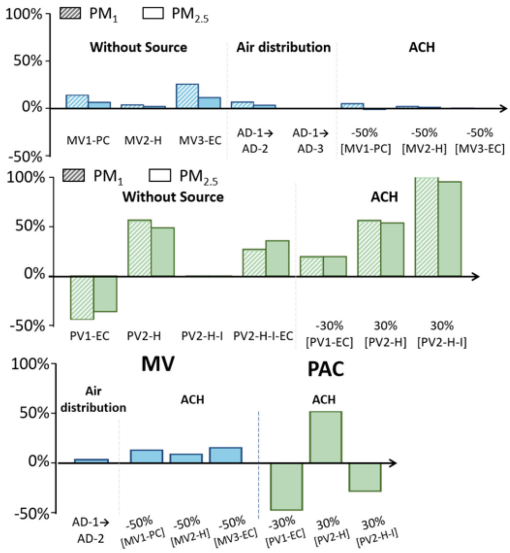


Fig. 4. The impact of different factors on purification efficiency.

3.3 Establishment of Combined Systems

The γ_i, η_i, and k values from single-system fitting were applied to the MV-PAC combined model. Under identical conditions, computed IAP concentrations showed >90% agreement with measurements for PM and O_3 (see Fig. 5), confirming model validity. This indicates no efficiency gains or losses for MV or PAC in combined operation. Model validation enables quantifying PAC's partial MV replacement and subsequent combined system energy studies.

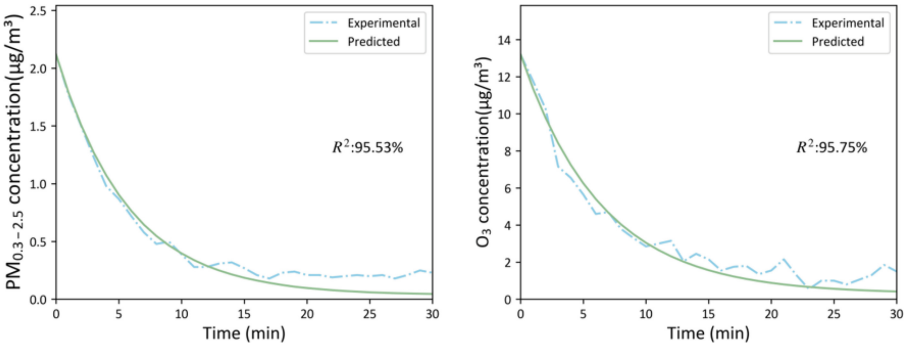


Fig. 5. Examples of the experimental and predicted concentrations comparison of IAPs.

3.4 Energy Consumption

Under similar indoor and outdoor enthalpy conditions, the Overall energy consumption of MV was substantially higher than PAC for the same operating duration, confirming a distinct energy advantage of PAC (see Fig. 6). Consequently, a system where PAC replaces part of the MV offers significant energy-saving potential.

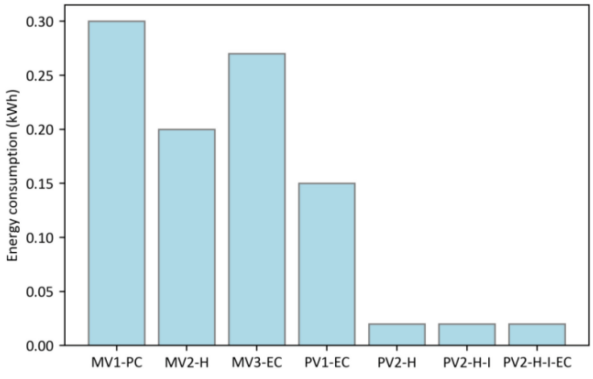


Fig. 6. Comparison of energy consumption.

4 Conclusions

This study compared MV and PAC systems for IAQ maintenance. Through pollutant modeling and twin-chamber experiments, key conclusions emerge:

1. MV and PAC exhibit distinct efficiencies for different IAPs. MV demonstrates greater stability without indoor emissions, while PAC excels with emissions, especially for $PM_{0.3–10}$ and UFPs, with particle size minimally influencing advantages.
2. Multiple factors affect purification: MV showed superior PM: control without emissions, ceiling supply (AD-1 and 3) outperforming floor supply (AD-2). Emission absence most enhances MV stability. PAC showed greater sensitivity, particularly to ACH. For O_3, the purification efficiency of MV rose slightly at lower ACH, while PAC exhibited inconsistent trends. Air distribution affected O_3 differently than PM.
3. This validates the accuracy of the combined model for IAP prediction, establishing PAC's partial MV replacement potential. The additive effect and low PAC energy consumption enable exploring integrated systems' efficiency advantages without compromising air quality.

Future studies should holistically consider the energy consumption in different conditions to comprehensively assess the energy-efficiency advantages of integrated systems, thereby offering more practical design schemes to address building ventilation systems' high energy consumption issues.

References

1. Geng, Y., Ji, W., Wang, Z., Lin, B., Zhu, Y.: A review of operating performance in green buildings: energy use, indoor environmental quality and occupant satisfaction. Energ. Buildings. **183**, 500–514 (2019)
2. Pei, J., Dai, W., Li, H., Liu, J.: Laboratory and field investigation of portable air cleaners' long-term performance for particle removal. Build. Environ. **181**, 107100 (2020)
3. Zhang, S., Ai, Z., Lin, Z.: Occupancy-aided ventilation for both airborne infection risk control and work productivity. Build. Environ. **188**, 107506 (2021)
4. Zhang, S., Ai, Z., Lin, Z.: Novel demand-controlled optimization of constant-air-volume mechanical ventilation for indoor air quality, durability and energy saving. Appl. Energy. **293**, 116954 (2021)
5. Luo, M., Hong, Y., Pantelic, J.: Determining building natural ventilation potential via IoT-based air quality sensors. Front. Environ. Sci. **9**, undefined-undefined (2021)
6. Pérez-Lombard, L., Ortiz, J., Pout, C.: A review on buildings energy consumption information. Energ. Buildings. **40**, 394–398 (2008)
7. ASHRAE: Control of Infectious Aerosols (Standard 241-2023). American Society of Heating, Refrigerating and Air-Conditioning Engineers (2023)
8. Blocken, B., van Druenen, T., Ricci, A., Kang, L., van Hooff, T., Qin, P., Xia, L., Ruiz, C.A., Arts, J.H., Diepens, J.F.L., Maas, G.A., Gillmeier, S.G., Vos, S.B., Brombacher, A.C.: Ventilation and air cleaning to limit aerosol particle concentrations in a gym during the COVID-19 pandemic. Build. Environ. **193**, 107659 (2021)
9. Ren, J., Liu, J., Cao, X., Hou, Y.: Influencing factors and energy-saving control strategies for indoor fine particles in commercial office buildings in six Chinese cities. Energ. Buildings. **149**, 171–179 (2017)

10. Shaughnessy, R.J., Sextro, R.G.: What is an effective portable air cleaning device? A review. J. Occup. Environ. Hyg. **3**, 169–181; quiz D45 (2006)
11. Cortellessa, G., Canale, C., Stabile, L., Grossi, G., Buonanno, G., Arpino, F.: Effectiveness of a portable personal air cleaner in reducing the airborne transmission of respiratory pathogens. Build. Environ. **235**, 110222 (2023)
12. Gord, J., Vigil, C., Richards, S., Bertram, T.H.: Classroom scale measurements of the efficacy of ventilation, filtration, and electronic air cleaners for the removal of aerosol particles. Build. Environ. **244**, 110758 (2023)
13. Cai, J., Yu, W., Li, B., Yao, R., Zhang, T., Guo, M., Wang, H., Cheng, Z., Xiong, J., Meng, Q., Kipen, H.: Particle removal efficiency of a household portable air cleaner in real-world residences: a single-blind cross-over field study. Energ. Buildings. **203**, 109464 (2019)
14. Gore, R.B., Bishop, S., Durrell, B., Curbishley, L., Woodcock, A., Custovic, A.: Air filtration units in homes with cats: can they reduce personal exposure to cat allergen? Clin. Exp. Allergy. **33**, 765–769 (2003)
15. Sublett, J.L.: Effectiveness of air filters and air cleaners in allergic respiratory diseases: a review of the recent literature. Curr Allergy Asthma Rep. **11**, 395–402 (2011)
16. Zhang, X., Li, D., Xie, J., Liu, J.: Environmental perceptions, mental performance, and physiological responses of people with respiratory allergies exposed to reduced indoor air quality. Indoor Air. **31**, 1458–1472 (2021)
17. Joo, T., Rivera-Rios, J.C., Alvarado-Velez, D., Westgate, S., Ng, N.L.: Formation of oxidized gases and secondary organic aerosol from a commercial oxidant-generating electronic air cleaner. Environ. Sci. Technol. Lett. **8**, 691–698 (2021)
18. Khararoodi, M.G., Lee, C.-S., Haghighat, F.: Modelling of sorbent-based gas filters for indoor environment: a comprehensive review. Build. Environ. **208**, 108579 (2022)
19. Wu, Z., Chen, J., Qiu, W., Wu, J., Liang, S., Ye, Y., Li, X., Cai, J.: Preliminary analysis of the health risk of formaldehyde secondary pollution from air purifiers. Elect Appl China. **5**, 22–25 (2023)
20. Li, Y., Fan, Y., Wei, Y., Liu, M., Xu, B., Ye, W.: Can portable air cleaners reconcile conflicting needs for open-door/window autonomy and indoor air quality for occupants in densely populated offices? Appl. Energy. **358**, 122548 (2024)
21. Chen, D., Liu, M., Guo, W., Li, Y., Xu, B., Ye, W.: Energy-efficient operation of portable air cleaners based on real-time prediction of non-uniform concentrations of indoor air pollutants in open offices. Build. Environ. **256**, 111478 (2024)
22. Fischer, A., Izmailov, A.F., Solodov, M.V.: The Levenberg-Marquardt method: an overview of modern convergence theories and more. Comput. Optim. Appl. **89**, 33–67 (2024)
23. Chen, C., Zhao, B., Zhou, W., Jiang, X., Tan, Z.: A methodology for predicting particle penetration factor through cracks of windows and doors for actual engineering application. Build. Environ. **47**, 339–348 (2012)
24. Poppendieck, D., Hubbard, H., Ward, M., Weschler, C., Corsi, R.L.: Ozone reactions with indoor materials during building disinfection. Atmos. Environ. **41**, 3166–3176 (2007)

Author Index

A
Alanne, Kari 250
Amini, Hamed 250
Aruna, 132
Attia, Shady 458

C
Cai, Shanshan 296
Cao, Jian 114
Chen, Jiajie 97
Cui, Mengdi 182
Cui, Xiran 268

D
Dai, Baomin 154
Da-ji, Lu 374
Ding, Xianglu 467
Du, Yu 200
Duan, Haojun 217
Duan, Tongyu 154

F
Fan, Man 174
Fang, Can 406
Fei, Lin 385
Feng, Chenxin 277

G
Gao, Hao 494
Gu, Jiefan 315
Guan-yu, Chen 385
Guo, Rui 458
Guo, Yutao 143
Guoyuan, Ma 424

H
Hamdy, Mohamed 250
Han, Chong 3
Han, Xinrou 486
Han, Yunsong 268
Heng-lin, Shi 374, 385
Hou-ying, Li 374, 385
Hu, Changhua 209
Hu, Wenju 114
Hu, Xinyi 441
Hua, Tianyi 239
Huang, Guixin 449
Huang, Huadong 38
Huang, Huakun 326
Huang, Shifang 58

J
Jia, Encan 200
Jiang, Wei 231
Jiang, Zhike 143
Jin, Ruiying 315
Jin, Xinyue 86
Jin, Xu 132
Jin, Yixuan 38
Jokisalo, Juha 287, 441
Ju, Yuchen 287
Junrui, Nie 424

K
Karjalainen, Perttu 287
Kong, Xiangfei 174
Kosonen, Risto 250, 287, 441

L
Lai, Gaoqi 174
Lehtonen, Matti 441
Li, Chenxi 38
Li, Cui 364
Li, Dong 396
Li, Han 174
Li, Jing 209
Li, Junjie 315
Li, Xu 296
Li, Yiqun 506
Li, Zhe 486
Li, Zhengrong 354

© The Editor(s) (if applicable) and The Author(s), under exclusive license to Springer Nature Singapore Pte Ltd. 2025
L. Ni et al. (Eds.): CCHVAC 2025, ESE, pp. 517–519, 2025.
https://doi.org/10.1007/978-981-95-3253-7

Liang, Caihua 123
Lin, Guanjing 334
Li-rong, Pan 385
Liu, Hongzhi 48, 97
Liu, Jia 406
Liu, Jian 163
Liu, Kaiyue 432
Liu, Mingqi 506
Liu, Sheng 414
Liu, Shengchun 154
Liu, Yanchen 406
Liu, Yangming 334
Liu, Yongxin 467, 476
Liu, Zhaoyi 494
Liu, Zhe 432
Liu, Zhongyan 132
Long, Yan 239
López Salazar, Samanta 396
Lu, Changling 105
Lu, Qiuyan 239
Luo, Peng 467
Luo, Zhouyang 38
Lv, Jing 48, 97

M
Ma, Chenyu 432
Ma, Jingrong 268
Ma, Shuang 432
Ma, Zhenfang 97, 105
Mao, Ding 191
Meng, Hang 307
Meng, Xin 132
Miao, Ronghua 154

N
Ni, Long 3
Ni, Shijun 364
Ning, Haoran 13

P
Peng, Hao 38
Peng, Xiao 277
Peng, Zixuan 217

Q
Qi, Zhifu 38
Qiao, Tianzheng 26
Qiu, Guodong 75
Qiu, Zheng 132
Qu, Minglu 48, 97, 105

R
Ren, Tianshuo 467

S
Sang, Tong 174
Shangyu, Sun 424
Shen, Leshan 38
Shen, Zhen 38
Shu-hao, Tan 374
Shuxue, Xu 424
Simá, E. 396
Song, Tao 209
Su, Shirui 75
Su, Wei 132
Sun, Cheng 268
Sun, Junli 307
Sun, Shien 38
Sun, Ying 13
Sun, Yuying 66, 86, 143

T
Tan, Benying 326
Tang, Huiyan 354
Tang, Rui 66
Tao, Biaoqing 268
Teng, Weiming 38

W
Wang, Baolong 182
Wang, Bo 209
Wang, Dan 114
Wang, Feng 26, 123, 260
Wang, Gang 200
Wang, Guiqiang 449
Wang, Haiying 307
Wang, Hongxin 315
Wang, Jay 191
Wang, Peng 231, 345, 476
Wang, Shiquan 143
Wang, Wei 66, 86, 143
Wang, Weili 326
Wang, Yanfeng 406
Wang, Ying 13
Wang, Yongjie 334
Wang, Yumiao 163
Wang, Yunfeng 66

Wei, Wenzhe 66, 86, 143
Weilai, Rong 424
Wu, Huijun 326, 406
Wu, Jintao 296
Wu, Siqi 345
Wu, Xiaozhou 494

X
Xiang, Mengting 123
Xie, Xiaoyun 217
Xie, Zhuwei 406
Xin-ping, Qin 374
Xu, Fan 200
Xu, Jiayu 277
Xu, Peng 315
Xu, Xianglai 132
Xu, Xinhua 414

Y
Yan, Renjie 307
Yang, Bin 486
Yang, Lingyan 114
Yang, Qisheng 209
Yang, Ruitong 396
Yang, Weibo 26, 123
Yang, Xin 209
Yang, Yifan 38
Yao, Shicheng 13
Yao, YiNuo 3
Ye, Wei 506
Yin, Hang 250
Ying-de, Yin 374, 385
Yu, Diqi 494
Yu, Guoqing 105
Yu, Haochen 13
Yuan, Zhe 396
Yuan-yu, Li 374, 385

Z
Zhan, Changhong 334
Zhang, Chaobo 260
Zhang, Chunxiao 143
Zhang, Donghai 432
Zhang, Hao 132
Zhang, Jian 260
Zhang, Jianfei 86
Zhang, Jiapeng 132
Zhang, Ruyi 296
Zhang, Sijing 163
Zhang, Weixiong 326
Zhang, Xiaosong 58, 163
Zhang, Xinyu 143
Zhao, Haoqiang 105
Zhao, Jiayan 26
Zhao, Linjun 326
Zhao, Yang 277
Zhou, Bin 486
Zhou, Fang 163
Zhu, Liutao 58